High resolution modelling of flexible submerged vegetation in rivers

Tim Marjoribanks

Abstract

Vegetation is a common feature within natural river channels and exerts a profound influence on the functioning of the fluvial system. In particular, the interaction between vegetation and flow causes a reduction in conveyance, an alteration to the velocity profile and the generation of coherent turbulent structures which differ to those found in un-vegetated channels. Recognition of the influence of vegetation on open channel flow has led to an increased awareness of the importance of accurately representing the effects of vegetation within numerical models, across a range of spatial scales.

This thesis introduces two novel biomechanical models, capable of simulating the complex interaction between flow and vegetation at high spatial and temporal resolution. The development and validation of these models permits investigation of flow-vegetation interactions across a range of plant types and flow conditions. These models are applied to a range of scenarios providing new insight into the interaction mechanisms between the vegetation and the flow. In particular, this thesis focuses on the role of turbulent structures in driving flow-vegetation interaction.

The results presented in this thesis support existing theories for simple canopy flows, whilst also proposing additional interactions in the case of more complex canopies. In addition, key findings relating to the role of drag in controlling flow-vegetation interactions are explored.

Finally, through the development of a third, lower resolution, vegetation model, this thesis begins to explore how the process understanding gained from application of the high resolution models may be upscaled to the reach scale models which are central to river management.

High resolution modelling of flexible submerged vegetation in rivers

Timothy Ian Marjoribanks

Department of Geography
Durham University

Thesis submitted for the degree of Doctor of Philosophy

June 2013

Table of Contents

TABLE OF CONTENTS ..... **iii**

LIST OF FIGURES ..... **ix**

LIST OF TABLES ..... **xxi**

LIST OF NOTATION ..... **xxii**

LIST OF ABBREVIATIONS ..... **xxviii**

STATEMENT OF COPYRIGHT ..... **xxix**

ACKNOWLEDGEMENTS ..... **xxix**

CHAPTER 1: INTRODUCTION **1**

1.1 RATIONALE 1

1.2 RESEARCH AIM 4

1.3 RESEARCH QUESTIONS 4

1.4 OBJECTIVES AND THESIS STRUCTURE 6

CHAPTER 2: MODELLING FLOW-VEGETATION INTERACTIONS **10**

2.1 INTRODUCTION 10

2.2 FLOW STRUCTURE AND PROCESSES OVER TERRESTRIAL CANOPIES 10

2.2.1 Characteristic mean velocity profile *11*

2.2.2 Turbulence structure and characteristics *12*

2.2.3 Plant response and interaction with the flow: The role of plant biomechanics *17*

2.2.4 Transport between the canopy and surface layer *19*

2.2.5 Energy mechanisms within the flow *20*

2.3 FLOW STRUCTURE AND PROCESSES IN AQUATIC CANOPIES 21

2.3.1 Velocity and turbulence characteristics *22*

2.3.2 Plant response and interaction with the flow *26*

2.3.3 Transport and energy mechanisms within the flow *29*

2.3.4 Key differences between terrestrial and aquatic canopies *31*

2.4 NUMERICAL REPRESENTATION OF OPEN CHANNEL FLOW 33

2.4.1 The Navier-Stokes Equations *34*

2.4.2 Direct numerical simulation (DNS) *35*

2.4.3 The Reynolds averaged Navier-Stokes equations *36*

2.4.4 Large eddy simulation *37*

2.4.5 Dimensionality and process representation *38*

2.4.6 The Saint-Venant equations *38*
2.4.7 Bulk flow model *39*
2.4.8 Boundary layer flow *42*
2.5 VEGETATION AS FLOW RESISTANCE 43
2.5.1 A posteriori estimates of vegetative resistance *43*
2.5.2 A priori estimates of vegetative resistance *46*
2.5.3 Vegetation as a roughness height *48*
2.5.4 The problem with representing vegetation using a roughness approach *49*
2.6 PHYSICAL REPRESENTATION OF VEGETATION ELEMENTS WITHIN NUMERICAL MODELS 50
2.6.1 Reach-scale modelling of vegetation *50*
2.6.2 Plant-scale models *52*
2.6.3 Stem-scale models *53*
2.7 VEGETATION: A DYNAMIC BLOCKAGE? 55
2.7.1 Flexible stem models *56*
2.7.2 Representing highly flexible stems and foliage *57*
2.7.3 High-resolution dynamic blockage modelling *59*
2.8 CHAPTER SUMMARY AND CONCLUSIONS 59

CHAPTER 3: MODEL DEVELOPMENT 61

3.1 INTRODUCTION 61
3.2 NUMERICAL REPRESENTATION OF THE FLOW 61
3.2.1 Flow solver mechanics *61*
3.2.2 Turbulence closure modelling *63*
3.2.3 Mass flux scaling algorithm *68*
3.2.4 Free surface treatment *69*
3.2.5 Inlet and Outlet conditions *71*
3.2.6 Good practice in modelling *72*
3.2.7 CFD model verification *72*
3.2.8 Grid Convergence Index *77*
3.2.9 CFD model validation *84*
3.2.10 Summary *84*
3.3 VEGETATION CONCEPTUALISATION 85
3.4 FORCE CALCULATION FROM THE CFD MODEL 87
3.5 EULER-BERNOULLI BEAM EQUATION MODEL 88
3.5.1 Numerical Basis *89*

3.5.2 Explicit formulation *90*
3.5.3 Subcycling explicit formulation *94*
3.5.4 Implicit second-order formulation *95*
3.5.5 Implicit fourth-order formulation *97*
3.5.6 Verification of the model *100*
3.6 N-PENDULA MODEL 102
3.6.1 Numerical basis *102*
3.6.2 The zero rigidity approach *104*
3.6.3 Introducing flexural rigidity *105*
3.6.4 Verification of the model *106*
3.7 DRAG BACK-CALCULATION 106
3.7.1 Pressure coefficient approach *108*
3.7.2 Control volume approach *112*
3.8 CHAPTER SUMMARY AND CONCLUSIONS 113

CHAPTER 4: ANALYTICAL METHODS FOR FLOW CHARACTERISATION 114

4.1 CHAPTER INTRODUCTION 114
4.2 MEAN FLOW PROFILING 114
4.3 REYNOLDS DECOMPOSITION 117
4.4 QUADRANT ANALYSIS 119
4.5 SPECTRAL ANALYSIS 120
4.6 WAVELET ANALYSIS 123
4.7 EULERIAN VORTEX METHODS 125
4.7.1 The Q criterion *126*
4.7.2 The λ_2 criterion *127*
4.7.3 The Δ criterion *128*
4.7.4 Swirling strength criterion *129*
4.8 LAGRANGIAN VORTEX METHODS 130
4.9 VORTEX SIGNATURES IN VEGETATED FLOWS 139

CHAPTER 5: FLUME EXPERIMENTS AND VALIDATION WORK 141

5.1 INTRODUCTION 141
5.2 PARAMETERISATION OF FLEXURAL RIGIDITY 142
5.2.1 Flume work rigidity parameterisation *144*
5.2.2 Numerical simulation rigidity parameterisation *146*

5.3 EXPERIMENTAL FLUME SETUP 147
5.4 NUMERICAL DOMAIN SETUP 150
5.5 MODEL VALIDATION METHODS 151
5.6 RIGID VEGETATION 152
5.7 FLEXIBLE VEGETATION 160
5.7.1 Slow flow conditions ($\boldsymbol{u}_{z=0.4h}$ = 0.18-0.26m/s) 160
5.7.2 Medium flow conditions ($\boldsymbol{u}_{z=0.4h}$ = 0.36-0.52m/s) 165
5.7.3 Fast flow conditions ($\boldsymbol{u}_{z=0.4h}$ =0.59m/s) 169
5.8 REAL VEGETATION 172
5.9 WAVELET ANALYSIS 175
5.10 SUMMARY OF VALIDATION 178

CHAPTER 6: MODEL APPLICATION AND ANALYSIS 181

6.1 INTRODUCTION 181
6.2 VORTEX MECHANICS OVER RIGID VEGETATION 183
6.2.1 Experimental setup 183
6.2.2 Mean flow profiles and turbulence characteristics 185
6.2.3 Quadrant analysis 188
6.2.4 Vortex detection 190
6.2.5 Velocity spectra 195
6.2.6 Summary 197
6.3 PLANT AND FLOW DYNAMICS ABOVE A SMALL PATCH 198
6.3.1 Experimental setup 198
6.3.2 Mean flow profiles and turbulence characteristics 199
6.3.3 Quadrant analysis 202
6.3.4 Vortex detection 204
6.3.5 Velocity and plant spectra 210
6.3.6 Summary 214
6.4 PLANT AND FLOW DYNAMICS ABOVE A CANOPY 215
6.4.1 Experimental setup 215
6.4.2 Mean flow profiles and turbulence characteristics 216
6.4.3 Quadrant analysis 218
6.4.4 Vortex detection 220
6.4.5 Velocity and plant spectra 230
6.4.6 Summary 232

6.5 FLOW AND PLANT DYNAMICS AROUND A SMALL HIGHLY FLEXIBLE VEGETATION PATCH 233
6.5.1 Experimental setup 234
6.5.2 Mean flow profiles and turbulence characteristics 234
6.5.3 Quadrant analysis 236
6.5.4 Vortex detection 239
6.5.5 Velocity and plant spectra 241
6.5.6 Summary 243
6.6 FLOW AND PLANT DYNAMICS OVER A LARGE HIGHLY FLEXIBLE CANOPY 243
6.6.1 Experimental setup 243
6.6.2 Mean flow profiles and turbulence characteristics 244
6.6.3 Quadrant analysis 246
6.6.4 Vortex detection 248
6.6.5 Velocity and plant spectra 251
6.6.6 Summary 253
6.7 DRAG AS A DRIVER OF STEM MOTION 253
6.7.1 Experimental setup 254
6.7.2 Comparison of flow and vegetation data 254
6.7.3 Summary 258
6.8 CONCLUSION 259

CHAPTER 7: DISCUSSION OF MICRO-SCALE PROCESSES IN VEGETATED CHANNELS 261

7.1 INTRODUCTION 261
7.2 CLASSIFICATION BY FORCE BALANCE 261
7.3 PROCESSES IN SEMI-RIGID, BENDING CANOPIES 265
7.4 PROCESSES IN HIGHLY FLEXIBLE, TENSILE CANOPIES 267
7.5 COMPARISON BETWEEN VEGETATION TYPES 268
7.6 IMPLICATIONS FOR MODELLING VEGETATION 269
7.7 CHAPTER SUMMARY 270

CHAPTER 8: APPLYING PROCESS KNOWLEDGE TO THE REACH SCALE 271

8.1 INTRODUCTION 271
8.2 RIVER BROWNEY FIELDWORK 273
8.3 FIELD METHODOLOGY 274
8.4 NUMERICAL METHODOLOGY 277
8.4.1 Numerical model 277

8.4.2 Static vegetation density model *278*
8.4.3 Dynamic vegetation density model *280*
8.5 RESULTS 283
8.5.1 High resolution results *285*
8.5.2 Medium resolution results *290*
8.5.3 Low resolution results *293*
8.6 IMPACT OF RESOLUTION WITHIN THE DYNAMIC MODEL 296
8.7 COMPARISON WITH PREVIOUS WORK 300
8.8 CHAPTER SUMMARY 301
CHAPTER 9: CONCLUSIONS 305
9.1 INTRODUCTION 305
9.2 RESEARCH QUESTIONS 305
9.3 FURTHER RESEARCH 312
9.4 POTENTIAL APPLICATIONS 314
9.5 CONCLUDING REMARKS 314
REFERENCES 315

List of Figures

Figure 1.1: Schematic overview of how the objectives map onto the thesis chapters. 9

Figure 2.1: Mean vertical velocity profile of canopy flow, from Inoue (1963). The profile is split into 4 separate regions (region IV has been added to the figure). Here, H is the canopy height, d is the zero plane displacement, Z_0 is the roughness parameter and U_H is the velocity at the canopy top. 12

Figure 2.2: Evolution of K-H vortices over vegetation (Finnigan *et al.*, 2009). Figure shows (a) initial instability, (b) roll up into Stuart roller vortices, (c) vortex stretching and pairing and (d) pairs of H-D and H-U vortices, causing sweep and ejection events within the flow. 15

Figure 2.3: Schematized flow model for aquatic canopy flow (Nezu and Sanjou, 2008). Here the heights h_p and h_{log} delimit the 3 zones. The cause of sweep and ejection events is also hypothesised as relating to the passage of shear-scale eddies. 23

Figure 2.4: Development and evolution of vortices within aquatic flows (Ghisalberti, 2009). 24

Figure 2.5: Six scales of turbulence within vegetated channels, adapted and redrawn from Nikora (2010). 25

Figure 2.6: Example of simple channel flow model, where A is the cross-sectional area, P_W is the wetted perimeter and U is the downstream velocity. 40

Figure 2.7: Logarithmic flow profile for boundary layers. z_0 is the roughness height 42

Figure 2.8: The two zone model (from Huthoff (2007)). The vegetated zone of height k has the characteristic velocity U_r, whereas the surface layer has velocity U_s 47

Figure 2.9: Schematic of an LES canopy model (Shaw and Schumann, 1992). Here, h is the vegetation canopy height. 51

Figure 2.10: Comparison of field-scale and plant-scale representations (Yue *et al.*, 2007). Here, grid points are assigned either a stem (O) or leaf (X) drag treatment. 53

Figure 2.11: Isosurfaces of pressure fluctuations for three different vegetation densities (Stoesser *et al.*, 2010). 55

Figure 3.1: Examples of different topographic representation: (a) boundary fitting and (b) a mass flux scaling approach. Figure from Hardy *et al.* (2005) 68

Figure 3.2: Photo showing the surface expressions of submerged vegetation canopies. Flow is from bottom to top. The river is approximately 5m wide and 0.3m deep. The water surface deviations from the mean are estimated as less than 10% of the flow depth. 70

Figure 3.3: Schematic of the recirculating domain setup. 71

Figure 3.4: Normalised spot values of different variables (ϕ) plotted against sweeps, showing clear flat-lining. Rough 'convergence' points for each variable are labelled. 75

Figure 3.5: GCI cross-sections for (a) downstream, (b) cross-stream and (c) vertical velocity at two different resolutions. 79

Figure 3.6: CAFE curves, plotting the GCI error level against the cumulative percentage of domain volume with GCI greater than or equal to that GCI value. 81

Figure 3.7: Iterative calculations of p for the 3 flow velocities at a point. 83

Figure 3.8: Tandem plant and LES grid systems (Ikeda *et al.*, 2001). Here a stalk is conceptualised as a vertical array which then moves and maps onto the LES grid. 86

Figure 3.9: Porosity cut-cell treatment of vegetation. Here darker cells represent lower porosity values. 86

Figure 3.10: Comparison of stencils for the backward and central difference schemes. 90

Figure 3.11: Exponential solution instability in an explicit beam model run with k=0.001. . 94

Figure 3.12: Stencil for the 4^{th} order implicit scheme 97

Figure 3.13: Graph showing the change in end-node displacement with increasing node number. The change is shown as a percentage of the total displacement. 101

Figure 3.14: A schematic showing the basis for the N-pendula model. 102

Figure 3.15: A process diagram of the N-pendula model code. 103

Figure 3.16: Cylinder drag coefficient dependence on Reynolds number. Adapted from experimental data of Panton (1984). 107

Figure 3.17: Schematic diagram of the pressure integration around the cylinder. 108

Figure 3.18: Setup for the benchmark case 110

Figure 3.19: Distribution of pressure coefficient around a cylinder for different flow conditions. Characteristic profiles taken from Anderson (1984). 110

Figure 3.20: Vertical drag coefficient profile taken from the Euler-Bernoulli beam model. Three clear sections are identified: a) cylindrical drag behaviour, b) slight stalk bending and c) severe stalk bending. 111

Figure 4.1: Schematic of the mixing layer velocity profile. The flow is conceptualised as two layers of different velocity (U_1 and U_2), one through the vegetation canopy and one above. At the interface between the two zones, a shear instability develops. 115

Figure 4.2: Quadrant analysis of Reynolds decomposition in the x-z plane redrawn from Bennett and Best (1995). The dotted line defines a hole or threshold value often used to discount outliers, based upon the hole size, H. 119

Figure 4.3: Commonly used wavelets: (a) Haar, (b) Gaussian (order 1), (c) Daubechies (order 4) and (d) Morlet wavelets. Figure taken from Baker (2007). 124

Figure 4.4: A schematic diagram showing the relationships and regions of overlap between the λ_2, Δ and Q criteria. 129

Figure 4.5: Comparison of different ridge-tracking algorithms. The plots show a) the original FLTE plot, b) a simple peak method, c) shape function method d) shape function method using a smoothed gradient, e) the principal curvature method and f) the principal curvature method using a smoothed gradient. 135

Figure 4.6: Comparison of ridge tracking methods: a) search for peak condition in 4 primary directions, b) calculate the differentials in x and y in order to calculate the Hessian c) calculate the differentials in x and y, as an average over 3 cells, smoothing the data. 135

Figure 4.7: Gaussian curvature of different surfaces. The arrows indicate the directions of principal curvature for each case: (a) an elliptic surface, which is not necessarily a local maximum, (b) a parabolic surface with one principal curvature equal to zero and (c) a hyperbolic surface with one positive and one negative curvature component. 136

Figure 4.8: Comparison of the (a) two-dimensional and (b) three-dimensional FTLE snapshots. 138

Figure 4.9: Iso-surfaces of FTLE ridges taken from the 3D FTLE field, showing major structures have significant lateral extent. The iso-surface is coloured by cross-stream distance for clarity. Flow is from bottom right to top left. 138

Figure 4.10: Schematic of expected vorticity measure and FTLE results, for hairpin vortices in canopy flows, based on results from Finnigan *et al.* (2009) and Green *et al.* (2007). An arbitrary threshold for the vorticity isosurface has been used. 140

Figure 5.1: Values of flexural rigidity as used by previous studies. Values have been taken either directly from publications, or from subsequent citing articles. The black line indicates the range of values used, and the black marker either represents the mean value used, or the preferential value from within the range used by the authors. 143

Figure 5.2: Vegetation rigidity experiments for the (a) artificial and (b) real vegetation. .. 144

Figure 5.3: Graphs showing the numerator of Equation 5.2 plotted against the denominator, for a series of different measurements. The black line is a line of best fit and its gradient is equal to the flexural rigidity. 145

Figure 5.4: Flume setup for the rigid vegetation experiments, with a 0.3m ruler for scale. 149

Figure 5.5: Vegetation collection from the River Browney. Inset map shows location of site. Field assistant included for scale. 149

Figure 5.6: Map of locations in the domain used for the validation. The image behind shows an example mean velocity profile. The different coloured points refer to canopy (black), shear layer (grey) and boundary layer (white) locations. 151

Figure 5.7: Comparisons of modelled and measured downstream (a,c) and vertical (b,d) velocities for the 0.4m (top) and 0.2m (bottom) rigid canopies. The data are split into canopy (blue), shear layer (green) and boundary layer (red) points. The black line represents a 1:1 relationship. 153

Figure 5.8: Close-up of the above-canopy data for the 0.4m downstream velocity comparison in Figure 5.7a showing two different slopes present. 156

Figure 5.9: Shear layer velocity (left) and Reynolds stress (right) profiles for the 0.4m (top) and 0.2m (bottom) rigid canopies. 157

Figure 5.10: Mean vorticity plots for the (a) flume and (b) numerical 0.2m rigid canopies. The plot shows both clockwise (blue) and anticlockwise (red) vorticity. 158

Figure 5.11: Mean vorticity plots for the (a) flume and (b) numerical 0.4m rigid canopies. The plot shows both clockwise (blue) and anticlockwise (red) vorticity. 159

Figure 5.12: Comparisons of modelled and measured downstream (left) and vertical (right) velocities for the 0.4m (top) and 0.2m (bottom) flexible canopies in slow flow. The data are split into canopy (blue), shear layer (green) and boundary layer (red) points. The black line represents a 1:1 relationship. 161

Figure 5.13: Shear layer velocity (a,c) and Reynolds stress (b,d) profiles for the 0.4m (top) and 0.2m (bottom) flexible canopies in slow flow. 162

Figure 5.14: Mean vorticity plots for the (a) flume and (b) numerical 0.2m flexible canopies in slow flow. The plot shows both clockwise (blue) and anticlockwise (red) vorticity. The dotted line represents the rate of growth of the shear layer in the flume case. 163

Figure 5.15: Mean vorticity plots for the (a) flume and (b) numerical 0.4m flexible canopies in slow flow. The plot shows both clockwise (blue) and anticlockwise (red) vorticity. 164

Figure 5.16: Comparisons of modelled and measured downstream (a,c) and vertical (b,d) velocities for the 0.4m (top) and 0.2m (bottom) flexible canopies in medium flow. The data are split into canopy (blue), shear layer (green) and boundary layer (red) points. The black line represents a 1:1 relationship 165

Figure 5.17: Shear layer velocity (a,c) and Reynolds stress (b,d) profiles for the 0.4m (top) and 0.2m (bottom) flexible canopies in medium flow. 166

Figure 5.18: Mean vorticity plots for the (a) flume and (b) numerical 0.2m flexible canopies in medium flow. The plot shows both clockwise (blue) and anticlockwise (red) vorticity. . 167

Figure 5.19: Mean vorticity plots for the (a) flume and (b) numerical 0.4m flexible canopies in slow flow. The plot shows both clockwise (blue) and anticlockwise (red) vorticity. 168

Figure 5.20: Comparisons of modelled and measured (a) downstream and (b) vertical velocities for the 0.4m flexible canopies in fast flow. The data are split into canopy (blue), shear layer (green) and boundary layer (red) points. The black line represents a 1:1 relationship. 169

Figure 5.21: Mean velocity long-section for the 0.4m fast flow case..... 170

Figure 5.22: Shear layer velocity (a) and Reynolds stress (b) profiles for the 0.4m flexible canopies in fast flow. 171

Figure 5.23: Mean vorticity plots for the (a) flume and (b) numerical 0.4m flexible canopies in slow flow. The plot shows both clockwise (blue) and anticlockwise (red) vorticity. 171

Figure 5.24: (a) Shear layer velocity and (b) Reynolds stress profiles for the real vegetation experiments 173

Figure 5.25: Mean vorticity plots for the slow (top), medium (middle) and fast (bottom) 0.4m real canopies. The plot shows both clockwise (blue) and anticlockwise (red) vorticity. Dotted lines represent approximate shear layer angles..... 175

Figure 5.26: Mean vorticity plot for N-pendula canopy model. The plot shows both clockwise (blue) and anticlockwise (red) vorticity. 175

Figure 5.27: Wavelet spectra from a) a flexible flume canopy, b) a flexible canopy simulation, c) a real flume canopy and d) a highly flexible canopy simulation. The black dotted lines highlight dominant turbulent scales. 176

Figure 6.1: Graphical view of the rigid vegetation domain. The pink region represents the inlet, and the blue region represents the outlet. Physical dimensions shown in Figure 6.2. 183

Figure 6.2: Schematic of the rigid vegetation domain, not drawn to scale. The dotted line shows the boundary of the recirculation region. 184

Figure 6.3: Normalised downstream velocity (a) and Reynolds stress (b) vertical profiles for the rigid vegetation simulation. The black line represents the profile for an idealised shear mixing layer (Ghisalberti and Nepf, 2002). 185

Figure 6.4: Time-averaged long-section of downstream (u) velocity. 185

Figure 6.5: Time-averaged long-section of Reynolds stress 186

Figure 6.6: Time-averaged long-section of turbulent kinetic energy 187

Figure 6.7: Time-averaged long-section of turbulence production..... 187

Figure 6.8: Vertical profiles of quadrant occurrence as a percentage of the total time series, with a hole size of (a) H=0 and (b) H=2. The dotted line shows the canopy top. 188

Figure 6.9: Quadrant dominance across the domain using a hole size of H=2. 189

Figure 6.10: Quadrant occurrence as a percentage of total time series, using hole size H=0. 190

Figure 6.11: Vorticity plot showing a downstream snapshot of clockwise (blue) and anticlockwise (red) spanwise vorticity. The oval highlights the shear-scale vortex. 191

Figure 6.12: Eulerian vortex methods, showing regions of vorticity in black. 192

Figure 6.13: FTLE plot showing areas of flow attraction. Areas in white represent regions where the trajectories could not be tracked sufficiently to give a reliable estimate. 193

Figure 6.14: Vortex evolution through time. The x-axis is the downstream coordinate and the y-axis is time. The black region represents the vortex, and the portion of the domain it covers at different time-steps 194

Figure 6.15: Vortex growth through time, measured using vertical (red) and horizontal (blue) width. The black line shows the predicted vortex growth rate. 195

Figure 6.16: Velocity power spectra from a single point above the canopy. The Kolmogorov decay rate is also shown in black for reference. 196

Figure 6.17: Wavelet spectra of the same time series as the power spectra. Here the colour scale indicates magnitude (power). The dotted line indicates the shear layer scale. 197

Figure 6.18: Side view of the domain with the stalks in red, captured during the simulation. Flow is from left to right. 198

Figure 6.19: Schematic of the numerical domain for the patch model. The dotted line indicated the recirculation region. This diagram is not to scale. 199

Figure 6.20: Normalised vertical profiles of horizontally and temporally averaged downstream velocity(a) and Reynolds stress (b). The idealised shear layer profiles are shown in black 200

Figure 6.21: Long-section of time-averaged downstream velocity. An approximate vegetation mask is included. 200

Figure 6.22: Long-section of time-averaged Reynolds stress. An approximate vegetation mask is included. 201

Figure 6.23: Long-section of time-averaged turbulent kinetic energy. An approximate vegetation mask is included. 201

Figure 6.24: Quadrant dominance over the entire simulation with a) H=0 and b) H=2. 202

Figure 6.25: Dominant quadrants across the domain using H=2. 203

Figure 6.26: Occurrence of different quadrant events as a percentage of the total simulation time, using a threshold hole size of H=2. Approximate canopy positions are shown in green 204

Figure 6.27: FTLE (left) and vorticity (right) long-sections at a series of time-steps. The positions of identified vortices are shown using the dotted ovals. The white regions in the FTLE plot correspond to regions where the trajectories could not be fully tracked. In the vorticity plots, blue corresponds to clockwise vorticity and red to anti-clockwise vorticity. 205

Figure 6.28: Series of snapshots through time of vortex detection using the three Eulerian vortex methods (Q=top, λ_2=middle, Δ=bottom) 208

Figure 6.29: Downstream velocity (red) and plant canopy height (blue) power spectra. The Kolmogorov -5/3 decay rate is also plotted in black for reference. 210

Figure 6.30: Wavelet power spectra for the velocity (a) and canopy height (b) series and (c) cross spectra between the two time series. 212

Figure 6.31: Plot of the (a) velocity and (b) canopy height time series used in the spectral analysis. 213

Figure 6.32: Schematic of the numerical domain for the canopy simulation. The dotted line indicated the extent of the recirculation region. This diagram is not to scale. 215

Figure 6.33: Normalised vertical profiles of the horizontally and temporally averaged downstream velocity (a) and Reynolds stress (b). The idealised shear layer profiles are shown in black for comparison. 216

Figure 6.34: Long-section of the time-averaged downstream (u) velocity. Due to the dynamic nature of the vegetation, it has not been blocked out. 217

Figure 6.35: Long-section of the time-averaged Reynolds stress. 217

Figure 6.36: Long-section of the time-averaged turbulent kinetic energy. 218

Figure 6.37: Quadrant dominance over the entire simulation with a) H=0 and b) H=2. 218

Figure 6.38: Quadrant dominance using a threshold hole size of H=2. 219

Figure 6.39: Quadrant occurrence expressed as a percentage using a hole size H=2. 220

Figure 6.40: FTLE vortex tracking. Areas in white represent regions where the trajectories could not be tracked sufficiently to give a reliable estimate. Ridges represent areas of greatest flow attraction. 221

Figure 6.41: Q criterion vortex detection results through time. Black areas represent vortices. 222

Figure 6.42: Δ criterion vortex detection results. Black areas represent vortices 223

Figure 6.43: λ_2 criterion vortex detection results. Black areas represent vortices 224

Figure 6.44: Vorticity snapshot taken at t=24.4s, showing clockwise (blue) and anti-clockwise (red) vorticity. 225

Figure 6.45: Comparison between different vortex methods for t=24.4s. Q criterion vortices are shown in blue, λ_2 criterion vortices in green, Δ criterion vortices in red and FTLE ridges in black. 225

Figure 6.46: Change in vortex thickness through time, using the Q (blue), λ_2 (green) and Δ (red) vortex criteria. The predicted growth rate is shown in black 227

Figure 6.47: Evolution and breakup of the vortex as detected by the Q criterion. The frames are taken at 0.2s intervals, between 24.8s (top) and 25.4s (bottom). 227

Figure 6.48: Images of the 3D FTLE ridges viewed from (a) side-on to the domain with flow from left to right and (b) from the outlet, looking upstream. The surfaces are coloured according to their y-coordinate for visualisation purposes. The annotations in red highlight potential vortex structure. 229

Figure 6.49: Velocity (red) and canopy height (blue) spectra. The black line shows the Kolmogorov rate of decay. The dotted line is located at 0.5Hz. 230

Figure 6.50: Wavelet spectra for a) the velocity and b) the canopy height and c) cross-spectra between the two time-series. The dotted line highlights the observed increase in scale through time. 232

Figure 6.51: Schematic of the numerical domain used for the small patch. The dotted line indicates the recirculation region. 234

Figure 6.52: Vertical profiles of a) downstream velocity and b) Reynolds stress. 235

Figure 6.53: Time-averaged long-section of the mean downstream (u) velocity field. Vegetation cannot be masked as it is dynamic. 235

Figure 6.54: Long-section of time-averaged Reynolds stress. 236

Figure 6.55: Long-section of time-averaged TKE. 236

Figure 6.56: Vertical profiles of quadrant occurrence using a) H=0 and b) H=2 threshold. 237

Figure 6.57: Quadrant dominance using a threshold hole size of H=2. 237

Figure 6.58: Quadrant occurrence across the long-section as a percentage with H=2 238

Figure 6.59: Vorticity snapshot showing clockwise vorticity (blue) and anti-clockwise vorticity (red). 239

Figure 6.60: Eulerian vortex detection results. Areas of black represent vortices. 240

Figure 6.61: FTLE vortex tracking. Areas in white represent regions where the trajectories could not be tracked sufficiently to give a reliable estimate. Ridges represent areas of greatest flow attraction. 241

Figure 6.62: Velocity (red) and canopy height (blue) spectra. The black line shows the Kolmogorov decay rate. 242

Figure 6.63: Wavelet spectra for a) the velocity and b) canopy height time series and (c) cross spectra between the two time series. 242

Figure 6.64: Schematic of the domain for the canopy simulation. The dotted line indicates the extent of the recirculation region. This diagram is not to scale. 244

Figure 6.65: Normalised vertical velocity profiles of the horizontally and temporally averaged (a) downstream velocity and (b) Reynolds stress. The idealised shear layer profiles are shown in back for comparison 244

Figure 6.66: Long-section of the time-averaged downstream (u) velocity. 245

Figure 6.67: Long section of the time-averaged Reynolds stress. 245

Figure 6.68: Long-section of the time-averaged turbulent kinetic energy 246

Figure 6.69: Quadrant dominance over the entire simulation with a) H=0 and b) H=2 246

Figure 6.70: Quadrant dominance using a threshold hole size of H=2. 247

Figure 6.71: Quadrant occurrence across the long-section as a percentage with H=2. The figures for Q2 and Q3 contained no signal and therefore have not been included. 247

Figure 6.72: Snapshots from the FTLE field at particular time-steps showing different vortex generating mechanisms. 249

Figure 6.73: Snapshots from the vorticity field at particular time-steps showing clockwise (blue) and anticlockwise (red) vorticity. 250

Figure 6.74: Velocity (red) and canopy height (blue) spectra. The black line shows the Kolmogorov rate of decay 251

Figure 6.75: Wavelet spectra for a) the velocity and b) canopy height time series and (c) cross-spectra between the two time series. 252

Figure 6.76: Schematic of the numerical domain for the single stem simulation. 254

Figure 6.77: Canopy height time series from the constant (red) and variable (blue) drag coefficient simulations. 255

Figure 6.78: Flow and canopy height spectra from the constant (left) and variable (right) drag coefficient simulations 255

Figure 6.79: Time series for the (a) flow, (b) canopy height and (c) drag coefficient for the variable drag simulation. 256

Figure 6.80: Drag coefficient profile along the stalk and through time. 257

Figure 6.81: Wavelet spectra for the variable drag simulation. The three graphs correspond to the (a) flow, (b) canopy height and (c) cross wavelet spectra 257

Figure 6.82: Wavelet spectra for the constant drag coefficient simulations. The three graphs show the (a) flow, (b) plant and (c) cross wavelet spectra. 258

Figure 7.1: Schematic diagram showing the canopy layer velocity and shear profiles (a & b), and turbulent processes within sparse (c & d) and dense (e & f) canopies. The canopies are split by Nikora's (2010) classification into semi-rigid (bending) plants and highly flexible (tensile) plants. 264

Figure 7.2: Model for canopy turbulence structure from Finnigan *et al.*, (2009). 266

Figure 7.3: Model for boundary layer turbulence structure from Adrian *et al.*, (2000)..... 266

Figure 8.1: The field site location shown in OS 1:25 000. The river reach is shown in the red oval and the coordinates are given with respect to the British National Grid. 273

Figure 8.2: Aerial photo of the field site, with the reach indicated by the red line. The river flows from North to South. 273

Figure 8.3: Photo of the field site, taken in September, looking downstream. Field assistant shown for scale. 274

Figure 8.4: Patch of Ranunculus penicillatus within the river reach. The water depth was approximately 0.2m. 274

Figure 8.5: Map of the (a) DEM point densities across the numerical domain and (b) topography across the domain. The white contours mark every 0.1m change in topography. Green areas show vegetation patches. The water surface edge is shown by the black/blue line with different colours used for clarity. 275

Figure 8.6: Location of the ADV measurement points (red dots) and associated cross-sections. The cross-sections are referred to by these numbers throughout. 276

Figure 8.7: Vegetation sample collected from the field. 279

Figure 8.8: Schematic showing the lateral motion of the drag mask. The solid grid represents the domain grid whereas the dotted grid represents the plant grid. Darker values correspond to higher drag values. The original plant position (a) is altered as each section shifts laterally (b) according to the wave equation (Equation 8.2). 280

Figure 8.9: Lateral velocity power spectra for the time series taken behind the vegetation patch. The red circles highlight two key frequencies, which it is suggested correspond to the (a) shear and (b) flapping scale. 282

Figure 8.10: Comparison between downstream velocities from the a) RNG k-e, b) LES and c) dynamic LES models. The dots show the corresponding field-measured values. The thick black lines show the measured water surface edge. The dashed circles highlight changes in wake shape and the dotted circles highlight changes in wake velocity magnitude. 284

Figure 8.11: Comparison between lateral velocities from the a) RNG k-e, b) LES and c) dynamic LES models. The dots show the corresponding field-measured values. The thick

black lines show the measured water surface edge. The dotted circles highlight changes in wake velocity magnitude. 284

Figure 8.12: Downstream velocity maps for the (a) static and (b) dynamic high resolution models. The circles show values measured in the field. 286

Figure 8.13: Lateral velocity maps for the (a) static and (b) dynamic high resolution models. Flow from true right to true left is considered positive. The circles show values measured in the field. 287

Figure 8.14: Scatter plots showing agreement between measured and modelled (a) downstream and (b) lateral velocities. The black line represents a perfect fit. 288

Figure 8.15: Downstream velocity maps for the (a) static and (b) dynamic medium resolution models. The dots show values measured in the field. The dotted line indicates the region of faster streamlined flow and the circle represents a region of diffuse wakes. 291

Figure 8.16: Lateral velocity maps for the (a) static and (b) dynamic medium resolution models. Flow from true right to true left is considered positive. The circles show values measured in the field. 292

Figure 8.17: Scatter plots showing agreement between measured and modelled (a) downstream and (b) lateral velocities. The black line represents a perfect fit. The ovals highlight regions of poor fit associated with cross-section 3. 292

Figure 8.18: Downstream velocity maps for the (a) static and (b) dynamic low resolution models. The dots show values measured in the field. The dashed line highlights the region of fast flow. 294

Figure 8.19: Lateral velocity maps for the (a) static and (b) dynamic low resolution models. Flow from true right to true left is considered positive. The dots show values measured in the field. 295

Figure 8.20: Scatter plots showing agreement between measured and modelled (a) downstream and (b) lateral velocities. The dotted circle highlights poor data relating to cross-section 3. The black line represents a perfect fit. The dotted line shows the offset, 296

Figure 8.21: Downstream velocity as predicted by the dynamic model for (a) low, (b) medium and (c) high resolution grids. The thick black lines show the measured water surface edge. The dots represent the field-measured velocities. 297

Figure 8.22: Lateral velocity as predicted by the dynamic model for (a) low, (b) medium and (c) high resolution grids. The thick black lines show the measured water surface edge. The dots represent the field-measured velocities 298

Figure 8.23: Dynamic model velocity plotted against static model velocity for (a) downstream and (b) lateral velocities at each of the ADV measurement locations. Each graph shows the low (green), medium (green) and high (red) resolution results. 299

Figure 8.24: Dynamic model downstream (top) and lateral (bottom) velocity plotted against static model velocity for the whole domain with grid resolutions (a) 0.2m, (b) 0.1m and (c) 0.05m. 299

Figure 9.1: The six scales of turbulence within vegetated channels as proposed by Nikora (2010). The six scales are; 1) boundary layer; 2) canopy shear layer; 3) leaf boundary layer; 4) leaf mixing layer; 5) stem wake and; 6) plant flapping scale. 306

Figure 9.2: Schematics of the (a) Euler-Bernoullli beam and (b) N-pendula models above an excerpt of Figure 7.1 showing the differences in vortex generation between the two vegetation types. 308

Figure 9.3: Downstream velocity and canopy height spectra showing interaction and feedback between the two as shown in Figure 6.29. The circles highlight the potential shear layer signals (A and D) and the natural frequency signals (B and C). 309

Figure 9.4: Vertical drag coefficient profile taken from the Euler beam model at different points downstream through the canopy as shown in Figure 3.20 311

List of Tables

Table 4.1: Criteria for vortex detection in canopy flows 139

Table 5.1: Flexural Rigidity choice for the different simulations in Chapter 6 146

Table 5.2: Inlet velocities for the validation runs. Absent figures imply unreliable results. 147

Table 5.3: Linear regression data for the entire datasets 154

Table 5.4: Linear regression data for downstream velocity (U) in the individual regions of the flow 155

Table 5.5: Linear regression data for vertical velocity (W) in the individual regions 155

Table 5.6: Averaged velocities for the real vegetation runs 172

Table 6.1: Outline of all the numerical simulations presented in Chapter 6. *The Reynolds numbers are low due to the size restriction and shape of the numerical domain. In practice, the scenarios are analogous to higher Reynolds number natural flows. 182

Table 6.2: Key frequencies active within the flow: f_W is the wake shedding frequency and f_{KH} is the Kelvin-Helmholtz vortex frequency as discussed in Chapter 4. 196

Table 6.3: Key frequencies active within the flow: f_W is the wake shedding frequency, f_N is the natural frequency of the vegetation and f_{KH} is the Kelvin-Helmholtz vortex frequency as discussed in Chapter 4. 211

Table 6.4: Key frequencies active within the flow: f_W is the wake shedding frequency, f_N is the natural frequency of the vegetation and f_{KH} is the Kelvin-Helmholtz vortex frequency as discussed in Chapter 4. 230

Table 6.5: Key frequencies active within the flow. f_{KH} is the Kelvin-Helmholtz frequency. Wake-scale turbulence is not included her as the inclination of the stems means that the effective radius is substantially different. 252

Table 8.1: RMSE values for the different model simulations 288

Table 8.2: Regression coefficients and R^2 values for downstream velocity 288

Table 8.3: Regression coefficients and R^2 values for lateral velocity 288

List of Notation

Upper-case Roman

A	Channel cross-sectional area
A_f	Plant flapping signal amplitude
A_i	Actual fractional error
A_p	Stem cross-sectional area
A_V	Vortex areas
$A_{0,k}$	Fourier coefficients
B	Buoyancy number
B_k	Fourier coefficient
B^{SA}	Surface-area based blockage value
B^V	Volume based blockage value
B^X	Cross-section based blockage value
C	Chezy coefficient
Ca	Cauchy Number
C_D	Drag coefficient
C_k	Fourier coefficient
C_M	Coefficient of added mass
C_p	Pressure coefficient
C_s	Smagorinsky constant
D_i	i^{th} percentile of the grain size distribution
E	Modulus of elasticity
E_i	Estimated fractional error
$E_{x,z}$	External fluid forces in x and z directions
F	Force/Loading
F_B	Buoyancy force
F_D	Drag force
F_i	ith component of the Force vector
F_i^{TEN}	Tension force at the ith node
F_i^{TOR}	Torsion force at the ith node

F_P	Pressure force
Fr	Froude number
F_R	Bending force
F_s	Sampling frequency
$\widetilde{F_D}$	Drag force correction
GCI	Grid convergence index
H	Hole size
$H(f)$	Hessian matrix
I	2nd moment of inertia
$J = EI$	Flexural rigidity
K	Gaussian curvature
L	Courant number
$\mathcal{L}_i$	ith Lyapunov exponent
L_S	Length scale
L_2 , $\|.\|_2$	Euclidean Norm
L_∞ , $\|.\|_\infty$	Infinity Norm
M	Stem density
P	First invariant of ∇u
P_e	Effective wetted perimeter
P_T	Turbulent production rate
P_W	Wetted perimeter
Q	Second invariant of ∇u
$\mathrm{Q_E}$	Threshold on Q
Q_i	ith quadrant
Q_i^n	Computational force vector
R	Third invariant of ∇u
Re	Reynolds number
R_h	Hydraulic radius (A/P)
R^2	Coefficient of determination
S	Channel/bed slope
S_f	Friction slope

$S(f)$	Power spectral density
S_{ij}	Strain
T_1	Given time period for FTLE calculation
T	Vegetation cross-sectional variability parameter
$\overline{U}$	Time-averaged downstream velocity
U_1	Canopy downstream velocity
U_2	Above-canopy downstream velocity
U_*	Shear velocity
U^*	Normalised downstream velocity
V	Total fluid volume

Lower-case Roman

a	Vegetation frontal area
a_p	Plant acceleration
$a_{1,2,3}$	Real-valued exponents
c	Real constant
f	Frequency
f_{DW}	Darcy-Weisbach friction factor
f_{KH}	Kelvin-Helmholtz vortex shedding frequency
f_N	Natural frequency
f_v	Vegetation flapping frequency
f_{v1}	Spalart-Allmaras function
f_W	Wake shedding frequency
$f_{1,2}$	Numerical solutions using grid spacing $h_{1,2}$
f^*	Exact solution
g	Gravitational acceleration
g_i	Arbitrary continuous functions
$\tilde{g}$	Amplification factor
h	Vegetation canopy height

h_w	Water height
i	Imaginary unit number
k	Turbulent kinetic energy
$k_{1,2}$	Principal curvatures
k'	Instantaneous kinetic energy
l	Beam length
l_b	Blade/stem length
l_t	Turbulent length scale
m	Sinuosity-induced roughness coefficient
n	Manning's friction coefficient
n_b	Base roughness value
$n_{1,2,3,4}$	Roughness components
p	Pressure
p_c	Order of convergence
p_∞	Free-stream pressure
$\bar{p}$	Time-averaged pressure
q	External force term
r	Grid refinement ratio
r_p	Plant radius
r_V	Vortex radius
t	Time
t_b	Blade thickness
tr(.)	Trace
u_f	Local average fluid velocity
u_p	Plant velocity
u_{RMS}	Root mean square downstream velocity
u_t	Velocity scale
$u_i{}'$	ith component of the instantaneous velocity (also $u', v'w'$)
$\overline{u'w'}^*$	Normalised Reynolds stress
$\bar{u}_i$	ith component of the time-averaged velocity

$\langle u \rangle$	Resolved velocity component (LES)
$\tilde{u}$	Unresolved velocity component
v	Vortex propagation speed
w	Channel width
w_b	Blade width
w_{RMS}	Root mean square vertical velocity
x	1st Cartesian coordinate
x_i	ith Cartesian coordinate
y	2nd Cartesian coordinate
z	3rd Cartesian coordinate
z_0	Roughness height
z^*	Normalised height
$\overline{z_p}$	Mean canopy height (roughness height)

Upper-case Greek

Δ	Cubic discriminant
Δ_f	LES filter width
Δ_t	Temporal grid resolution
ΔU	Shear layer velocity difference
Δ_x	Spatial grid resolution
ΔX_i	Incremental distance from X_i
K	Generic roughness coefficient
Ω	Rotation tensor

Lower-case Greek

δ	Shear layer width
δ^i	ith order central differencing scheme
δ_{ij}	Kronecker delta function
δ_0	Initial shear layer width
ε	Numerical error

ϵ	Turbulent energy dissipation rate
ϵ_{ijk}	Levi-Civita symbol
θ_i	Angle from the horizontal at the ith node
θ_M	Momentum thickness
κ	Karman constant
λ	Wavelength
λ_{ci}	Imaginary part of the complex eigenvalue
λ_{cr}	Real part of the complex eigenvalue
λ_i	ith eigenvalue
λ_{max}	Maximum eigenvalue
λ_r	Real eigenvalue
μ	Dynamic viscosity
μ_M	Mass per unit length
ν_t	Eddy viscosity
$\tilde{\nu}$	Spalart-Allmaras viscosity-like variable
ξ	Displacement
ξ_i^n	Displacement value at the ith node at time n
ξ_0	Vibration amplitude
ρ	Density of water
ρ_p	Plant material density
σ_1^T	Coefficient of maximum expansion
τ^{ij}	LES/Reynolds stress components
τ_0	Bed shear stress
ψ	Wavelet function
ω_i	ith component of the vorticity vector
ω	Specific turbulent energy dissipation rate

Symbols

∇^i	ith order backward differencing scheme
∇	Gradient differential operator
$\|.\|_F$	Frobenius norm
$\emptyset$	Vegetation volume fraction

List of Abbreviations

ADV	Acoustic Doppler Velocimeter
CFD	Computational Fluid Dynamics
DEM	Digital elevation model
DNS	Direct Numerical Simulation
LES	Large Eddy Simulation
MFSA	Mass flux scaling algorithm
PIV	Particle Image Velocimetry
RMS	Root mean square
RANS	Reynolds Averaged Navier-Stokes
SGS	Sub-grid scale
TKE	Turbulent Kinetic Energy
URANS	Unsteady Reynolds Averaged Navier-Stokes
UVP	Ultrasonic velocity profiling

Statement of Copyright

Acknowledgements

There are a number of people without whom this thesis would simply not have been written.

Firstly, I owe a debt of gratitude to my three supervisors. To Rich, for introducing me to the world of turbulence and flapping vegetation, and for his constant support, encouragement and advice throughout the last 3 years. To Stuart, for his enthusiasm, ideas and insight into the PhD and for correcting my numerous grammatical errors! And to Dan, for his help with the flume experiments, and advice and encouragement throughout the project. I feel extremely privileged to have been supervised by three great academics, who have constantly believed in me, even when I have not.

Secondly, there are a vast number of people in the geography department who have helped me over the past 4 years. I am very grateful for all the help and advice I have received and I would also like to thank those friends and fellow PhD students who have made the department such a pleasant place to study. In particular, I would like to thank Matthew, with whom I have spent a great deal of time, in the office and in the field, and who has provided much support; academic and beyond.

Finally, I would like to thank my family and in particular, Katherine, for her unending support over the last four years, and for suffering endless hours of listening to me talk about vegetation in rivers and moan about my various programming woes.

Chapter 1: Introduction

1.1 Rationale

Vegetation is a ubiquitous feature of riverine environments. Whether located on the floodplain, along the banks or in the channel, it can strongly impact upon the behaviour of the river system. This thesis focuses on in-channel aquatic macrophytes (plants visible to the naked eye), which are a fundamental component of many lowland river ecosystems (Clarke, 2002; Franklin *et al.*, 2008). Traditionally, in-channel vegetation has been viewed as problematic due to the increase in flow resistance it can cause (Kouwen and Unny, 1973), which for a given flow, leads to an increase in water level. Flow resistance extracts energy from the flow, via drag, which transfers energy from the mean flow to both heat and to stem-scale turbulence (Yagci and Kabdasli, 2008; Zong and Nepf, 2010). An increase in flow resistance therefore leads to a decrease in mean velocity and thus conveyance (Jarvela, 2002; Nepf *et al.*, 2007), which for a constant discharge implies that the river must increase its cross-sectional area. For confined channels, this leads to an increase in depth (Petryk and Bosmajian, 1975; Nepf, 1999) and consequently poses a significant flood risk. Therefore, vegetation has historically been removed from channels to accelerate flow and decrease potential flood risk (Luhar *et al.*, 2008; Nepf and Ghisalberti, 2008).

However, over the last few decades, the positive effects of vegetation in terms of ecology and flood conveyance have been realised (Nezu and Onitsuka, 2001; Wilson *et al.*, 2003). Vegetation canopies provide areas of decreased bed shear stress (Sukhodolov and Sukhodolova, 2010), which may increase sedimentation (Sand-Jensen *et al.*, 1989; López and García, 1998) and can create sediment and nutrient sinks that enable the development of stable habitats for terrestrial and aquatic wildlife (Lopez and Garcia, 2001; Liu and Shen, 2008; Liu *et al.*, 2008). In addition, by creating spatial heterogeneity within the flow, and encouraging the development of different habitats, vegetation promotes biodiversity within rivers (Kemp *et al.*, 2000). Through the uptake of heavy metals and nutrients (Kadlec and Knight, 1996)

and the production of oxygen, the biological interaction between flow and vegetation can significantly improve water quality (Ghisalberti and Nepf, 2006). Consequently, vegetation has become central to many river restoration schemes (Wilson *et al.*, 2003).

Vegetation can also be used to actively manage flood risk. By allowing channels in flood-suitable areas to return to their natural vegetated state, the potential for overbank flows increases and therefore flood risk in urban areas downstream decreases (Evans *et al.*, 2009). Hence, in addition to its ecological impacts, vegetation can be used as a catchment-scale flood management tool. Such factors thus have environmental, geomorphological and ecological implications which create a number of issues and uncertainty as to how best to manage the river corridor.

Aquatic vegetation can be seen to have both beneficial and detrimental effects on the river system (Haslam *et al.*, 1975) and exhibits complex relationships with the flow and the landscape (Nepf, 2012b; Gurnell, 2013). Due to the lack of a full process understanding of flow-vegetation interactions, there is a tension between the positive and negative impacts within river management schemes. This tension was highlighted most notably in the Pitt Review (2008), written following the 2007 summer floods in the UK. The 2007 flooding was the UK's largest peacetime emergency since World War II with a cost of 13 lives and over £3 billion. One of the key observations of the Pitt review, in relation to the problem of vegetation, was that management processes such as dredging and vegetation clearance were no longer being performed as frequently in UK rivers because the management focus has shifted to flood control as an integrated part of river restoration and ecological integrity. One of the contributing factors, cited by the flood victims, to the cause of the flooding was the extent and slow recession of the flood waters (Pitt, 2008), potentially caused by undredged channels. Therefore, there is still a concern that vegetation is a significant driver of flood risk (Evans *et al.*, 2009), and the debate, as to the trade-off between flood and ecosystem management, is ongoing.

This ecological approach is central to the EU Water Framework Directive (WFD) (2000/60/EC) established in 2000, which requires EU member states to adopt river management policy which *'prevents further deterioration and enhances the status of aquatic ecosystems'* (WFD, p.6). The abundance and composition of aquatic macrophytes are key criteria used within the framework as indicators of the ecological status of rivers and therefore vegetation clearance is discouraged (O'Hare *et al.*, 2010). Other EU directives such as the Habitats directive (92/43/EEC), and more recently the Biodiversity Framework (2011/2307(INI)) have also highlighted the current negative implications of human impact and channel modification (ETC/BD, 2008) and advocated the restoration and preservation of ecosystem services.

Recognition of these issues has led to significant research on vegetated flows over the last two decades (Luhar and Nepf, 2013). This work, much of it based upon work in terrestrial environments (e.g. Raupach *et al.*, 1996; Finnigan *et al.*, 2009), has led to an improvement in our understanding of the quantitative effects of vegetation canopies on flow in open channels (e.g. Ghisalberti and Nepf, 2002; Nepf, 2012a; Nepf, 2012b). However, despite improvements in our understanding of the dynamic process interactions between flow and vegetation, this process understanding has not been transferred to our reach-scale field-based predictive tools or incorporated in our modelling approaches where empirical roughness relationships still dominate (Lane and Hardy, 2002; Luhar and Nepf, 2013).

It is suggested herein that empirical roughness values are limited in accuracy as they fail to quantify the spatial and temporal variation in roughness due to plant and patch characteristics (Rhee *et al.*, 2008; O'Hare *et al.*, 2010). Therefore, empirical roughness-based models are unable to predict local flow structure which prevents the prediction of spatially dependent sediment transport dynamics and ecohydraulic variables necessary for ecological evaluation in line with the WFD. Effective river management requires a detailed knowledge of the effects of vegetation and an ability to predict, with accuracy, the local impact of vegetation on flow and morphology (Stoesser *et al.*, 2009). However, much of the aquatic research to date has involved simple, idealised canopy models, or has been flume-

or field-based where accurate, spatially-intensive, concurrent measurements are not feasible at the local scale. The trade-off between flood and ecological management highlights the need for reliable methods of accurately calculating vegetative resistance (Nepf, 2012b) and therefore further work is required to better model the effect of macrophytes on channel hydraulics (Kemp *et al.*, 2000).

Improving our process understanding of energy extraction and turbulence production at the stem-scale is key to moving away from empirical resistance methods (Naden *et al.*, 2006). In particular, it is important to characterise the time-dependent interaction between flow and vegetation at the stem-scale and to identify the key processes in order to determine an appropriate modelling strategy at the canopy-scale and beyond.

1.2 Research Aim

The overall aim of this thesis is to further our understanding of the effect of vegetation on flow in rivers. More specifically, this thesis aims to study the effects of submerged, flexible vegetation within open channel flows as this represents the most complex and realistic scenario for aquatic macrophytes. This thesis will focus on the stem-scale flow-vegetation interactions as this is the scale at which energy is extracted from the flow. This overall aim is further divided into a methodological aim (*A1*) and a research aim (*A2*).

A1. To develop a model capable of simulating the interaction between flow and vegetation from the individual plant scale through to the canopy scale;

and to use this new modelling approach in order;

A2. To investigate the controls on the turbulent processes exhibited in canopy flows.

1.3 Research Questions

In order to achieve the aims, a number of key questions have been identified which are addressed and answered throughout the thesis. These research questions are a product of both the methodological and research aims and include;

Q1. What turbulent processes are present within canopy flows?

This question has been formulated as it is central to understanding the interaction between flow and vegetation at the stem-scale and characterising how the turbulence differs from non-vegetated channels. A full process understanding of the turbulence is essential in developing a vegetative resistance model (Naden *et al.*, 2006).

Q2. How do aquatic canopy flows differ from terrestrial canopy flows?

This question addresses the extent to which our process understanding obtained from the terrestrial environment (e.g. Finnigan *et al.*, 2009) is applicable to the aquatic case. It is necessary to identify any similarities or differences in the processes before being able to generalise terrestrial canopy flow models for the aquatic case.

Q3. How do structural and biomechanical properties of river plants determine turbulence dynamics within plant canopies?

In order to understand the controls on turbulence within vegetated channels, and subsequently develop an effective, physically-based vegetative resistance model, it is important to identify the key vegetation characteristics which determine the vortex dynamics.

Q4. What feedback mechanisms are present between the flow and vegetation characteristics?

To date, one of the key areas of research into canopy layers has been the feedbacks between the flow and vegetation. These feedback mechanisms are important to define as they dictate which flow and vegetation characteristics determine the turbulent flow field. Furthermore, they also define the processes which need to be included in the conceptual model.

Q5. What key processes need to be represented within high-resolution vegetation models?

This question is crucial to the methodological aim, in defining the conceptual model, as it determines the necessary level of complexity and process representation required to fully model flow-vegetation interactions. However, this process information is not known *a priori* and therefore will be addressed throughout the process of model development and application.

Q6. Is it possible to improve the representation of vegetation in management-scale models, by applying a more process-based approach?

Current numerical models of flow-vegetation interaction rely on empirical roughness relationships rather than process-informed parameters. Throughout this thesis it is suggested that these empirical relationships represent flow through vegetation poorly. In order to justify this hypothesis it is important to assess the discrepancy between these current approaches and more physically-based models.

1.4 Objectives and Thesis Structure

The thesis aims and research questions are addressed through a set of methodological objectives. In order to be able to answer the research questions it is first necessary to critique our current understanding of canopy flows as well as the variety of modelling approaches previously applied to vegetated flows across a range of spatial scales (**O1**). This will also include reviewing appropriate methods of analysing the numerical data produced by such models in order to assess whether the models are correctly representing the natural environment.

In order to fulfil the methodological aim (*A1*), two novel vegetation models will be developed which are capable of simulating the time-dependent interaction between the flow and vegetation at the stem scale (**O2**). The new models need to be fully assessed to quantify their suitability and accuracy. To achieve this, it is necessary to validate the models against a set of highly controlled flume data (**O3**). The successful development and validation of these models will allow an investigation of the dominant controls on the turbulence structures within vegetated channels by applying the model to a range of different scenarios (**O4**).

Finally, in order to evaluate the applicability of the high-resolution results at the reach-scale it is necessary to incorporate the key processes within a reduced complexity reach-scale model (**O5**). This will allow a comparison between the new model and existing methodologies in order to evaluate any improvement in performance.

These five methodological objectives map onto the structure of the thesis as shown in Figure 1.1 and discussed below.

Objective 1: Critique of our current understanding of canopy layer theory in order to: develop a suitable modelling methodology, obtain a valid analysis framework and explore potential reach-scale modelling methods.

This objective is addressed in Chapters 2, 3, and 4 and can be divided into two sections; one focussing on the theory of canopy flows and how they have been previously modelled, and the other on specific methodological aspects of the thesis such as appropriate modelling and analysis frameworks. Chapter 2 deals with the theory of canopy flows and discusses how the interactions between flow and vegetation have previously been incorporated into models of different complexity. In order to do this, the chapter begins by reviewing the underlying theory of flow-vegetation interaction before summarising the different numerical modelling approaches which have previously been used. Finally it examines how vegetation has been included within previous models.

Thus, within Chapter 2, some key numerical methods are discussed, though the details regarding specific methodologies are addressed in more depth in Chapter 3. In Chapter 3, previous modelling methodologies are critiqued before the methodological approach to be used in the thesis is formulated. In Chapter 4, a synthesis of techniques used for investigating flow structure is presented which enables a useful and appropriate flow and vegetation data analysis approach to be devised.

Objective 2: Development of biomechanical models capable of representing flexible vegetation.

Objective 2 is addressed in Chapter 3, where two different models, which incorporate vegetation within a Computational Fluid Dynamics (CFD) framework, are proposed and developed. The first of these models is based upon the Euler beam equation and is designed to replicate semi-rigid vegetation. The second model uses an N-pendula approach to represent highly flexible vegetation. As well as the initial development of these models, Chapter 3 includes the verification and stability testing of the two models. Furthermore, attention is given to the various CFD solver options and boundary conditions, and the parameters used for the rest of the thesis are set out.

Objective 3: Validation of the biomechanical models against experimental flume data.

Chapter 5 covers the validation of the two numerical models against controlled experimental flume data. This is an important step to demonstrate the applicability of the two vegetation models developed as part of Objective 2, before the models are applied to a wide range of scenarios. In order to fully validate the models, key flow parameters including both mean flow and turbulent properties are compared against the flume data.

Objective 4: Investigation of the dominant controls on turbulent structure within vegetated channels.

Objective 4 is addressed in Chapters 6 and 7 where results from the numerical models are applied and discussed. Chapter 6 includes results from a range of numerical simulations using rigid, semi-rigid and highly flexible vegetation. The results are analysed according to the analysis criteria developed in Objective 1. The key aim is to elucidate the key controls on canopy flow, to inform Objective 5, and compare the results against our current understanding of flow-vegetation interaction.

Objective 5: Incorporation of high resolution process understanding into reduced complexity reach-scale models.

The final objective involves incorporating the improved process understanding into a lower spatial resolution reach-scale model. Accordingly, the dominant features and mechanisms within the flow, such as drag and vortex production, are identified and represented in a simplistic way within a reach-scale CFD model. The results from this new model are compared to results obtained from applying an existing methodological approach as well as field data in order to quantify accuracy and process representation within the two models.

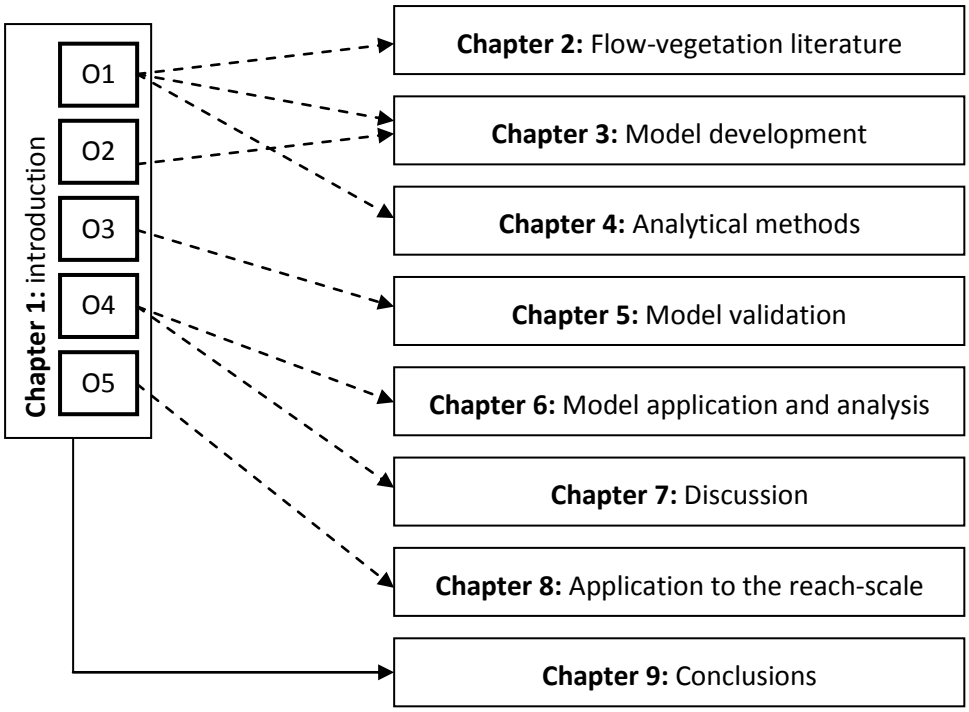

Figure 1.1: *Schematic overview of how the objectives map onto the thesis chapters.*

By following such a research design it is suggested that a suitable high resolution space-time model of flow-vegetation interaction will be developed. This will not only improve our process understanding of flow-vegetation interaction but also enable an enhanced processes-informed model for future management of the riverine environment.

Chapter 2: Modelling flow-vegetation interactions

2.1 Introduction

Chapter 1 highlighted the importance of vegetation within river channels and the need for accurate vegetation modelling methods to enable effective river management. The effects of vegetation within rivers have been studied since the 1950s (e.g. Cowan, 1956), right from the earliest attempts at quantifying roughness in open channels, however the literature is neither as extensive nor as developed as the research on non-vegetated gravel and sand bed rivers. There has, however, been a large amount of research conducted concerning terrestrial canopy flows. Whilst there are important differences between the two, which are discussed in Section 2.3.4, there are also important similarities, which have served as a basis for the emergence of aquatic canopy flow studies over the last two decades.

Therefore, this chapter begins with a review of terrestrial canopies before moving on to consider the aquatic case. Having established a good understanding of the theory behind canopy flows, Section 2.4 reviews different methods of numerically representing open-channel flows, with a particular focus on the trade-off between process representation and computational cost. The remainder of the chapter then reviews the different ways in which vegetation has been incorporated into such models, from the simplest management models through to complex three-dimensional research tools.

2.2 Flow structure and processes over terrestrial canopies

The theoretical foundations for canopy layer theory within vegetated channels are found within the terrestrial canopy literature. Therefore, prior to examining flow structure within aquatic flows, this section provides an overview of the vast amount

of research conducted in terrestrial environments, out of which some of the key ideas have emerged.

2.2.1 Characteristic mean velocity profile

One of the most significant challenges in understanding the impact of vegetation has been characterising the effect of vegetation on the mean velocity profile. Individual vegetation elements represent significant mass blockages and roughness elements within the flow. In addition, as a collective entity, plant canopies also act as a porous blockage (Shaw and Schumann, 1992; Ghisalberti and Nepf, 2009), restricting flow but not preventing it. This porous blockage effect creates two very different flow regimes: one above and one within the vegetation canopy. The within-canopy zone is characterised by a region of low longitudinal velocity, due to energy extraction from the flow by the canopy elements, a mechanism which will be explored in more detail in Section 2.2.5. This region is also characterised by a very low longitudinal velocity gradient in the vertical direction $\left(\frac{\partial U}{\partial z} \approx 0\right)$ (Finnigan, 1979a).

Whilst the velocity profile in non-vegetated channels is often approximated to the standard boundary layer profile (see Section 2.4.8), this is not an accurate approximation in vegetated channels as the porous canopy zone, and consequent creation of two distinct flow regimes, has a significant impact on the shape of the velocity profile. Instead it has been hypothesised that the canopy layer is more analogous to a mixing layer or free shear layer (Raupach *et al.*, 1996). A mixing layer is defined by Raupach *et al.* (1996) as the region of mixing of two co-flowing streams of different velocities.

The vertical velocity profile for canopy flows was first formally conceptualised by Inoue (1963) as shown in Figure 2.1. He hypothesised that there were three different velocity regimes: (I) canopy, (II) boundary layer and (III) a small zone at the bed where both vegetation and the channel bottom affect the flow. He also noted the presence of a fourth layer, the honami layer (added to the original diagram as IV), which acted as a smooth transition between (I) and (II). Remarkably, over half a

century this conceptual model has changed only slightly. Current models, based on the mixing layer analogy, identify two separate velocity regimes: a canopy region of slow flow as explained above (I & III) and a region above the canopy top, which is more analogous to a boundary layer profile (II). Where these two zones join, an inflection point is formed and the profile resembles a hyperbolic tangent curve (IV) (Rogers and Moser, 1992).

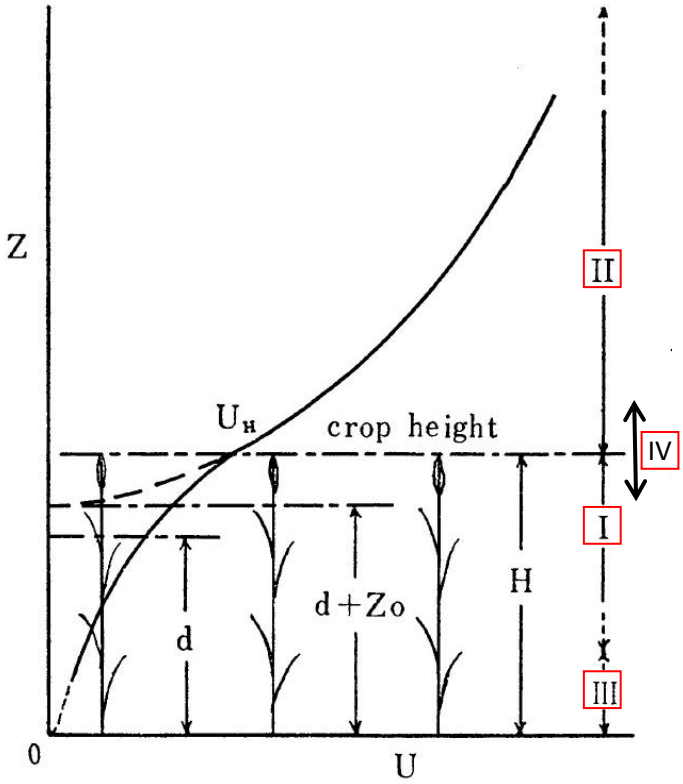

Figure 2.1: *Mean vertical velocity profile of canopy flow, from Inoue (1963). The profile is split into 4 separate regions (region IV has been added to the figure). Here, H is the canopy height, d is the zero plane displacement, Z_0 is the roughness parameter and U_H is the velocity at the canopy top.*

The inflection point in the mean velocity profile at the top of the canopy is a key feature of the flow regime, as it represents a highly unstable region of high shear, which acts as the main driver for canopy shear layer (CSL) turbulence.

2.2.2 Turbulence structure and characteristics

The turbulence structure of the CSL can be split into three distinctive length scales, defined as fine-scale, active and inactive (Raupach *et al.*, 1996). These three different scales can be characterised by their typical length scale (L_S) as defined in Equation 2.1.

$$L_S = U_h / \left(\frac{dU}{dz}\right)_{z=h} \quad (2.1)$$

Here, U_h is the longitudinal velocity at the top of the vegetation canopy. Using the definitions from Raupach *et al.* (1996), L_S is the length scale of the turbulence associated with the shear layer at the canopy top and is therefore labelled the 'active turbulence'. As the canopy is a component within a planetary boundary layer there exists much larger scale turbulence (>>L_S), usually scaling with the depth of the entire boundary layer. This turbulence will interact with the shear-scale eddies. However, at the height of interest ($z = h$) it is unlikely to impact largely on the turbulence statistics and is therefore termed 'inactive turbulence'. At the other end of the spectrum, wake-scale eddies are formed in the lee of individual stems with a length scale much smaller than the shear length scale (<<L_S). These vortices are usually Karman vortices shed due to flow separation around individual stalks. This 'fine-scale' turbulence plays a vital role in the development of the characteristic mean velocity profile through energy extraction, but is less significant within the turbulent energy budget as it is of a significantly small scale that it quickly dissipates away into heat.

Instead, the shear-scale active turbulence dominates the TKE budget within the canopy (Raupach *et al.*, 1996). These vortices are generated by the Kelvin-Helmholtz (K-H) instability mechanism (Ho and Huerre, 1984) as a result of the inflected velocity profile of the free shear layer. The initial instability develops into a series of waves which grow downstream before rolling up into vortices. The frequency at which these vortices are generated depends on the characteristics of the free shear layer; namely the momentum thickness (θ_M) and the mean velocity ($\overline{U}$) of the flow and is shown in Equation 2.2 (Ho and Huerre, 1984).

$$f_{KH} = 0.032\left(\frac{\overline{U}}{\theta_M}\right) \quad (2.2)$$

The momentum thickness is a measure of the thickness of the shear layer and the mean velocity is assumed to be the arithmetic mean of the two free stream velocities. Equation 2.2 is in fact a re-arrangement of the formula for the Strouhal

number, which is set equal to 0.032. This assumption follows from a linear stability analysis of the free shear layer instability, in which this value of the Strouhal number correlates with the most amplified wave, which in turn is associated with the natural frequency of the mixing layer (f_{KH}) (Ho and Huerre, 1984).

These Kelvin-Helmholtz instabilities evolve as they progress downstream, becoming distinct transverse Stuart roller vortices (Finnigan, 2000). In between these spanwise rollers, braid regions develop exhibiting high strain rates. Pairs of counter-rotating streamwise rib vortices form in these regions (Rogers and Moser, 1992) and interact with the roller vortices. Ambient turbulence within the flow then causes pairing of the roller vortices and the interaction between the pair's vorticity fields causes them to converge and rotate around one another (Finnigan *et al.*, 2009). Figure 2.2 shows a schematic of the process, which eventually leads to the development of pairs of head-up (H-U) and head-down (H-D) vortices.

This is a key theory as it links two prominent aspects of turbulence research within canopy flows: the development of Kelvin-Helmholtz instabilities and the occurrence of coherent sweep and ejection motions within the canopy. Following Lu and Willmart (1973), sweeps are defined as events with larger than average downstream velocity and smaller than average vertical (upward) velocity, and ejections as events with a smaller than average downstream velocity and a larger than average vertical velocity. They are explained in detail in Section 4.4.

Research into the occurrence of such sweep and ejection events within and above plant canopies predates the shear layer analogy and consequently the vortex work by over a decade. Maitani (1977) was one of the first authors to study the coherence of flow events, though not within the framework of sweeps and ejections. He studied the vertical kinetic energy flux, which is inherently correlated with the longitudinal and vertical velocity components. His results showed that, in contrast to results obtained in boundary layer experiments, downward energy fluxes were indeed dominant over vegetation canopies.

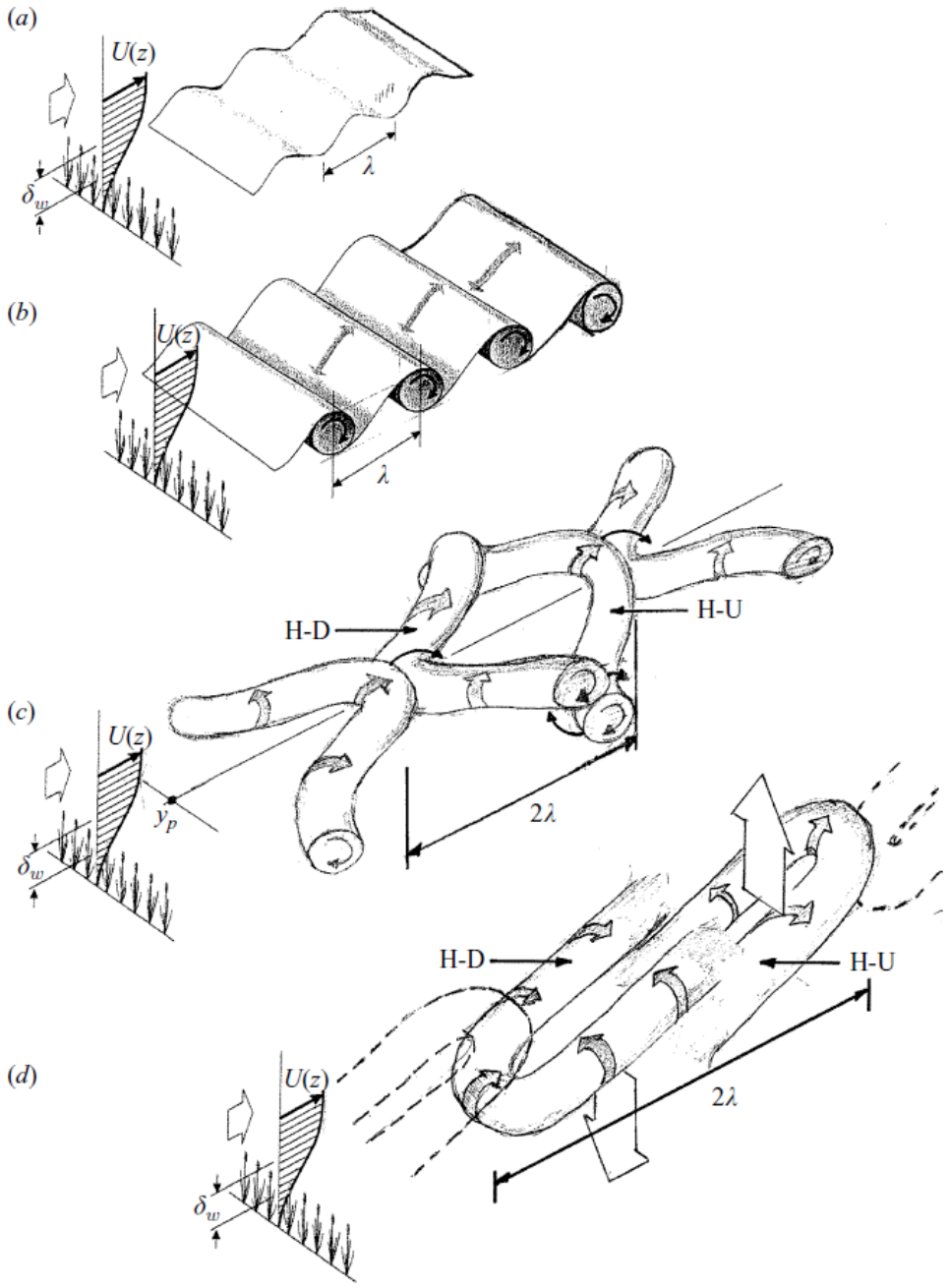

Figure 2.2: *Evolution of K-H vortices over vegetation (Finnigan et al., 2009). Figure shows (a) initial instability, (b) roll up into Stuart roller vortices, (c) vortex stretching and pairing and (d) pairs of H-D and H-U vortices, causing sweep and ejection events within the flow.*

Another study by the same author showed a significant positive and negative skew in the horizontal and vertical velocity probability distributions respectively (Maitani, 1979). This alludes to the presence of sweep motions above the canopy and a dominance of instantaneous downward momentum fluxes into the canopy.

This theory was confirmed by using conditional sampling to illustrate the dominance of sweeps/inrushes compared to ejections within the flow (Maitani, 1978). It was found that it was this imbalance which leads to a skewed non-Gaussian velocity distribution. Furthermore it was hypothesised for the first time that the inrush-ejection cycle played an important role in momentum and energy transfer (Maitani, 1978).

Finnigan (1979a) developed further the idea that the majority of the momentum transport is achieved by flow that is not representative of the mean flow. Instead, it is achieved as the result of intermittent, high momentum gusts (sweeps) which penetrate the canopy (Finnigan, 1979b). He found that within the canopy itself, the gusts (sweeps) and outward interactions were dominant, but that above the canopy, bursts (ejections) became more frequent. Moreover, Finnigan (1979b) was the first to link these sweep-ejection cycles to the passage of coherent eddies.

Kanda and Hino (1994) confirmed this link between coherent eddies and turbulent quadrant events through a model experiment, which illustrated the presence of sweep and ejections linked to the passage of inclined coherent vortices. Thus, in contrast to Finnigan *et al.* (2009) they hypothesised that sweep and ejection events are merely manifestations of the vortex within the velocity signal.

Much of the research above was conducted with vegetation of a simple form with little foliage. Within more complex canopies, there exist a number of other scales of turbulence relating to the different components of each plant. For example, foliage and leaves may generate turbulence of a different length-scale to any of the three mentioned above. However, due to its flexibility, foliage is most likely to reconfigure significantly, to produce turbulence with a length-scale more similar to that of the fine wake-scale turbulence than that of the canopy-scale, and it is therefore unlikely that the presence of foliage will contribute significantly to the large scale turbulence in terrestrial canopies.

Nevertheless it acts as a reminder that whilst the theory has been presented as uniform for all canopies, velocity profiles and turbulence statistics will naturally have a dependence on the plant form and biomechanics.

2.2.3 Plant response and interaction with the flow: The role of plant biomechanics

The first study to consider the effect of velocity fluctuations at the top of the canopy on its movement was that by Inoue (1955a). It was shown that the maximum longitudinal displacement of stalks correlated well with wind velocity and minimum surface drag. In a paired paper (Inoue, 1955b) the author also suggested a theoretical -7/3 power law for plant vibrations, but did not have the experimental data to test the theory.

However, by far the most influential impact of these two papers was the introduction of the concept of 'Honami', (from *ho*=cereal and *nami*=wave), which refers to the coherent wave-like movement of the canopy in response to velocity fluctuations. This is a term which has been used extensively in the literature since, and has also been adapted to 'monami' for the aquatic case (see Section 2.3.2).

Inoue (1955a) noticed that the waving of the canopy occurred at the natural frequency of the vegetation. This idea was reinforced by Maitani (1979), who observed a peak in the longitudinal velocity spectra at the natural frequency of the vegetation for wheat canopies. This raised an interesting question as to whether or not the vegetation canopy acts to modulate the velocity fluctuations, creating a feedback between the vegetation and the flow. He also found experimental evidence for the -7/3 spectral slope, as proposed by Inoue (1955b), for canopies of rush plants, which appeared to correspond to velocity fluctuations and downward momentum fluxes. In fact, this -7/3 trend corresponds to the spectral slope for pressure fluctuations in homogeneous turbulent flows (see George *et al.*, 1984 and references therein). This suggests that the plant motion is perhaps responding to the pressure signal rather than the velocity signal.

Finnigan (1979a) modelled the vegetation canopy response to the flow as a travelling wave equation (Equation 2.3), an approach that has been subsequently used by a number of different authors (e.g. Doare *et al.*, 2004; Py *et al.*, 2004). Here, $\xi(x,t)$ is the displacement of a stalk in the canopy from its rest position and is formulated as a function of the vibration amplitude ($\xi_0(x)$) and the wavelength (λ)

and frequency (f) of the stalk vibration. A useful quantity to define is the phase velocity ($\theta = \lambda f$) of the honami wave. These phase velocities are dependent on the velocity field and act as 'frozen histories' of the gust velocities.

$$\xi(x,t) = \xi_0(x) \exp\left(2\pi i \left(\frac{x}{\lambda}\right) - ft\right) \tag{2.3}$$

However, once the plants have begun vibrating, the stalks act to modulate the velocity fluctuations through aerodynamic drag (Finnigan, 1979a). Thus the canopy signal switches from velocity-driven to plant-driven, governed by the biomechanical properties of the vegetation. Therefore, the overall vegetation motion is determined by both wind and plant characteristics (Flesch and Grant, 1991). It is no surprise therefore that the strongest honami occurs when the wind velocity coincides with the natural frequency of the canopy (Raupach *et al.*, 1996).

As well as altering the velocity through drag, the waving plants are also the prime producer of pressure fluctuations at the canopy top whose frequencies correspond to the natural frequency of the stems (Finnigan, 1979b; Raupach and Thom, 1981). It is these pressure fluctuations, along with momentum transfer, that propagate the velocity waves (Finnigan, 1979a). These studies highlight the role of natural frequency and thus the biomechanical properties, such as flexural rigidity, in determining and characterising the interaction between vegetation and flow.

There are other, larger scale vegetation properties that can also affect the flow. Doare *et al.*, (2004) used a mass-spring model to highlight the importance of vegetation collisions within the canopy in controlling the plant response to velocity fluctuations. This can be characterised as a canopy property linked to the spacing of elements as well as the form of the individual plants. Vegetation spacing also determines the extent to which plants further within the canopy are sheltered from the flow (Raupach and Thom, 1981). This sheltering significantly reduces the drag experienced by the canopy.

2.2.4 Transport between the canopy and surface layer

One of the main motives for studying flow and turbulence over canopies has been to gain a better understanding of transport processes between the canopy and the open flow (Raupach and Thom, 1981). The transport of momentum, stress and energy is key in determining the transfer of scalars such as pollen and nutrients which can have a significant ecological impact.

It has long been known that transport within canopy flows is not, in the most part, achieved by the representative mean flow (Finnigan, 1979a), and neither can the transport of scalars be predicted using simple gradient-diffusion theory (Raupach, 1989). Instead, the majority of transport is intermittent (Finnigan, 1979b) and occurs as a result of coherent turbulent motions (Bergström and Högström, 1989; Gao *et al.*, 1989). Therefore, a good knowledge of turbulence is essential in understanding the transport of scalars (Wilson *et al.*, 1982). Thus, the transport of flow properties (momentum, stress and energy), and consequently scalars (heat, pollen and nutrients), is considered here with reference to the dominant turbulence mechanisms described in the preceding sections.

Shear-scale turbulence in the form of sweeps and ejections is the main driver of transport. Maitini (1978; 1979) found that over canopies, downward energy fluxes dominate, implying that turbulence is transported from the canopy top into the canopy due to the dominance of sweeps over ejections in this region. Similarly the main contributors to momentum transfer are sweeps, followed by ejections (Finnigan, 2000). In terms of stress, sweep and ejection events are particularly important as they both represent a net downward flux of stress (Raupach and Thom, 1981). Therefore, over canopies, where both sweeps and ejections outnumber the inward and outward interactions (which represent upward transport) stress will be transported predominantly into the canopy. Thus transport of the flow variables greatly outweighs production as a source term within the top part of the canopy (Dwyer *et al.*, 1997).

Within the canopy, momentum and scalar transport is driven by diffusion (Raupach and Thom, 1981) and wake-scale vortex dynamics. Here there is very little vertical

velocity gradient and consequently transport, and instead longitudinal diffusion dominates.

Two key variables which have not been discussed here are heat flux and the transport of water. While these are important in the terrestrial environment, they are not discussed as the ultimate focus of this thesis is aquatic canopies. Although heat flux can still be important it is not solved within the numerical schemes used in this study.

2.2.5 Energy mechanisms within the flow

The key process which drives the development of the canopy shear layer and the turbulent structure, governs transport processes and is also responsible for determining plant motion is the transfer of energy within the flow. There are three main energy transfer mechanisms which drive canopy flow: 1) the transfer of energy from the flow to the plant and vice versa, 2) the transfer of energy from the mean flow to turbulent flow and 3) the transfer of energy from turbulent kinetic energy into heat due to viscosity.

Mechanisms (2) and (3) describe the turbulent energy cascade described by Kolmogorov's (1941) -5/3 law, whereby energy is transferred from the mean flow, to large eddies, which then decay into much smaller scale vortices until eventually, at the molecular level, viscous effects cause the dissipation of energy into heat. The rate of decay with respect to frequency within the energy spectrum of a typical turbulent flow follows a -5/3 gradient in log-log space. This process is common to any turbulent flow, though the original method of turbulence production, and therefore dominant turbulent length scale, will vary.

Within canopy flows, as discussed in Section 2.2.2, there are three main scales of turbulence production: wake, mixing layer and boundary layer. Wake formation removes energy from the mean flow via drag, transferring it into small scale turbulence. Due to the size of these vortices, they quickly dissipate away into heat and therefore do not contribute significantly to the TKE budget, accounting for

roughly 10% of the total in-canopy turbulence (Seginer *et al.*, 1976). However, drag also acts on the turbulent flow and will therefore impact upon the TKE budget.

When large-scale, high energy, mixing layer or boundary layer turbulent structures interact with plant stems, the wake shedding process represents a transfer of energy within the turbulent energy spectrum, from the high wavenumbers to the much smaller-scale structures. This is a deviation from the traditional Kolmogorov (1941) spectrum, as the middle sections of the spectrum are bypassed. This phenomenon has been termed a 'Spectral shortcut' (Finnigan, 2000).

Stem-scale drag also transfers energy from both the mean and the turbulent kinetic energy budgets into plant strain energy, depending on the local flexural rigidity of the plant. For a rigid stem, no energy will be converted into strain, whereas for a flexible plant, a significant portion of the energy will be transferred to the plant, as potential energy. Once the vortex passes and the ambient velocity is lower, the plant then releases the stored elastic potential energy through rebounding to its initial position. In doing so, the plant moves against the flow, causing drag and therefore the transfer of energy into wake-scale turbulence. It is this process which acts to dampen the plant oscillations.

Thus, for all canopies, whether rigid or flexible, drag acts as the major driver for energy transfer within the flow. Counteracting the drag force is the flexural rigidity of the vegetation. These forces control both the magnitude of energy exchange and the proportion converted to both plant potential energy and turbulent kinetic energy. This force balance is discussed further in Sections 2.3.2 and 2.6.

2.3 Flow structure and processes in aquatic canopies

The study of flow structure in aquatic canopies evolved out of terrestrial observations and in many cases the terminology and ideas are borrowed from the literature outlined above. The two environments do, however, present very different problems, and therefore must be seen as distinct cases. Here, the

characteristics of aquatic canopies are discussed, followed by analysis of the key differences between aquatic and terrestrial canopies.

2.3.1 Velocity and turbulence characteristics

One of the first studies of flow structure within an aquatic environment was undertaken by Ackerman and Okubo (1993). They conducted experiments on marine eelgrass canopies and observed low frequency velocity fluctuations evidenced by movement of the vegetation canopy. They noted that these velocity fluctuations did not correlate with any surface generated waves or with ambient turbulence, suggesting the existence of a canopy shear layer, analogous to a mixing layer, as the primary driver of the motion.

Grizzle *et al.* (1996) also worked on marine sea grasses, and discovered particular velocity fluctuations within the flow, whereby regions just above the canopy would experience a sudden drop in velocity, accompanied by an increase in velocity immediately above and below. This suggested the presence of spatially coherent vortices within the flow, though the exact cause for these patterns was not hypothesised by the authors.

Ikeda *et al.* (1996) were the first to provide quantitative evidence of the inflected velocity profile above aquatic canopies. This result is not surprising given results in terrestrial canopies, and consequently little attention has been given within the aquatic literature to the mean velocity profile itself. However, Nezu and Sanjou (2008) did characterise the velocity profile into three regions based on previous experimental studies. They define the emergent zone, the mixing zone and the log law zone as shown in Figure 2.3.

The emergent zone is the zone closest to the bed where the flow is pressure driven, mechanical turbulence production dominates and therefore the flow profile is constant (Nepf and Vivoni, 2000). The mixing zone is characterised by an inflection in the velocity profile and is dominated by the large shear-scale vortices which are discussed below. The log law zone describes the region above the canopy top, where the flow profile is logarithmic (Lopez and Garcia, 2001) as in a boundary layer,

however in reality this is unlikely to occur in canopies with a low submergence depth.

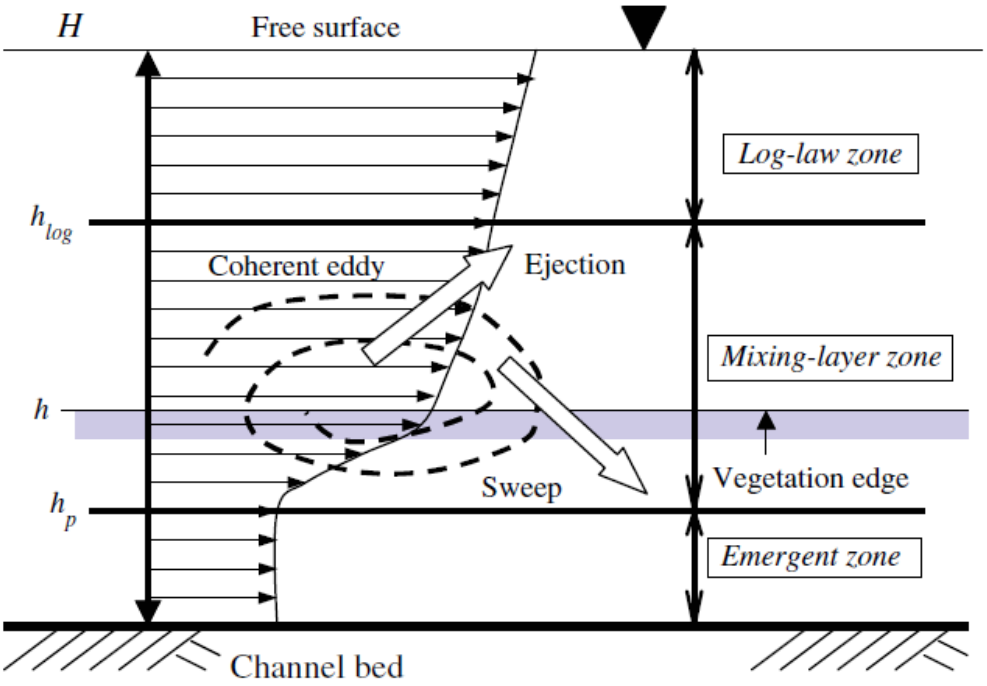

Figure 2.3: *Schematized flow model for aquatic canopy flow (Nezu and Sanjou, 2008). Here the heights h_p and h_{log} delimit the 3 zones. The cause of sweep and ejection events is also hypothesised as relating to the passage of shear-scale eddies.*

Ikeda *et al.* (1996) were also the first to provide quantitative evidence of coherent vortices over aquatic canopies. They observed pairs of counter-rotating elliptical K-H vortices, centred slightly above the canopy, moving downstream at a speed greater than the mean flow. These vortices were inclined downwards towards the front and were preceded by a strong upward motion. Evidence of these inclined vortices was also found by Ghisalberti and Nepf (2006).

These K-H vortices generate through the shear instability (Nezu and Onitsuka, 2001). As they evolve (see Figure 2.4), the height of the vortex centre increases due to the canopy drag, and they also expand with distance and time (Ghisalberti and Nepf, 2002). However unlike free shear layer vortices, vegetated shear layer vortices only grow to a finite thickness (Ghisalberti and Nepf, 2006). Vortex growth stops when turbulent energy production equals dissipation (Ghisalberti and Nepf, 2004) and this equilibrium can be estimated by balancing shear production and canopy

dissipation, under the assumption that the other terms in the budget are negligible (see Nepf *et al.*, 2007).

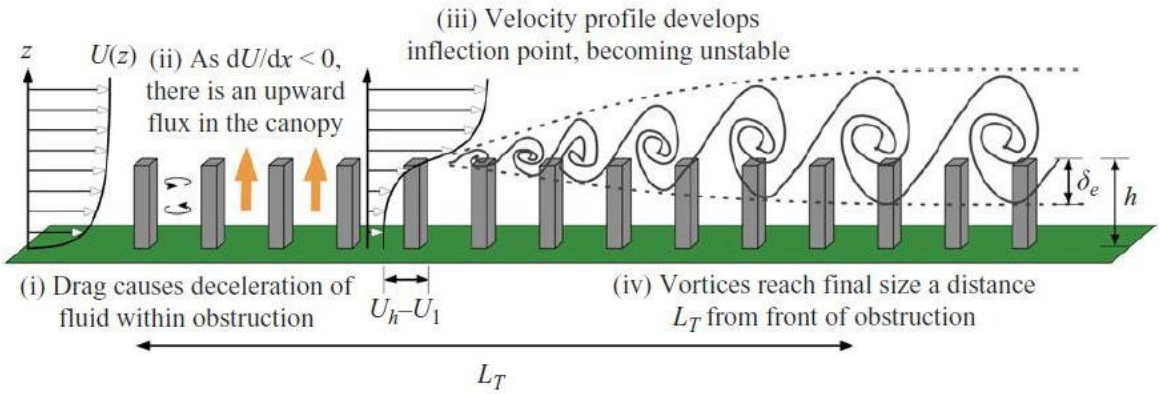

Figure 2.4: *Development and evolution of vortices within aquatic flows (Ghisalberti, 2009).*

As with the terrestrial case, alongside the discovery of these coherent turbulent structures, there has been a considerable amount of research into the presence of sweep and ejection events over the canopy top. Ghisalberti and Nepf (2006) observed a sweep-ejection cycle consisting of a strong sweep followed by a weak ejection. They hypothesised that the reason for the weaker ejection was energy loss during the sweep stage due to vegetation drag. They also found that statistically, sweeps dominate ejections in the canopy, with the pattern reversed above the canopy. These results have been confirmed by Maltese *et al.* (2007).

The shear-scale K-H vortices appear to be responsible for the sweep and ejection events observed at the canopy top. Okamoto and Nezu (2009) noted the periodical nature of sweeps and ejections at the canopy top, suggesting they corresponded to the front and back ends of vortices. Working in lateral canopy shear layers, White and Nepf (2007) noted that sweeps are key to vortex production, with ejections occupying a smaller yet significant role as a transport mechanism. Finally, Nezu and Sanjou (2008) note that inward and outward interactions diminish near the canopy top, suggesting an increase in coherence, observed as the passage of K-H vortices. Thus it is clear that the two key observable properties of shear-scale turbulence, namely turbulent quadrant events (sweeps and ejections) and mixing layer vortices are mechanistically linked. However, the nature of this link and interdependence within aquatic flows is not yet fully understood.

As well as the shear-scale turbulence, there are a number of other length scales of turbulence within the canopy. Nikora (2010) identifies six distinct turbulence scales, as shown in Figure 2.5. Using the Nikora numbering system, the different scales sit within three broad turbulence regimes: boundary layers (1 & 3), mixing layers (2 & 4) and wakes (5). Plant flapping (6) does not fit naturally into any of these regimes, but in reality is most likely to be caused either by a mixing layer instability or by wake vortex shedding similar to a flapping flag (e.g. Zhang *et al.*, 2000; Connell and Yue, 2007). This mechanism of turbulence production is of great interest as it is likely to be closely related to the plant form and will therefore vary across different plant types.

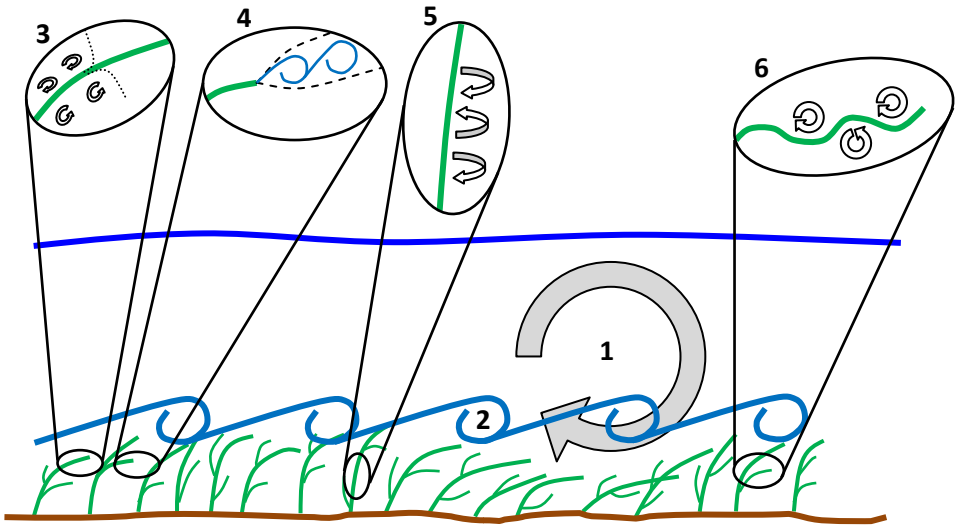

Figure 2.5: *Six scales of turbulence within vegetated channels, adapted and redrawn from Nikora (2010).*

Although all six scales are likely to be present within canopy flows, the most dominant scales are likely to be the depth-scale boundary layer, the shear-scale mixing layer and the stem-scale turbulence (whether that be wakes or mixing layers). It is suggested that it would be unlikely that, in any experimental setup, vortices originating from the steam/leaf scale boundary layer would ever be identified.

2.3.2 Plant response and interaction with the flow

Ackerman and Okubo (1993) were the first to analyse plant motion within aquatic canopies. With a backdrop of the previous work done in terrestrial canopies, coherent movement of the canopy was one of the benchmark characteristics they used to investigate whether aquatic canopies behaved similarly to terrestrial canopies. In fact, in the earliest aquatic studies, where velocity measurements were few, coherent moving of the canopy was used as the primary evidence of vortices within the flow.

Due to the observed similarities between the aquatic and terrestrial waving of vegetation, Ackerman and Okubo (1993) named the aquatic phenomenon 'monami' (from honami). Working within a very similar setup, Grizzle *et al.* (1996) also observed synchronous waving of the canopy. They also noted the existence of a clear threshold velocity below which coherent waving did not occur. This suggests that the coherent flapping is a response of the vegetation to flow of a particular magnitude, potentially related to the natural frequency of the vegetation.

Similar to the terrestrial case, evidence has been found of a feedback effect on the velocity field caused by the vegetation. Ikeda *et al.* (1996) found that flow at the top of the canopy appeared to have been modulated by the vegetation motion, as the flow exhibited a -7/5 power spectrum, rather than the standard -5/3 Kolmogorov turbulent spectrum. However, this figure differs substantially from the figure of -7/3 associated with plant motion, observed on occasions in both terrestrial and aquatic canopies (e.g. Inoue, 1955b; Maitani, 1979; Ikeda *et al.*, 1995).

The spectrum of plant motion in response to the flow can be broadly categorised into four distinct regimes. These are erect, gently swaying, monami (coherently waving) and prone (Kouwen and Unny, 1973; Nepf and Vivoni, 2000). The regime of motion observed for a particular canopy will be determined by the vegetation biomechanics as well as the flow velocity. While these regimes could also be used for the terrestrial case, aquatic plants tend to have greater flexibility leading to a greater range of plant motion (Nepf and Vivoni, 2000).

In reality, flexible aquatic canopies under normal conditions will experience either gently waving or coherently waving canopies. As first noted by Grizzle *et al*. (1996), there is a clear velocity threshold between these two regimes, and this threshold value changes with flexural rigidity (Ghisalberti and Nepf, 2006).

One of the key challenges in conducting experiments with simple artificial vegetation is making sure that the findings are applicable to real aquatic vegetation, which exhibits a wide range of forms. Wilson *et al.* (2003) addressed the issue of scaling biomechanical properties between real and artificial plants. They noted the huge difficulty in comparing the biomechanical properties of very different materials. In particular, flexural rigidity can be difficult to measure and scale as the artificial stems will most likely have constant rigidity, whereas in real stems, this will vary considerably along the stem. Nevertheless, it has been shown that shear instability characteristics appear to generalise over a range of flexibilities (Ghisalberti and Nepf, 2002; Velasco *et al.*, 2003) and therefore flume experiments with artificial vegetation represent valid contributions to theory over natural canopies.

Ghisalberti and Nepf (2002) used prototype vegetation, and found good agreement between monami frequencies and predicted mixing layer instabilities. They defined monami as the observed downstream progression of plant deflection due to high vortex velocities. In a different study, the same authors identified a lag time between vortex passage and plant motion (Ghisalberti and Nepf, 2006). This suggests that the vegetation has an active role in controlling the monami characteristics and therefore the feedback with the flow.

Okamoto and Nezu (2009) also conducted a series of experiments with artificial vegetation. They observed that when monami was present, the oscillating canopy absorbed significantly more momentum than the rigid vegetation canopy, thus regulating the turbulence at the canopy top. This momentum absorption can also be enhanced by the presence of foliage. Foliage can represent a significant increase in momentum absorbing area (MAA) and despite increasing the drag force, it also inhibits momentum exchange, reducing in-canopy velocities (Wilson *et al.*, 2003).

In response to the drag force acting on canopies with foliage, reconfiguration commonly occurs. Here, streamlining of the plant foliage is more important in terms of drag reduction than stem bending (Jarvela, 2002) and represents a significant reduction in form drag. This can occur at a range of scales from the leaf scale right through to the patch-scale (Albayrak *et al.*, 2011). Two important parameters which govern reconfiguration are the Cauchy number (Ca) and Buoyancy number (B) (Nikora, 2010; Luhar and Nepf, 2011) which describe the force ratios between the drag and rigidity, and buoyancy and rigidity forces respectively.

$$Ca = \frac{1}{2}\frac{\rho C_D w_b U^2 {l_b}^3}{EI} \tag{2.4}$$

$$B = \frac{\Delta\rho g w_b t_b {l_b}^3}{EI} \tag{2.5}$$

Here, t_b is the blade thickness, l_b is the length of the blade, w_b is the blade width, C_D is the drag coefficient and EI is the flexural rigidity.

Similar to the terrestrial case, larger scale vegetation properties can also affect the overall flow regime. The shear region within canopy flows is caused by a bulk drag discontinuity (Nepf *et al.*, 2007). The term $C_D ah$ is often used to categorise the scale of the drag discontinuity, where C_D is the drag coefficient, a is the frontal area per volume and h is the canopy height. While C_D and h represent a dependence on the individual plant form (e.g. foliage and length), a represents a dependence on a patch-scale property (e.g. stem density).

Nepf and Ghisalberti (2008) note that the velocity inflection point which governs the entire canopy flow only exists for canopies with $C_D ah > 0.1$. Furthermore, stem density controls the turbulence regime within the canopy. For canopies with $C_D ah > 0.3$, shear-scale turbulence cannot penetrate into the canopy and therefore the entire canopy is dominated by stem scale vortex shedding.

Similarly, hydraulic resistance is directly linked to the term *MEI* (Wilson *et al.*, 2003), where *M* is the stem density and *EI* is the flexural rigidity. This represents another feedback between the flow and vegetation, as *MEI* alters with streamlining.

Thus plant biomechanics not only modulate the velocity field at the top of the canopy, they are also vital in characterising the flow profile throughout the entire flow depth, and in determining transport between the canopy and the open flow.

2.3.3 Transport and energy mechanisms within the flow

Within canopy flow, momentum transfer characteristics are responsive to both flow configuration and vortex organisation (Velasco *et al.*, 2003). The canopy itself can be split into two vertical regions, one of rapid exchange and one of slower exchange (Nepf and Vivoni, 2000). The height of the boundary between these two zones marks the point at which the shear-scale vortices no longer penetrate into the canopy. The lower zone is therefore characterised by transversal stresses related to stem-scale turbulence, whereas the upper zone is dominated by vertical Reynolds stresses caused by the shear-scale turbulence (Nepf and Vivoni, 2000; Nepf *et al.*, 2007).

Wake driven transport results from the pressure distribution around each stem, described in terms of the pressure coefficient (see Section 3.7.1 for further discussion of the pressure coefficient). Upstream of the obstacle, the pressure coefficient is equal to 1, and therefore stagnation occurs and downward flow is created due to the vertical gradient in longitudinal velocity (Nepf and Koch, 1999). In contrast, downstream of the obstacle, the pressure coefficient is negative, leading to upwards flow. This flow controls the availability and distribution of potentially sediment and nutrient rich water from the bed, and therefore has implications for biological function within the canopy (Nepf and Koch, 1999).

Vortex driven momentum transport is an order of magnitude higher than wake driven transport (Ghisalberti and Nepf, 2006), and therefore the upper region experiences much faster renewal. Ghisalberti and Nepf (2009) found that within this upper zone, coherent vortices generate up to 80% of the momentum transport between the canopy and the open flow. They also noted that because of the nature of the K-H vortices, this transport process is both highly periodic and spatially non-uniform. Furthermore, the study found that rates of mass transport were three times higher than momentum transport rates. This reinforces the analogy with the

mixing layer, where this is also the case (Raupach *et al.*, 1996). This also has implications for scalar transport, which will most likely follow the same rates as mass transport, although scalar transfer has yet to be investigated.

The impact of monami on transfer has also recently been investigated. Ghisalberti and Nepf (2009) found that monami causes the canopy to behave in a similar manner to that of a sparser canopy, increasing vertical transfer and therefore causing greater flushing. They found that residence times within the canopy were four times greater for non-flexible canopies. However it has also been noted that waving vegetation decreases the stress peak at the canopy top and therefore reduces momentum transport by up to 40% compared to rigid canopies (Ghisalberti and Nepf, 2006). The decrease in stress at the canopy top leads to weaker vortices and hence less efficient exchange (Nepf and Ghisalberti, 2008).

Intuitively, as vortices govern mass and momentum exchange, they are also responsible for the transport of suspended sediment (Okamoto and Nezu, 2009). Therefore knowledge of vortex driven exchange is central to river management. At the heart of understanding vortices are the energy mechanisms within the flow.

The energy mechanisms within aquatic flows are largely similar to those found within terrestrial canopies, however aquatic flows are bounded (depth-limited) and this usually prevents the production of large boundary layer vortices. Therefore, whereas in terrestrial canopies, an important mechanism is the interaction between boundary layer vortices and K-H vortices, in most shallow aquatic flows K-H vortices dominate the flow (Nepf and Ghisalberti, 2008).

Thus the three dominant turbulent length scales become stem, shear and water depth scale (White and Nepf, 2007). The shear length can be related to the drag discontinuity $C_D a^{-1}$ which characterises the inflection point in the velocity profile.

The stem-scale drag mechanism is largely similar to that of the terrestrial canopy case, where energy is extracted from both the mean and turbulent kinetic energy and converted to smaller scale turbulent kinetic energy, before dissipating into heat. The fraction of energy which is converted by the vegetation into turbulent kinetic

energy depends on the ratio of form and viscous drag, which in turn is dependent on the plant morphology and biomechanics as well as the flow velocity (Nepf, 1999). Similarly, within a canopy, drag values can be affected by the impact of upstream separation and wakes (Ghisalberti, 2009).

Thus the driver of all the canopy scale turbulence (both stem and shear scale) is the magnitude of the drag force. Therefore, it is imperative that the drag be calculated accurately to ensure a correct understanding of the turbulent flow regime. This issue is discussed further in Section 3.7.

2.3.4 Key differences between terrestrial and aquatic canopies

In comparing terrestrial and aquatic canopies, there are two key differences which have emerged in this review. The first is the depth-limited nature of aquatic canopy flows. The major impact of this is to alter the turbulent spectrum, increasing the dominance of K-H vortices within the turbulence regime (Nepf and Ghisalberti, 2008). A subsequent impact is that in particular cases, with very small submergence depth, there is limited development of a shear layer at the canopy top, and the mixing layer is not symmetrical.

The second is the significant difference in plant form and biomechanics. One of the major drivers of difference in plant form and biomechanics is density. Whereas terrestrial vegetation is universally denser than the fluid it resides in, many aquatic species have a lower density than the surrounding fluid and thus are positively buoyant (Luhar and Nepf, 2011), creating a very different force balance. While terrestrial vegetation relies upon high flexural rigidity to counteract gravitational forces (in order to grow and reach sunlight in a competitive environment), this is much less of an issue in aquatic canopies where buoyancy can, to a certain degree, control the plant position. Rigidity can still be important and there are examples of aquatic plants which have relatively high rigidity (e.g. reeds, grasses) however these tend to be emergent plants. The majority of submerged macrophytes exhibit a low flexural rigidity. Therefore aquatic plants can be split into two main types: those

which are highly flexible and are controlled predominantly by tensile forces, and those which are more rigid and are controlled by bending forces (Nikora, 2010).

In the former category, in particular, buoyancy will act as a major control on plant position, acting against drag. Thus, the force balance is notably different to the terrestrial case where gravity acts predominantly in the same direction as drag. This has important implications for modelling aquatic canopies as distinct from terrestrial canopies.

Another result of lower flexural rigidity is an increased ability to reconfigure. As mentioned above, reconfiguration is a key element in reducing drag. Aquatic vegetation must find a balance between drag reduction and photosynthetic capacity (Albayrak *et al.*, 2011; Bal *et al.*, 2011). Aquatic vegetation commonly has substantial foliage with a large surface area to enable light capture. However, plant survival within a high drag environment is dependent on morphological adaptations and streamlining to prevent uprooting or physical damage (Sand-Jensen, 2003). Aquatic plants can experience a drag force 25 times larger than terrestrial plants, for a given velocity (Denny and Gaylord, 2002), so a plant's ability to reconfigure is crucial as it enables it to become more streamlined, reducing the form drag exerted on it.

Finally, terrestrial research has predominantly been undertaken over forest/tree canopies and simple crop canopies. Aquatic macrophytes generally present a more complex form and also encompass a range of forms within themselves. It is likely that the flow regimes, and in particular turbulence characteristics, will reflect that.

One notable difference in form is that many aquatic plants adopt a horizontal position within the flow, which is a departure from the idealised canopy structure used within terrestrial canopies and many aquatic experiments. This is likely to affect the dominant mechanisms of turbulent production. Here, plant-flapping-scale turbulence may become significant (see Section 2.7.2)

2.4 Numerical representation of open channel flow

Fluid and continuum mechanics describes an extensive field of research, one that has developed over many centuries and with an extensive literature. This section presents an overview of key ideas with respect to a subset of this literature and concerning open channel flow. Section 2.5 then introduces the concept of incorporating vegetation into models of fluid flow. This section begins with the three dimensional physics of flow, and then progresses through to the more simplified models used within river management models.

Water can be described as an incompressible, Newtonian fluid. This implies that viscosity and density can both be considered constant, within the temperature limits observed in natural channels, providing the water does not change state. Models of fluid flow also rely upon the assumption that fluid can be considered as a continuum (Tritton, 1988) and thus Newton's laws are considered in an Eulerian form (Lane, 1998; Pope, 2000). Finally, natural flows are viscous and typically turbulent. Turbulence is hard to define, but is observed as the presence of multi-scale unsteady fluctuations within the flow, which behave in an apparently chaotic manner (Tennekes and Lumley, 1972; Davidson, 2004; Lesieur, 2008). Here, the term 'chaotic' is used in the deterministic, mathematical sense, indicating an apparently random process with underlying organisation (Devaney, 2003).

In order to characterise the turbulent nature of a flow, the Reynolds number (Equation 2.6) is used. The Reynolds number is non-dimensional, and is the ratio of inertial to viscous forces. Flows with $Re < 500$ are classified as laminar, and flows with $Re > 2000$ are considered fully turbulent while flows in between are considered transitional flows (Graf, 1998). The Reynolds number is important to quantify as key forces such as drag exhibit a Re dependence (Panton, 1984).

$$Re = \frac{UR_h}{\mu} \tag{2.6}$$

Another useful quantity when analysing flow is the Froude number (Equation 2.7), which is defined as the ratio of the inertial to gravitational forces and determines the behaviour of the flow in response to the relative dominance of the internal forces. The Froude number can be used to define subcritical ($Fr < 1$) and supercritical flows ($Fr > 1$). This is a key distinction to make as it will impact on model suitability and free surface approximations (Section 3.2.4).

$$Fr = \frac{U}{\sqrt{gA/w}} \tag{2.7}$$

Fluvial open channel flows are predominantly shallow (Jirka and Uijttewaal, 2004) and therefore the effects of topography (and by extension, vegetation) extend throughout the flow depth (Lane *et al.*, 2005). The effects of the topography are two-fold. First, the topography represents a no-slip channel boundary, exerting friction on the flow. A no-slip condition states that for a viscous flow, the fluid will have zero velocity relative to the boundary at the interface with the boundary (Anderson, 1984). Secondly, the topography represents a physical blockage protruding into the flow. This will cause flow separation, generation of turbulent structures within the flow and consequently momentum loss. Therefore, accurate representations of topography and vegetation are vital elements of any model used to predict channel flow.

However, models are limited by spatial resolution and therefore require discrete sampling of the continuous bed surface and vegetation interface. Thus, some of the topography and vegetation will always be 'sub-grid' or 'sub-scale' and must be represented through roughness parameters rather than explicit representation. Here, the merit of this parameterisation is considered at a range of scales and dimensions.

2.4.1 The Navier-Stokes Equations

The Navier-Stokes equations (Equations 2.8 and 2.9) are a set of mass and momentum conservation equations for, in the simplest case, incompressible and

Newtonian fluids (Hinze, 1975; Ingham and Ma, 2005). They can be written in a number of different formulations; here the Einstein summation convention is used.

$$\rho\left(\frac{\partial u_i}{\partial t}+u_j\frac{\partial u_i}{\partial x_j}\right)=-\frac{\partial p}{\partial x_i}+\mu\left(\frac{\partial^2 u_i}{\partial x_j \partial x_j}\right)+F_i \qquad (2.8)$$

$$\frac{\partial u_i}{\partial x_i}=0 \qquad (2.9)$$

where ρ is the fluid density, μ is the dynamic viscosity, p is the pressure, u_i is the velocity component in the x_i direction and F_i represents additional forces on the flow. Equation 2.8 ensures momentum conservation and Equation 2.9 represents mass continuity. The existence and smoothness of these equations has yet to be solved analytically even for the simplest flows (Moin and Mahesh, 1998). However, they are still extremely useful as the basis for modelling three dimensional turbulent flows, and they can be solved numerically in a variety of ways.

2.4.2 Direct numerical simulation (DNS)

The most accurate method for solving the Navier-Stokes equations is to solve them fully, resolving all turbulent scales down to the smallest scales at which energy is dissipated into heat by molecular forces (Sotiropoulos, 2005). Here, blockages which are greater than the grid size are explicitly represented in the model as no-slip boundary conditions. Due to the nature of the simulation, this grid size is typically very small and therefore captures all the elements that would constitute roughness in a river. This is a promising method which has been used for a variety of fundamental flow problems such as boundary layer flow (Spalart, 1988; Na and Moin, 1998), plane channel flow (Kim *et al.*, 1987), flow over a step (Le *et al.*, 1997) and flow over simple dunes (Shimizu *et al.*, 2001). However, at present it is still impractical for most environmental purposes due to the computational cost, particularly for simulations which exhibit a large range of turbulent scales (Moin and Mahesh, 1998; Ingham and Ma, 2005).

Instead, the equations must be partially solved, with the help of a modelled component. There are two main methods for doing this, which are now discussed.

2.4.3 The Reynolds averaged Navier-Stokes equations

The Reynolds-averaged Navier-Stokes (RANS) equations are formulated by decomposing the velocity signal into two components: a time-mean component, averaged over a certain time period, and an instantaneous fluctuating component (Reynolds, 1895).

$$u_i = \bar{u}_i + u_i' \tag{2.10}$$

This decomposition can then be substituted back into the Navier-Stokes equations. After applying ensemble averaging the equations become

$$\frac{\partial \bar{u}_i}{\partial t} + \bar{u}_j \frac{\partial \bar{u}_i}{\partial x_j} = -\frac{1}{\rho}\frac{\partial \bar{p}}{\partial x_i} + \frac{1}{\rho}\frac{\partial}{\partial x_j}\left(\mu \frac{\partial \bar{u}_i}{\partial x_j} - \rho\overline{u_i' u_j'}\right) \tag{2.11}$$

$$\frac{\partial \bar{u}_i}{\partial x_i} = 0 \tag{2.12}$$

In Equation 2.11 all the terms are now expressed as average quantities, except for the final term, which is called the Reynolds stress, and involves terms originating from the product of the different fluctuating velocity components. There is no direct way of calculating these terms (Lane, 1998), and therefore in order to solve the equation for the mean flow, an approximation for the Reynolds stress is required. This is provided by turbulence closure models, which are discussed in detail in Section 3.2.2.

Nevertheless, using closure models, these equations provide a method of calculating mean velocities and turbulence quantities in three dimensions at a high spatial resolution. Within the RANS models, roughness and resistance are incorporated in two different ways. Firstly, large roughness elements and blockages are explicitly represented within the numerical grid and are therefore accounted for through no-slip boundary conditions, provided at the interface between the fluid and the solid boundary, similar to the DNS case. However, in order to avoid the high computational cost of solving the flow near this boundary condition explicitly, a wall function is often used instead. These functions are based an approximation of the flow close to the boundary, which is usually based on the assumption of the

logarithmic law of the wall, described in Section 2.4.8. Smaller, sub-grid blockages are accounted for within the roughness height specified in the law of the wall framework. Here the roughness must account for the viscous drag at the surface as well as the form drag induced by sub-grid topography (Hardy *et al.*, 2005).

RANS models have been applied to a range of problems within fluvial geomorphology including channel confluences (Weerakoon and Tamai, 1989; Bradbrook *et al.*, 1998), channel bifurcations (Hardy *et al.*, 2011), meander bends (Hodskinson and Ferguson, 1998; Ferguson *et al.*, 2003), pools and riffles (Booker *et al.*, 2001) and flow through vegetation (see Section 2.6).

2.4.4 Large eddy simulation

While RANS modelling can predict the mean velocity and turbulence characteristics, it is unable to provide the time-dependent results, that are necessary for fully analysing the dynamics of turbulence. Unsteady versions of the RANS equations have been developed (URANS) which can resolve variations greater than the integral timescale (i.e. variations in the mean flow but not the turbulent flow), however they still fail to resolve turbulence over a range of scales smaller than the integral timescale (Keylock *et al.*, 2005). This is a severe limitation in applications where the turbulent flow field is of most interest.

Large eddy simulation (LES) provides an alternative method to the RANS equations, whereby the signal is filtered into a resolved scale and an unresolved scale, based on a spatial filter. This allows a far greater range of turbulent length scales to be resolved, and only the small scales, which are less likely to be affected by boundary conditions are modelled (Rodi, 1997). These scales of motion are modelled using a sub-grid model. Section 3.2.2 describes the most common sub-grid scale models in detail.

Similar to RANS models, sub-grid scale blockages and roughness at the solid boundaries must still also be modelled using an approximation. Due to the additional turbulence resolution within LES, a finer grid may be used at boundaries in order to resolve the majority of scales of turbulence, thus restricting the use of

the wall functions to a much smaller scale. However, this is not always a realistic option when modelling large distances downstream, and therefore, where the boundary flow is not of particular interest, wall functions are used (Ingham and Ma, 2005).

LES has also been used extensively within fluvial geomorphology to investigate problems such as channel confluences (Bradbrook *et al.*, 2000; Constantinescu *et al.*, 2011), flow over gravel beds (Hardy *et al.*, 2007), flow in pool and riffle sequences (Stoesser *et al.*, 2010) and flow through rigid vegetation (see Section 2.6).

2.4.5 Dimensionality and process representation

Model choice always involves a trade-off between process representation and simplicity and must be informed by the requirements of the study in combination with the computational limitations at the scale of interest (Lane *et al.*, 1999). Whilst LES may be more accurate, it is sometimes considered to be too computationally expensive, particularly in modelling the boundary layer (Spalart, 2008). A number of hybrid models have been developed which seek to combine the resolution of LES and the computational efficiency of RANS models. One example is detached eddy simulation (DES) which uses LES in key areas of detached turbulence, but the simplified RANS model throughout the rest of the domain and particularly near boundaries (Spalart, 2008).

However, for many engineering and management applications any three-dimensional model, even RANS modelling, will be too computationally expensive and may not be necessary. In this case, models of lower dimensionality must be used. These inherently involve averaging in one or more dimensions, thus losing significant process representation, however enable modelling on a much larger scale.

2.4.6 The Saint-Venant equations

The St. Venant (or shallow water) equations, derived from the Navier-Stokes equations by averaging in one or more dimensions, provide a depth-averaged simplification particularly pertinent to environmental flows (Wright, 2005). In

addition to the depth-averaged two-dimensional formulation (Equations 2.13-2.15), they may be simplified further by averaging in the cross-stream dimension to provide a one-dimensional model.

$$\frac{\partial h_w}{\partial t} + \frac{\partial (h_w u)}{\partial x} + \frac{\partial (h_w u)}{\partial y} = 0 \tag{2.13}$$

$$\frac{\partial h_w u}{\partial t} + \frac{\partial}{\partial x}\left(u^2 h_w + \frac{g h_w^2}{2}\right) + \frac{\partial}{\partial y}(uv h_w) + S_f = 0 \tag{2.14}$$

$$\frac{\partial h_w v}{\partial t} + \frac{\partial}{\partial x}(uv h_w) + \frac{\partial}{\partial y}\left(v^2 h_w + \frac{g h_w^2}{2}\right) + S_f = 0 \tag{2.15}$$

These equations are obtained by integrating the Navier-Stokes equations throughout the flow depth (h_w) to give the new mass and momentum equations. The formulation shown here is the inertial form whereby convective acceleration is ignored (Bates *et al.*, 2010). Here S is the friction slope which represents the rate at which energy is lost due to friction.

These equations, in both one- and two-dimensional form have been used extensively within reach-scale management models (e.g. ISIS, MIKE11, LISFLOOD, HEC-RAS) and enable accurate prediction of flow across large domains. However, while this is still a sophisticated and physically accurate flow model, all of the flow resistance terms are now grouped into a bulk resistance term (S_f). This term must account for the effects of both bed and vegetative friction and is typically calculated using a bulk flow model approximation which is often empirically based and lacks local accuracy (Lane and Hardy, 2002).

2.4.7 Bulk flow model

As discussed in the previous section, the simplification of the Navier-stokes equations into the St. Venant equations requires a parameterisation of the effects of friction on the flow. There have been numerous suggestions of different methods for predicting this roughness term (or friction slope), the most prominent being those of Manning, Chezy and Darcy-Weisbach. All of these equations follow the same general form (Equation 2.16) whereby the friction slope is given as a

function of velocity (U), hydraulic radius (R), which is calculated as the ratio between the channel cross-sectional area and the wetted perimeter, and a roughness coefficient (K). The exponents within the equation (a_1, a_2, a_3) vary between the three formulae. Discussion here will therefore be limited to those 3 models, though it is noted that a wide variety of similar equations exist.

$$S_f = \left(\frac{U^{a_1}\mathrm{K}}{{R_h}^{a_3}}\right)^{a_2} \tag{2.16}$$

As well as providing friction approximations for use within other models such as the shallow water equations, bulk models themselves can be re-arranged to solve for velocity, given prior knowledge of the roughness coefficient. These represent highly simplified flow models which assume steady, uniform flow; in other words, flow with no spatial or temporal acceleration. The flow is considered to be one dimensional and laminar, with a single representative velocity (as shown in Figure 2.6). Resistance (or roughness) is therefore modelled as a retardation of the bulk flow.

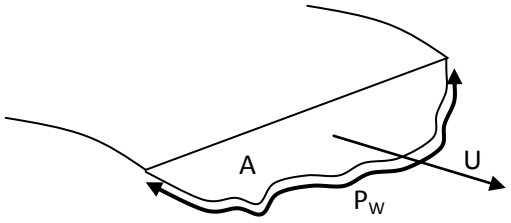

Figure 2.6: *Example of simple channel flow model, where A is the cross-sectional area, P_W is the wetted perimeter and U is the downstream velocity.*

The most commonly used resistance formula is Manning's equation (Equation 2.17). Under the assumption of steady, constant-depth flow, the friction slope can be equated to the water surface slope, which in term can be equated to, *S,* the bed slope (De Doncker *et al.*, 2009).

$$U = \frac{1}{n} R_h^{\frac{2}{3}} S^{\frac{1}{2}} \tag{2.17}$$

This equation was formulated as a correction to the Chezy formula (Equation 2.18) as experience showed that *C* (the Chezy roughness coefficient) exhibited a dependence on flow depth (Ferguson, 2010).

$$U = C(R_h S)^{\frac{1}{2}} \tag{2.18}$$

Thus, in Manning's formulation, the roughness coefficient is invariant with stage, enabling a reach-scale value to be used across a range of different flow conditions (Ferguson, 2010). However, both the Manning and Chezy equations produce roughness coefficients with unintuitive physical dimension. An alternative to the Manning equation is the Darcy-Weisbach equation (Equation 2.19). This equation is preferable as it produces a dimensionless coefficient (f_{DW}), however in practical river management, Manning's n is still dominant (Jarvela, 2002), providing the default roughness measure within more hydrodynamic models (e.g. HEC-RAS, ISIS, LISFLOOD).

$$U = \sqrt{\frac{8gR_h S}{f_{DW}}} \tag{2.19}$$

One of the key problems with all three friction parameters $(n, C \,\&\, f_{DW})$ is the reliance upon empirical relations rather than process representation. There have been attempts to link Manning's n to physical channel characteristics such as bed grain size as well as vegetation (discussed in Section 2.5). The most widespread method for grain size is that of Strickler shown below (Ferguson, 2010).

$$n \approx 0.047 D_{50}^{1/6} \approx 0.039 D_{84}^{1/6} \tag{2.20}$$

While this aims to provide a physical basis for the choice of n, it is still dependent on empirical constants which will vary locally. In reality, in many models Manning's *n* represents a calibration parameter (Lane, 2005) which is altered, not for physical accuracy in process representation, but rather to calibrate model data to real data. Thus, instead of accounting for roughness, it is a term which accounts for all processes not included within the model.

2.4.8 Boundary layer flow

The main alternative to bulk roughness coefficients is the use of roughness heights. This is based upon a boundary layer flow model. Both the RANS and LES models can use the log law of the wall to approximate the velocity distribution in the vicinity of boundaries. This model describes how the velocity of the flow over a surface or boundary varies with distance away from the surface (z) due to the effects of friction or resistance at the boundary.

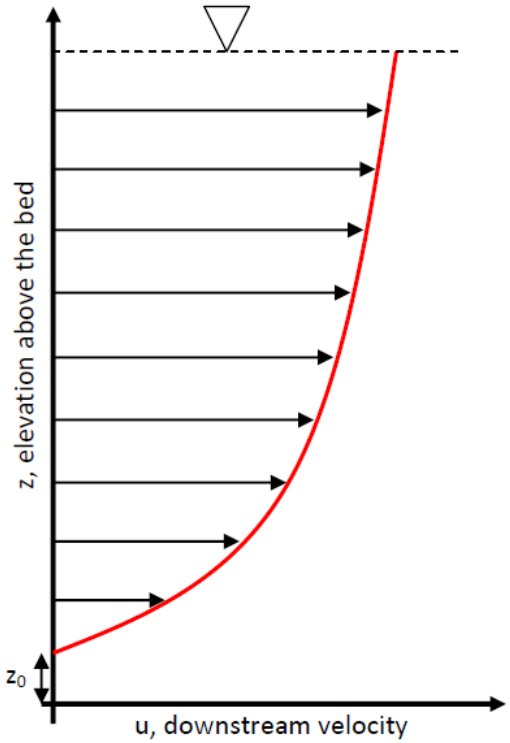

Figure 2.7: *Logarithmic flow profile for boundary layers. z_0 is the roughness height*

The basic model is shown in Figure 2.7 and follows a logarithmic velocity profile. The corresponding equation for the boundary layer flow profile is

$$\frac{U}{U_*} = \frac{1}{\kappa}\ln\left(\frac{z}{z_0}\right) \tag{2.21}$$

Here, U_* is the shear velocity and κ is the Karman constant (≈0.41). A key parameter in this model is the roughness height, z_0, which is conceptualised as the height at which the average velocity is zero. This roughness height varies greatly between surfaces, depending on the topography. It is worth noting here that as this

in an empirical relation, there exist a number of different forms of Equation 2.21. However, the principle is the same throughout.

While the RANS and LES models described above use this model as merely treatment for boundary conditions, similar to the bulk flow models, the log law of the wall is in its own right a popular model for representing flow within terrestrial and aquatic environments, where it is used to estimate the velocity throughout the flow depth rather than merely at the boundaries. Within this model, the effects of any roughness or blockage within the channel must be incorporated within the roughness height. Therefore a number of different relationships have been derived linking the roughness height to the physical characteristics of the channel. Two common examples which link the roughness height to the grain size distribution, based on field investigations, are $z_0 = 0.1D_{84}$ and $z_0 = (6.8/30)D_{50}$ (Nicholas, 2001). However, such a relation is hard to define for complex beds with large scale roughness and blockages.

2.5 Vegetation as flow resistance

The earliest models to include some treatment of vegetation involved altering a channel roughness coefficient to account for the additional resistance created by vegetation (e.g. Chow, 1959). Here, two main approaches are covered; *a posteriori* methods which find empirical values for vegetative resistance from previous experiments, and *a priori* methods which seek to predict the resistance based upon other channel characteristics. The latter is obviously preferable as it aims to link the concept of roughness to a good process understanding. However, river engineers have traditionally relied more heavily on empirical *a posteriori* estimates, based upon pictures and tables found in reference publications, which are unreliable and lack local accuracy (Lane, 2005; Green, 2005b).

2.5.1 *A posteriori* estimates of vegetative resistance

Traditionally, as empirical estimates of roughness were used by engineers, little distinction was made between channels with vegetation and those without. Instead, vegetation was one of many different factors which were used as a descriptor when

choosing roughness values. Typically, roughness values are selected from tables, according to a description of the channel, which takes into account features such as channel shape, bed material, irregularity and vegetation (e.g. Chow, 1959).

One of the earliest treatments of vegetative resistance as an entity of its own was introduced by Cowan (1956). This conceptualised channel roughness as the sum of its component parts as shown in Equation 2.22.

$$n = (n_b + n_1 + n_2 + n_3 + n_4)m \qquad (2.22)$$

Here n_b is the roughness of a straight, uniform and smooth channel. The next four n_i terms correspond to the additional resistance effects due to surface irregularities, cross section characteristics, in-channel obstructions and vegetation respectively. The multiplying term (m) corresponds to the sinuosity of the channel. This conceptual model of additive roughness is promising as it has the potential for each component to be calculated individually and preferably related to the key physical characteristics governing each term. The Conveyance Estimation System, a model developed by the Environment Agency (E.A., 2004), uses a similar scheme whereby roughness is split into a number of components, one of which is due to the effects of vegetation.

A number of authors have sought to improve this approach through linking the vegetation component of the roughness to plant characteristics. Although this may seem more appropriate to the next section, the studies described below are classed as *a posteriori* methods due to the heavy reliance they exhibit on measurements to inform empirical relations and coefficients rather than physical reasoning to inform understanding.

A common relationship which has been exploited is the *n-UR* relationship, whereby Manning's coefficient is found to correlate well with the product of the mean flow velocity and the channel hydraulic radius. This is in effect an *n-Re* relationship (Rhee *et al.*, 2008) as the Reynolds number (Equation 2.6) depends only on the velocity, hydraulic radius and viscosity (which is assumed constant). The idea is that for every

type of vegetation, there is a unique, linear relationship between the two variables. However, there is no scientific justification for the approach (Wilson *et al.*, 2005).

Kouwen and Unny (1973) found that while the *n-UR* relationship agreed well for prone vegetative roughness, for rigid or waving canopies Manning's *n* appeared to be primarily a function of relative roughness. Other studies have shown that the *n-UR* relationship does not hold for emergent canopies, short, stiff vegetation or shallow slopes (Ree, 1958; Kouwen, 1980). Therefore its usefulness is severely limited. Furthermore, it has been argued that as both sides depend on velocity and channel dimensions, there is a degree of circularity about the relationship (Lane and Hardy, 2002)

Fisher (1992) developed a method for calculating Manning's n based on the blockage characteristics of the vegetation within the channel. Blockage can either be defined as the proportion of the plan surface area containing vegetation, (B^{SA}), the proportion of the volume containing vegetation (B^{V}), or the proportion of each cross-section containing vegetation (B^{X}). Fisher suggested that B^{SA} should be used as it is the easiest to quantify. Using this measure, she came up with

$$n = 0.0337 + 0.0239\left(\frac{B^{SA}}{UR_h}\right) \qquad (2.23)$$

Here, the first term is the assumed value of *n* for a river clear of vegetation. Although B^{SA} may be the easiest to measure, it is not the most intuitive choice as it does not take into account changes with water depth or variation in blockage throughout the depth (Green, 2005a).

Green (2005a) tested all three blockage metrics at a range of field sites. The best equation for calculating the vegetative roughness was shown to be

$$n_4 = 0.0043B^{X} - 0.0497 \qquad (2.24)$$

This equation is based on regression analysis from field data, and so has some limitations, particularly with regards to applicability to other reaches with different vegetation types. Furthermore, in the absence of any vegetation, the model predicts a negative vegetative resistance which is counter-intuitive.

Green (2006) developed this theory further, by introducing a new vegetation parameter which affects the resistance

$$T = \frac{P_e}{P_W} \tag{2.25}$$

Here P_W is the wetted perimeter and P_e is the effective wetted perimeter, measured as the wetted perimeter plus the non-coincidental vegetation boundary length i.e. the total solid boundary encountered by the fluid. Through performing multiple regression on a dataset from 35 different field sites, all of which were dominated by the *Ranunculus* species, a new equation was produced (Green, 2006)

$$n_4 = 0.0432e^{0.0281B_{69}^X} + 0.1361T_{16} - 0.205 \tag{2.26}$$

This equation uses the 16th and 69th percentiles repectively of T and B^X, chosen due to their maximal R^2 values. He tested this equation using three different field sites, and achieved relatively low error estimates (<20%) suggesting the model may be valid for other vegetation types. However, despite the complexity of the equation, it still gives a significant negative value of vegetative resistance for channels with no vegetation. Additionally, it is questionable whether the crude nature of the output justifies the effort required to obtain the data necessary to calculate the estimate.

2.5.2 *A priori* estimates of vegetative resistance

There have been a number of studies which have aimed to improve the *a priori* calculation of vegetation-induced roughness. These models attempt to relate the concept of vegetative roughness to the physical characteristics of the vegetation within the channel, in a similar manner to some of the methods developed which link bed roughness to bed characteristics such as grain size. The earliest relationship was developed by Petryk and Bosmajian (1975). They used a momentum balance approach

$$\rho g A S = F_D + \tau_0 P_W \tag{2.27}$$

where A is the cross sectional area of the flow, S is the bed slope, D is the vegetative drag force and $\tau_0 P_W$ is the product of the bed shear stress and the wetted perimeter. This equation can be used in conjunction with both Equations 2.17 and 2.22 to derive a formula for n_4 and consequently the total resistance, n.

$$n = \sqrt{n_b^2 + \frac{R^{\frac{4}{3}}}{2gA}\left(C_d \sum a_i\right)} \tag{2.28}$$

There have been a number of other studies which have linked the Manning's n coefficient to the vegetative drag force (e.g. Hoffmann, 2004; James *et al.*, 2004) and developed similar equations. For a comparison of the performance of these models, a review is provided by Shucksmith *et al.* (2011).

Stone and Shen (2002) developed a momentum balance model for predicting channel velocity based on the Darcy-Weisbach resistance equation, with an additional drag term to account for vegetative roughness. The model was designed so that in the absence of vegetation, it simplifies to the standard Darcy-Weisbach method. The model is also suitable for both emergent and submergent vegetation. However, it only deals with rigid vegetation.

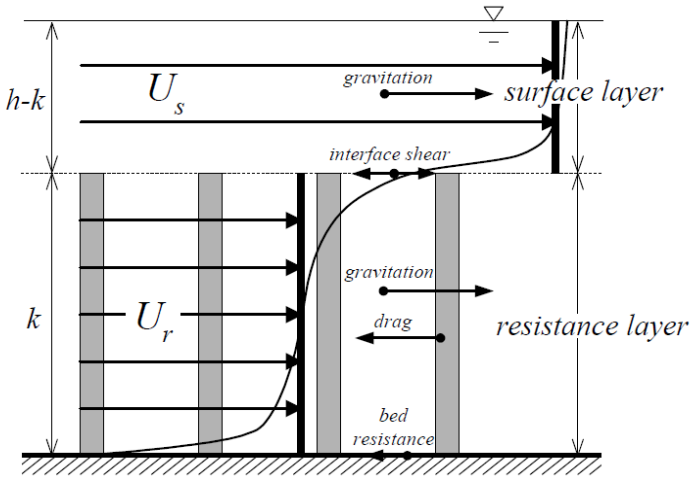

Figure 2.8: *The two zone model (from Huthoff (2007)). The vegetated zone of height k has the characteristic velocity U_r, whereas the surface layer has velocity U_s*

Huthoff *et al.* (2007) used a similar approach to develop a depth-averaged flow velocity model, again with an additional drag term to deal with the resistance due to the vegetation. Both these models use a two zone approach (see Figure 2.8), splitting the flow into two distinct zones: a roughness/resistance layer and a surface

layer. The surface layer is treated as a logarithmic flow profile while the roughness layer is treated using a momentum balance which takes into account the vegetative drag.

Konings *et al.* (2012) developed a more complex model, which calculates the velocity based on knowledge of the dominant momentum transferring vortex size. The model performs well, but still fails to fully account for the flexibility of the vegetation resulting in a lower performance with flexible vegetation.

2.5.3 Vegetation as a roughness height

Vegetation can alternatively be conceptualised within the boundary layer model as a roughness height. A number of different adaptations to the standard boundary layer model have been devised. A substantial review of these can be found in Stephan and Gutknecht (2002). Most of these methods replace the logarithmic term in Equation 2.21 with z/h. Here h is the vegetation height. In other words, the roughness height is considered to directly correspond with the canopy height. It should be noted that this in itself is incorrect as this implies a zero net velocity throughout the canopy. Whether the rigid or deflected vegetation height is used in this approximation make little difference, as in either way it represents a rigid treatment of the vegetation (Green, 2005b).

Kouwen *et al.* (1969) used the ratio of the total cross-sectional area of the channel to the area blocked by vegetation (A/a) instead of the standard z/h model. In the presence of dense vegetation, this reduces to the z/h model, but it will differ significantly for sparser canopies. However the applicability of this method to natural channels with non-uniform boundaries is unclear (Green, 2005b).

Stephan and Gutknecht (2002) devise their own formulation of the boundary layer equation based on experiments with live vegetation.

$$\frac{U}{U_*} = \frac{1}{\kappa}\ln\left(\frac{z-\overline{z_p}}{\overline{z_p}}\right) + c \qquad (2.29)$$

Here, they claim a typical mean vegetation canopy height ($\overline{z_p}$) can be used to represent the roughness height and that the wavy motion of the vegetation does not appear to affect the resistance (Stephan and Gutknecht, 2002).

However, as research into canopy flow has progressed, it has become clear that the boundary layer approximation itself is not appropriate for representing flow structure over vegetation canopies. Therefore, this approach is inappropriate except on large scales of enquiry, where canopy scale turbulence is on a scale much smaller than that of interest and consequently the canopy simply represents a roughness layer ($\overline{z_p} \ll z$).

2.5.4 The problem with representing vegetation using a roughness approach

The problems associated with using a roughness approach within river channel models in general have been highlighted in Section 2.4.7. However, there are a few further issues raised by the addition of vegetation to the channel. Vegetation represents a significant mass blockage within the channel, causing both volume displacement and friction effects throughout the flow depth (Green, 2005b). Roughness approaches assume friction only acts at the interface between the water and the bed, and therefore do not account for the effects of these larger scale elements (García Díaz, 2005). Therefore, flow resistance caused by vegetation represents a three dimensional effect on the velocity field, and a departure from the depth-averaged velocity assumption used within many management models (Naden *et al.*, 2006). These effects will also be linked inextricably to spatially and temporally dynamic factors such as plant position (governed by biomechanics), patch location and seasonality.

From the outset it seems highly improbable that a single coefficient could ever fully represent the effects of the complex interaction between flow and vegetation (Green, 2005b). Even models which seek to improve the estimation of roughness within vegetated channels still fail to capture fully the high spatial and temporal heterogeneity in macrophyte distribution and hence resistance (Green, 2005b). Therefore, there is the need to develop more accurate models of vegetative

resistance. One of the most straightforward ways to accurately represent the effects of vegetation within channels is to attempt to physically model the interaction between the flow and vegetation.

2.6 Physical representation of vegetation elements within numerical models

Based upon the development of canopy layer theory, a significant number of researchers have sought to represent vegetation canopies physically within models, rather than as a roughness element. Here, 'physical' refers to any treatment of vegetation which directly resolves the *processes* operating within canopies. This has been undertaken both at a canopy scale and at a single stem scale. Here, discussion is focussed on two main ideas: introduction of bulk drag terms as reach (field) and plant scale treatments, and explicit stem scale modelling. It is important to note that there are some models that combine these two approaches.

2.6.1 Reach-scale modelling of vegetation

Within this section, the terms field-scale and reach-scale are used interchangeably for similar scale models within the terrestrial and aquatic literature respectively. These models are designed to resolve the large scale shear eddies whereas the smaller wake-scale eddies are modelled. In other words, the entire canopy structure is assumed to be of a sub-grid scale. As such, bulk source and sink terms must be added into the equations to represent the vegetation. For example, Fischer-Antze *et al.* (2001) introduced a drag term into a steady RANS model with a standard κ-ε turbulence closure model. The drag force term was based on a plant density term, and the assumption of rigid, cylindrical vegetation. Their results agree well with experimental work, but they only report on the mean velocity, not the turbulent quantities.

Lopez and Garcia (2001) used both a κ-ε model and a κ-ω turbulence closure model with a double-averaging scheme (Raupach and Shaw, 1982) to model regular rigid vegetation. Both models reproduced mean and turbulent quantities well. However, Defina and Bixio (2005) also used the same κ-ε model alongside an analytical model

for comparison. They found that while both models reproduced mean flow quantities well, neither managed to effectively predict quantitative turbulence. Prediction of turbulence within vegetation canopies is essential as it drives many of the canopy processes as discussed in Section 2.3.

Regardless of whether the RANS models are capable of reproducing the bulk turbulent quantities or not, they are unable to capture the unsteady flow, and vortex dynamics within the flow. In particular, they struggle to account for both the shear and wake turbulence scales (Defina and Bixio, 2005). LES models are therefore more appropriate for modelling turbulence across a range of scales (Keylock *et al.*, 2005).

One of the earliest LES models was by Shaw and Schumann (1992) who modelled airflow above and within a forest (see Figure 2.9). They treated the canopy as a porous body with a constant depth-dependent drag coefficient, using a profile based on data from a deciduous forest. Their model replicated the inflected velocity profile and shear profile from experimental studies well. A number of authors have used a similar approach, treating drag as a constant force throughout the canopy (e.g. Dwyer *et al.*, 1997; Watanabe, 2004)

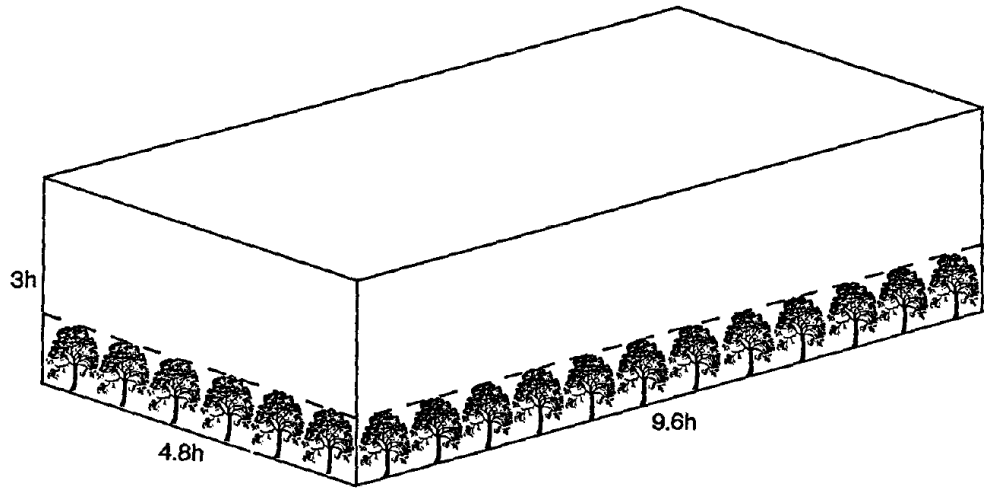

Figure 2.9: *Schematic of an LES canopy model (Shaw and Schumann, 1992). Here, h is the vegetation canopy height.*

Kanda and Hino (1994) used a similar but more sophisticated model, introducing a drag term into the Navier-Stokes equations, based on leaf area density. A similar

approach was used by Dupont and Brunet (2008b) to study the effect of foliage density on canopy flow.

Py *et al.* (2006) extended the classical field-scale model by introducing the effects of plant motion. Here, the canopy is treated as a poroelastic medium which is coupled to the wind velocity profile by the drag term. The canopy can be viewed discretely as a system of connected oscillators representing the stems. They used a piece-wise velocity profile to represent the mixing layer. The stability of the fundamental vibrating frequency of the canopy is examined by solving the perturbation mass and momentum equations. Their results show a lock-in mechanism between the vegetation and the flow, highlighting the importance of fully coupled and interacting vegetation and flow models.

This model has been developed and expanded by other authors. Doare *et al.* (2004) added an option for elastic collisions mechanisms to be incorporated into the model to deal with plant interaction within the canopy. Gosselin and de Langre (2009) also adapted the model by adding a free surface treatment so that the model was applicable to aquatic cases too. Their results show that the aquatic version of the model agrees well with experimental data from aquatic canopies, recreating monami.

Dupont *et al.* (2010) also developed a similar plant motion model within the LES model used in previous studies by the same author (e.g. Dupont and Brunet, 2008a; Dupont *et al.*, 2008). The advantage of this model is that the fluid motion is solved using large eddy simulation which allows turbulence to be resolved to a much greater extent than the simpler hydrodynamic models used in the previous studies that account for plant motion.

2.6.2 Plant-scale models

Plant-scale models don't fully resolve each stem, but make some distinction between canopy characteristics at the plant scale. Classed as a hybrid between the field and stem scale approaches, this method is less common but has nevertheless been used to good effect. Yue *et al.* (2007) developed an LES model which

distinguishes between stem and leaf drag. Stem drag was modelled as basic cylinder drag, whereas leaf drag was modelled using an estimated leaf area index. They compared the model performance with a field-scale approach which uses a standard leaf drag treatment throughout (see Figure 2.10). They found that both models predicted the same spectral slope, but that the field scale model under-predicted the RMS velocity values, effectively damping the instability. Furthermore, the plant-scale approach showed good agreement with PIV data (Yue *et al.*, 2007). Thus, plant-scale LES has been shown to be a reliable tool for investigating turbulence and momentum transport over canopies.

2.6.3 Stem-scale models

To investigate the effect of turbulence production at the wake and leaf scales on turbulence structure and momentum transport, vegetation elements must be modelled at a scale at which they are not sub-grid, i.e. the vegetation diameter significantly exceeds the cell width of the model. This constraint on model resolution has meant that to date, most stem-scale models have focussed on smaller-scale canopy properties and have not considered large or highly submerged canopies.

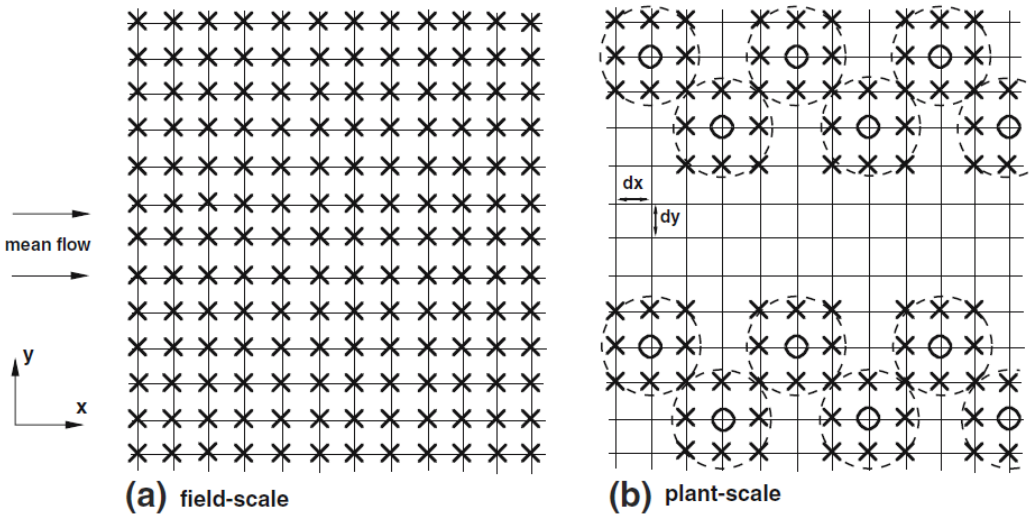

Figure 2.10: *Comparison of field-scale and plant-scale representations (Yue et al., 2007). Here, grid points are assigned either a stem (O) or leaf (X) drag treatment.*

Stoesser *et al.* (2006) performed numerical LES experiments on an array of submerged cylinders using a very fine grid. Their results agreed well with previous experimental results, as well as replicating the classical vortex regimes known to be

present (e.g. horseshoe, von Karman, rib and roller vortices as well as trailing vortices from the vegetation tops). A key feature of this representation of the vegetation is that pressure and friction drag are directly accounted for (Stoesser *et al.*, 2009), removing the need for empirical drag coefficients.

Subsequent papers have developed this analysis further, and begun use larger domains, enabling patch-scale analysis at stem-scale resolution. Stoesser *et al.,* (2010) conducted LES experiments on a patch of emergent vegetation using a combination of high resolution Cartesian and curvilinear grids. They used a range of different vegetation densities and were able to investigate the structural changes to wake turbulence patterns caused by changes in vegetation density (see Figure 2.11). They achieved this via identification and visualisation of turbulent structures as well as through calculating the drag terms acting on the vegetation directly.

The latter point is of particular interest. Through high resolution modelling, it is possible to directly calculate the form and skin drag forces acting the vegetation purely from the velocity and pressure signals, thus enabling comparison with empirical drag values. However, the high computational demands of LES mean this is not useful as a management tool. To address this, Kim and Stoesser (2011) developed a low resolution LES method. Here, instead of using body fitted grids, an immersed boundary method was used within a Cartesian grid which was 20 times coarser than the higher resolution LES model used by Stoesser *et al.* (2010).

Around the circumference of each stalk, a cut-cell treatment was used to represent numerical cells partially filled with vegetation (see Section 3.3). The vegetation radius was approximately four times the grid resolution, and therefore, crucially, wake turbulence was produced by the model, thus removing the need for an empirical drag treatment. This model reproduced the results from the validated high resolution model with reasonable accuracy, including the streamwise and spanwise velocity gradients, wake structure and secondary currents (Kim and Stoesser, 2011). The computational demands of the model are such that it could be used as a management tool at a canopy scale.

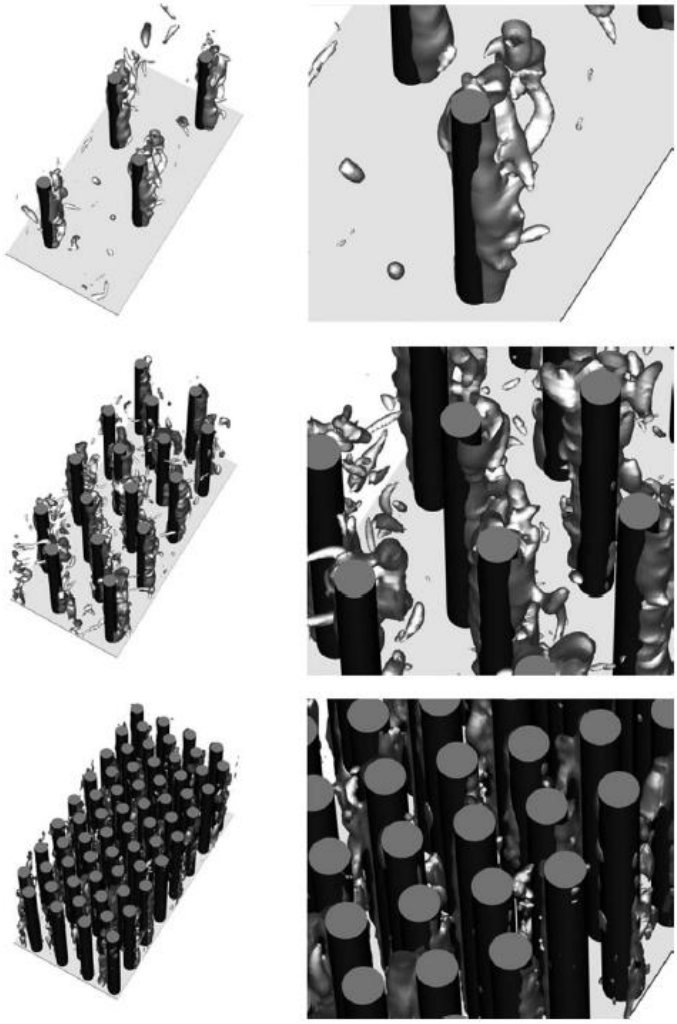

Figure 2.11: *Isosurfaces of pressure fluctuations for three different vegetation densities (Stoesser et al., 2010).*

While these stem scale models are capable of capturing the fine turbulence structure with great accuracy, it is worth noting that they do not include any treatment of flexible vegetation. They are therefore unable to capture the complex feedbacks between flow and vegetation, which may influence canopy processes (Nepf and Ghisalberti, 2008; Okamoto and Nezu, 2009).

2.7 Vegetation: A dynamic blockage?

From the preceding sections of this chapter there are two main factors that emerge as crucial in predicting flow through canopies: drag and biomechanics.

1. Drag acts as the driver for canopy flow, dissipating energy through wake production and determining the shear instability (Nepf *et al.*, 2007). Therefore it is vital to predict the drag force accurately. To avoid the use of empirical and often inaccurate drag coefficients, wake production must be explicitly represented within the model (e.g. Stoesser *et al.*, 2010; Kim and Stoesser, 2011). In other words, the vegetation must represent a physical mass and momentum blockage.
2. Plant biomechanics also determine the flow characteristics. Most notably, flexible plants vibrate in response to the flow, modulating the velocity signal (Finnigan, 1979a). Therefore in order to accurately represent real vegetation canopies, the vegetation must be treated as dynamic.

Thus, it is argued here that vegetation represents a dynamic blockage within the flow, and should be modelled as such. A number of authors have sought to include vegetation as a dynamic blockage, to varying levels of complexity. Here, the merits and drawbacks of each method are discussed. The methods fall largely into two categories, flexible and highly flexible, which is similar to Nikora's (2010) classification of macrophytes as being controlled either by tensile forces or bending forces. In practical terms, there is a structural difference between these two model types, in terms of how stiffness is incorporated into the model and this is explained below.

2.7.1 Flexible stem models

The first study to include flexible stems was conducted by Ikeda *et al.* (2001). They developed a biomechanical plant model within a two dimensional LES framework. The model was based upon the dynamic Euler-Bernoulli cantilever beam equation (see Section 3.5 for details). This partial differential equation calculates the displacement from the flexural rigidity and the dynamic loading of the wind. They used two independent grids in their model, one LES and one plant grid. Properties such as drag and velocity were exchanged between the two grids. Therefore although there was no strict blockage treatment, local grid values of leaf drag were read in from the plant grid, representing spatially heterogeneous drag values and

effectively producing a porous blockage effect. However, this model still relied upon an empirical drag coefficient.

Another issue with the model is that the standard Euler-Bernoulli beam equation is only suitable for relatively small deflections due to flexure of the entire stem. Such assumptions may not be accurate enough when considering vegetation with very high flexibility (Li and Xie, 2011). However, the Euler-Bernoulli equations can be altered to account for larger deflections. Li and Xie (2011) used an extension of the beam equation to model submerged and highly flexible vegetation. However, they modelled at a relatively coarse scale, using very large eddy simulation (VLES) with a fixed width filter. Due to the resolution, individual stalks were sub-grid and the vegetation was represented by a bulk drag force throughout the canopy. The height of the canopy was determined using an empirical relationship calculated using the large deflection analysis. Therefore, despite the complexity of the model equations used, the results were reduced to the plant scale.

2.7.2 Representing highly flexible stems and foliage

In contrast to those flexible vegetation models described above which have a heavily reliance on flexural rigidity, very flexible vegetation models tend to assume that the effect of rigidity is minimal.

One of the simplest examples of this is the model by Backhaus and Verduin (2008). They created a simple model for seagrass motion in which plant geometry and morphology was conceptualised using a cone of permitted movement. This cone effectively introduced a permitted circle of movement at each vertical slab, the radius of which increased which height. The plant was conceptualised as a stack of vertical sections, each of which moved entirely independently of the rest of the plant. While the plant was within the permitted cone, the plant moved freely with the flow in a ‘flapping mode’. Once the vegetation moved beyond the permitted zone, a drag force was applied to the flow, representing the position of maximum stretching of the plant, named the plant ‘trapping mode’. Thus the permitted cone of movement is the main representation of the plant biomechanical data including the rigidity. The model is very simplistic, and given that each vertical section of the

plant is entirely independent there is huge scope for error, although the authors noted that in their study this was not the case due to the prevalence of the trapping mode (Backhaus and Verduin, 2008).

Abdelrhman (2007) developed a more sophisticated model based on a very simple multiple pendula (N-pendula) basis. Here the vegetation is conceptualised as a series of elements connected by hinge-like joints. Each element is subject to a moment, depending on both the force induced by the flow and the tension force from other elements. The hinges are allowed to move freely, thus representing vegetation with zero rigidity. The assumption therefore is that this vegetation is predominantly driven by the balance between drag and buoyancy forces, which was backed up by laboratory results (Abdelrhman, 2007). The model was implemented within a very simple hydrodynamic model, which calculated the velocity at different heights based upon known velocity profiles. Energy loss from the flow was represented by introducing a simple force balance into the flow equation, similar to that used in the plant model. The model was able to replicate the familiar mean velocity profile, but due to its simplicity could not predict turbulent properties of the flow with any accuracy.

Dijkstra and Uittenbogaard (2010) developed a more complex model which used a very similar basis. The main development was the introduction of rigidity in the plant equations, allowing the model to be used more widely for plants exhibiting a range of flexibilities. It is important to note however, that this approach represents a much more local flexibility model than the Euler-Bernoulli beam equation which treats the flexibility as a global, smooth and continuous variable. The model was also used in conjunction with a RANS model, representing an improvement in accuracy on Abdelrhman's model. The results showed that this vegetation model offered a significant improvement over rigid vegetation approximations and roughness coefficients. However, the model also appeared to be very sensitive to rigidity, which is difficult to measure accurately. Furthermore, the model was only RANS-based and therefore was unable to fully predict turbulence characteristics.

A very similar model was used by Farnell *et al.* (2004) within a very different context to model a filament in a soap film. The model is again based on an n-pendula system, with a local treatment of rigidity. The equations are solved using an energy approach within a simple 2D finite-element model. The model reproduces vortex shedding off the end of the filament. However, the equations do contain an empirical damping term. Furthermore, the model is used within a much simpler environment than a canopy flow. There are a number of similar models which have been used to simulate flapping flags/filaments (e.g. Alben and Shelley, 2008; Michelin *et al.*, 2008). While they have not been applied within a canopy environment, they are valuable contributions to methodology.

Moreover, they also introduce another important vortex regime, mentioned earlier in Section 2.3 with regard to plant-flapping-scale turbulence, which is a combination of mixing layer and wake production vortex shedding in the lee of a flexible filament. This vortex production mechanism is usually neglected within canopy flow studies, which for the most part deal with moderately flexible plants (Dijkstra and Uittenbogaard, 2010) but may prove to be more important in highly flexible canopies.

2.7.3 High-resolution dynamic blockage modelling

While these studies have greatly advanced modelling techniques, there is still an absence of high resolution LES models which can incorporate flexible vegetation. Such a model would permit a much fuller understanding of vortex dynamics over flexible vegetation, and shed new light on the exact nature of the interaction between vegetation canopies and the turbulent flow field.

2.8 Chapter summary and conclusions

This chapter has demonstrated the complexity associated with vegetated channels. Previous research has illustrated that vegetation has a profound effect on flow in open channels, altering the mean flow, turbulence characteristics and thus impacting on key processes such as particle transport, erosion and deposition. It is

therefore important to accurately include the effect of vegetation in management models.

Current representation of vegetation within management-scale models relies heavily on the use of inaccurate and inappropriate empirical constants. In particular, current models fail to represent vegetation as a blockage which is both dynamic and porous. In order to better incorporate these characteristics within reach-scale management models, there is therefore a need to further our understanding of how these two properties affect the larger-scale flow characteristics.

The final section of this chapter argued that it is necessary to develop a dynamic blockage model within a high-resolution LES framework in order to conduct a thorough investigation regarding the complex interactions between flow and vegetation. The focus of Chapter 3 is to develop such a model.

Chapter 3: Model development

3.1 Introduction

Chapters 1 and 2 have highlighted the importance of understanding the complex relationships between flow and vegetation. It was argued that there is a need to develop new high-resolution modelling techniques in order to further our process understanding. Therefore, the focus of this chapter is the development of two novel biomechanical vegetation models, capable of simulating the time-dependent interaction between flow and flexible vegetation at a millimetre and Hertz scale. These biomechanical models are incorporated within a pre-existing industry-standard CFD model, PHOENICS (CHAM, 2005). PHOENICS has previously been used to successfully simulate a number of geomorphological applications such as confluences (e.g. Bradbrook *et al.*, 1998), meander bends (Hodskinson and Ferguson, 1998) and flow over gravel (Hardy *et al.*, 2007) and therefore provides a sound basis upon which to develop the models. The first half of the chapter focuses on describing and justifying the generic aspects of the Computational Fluid Dynamics (CFD) model, such as boundary conditions and model specification. The second half of the chapter focuses on the development of the new biomechanical models.

3.2 Numerical representation of the flow

The main concepts and methods involved with numerically representing flow such as the Reynolds Averaged Navier-Stokes (RANS) equations and Large Eddy Simulation (LES) modelling were introduced in Chapter 2. Whilst the general equations were provided, the details as to how the equations were solved were not covered. Details such as the computational scheme, the choice of turbulence closure scheme and boundary conditions are important as they can all substantially affect the numerical result. Here, those methods are expanded upon, and the choice of methods used for this study is justified.

3.2.1 Flow solver mechanics

PHOENICS solves the Navier-Stokes mass and momentum equations in a semi-coupled manner via the SIMPLEST algorithm (CHAM, 2005). This is a variant of the SIMPLE (semi-implicit method for pressure linked equations) algorithm (Patankar and Spalding, 1972) which solves the velocity field based on an estimated initial pressure field, before applying a pressure correction. Thus the velocities are solved using the momentum equation and the pressure correction formula is used to ensure that calculated velocity field is divergence free and consequently the continuity equation is satisfied (Anderson, 1984). The velocity field can then be recalculated using the new pressure values, and the process repeated iteratively until the error is significantly diminished.

There have been two significant improvements to this algorithm. Firstly SIMPLER (SIMPLE–revised) uses an initial estimated velocity field rather than a pressure field to begin the iteration procedure (Pantakar, 1980). An initial pressure field is then estimated from this velocity field. This improvement results in faster convergence. The method does involve solving a pressure equation rather than just applying a pressure correction formula, which is more computationally intensive, but the improvements in convergence rate more than compensate for the additional computational time (Pantakar, 1980). Finally, SIMPLEST (SIMPLE-ShorTened) is a further improvement of the SIMPLER algorithm, whereby convective and diffusion terms are treated separately within the finite volume equation (Spalding, 1980). This method produces convergence more smoothly than the SIMPLE algorithm (CHAM, 2008).

The difference equations used to solve the finite volume system are formulated in an implicit manner in order to ensure universal stability of the scheme. The finite volume scheme involves calculation of the convected variables at the faces of the control volume. The most straightforward way of calculating this is to use a second order accurate central difference scheme to estimate the value between the two known cell centres. However, this scheme is unbounded and can cause unphysical oscillations in regions of strong convection (CHAM, 2005). An alternative is to use

an upwind scheme, whereby the convected variable value at the cell face is assumed to be equal to its value at the upwind cell centre. This scheme is stable and unconditionally bounded, but only first order accurate (Pantakar, 1980). The compromise is to use a hybrid scheme whereby the central difference scheme is used in regions of low convection and the upwind scheme is used in areas of high convection. This threshold is defined using the Peclet number (Pe) which is the ratio of convective and diffusive terms acting across a particular face (Lane *et al.*, 2005). The threshold above which the upwind scheme is used is then set to $Pe = 2$. Due to the improvement in accuracy of the hybrid scheme, it was used in all of the simulations carried out in this study.

3.2.2 Turbulence closure modelling

As discussed in Section 2.4, both the RANS and LES formulations of the Navier-Stokes equations require the use of a turbulence closure model to represent the unresolved component of the turbulence. Within RANS modelling, the majority of these models link the resulting unknown Reynolds stresses to time-averaged flow properties (Keylock *et al.*, 2005) using the Boussinesq (1877) approximation. This states that there is a linear relationship between the Reynolds stresses and the mean flow strain field. This general relationship is shown below.

$$-\overline{u_i' u_j'} = \nu_t \left(\frac{\partial \bar{u}_i}{\partial x_j} + \frac{\partial \bar{u}_j}{\partial x_i} \right) - \frac{1}{3} k \delta_{ij} \qquad (3.1)$$

Here ν_t is the eddy viscosity, k is the turbulent kinetic energy and δ_{ij} is the Kronecker delta function. The $\bar{u}_i$ and u_i' velocity terms are the mean and fluctuating parts of the velocity signal, calculated using Reynolds decomposition. The first term on the right hand side represents the mean strain rate multiplied by a factor (ν_t) and the second term accounts for the turbulent kinetic energy contribution. The different methods for calculating ν_t define the different turbulent closure methods. The overarching concept is that the eddy viscosity can be expressed as a product of a turbulent length scale (l_t) and a turbulent velocity scale (u_t). There are four main types of method for calculating the eddy viscosity.

The most basic methods, the zero-equation algebraic models, specify both the length and velocity turbulent scales in terms of a single algebraic expression (Sotiropoulos, 2005). One of the most commonly used zero-equation models is the Prandtl (1925) mixing length model (Equation 3.2).

$$\nu_t = l_t^2 \left|\frac{\partial u_1}{\partial x_2}\right| \tag{3.2}$$

This follows from the assumption that the velocity scale is proportional to the length scale multiplied by the velocity gradient $\left(u_t = l_t \left|\frac{\partial u_1}{\partial x_2}\right|\right)$ which should intuitively hold for ideal, isotropic turbulent eddies.

The Prandtl model is only valid for two dimensional boundary layers, but it can be generalised in three dimensions as

$$\nu_t = 2l_t^2 \sqrt{S_{ij}S_{ij}} \tag{3.3}$$

where S_{ij} is the strain tensor. The length scale is then chosen empirically to obtain the eddy viscosity (e.g. $l_t = 0.07l$ for a mixing layer, where l is the half-width of the shear layer). While this method is quick and easy, it assumes that the turbulent length scale is constant, which limits its applicability.

One-equation models involve solving one additional equation to obtain the eddy viscosity. Therefore, they represent a more complex solution, but one which is more accurate and applicable to a wider range of flows. The most common one-equation model is the Spalart-Allmaras model (Spalart and Allmaras, 1994). This model solves a single partial differential equation for a viscosity-like variable, $\tilde{\nu}$.

$$\nu_t = \tilde{\nu} f_{\nu 1} \tag{3.4}$$

The term $f_{\nu 1}$ is itself a function of $\tilde{\nu}$ as well as other flow properties and a range of empirical coefficients (Deck *et al.*, 2002). This method was used as the standard model within the development of detached eddy simulation (DES) and has consequently gained in popularity.

By far the most common turbulence closure models used to date are the two-equation $\kappa - \epsilon$ and $\kappa - \omega$ models. These models both involve solving two additional transport equations: one for the kinetic energy (κ) and one for either the dissipation (ϵ) or the specific dissipation rate ($\omega \equiv \epsilon/\kappa$).

For the $\kappa - \epsilon$ model, the equation for the eddy viscosity becomes

$$\nu_t = \frac{k^2}{\epsilon} \tag{3.5}$$

Here the velocity scale becomes $u_t = \sqrt{k}$ and the length scale becomes $l_t = k^{3/2}/\epsilon$. Yakhot and Orszag (1986) developed an alternative $\kappa - \epsilon$ model using Re-Normalization Group (RNG) methods which has been widely used in geomorphological applications (e.g. Bradbrook *et al.*, 1998). This model did not start with the $\kappa - \epsilon$ model as a premise, but rather developed through the application of RNG methods to the Navier-Stokes equations. The solution showed that the resulting transport equation for ϵ was identical to that used for the $\kappa - \epsilon$ model except for one coefficient, while the transport equations for κ were identical. The difference between the two methods arises because the RNG $\kappa - \epsilon$ method calculates diffusion across the spectrum of scales whereas the standard $\kappa - \epsilon$ model only accounts for diffusion at a single scale (Yakhot and Orszag, 1986).

The performance of the RNG model is broadly similar to the standard $\kappa - \epsilon$ model though it has been shown to offer improved performance in specific cases such as flow over a backward facing step and, more generally, areas of high strain (e.g. Lien and Leschziner, 1994; Bradbrook *et al.*, 1998). However, one disadvantage of the $\kappa - \epsilon$ models is that they require a separate near-wall treatment, to account for the effects of eddy distortion, turbulent production and damping associated with the wall (Sotiropoulos, 2005). The $\kappa - \omega$ model is very similar in form to the $\kappa - \epsilon$ model but removes this problem, as in this formulation ω naturally approaches zero at the boundaries meaning an additional model is not required for near-wall regions.

The eddy viscosity for the $\kappa - \omega$ is written as:

$$\nu_t = \frac{k}{\omega} \tag{3.6}$$

Here, the velocity scale is again $u_t = \sqrt{k}$ and the length scale is $l_t = \sqrt{k}/\omega$.

The most complex RANS turbulence closure model is Reynolds Stress modelling. In this scheme, instead of approximating the Reynolds stress tensor by estimating the eddy viscosity, the transport equations for the Reynolds stress terms themselves are solved (Rotta, 1951; Launder *et al.*, 1975). Equation 3.7 shows qualitatively the different terms in the equation which must be solved (Hanjalic and Launder, 1972).

$$\text{Convection} = \text{Generation} - \text{Destruction} + \text{Redistribution} - \text{Diffusion} \tag{3.7}$$

Some of the terms in this equation are still unknown and unsolvable and therefore simplifications are still required before this equation can be used. In particular, some of the terms involve triple correlations between the fluctuating velocity components which must be expressed alternatively as second order terms (Speziale, 1991). Whilst this method is the most accurate, it is still statistically based and therefore fails to capture the large eddy structures, which dominate processes such as vortex shedding, that are present in unsteady flows (Rodi, 1997). Here, large eddy simulation provides a conceptually better approach.

The assumptions and equations used for Large Eddy Simulation (LES) are broadly similar in appearance to those used for RANS models. Instead of separating variables into mean and fluctuating parts as in RANS, LES involves splitting the variables into resolved and unresolved parts

$$u = \langle u \rangle + \tilde{u} \tag{3.8}$$

The resolved part of the signal is calculated using a low pass filter, with a particular filter width (Δ_f). This convolution of the flow field at every point can be achieved by applying a range of different filters but the box (top-hat) filter is the most commonly used (Keylock *et al.*, 2005). The filter width should be chosen such that the filter retains the anisotropic turbulence and averages out the isotropic

component. Within a computational context it is convenient to consider only the discrete centre points of each cell rather than the continuous flow field. In this case, the size of the spatial discretisation is the natural choice of filter width, and thus the box filter becomes the average over the cell volume. As such, fluctuations smaller than the grid cell size are necessarily considered sub-grid scale whilst fluctuations larger than the grid size are resolved explicitly (Deardorff, 1970).

Applying the decomposition in Equation 3.8 to the Navier-Stokes equations leads to a set of equations very similar to the RANS equations, but with two key differences. Firstly, a time derivative term is preserved and secondly, the sub-grid stress (SGS) term in the LES equations is more complex than the Reynolds stress term (Keylock *et al.*, 2005). Similar to the RANS equations, a model must be introduced to account for the effects of the SGS term.

The original and most commonly used SGS closure model is the Smagorinsky (1963) model. This model relies upon the mixing length hypothesis (Equation 3.2) and defines the mixing length as the cubic root of the grid volume. This simplifies to the filter width (Δ_f) for a grid with equal grid spacing in each direction. The Smagorinsky model can be written using the Boussinesq (1877) approximation in Equation 3.1 in terms of the SGS stress tensor (τ^{ij}) as

$$\tau^{ij} = \nu_t \left(\frac{\partial \bar{u}_i}{\partial x_j} + \frac{\partial \bar{u}_j}{\partial x_i} \right) + \frac{1}{3} \tau^{kk} \delta_{ij} \tag{3.9}$$

with $\nu_t = \left(C_s \Delta_f\right)^2 \left|\sqrt{2 S_{ij} S_{ij}}\right|$. Here, C_s is the Smagorinsky constant which depends on the flow characteristics. In reality, C_s varies both in space and time (Rogallo and Moin, 1984). However, for the standard model it is assumed constant ($C_s = 0.1 - 0.2$). Dynamic models have been developed which alter C_s based upon filtering at two different scales. Here, the coefficient is chosen locally as part of the numerical procedure rather than being given *a priori* (Germano *et al.*, 1991). There are a number of different dynamic models which have been suggested, based upon Germano's (1991) model, which aim to deal with the key limitations of the original model such as the inclusion of the backscatter of energy up the energy cascade. At present, PHOENICS does not contain a built-in dynamic Smagorinsky turbulence

model, and it was considered beyond the scope of this study to develop one. Instead, comparison of different closure models is noted as a potential avenue for further research.

Given the requirement of high-resolution, time-dependent modelling, and the focus of this study on coherent turbulent structures, LES is the most suitable choice of model, given that it is the most accurate method for capturing dynamic turbulent structures over a range of spatial scales (Keylock *et al.*, 2005). Therefore, all simulations were run using LES with the standard Smagorinsky model, but to aid convergence they were 'hot-started' from a converged steady state solution solved using the RANS equations with a RNG $\kappa - \epsilon$ turbulence closure scheme.

3.2.3 Mass flux scaling algorithm

One of the challenges in high resolution modelling is the appropriate representation of boundary conditions. In the case of natural river channels, this most commonly refers to the discretisation of complex topography which can strongly affect the generation of turbulent structures (Lane *et al.*, 2004; Hardy *et al.*, 2007) and thus influence the flow dynamics. There are two main approaches which can be used here. The first involves adapting the numerical mesh to fit the topography (e.g. Figure 3.1a). These boundary fitted coordinate (BFC) grids alter grid size and shape in order to fit the grid to the topography. This distortion of grid shape can lead to artificial diffusion and numerical instability (Hardy *et al.*, 2005). Furthermore, the variation in grid size can cause problems in testing the grid independence of numerical solutions as well as choosing the filter width for LES (Hardy *et al.*, 2005). Grid independence testing is covered further in Section 3.2.8.

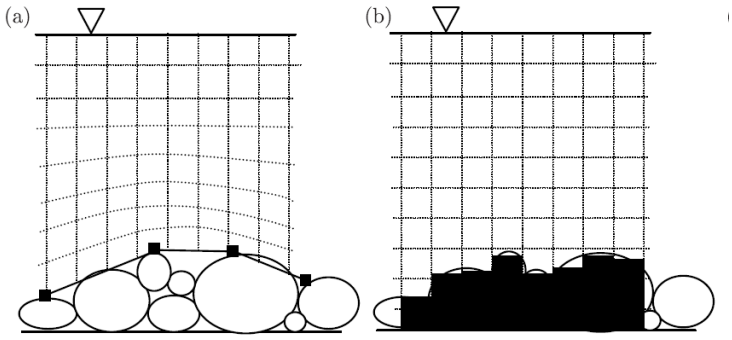

Figure 3.1: *Examples of different topographic representation: (a) boundary fitting and (b) a mass flux scaling approach. Figure from Hardy et al. (2005).*

An alternative approach to BFC grids is to represent the topography using a mass flux scaling algorithm (MFSA) as shown in Figure 3.1b. Here, a hexahedral Cartesian grid is used, and complex boundaries are incorporated by setting cell porosity values. This porosity approach was first suggested by Olsen and Stokseth (1995) and was developed further by Lane *et al.* (2002; 2004). Hardy *et al.* (2005) added an additional drag treatment within the momentum equations to deal with the changes in porosity between cells. The approach has successfully been used to model flow over complex granular surfaces (Hardy *et al.*, 2007) .

In the vegetation model simulations, only a simple flat boundary was used, in order to fully investigate the contribution of vegetation to the turbulent structure and minimise any significant bed-generated turbulence. However, the model contains the capability to include more complex surfaces. While the MFSA was not implemented at the bed in this thesis, it was developed further to represent the vegetation and is fully explained in Section 3.3.

3.2.4 Free surface treatment

The free surface represents another important boundary condition within natural channel flows, and will be most important in situations with a high surface slope or where the effects of turbulent motions at the scale of interest extend to the free surface. There are three main approaches to modelling the free surface.

The first and most straightforward, scheme is a rigid lid approach. Here the computational grid is set up with a planar solid boundary at the top of the domain. As such, variations in water surface elevation are not directly accounted for, but are represented as deviations from zero pressure in the top cell. Thus, the effects of the water surface are accounted for in the pressure gradient term within the momentum equation, but it does not affect the mass continuity equation. This can lead to over-prediction of velocity in areas of superelevation (Weerakoon and Tamai, 1989).

Bradbrook *et al.* (1998) implemented a more sophisticated treatment of the free surface using the mass flux scaling algorithm. Here, the free surface layer of cells is

treated as a porous domain. Thus areas of depression are assigned values of less than 1 and areas with superelevation are assigned porosities greater than 1 (Spalding, 1985). This method represents a mass treatment of the flow, as the porosity allows the correct discharge to pass through, and the free surface effects to be fully represented. This approach has been successfully applied to geomorphological flows through confluences and over gravel surfaces (Bradbrook *et al.*, 2000; Hardy *et al.*, 2007).

The third method is through multiphase modelling where the air-water surface is modelled directly. However, this method is very computationally expensive and is only advisable strictly when the surface perturbations are the main feature of interest.

Throughout model application, the water surface slope was considered to be negligible and therefore the basic rigid-lid approximation was used in order to simplify the simulations. It is worth noting that in many natural channels, due to the low submergence depth, surface expressions of vegetation-induced turbulence are significant (as seen in Figure 3.2) and so there may be merit in using a more sophisticated surface treatment. However, these schemes are far more complex and potentially unstable, and are therefore beyond the scope of this study.

Figure 3.2: *Photo showing the surface expressions of submerged vegetation canopies. Flow is from bottom to top. The river is approximately 5m wide and 0.3m deep. The water surface deviations from the mean are estimated as less than 10% of the flow depth.*

3.2.5 Inlet and Outlet conditions

Inlet and outlet conditions are key boundary conditions which must be specified in any CFD model. All simulations in this thesis were performed on a high-specification desktop computer rather than a supercomputer, and therefore were subject to significant memory constraints. This meant that domain size and spatial resolution were both constrained. In order to capture the evolution of the flow through vegetation over an extended domain length, cyclic inlet and outlet boundary conditions were used. With this method, the end of the domain is mapped onto the beginning of the flume to effectively create a recirculating flume.

Typically, using cyclic boundary conditions involves solving the difference equations between the outlet and inlet cells to derive flow across the boundary. Though PHOENICS has an in-built cyclic boundary conditions setting, it was found that it was not sufficient, due to the fact that the inlet dampened the turbulence levels from the outlet, and there was no sign of larger-scale turbulent structures being recirculated.

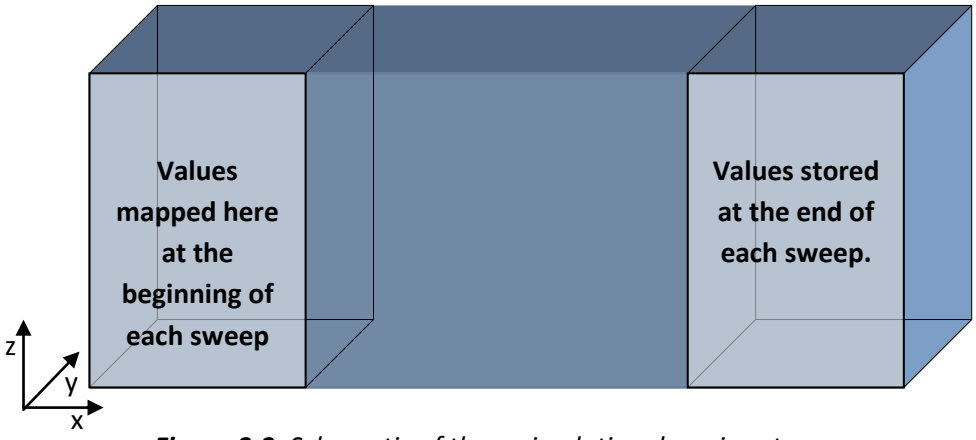

Figure 3.3: *Schematic of the recirculating domain setup.*

Therefore a new recirculation scheme was developed, as shown in Figure 3.3, whereby a larger section of the domain (roughly 0.05-0.2x/l), rather than simply one cross-stream slice, was mapped onto the beginning of the domain. These values were mapped at every sweep, to ensure that there was no dampening. The pressure and velocity values were mapped for all of the recirculating except for the cross-sections corresponding to the inlet and outlet. Here the outlet pressure was discarded and the new value for the dynamic pressure was calculated from the

mapped velocities. This ensured that the correct pressure gradient was maintained within the channel.

The introduction of recirculation creates the potential for the appearance of channel-length scale turbulent motions within the results. Therefore, care must be taken when analysing the results to ensure that such motions are detected and characterised correctly.

3.2.6 Good practice in modelling

The preceding sections have outlined the necessary methods employed in applying the CFD model. The methods have been justified, and have been shown to be robust. However, sound modelling still requires good practice to ensure that the results are valid. This involves verifying and validating the model thoroughly to ensure that the application of the model is suitable and appropriate. The methods of verification and validation of the CFD model used in this thesis are outlined below.

3.2.7 CFD model verification

Model verification is the process of checking whether the model is solving the equations correctly as opposed to model validation which involves checking whether the model solves the correct equations (Roache, 1994). The word 'verify' means an assertion or establishment of truth and therefore in modelling terms, a verified model is one whose truth has been demonstrated, which implies its suitability as a basis for decision making (Oreskes *et al.*, 1994).

As mentioned in Section 3.2.1, the CFD model PHOENICS solves the Navier-Stokes equations over a discrete number of points using a finite volume method. It is well recognised that these equations are an accurate simulation of fluid flow and therefore the issue of verifying such schemes centres on the discretisation of the continuum mechanics problem into a finite volume scheme rather than the equations themselves (Hardy *et al.*, 2003). The idea behind such finite-volume schemes is that for an appropriate grid with spacing h between neighbouring points, the discrete solution should tend to the exact solution as h tends to zero. However

there is a hidden intricacy within turbulent flow solvers. As discussed in Section 2.4, the majority of such methods solve directly down to a particular spatial scale below which turbulence models are used to save computational time and memory. Therefore if the discretised solution converged perfectly to the exact solution then the turbulence models would introduce 'double-counting' (Roache, 1997).

In most applications this is not an issue because complete convergence is not attained. Instead the solution is deemed to be close enough to the exact solution to be considered sufficiently accurate to use as a basis for decision making. This requires the definition of a threshold for convergence of the solution beyond which the model is assumed suitably accurate. Thus the focus of verification within modelling tends to be error calculation and minimisation rather than elimination.

The American Society of Mechanical Engineers (ASME) have a particular policy regarding verification of open channel models used within its journals. Lane *et al.* (2005) provide a useful critique of these criteria with particular consideration for the use of numerical models within fluvial geomorphology. They conclude that the guidelines whilst being necessary, may not be sufficient in natural fluvial systems.

Here, the main distinct criteria for model verification are described, with reference to both the original ASME guidelines (1993) and the critique by Lane *et al.* (2005). Where appropriate, reference is made specifically to the case of vegetated channels. In particular, a test domain filled with a canopy of rigid vegetation was used to elucidate the issues faced with general canopy flows.

a) Solution accuracy in space

As mentioned in Section 3.2.1 it is important that the order of accuracy of any system of equations used is known and reported alongside the results. The normal requirement for numerical models is that they are at least second order accurate in space. However, as is also explained in Section 3.2.1, within CFD solvers a compromise is often used. This means that strictly this cannot be classed as a second order method, and instead the order must be calculated experimentally using the grid convergence index method, as explained in Section 3.2.8.

b) Grid independence testing

The second criterion is that the solution should be shown to be independent of the grid or mesh size used. In other words the grid should not be subject to large discretisation error. This is a key issue, particularly when using Large Eddy Simulation, as grid resolution can have a critical impact upon the solution. Arguably the most common, straightforward and reliable methods are grid convergence studies (Roache, 1998). Therefore, grid convergence is further discussed in detail in Section 3.2.8.

c) Determination of solution convergence

A solution is said to have converged for a particular variable when the sum of the absolute values of the residuals for that variable falls below a pre-specified tolerance (Lane *et al.*, 2005). In PHOENICS, this tolerance is set to 0.1% of the original error (CHAM, 2007). However this level of convergence is very rarely obtained for high resolution fluvial problems, especially when complex topography is present (Lane *et al.*, 2005). An alternative approach is to analyse the spot values visually for each variable of interest at particular locations throughout the flow field after each sweep (iteration over the entire domain) and to define the solution as converged when all variables have 'flat-lined', as shown in Figure 3.4.

The idea of a fully converged solution is a myth as there can always be constructed a variable that has not converged fully (Roache, 1997). Instead, the variables being investigated should be checked for convergence as well as any others that drive key processes being investigated, and as discussed earlier, analysis should not extend beyond the variables that have been shown to be converged (Roache, 1997). The order in which different variables converge is clear in Figure 3.4.

Steps can be taken to improve the rate of convergence of the solution. Firstly, the inlet velocity profile can be used to initialise the entire flow field, thereby providing a more accurate starting value. Alternatively, a converged whole-field solution from a previous run can be used to provide starting values for the entire field. This can be particularly useful for starting high resolution models from converged lower

resolution models, or to start more complex turbulence models from simpler ones. As mentioned in Section 3.2.2 this technique was used to hot-start the LES simulations in this study.

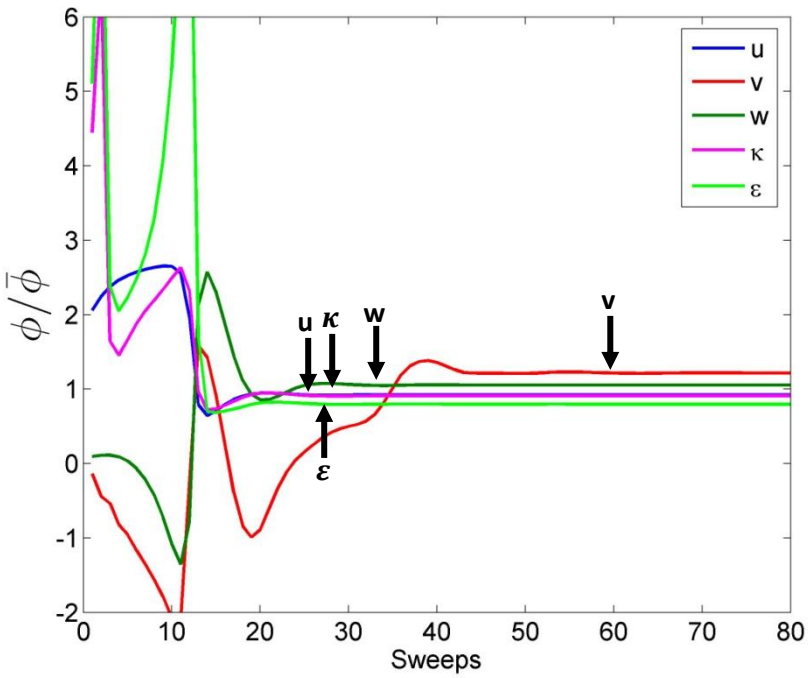

Figure 3.4: *Normalised spot values of different variables (φ) plotted against sweeps, showing clear flat-lining. Rough 'convergence' points for each variable are labelled.*

In vegetated channels, the success of this technique, particularly starting from lower resolution models, may be highly dependent on the grid resolutions used. As long as the grid size is smaller than half the diameter of the vegetation elements, this technique is likely to be useful. However, as the resolution decreases the solution changes sufficiently such that it no longer provides a useful starting value for a higher resolution model run. Computational experiments carried out at the same resolution as the plant diameter showed substantial error and no convergence even over 2 500 iterations.

d) Solution accuracy in time

The final consideration that relates to the numerical solution is its temporal accuracy. All of the methods so far have in effect considered a steady state solution. However, the analysis in this thesis requires unsteady temporal data, and this introduces another source of potential error. Choice of an inappropriate time-step

can cause unphysical oscillations in the solution and therefore it is essential that the time-step is chosen correctly. The standard equation used is the Courant number

$$L = u\frac{\Delta_t}{\Delta_x} \tag{3.10}$$

This is the product of the downstream velocity and the ratio of the temporal (Δ_t) and spatial resolution (Δ_x). Essentially, this calculates the proportion of a single computational cell that the fluid travels through in a single timestep. For an explicit first order method, the time-step must be small enough such that a change in one variable does not propagate across a distance greater than one cell before re-evaluation (Lane, 1998). This imposes severe restrictions on time-step, for a simulation with high spatial resolution and moderate velocities. This condition is not as strict in implicit models, and PHOENICS can handle time-steps which exceed the Courant limit by many orders of magnitude (CHAM, 2007) and therefore Courant numbers are not reported for each case. However, care has still been taken in this thesis to ensure that the lowest possible Courant number is used without imposing prohibitive constraints on the temporal resolution and thus computational time.

e) Specification of boundary conditions

Boundary conditions can affect the overall accuracy of a simulation and therefore the choice and justification of boundary conditions should be specified. This includes spatial boundary conditions such as the free surface approximation, topographic representation, inlets and outlets as well as temporal boundary (initial) conditions. Each of these has been explained in some detail earlier in this chapter.

f) Reporting of code:

Finally, when using commercial CFD codes it is important to report any changes or alterations made to commercial code that could compromise its performance. In other words, any additional code, such as the mass flux scaling algorithm, or alteration to the momentum equations should be adequately reported, to allow scrutiny of the adapted scheme.

3.2.8 Grid Convergence Index

As discussed in Section 3.2.7, the Grid Convergence Index (GCI) is one of the most reliable methods for assessing grid independence. The GCI is a method, developed by Roache (1993), based on Richardson extrapolation which can be applied either to a single point, a group of points or the entire domain and is formulated as follows.

Assuming the solutions, f_1 and f_2, to the same equation are calculated on two grids with even spacing h_1 and h_2 then they can be represented as series expansions,

$$f_1 = f^* + g_1 h_1 + g_2 h_1^2 + g_3 h_1^3 + H.O.T \quad (3.11)$$

$$f_2 = f^* + g_1 h_2 + g_2 h_2^2 + g_3 h_2^3 + H.O.T \quad (3.12)$$

where g_i are functions defined on the continuum which do not depend on any discretisation and f^* is the exact solution to the equations. Here, $H.O.T$ represents the higher order terms. In second order methods g_1 is, by definition, zero and the exact solution can be written as

$$f^* = (h_2^2 f_1 - h_1^2 f_2)/(h_2^2 - h_1^2) + H.O.T. \quad (3.13)$$

Defining the grid refinement ratio as $r = h_1/h_2$, this can be rewritten as a correction to the finer grid (h_1) solution

$$f^* = f_1 + (f_1 - f_2)/(r^2 - 1) + H.O.T. \quad (3.14)$$

Dropping higher order terms and generalising for order of convergence p_c, the estimated fractional error for the fine grid can be expressed as

$$E_1(fine) = \varepsilon/(r^{p_c} - 1) \quad (3.15)$$

$$\varepsilon = (f_2 - f_1)/f_1 \quad (3.16)$$

Defining the actual fractional error as

$$A_1 = (f_1 - f^*)/f^* \quad (3.17)$$

and using the previous results and a binomial expansion, the actual error can be expressed in terms of the estimated error:

$$A_1 = E_1 + O(h^{p_c+l}, E_1^2) \tag{3.18}$$

Here $l = 1$ generally, or 2 if centered differences have been used (Roache, 1994). Equation 3.17 shows that the estimated fractional error is a good estimate for the actual fractional error, if $E_1 \ll 1$. This is extremely useful as it provides an error estimate for the discrete solution that does not require prior knowledge of the exact solution, which in the majority of CFD problems is not known.

The GCI is then defined as the estimated error multiplied by a safety factor.

$$GCI(fine) = 3|\varepsilon|/(r^{p_c} - 1) \tag{3.19}$$

It is equally likely that the actual error will lie above the estimated error as below it and so the estimated error does not represent an error bound. By including a safety factor, the GCI then becomes a conservative upper bound for the error, equivalent to a 99.9% confidence interval (Hardy *et al.*, 2003).

In order to be able to quantify the global GCI, L_∞ and L_2 norms can be used to calculate characteristic statistics for entire domains. These norms are calculated as follows

$$L_2(A) = \sqrt{\sum_{i=1}^{n} A(i)^2} \tag{3.20}$$

$$L_\infty(A) = \max\big(A(i)\big) \tag{3.21}$$

There is some debate as to whether either of these norms is a representative or reliable measure for representing the entire domain (Westerlink and Roache, 1997). The L_∞ norm is very sensitive to occasional outlying errors that are not representative of the error across the entire domain. This is particularly significant in domains that contain areas in which the local error may be especially high, for example areas of high shear, or near to walls or other boundaries. However the L_∞

norm may be useful if one requires an absolute bound on the estimated error within a relatively well-behaved domain.

Conversely the L_2 norm can average out regions of very low error and regions of very high error into a single statistic portraying a domain with medium error throughout. This can be avoided by choosing an appropriate domain over which to average although this may not be instinctively obvious prior to the calculation. Instead it can be more helpful to plot how the GCI changes across a particular 2D slice of the domain. Such analysis can help identify spatial patterns of convergence and can also inform the decision as to which domain to calculate the L_2norm over.

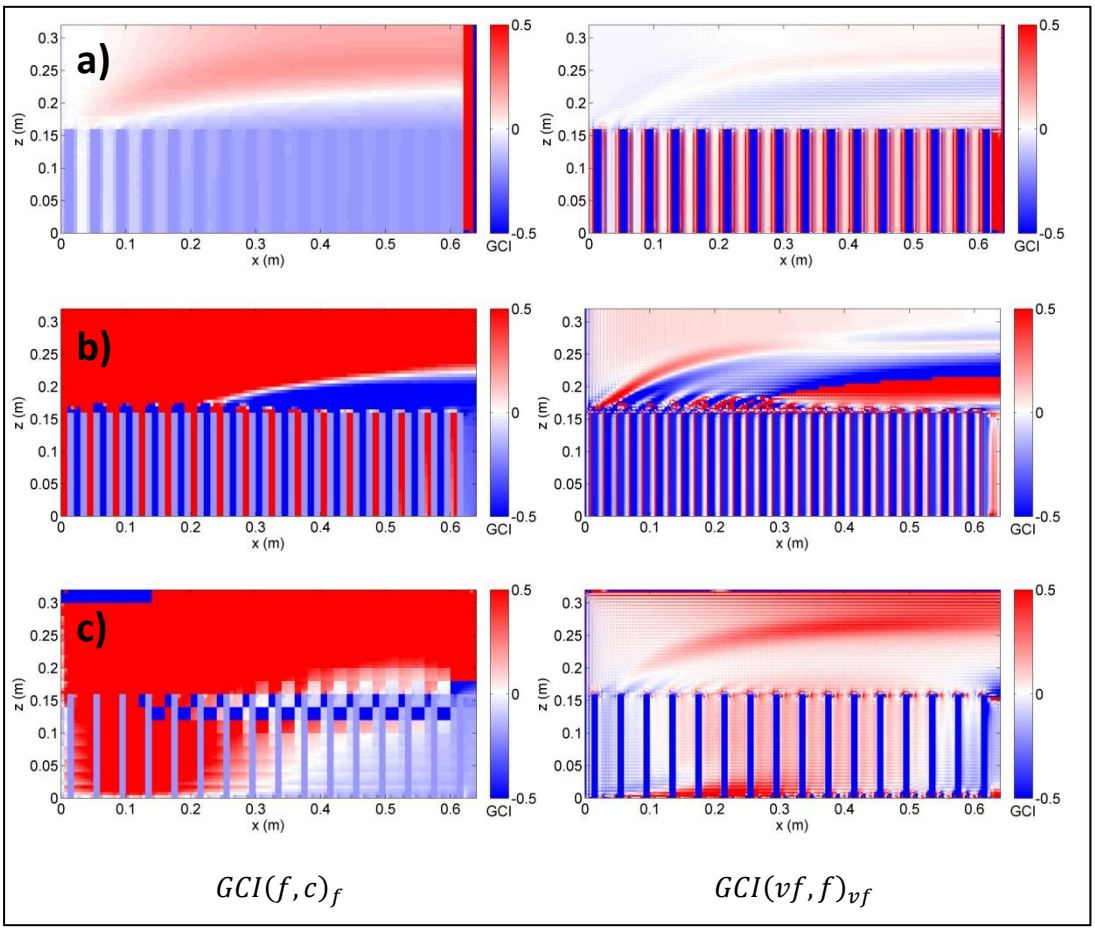

Figure 3.5: *GCI cross-sections for (a) downstream, (b) cross-stream and (c) vertical velocity at two different resolutions.*

Figure 3.5 shows a series of GCI cross-sections from a test simulation. The test domain was 0.64m long, 0.32m wide and 0.32m high. A canopy of stems, each 0.01m in diameter were placed in a staggered arrangement, with a separation of 0.01m between each stalk. Each stalk was 0.16m high i.e. half the total depth. Four

different resolution grids were used: 0.02m (coarse), 0.01m (medium), 0.005m (fine) and 0.0025m (very fine). For the medium grid size, the grid spacing was equal to the vegetation diameter. The results at this resolution were numerically inaccurate and the solution failed to converge at all. Therefore the medium grid results were discarded. The inlet velocity for all the runs was set at 0.3m/s.

The GCI plots in Figure 3.5 show that in all three velocity signals, there is a clear spatial pattern to the error magnitude which appears to relate to flow separation regions at the canopy top. In general, the very fine grid shows a decrease in error compared to the fine grid, and one would expect the coarse grid to perform considerably worse than the fine grid. It is also clear that of the three, lateral velocity seems most susceptible to high error values even at the very fine resolution. While these cross-sections are useful, they do not allow analysis of the variability of the GCI across the entire domain.

Cumulative area fraction error (CAFE) curves are a helpful way of investigating global GCI (Luettich and Westerlink, 1994). These curves plot the percentage of the total domain that exceeds a particular error level (y axis), against the error level itself, ε (x axis). These graphs highlight any extreme anomalies whilst also indicating the median error.

Figure 3.6 shows the CAFE curves calculated for a patch just above a rigid vegetation canopy for the same two resolution comparisons as Figure 3.5. The figure indicates that in order to achieve the best results, the very fine grid size is required, at which, 90% of the domain has a GCI of under 0.1 compared to the fine grid which drops off more slowly. However, Figure 3.6 also shows that the three velocity components display very different trends, with the lateral and vertical velocities showing worse convergence. This highlights the need to consider all variables of interest.

Hardy *et al.* (2003) applied the GCI approach to two typical fluvial modelling applications, namely a meander bend and a zero degree confluence. They calculated global convergence indices and looked at the distribution of GCI at particular cross-sections. The results showed good convergence for the

downstream velocity. However, GCI values for other variables were not as good. In particular, the locally dominant processes seem to affect the convergence of variables. For example, in the meander bend, lateral velocity showed poor convergence due to the secondary circulation. Similarly in the confluence there was poor convergence of the vertical velocity component. This reiterates the importance of considering the variable of interest when seeking to verify a numerical scheme. Otherwise a numerical scheme may be verified for a variable lower down the convergence order and used to study higher order processes governed by variables that have not yet converged.

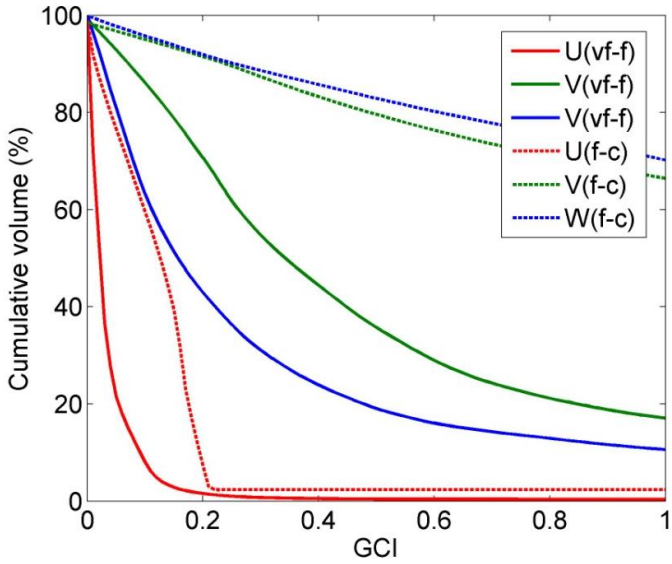

Figure 3.6: *CAFE curves, plotting the GCI error level against the cumulative percentage of domain volume with GCI greater than or equal to that GCI value.*

In addition, Hardy *et al.* (2003) also showed that a grid independent steady RNG turbulence model solution can lose its grid independence when used to hot-start a LES simulation. Therefore, a low GCI for a steady simulation is not sufficient enough to be able to conclude that the LES simulation will be converged. However it is impractical to test the LES solution for convergence at every time step. Instead one could analyse the GCI of the time averaged LES solution.

For LES simulations in particular, an apparently grid-independent solution can be misleading as it may still neglect important processes operating at a sub-grid scale. Therefore in addition to choosing a grid with a low GCI it is important to choose a grid which accounts for the scale of the processes being investigated (Hardy *et al.*,

2003). Finally, the idea of selecting a grid with 'a low GCI value' is still a vague term. There are no formal definitions of thresholds between acceptable and unacceptable levels of error and indeed this threshold may depend on the domain being solved.

Vegetated channels present a difficult challenge when calculating GCI values as vegetation elements can be sub-grid, meaning a change in resolution can dramatically alter the flow patterns observed. Therefore there is high grid dependence where the resolution is similar to the size of the vegetation elements. The implication of this is that where small vegetation diameters are being used, a very high resolution grid must be used to obtain grid independence. With a given computational power this limits the spatial extent of any investigation. This is significant as many of the process operating at the top of vegetation canopies do so over relatively long downstream distances (Ghisalberti and Nepf, 2002).

Vegetated channels are also likely to exhibit a higher GCI as a much larger proportion of the domain is in the proximity of a boundary. For this reason spatial analysis of the GCI is vital in determining whether or not the solution is suitably converged in the area of interest. There are further potential problems when the GCI is extended to unsteady LES simulations involving flexible vegetation, as the vegetation blockage will vary between time steps making grid comparison very difficult. This may be partly solved by using a time-averaged solution derived from the LES simulation for comparison between grid resolutions.

The above calculations of the GCI all require a prior knowledge of the order of convergence *p*. However similar methods can be used to calculate *p* using solutions from three different resolution grids. If the grid refinement factor is the same between the 3 grids (i.e. $h_1/h_2 = h_2/h_3$) then this is simply calculated by:

$$p_c = \ln\left(\varepsilon_{23}/\varepsilon_{12}\right)/\ln\left(r\right) \tag{3.22}$$

If the grid refinement factor is different *p* can still be calculated iteratively using the relation:

$$p_{c,n+1} = \omega p_{c,n} + (1-\omega)\ln(\beta)/\ln\left(r_{12}\right) \tag{3.23}$$

where

$$\beta = \frac{r_{12}^{p_{c,n}} - 1}{r_{23}^{p_{c,n}} - 1} \varepsilon_{23}/\varepsilon_{12}. \quad (3.24)$$

A value of ω = 0.5 tends to work well for well-behaved cases (Roache, 1997). This calculation was carried out for the 3 grid resolutions mentioned above at a single point, in the middle of the domain above the canopy. The results are shown in Figure 3.7. These show that the actual convergence is significantly lower than 2, particularly for the lateral and vertical velocity components. However, in order to achieve an accurate result, *p* should be calculated throughout the domain and then averaged. This still does not guarantee valid results however, as there can be significant discrepancy across the domain, as shown by Flynn and Eisner (2004) who obtained only a small percentage of values within the theoretical order of accuracy ($1 < p_c < 2$) for simulations of flow around a cylinder. This is complicated for vegetated flows by the presence of additional solid blockages in the domain which do not necessarily translate naturally between the different resolutions.

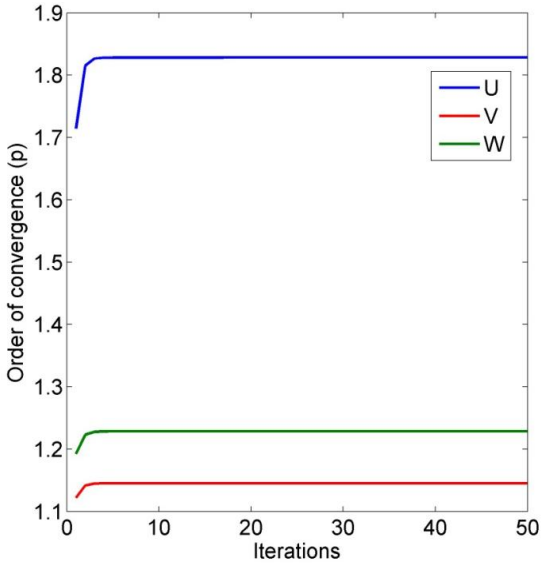

Figure 3.7: *Iterative calculations of p for the 3 flow velocities at a point.*

In summary, grid convergence is a key aspect of model verification, particularly in LES simulations where there can be a strong dependence on grid resolution. This section has outlined various methods for assessing the accuracy of simulations through idealised vegetation canopies. Applying GCI methods to vegetation simulations, it has been shown that to maximise convergence a very fine grid

should be used. In this instance, the vegetation diameter was four times the grid resolution, and this was shown to increase convergence dramatically compared to the other grid resolutions. Consequently, this ratio of vegetation diameter to grid resolution will be considered the minimum acceptable throughout this thesis. It is hard to assess convergence within the canopy, as the changes in vegetation discretisation between grid resolutions affect the results. Furthermore, flexible canopies represent a more complex situation. Nevertheless, these results are used to inform the vegetation modelling, to ensure the best possible numerical convergence.

3.2.9 CFD model validation

Validation of numerical models is equally as important as verification. However, it can prove challenging. One of the key drivers for the use of numerical modelling is the ability to capture processes at a resolution which cannot be measured in the field, or over a wider parameter space than is measurable in the field. Therefore, it can be difficult to collect sufficiently accurate validation data. For the numerical experiments carried out in this thesis, analogous flume experiments were conducted as validation data and these results are reported in Chapter 5. However, even with high resolution models, there will be some processes and levels of complexity not represented within the model. Therefore, some disagreement between the datasets is inevitable, meaning the broad patterns and values, rather than individual results, must be compared.

An alternative method of validation is the use of benchmark solutions. In some cases this is appropriate as in Section 3.7 when the benchmark solution for a cylinder is used as a reference. However, this is not a useful method for complex situations such as entire canopy flows, for which no benchmark solutions exist.

3.2.10 Summary

The first half of this chapter has outlined the considerations required in formulating and applying a CFD model. The choice of appropriate solution techniques, turbulence models and boundary and initial conditions has been justified with

reference to the relevant literature. Issues of good practice within modelling have been discussed and key criteria drawn out, with reference to the discussion by Lane *et al.* (2005). With respect to each of the criteria, the model specification used within this thesis has been addressed and thus the CFD aspect of the simulations has been justified. The remainder of this chapter focuses on the other coupled aspect of the modelling undertaken in this thesis: the inclusion of vegetation within the CFD framework.

3.3 Vegetation Conceptualisation

The term 'vegetation' covers a whole range of different species with very different structures and characteristics. Therefore, prior to model design it is necessary to define which types of vegetation will be the focus of this thesis. For the purpose of this research, two main types of vegetation are considered. These fit broadly into the categories of a) relatively high rigidity reed and grass-like stems (e.g. *Phragmites australis*) and b) low rigidity submerged macrophytes (e.g. *Ranunculus penicillatus, Callitriche platycarpa*). As discussed in Chapter 2, these can be classed broadly as those that are controlled by bending and tensile forces respectively (Nikora, 2010). Therefore, two different models are developed which represent different physical force balances. The Euler-Bernoulli Beam model was developed to model semi-rigid vegetation whilst the N-pendula model was developed to simulate highly flexible vegetation. These models are each described in detail in Sections 3.5 and 3.6. However, the conceptualisation of the vegetation itself is very similar between the models.

The process of conceptualisation necessarily involves a number of simplifications. Firstly the models only deal with single-stemmed plants. Foliage and more complex plant form is something which could be developed at a later stage, although this would require significant extensions to the equations used here. While this may seem a significant limitation, the model does allow for a large number of individual stems to be modelled simultaneously, allowing the representation of realistic vegetation patches.

Secondly, the plant is assumed to be made up of discrete components (see Figure 3.8). The exact nature of this varies between the two models used. However, in both cases, the stem is conceptualised as a set of discrete connected masses. This means that at a very fine scale the vegetation does not retain its shape, although plant mass is preserved (Ikeda *et al.*, 2001).

In both models, each discrete component of the stem is treated as a fixed shape. The centre of mass of the shape is treated as the stem centre, which then moves according to the equations set out later in this chapter. As the cente of mass moves at each time-step, so the original shape of each plant section is remapped separately.

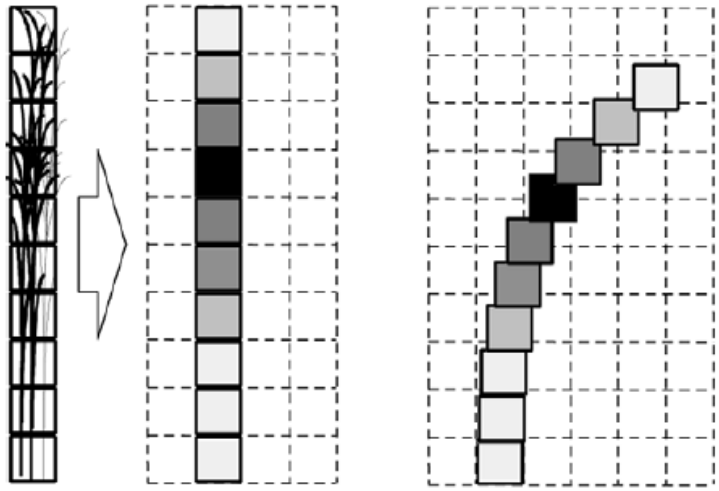

Figure 3.8: *Tandem plant and LES grid systems (Ikeda et al., 2001). Here a stalk is conceptualised as a vertical array which then moves and maps onto the LES grid.*

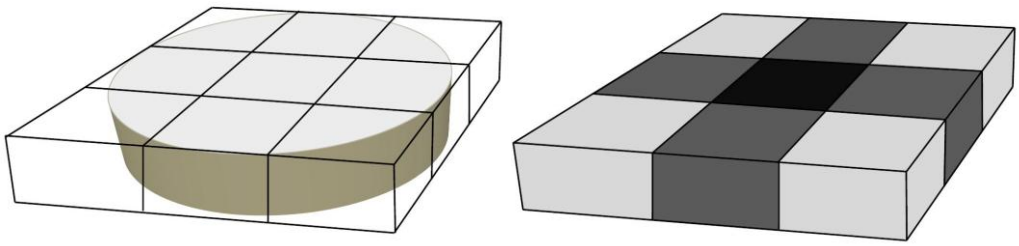

Figure 3.9: *Porosity cut-cell treatment of vegetation. Here darker cells represent lower porosity values.*

The vegetation is treated as an immersed boundary, using a dual grid system similar to Ikeda *et al.* (2001) whereby the vegetation grid and the LES grid interact at each timestep in a sequentially staggered manner (Felippa *et al.*, 2001). Velocity data passes to the plant grid, and is used to calculate plant motion before the new plant

mass data passes back to the LES grid for the next flow calculation. Plant mass is represented as porosity (Lane and Hardy, 2002) within the LES grid, as an extension of the MFSA approach described in Section 3.2.3. This acts as a partial, or full mass blockage, which is represented as a porosity value between 0 and 1 (where 0 is fully blocked and 1 is no blockage) and is a simpler form of the cut-cell method used by Kim and Stoesser (2011). The key difference between the model developed below and that of Ikeda (2001) is that here the grid resolution is smaller than the vegetation stalk diameter, and therefore the porosity is not used to represent stem density (as in Figure 3.8) but rather to represent volume blockage due to a single stem (Figure 3.9).

3.4 Force calculation from the CFD model

In the same way that mass information is transferred to the LES grid, flow data is passed to the plant grid in order to calculate the dynamic force balance. The external forces acting on the vegetation can be described as drag (both form and skin), buoyancy, and lift, or more generally, pressure driven movement.

The buoyancy force is calculated as the difference in density between the vegetation (ρ_p) and fluid (ρ), multiplied by the gravitational acceleration and the volume, which is assumed to be a cylinder of radius r_p and height h.

$$F_B = \left(\rho - \rho_p\right) g \pi {r_p}^2 h \tag{3.25}$$

The drag force was initially calculated using the drag equation with a drag coefficient (C_D) set equal to the value for a rigid cylinder. Here u_f is the local fluid velocity averaged over the neighbouring cells and u_p is the plant velocity. The modulus of the velocity difference is used here instead of simply $\left(u_f - u_p\right)^2$ in order to maintain the directionality of the drag force. This drag approximation is a crude and potentially inaccurate representation of the drag force but is the standard method for incorporating drag and served as the basis for model development. Section 3.7 discusses an improved alternative approach to calculating the drag force which was also implemented within the model at a later stage.

$$F_D = \frac{1}{2}\rho C_D \pi r h (u_f - u_p)\left|u_f - u_p\right| \quad (3.26)$$

These two forces, drag and buoyancy, are generally the highest magnitude forces, and the N-pendula model was run using simply these forces. However, following Ikeda *et al.* (2001) an additional force term was incorporated into the Euler-Bernoulli beam equation model to account for unsteady pressure fluctuations.

$$F_P = \frac{\partial u_f}{\partial t}(1 + C_M)\rho\pi r^2 h \quad (3.27)$$

Here C_M is the coefficient of added mass, which is taken as equal to 1. The forces described above were assumed to act in either the downstream (x) or vertical direction (z). In some cases, such as with the drag force, a component was calculated for both directions. The forces were then resolved into the correct plant directions using trigonometry and appear in the following model descriptions as external force terms (q for the beam model and $E_{x/z}$for the N-pendula model).

It was also necessary to take into account the effect of shading, as when the plant bent, the full frontal surface of the top cells was not exposed to the fluid forces (see Figure 3.8). Therefore, the forces were scaled linearly, dependent on their vertical position relative to the neighbouring cells in the vertical direction.

3.5 Euler-Bernoulli beam equation model

The dynamic Euler-Bernoulli beam equation solves the deflection of a thin beam under external loading. It represents a simplification of linear elasticity theory and balances the external force with the rigidity of the beam. Thus, it is appropriate for modelling vegetation with low flexibility which is controlled by bending forces. Due to its simplicity it has a number of limitations. Firstly, it does not account for shear deformation. Secondly, it is only applicable for small deflections, although it can be extended for larger perturbations (Li and Xie, 2011). It was chosen as it has been used in previous studies, both to model explicit vegetation elements (Ikeda *et al.*, 2001) as well as to drive canopy scale models (Finnigan and Mulhearn, 1978; Erduran and Kutija, 2003).

3.5.1 Numerical Basis

The dynamic version of the Euler-Bernoulli beam equation is shown in Equation 3.28. It can be split into 3 terms: a bending stiffness term, an inertial term and an external force term, labelled 1, 2 and 3 respectively. It is these three forces which must be balanced to ascertain the plant movement and position.

$$\underbrace{\frac{\partial^2}{\partial z^2}\left(EI\frac{\partial^2\xi(z,t)}{\partial z^2}\right)}_{1} = \underbrace{-\mu_M\frac{\partial^2\xi(z,t)}{\partial t^2}}_{2} + \underbrace{q(z,t)}_{3} \qquad (3.28)$$

The equation assumes that the beam is initially straight and under no load. Given a load, $q(z)$, along the beam, the perpendicular displacement, $\xi(z)$, from this initial straight position at a point x along the beam can then be solved. The flexural rigidity (EI), defined as the product of the elastic modulus (E) and the second moment of inertia (I), and the mass per unit length (μ_M) both feature within the equation. For simplicity, these have been assumed constant although this is not necessarily the case. Many plants will exhibit variations in flexural rigidity along the stem and it is likely that most vegetation stalks will also differ in diameter along the stalk (Miler *et al.*, 2012). This would lead to a z-dependence in both flexural rigidity and mass per unit length. For the mass term this is straightforward and could be implemented at a later stage. However, the flexural rigidity term lies within a differential operator, and therefore adding an z-dependence will alter the numerical scheme considerably. Therefore, the model described below is only valid for stems of constant rigidity.

This is justifiable for two reasons. Firstly, the method used to calculate the flexural rigidity of the prototype and real vegetation (discussed in Section 5.2.1) relies upon the assumption of a constant flexural rigidity along the stem. Even if the model did exhibit variations in rigidity, it could not be calibrated experimentally. Secondly, the prototype vegetation used was of a constant diameter, and so it is unlikely that there is much variation in the rigidity. Therefore, this is only a problem for the real vegetation.

The equation can be solved using a number of different formulations. During model development, these different formulations were investigated, ranging from the simplest explicit formulation through to complex change-of-variables methods. Here, is presented an overview of the development process.

3.5.2 Explicit formulation

For the explicit formulation, the equation is discretised using a scheme that is backward in space and central in time as shown in Eq. 3.29.

$$\frac{EI}{(\Delta_z)^4}\nabla_z^4\xi_j^n - \frac{\mu_M}{(\Delta_t)^2}\delta_t^2\xi_j^n = Q_j^n \qquad (3.29)$$

Here, ∇_v^m and δ_v^m are the m^{th} order backward and central difference schemes respectively with respect to the variable v. Whilst this scheme is a lower-order-accurate method than a fully central scheme (Wilmott, 1995), it relies on boundary conditions only at the attached, bottom end of the stem where movement is likely to be minimal, rather than at both ends. This leads to a more accurate prediction at the free end of the plant stem, where movement is likely to be greatest. This is highlighted in Figure 3.10 which shows the stencil for the two schemes. The stencil is an illustration of the discrete space/time values used in the equation.

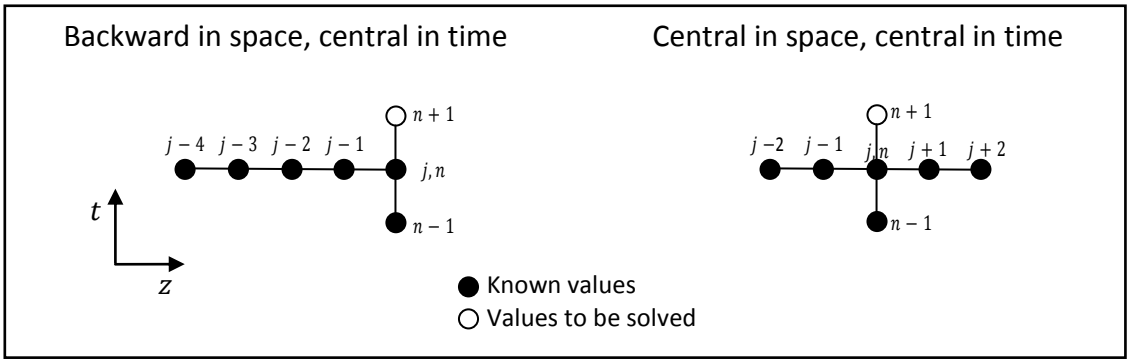

Figure 3.10: *Comparison of stencils for the backward and central difference schemes.*

Equation 3.30 describes the fully expanded version of Equation 3.29. Once re-arranged to solve for the correct node, this equation becomes

$$\xi_j^{n+1} = \frac{\Delta_t{}^2}{\mu}Q_k^{n+1} - \frac{EI}{\mu}\frac{\Delta_t{}^2}{\Delta_z{}^4}\left(\xi_j^n - 4\xi_{j-1}^n + 6\xi_{j-2}^n - 4\xi_{j-3}^n + \xi_{j-4}^n\right) + 2\xi_j^n - \xi_j^{n-1} \qquad (3.30)$$

where h is the spatial discretisation and k is the temporal discretisation, and n and j are node locations in time and space respectively. This equation contains only one unknown on the left hand side and so can be solved given sufficient initial and boundary conditions. The necessary initial and boundary conditions for this scheme are:

$$\xi_j^0 = 0, \xi_0^n = 0, \quad \xi_1^n, \xi_2^n, \xi_3^n, \xi_4^n = \text{modelled}$$

As far as the author is aware, there is no pre-existing model within the literature which can be used to calculate these boundary conditions. Thus, a simple linear model has been used, whereby it is assumed that for the first 4 nodes of each stem, the displacement (ξ) increases linearly according to the displacement of the 5th node at the previous time step. In other words, for $j = 1$ to 4

$$\xi_j^n = \frac{j\xi_5^{n-1}}{5} \tag{3.31}$$

In effect, this assumes that the bottom of the stalk is a rigid element, pivoting about the base. This assumption should not have a significant influence on the model, as movement within the bottom few nodes is likely to be minimal and the linear approximation does not introduce a fourth order derivative.

The explicit formulation is the easiest to solve, however the limitation of this is that the scheme is prone to becoming numerically unstable. This can be seen by examining the Fourier/von Neumann stability for the scheme. By assuming that the round-off error (ε) satisfies the discretised equation (Equation 3.30), and neglecting the external force term, the error can be written as:

$$\varepsilon_j^{n+1} = -\tilde{\mu}\left(\varepsilon_j^n - 4\varepsilon_{j-1}^n + 6\varepsilon_{j-2}^n - 4\varepsilon_{j-3}^n + \varepsilon_{j-4}^n\right) + 2\varepsilon_j^n - \varepsilon_j^{n-1} \tag{3.32}$$

where, $\tilde{\mu} = \frac{EI}{\mu}\frac{{\Delta_t}^2}{{\Delta_z}^4}$. The error is now expressed as a Fourier series, and for the rest of the analysis, only a single arbitrary mode of the series is considered.

$$\varepsilon_j^{n+1} = \tilde{g}^n e^{i\beta jh} \tag{3.33}$$

Here $\tilde{g}$ is the amplification factor (i.e. the growth of error between time steps), and the choice of β is arbitrary. Substituting (3.33) into (3.32) and simplifying gives

$$\tilde{g} = -\tilde{\mu}\left(e^{2i\beta h} - 4e^{i\beta h} + 6 - 4e^{-i\beta h} + e^{-2i\beta h}\right) + 2 - \tilde{g}^{-1} \tag{3.34}$$

Converting this into trigonometric identities and multiplying by g, gives

$$\tilde{g}^2 = \underbrace{(\tilde{\mu}(8\cos(\beta h) - 4\cos^2(\beta h) - 4) + 2)}_{\varphi}\ \tilde{g} - 1 \tag{3.35}$$

This is a quadratic equation of the form $a\,\tilde{g}^2 + b\,\tilde{g} + c = 0$. A simple relation for the roots of quadratic equations can be used to characterise the roots, $\tilde{g}_1$ and $\tilde{g}_2$.

$$\tilde{g}_1.\ \tilde{g}_2 = \frac{c}{a} \tag{3.36}$$

This shows that the product of the two roots is 1. For stability it is required that the modulus of all roots (amplification factors) be less than or equal to 1 (i.e. $|\tilde{g}| \leq 1$). Given (3.36), this is only possible for a non-positive discriminant ($b^2 - 4ac \leq 0$). In other words, Equation 3.36 implies that there are not two real roots, as one would have to be the reciprocal of the other, and thus both could not be less than or equal to one. The only remaining possibilities are that both roots are either equal ($b^2 - 4ac = 0$), or that both roots are complex numbers ($b^2 - 4ac < 0$). Therefore the stability condition becomes

$$\varphi^2 \leq 4 \tag{3.37}$$

A new variable, α, is now introduced such that

$$\alpha = 8\cos(\beta h) - 4\cos^2(\beta h) - 4 \tag{3.38}$$

$$\varphi = \tilde{\mu}\alpha + 2 \tag{3.39}$$

It is now straightforward to work out the maximum and minimum values of α,

$$-16 \leq \alpha \leq 0 \tag{3.40}$$

Rewriting the stability condition (3.39), two separate conditions emerge

$$\tilde{\mu}\alpha \leq 0 \tag{3.41}$$

$$\tilde{\mu}\alpha \geq -4 \tag{3.42}$$

Using (3.40), the first condition (3.41) holds unconditionally for $\tilde{\mu}$. The second condition (3.42) holds for $\tilde{\mu} \leq \frac{1}{4}$. Hence this is the necessary condition for a stable solution.

To illustrate the significance of this, consider a typical simulation setup, with $EI = 0.02Nm^2$ and a plant with stem radius of $r_p = 0.005m$ and density $\rho_p = 700kg/m^3$. This density was chosen to be within the range used by other authors (e.g. Luhar and Nepf, 2011). The mass per unit length is therefore $\mu_M = 0.0549kg/m$. Given that

$$\tilde{\mu} = \frac{EI}{\mu_M}\frac{{\Delta_t}^2}{{\Delta_z}^4}, \tag{3.43}$$

the condition on the spatial and temporal discretisation becomes

$$\frac{{\Delta_t}^2}{{\Delta_z}^4} \leq 0.686. \tag{3.44}$$

Given the plant radius, and assuming that for simplicity of calculation the plant grid resolution is the same as the LES grid and that $\Delta_x = \Delta_y = \Delta_z$, according to the grid resolution restriction set out in Section 3.2.8 the largest appropriate value of Δ_z might be taken as 0.0025m. The restriction in Equation 3.44 would in this case require a time step smaller than 0.0000052s to guarantee a stable solution. Figure 3.11 shows the dramatic effects the unstable scheme has on the solution through time, when a larger time step (0.001s) is used. It is clear that this scheme is not practical, as to run the fluid dynamics solver at a high enough resolution would be too computationally expensive. Therefore, an alternative method is required.

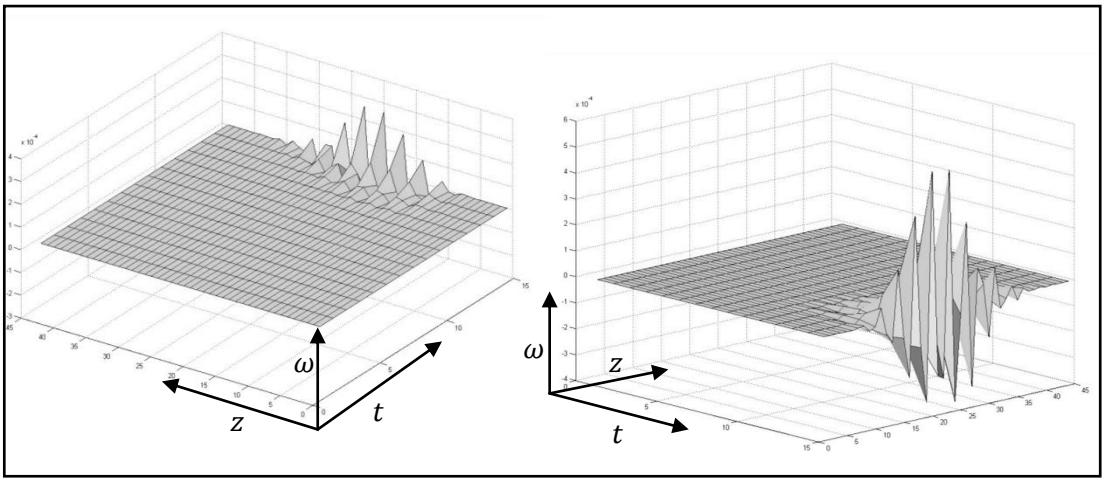

Figure 3.11: *Exponential solution instability in an explicit beam model run with k=0.001.*

3.5.3 Subcycling explicit formulation

Given the attractive simplicity of the explicit method, an appealing modification to the explicit model is to create a subcycling model (Felippa *et al.*, 2001), whereby the fluid mechanics solver and the plant motion solver run at different temporal resolutions. Whereas the fluid solver requires a number of minutes for a typical domain, the plant solver requires considerably less than a second, enabling it to run at the sufficient resolution within a short period of time.

Therefore, the numerics are identical to the explicit scheme described above, except that the plant solver is run 10 000 times (subcycles) per fluid time step. With a fluid time step of 0.01s, this provides a plant model temporal resolution of 0.000001s, which given the above spatial discretisation, should be sufficient for model stability according to Equation 3.44.

There is one other important change to the model, however. As the fluid solver is not being run every subcycle, it is not possible to calculate the forces directly at this resolution. Instead, the forces must be estimated from the most recent fluid time step. This creates a problem, because the plant velocity will increase between fluid time steps, but the corresponding drag force will not. Therefore, there will be excessive plant motion in these periods. To counter this, a drag correction must be introduced at each subcycle. This correction, $\widetilde{F_D}$ is calculated as an addition to the existing drag force and represents the drag of the new relative velocity.

$$\widetilde{F_D} = \left(u_P^s - u_p\right)\left(\left|u_P^s - u_f\right| \pm \left(u_p - u_f\right)\right) \tag{3.45}$$

In this equation, u_P^S is the plant velocity at the subcycle, and u_p and u_f are the plant and water velocities at the most recent time-step. The sign of the last term depends on the sign of plant velocity.

While this should in theory curtail excessive plant motion, it was found that the inertial term within the equation was too dominant, and that the bending-stiffness term and external force term were having little, if any, effect. In other words, it was very difficult for the external or internal forces to override the plant velocity signal. It would seem that despite the drag correction, the lack of fluid force information at the subcycle is critical. Therefore this method was abandoned in favour of the original sequentially staggered model.

3.5.4 Implicit second-order formulation

As the explicit formulation suffered from a lack of stability, the next step was to switch to an implicit formulation, as they are commonly more stable. The harsh stability criterion in the explicit model comes in part from the 4th order differencing, and therefore, to further improve the chances of stability, a second order approach was investigated. The implicit formulation of the model is different from the explicit version in that it does not solve a single unknown based upon a series of known values. Instead it solves for all dependent variables simultaneously via matrix algebra. This leads to a more complex solver, but one which is more stable. In order to simplify the equations into a 2nd order scheme, this method involves a switch in variables. First, two new variables are defined as,

$$v = \frac{\partial \omega}{\partial t}, w = \frac{\partial^2 \omega}{\partial z^2} \tag{3.46}$$

These are then substituted into (3.28) to give

$$EI\frac{\partial^2 w}{\partial z^2} + \mu_M \frac{\partial v}{\partial t} = q(z,t). \tag{3.47}$$

This can be solved for each of these variables using

$$\frac{\partial v}{\partial t} = \frac{1}{\mu_M} q(z,t) - \frac{EI}{\mu_M} \frac{\partial^2 w}{\partial z^2} \tag{3.48}$$

$$\frac{\partial w}{\partial t} = \frac{\partial v}{\partial z^2} \tag{3.49}$$

These equations can be written using a backward in time and backward in space scheme. Similarly to the explicit case, the central scheme would be give higher order accuracy but would require boundary conditions at the free end of the stem.

$$\frac{v_j^{n+1} - v_j^n}{\Delta_t} = \frac{1}{\mu_M} Q_j^{n+1} - \frac{EI}{\mu_M} \frac{w_j^{n+1} - 2w_{j-1}^{n+1} + w_{j-2}^{n+1}}{{\Delta_z}^2} \tag{3.50}$$

$$\frac{w_j^{n+1} - w_j^n}{\Delta_t} = \frac{v_j^{n+1} - 2v_{j-1}^{n+1} + v_{j-2}^{n+1}}{{\Delta_z}^2} \tag{3.51}$$

This can be written in matrix form, combining the two equations into one

$$A\underline{p}^{n+1} = \underline{p}^n + \underline{q}^{n+1} + \underline{d}^{n+1} \tag{3.52}$$

where,

$$A = \frac{k}{h^2}\begin{bmatrix} 2 & 1 & 1 & 0 & & \\ 1 & -2\sigma & 0 & 1 & \cdots & 0 \\ 1 & 0 & 2 & 1 & & \\ 0 & 1 & 1 & -2\sigma & & \\ & \vdots & & & \ddots & \vdots \\ & 0 & & & \cdots & \begin{matrix} 2 & 1 \\ 1 & -2\sigma \end{matrix} \end{bmatrix}, \quad \sigma = \frac{EI}{\mu}$$

$$\underline{p}^{n+1} = \begin{bmatrix} v_1^{n+1} \\ {w_1}^{n+1} \\ v_2^{n+1} \\ w_2^{n+1} \\ \vdots \end{bmatrix}, \qquad \underline{q}^{n+1} = \frac{1}{\mu_M}\begin{bmatrix} q_1^{n+1} \\ 0 \\ q_2^{n+1} \\ 0 \\ \vdots \end{bmatrix}, \qquad \underline{d}^{n+1} = \begin{bmatrix} v_1^{n+1} \\ {w_1}^{n+1} \\ v_2^{n+1} \\ w_2^{n+1} \\ 0 \\ \vdots \end{bmatrix}$$

Despite the complexity, this system is of the generic form $A\underline{x} = \underline{b}$ and can be solved very quickly and easily, using matrix algebra. The boundary conditions are given within d, and the initial conditions are contained within p^0. Once v has been solved, it is then straightforward to solve for the displacement, ω.

$$\omega^{n+1} = kv^{n+1} + \omega^n \tag{3.53}$$

The problem with this formulation arises in specifying the boundary and initial conditions. The variables now being dealt with are the vegetation speed (v) and the

second derivative of the displacement with respect to distance along the stem (w). Vegetation speed is a familiar variable as it has already been calculated in previous models to work out the drag force, and so it is relatively easy to estimate its value for the bottom few nodes of the stem. However, w is far less intuitive and it is difficult to estimate what this value should be. Therefore this model was discarded in favour of the fourth order implicit version.

3.5.5 Implicit fourth-order formulation

The fourth-order version of the implicit method is less convoluted than the second order change of variables. Due to the higher derivatives, there is the possibility of a harsher stability restriction, however as this is an implicit scheme it is not the case.

$$\frac{EI}{{\Delta_z}^4}\nabla_z^4\xi_j^n - \frac{\mu_M}{{\Delta_t}^2}\nabla_t^2\xi_j^n = Q_j^n \tag{3.54}$$

With this formulation (Equation 3.54), two backwards difference schemes are used. The stencil is shown in Figure 3.12.

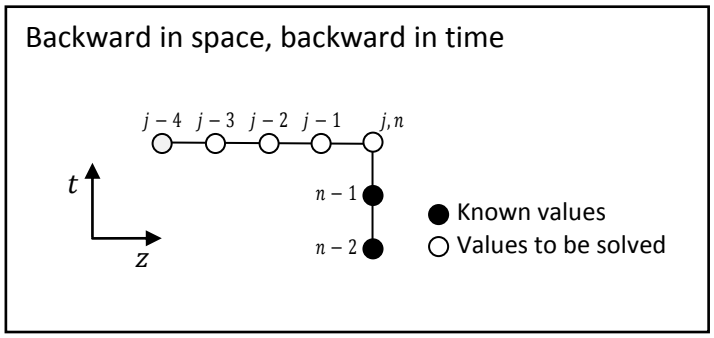

Figure 3.12: *Stencil for the 4th order implicit scheme*

$$\xi_j^{n+1} - 2\xi_j^n + \xi_j^{n-1} = \frac{{\Delta_t}^2}{\mu_M}Q_j^{n+1} - \frac{EI{\Delta_t}^2}{\mu_M}\frac{\xi_j^{n+1} - 4\xi_{j-1}^{n+1} + 6\xi_{j-2}^{n+1} - 4\xi_{j-3}^{n+1} + \xi_{j-4}^{n+1}}{{\Delta_z}^4} \tag{3.55}$$

Expanding the difference equation (Equation 3.55) and writing it in matrix form gives

$$\frac{EI}{\mu_M}\frac{\Delta_t}{{\Delta_z}^2}\boldsymbol{A}\underline{\xi}^{n+1} = \frac{1}{\mu_M}\underline{q}^{n+1} + \underline{\xi}^n - \underline{\xi}^{n-1} - c^{n+1} \tag{3.56}$$

where,

$$A=\begin{bmatrix}
\varphi & & & & & & & & & & & \\
-4 & \varphi & & & & & & & & & & \\
6 & -4 & \varphi & & & & & & & & & \\
-4 & 6 & -4 & \varphi & & & & & & & & \\
1 & -4 & 6 & -4 & \varphi & & & & & & & \\
 & 1 & -4 & 6 & -4 & \varphi & & & & & & \\
 & & \vdots & & & & \ddots & & & \vdots & & \\
 & & & & & & & \varphi & & & & \\
 & & & & & & & -4 & \varphi & & & \\
 & & 0 & & & & \cdots & 6 & -4 & \varphi & & \\
 & & & & & & & -4 & 6 & -4 & \varphi & \\
 & & & & & & & 1 & -4 & 6 & -4 & \varphi \\
 & & & & & & & & 1 & -4 & 6 & -4 \\
 & & & & & & & & & 1 & -4 & 6
\end{bmatrix},$$

$$\underline{c}^{n+1}=\begin{bmatrix}
\xi_1^{n+1}-4\xi_2^{n+1}+6\xi_3^{n+1}-4\xi_4^{n+1} \\
\xi_2^{n+1}-4\xi_3^{n+1}+6\xi_4^{n+1} \\
\xi_3^{n+1}-4\xi_4^{n+1} \\
\xi_4^{n+1} \\
0 \\
\vdots \\
0
\end{bmatrix}, \quad \underline{q}^{n+1}=\begin{bmatrix}
q_1^{n+1} \\
q_{12}^{n+1} \\
0 \\
\vdots \\
0
\end{bmatrix}$$

As with the second order method, this has the form $A\underline{x}=\underline{b}$ and so can be solved simply using matrix techniques such as LU decomposition.

The Fourier/von Neumann stability can be calculated in a similar manner to the method used for the explicit method. The discretised equation for the error becomes

$$\varepsilon_j^{n+1}-2\varepsilon_j^n+\varepsilon_j^{n-1}=-\frac{EI{\Delta_t}^2}{\mu_M}\frac{\varepsilon_{j+2}^{n+1}-4\varepsilon_{j+1}^{n+1}+6\varepsilon_j^{n+1}-4\varepsilon_{j-1}^{n+1}+\varepsilon_{j-2}^{n+1}}{{\Delta_z}^4} \qquad (3.57)$$

Expanding this as a Fourier series, selecting a single node and simplifying produces

$$\tilde{g}^2-2\tilde{g}+1=\tilde{\mu}\tilde{g}(e^{2i\beta h}-4e^{i\beta h}+6-4e^{i\beta h}+e^{2i\beta h)} \qquad (3.58)$$

This forms a quadratic equation of the form

$$\tilde{g}^2\left(\underbrace{1-\tilde{\mu}\left(e^{2i\beta h}-4e^{i\beta h}+6-4e^{i\beta h}+e^{2i\beta h)}\right)}_{\varphi}\right)-2\tilde{g}+1=0 \qquad (3.59)$$

Here the value of φ is subtly different to the value in the explicit case. The quadratic formula can now be solved as

$$\tilde{g} = \frac{2 \pm \sqrt{4 - 4\varphi}}{2\varphi} \tag{3.60}$$

This simplifies to

$$\tilde{g} = \frac{1 \pm \sqrt{1 - \varphi}}{\varphi} \tag{3.61}$$

Using similar notation to Section 3.5.2 it is possible to define $\varphi = 1 - \tilde{\mu}\alpha$. Here α has the same value as it did in the explicit case, and therefore the same maximum and minimum values (Equations 3.41 and 3.42) apply. Substituting in the value for φ this simplifies further to

$$\tilde{g} = \frac{1 \pm \sqrt{\tilde{\mu}\alpha}}{1 - \tilde{\mu}\alpha} \tag{3.62}$$

The denominator here is the difference of two squares so can be expressed as

$$\tilde{g} = \frac{1 \pm \sqrt{\tilde{\mu}\alpha}}{\left(1 + \sqrt{\tilde{\mu}\alpha}\right)\left(1 - \sqrt{\tilde{\mu}\alpha}\right)} \tag{3.63}$$

Therefore, dividing through, the stability criteria can be written as

$$|\tilde{g}| = \left|\frac{1}{1 \pm \sqrt{\tilde{\mu}\alpha}}\right| \leq 1 \tag{3.64}$$

The limits on α dictate that the term $\tilde{\mu}\alpha$ is non-positive for all values of $\tilde{\mu}$. Therefore the denominator is a complex number. It is therefore possible to rewrite (3.64) as

$$\left|\frac{1}{1 \pm i\sqrt{-\tilde{\mu}\alpha}}\right| \leq 1 \tag{3.65}$$

Here the term within the square root is now non-negative. For a complex number $= a + bi$, the modulus is calculated as $|z| = \sqrt{a^2 + b^2}$. Rearranging (3.65) gives the stability condition

$$\left|\sqrt{1-\tilde{\mu}\alpha}\right| \geq 1 \qquad (3.66)$$

As has been established, the term $-\tilde{\mu}\alpha$ is non-negative for all values of $\tilde{\mu}$ and therefore it follows that the condition in Equation 3.66 holds for all values of $\tilde{\mu}$. Therefore, this numerical scheme is unconditionally stable, with no restriction on spatial and temporal discretisation.

The stability analysis above ignored the external force term. Therefore, there is the possibility that this term could affect the stability detrimentally. However, the force term is calculated from the output of a commercial CFD model, which itself has its own stability tests. It is therefore concluded that providing both the CFD model and the plant model are independently stable, there should be no instability introduced by coupling the two together.

In summary, four different formulations of the beam equation were investigated. Initially an explicit formulation was used due to the relative simplicity. However, this method placed harsh restrictions on the timestep in order to guarantee stability and therefore the use of this model was not practical. The subcycling explicit model aimed to deal with the stability problems while retaining the simpler explicit formulation. However, this proved unhelpful as the subcycle force interactions could not be modelled and this led to unrealistic plant motion.

Therefore the explicit formulation was abandoned in favour of an implicit form. Initially, a second order method was used to further improve the likelihood of stability. This method showed promise, but the change of variables meant that it was difficult to accurately prescribe boundary conditions with confidence. Instead, a 4^{th} order implicit method was used. This model was shown to be unconditionally stable and solvable using matrix decomposition. For this reason, this model was the optimal choice, and was the version used throughout this thesis.

3.5.6 Verification of the model

The issue of verification of numerical schemes has been discussed in Section 3.2.7. Here, the emphasis is purely on verifying the numerical vegetation model itself. Therefore, there are three main elements to verification: grid convergence,

accuracy and code error. The scheme derived above is first order accurate. This is not ideal, as second-order accuracy is preferred. However, as explained in Section 3.5.2, use of the second order accurate central differencing would result in boundary conditions needing to be specified at the top of the stem, which in itself introduces inaccuracy.

Grid convergence tests were run on a steady state solution of the beam equation model. The model was set up so that the beam was subject to a constant, equally distributed force (F). The local force at each node was therefore F/n where n is the number of nodes on the stem. The model was run with the linear boundary conditions as described above and was tested for the range $5 < n < 1000$.

Figure 3.13 shows the change in calculated displacement of the top node of the stalk with increasing node number. The change has been expressed as a percentage of the total displacement. This shows that grid refinement has a decreasing impact as the resolution increases. For $n > 34$ the error is less than 2%, and the error drops away to less than 1% for node numbers greater than 89. With these considerations, the resolution for the numerical simulations was chosen to ensure minimal discretisation error, without imposing overly harsh computational time restrictions.

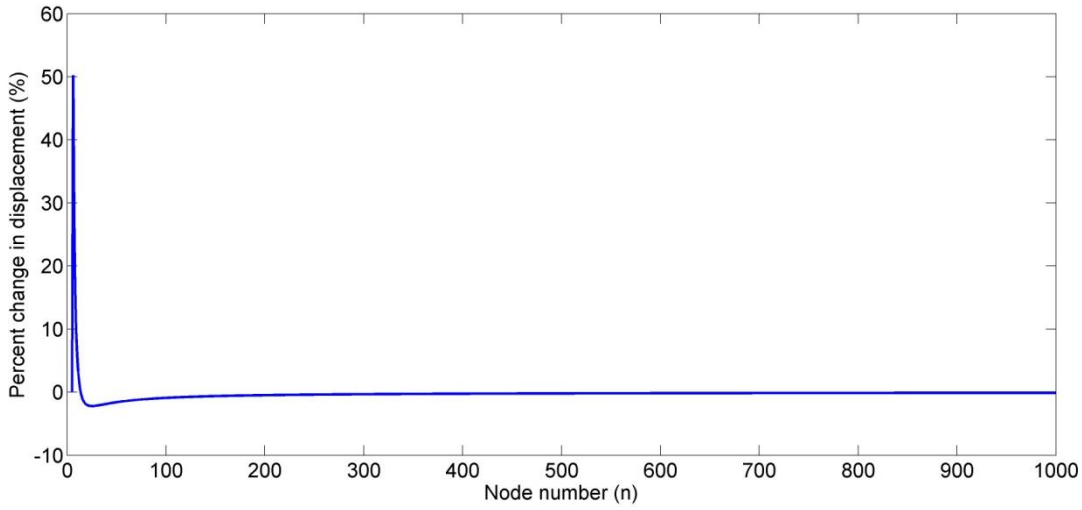

Figure 3.13: *Graph showing the change in end-node displacement with increasing node number. The change is shown as a percentage of the total displacement.*

3.6 N-pendula model

The N-pendula model is the second vegetation model developed within this thesis. As discussed in Section 3.3, the N-pendula model is conceptually very different to the Euler-Bernoulli beam model in terms of mechanics. Whereas the beam model considers the global behaviour of the plant through a partial differential equation, the N-pendula model considers the local behaviour of the plant, and then solves for the globally most efficient combination of local behaviours (Farnell *et al.*, 2004). This treatment of plant movement and flexibility lends itself to systems which are highly flexible with low rigidity values (e.g. macrophytes). In fact, similar models are used extensively within different disciplines to model flapping of flag-like structures (e.g.Farnell *et al.*, 2004; Michelin *et al.*, 2008). Therefore, instead of offering an alternative to the beam equation, this model provides a method for modelling vegetation of a different structural nature to that modelled by the beam equation.

3.6.1 Numerical basis

The model is conceptualised as a series of connected pendula of length l. Each pendulum is subject to a moment, about its pivot, which is a combination of the external fluid forces and the internal resistive forces.

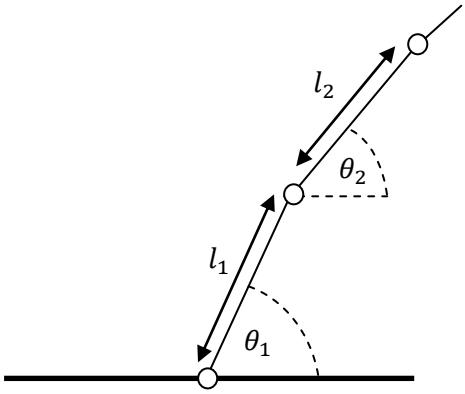

Figure 3.14: *A schematic showing the basis for the N-pendula model.*

A number of different global models were considered. The first to be used was similar to the method used by Farnell *et al.* (2004). This method solves for the minimal energy solution for the entire system using the Lagrangian to ensure that all the individual motions correspond to the most efficient global solution. However, this method was developed for simpler flow conditions and failed to produce

realistic results, most likely due to the relatively complex flow field, in comparison to other applications of the model. Therefore, this relatively complex model was not used but is noted as a further extension of this work.

Instead, a simpler model was developed, whereby the behaviour of the system is still treated in a global sense but in a simpler formulation similar to that used by Abdelrhman (2007). The torsion and tension forces at each hinge are linked such that:

$$F_i^{TOR} = E_z \cos\theta_i - E_x \sin\theta_i + F_{i+1}^{TEN} \sin(\theta_i - \theta_{i+1}) - EI * \delta_x^2 \theta \qquad (3.67)$$

$$F_i^{TEN} = E_x \cos\theta_i + E_z \sin\theta_i + F_{i+1}^{TEN} \cos(\theta_i - \theta_{i+1}) \qquad (3.68)$$

In these equations, E_x and E_z are the external fluid forces in the horizontal and vertical directions respectively. δ_x^2 is the second order difference scheme in line with previous notation and θ is the angle between the horizontal and the pendulum as marked on Figure 3.14. The process diagram of the model is shown in Figure 3.15.

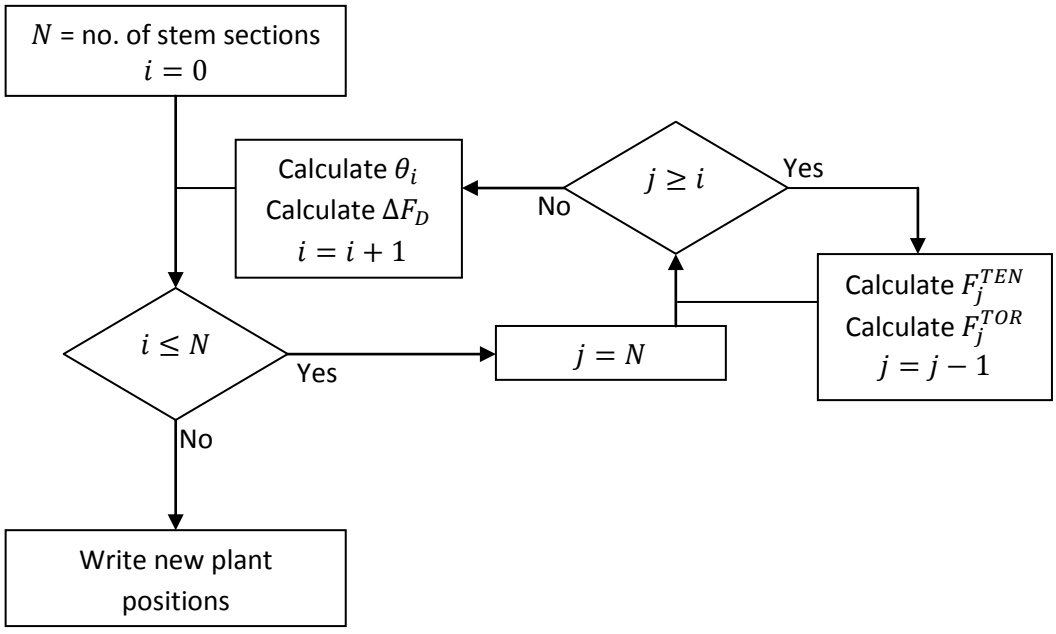

Figure 3.15: *A process diagram of the N-pendula model code.*

The model calculates the change in angle at each joint up the stem in turn, by resolving the forces at each joint further up the stalk into radial and transversal forces. After each angle change has been calculated, the resulting movement of the

sections higher up the stem caused by the angle change lower down is taken into account by an additional drag force ΔF_D which is added to the force calculations for subsequent nodes. The angle at each node, θ_i^t, was calculated using finite difference methods. First, the angular acceleration (${a_p}_i^t$) was calculated based on the known mass and force.

$${a_p}_i^t = F_i/m \tag{3.69}$$

From this, the angle and then velocity (${u_p}_i^t$) were calculated, using second order and first order backwards scheme respectively.

$$\theta_i^t = {a_p}_i^t(\Delta_t)^2 - \theta_i^{t-2} + 2\theta_i^{t-1} \tag{3.70}$$

$${u_p}_i^t = \frac{\theta_i^t - \theta_i^{t-1}}{\Delta_t} \tag{3.71}$$

The stability check was then applied, before the change in angle was either confirmed or re-calculated.

3.6.2 The zero rigidity approach

Initially the model was run with zero rigidity. The justification for this was twofold. First, the model is designed to replicate vegetation with very low rigidity, and therefore rigidity should not play a major role in determining plant shape. Second, moving to a hinge model such as the N-pendula model creates difficulties in determining accurate rigidity parameters. It is no longer possible to use global measures such as the one used in the Euler-Bernoulli beam model. Instead, a local treatment must be devised and this is less intuitive to relate to the physical characteristics of the vegetation.

However, experiments with zero rigidity highlighted problems with the stability of the model in this setup. With no damping or smoothing of forces over nearby joints, individual joints throughout the plant experienced large instantaneous forces. This then initiated a chaotic N-pendula regime whereby joints freely rotated through more than 360^o. This is unrealistic and therefore, to maintain model stability, a rigidity term had to be introduced.

3.6.3 Introducing flexural rigidity

The introduction of rigidity into the equations outlined above can be achieved by two different means. Firstly, the vegetation rigidity can be treated as a local force, acting at each hinge. This is the simplest model, and fits in well with the existing model framework. As it is based purely on a single local hinge, this force cannot depend on the shape of the stem at neighbouring nodes and therefore effectively represents a damping force, or numerical restraint on motion. This can either be set as a maximum change in angle per time-step or as a resistive force, that is proportional to the velocity. In order to minimise the restriction on the model, and limit parameterisation strictly to the cases where it is required for stability, the rigidity term was set as a maximum change in angle per time step.

In practical terms, this represents a limit on $\partial\theta/\partial t$. The limit was set to the angular velocity at which, assuming constant angular velocity along the stalk, the tip of the stalk would be moving at twice the fluid inlet velocity. Therefore, the restriction should only apply to extreme cases, such as when the plant is initially configuring into a stable position.

The second method for introducing rigidity involves the introduction of a term which is calculated based on the neighbouring hinges. Dijkstra and Uittenbogaard (2010) use such a term in their model, including an internal moment dependent on $\partial\theta/\partial s$ where s is the distance up-stalk. A similar term was implemented into the model based on a central difference scheme about each node. However, as the flexural rigidity was low, this force term had little effect on the vegetation, except for when instability occurred, when the term introduced strong oscillating forces into the equation.

Therefore, in the model application, both representations of rigidity were implemented, one as a physical rigidity which in practice had little impact on the mechanics, and one as a stability parameter which only acts to prevent highly unrealistic motion during initial reconfiguration. This model still has the benefit of not being driven by rigidity, but offered a more stable solution to the model with no rigidity.

3.6.4 Verification of the model

This method presents a very different problem to the differential equation based Euler-Bernoulli beam model, and therefore cannot be evaluated in the same way. While elements of the model are governed by finite difference approximations of differential equations, the overall motion is not, instead being calculated on a pivot by pivot basis. The method therefore contains inherent resolution dependence. The question which must instead be addressed is whether the model has a high enough spatial resolution (small enough length, l) to capture the plant and flow dynamics that are being investigated. In other words, the length should be small enough that the model is able to adequately replicate plant shape.

The pendula were represented within the model as cubes, with the pendula fixed to the centre of mass. Cubes were used instead of cylinders, as under significant reconfiguration, cylinders became a poor approximation of plant shape. The resolution of the model was set so that the cube size, and consequently pendula lengths l_i, were equal to three times the spatial resolution of the fluid model. This ensured that the blockage in the flow was significant enough to resolve some wake-scale turbulence whilst keeping the pendula lengths small enough to accurately reproduce the plant motion at small scales.

Because of the use of first-order accurate schemes in the time-integration used in the n-pendula model, it can only be considered as first-order accurate. This is a limitation of the model, which could be improved through further development.

3.7 Drag back-calculation

As discussed in Sections 2.2.5 and 3.4, one of the main driving forces in moving the vegetation is the drag force. Traditionally drag is calculated using the drag coefficient of a cylinder. The drag coefficient for a cylinder has been tested experimentally and is hence well known for a range of Reynolds numbers (see Figure 3.16). However, this is a good approximation only for rigid cylindrical vegetation. Flexible vegetation reconfigures in order to minimise form drag (Sand-Jensen, 2003) and therefore the frontal area and drag coefficient alter too. The

frontal area change is not in itself enough to describe the change in drag force, as this simply represents the presence of a shorter cylinder, whereas in reality the vegetation has reconfigured into a more streamlined shape.

It is hypothesised in this thesis that drag is a force which is spatially and temporally dynamic. Vegetation form often differs from the cylindrical form assumed by use of $C_D=1$ and vegetation form also changes through time. Therefore, it is suggested that the use of a constant drag coefficient is inappropriate and inaccurate. Thus a new method for calculating the drag force from the flow was developed.

Drag consists of two components: a skin drag (friction) component and a form drag component. Within the CFD model, the skin drag is caused by friction and is calculated and accounted for along the edges of the vegetation, on the plant/fluid boundaries by a no slip condition and roughness height. This force is included within the generic drag term in the vegetation model, though its relative contribution is small for cylindrical objects. The form drag (or pressure drag) is a result of the mass blockage and subsequent flow routing and is the dominant component for bluff objects. Initially this was estimated within the model using the drag equation (as described in Section 3.4). However, as discussed, this equation offers a very rough estimate of the drag which is often inaccurate (Kim and Stoesser, 2011), and so is unsuitable for such a high resolution model.

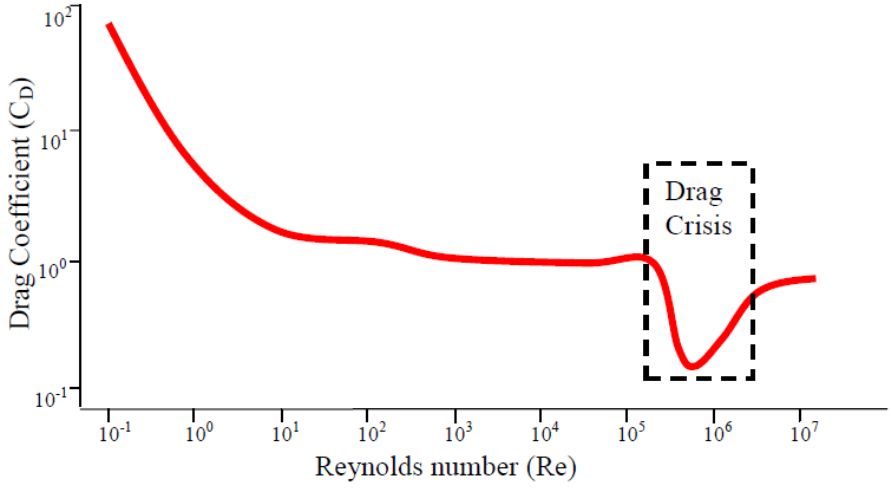

Figure 3.16: *Cylinder drag coefficient dependence on Reynolds number. Adapted from experimental data of Panton (1984).*

Within CFD models, all the velocity and pressure data are readily accessible, and so it is possible to back-calculate the form drag force directly using that data (Stoesser

et al., 2009; 2010). This removes the need for an empirical coefficient, potentially increasing accuracy. Two methods of calculating the drag have been investigated in this study.

3.7.1 Pressure coefficient approach

This is a standard method within aerodynamics for calculating drag from pressure fields (Anderson, 1984). However, as far as the author is aware, it has not yet been incorporated into a flexible vegetation model. As shown in Equation 3.72, the pressure (p) surrounding the vegetation element is resolved in the downstream direction and integrated over the vegetation surface area, thus calculating the net downstream force exerted on the vegetation stalk. Here θ is taken as the angle of the pressure component relative to the upstream direction, measured clockwise from above the vegetation as shown in Figure 3.17.

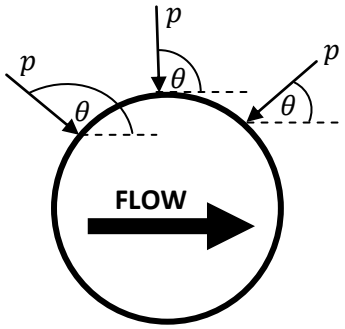

Figure 3.17: *Schematic diagram of the pressure integration around the cylinder.*

The pressure component acts normal to the surface of the vegetation at all locations therefore the force can be expressed as

$$F_D = \int_A p \cos\theta \; dA. \tag{3.72}$$

This can be split into two integrals, one over an angle and another over the height.

$$F_D = \int_0^h \int_0^{2\pi} p \cos\theta \; r_p d\theta dh. \tag{3.73}$$

Here, $\boldsymbol{r_p}$ is the vegetation radius and $\boldsymbol{h}$ is the vegetation height. This equation can be discretised (Equation 3.74) using a simple trapezium rule, numerical integration between known pressure values in cells around the edge of the vegetation.

$$F_D = rh\sum_{i=1}^{n}\frac{1}{2}(P_{i+1}+P_i)(\theta_{i+1}-\theta_i) \qquad (3.74)$$

Here $P_i = (p - p_\infty)\cos\theta_i$ is the resolved relative pressure at a distance of $\theta_i r_p$ around the circumference of the vegetation stalk. This equation can be re-arranged to solve for the drag coefficient, in terms of the pressure coefficient $\left(C_P = \frac{p-p_\infty}{0.5\rho U^2}\right)$ as

$$C_D = \sum_{i=1}^{n}\frac{1}{2\pi}\left(C_{P,i+1}\cos\theta_{i+1} + C_{P,i}\cos\theta_i\right)(\theta_{i+1}-\theta_i) \qquad (3.75)$$

In this formulation, a cylindrical plant form has been assumed. It is possible to generalise this for plants of any shape and form by considering the area of each discrete section of the plant surface separately and using the vertices of each section to calculate the angle in order to resolve the pressure into the downstream direction. These individual sections can then be summed in a similar manner to Equation 3.75. This is slightly more computationally expensive to solve, so initially the focus will be on cylindrical forms, but it is noted that the scheme could be extended to more complex plant forms in future.

This method was tested on a benchmark case, as well as with the two biomechanical models mentioned above. The benchmark case consisted of a simple cuboidal domain, with a single rigid cylinder as shown in Figure 3.18. The inlet flow velocity was set at 0.3m/s to ensure the Reynolds number was in the range where the drag coefficient can be approximated as 1. The model was run for long enough to ensure convergence of the key flow variables.

Figure 3.19 shows the distribution of the pressure coefficient around the cylinder in comparison to the idealised profiles. The shape of the profile shows good agreement with the overall pattern of the characteristic turbulent profile. The variation from the exact profile is expected as the exact values are likely to vary with Reynolds number. The average drag coefficient for the entire cylinder is 0.9614, with a standard deviation of 0.0113. This value is in good agreement with the

expected value as shown in Figure 3.16 and demonstrates the accuracy of the method throughout the flow depth.

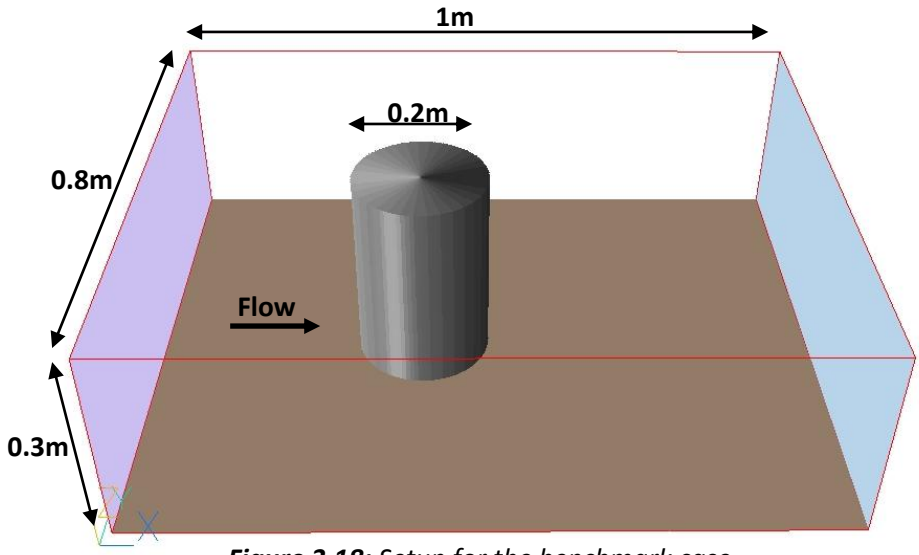

Figure 3.18: *Setup for the benchmark case*

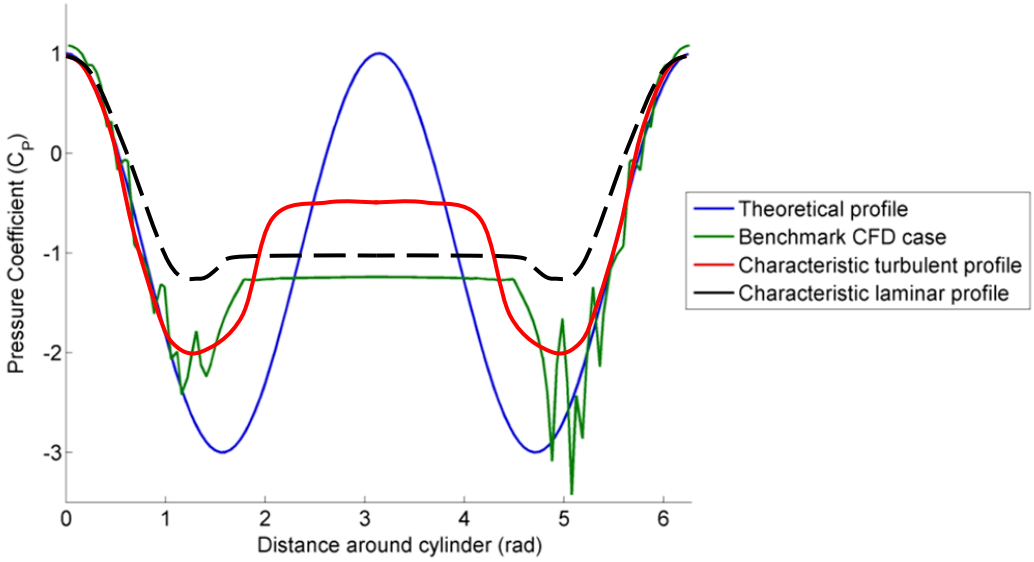

Figure 3.19: *Distribution of pressure coefficient around a cylinder for different flow conditions. Characteristic profiles taken from Anderson (1984).*

Figure 3.20 shows the distribution of the drag coefficient up a series of stalks taken from the Euler-Bernoulli beam model. The profile can be split into three clear sections. In the first (A), the stems act as rigid stems, with drag coefficients similar to those observed for rigid cylinders. At the bed there are higher drag coefficients, corresponding to the contribution of bed drag. In the second region (B) the stalks experience slight bending, which has two effects on the drag coefficient. Firstly, the pattern becomes much less smooth. This is due to the fact that vegetation is represented by porous blocks rather than smooth boundaries.

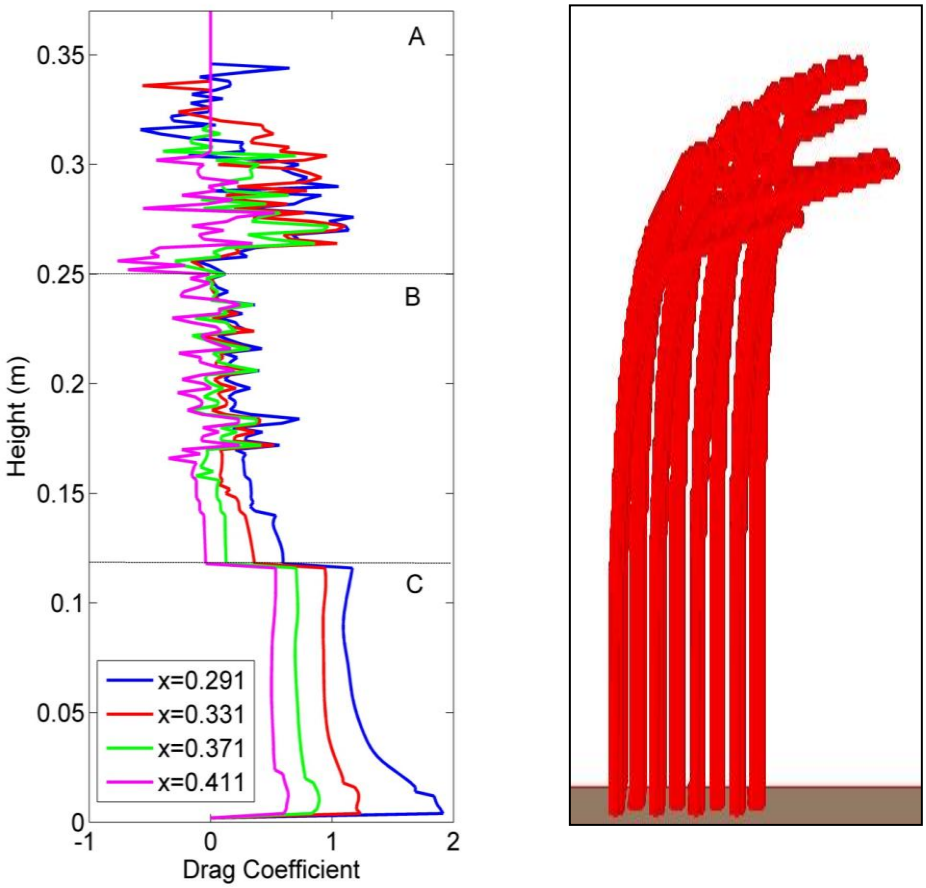

Figure 3.20: *Vertical drag coefficient profile taken from the Euler-Bernoulli beam model. Three clear sections are identified: a) cylindrical drag behaviour, b) slight stalk bending and c) severe stalk bending.*

Secondly, there is a reduction in drag due to the bending. This is expected as the vegetation is dynamic in this region and therefore reconfigures to minimise drag. Furthermore, because the vegetation position is not static, there is less likelihood that a stable pressure distribution will form immediately around the vegetation from which the drag is calculated. The third region (C) occurs at the top of the stem, where there is major plant bending. This region is characterised by higher drag coefficients, but with high variability. The higher values are expected as these horizontal slabs of the domain contain a higher mass of vegetation due to bending.

At several points up the stalk, negative drag coefficients seem to exist. This is clearly unphysical but from the drag equation (Equation 3.26), it can be seen that in this context it merely corresponds to a force in the opposite direction. In other words, regions with a negative drag coefficient are experiencing a net upstream force. The region that experiences the most negative drag coefficient and thus force is the

stalk at the rear of the canopy, which is most likely to experience high pressure from patch wake scale recirculation, combined with lower pressure at the front of the stems. Similarly, the tops of some stems experience negative drag and this could be due to streamlining reducing the pressure at the front of the stem, combined with high pressure behind due to recirculation.

Figure 3.20 highlights two key issues with the modelling of drag coefficients. Firstly, there is clear spatial variability in drag both on a stem and patch scale. Therefore it is not appropriate simply to assume a drag coefficient of 1. The second issue relates to this, in that the spatial distribution of drag corresponds directly to plant bending. Such reconfiguration is a dynamic process and thus it can be inferred that the drag coefficient will also exhibit significant temporal variation. Thus, the case is made for the inclusion of a dynamic drag coefficient within the biomechanical model, calculated directly from the flow data. Due to time constraints, it was not possible to apply this drag model to all the simulations carried out in Chapters 5 and 6. However, it was used on a prototype run, the results of which are presented in Section 6.7.

3.7.2 Control volume approach

In addition to the pressure coefficient method, a control volume method can also be used. Kim and Stoesser (2011) devised a patch-scale control volume method, based on the pressure loss across the volume containing the vegetation patch. This is based upon the theory discussed by Tanino and Nepf (2008), which links the bulk drag coefficient to the downstream pressure gradient. This method, shown in Equation 3.76, calculates a drag coefficient for both the vegetation and the bed, though in most cases the bed drag is considered negligible in comparison to the vegetative drag.

$$C_D = \frac{2\left(\frac{\partial p}{\partial x}\right) V(1-\emptyset)}{u^2 M h_w 2 r_p} \tag{3.76}$$

In this equation, $\partial p/\partial x$ is the downstream pressure gradient, V is the flow volume, $\emptyset$ is the vegetation volume fraction, u is the bulk velocity, M is the number of stalks

per area, h_w is the water depth and r_p is the plant radius. This is a useful method for reach-scale models, but cannot be used to drive plant motion in a high resolution model where each stalk is resolved.

3.8 Chapter summary and conclusions

This chapter has explained and justified in detail the methods used throughout the numerical experiments presented in Chapters 5 and 6. This includes the development of two novel biomechanical models which have shown to be robustly and rigorously derived. Several different formulations were tested for both, and the best methods selected based on stability and physical representation. Their reliability as a research tool has been verified, and will be validated against flume data in Chapter 5.

This chapter has also discussed the key general modelling considerations including turbulence modelling, solution methods and boundary conditions that must be considered when applying CFD models in a geomorphological context. Thus the biomechanical vegetation models can now be implemented within the CFD framework with confidence.

Chapter 4: Analytical methods for flow characterisation

4.1 Chapter Introduction

Chapter 2 highlighted the importance of understanding turbulent characteristics of the flow within vegetated canopies. It was demonstrated that, due to the presence of the vegetative drag within the canopy, a shear layer forms at the canopy top as a result of the drag discontinuity. This shear layer generates large-scale coherent structures which dominate mass and momentum exchange, and are therefore a crucial part of canopy flows. These vortices develop via the Kelvin-Helmholtz instability at the canopy top, evolving into roller vortices which then stretch and fold to become pairs of hairpin vortices.

One of the aims of this project, and specifically research question 3, focuses on the effect of vegetation characteristics and configuration on the vortex dynamics. In order to investigate this it is necessary to be able to quantify the presence and physical characteristics, such as size and shape, of the vortices. This requires the use of a range of different analysis methods which are capable of detecting and visualising vortices within the flow. Vortices are complex and dynamic, and hence there is no single analysis method which is proven to detect them with 100% accuracy.

A suite of different methods have therefore been developed and employed to extract the turbulence characteristics and vortex signatures from the data produced from the numerical and flume experiments. In this chapter, the various techniques used to analyse the data in Chapters 5 and 6 are explained and justified. Where appropriate, the same methods have been used for both the flume and numerical data sets to ensure comparability.

4.2 Mean flow profiling

A key element in canopy layer theory is the alteration of the characteristic mean velocity profile and the effect this has on turbulence generation (Raupach *et al.*, 1996). Therefore, the initial method of analysis is vertical profiling of the mean flow. This is useful as it illustrates the difference in velocity between the canopy zone and the flow above. Furthermore, it shows the mean velocity gradient which can be used to calculate the shear stress. As the experiments were carried out over a range of different depths and Reynolds numbers, it is necessary to normalise the results to enable effective inter-comparisons. The normalisation, whereby the velocity and height variables are normalised using three characteristic mixing layer variables defined below; the mean velocity $(\overline{U})$, the velocity difference (ΔU) and the momentum thickness (θ_M), follows the method used by Ghisalberti and Nepf (2002; 2006), which was in turn based on the method used by Rogers and Moser (1994).

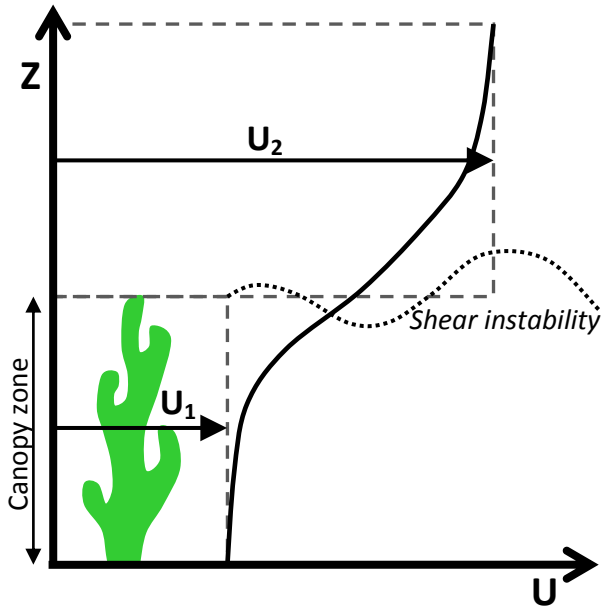

Figure 4.1: *Schematic of the mixing layer velocity profile. The flow is conceptualised as two layers of different velocity (U_1 and U_2), one through the vegetation canopy and one above. At the interface between the two zones, a shear instability develops.*

This method therefore works on the assumption that the flow profile resembles the hyperbolic tangent curve of a classical mixing layer as discussed in Chapter 2 (Rogers and Moser, 1992). Consequently, the mean velocity is defined as the arithmetic mean of the two co-flowing velocities as illustrated in Figure 4.1 and the velocity difference as the difference between the two co-flowing velocities.

$$\overline{U} = \frac{U_1 + U_2}{2} \tag{4.1}$$

$$\Delta U = U_2 - U_1 \tag{4.2}$$

Hence the normalised velocity, (U^*), is calculated as:

$$U^* = \frac{U - \overline{U}}{\Delta U} \tag{4.3}$$

The momentum thickness is calculated from the mean velocity profile as

$$\theta_M = \int_{-\infty}^{\infty} \left[\frac{1}{4} - \left(\frac{U - \overline{U}}{\Delta U} \right)^2 \right] dz \tag{4.4}$$

This is effectively a measure of the momentum deficit within the flow, due to the presence of the mixing layer (Anderson, 1984). This can be calculated numerically using the trapezium rule. If we define the heights z_1 and z_2 such that

$$U_1 = U(z_1) \tag{4.5}$$

$$U_2 = U(z_2), \tag{4.6}$$

then the integral (4.4) can be evaluated using the fact that the limit of the integral is zero for $z \leq z_1$ and $z \geq z_2$. The numerical formula then becomes

$$\theta_M = \frac{h}{2} \sum_{i=1}^{n} \left[\frac{1}{2} - (U_{i+1}^*)^2 - (U_i^*)^2 \right], \tag{4.7}$$

where $n = (z_2 - z_1)/h$ and h is the spatial resolution in z. Once θ has been calculated, the normalised height (z^*) can be calculated in a similar way to the velocity as

$$z^* = \frac{z - \bar{z}}{\theta_M} \tag{4.8}$$

Here $\bar{z}$ is the height at which the mean velocity $(\overline{U})$ occurs. This is calculated directly from the data as the lowest point in the velocity profile where the velocity is equal to, or exceeds, the mean velocity. In addition to the velocity, the shear stress can also be normalised in a similar way. Rogers and Moser (1994) give the equation for normalised Reynolds stress as

$$\overline{u'w'}^{*} = \frac{\overline{u'w'}}{(\Delta U)^2} \tag{4.9}$$

Conversion of the original data into these new variables, U^*, $\overline{u'w'}^{*}$ and z^*, creates normalised mixing layer velocity profiles which allow direct comparison between the data from different experiments, collected in different conditions.

This technique is valuable as the characteristics of the mixing layer velocity profile in turn determine the characteristics of the turbulence. Notably, as mentioned in Chapter 2, the Kelvin-Helmholtz instabilities that are generated at the mixing layer and lead to the development of roller vortices at the canopy top, can be characterised by their frequency (Ho and Huerre, 1984; Ghisalberti and Nepf, 2002):

$$f_{KH} = 0.032\frac{\overline{U}}{\theta_M} \tag{4.10}$$

Thus, the expected dominant turbulent length scale can be calculated from the mean shear velocity profile characteristics described above. However, to fully answer the research questions, more detail regarding the nature of the vortices is required and therefore more sophisticated techniques are employed.

4.3 Reynolds decomposition

The principle behind Reynolds decomposition has been outlined in Section 2.4.3. Decomposition of the signal into mean and fluctuating (turbulent) components permits analysis of the turbulent signal. There are a number of useful quantities which can be defined using the turbulent signal.

The instantaneous turbulent kinetic energy (TKE) is defined as

$$k' = \frac{1}{2}\rho(u'^2 + v'^2 + w'^2) \tag{4.11}$$

Here, u', v' and w' are the fluctuating parts of the three orthogonal velocity components and ρ is the fluid density. The mean TKE for a time series can also be calculated as

$$\overline{k'} = \frac{1}{2}\rho\left(\overline{u'^2} + \overline{v'^2} + \overline{w'^2}\right) \quad (4.12)$$

Here the overbar denotes the time-averaged value. It is therefore possible to estimate the average amount of energy contained within the turbulent signal. This is an important variable to quantify as it has been shown that TKE can be used as a good indicator for investigating important processes such as erosion and deposition within canopies (Nepf *et al.*, in press). It can also be useful to look at the individual component contributions to the turbulent kinetic energy as this indicates whether the turbulence is isotropic or anisotropic. Isotropic turbulence is spatially homogeneous with no preference for direction (Hinze, 1975). Anisotropy within the turbulent kinetic energy therefore alludes to coherent, directional structure within the turbulence which may be the signature of large scale vortices.

It is possible to calculate the production rate of turbulent kinetic energy by comparing the budgets for the mean and turbulent components of the kinetic energy (see (Hinze, 1975)). The turbulent production term is so named because it appears in both the mean and turbulent budgets with opposite signs. Therefore, it can be viewed as the rate of transfer of energy between the mean and kinetic budget. It is given by:

$$P_T = -\overline{u'w'}\frac{\partial \bar{u}}{\partial z} \quad (4.13)$$

Plotting the turbulent production rate highlights regions within the flow where turbulence is being generated and can thus indicate sources of turbulence within the flow. The turbulence production rate is the product of the mean velocity gradient and the mean product of the instantaneous velocities. This second term is very similar to the time-averaged Reynolds stress which is defined as:

$$\tau^{ij} = -\rho\overline{u'w'} \quad (4.14)$$

and represents the stress which arises from the momentum transfer by the fluctuating velocity field (Pope, 2000). The Reynolds stress is itself a useful flow quantity which can be used to estimate momentum absorption by the plant canopy, and the potential plant deformation response to the flow (Velasco *et al.*, 2003).

4.4 Quadrant analysis

A useful by-product of the Reynolds decomposition is the development of quadrant analysis; a method for analysing turbulence within a flow time series using conditional sampling (Lu and Willmart, 1973) which has been used extensively to describe vegetated flows (see Chapter 2). If just the fluctuating components of the Reynolds-decomposed velocity signal are considered, then different, orthogonal components of the instantaneous velocity can be plotted on a quadrant graph as seen in Figure 4.2. Here the vertical and downstream velocities are used, as is most common practice within canopy flows. However, it is worth noting that the lateral component may be more insightful in certain situations (e.g. White and Nepf, 2007) when the area of interest is the lateral shear layer.

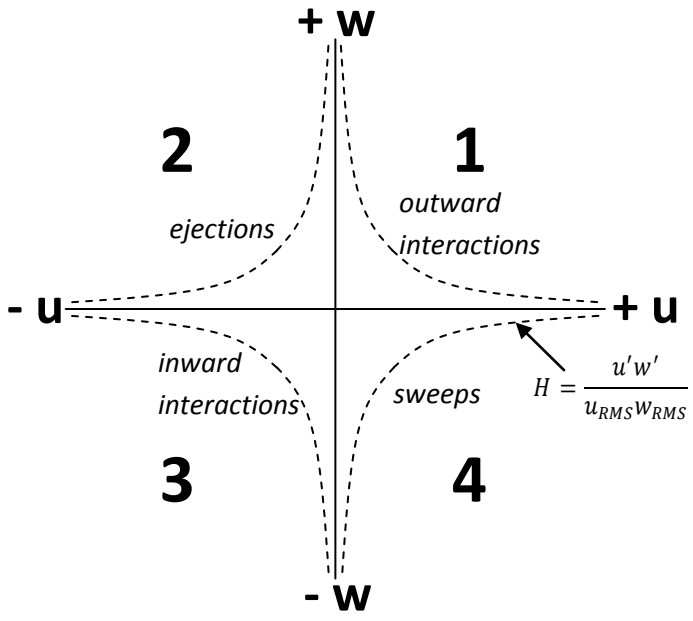

Figure 4.2: *Quadrant analysis of Reynolds decomposition in the x-z plane redrawn from Bennett and Best (1995). The dotted line defines a hole or threshold value often used to discount outliers, based upon the hole size, H.*

In Figure 4.2 the origin represents the mean flow, and deviations from the mean represent turbulent events. The turbulent events can be categorised by quadrants 1-4 as outward interactions, ejections, inward interactions and sweeps (or inrushes) respectively (Bennett and Best, 1995). This technique has been used extensively in order to detect coherence within a range of vegetated flow time series, as discussed in Sections 2.2.2 and 2.3.1.

It is often preferable to ignore small scale fluctuations as it is usually the larger scale fluctuations which relate to coherent turbulent structures. One way to do this is to impose a 'hole size' as a further condition. Here, values lying within the hole, corresponding to small scale fluctuations about the mean, are disregarded while larger magnitude turbulent events are retained (Lu and Willmart, 1973). The hole size is set as:

$$H = \frac{u'w'}{u_{RMS}w_{RMS}} \tag{4.15}$$

Therefore, increasing the hole size increases the amount of data discarded. In most anisotropic turbulent data sets, the larger the hole size, the greater the bias between quadrants and thus the more evident any coherence becomes. This is based on the assumption that the statistical component of the turbulence will resemble a Gaussian white noise distribution, evenly spread between the quadrants. Therefore, as the hole size is increased, the contribution to the remaining data from the Gaussian noise distribution diminishes rapidly. Furthermore, as mentioned in the previous section, the product of these velocity components is the Reynolds stress. Therefore, the hole size also sets a minimum Reynolds stress value, below which turbulent events are considered insignificant.

Some studies have also looked at the time sequencing of quadrant events (e.g. Buffin-Bélanger *et al.*, 2000; Marquis and Roy, 2011). This can reveal both the ordering of different turbulent quadrant events, as well as the frequency and duration.

4.5 Spectral analysis

Another method for extracting coherent data from a turbulent time series is to use spectral analysis. This method uses a Fourier transform to analyse the energy present within the signal and permits investigation of the periodicities at different time-scales present within the data. Fourier (1878) theory states that any smooth continuous signal, $u(t)$, can be written as a function of sine and cosine waves (Equation 4.16).

$$u(t) = A_0 + \sum_{k=1}^{\infty} A_k \sin(2\pi kt) + B_k \cos(2\pi kt) \quad (4.16)$$

Here, A_k and B_k are coefficients. For a discrete, finite-length time series, the number of waves is not infinite but is instead limited by resolution, and therefore the equation for a time series $\{u_1, u_2, \dots, u_N\}$ can be rewritten as

$$u_t = A_0 + \sum_{k=1}^{N/2} A_k \sin(2\pi kt/N) + B_k \cos(2\pi kt/N) \quad (4.17)$$

This can be simplified into the complex exponential form

$$u_t = \sum_{k=-N/2}^{N/2} C_k e^{i2\pi kt/N} \quad (4.18)$$

This is, in fact, a generalisation of (4.16) into complex space. Parseval's theorem (1799) states that the energy contained within the Fourier transform, calculated as the sum of the different wave energies is equal to the energy contained within the original velocity time series. Therefore, whereas calculating the turbulent kinetic energy of the signal gives an idea of the total energy, through using the Fourier transform it is possible to analyse the energy contained within different frequencies in the signal. Hence it is possible to identify frequencies with high energy which may correspond to large scale coherent turbulence.

As mentioned in Section 2.2.5, Kolmogorov (1941) discovered that the decay of homogeneous, isotropic turbulence followed the -5/3 spectrum, as energy was transferred from large, low frequency eddies to much smaller, high frequency eddies. By analysing the energy contained within individual frequencies, it is possible to detect deviation from this spectrum, through the presence of peaks and troughs, as well as changes in spectral slope or spectral shortcuts, which may indicate the presence of additional turbulence-generating mechanisms within the flow (Naden *et al.*, 2006).

In assuming that the signal comprises of sinusoidal waves, Fourier analysis inherently assumes that the signal is periodic and infinite. The signal therefore has

infinite energy. Consequently, instead of directly measuring the energy within the spectra, it is more appropriate to measure the average power of the signal. Given that a wave's power is proportional to the square of the amplitude, the power within the Fourier spectrum can be calculated directly from the amplitudes, C_k. In order to calculate the amplitude of each wave, Equation 4.17 can be re-arranged as:

$$C_k = \sum_{t=-N/2}^{N/2} u_t \, e^{-i2\pi kt/N} \tag{4.19}$$

The power spectral density of the signal can be estimated using the periodogram method (Schuster, 1898) as:

$$S(f) = \frac{1}{NF_s}\left|\sum_{t=1}^{N} u_t e^{-i2\pi ft/NF_s}\right|^2 \tag{4.20}$$

This formulation has been scaled to the physical frequency (f) rather than the wavenumber using the sampling frequency (F_s). Combining Equations 4.19 and 4.20 it is clear that, as expected, the periodogram estimation of power spectral density at a frequency f_i can be equated to the square of the Fourier transform coefficient C_{f_i}, scaled appropriately.

$$S(f_i) = \frac{1}{NF_s}\left|C_{f_i}\right|^2 \tag{4.21}$$

Spectral plots created using the periodogram method can be very noisy and therefore it is not always easy to distinguish trends. Therefore in some cases the Welch method (1967) has been used to average the periodograms. In this method the time series is split into a number of smaller, overlapping intervals over which the periodogram is calculated. The non-overlapping version of the Welch method is called the Bartlett method (1948). These periodograms can then be averaged, thus in theory, removing the random noise element and picking out elements of the signal which are consistent throughout. An important consideration when using these methods is that the averaging process limits the resolution as wavelengths longer than interval size are not considered (Stoica and Moses, 1997). Therefore,

these methods are only appropriate for time series where the resolution of enquiry is significantly smaller than the length of the time series.

4.6 Wavelet analysis

Wavelet analysis provides another method for analysing periodicities within data. It is a similar in approach to spectral analysis, but provides a more powerful tool as it is applied locally rather than globally and is therefore capable of analysing time series which contain intermittency or non-stationary periodicities (Daubechies, 1990; Farge, 1992). As with spectral analysis, wavelet analysis involves the fitting of a known function to a signal, though in this case the functions fitted are wavelets rather than trigonometric functions. There are two main characteristics to wavelet functions (Percival and Walden, 2000). Firstly, for a given wavelet function $\psi(t)$, the integral must be zero (Equation 4.22). This ensures that the wavelet is in fact a wave function.

$$\int_{-\infty}^{\infty} \psi(t)dt = 0 \tag{4.22}$$

The second condition is that the square of the wavelet must integrate to a constant (Equation 4.23). This ensures that the wavelet is finite and non-zero. This constant is often arbitrarily taken as one.

$$\int_{-\infty}^{\infty} \psi^2(t)dt = 1 \tag{4.23}$$

Figure 4.3 shows some common examples of wavelet functions. One of the major advantages of wavelet analysis over spectral analysis is the variety of different wavelet shapes available. Whereas trigonometric functions contain the restriction that every positive peak in the data must exist alongside an equal and opposite negative peak, wavelets provide a variety of different options, which can be chosen to fit the characteristic shape of structures within the signal. Within turbulence data, it has been suggested that the Morlet wavelet is the most appropriate due to its similarity with the decomposition of turbulent energy from a characteristic eddy

(Hardy *et al.*, 2009). In order to study periodicities of different frequencies, the Morlet wavelet may be scaled linearly.

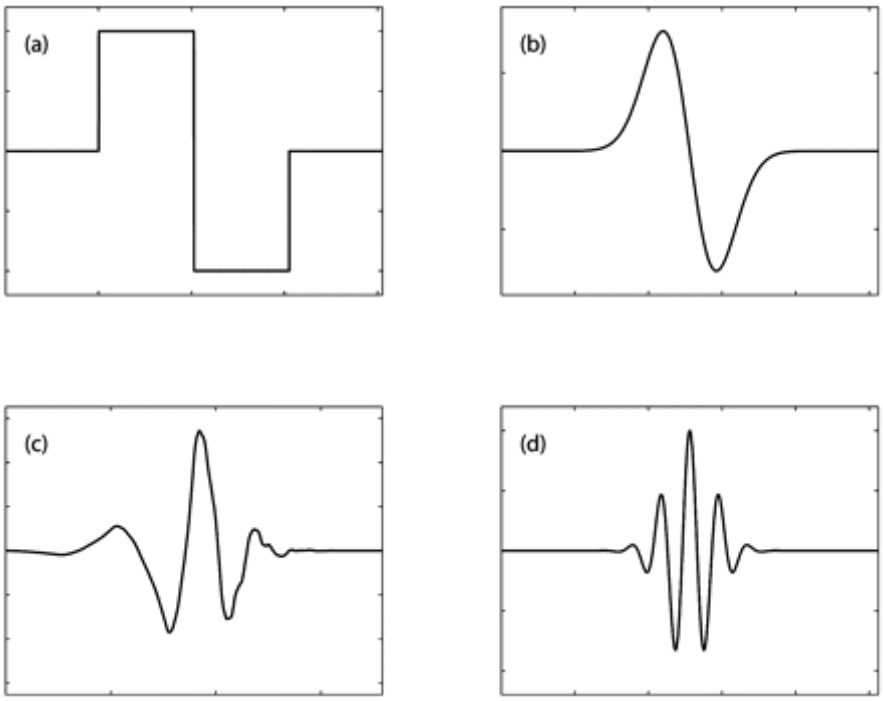

Figure 4.3: *Commonly used wavelets: (a) Haar, (b) Gaussian (order 1), (c) Daubechies (order 4) and (d) Morlet wavelets. Figure taken from Baker (2007).*

The wavelet power spectrum is calculated by fitting the characteristic wavelet to the time series, centered at each point in turn, over a range of different scales. Thus for a series of length *N*, at each different time scale, *N* different wavelets may be fitted (Kaiser, 1994), under the assumption that the time series is periodic. This convolution can be performed simply using the discrete Fourier transform (Torrence and Compo, 1998). If the time series is not periodic, the values at either end of the spectrum will be affected by edge effects and therefore must be discarded from the final dataset. The size of this region, called the cone of influence, will vary with scale.

Similar to spectral analysis, each time a wavelet is fitted, the resulting wavelet magnitude (power) is calculated. The distribution of energy across different time scales (inversely related to frequency), throughout the time series can then be assessed by identifying peaks in the wavelet power spectrum.

Analysis of turbulent spectra, via spectral or wavelet analysis, enables identification of dominant frequencies within the flow. Within canopy flows, there are typically

three key vortex frequencies which can be identified. The first is the Kelvin-Helmholtz frequency (f_{KH}) which relates to shear-scale vortex shedding (Equation 4.10). The other two are the wake-shedding frequency (f_W), which corresponds to the rate at which vortices are shed from individual stem wakes, and the natural frequency (f_N) which is a material property of the vegetation. The equations for the wake and natural frequencies are given in Equations 4.24 and 4.25 respectively.

$$f_W = \frac{0.2U}{2r_p} \tag{4.24}$$

$$f_N = \frac{22.4}{2\pi {l_b}^2}\sqrt{\frac{EI}{\rho A_p}} \tag{4.25}$$

In the above equations, U is the fluid velocity, r_p is the stem radius, l_b is the stem length, EI is the flexural rigidity of the stem and A_p is the cross-section of the beam. These frequencies can be used to identify key controls on the fluid and plant spectra.

4.7 Eulerian vortex methods

While the methods described above can help identify vortices within a single-point velocity signal, vortices are spatial by nature and therefore more easily detected within a spatial dataset such as those provided by Particle Image Velocimetry (PIV) and CFD (see Chapters 5 and 6). There are a number of techniques which have been developed to extract vortex signals from a two-dimensional velocity field. The Eulerian vortex methods described here detect vortices within an instantaneous 2D or 3D snapshot of the flow, by analysing spatial patterns in the velocity gradient field and its invariants (Green *et al.*, 2007).

The rotation tensor for a 3 dimensional velocity field (u) is defined as

$$\Omega = \frac{1}{2}(\nabla u - (\nabla u)^T) \tag{4.26}$$

Another useful, and similar, definition is that of the rate-of-strain tensor

$$S = \frac{1}{2}(\nabla u + (\nabla u)^T) \tag{4.27}$$

Together, these are the symmetric and anti-symmetric components of the divergence of the velocity field (∇u) (Chakraborty *et al.*, 2005). From Equation 4.26 the individual components of the vorticity can be derived as

$$\omega_i = \frac{1}{2}\epsilon_{ijk}\Omega_{\mathrm{jk}} = \epsilon_{ijk}\partial_j u_k \tag{4.28}$$

Here Einstein notation has been used for simplicity. This vorticity can, in the fluvial context, be considered as streamwise (ω_1), spanwise (ω_2), and vertical vorticity (ω_3). These three definitions will be used in the analysis in Chapters 5 and 6. While this definition of vorticity as the curl of the velocity field is useful, it does not necessarily highlight the presence of vortices within the flow. For example, regions of high lateral shear result in rotational flow and high values of vorticity, which cannot be distinguished from actual swirling motions using just vorticity (Cucitore *et al.*, 1999). Therefore, other more sophisticated identification methods are often required.

4.7.1 The Q criterion

The earliest vortex identification method proposed was the Q criterion (Hunt *et al.*, 1988). Here Q is the second invariant of ∇u and a vortex centre is associated with values of $\mathrm{Q} > \mathrm{Q_E}$, where $\mathrm{Q_E}$ is some threshold, although most subsequent studies have simply taken $\mathrm{Q_E} = 0$.

$$Q = \frac{1}{2}(\|\Omega\|^2 - \|S\|^2) \tag{4.29}$$

Here $\|.\|$ is the matrix norm, which can either be calculated as the Frobenius norm $\left(\|\mathrm{X}\|_F = \sqrt{\mathrm{tr}(XX^T)}\right)$ (e.g. Jeong and Hussain, 1995; Chakraborty *et al.*, 2005) or the Euclidean norm $\left(\|\mathrm{X}\|_2 = \sqrt{\lambda_{max}(XX^T)}\right)$ (e.g. Haller, 2005). Whilst these two norms are often very similar it is worth noting that the Frobenius norm is based upon all the eigenvalues whereas the Euclidean norm is based purely upon the largest eigenvalue. Therefore, where the relative magnitudes of the eigenvalues differ between the strain and vorticity tensor, choice of norm may have an impact on the

results. In this study the broader Frobenius norm is used in line with Chakraborty *et al.* (2005) and the majority of other studies.

The Q criterion carries a second condition, that the local pressure be lower than the ambient pressure. $Q > 0$ does not guarantee the existence of such a minimum, however, in most cases it is sufficient (Jeong and Hussain, 1995), and therefore, in this study only the primary condition is used (Chakraborty *et al.*, 2005).

The physical interpretation of the Q criterion is that it assumes that a vortex is present if the magnitude of the vorticity tensor is greater than that of the rate of strain tensor and there exists a localised pressure minimum.

4.7.2 The λ_2 criterion

The λ_2 criterion (Jeong and Hussain, 1995) extends the idea that vortex centres correspond to the occurrence of localised pressure minima. By considering the symmetric component of the divergence of the Navier-Stokes equations and discarding the unsteady irrotational straining and viscous effects, it can be shown that

$$\Omega_{ik}\Omega_{kj} + S_{ik}S_{kj} = -\frac{1}{\rho}p_{ij} \tag{4.30}$$

Here p_{ij} is the Hessian (second derivative matrix) of the pressure and Ω and S are the vorticity and strain tensors respectively, as defined earlier. In order that a local planar minimum of pressure exists, two eigenvalues of p_{ij} must be positive. By Equation 4.30, this condition must also hold on $\Omega^2 + S^2$.

Equation 4.30 is symmetric and therefore has only real eigenvalues. Therefore, if the eigenvalues are ordered arbitrarily so that $\lambda_1 \geq \lambda_2 \geq \lambda_3$, this condition holds as long as $\lambda_2 \leq 0$; hence why it is called the λ_2 criterion. These eigenvalues can be linked to the Q criterion by the following equation.

$$Q = -\frac{1}{2}\mathrm{tr}(S^2 + \Omega^2) = -\frac{1}{2}(\lambda_1 + \lambda_2 + \lambda_3) \tag{4.31}$$

Thus, the λ_2 condition can be seen as a localisation of the Q criterion onto a single plane (Jeong and Hussain, 1995). Physically speaking, the λ_2 criterion assumes that a vortex corresponds to a pressure minimum within a plane, when the contributions of irrotational straining and viscous terms in the Navier-Stokes equations are discarded (Jeong and Hussain, 1995). If included, these two terms can both create false pressure minima and eliminate existing minima caused by vortices.

4.7.3 The Δ criterion

The Δ criterion (Chong *et al.*, 1990) defines a vortex as the region where the divergence of the velocity field, ∇u, has complex eigenvalues. This is the least physically intuitive, but the criterion essentially assumes that flow is rotational in one plane. The identity $|\lambda I - \nabla u| = 0$ can be used to calculate the characteristic equation for the eigenvalues (λ) and as the matrix is of rank 3, the equation becomes

$$\lambda^3 + P\lambda^2 + Q\lambda + R = 0 \tag{4.32}$$

It is possible to calculate the characteristic equation and show that

$$P = -\mathrm{tr}(\nabla u) = -\nabla \cdot u \tag{4.33}$$

$$Q = \frac{1}{2}(\|\Omega\|^2 - \|S\|^2) \ \text{[as above]} \tag{4.34}$$

$$R = -\mathrm{Det}(\nabla u) \tag{4.35}$$

Using the formula for a cubic discriminant (Δ), and applying the formula to purely incompressible cases ($P = 0$), gives the requirement for complex eigenvalues of

$$\Delta = \left(\frac{R}{2}\right)^2 + \left(\frac{Q}{3}\right)^3 > 0 \tag{4.36}$$

Note that this requirement can still hold for a negative value of Q and therefore, the Q criterion is a subset of the Δ criterion.

Figure 4.4 shows schematically how the different vortex methods are linked. The key point this illustrates is that the three vortex methods described above are

similar in nature and all have a similar theoretical basis, however each will give slightly different results.

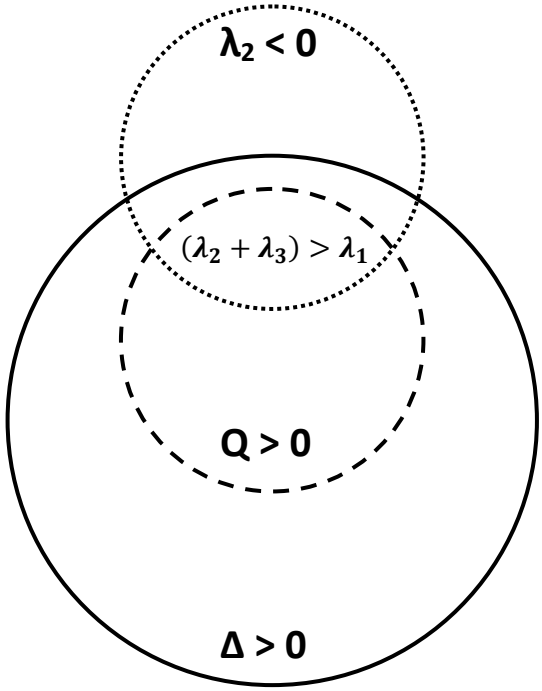

Figure 4.4: *A schematic diagram showing the relationships and regions of overlap between the λ_2, Δ and Q criteria.*

4.7.4 Swirling strength criterion

Zhou *et al.* (1999) proposed the swirling strength criterion as an extension of the Δ criterion, whereby the complex conjugate eigenvalues of ∇u are used to identify vortices. Providing the Δ condition holds, then the eigenvalues of the flow can be written as a real eigenvalue, $\lambda_1 = \lambda_r$ and a complex conjugate pair, $\lambda_{2,3} = \lambda_{cr} \pm i\lambda_{ci}$. The real eigenvalue represents a stretching or compressing of the flow whereas the complex pair define the swirling motion.

Therefore, λ_{ci} can be referred to as the swirling strength of the vortex (Zhou *et al.*, 1999) and iso-surfaces of constant λ_{ci} may be used to visualise the vortices.

$$\lambda_{ci} \geq \epsilon \tag{4.37}$$

Chakraborty *et al.* (2005) extended this idea by adding a further constraint

$$-\kappa \leq \frac{\lambda_{cr}}{\lambda_{ci}} \leq \delta \tag{4.38}$$

Here, κ and δ are both positive thresholds. The vortex core is therefore visualised as the intersection of these two sets. In addition to the threshold of swirl strength, which excludes slowly swirling motions (ϵ), this method also excludes regions with low orbital compactness. Orbital compactness can be measured as the degree to which the distance between initially close particles varies with time. If orbital compactness is only required in the vortex plane, only the right hand side of Equation 4.38 is required. If three-dimensional compactness is required, then a lower limit must be set, to ensure that high compactness within the vortex plane is not causing very low compactness in the direction of the real eigenvalue.

This method can be directly linked back to all three of the methods described above, and Chakraborty *et al.* (2005) define formal equivalence thresholds between the schemes, though they also note that these are general guidelines and the different methods will not necessarily reproduce each other precisely. The swirling strength criterion requires specification of at least one positive threshold related to a critical orbital compactness. The results are therefore not directly comparable to the other methods, unless a threshold of $\epsilon = 0$ is applied. In this case, the results are the same as the Δ criterion (Chakraborty *et al.*, 2005). For these reasons, the swirl strength was not utilised as a vortex detection method in this thesis.

4.8 Lagrangian vortex methods

Where both spatial and temporal data are available, as is the case for LES and PIV, they can be used in conjunction to help define vortex cores. In particular, a series of spatial snapshots can be used to identify the temporal convergence (or divergence) of flow into vortices. This method uses a similar idea to the orbital compactness described above, but analyses how the separation and compaction of phase space changes through time.

The approach uses a Lagrangian formulation whereby individual particles within the fluid are tracked through time, and their progressive separation is calculated. The change in relative distance between neighbouring trajectories through time can be quantified using Lyapunov exponents.

Lyapunov exponents are a tool used to investigate the chaotic nature of dynamical systems and are one of the primary indicators used to infer the presence of chaos within a dynamical system (e.g. Sprott, 2003). Specifically, Lyapunov exponents measure the degree to which the phase space is stretched and folded through time and hence reveal any sensitivity to initial conditions.

The concept is demonstrated most simply for a generic one-dimensional map of the form $X_{n+1} = f(X_n)$. Classic examples of such maps include the logistic map and the tent map. If we consider two points X_0 and $X_0 + \Delta X_0$ for some small and arbitrary ΔX_0, then we can calculate the separation between the two points after one iteration as:

$$\Delta X_1 = f(X_0 + \Delta X_0) - f(X_0) \approx \Delta X_0 f'(X_0) \tag{4.39}$$

As shown, the separation can be equated to the derivative, $f' = df/dX$, using the standard definition of a derivative, in the limit of $\Delta X_0 \to 0$. The implication of the above is that f' is equal to the ratio of the separation between successive time steps ($\Delta X_1/\Delta X_0$).

The local Lyapunov exponent ($\mathcal{L}$) is defined as the rate of exponential divergence of trajectories such that

$$\mathcal{L} = \ln|\Delta X_1/\Delta X_0| = \ln|f'(X_0)| \tag{4.40}$$

Thus, trajectories that experience divergence exhibit $\mathcal{L} > 0$, systems with contraction exhibit $\mathcal{L} < 0$ and systems which retain constant separation exhibit $\mathcal{L} = 0$.

This stretching or contracting of phase space can occur in each dimension of phase space and therefore the number of Lyapunov exponents for a given dynamical system is equal to the physical dimension of the phase space. Together, these exponents form the Lyapunov spectrum $\{\mathcal{L}_1, \dots, \mathcal{L}_n\}$. The spectrum is ordered such that $\mathcal{L}_1$is the most positive Lyapunov exponent and $\mathcal{L}_n$is the most negative.

Thus, the exponents that are usually of most interest are the maximal ($\mathcal{L}_1$) and minimal ($\mathcal{L}_n$) exponents as these represent bounds on the deformation of the

phase space. With regards to chaotic analysis, the presence of at least one positive Lyapunov exponent within a system indicates chaotic mixing, and therefore the standard condition for chaos within a system is $\mathcal{L}_1 > 0$.

In many respects Lyapunov exponents are an extension of eigenvalues (Sprott, 2003) in that they describe the magnitude of distortion with respect to principal directions, analogous to eigenvectors. However, whereas eigenvalues are local, Lyapunov exponents are usually considered in a global sense, in that they are usually averaged to obtain the infinite-time behaviour of the entire system. In the case of the one dimensional map this becomes

$$\mathcal{L} = \lim_{N\to\infty} \frac{1}{N} \sum_{n=0}^{N-1} \ln|f'(X_0)| \tag{4.41}$$

However, there is merit in studying the local Lyapunov exponents. These are more commonly called the finite-time Lyapunov exponents (FTLE) and refer to the local deformation of phase space over a determined period of time.

Another very similar technique to the FTLE is the finite-size Lyapunov exponent (FSLE). Here, instead of investigating the separation between neighbouring points over a finite time period, the time taken for the flow to achieve a certain separation is calculated. In other words, the FTLE method holds the time period constant in order to analyse difference in spatial separation, whereas the FSLE method investigates the variation in time taken for phase space to achieve a particular level of separation. Given the similarity between the two methods, only the FTLE is discussed in depth here, but a detailed discussion of the FSLE method can be found in Aurell *et al.* (1997).

The FTLE can be calculated by analysing trajectories calculated from velocity data. The particle trajectories can be evolved using a series of velocity maps and a finite difference approximation of the flow velocity. The simplest method is a rearrangement of a forward difference scheme (Pierrehumbert and Yang, 1993).

$$\boldsymbol{x}_{t+1} = \boldsymbol{x}_0 + \boldsymbol{u}(x_0, t)\Delta_t \tag{4.42}$$

Although the accuracy of this calculation could be increased via use of schemes such as Runge-Kutta-Fehlberg algorithms (Shadden *et al.*, 2005), the simplicity of this scheme dramatically reduces the computational time required for the analysis, and therefore this scheme was used throughout the analysis presented herein.

Once the particle trajectories have been calculated for the appropriate time period (T_1), the maximum FTLE can be calculated by defining the coefficient of maximum expansion (σ_1^T) as the square of the largest singular value of the 'deformation gradient' (Green *et al.*, 2007).

$$\sigma_1^{T_1}(\boldsymbol{x}_0, t_0) = \lambda_{max}\left(\left[\frac{\partial \boldsymbol{x}(t_0 + T_1, \boldsymbol{x}_0, \boldsymbol{t_0})}{\partial \boldsymbol{x}_0}\right]^T \left[\frac{\partial \boldsymbol{x}(t_0 + T_1, \boldsymbol{x}_0, \boldsymbol{t_0})}{\partial \boldsymbol{x}_0}\right]\right) \tag{4.43}$$

The deformation gradient represents the rate of deformation in each Euclidean dimension with respect to perturbations in each dimension and is therefore a square matrix, with a size equal to the phase space dimension. There is no guarantee that the maximum deformation will occur along one of the Euclidean axes and therefore, calculating the maximum singular value ensures that the maximum separation is calculated in an appropriate direction. For the purposes of this analysis, the actual direction of maximum separation is of little importance; however, the direction can be obtained from the eigenvectors of the deformation gradient tensor.

The formula for the FTLE can be derived by noting that, under the assumption of a constant Lyapunov exponent along trajectories through time, the separation at time *T* can be calculated as:

$$\Delta \boldsymbol{x}_{T_1} = e^{\mathcal{L}T_1} \Delta \boldsymbol{x}_0 \tag{4.44}$$

Hence, this can be re-arranged (Pierrehumbert and Yang, 1993; Shadden *et al.*, 2005; Green *et al.*, 2007) to give the maximal FTLE over a certain time period *T* as

$$\mathcal{L}_1^{T_1}(\boldsymbol{x}_0, t_0) = \frac{1}{T_1}\ln(\sigma_1^{T_1}) \tag{4.45}$$

Here the coefficient of maximum expansion $\left(\sigma_1^{T_1}\right)$ is used to represent the largest value of the ratio $\Delta\boldsymbol{x}_{T_1}/\Delta\boldsymbol{x}_o$.

While Lyapunov exponents are traditionally employed to identify chaotic mixing within flows, FTLEs have also been shown to be a useful tool for identifying vortices (or coherent structures) within flows (Haller, 2000; Haller and Yuan, 2000; Haller, 2005). If particle trajectories are projected backward in time, the FLTE can be used to highlight regions of the flow which act as attractors within the flow (Haller and Yuan, 2000). Similarly, if projected forward in time, the FTLE can be used to identify repelling regions in the flow (Green *et al.*, 2007). This leads to the idea that regions of high FTLE identify vortices otherwise known as Lagrangian coherent structures (LCS) within the flow (Haller, 2000; Haller and Yuan, 2000).

In particular, ridges within the FTLE field correspond to local LCSs (Shadden *et al.*, 2005), and therefore in order to identify vortices within the flow, it is necessary to study the derivative of the FTLE field to identify local maxima, rather than simply find the globally extreme values. Shadden *et al.,* (2005) define a ridge intuitively using two criteria: 1) it should be locally at the highest point in the field transverse to the ridge and 2) the topography should drop off steepest in the transverse direction. A number of ridge tracking techniques and algorithms exist, most of which use the Hessian of the FTLE field to infer the presence of ridges (e.g. Shadden *et al.*, 2005; Lipinski and Mohseni, 2010).

Figure 4.5 shows a comparison between three different ridge-tracking algorithms. The simplest one looks merely for the existence of a local peak in the data, represented by a change in sign of local slope such that the point is a peak rather than a trough. This peak is analysed with respect to the central reference cell, and as long as a peak occurs in one of the four primary directions shown in Figure 4.6a then the cell is counted as a ridge.

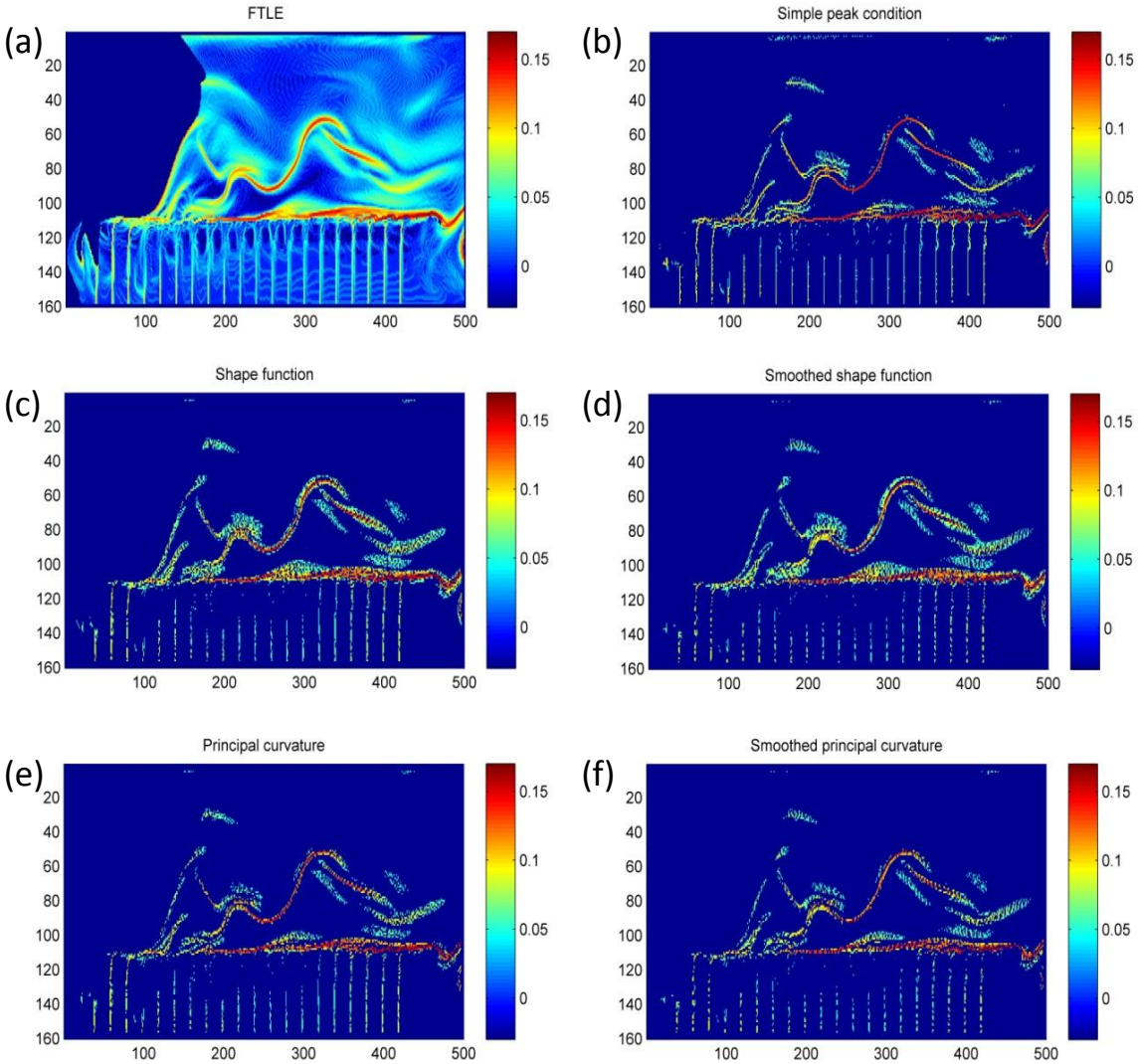

Figure 4.5: *Comparison of different ridge-tracking algorithms. The plots show a) the original FLTE plot, b) a simple peak method, c) shape function method d) shape function method using a smoothed gradient, e) the principal curvature method and f) the principal curvature method using a smoothed gradient.*

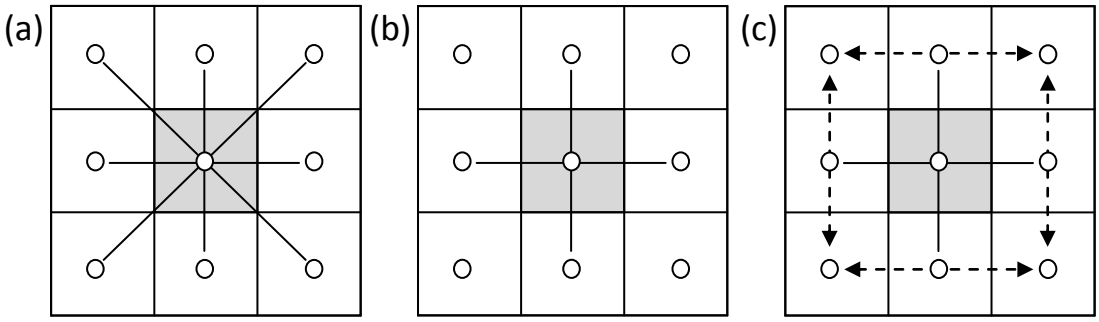

Figure 4.6: *Comparison of ridge tracking methods: a) search for peak condition in 4 primary directions, b) calculate the differentials in x and y in order to calculate the Hessian c) calculate the differentials in x and y, as an average over 3 cells, smoothing the data.*

A more thorough condition is to check the determinant of the Hessian ($H(f)$) for the same local grid around the reference cell.

$$H(f) = \begin{pmatrix} \frac{\partial^2 f}{\partial x^2} & \frac{\partial^2 f}{\partial x \partial y} \\ \frac{\partial^2 f}{\partial y \partial x} & \frac{\partial^2 f}{\partial y^2} \end{pmatrix} \tag{4.46}$$

Here f is the FTLE, and is assumed to be a smooth continuous surface. The Hessian permits calculation of the Gaussian curvature (K), the determinant of $H(f)$, which is effectively a shape function in that its value determines the local shape of the surface as shown in Figure 4.7. A ridge is thus defined as a region with $K \leq 0$ in addition with a local value threshold which ensures it is a peak rather than a trough.

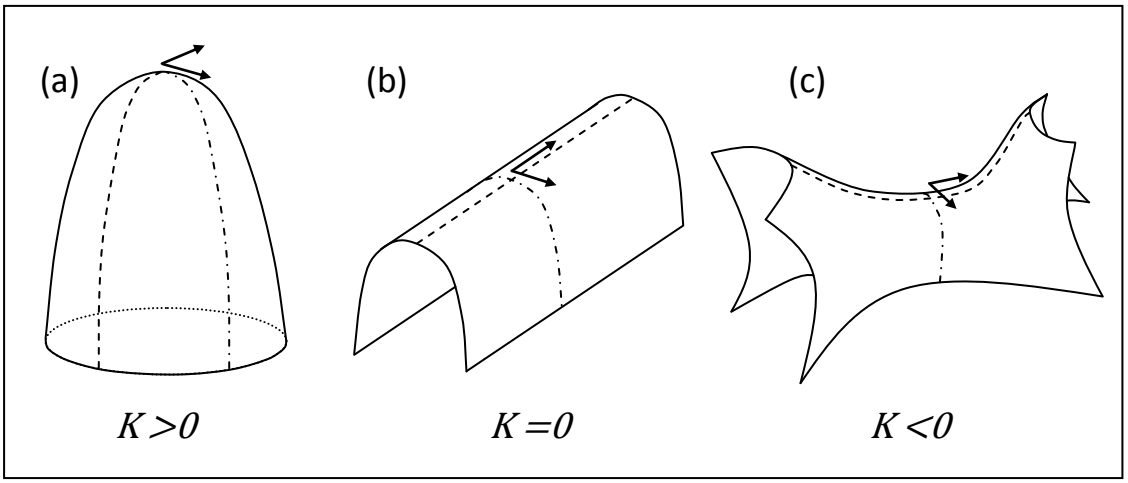

Figure 4.7: *Gaussian curvature of different surfaces. The arrows indicate the directions of principal curvature for each case: (a) an elliptic surface, which is not necessarily a local maximum, (b) a parabolic surface with one principal curvature equal to zero and (c) a hyperbolic surface with one positive and one negative curvature component.*

The final algorithm extends the previous method further by considering the two principal curvatures, the product of which is equal to the Gaussian curvature.

$$K = k_1 k_2 \tag{4.47}$$

These can be calculated as the eigenvalues of H. This allows distinction of ridges as regions only where the lateral gradient is larger than the along-ridge gradient. Assuming that k_1 is the most positive curvature, the condition for a ridge then becomes:

$$k_1 \geq 0 \text{ and } |k_2| < |k_1| \quad (4.48)$$

The latter two methods both involved the calculation of the first order and then second order derivatives in the x and y directions. This was achieved by a simple difference method about the reference cell (Figure 4.6b). However this method could potentially be very sensitive to noise in the data, so a smoothed version was also calculated, whereby the derivatives were averaged over three adjacent cells (Figure 4.6c). The results in Figure 4.5 show that the more complex methods fail to improve the accuracy noticeably and therefore the simplest method is used throughout this study.

A ridge in an FTLE field is alone not sufficient to conclude that a vortex is present. Regions of high shear also produce regions of high FTLE (Green *et al.*, 2007) and therefore it is strictly necessary to confirm that they do correspond to LCS's by calculating the strain rate normal to the ridge. However, this can often be inferred through interpretation of the flow dynamics.

It is important to note that this method is being applied to two-dimensional snapshots of three dimensional datasets. The assumption made in doing so is that the lateral velocity, which is not considered, is equal to zero, and that the flow is planar. This is evidently not the case, and is a source of error within the FTLE calculations, however, the main characteristics of flow above canopies, as introduced in Chapter 2, are based on a broadly planar model and therefore it is hypothesised that the error is relatively small.

For the flume data, three dimensional data were not collected, but for the numerical experiments three dimensional data were available and therefore an analogous three dimensional FTLE calculation was carried out to ascertain an estimate of the error in the planar assumption. Figure 4.8 shows a comparison between the two methods for an identical snapshot. It is clear that the overall vortex structure is broadly similar with the same ridges being identified and having a similar magnitude. Figure 4.9 supports this idea, showing that whilst there is clear three dimensional structure to the flow, the largest structures are relatively consistent throughout the width.

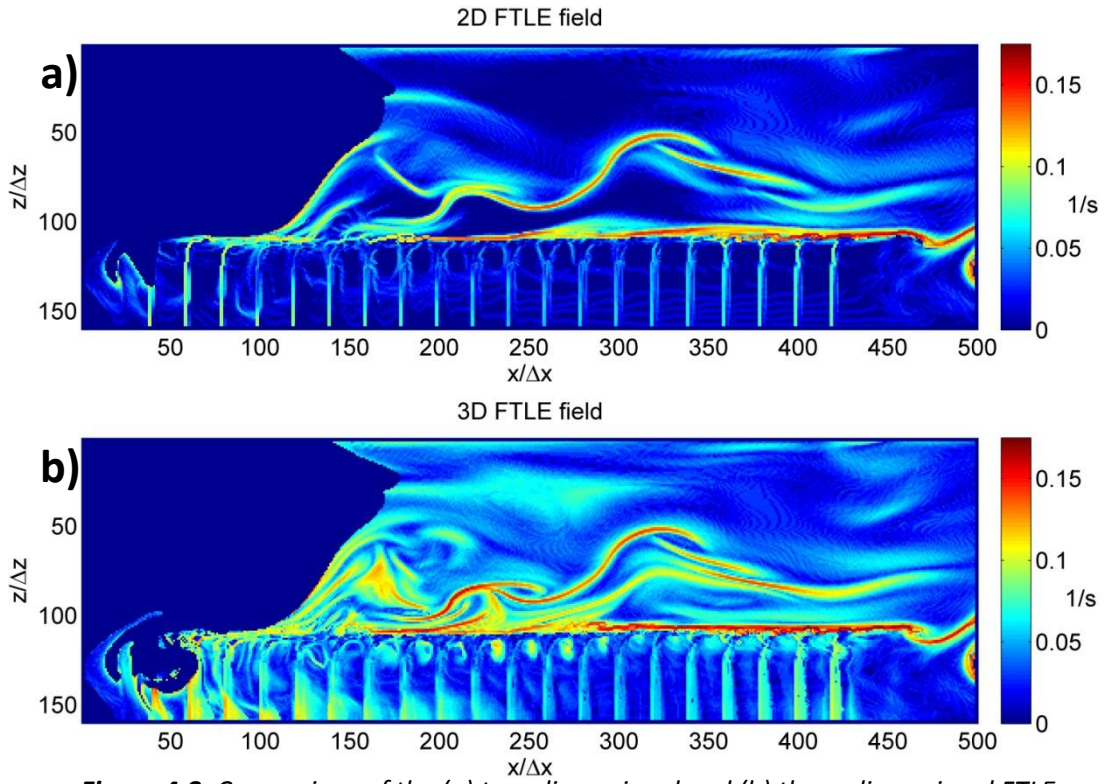

Figure 4.8: *Comparison of the (a) two-dimensional and (b) three-dimensional FTLE snapshots.*

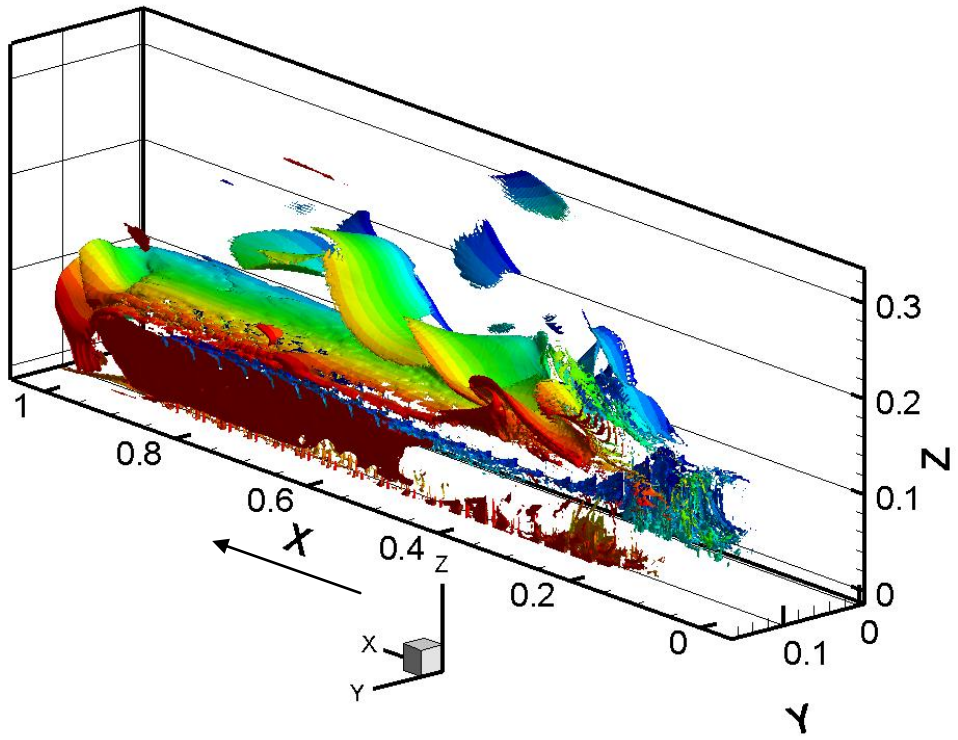

Figure 4.9: *Iso-surfaces of FTLE ridges taken from the 3D FTLE field, showing major structures have significant lateral extent. The iso-surface is coloured by cross-stream distance for clarity. Flow is from bottom right to top left.*

There are a few notable differences however, which are illustrated in Figure 4.8. Within the canopy, where the lateral velocity has the potential to be largest, there is some difference, as the three dimensional image identifies regions of convergence linked to wake reattachment, which will not be shown in the two dimensional case. Similarly, above the canopy there are regions of lateral convergence. However, the areas of highest convergence are found in both images.

While the three dimensional method appears to offer a small improvement, it also increases the computational cost considerably. Due to memory constraints on the desktop computer used, the three dimensional method required a calculation time roughly 180x the time required for the two dimensional method. Therefore, given the effectiveness of the two dimensional method, analysis is restricted to this method throughout, except for a select few, most interesting cases, where the three dimensional case is investigated.

4.9 Vortex signatures in vegetated flows

In summary, it has been shown in this chapter that there are a number of different, complementary methods which can be used to analyse coherent flow structures. Having explained the methods in detail, it is possible to propose a number of criteria to which the numerical and experimental results can be compared (see Table 4.1). This is neither a definitive nor an objective list, but instead highlights some of the characteristics of vortices which one would expect to find within canopy flows. These characteristics are based upon the previous research in canopy flows discussed in Chapter 2.

	Criteria	Methods
1.	The Kelvin-Helmholtz frequency (f_{KH}) should correspond to a peak in the velocity power spectra and wavelet spectra.	Mean flow profiling Spectral analysis Wavelet analysis
2.	The flow at the canopy top should show a dominance of Q4 (sweep) and Q2 (ejection) events	Quadrant analysis
3.	The Eulerian and Lagrangian vortex methods should produce results similar to those shown in Figure 4.10	$\|\omega_i\|, Q, \Delta, \lambda_2$ FTLE

Table 4.1: *Criteria for vortex detection in canopy flows*

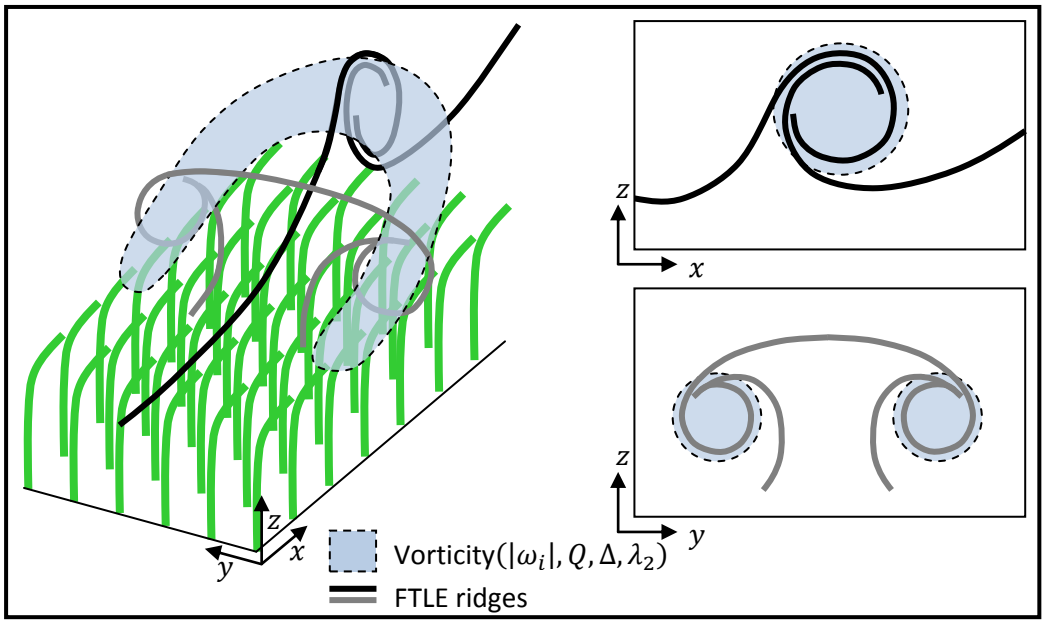

Figure 4.10: *Schematic of expected vorticity measure and FTLE results, for hairpin vortices in canopy flows, based on results from Finnigan et al. (2009) and Green et al. (2007). An arbitrary threshold for the vorticity isosurface has been used.*

The first characteristic demonstrates that the flow is governed by a mixing layer instability, which produces shear-scale vortices. The second implies the presence of coherent turbulent events at the canopy top. Furthermore, based on existing theory (see Chapter 2) the dominance of sweep and ejection events implies the presence of roller vortices along the canopy top. The third criterion indicates the existence of hairpin vortices above the canopy (see Figure 4.10).

All three of these measures are likely to be disrupted in reality by noise. In particular, the third criterion assumes the development of an idealistic hairpin vortex, which is highly unlikely to be easily detected even within numerical simulations. It is more likely that only the roller vortex part of the signature would be detected and not the trailing legs of the structure. Nevertheless, these criteria serve as an initial benchmark for the analysis of results presented in Chapters 5 and 6.

Chapter 5: Flume experiments and validation work

5.1 Introduction

Chapters 1 and 2 showed that there is the need for high resolution data that capture the interaction between flow and vegetation, in order to advance our understanding of the role and influence of vegetation on reach-scale processes. In Chapter 3, a rigorous numerical methodology was outlined for modelling such interactions. Chapter 4 then proceeded to develop an analytical method by which to analyse and to interpret relevant data. Thus, having established the reliability and physical basis of the model and having developed appropriate methods and criteria by which to analyse flow data, the numerical simulation data collected can now be validated. As discussed in Chapter 3, validation of the models is key to establishing and justifying their use as research tools.

In this chapter, all the models applied in Chapter 6 are validated against flume data. First, results are presented from a simulation using rigid vegetation. Similar models have been validated, and applied in the past (e.g. Stoesser *et al.*, 2009; 2010), and therefore there is less need to validate the methodology for this model. However, to ensure comparability, and test the similarity between flume and numerical model for a benchmark case, the numerical results are validated against flume data.

The Euler-Bernoulli beam model developed in Chapter 3 is novel and previously untested within a three-dimensional CFD framework, and therefore is implemented over a range of different flow conditions, corresponding to a series of analogous, high resolution, flume experiments. Results are also presented from experiments using real vegetation (*Ranunculus penicillatus*) for comparison with the N-pendula model results. The N-pendula model was developed after the flume experiments, in response to the results from the real vegetation experiments and therefore there were no analogous experiments conducted by which to validate the N-pendula model. Instead, key features of the flow in the real vegetation experiments were

used as comparison for the N-pendula data presented in Chapter 6. Finally, although it was not possible to validate the instantaneous turbulent flow quantities, wavelet results from the flume experiments are compared to similar numerical simulations presented in Chapter 6, as qualitative validation.

A key aspect of validating and implementing the models was ensuring that the representation of the flexural rigidity parameter was correct. Therefore before validating the vegetation models, the first section discusses flexural rigidity, and how the rigidity was measured and implemented within the validation models. Furthermore, this section justifies the choice of the flexural rigidity parameter within the models in Chapter 6.

5.2 Parameterisation of flexural rigidity

The term flexural rigidity refers to the material properties that dictate the relation between stress and strain within an object (Kouwen *et al.*, 1981; Niklas, 1992). It is therefore a key parameter within elastic structure models. In particular, it is popular within the vegetation literature because it features in equations such as the Euler-Bernoulli beam equation which are often used to approximate plant motion (e.g. Finnigan and Mulhearn, 1978; Kutija and Hong, 1996; Ikeda *et al.*, 2001). The flexural rigidity (*J*) is calculated as the product of the elastic (or Youngs) modulus (*E*), and the second moment of the area (*I*), as shown in Equation 5.1.

$$J = EI \tag{5.1}$$

In terms of vegetation, *E* can be considered an anatomical property, whereas *I* reflects the plant morphology (Niklas, 1992). The value of the flexural rigidity for a material can be calculated experimentally by performing bending tests under the assumption that at least over a selected region, the material behaves according to the Euler-Bernoulli Beam equation (e.g. Miler *et al.*, 2012). As discussed in Chapter 2, there exists a vast range of literature regarding flow over vegetation and many of these studies make some effort to quantify the flexural rigidity term (See references in Figure 5.1). Figure 5.1 shows a range of values for the flexural rigidity drawn from various previous studies looking at terrestrial, aquatic and marine vegetation. The

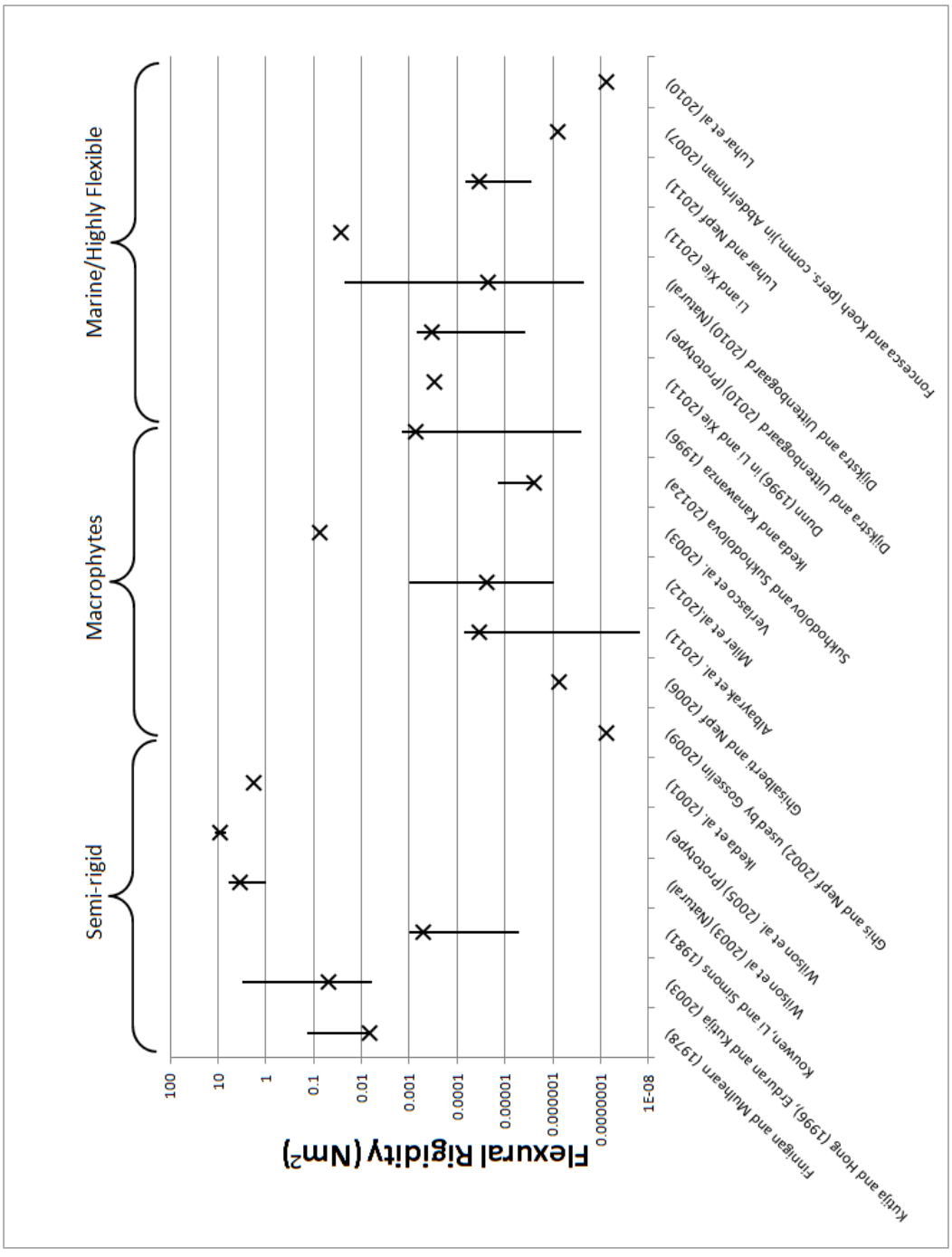

Figure 5.1: *Values of flexural rigidity as used by previous studies. Values have been taken either directly from publications, or from subsequent citing articles.*

The black line indicates the range of values used, and the black marker either represents the mean value used, or the preferential value from within the range used by the authors.

values and ranges used vary over several orders of magnitude. In some cases, this variation can be attributed to obvious differences in plant form. Figure 5.1 classifies three such distinctions, however there is a noticeable variation in values within plants of the same broad morphology and species. This suggests that the accurate parameterisation of the flexural rigidity within models is potentially problematic.

5.2.1 Flume work rigidity parameterisation

In order to be able to validate the model against the flume data correctly, it was necessary to conduct experiments on the different vegetation types used, to calculate a value for the flexural rigidity. The flexural rigidity was calculated using Equation 5.2 (Niklas, 1992)

$$EI = \frac{Fl^3}{3\omega} \tag{5.2}$$

Here, F is a point load, applied to the end of a beam of length l, causing a displacement of ω at the end of the beam. In order to improve the accuracy of the results, this calculation was performed for a number of different set displacements (0.05-0.07m) and lengths (0.08-0.14m). The force was then the measured variable.

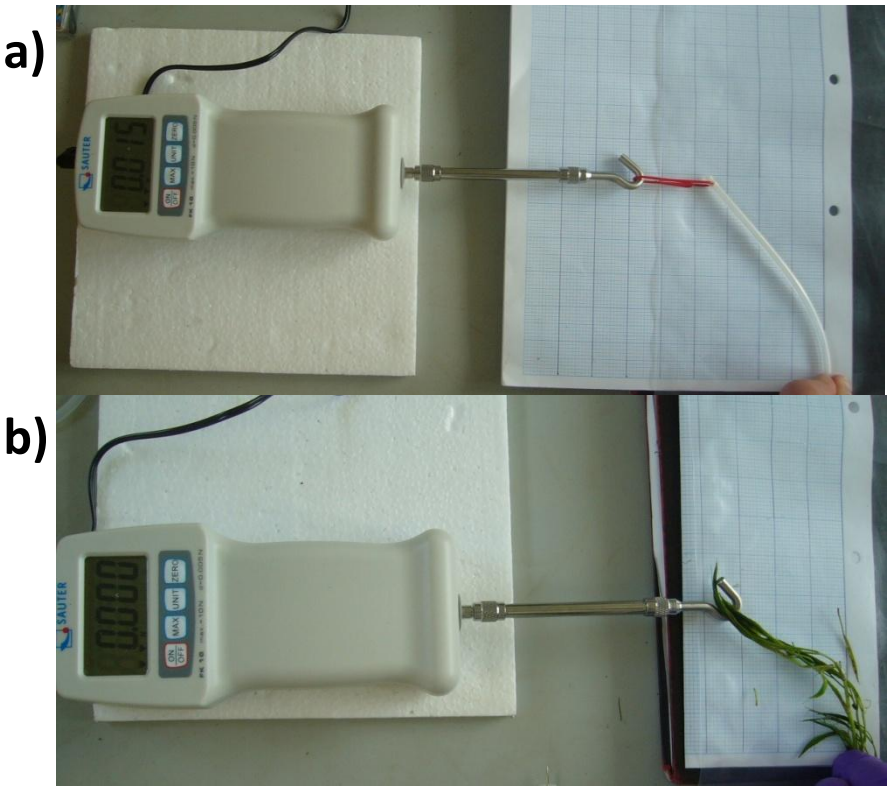

Figure 5.2: *Vegetation rigidity experiments for the (a) artificial and (b) real vegetation.*

The experimental setup is shown in Figure 5.2. The force was measured using a Sauter FK10 Force Gauge with a resolution of 0.005N. The vegetation was clamped manually at one end, and the force gauge applied perpendicular to the original vegetation position, until the desired displacement was achieved. In order to ensure that the force was always applied perpendicular, and avoid the force gauge slipping, a paperclip was used to attach the gauge to the artificial vegetation. Figure 5.3 shows the numerator of Equation 5.2 plotted against the denominator. The flexural rigidity can therefore be estimated as the slope of a line of best fit applied to the data. This line was fitted using linear least squares regression. This gave a value of $J = 0.0003Nm^2$ for the artificial vegetation. This compares well with the mean value of all the individual measurements ($J = 0.000313Nm^2$).

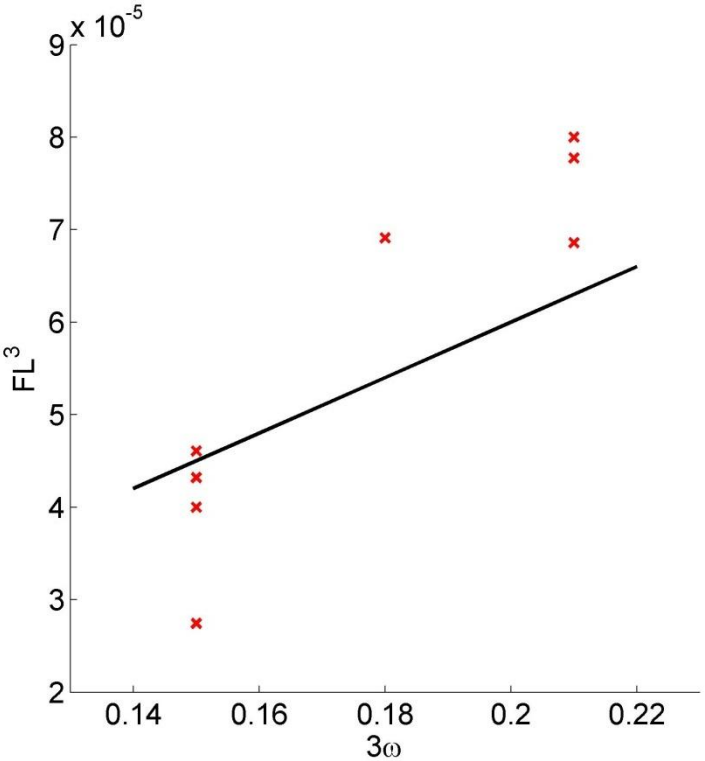

Figure 5.3: *Graphs showing the numerator of Equation 5.2 plotted against the denominator, for a series of different measurements. The black line is a line of best fit and its gradient is equal to the flexural rigidity.*

The same method was applied to the real vegetation. However, the vegetation was too flexible (Figure 5.2b) and the resolution of the force gauge too low to get any results from the bending tests. This is not too problematic as direct validation experiments were not conducted for the real vegetation, but nevertheless this must

be considered when comparing the numerical and experimental data with the real vegetation.

5.2.2 Numerical simulation rigidity parameterisation

The flexural rigidity is one of the key parameters in the Euler-Bernoulli Beam model and therefore it was vital that a realistic value was used throughout all the simulations. All the values used in Chapter 6 were either chosen in line with the literature or with the flume values. There were three different flexural rigidity values used (See Table 5.1), which correspond to three different setups used in Chapter 6.

Numerical simulation	Model	J=EI (Nm^2)	Basis for choice
Small patch of tall, reed-like stems (Section 6.3)	Euler-Bernoulli Beam	0.02	Literature (Figure 5.1)
Canopy of shorter stems, more analogous to the flume setup (Section 6.4)	Euler-Bernoulli Beam	0.0003	Analogy with artificial flume vegetation
Highly flexible macrophytes (Sections 6.5 & 6.6)	N-pendula	0.001	Literature (Figure 5.1)

Table 5.1: *Flexural Rigidity choice for the different simulations in Chapter 6*

The original simulation with a small patch of reed-like stems was chosen to be in-line with the studies which also used the Euler-Bernoulli Beam equation, and lies within the semi-rigid region in Figure 5.1. The full canopy simulation was designed to be as similar to the flume experiments as possible, though not analogous due to domain constraints. Therefore, the rigidity was chosen to equal that of the artificial flume vegetation, even though this represented a relatively low rigidity. The N-pendula model run was designed to be highly flexible and therefore a rigidity value was chosen to fall within the macrophyte and marine range. However, the stem area was significantly larger than many of those used in the literature and therefore a value towards the top of the range (0.001) was used. Although this value is actually larger than the validation run, due to the fact that the model is not driven by the Euler-Bernoulli Beam model, it represents a more flexible stem as the model is primarily tension driven rather than rigidity driven as discussed in Section 3.6.

5.3 Experimental flume setup

The flume experiments were carried out at the Sorby Environmental Fluid Dynamics Laboratory (SEFDL) at the University of Leeds. The recirculating flume was 10m long and 1m wide. The slope was set at a constant value of 0.01. Two different depths were used (0.2m and 0.4m) as well as range of velocities. These velocities were categorised into slow ($\overline{U}$ =0.18-0.26m/s), medium ($\overline{U}$ =0.36-0.52m/s) and fast ($\overline{U}$ =0.59m/s) flows, where the actual velocities depended upon the flow depth (see Table 5.2). For all the experiments, the flow was fully turbulent and also subcritical, with Froude numbers within the range 0.01-0.22. The flexible, 0.2m, fast experiment is not reported here as the results contained a high proportion of error due to free-surface interference with the data.

The suite of experiments were designed to produce a range of depths and flow conditions representative of those found within small, lowland river systems similar to the River Browney (see Chapter 8). The slow flow condition corresponds to mean base-flow conditions, as observed during the fieldwork ($\overline{U} \approx$ 0.21m/s) in similar depth flows, whereas the fast flow is representative of the fastest local inlet velocity recorded (U =0.56m/s). The artificial vegetation dimensions were designed to be similar to previous studies (e.g. Ghisalberti and Nepf, 2006), whilst providing realistic canopy characteristics as well as optimal conditions in which to evaluate model performance. The real vegetation was sourced from the River Browney.

Run (type,depth,speed)	Velocity (m/s)	Reynolds number
Rigid, 0.2m, medium	0.44	62,900
Rigid, 0.4m, medium	0.38	84,400
Flexible, 0.2m, slow	0.26	37,100
Flexible, 0.2m, medium	0.52	74,300
Flexible, 0.2m, fast	--	--
Flexible, 0.4m, slow	0.18	40,000
Flexible, 0.4m, medium	0.36	80,000
Flexible, 0.4m, fast	0.59	131,100

Table 5.2: *Inlet velocities for the validation runs. Absent figures imply unreliable results.*

The velocity data were collected using a DANTEC two-dimensional digital particle image velocimetry system (2-D DPIV) which is a nonintrusive, whole flow field technique for velocity measurement (Hardy *et al.*, 2005). A major advantage of this technique is that it allows quantitative flow visualisation of the entire flow field through time (Hardy *et al.*, 2009). Measurement was based upon seeding of the flow with neutrally buoyant tracer particles (hollow reflective glass spheres with a mean diameter of 10µm) and illuminating the flow field with a single pulsed Litron Nano laser light sheet. A charge-coupled device (CCD) camera was positioned perpendicular to the light sheet to capture the illuminated flow field at a resolution of 50Hz.

The downstream and vertical velocity maps were derived by draping a digital mesh of 8 x 8 pixel interrogation regions over the image, where the dimension of each pixel was approximately 0.6mm. In each interrogation region, a fast Fourier transform (FFT)-based spatial cross-correlation technique was applied to consecutive images to determine both velocity components (Westerweel, 1997). In order to maximise the signal-to-noise ration of the particle cross-correlations in the PIV analysis, six quality checks were applied to the data (Hardy *et al.*, 2005) including a 25% overlap between interrogation regions. In addition, an adaptive correlation method was used whereby initially, interrogation regions of size 32 x 32 pixels and subsequently 16 x 16 pixels were used to increase the accuracy of the eventual 8 x 8 pixel cross-correlation. With this methodology, the mean bias error (accuracy) and RMS error (precision) of the derived velocities is in the order of 0.1 pixels (Huang *et al.*, 1997) and the uncertainty in the velocity measurements was therefore in the order of 0.003m/s. The resulting velocity map had a spatial resolution of 0.0038m at 50Hz over a time length of 1 minute to provide a stationary time series.

The rigid vegetation (Figure 5.4) was represented using solid plastic cylinders which, within the flow ranges used, exhibited no bending. The flexible artificial vegetation consisted of Versilic® Peroxide-cured silicone tubing. Hollow tubing was selected to allow for the possibility of experiments using Laser induced Fluorescence (LIF). The stems were 0.1m in length with a diameter of 0.005m. Both the rigid and flexible

stems were set out in a staggered layout, with 0.05m separation between stems in the lateral direction and 0.1m between stems in the downstream direction.

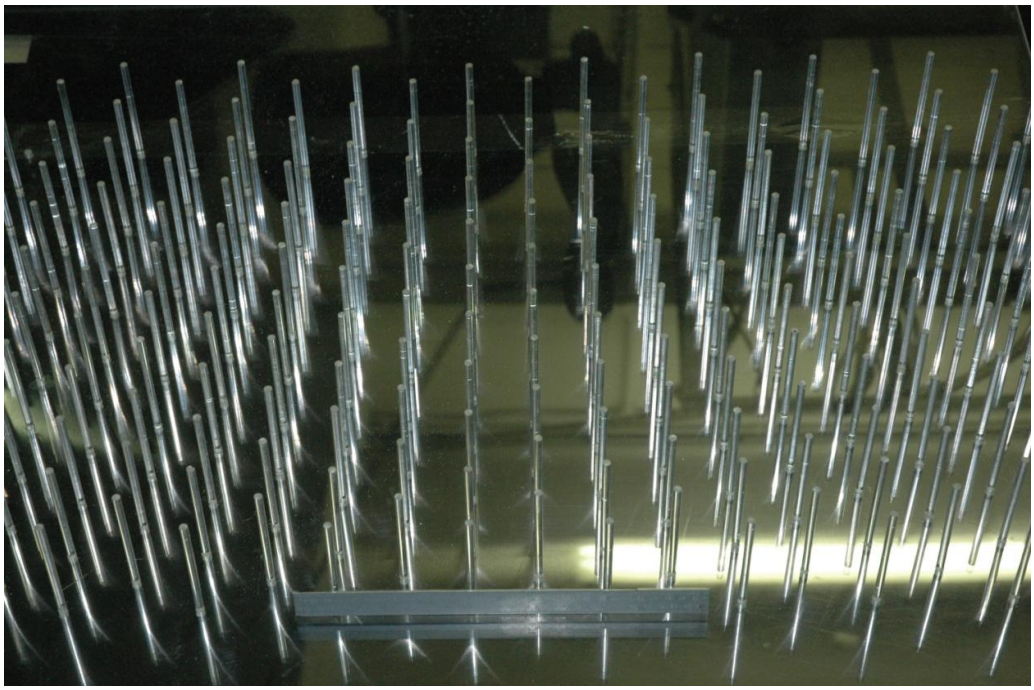

Figure 5.4: *Flume setup for the rigid vegetation experiments, with a 0.3m ruler for scale.*

Figure 5.5: *Vegetation collection from the River Browney. Inset map shows location of site. Field assistant included for scale.*

For the real vegetation experiments, samples of *Ranunculus penicillatus* were collected from a local field site on the River Browney, West of Durham (Figure 5.5) in early September. The vegetation was transported in wet sacks to the laboratory, and used in the flume on the same day to limit the effect of changes in plant biomechanics due to the vegetation having been removed from its natural environment, and consequent lack of light and nutrients. The vegetation was fixed to the bed of the flume using cable ties in order to try and replicate the patch configuration found in natural rivers.

5.4 Numerical domain setup

The numerical domain was set up to represent a section of the flume experiment. Due to the vegetation size, and subsequent limits on grid resolution, it was not possible to represent the full width and length of the domain numerically. Instead a section 0.5m long and 0.2m wide was used. Therefore, applying the vegetation configuration, the domain contained 35 individual stems. The flume experiments only allowed two dimensional flow data to be collected and therefore the width of the numerical domain was considered more than sufficient to reproduce the two dimensional flow dynamics. The grid resolution was set as 0.002m in the downstream and vertical direction and 0.001m in the lateral direction (nx=250,ny=200,nz=100/200). The grid was twice as fine in the lateral direction in order to adequately capture the stem-scale wake separation at the lowest possible computational cost. As mentioned in the previous section, the flexural rigidity was set at $0.003 Nm^2$ for all the numerical simulations. The model boundary conditions were setup as discussed in Chapter 3.

The inlet conditions of the numerical domain were set to match the mean flow conditions (Table 5.2) from the flume experiments. This mean value was used across the inlet rather than using a vertical profile. This potentially increases inaccuracy within the results, but ensures that all the flow structure created is due to the canopy rather than the boundary conditions.

5.5 Model validation methods

As stated in Chapter 4, the numerical data is to be interrogated against a set of criteria, using a range of analysis techniques. It is therefore important that the validation of the numerical models extends to that level of analysis. With this in mind, each of the three models was validated using a three criteria approach. First, downstream (u) and vertical (w) components of the velocity measurements from an (x - z) long-section taken down the middle of the domain (y/w=0.5) were compared. Samples were compared for the whole long-section with specific focus on the shear layer. The locations at which the measurements were taken is shown in Figure 5.6.

The points are split into three different regions; canopy (black), shear layer (grey) and boundary layer flow (white). These do not correspond to exact physical regions, but rather allow distinctions to be made in the analysis between the performance of the model in different flow regions, influenced by different flow processes. It is worth noting that in the 0.2m flow, there were no boundary layer points.

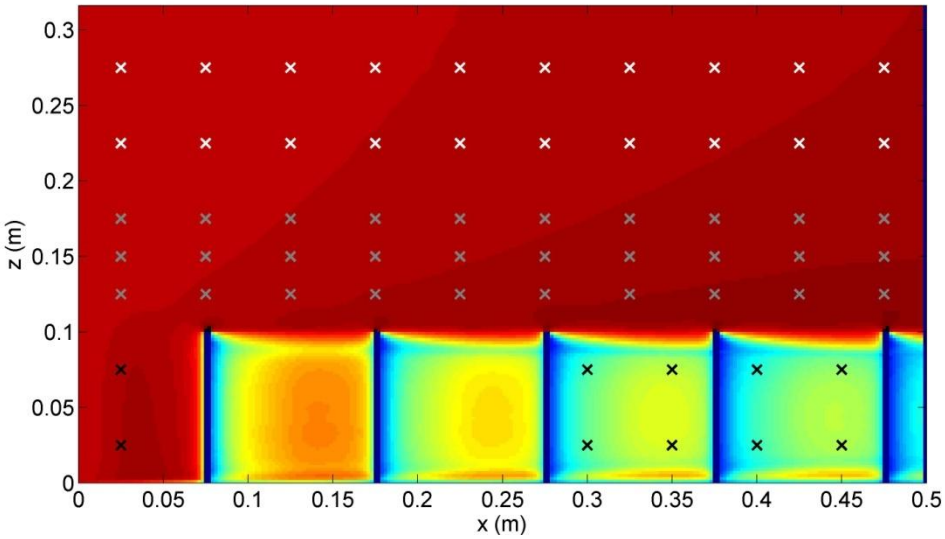

Figure 5.6: *Map of locations in the domain used for the validation. The image behind shows an example mean velocity profile. The different coloured points refer to canopy (black), shear layer (grey) and boundary layer (white) locations.*

Second, the normalised canopy shear layer profiles were examined. It is hypothesised that these profiles determine key turbulence length scales (Ho and Huerre, 1984; Ghisalberti and Nepf, 2002) and so it is important to investigate how

the predictions of the shape of the shear layer agree. Finally, as much of the analysis in Chapter 6 focuses on vortices, the mean (x-z) vorticity plots were compared. Due to the non-turbulent inlet conditions used in the validation simulations, the turbulence was not sufficiently developed to allow comparison with flume spectral data. Furthermore, due to the errors within the flume data, the instantaneous velocity signal contains a high level of noise. Therefore the validation is restricted to mean vorticity; however the flume wavelet plots are qualitatively compared to similar numerically obtained wavelet plots in Section 5.9. These three methods were designed to investigate the representation of canopy flow processes as well as the actual values obtained. All the analysis in Chapter 6 is restricted to velocity signals and therefore it is sufficient to only validate these variables.

5.6 Rigid vegetation

Due to the simple nature of the rigid model, and the wealth of literature regarding simulating rigid vegetation, this model was validated against only one flow condition at each depth. This was chosen as a medium flow condition, with an average downstream velocity of approximately 0.38m/s in the 0.4m flow and 0.44m/s in the 0.2m flow. As explained in Section 5.4 it was not possible to match the flume conditions exactly and the consequence of this was that the two Reynolds numbers of the flows were different. The decision was taken to replicate the velocity rather than the Reynolds number as the drag force which drives plant motion, and therefore canopy flow dynamics, exhibits a direct dependence on velocity, rather than Reynolds number.

Figure 5.7 shows the comparison between the measured and modelled velocities for both the 0.2m and 0.4m flows. There is a clear difference in the quality of prediction between the canopy region (blue) and the rest of the domain. Within the downstream velocity signal, the PIV canopy data is less variable than the corresponding CFD data, with a smaller range. There is also a large amount of scatter evident within the data.

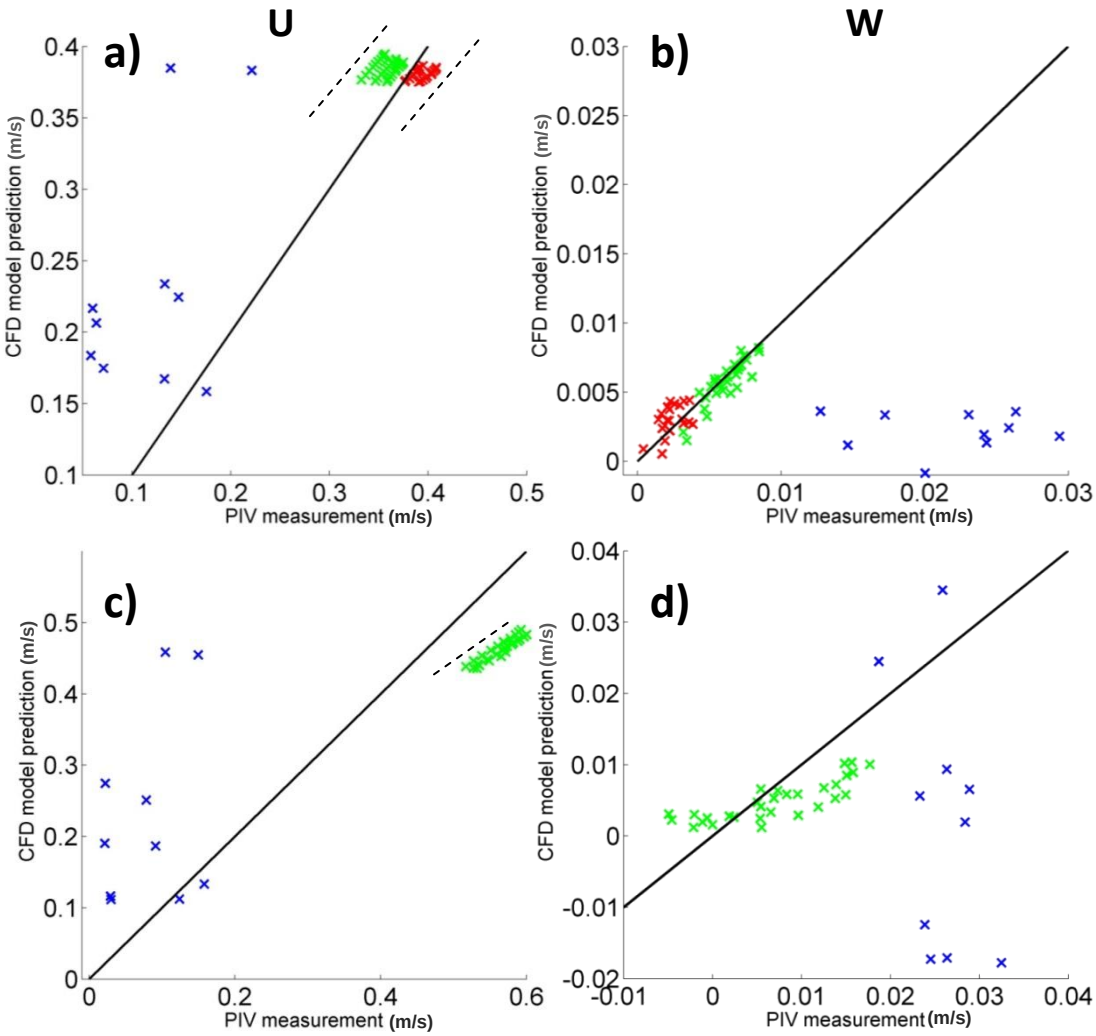

Figure 5.7: *Comparisons of modelled and measured downstream (a,c) and vertical (b,d) velocities for the 0.4m (top) and 0.2m (bottom) rigid canopies. The data are split into canopy (blue), shear layer (green) and boundary layer (red) points. The black line represents a 1:1 relationship.*

The suggested reason for this disparity and apparently poor prediction by the model of the canopy velocities is most likely due to error within the PIV data rather than model deficiency. Although every attempt was made to reduce the error within the PIV data, there were still significant sources of error related to the vegetation:

1) Much of the camera view of the canopy is obscured by stems, and therefore it is difficult to obtain accurate velocity readings from within the canopy.
2) Furthermore, it is likely that less light from the laser penetrated through the canopy and therefore the PIV image will be darker and less clear.

3) There is also the chance of reflection of light off the stems, obscuring the picture further.

Thus, it is assumed that the PIV data within the canopy contains significant errors. This assumption is supported by the fact that numerical simulations appear to represent flow structure within the canopy well, when compared to benchmark solutions and previous work on similar canopies (Stoesser *et al.*, 2006; Stoesser *et al.*, 2009).

Elsewhere in the domain, there is good qualitative agreement. The shear layer downstream (u-) velocities show a clear trend in both depths, though there is clearly some systematic error present causing both a translational shift and altering the gradient slightly. The regression figures shown in Table 5.3 give very low agreement with the expected slope of 1. However, the R^2 values indicate a good fit with the regression line, suggesting that although the regression line may differ substantially from $y = x$, the data do fit the given regression line well. One reason for this may be systematic error shifting the regression line. Figure 5.7 suggests that this single global figure is not representative of the different flow regions. Therefore a regional regression was conducted, as shown in Tables 5.4 and 5.5. This shows that for the 0.2m flow, the above-canopy flow fits the regression line well (R^2=0.877) whereas the canopy flow does not, suggesting more random error within the canopy.

Run (type, depth, speed)	**U**			**W**		
	Intercept	Gradient	R^2	Intercept	Gradient	R^2
Rigid, 0.2m, med.	0.188	0.489	0.745	0.005	-0.059	0.004
Rigid, 0.4m, med.	0.166	0.581	0.774	0.005	-0.057	0.037
Flexible, 0.2m, slow	0.138	0.467	0.810	0.002	-0.043	0.047
Flexible, 0.2m, med.	0.213	0.526	0.743	-0.001	0.604	0.191
Flexible, 0.4m, slow	0.060	0.376	0.550	0.002	-0.051	0.019
Flexible, 0.4m, med.	0.209	0.436	0.542	0.004	0.115	0.063
Flexible, 0.4m, fast	0.278	0.546	0.741	0.002	0.319	0.050

Table 5.3: *Linear regression data for the entire datasets*

U Run	Canopy			Shear			Boundary		
	Intercept	Gradient	R^2	Intercept	Gradient	R^2	Intercept	Gradient	R^2
Rigid, 0.2m, medium	0.167	0.765	0.094	0.109	0.627	0.877			
Rigid, 0.4m, medium	0.141	0.767	0.262	0.324	0.170	0.113	0.305	0.1093	0.248
Flexible, 0.2m, slow	0.174	-0.336	0.031	0.100	0.607	0.952			
Flexible, 0.2m, medium	0.245	0.562	0.352	0.408	0.241	0.223			
Flexible, 0.4m, slow	0.082	-0.485	0.244	0.109	0.133	0.072	0.110	0.102	0.133
Flexible, 0.4m, medium	0.353	-2.281	0.509	0.323	0.142	0.059	0.393	-0.069	0.045
Flexible, 0.4m, fast	0.249	0.614	0.366	0.761	-0.245	0.022	0.623	-0.042	0.266

***Table 5.4**: Linear regression data for downstream velocity (U) in the individual regions of the flow.*

W Run	Canopy			Shear			Boundary		
	Intercept	Gradient	R^2	Intercept	Gradient	R^2	Intercept	Gradient	R^2
Rigid, 0.2m, medium	0.052	-1.935	0.155	0.003	0.338	0.672			
Rigid, 0.4m, medium	0.002	-0.009	0.001	-0.001	1.059	0.783	0.001	0.651	0.250
Flexible, 0.2m, slow	-0.003	0.161	0.056	0.000	0.306	0.638			
Flexible, 0.2m, medium	0.003	1.146	0.312	0.002	0.226	0.085			
Flexible, 0.4m, slow	0.001	-0.02	0.004	0.001	0.475	0.418	0.001	0.120	0.118
Flexible, 0.4m, medium	0.002	0.193	0.111	0.002	0.533	0.388	0.001	0.307	0.336
Flexible, 0.4m, fast	-0.009	1.499	0.603	0.006	0.197	0.047	-0.001	0.262	0.361

***Table 5.5:** Linear regression data for vertical velocity (W) in the individual regions of the flow.*

In the 0.4m flow however, there is negligible improvement. However, the above-canopy data can be broken down further still into several smaller datasets, which follow a clear linear trend, shown approximately by the dashed line in Figure 5.7. This suggests that the model is representing the velocity gradient well, but that there is an error which varies throughout the domain, which is causing the values to be offset. From figure 5.8, which is a close up of the data in Figure 5.7, and using the locations in Figure 5.6 it is clear that there are three bands of shear layer data and two bands of boundary layer data each of which do follow a sensible trend, and therefore this error appears to relate to distance above the canopy.

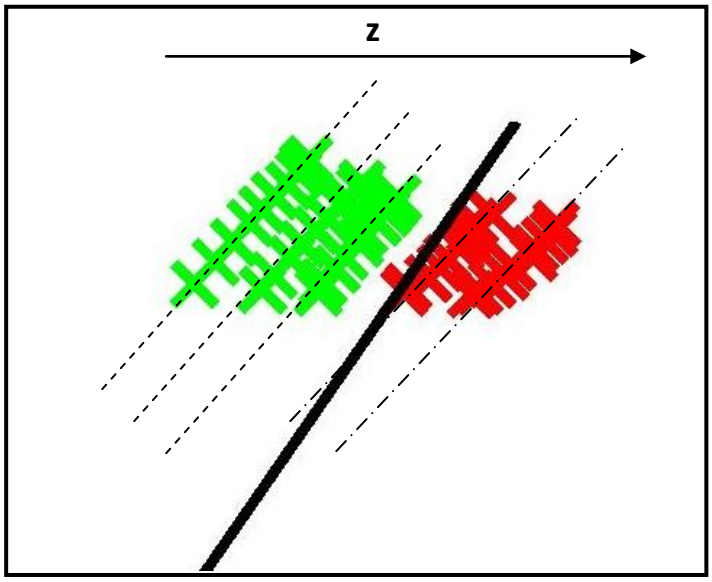

Figure 5.8: *Close-up of the above-canopy data for the 0.4m downstream velocity comparison in Figure 5.7a showing two different slopes present.*

The vertical velocity shows good agreement above the canopy, particularly in the 0.4m run, where the shear layer shows a regression gradient of 1.05 with an intercept of -0.001. Furthermore, the data fit the regression line well (R^2=0.783). This is encouraging as much of the data analysis within Chapter 6 focuses on the shear layer. The boundary layer data agrees well too, though has a gradient of 0.651. For the 0.2m flow conditions, the shear layer vertical velocities again show reasonable agreement with a gradient of 0.627.

The numerical shear layer velocity profiles for the two rigid cases show geometric agreement compared to the flume profiles though there is disparity in velocity magnitudes in the 0.4m case, and gradient in the 0.2m case (Figure 5.9 a & c).In

both cases the numerical model gives higher in-canopy velocities. As explained above, this is expected due to the inability of the PIV data to pick up the canopy flow structure well.

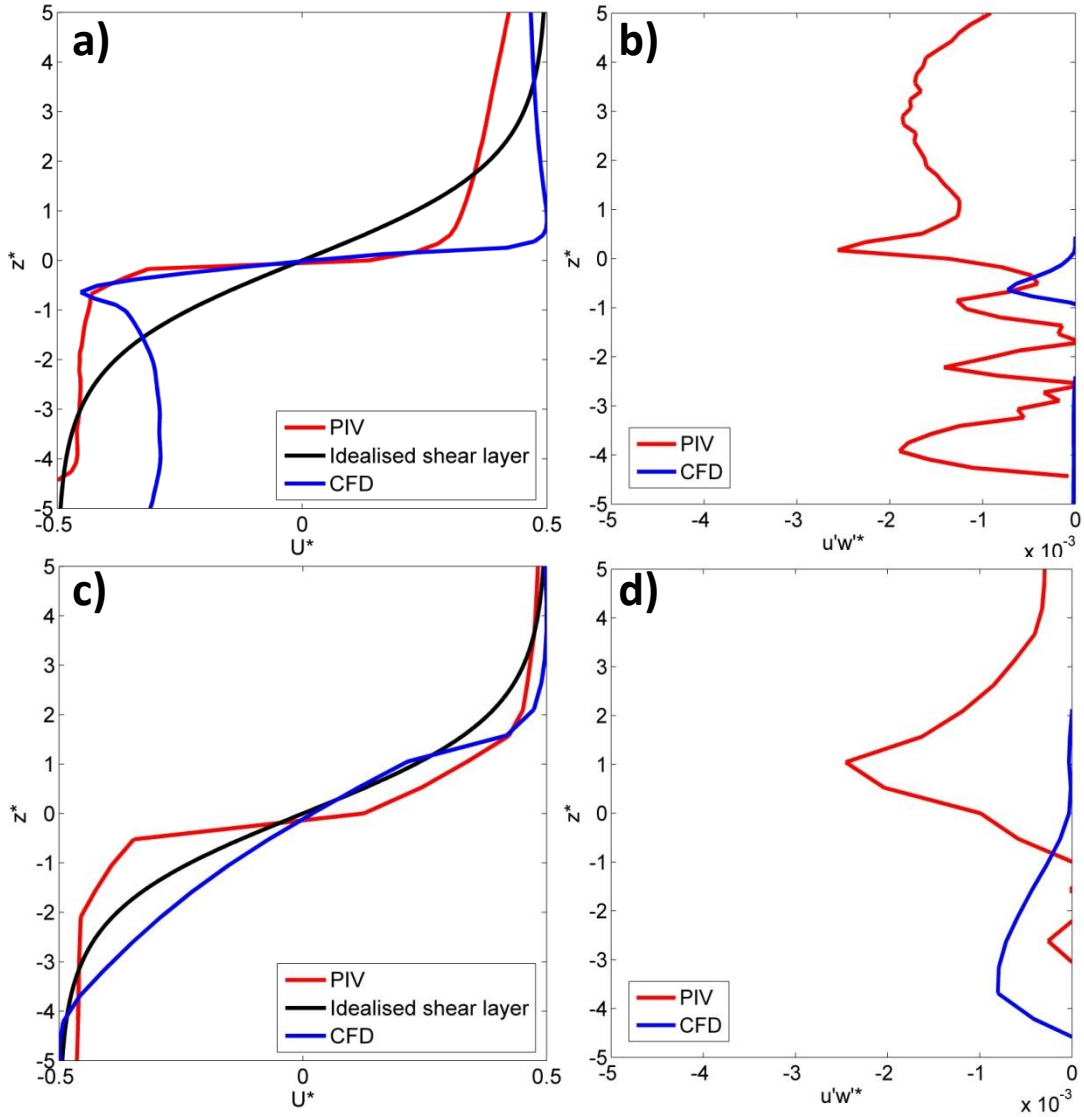

Figure 5.9: *Shear layer velocity (left) and Reynolds stress (right) profiles for the 0.4m (top) and 0.2m (bottom) rigid canopies.*

The Reynolds stress profiles (Figure 5.9 b &d) show less agreement. Both numerical plots show a single peak, which in theory should correspond well to the canopy top inflection point. This is the case for the 0.4m flow. However, the peak is significantly lower in the 0.2m case. It is suggested that this could be due to an in-canopy peak in Reynolds stress due to stem-induced turbulence. The PIV data is far noisier with multiple peaks, some perhaps relating to erroneous canopy data caused by over/under illumination. However, there is a clear peak around the canopy top in

both cases. For the 0.4m case, this peak occurs slightly higher in the flow than the peak predicted by the model.

Finally, the vorticity plots (Figure 5.10) for the 0.2m case show good visual agreement. Both highlight a region of strong clockwise vorticity at the canopy top of magnitude 20-30Hz. In the model this region is mainly confined to the top section of the canopy, whereas in the PIV data, this extends slightly into the flow above the canopy. The model picks up a significant amount of canopy turbulence, which is not picked up by the flume PIV for the reasons described above.

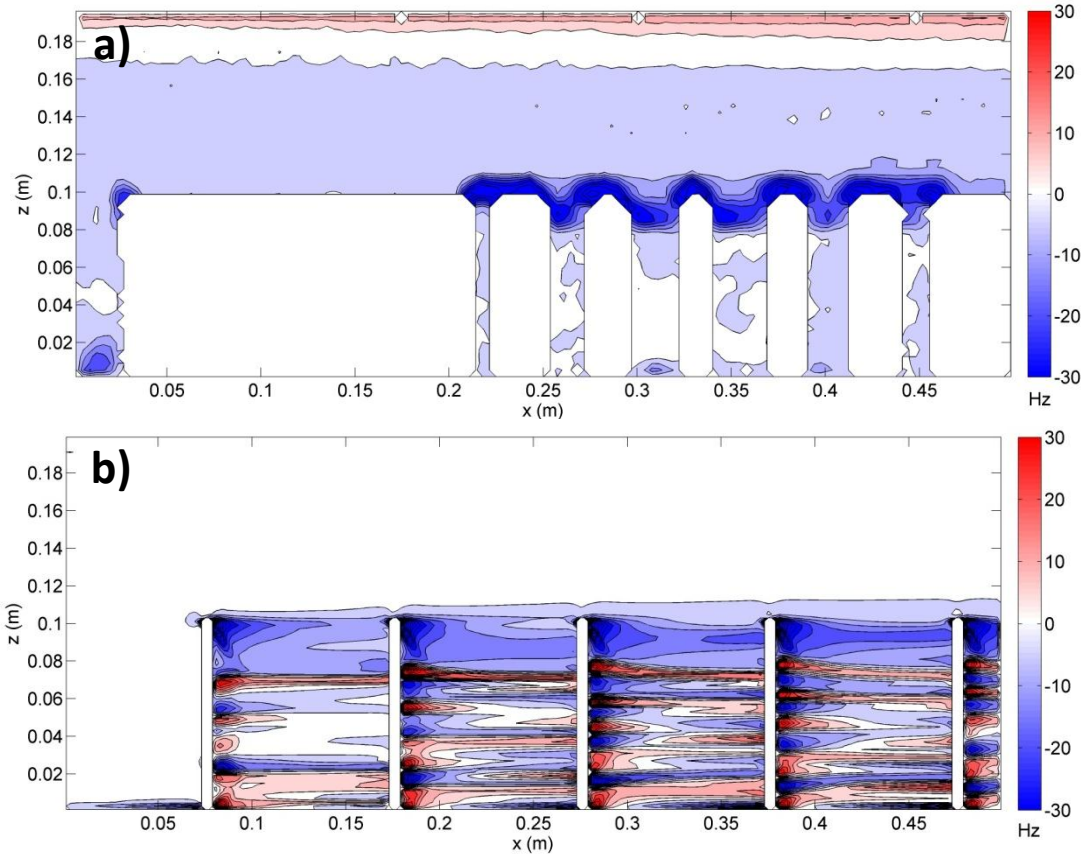

Figure 5.10: *Mean vorticity plots for the (a) flume and (b) numerical 0.2m rigid canopies. The plot shows both clockwise (blue) and anticlockwise (red) vorticity.*

The 0.4m flow (Figure 5.11) shows a very similar pattern of vorticity, occurring at the tops of the stems, related to the development of the canopy shear layer. Again the magnitudes are similar. Interestingly, the CFD model predicts far less in-canopy turbulence for this deeper flow.

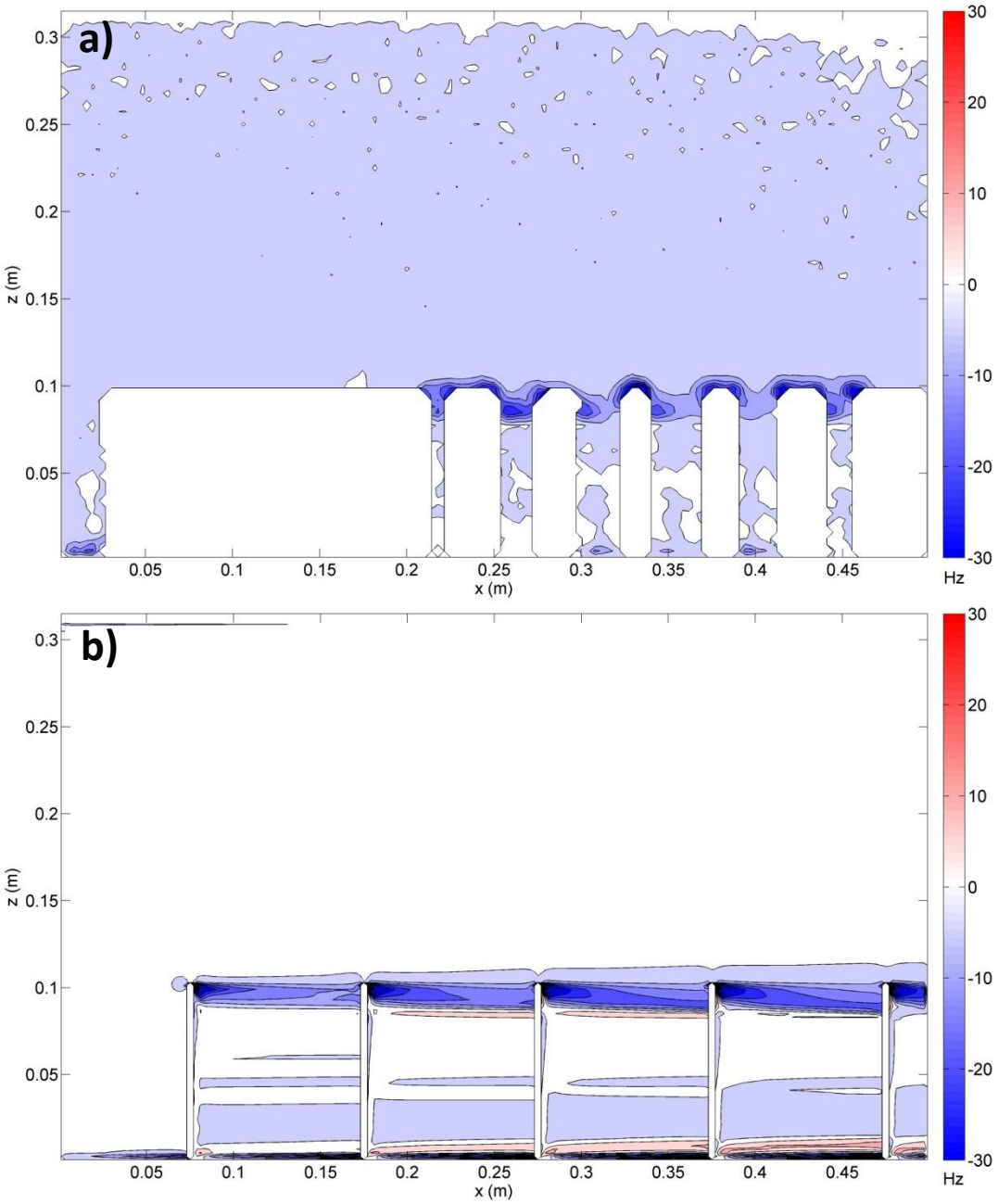

Figure 5.11: *Mean vorticity plots for the (a) flume and (b) numerical 0.4m rigid canopies. The plot shows both clockwise (blue) and anticlockwise (red) vorticity.*

Overall, it is suggested that the rigid stem model predicts the mean flow well, although in some places it fails to reproduce the large vertical velocity variations of the turbulent flow. Furthermore the vortex characteristics of the flow are also well reproduced with additional detail in the canopy which cannot be picked up using PIV, thus demonstrating the difficulty in using PIV for canopy flows.

5.7 Flexible vegetation

Due to the novel nature of the Euler-Bernoulli Beam model, described in Section 3.5, it has been validated across three different flow conditions to ensure that it performs well for each condition. Plant data were not collected simultaneously with flow data in the flume and therefore plant movement cannot be validated. Furthermore, the model assumes an initial vertical position for the vegetation. However, this was not the case as the artificial vegetation already had initial curvature. Nevertheless, the turbulent flow field should represent in some way the plant motion, and therefore it is assumed that by validating the flow field, it is possible to make assertions about the accuracy of the vegetation motion.

5.7.1 Slow flow conditions ($\overline{u}_{z=0.4h}$ = 0.18-0.26m/s)

Figure 5.12 shows the velocity comparisons for the flexible canopy experiments under the slow flow conditions. For the 0.4m flow, the downstream velocity (U) pattern (Figure 5.12a) looks very similar to the rigid case, with poor agreement in the canopy, and a clear pattern above the canopy. Again, the shear and boundary layer velocities group together in lines according to height, and each line shows qualitatively good agreement between measured and modelled values. The vertical velocities also show a similar pattern to the rigid case with relatively good agreement outside of the canopy though in general the data appears to fit less well with lower R^2 values.

For the shallower flow, again the patterns for both velocity components are similar to the rigid case, suggesting that flexibility does not alter the model performance significantly. Interestingly, for the 0.2m depth, the shear layer regression equation is nearly identical to that of the rigid canopy, with a very good fit (R^2=0.952). The gradient of the regression for all of the velocities in Figure 5.12 shows slightly weaker agreement with the expected 1:1 relationship than the rigid case, though this could be due to flow speed rather than simply flexibility.

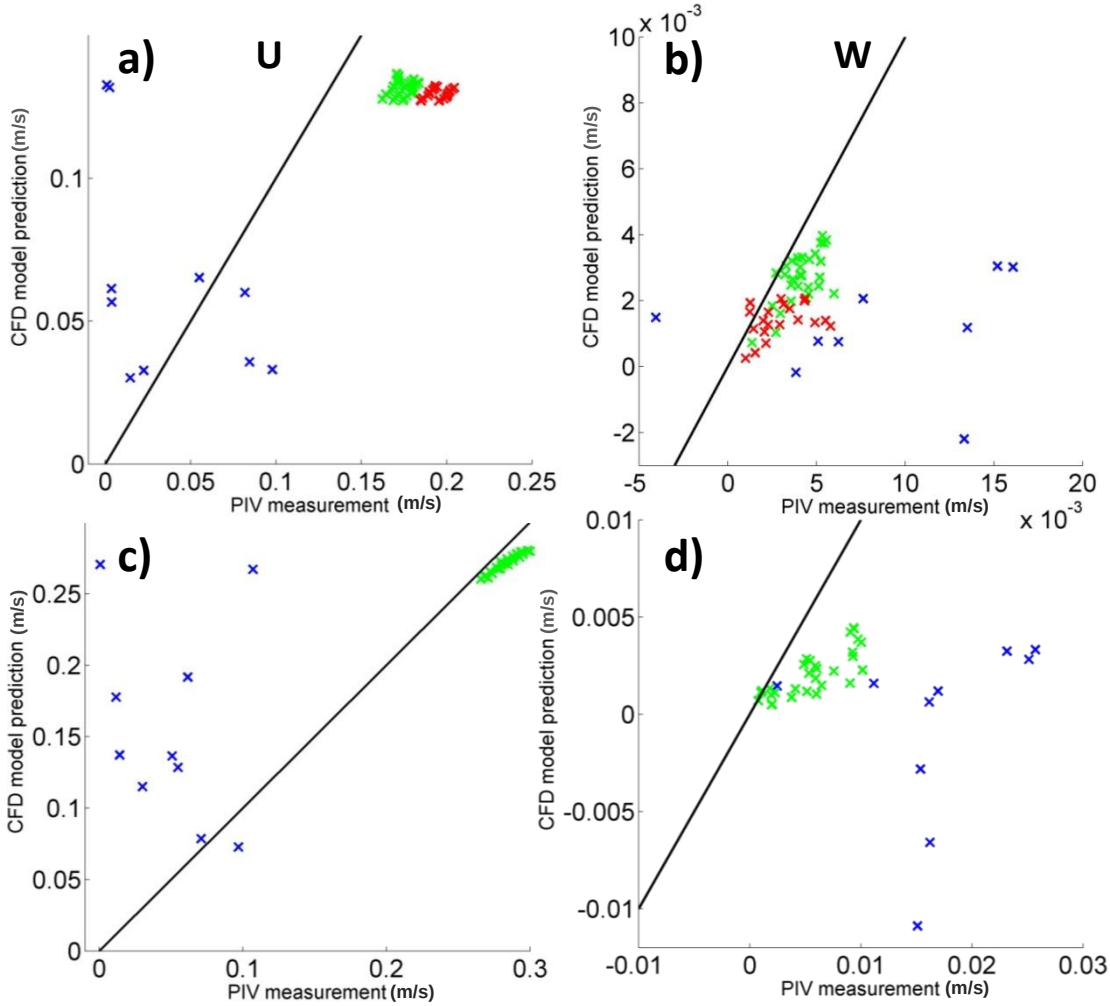

Figure 5.12: *Comparisons of modelled and measured downstream (left) and vertical (right) velocities for the 0.4m (top) and 0.2m (bottom) flexible canopies in slow flow. The data are split into canopy (blue), shear layer (green) and boundary layer (red) points. The black line represents a 1:1 relationship.*

The canopy shear layer profiles for the slow flow flexible experiments appear to highlight significant differences between the numerical prediction of the velocity in the 0.4m and 0.2m experiments (Figure 5.13 a & c). In the 0.4m flow, the PIV shear interface appears to be sharper, with a much more gradual shear layer in the CFD case. This is the opposite to the results for the rigid case above and could either be due to the increased wake effects of the top of individual stems in the slower flow or could simply be due to the approximation of the shear layer region. This approximation was done automatically to avoid bias. However, it could have led to an inappropriate choice of shear layer width, or at least a different estimated shear layer width between experiments.

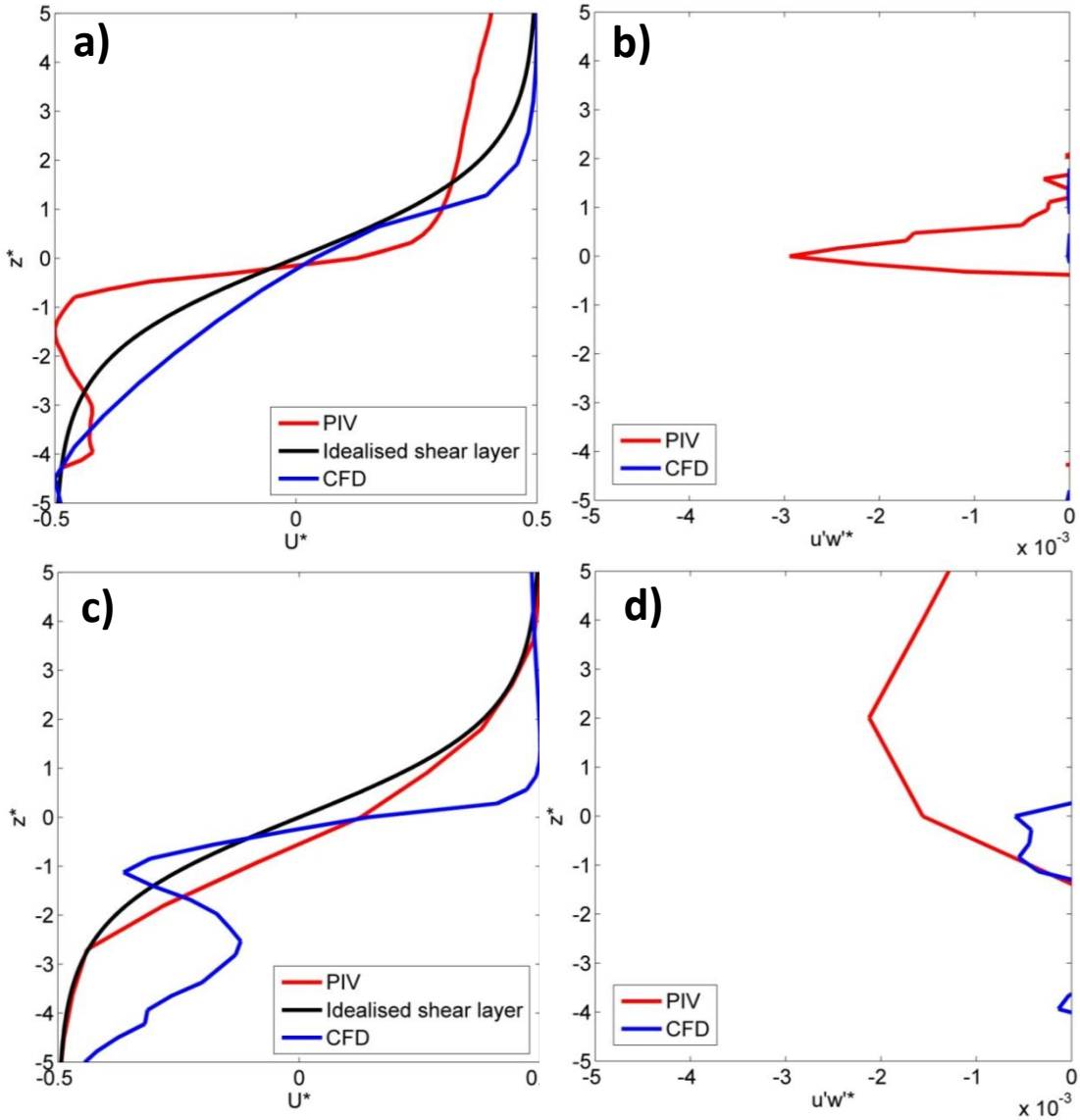

Figure 5.13: *Shear layer velocity (a,c) and Reynolds stress (b,d) profiles for the 0.4m (top) and 0.2m (bottom) flexible canopies in slow flow.*

The Reynolds stress profiles (Figure 5.13b&d) show that the Reynolds stress values are much higher in the flume than in the model as with the rigid case. In the 0.2m case, the flume experiments show a large peak in Reynolds stress, situated above the canopy, suggesting there may be erroneous values or the stress may not relate to the canopy shear layer. In contrast, for the 0.2m flow, the numerical model does show evidence of a peak at the canopy top. For the 0.4m flow, the experiment shows a clear Reynolds stress peak at the canopy top whereas the numerical model fails to predict any significant Reynolds stress at the canopy top.

The vorticity plots (Figure 5.14) show that for the 0.2m flow, the model predicts the vorticity magnitude at the top of the canopy well, peaking at approximately 30Hz.

There is some evidence of clockwise and anti-clockwise vorticity in the canopy region in the flume experiments, which the model resolves as stem-induced wake vorticity. The flume data shows the downstream expansion of the vorticity region into the flow above the canopy (as shown by the dotted line), probably due to growth of the shear layer from the canopy front. The numerical data also has evidence of this growth process; however the rate of increase is considerably lower.

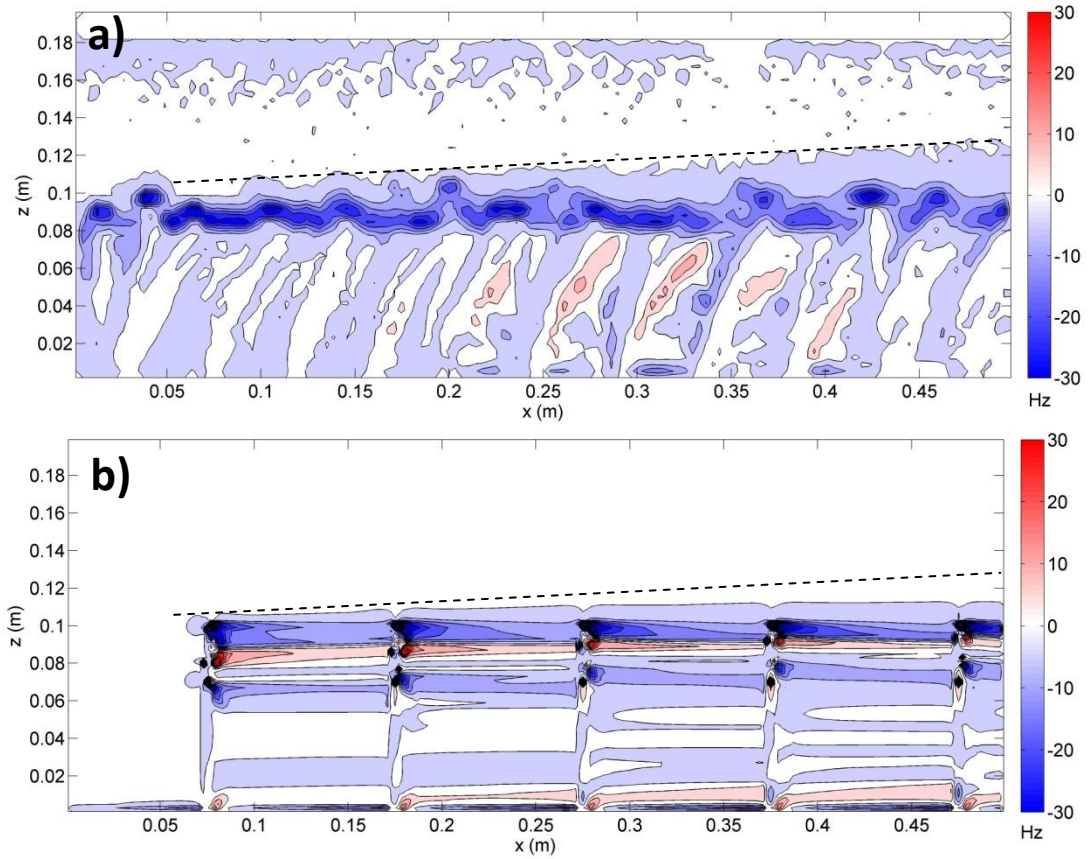

Figure 5.14: *Mean vorticity plots for the (a) flume and (b) numerical 0.2m flexible canopies in slow flow. The plot shows both clockwise (blue) and anticlockwise (red) vorticity. The dotted line represents the rate of growth of the shear layer in the flume case.*

The flume results from the 0.4m flow (Figure 5.15) show a lower magnitude of vorticity at the canopy top and this is reproduced in the numerical results. There is less evidence of shear layer growth in the experimental evidence, potentially obscured by the presence of smaller-scale random turbulence. However, the numerical results show that this process is still operating. Although the flume results pick up some anti-clockwise vorticity within the canopy, in this instance, the

numerical data does not pick up any wake-scale turbulence presumably because of its low magnitude.

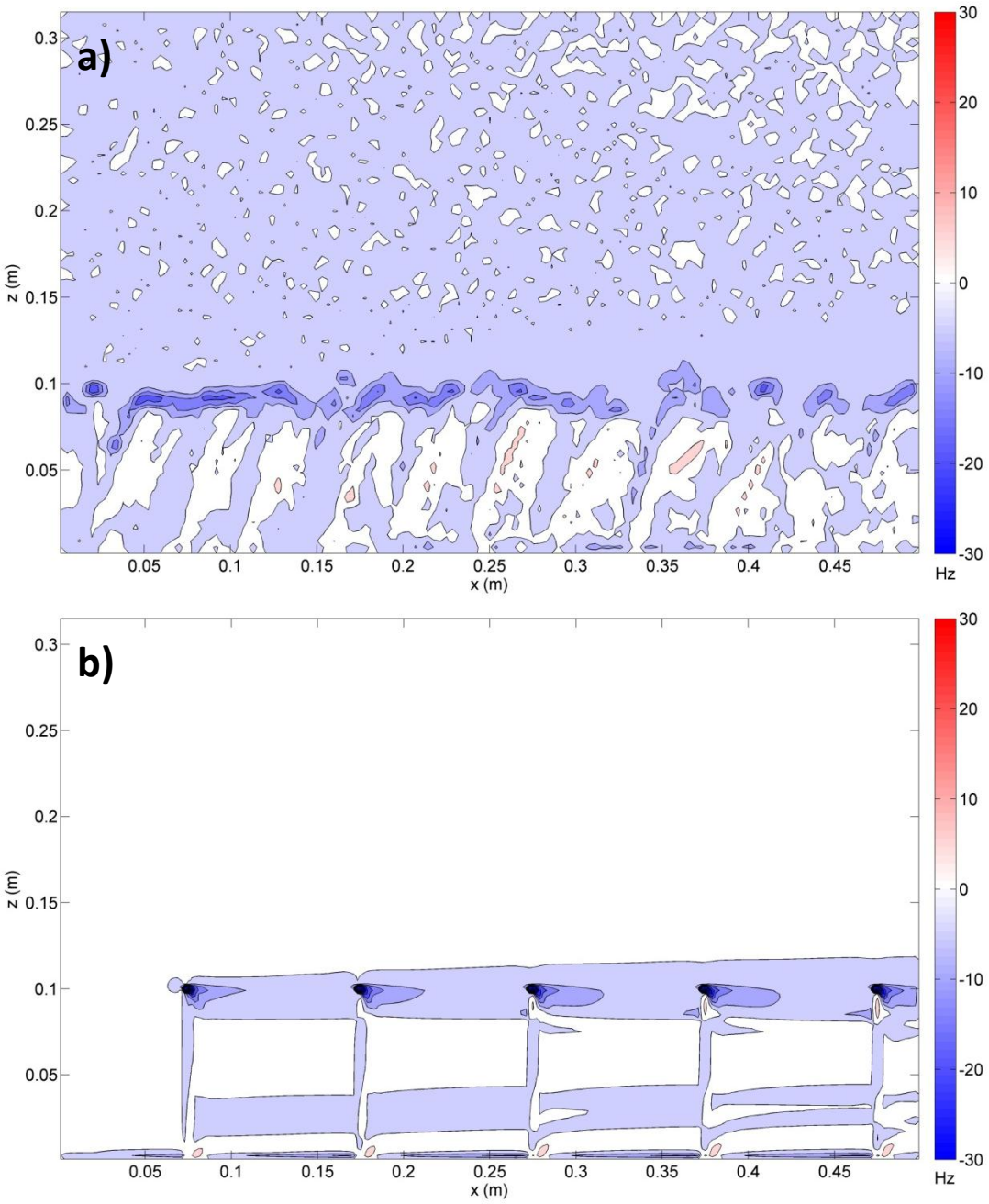

Figure 5.15: *Mean vorticity plots for the (a) flume and (b) numerical 0.4m flexible canopies in slow flow. The plot shows both clockwise (blue) and anticlockwise (red) vorticity.*

In summary, the results from the low flow conditions show that the flexible model exhibits a similar level of performance to the rigid model. Both the velocity and vorticity signals are similar. This is encouraging given that the rigid results agree well with the literature.

5.7.2 Medium flow conditions ($\overline{u}_{z=0.4h}$ = 0.36-0.52m/s)

The patterns are visually similar to the previous case for both velocity signals; however the regression gradients and corresponding R^2 values (See Tables 5.3-5.4) for the downstream velocity outside of the canopy are generally lower. This suggests either that on the whole the model performs a little worse, or the flume data contains greater errors. This increase in discrepancy is less obvious in the vertical velocity; however predictive performance is still poor.

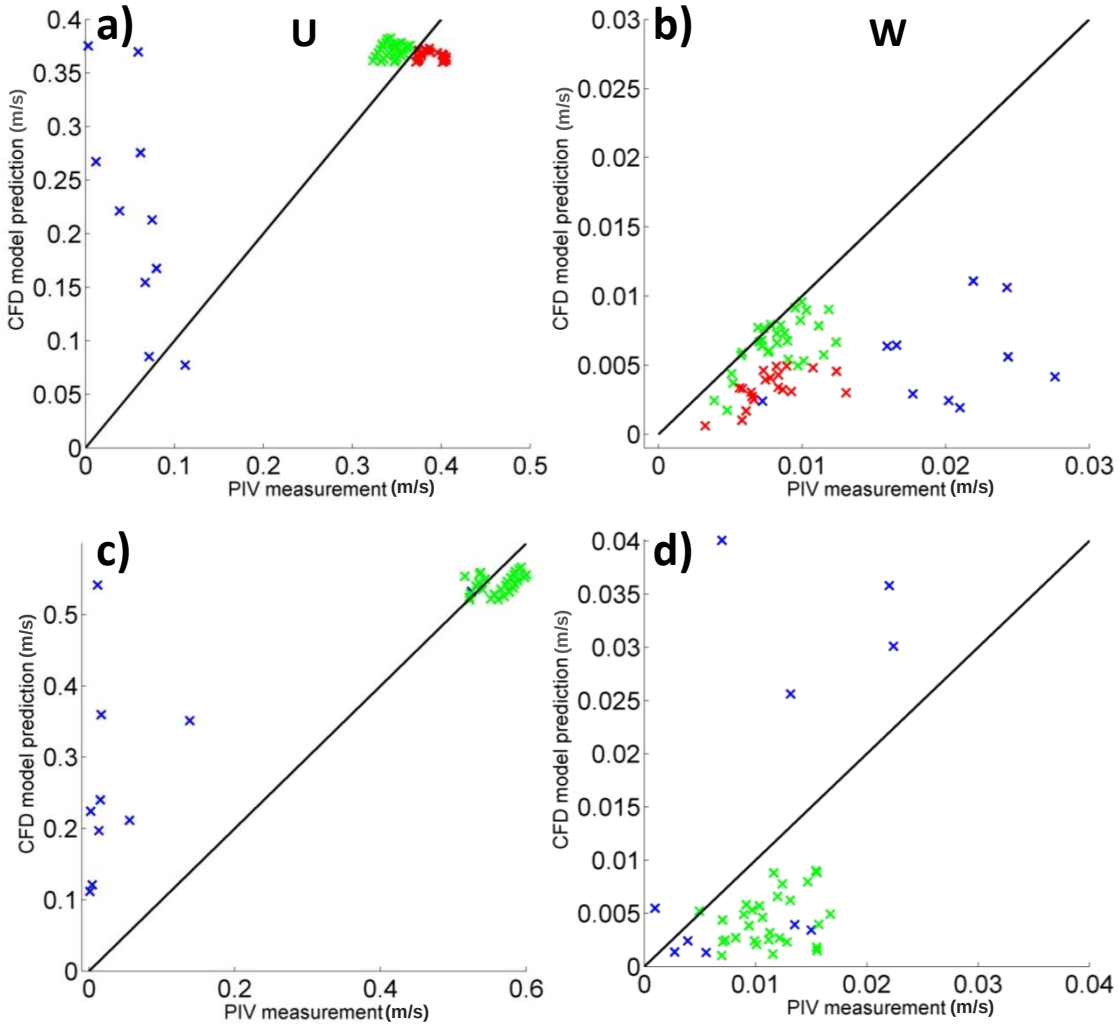

Figure 5.16: *Comparisons of modelled and measured downstream (a,c) and vertical (b,d) velocities for the 0.4m (top) and 0.2m (bottom) flexible canopies in medium flow. The data are split into canopy (blue), shear layer (green) and boundary layer (red) points. The black line represents a 1:1 relationship*

The shear layer velocity profiles (Figure 5.17a&c) show geometric agreement, particularly for the shallow 0.2m case, where the shape is very similar although the velocity magnitudes differ, which may be due to the normalisation process. Both depths show a higher velocity just above the canopy in the numerical simulations, consistent with lower vertical velocities and less mixing at the canopy top, than in the flume experiments. The flume experiments also fail to fully pick up the in-canopy flow as explained above, and for this reason, the numerical results contain a velocity peak in the canopy which is not present in the flume experiments. If the shear layer were assumed to start above this peak, the two profiles would look more similar.

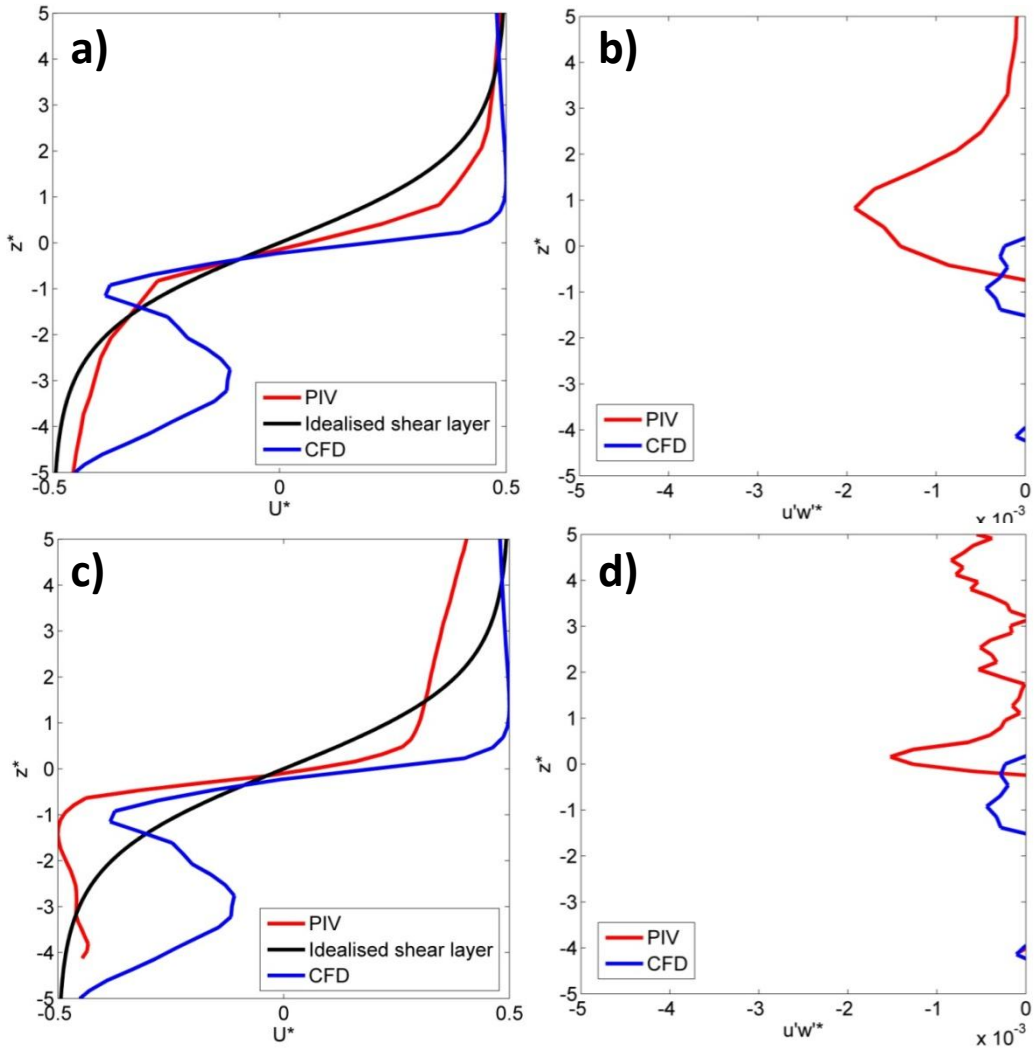

Figure 5.17: *Shear layer velocity (a,c) and Reynolds stress (b,d) profiles for the 0.4m (top) and 0.2m (bottom) flexible canopies in medium flow.*

The numerical Reynolds stress profiles (Figure 5.17b&d) both show a peak at the top of the canopy, though the magnitude is reduced. The flume experiments show a larger but more displaced peak. In particular, the 0.2m profile appears to contain a significant amount of noise above the canopy.

The vorticity plots (Figures 5.18 and 5.19) are consistent with the previous cases, in that both the flume and numerical results identify a clear shear layer vortex signal at the canopy top, and again the magnitudes are comparable (approximately 30Hz). The 0.2m flume results seem to show a region of strong anti-clockwise vorticity at the top of the domain, however, it is suggested that this is a non-physical signal, potentially relating to water-surface effects.

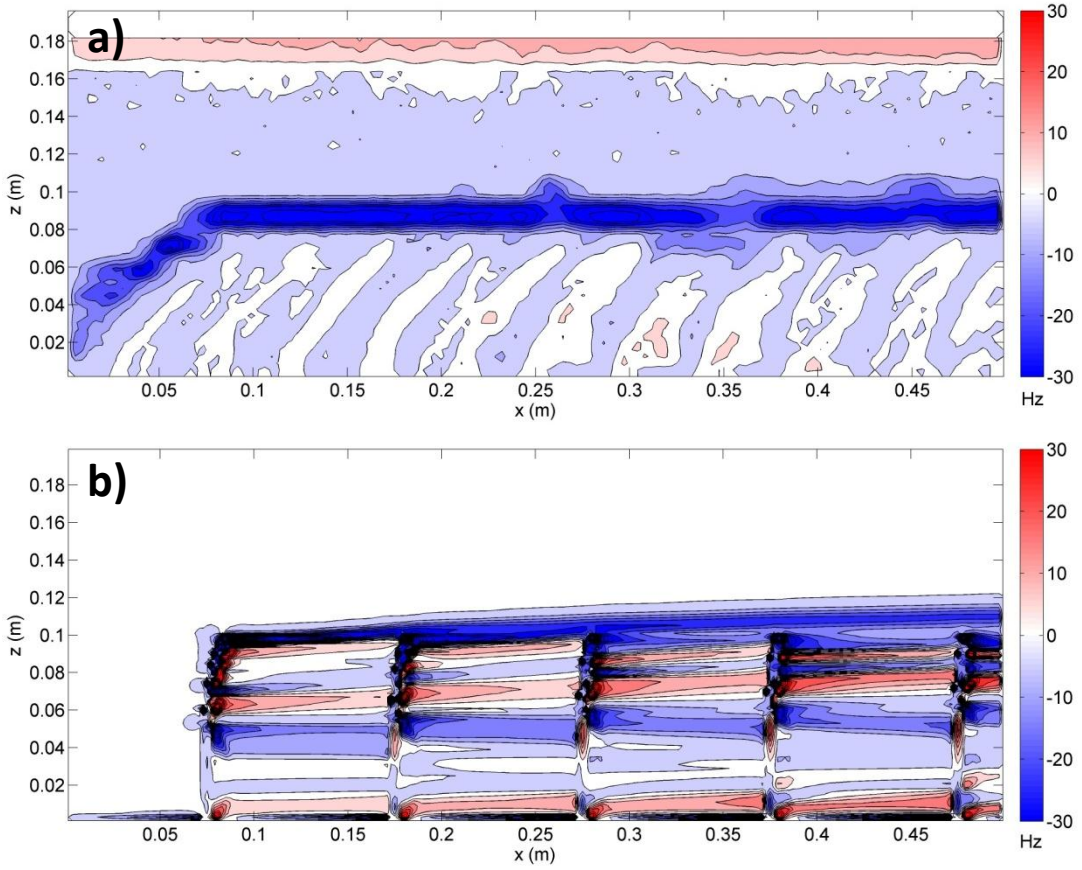

Figure 5.18: *Mean vorticity plots for the (a) flume and (b) numerical 0.2m flexible canopies in medium flow. The plot shows both clockwise (blue) and anticlockwise (red) vorticity.*

Neither of the flume experiments here detects significant shear layer growth along the canopy, whereas the numerical simulations both predict modest growth. However, this growth may be lost in the background turbulence signal in the flume experiments.

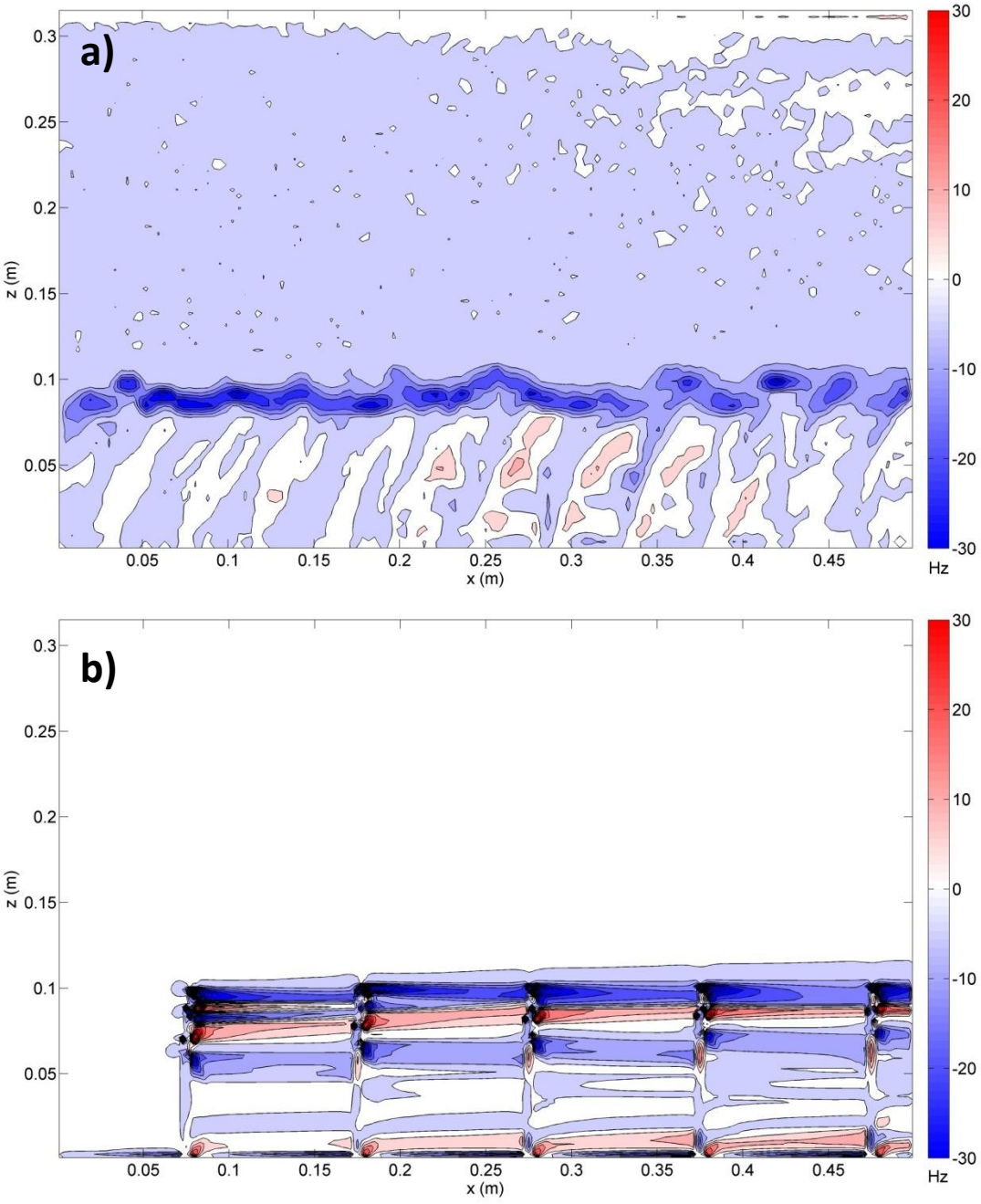

Figure 5.19: *Mean vorticity plots for the (a) flume and (b) numerical 0.4m flexible canopies in slow flow. The plot shows both clockwise (blue) and anticlockwise (red) vorticity.*

Overall, the medium flow conditions simulations again show good agreement between the overall pattern of velocities and vorticity, despite the discrepancy in spot-values. In particular, the normalised shear layer velocity and Reynolds stress profiles show good agreement in terms of shape and inflection point height, though there is still a difference in magnitude of Reynolds stress. Contrastingly, the numerical model appears to reproduce shear layer growth well, which is not visible in the experimental data.

5.7.3 Fast flow conditions ($\overline{u}_{z=0.4h}$ =0.59m/s)

For this faster flow case, only 0.4m flume experiments are reported due to errors in the 0.2m data caused by the free surface. The downstream velocity for the 0.4m flow shows visually poor agreement between the numerical and flume data, particularly in the boundary layer region (Figure 5.20). Here, the flume measurements occupy a range of approximately 0.3m/s whereas the numerical results have a range closer to 0.02m/s, highlighting the magnitude of the error. Figure 5.21 shows the time-averaged downstream velocity long-section for this case and shows a significant region of lower velocity at the top of the flume. This is non-physical and most probably corresponds to a lack of laser light at the top of the domain during this run.

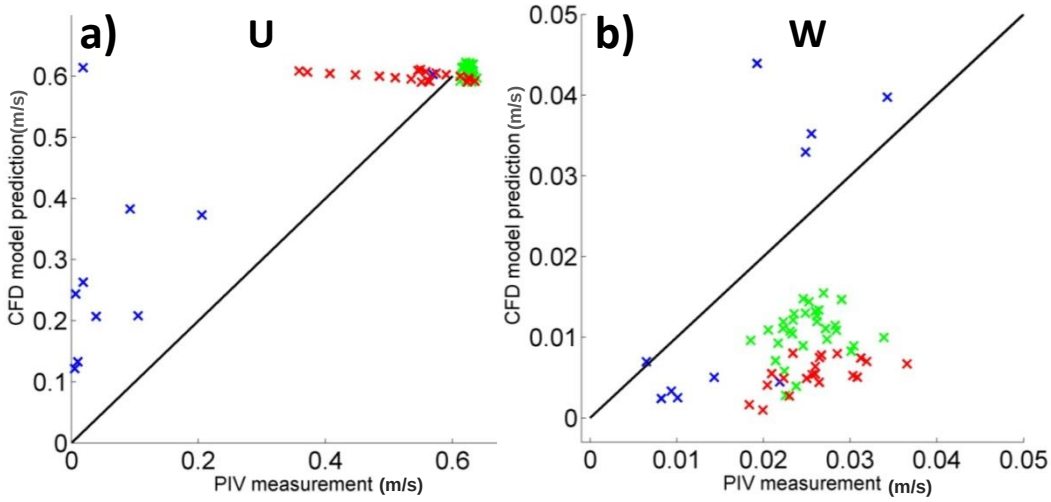

Figure 5.20: *Comparisons of modelled and measured (a) downstream and (b) vertical velocities for the 0.4m flexible canopies in fast flow. The data are split into canopy (blue), shear layer (green) and boundary layer (red) points. The black line represents a 1:1 relationship.*

Elsewhere in the domain, the performance is similar to the previous cases. The numerical canopy vertical velocity shows significantly improved agreement (Table 5.5) with the flume results. However, this may be due to the fact that the vegetation reconfiguration means that there is now minimal flow in the canopy.

Figure 5.22 shows that the central region of the shear layer is similar in both the numerical and flume results. However, there are significant differences in the canopy due to wake-scale turbulence, and at the top of the domain. The Reynolds

stress profiles (Figure 5.22b) both peak at or just above the canopy top. As before, there is a discrepancy between the magnitude of Reynolds stress due to the smaller vertical velocities in the numerical simulation. However, the difference in magnitude is less than any of the other cases. The flume Reynolds stress profile also does not drop off above the canopy, suggesting that other processes contribute to the stress, whereas the numerical data only picks up the shear layer processes.

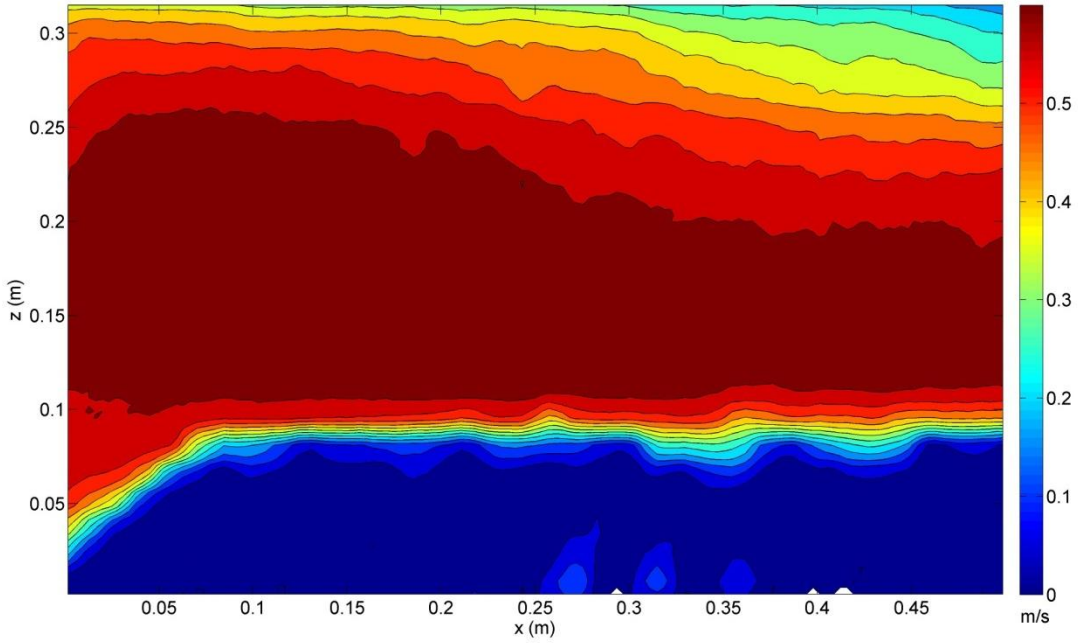

Figure 5.21: *Mean velocity long-section for the 0.4m fast flow case.*

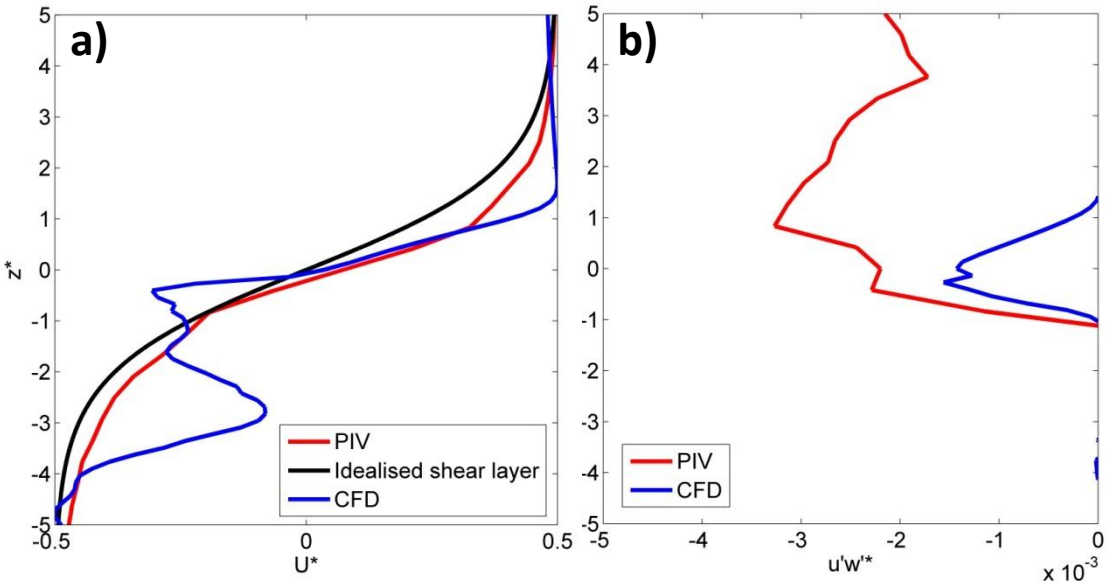

Figure 5.22: *Shear layer velocity (a) and Reynolds stress (b) profiles for the 0.4m flexible canopies in fast flow.*

As with all the other cases, the vorticity plots (Figure 5.23) show good agreement at the canopy top, in terms of spatial pattern and magnitude. In this particular case, the numerical simulation reproduces the downstream growth of the canopy shear layer better than the experimental data, as well as the in-canopy turbulence which is less evident in the flume data.

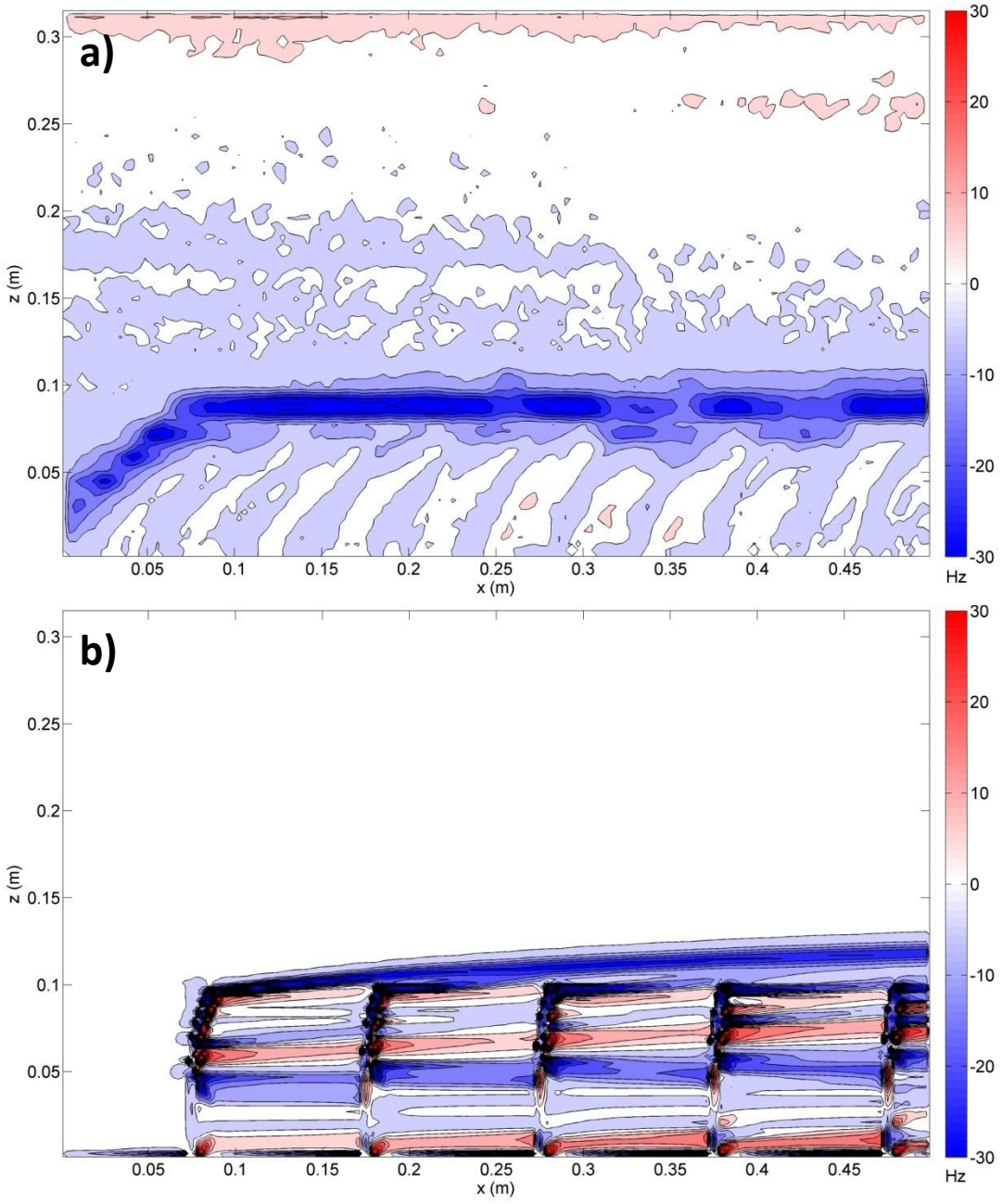

Figure 5.23: *Mean vorticity plots for the (a) flume and (b) numerical 0.4m flexible canopies in slow flow. The plot shows both clockwise (blue) and anticlockwise (red) vorticity.*

In summary, the fast flow cases show poorer agreement with the spot values, particularly for downstream velocity, though this is shown to be a result of

experimental error. Accounting for additional representation of wake turbulence in the numerical model, the shear layer approximations are geometrically similar, with a smaller discrepancy in Reynolds stress than the previous cases. Again, the growth of the shear layer is shown in the numerical vorticity data but is not as clear in the experimental data.

5.8 Real vegetation

Real vegetation presents a far more complex setup than the artificial vegetation. The plants used (*Ranunculus penicillatus*) were complex and varied in form, with multiple plants used, each with multiple stems. While the N-pendula model was developed to represent this type of vegetation, it was not developed to the same level of complexity as this vegetation and therefore direct comparison or validation of particular velocity values or plant motion would be unsuitable. However, it is still possible to assess the general characteristics of the flow, such as the canopy shear layer and the vorticity in order to inform how good a predictor the N-pendula model is for these type of flows. Therefore, in this section the flume and numerical results from the real vegetation experiments are compared.

Table 5.6 shows the time-averaged bulk velocities for the vegetation experiments and the N-pendula simulation. This shows that the hydraulic conditions should be similar, particularly between the medium and fast flows and the N-pendula model.

Run (type, depth, speed)	Velocity (m/s)	Reynolds number
Real, 0.4m, slow	0.13	28,889
Real, 0.4m, medium	0.24	53,333
Real, 0.4m, fast	0.30	66,667
N-pendula CFD,0.3m	0.28	12,000

Table 5.6: *Averaged velocities for the real vegetation runs*

Figure 5.24 shows the shear layer profiles for the flume experiments and the N-pendula simulation. The velocity profile shows good geometrical agreement between the different cases, with the clear development of a canopy shear layer in each case. The N-pendula profile is similar to the flume experiments though the

shear interface appears to be wider and shallower in slope. This may be due to the positioning of the vegetation and more effective streamlining of the canopy in the real vegetation than in the numerical canopy.

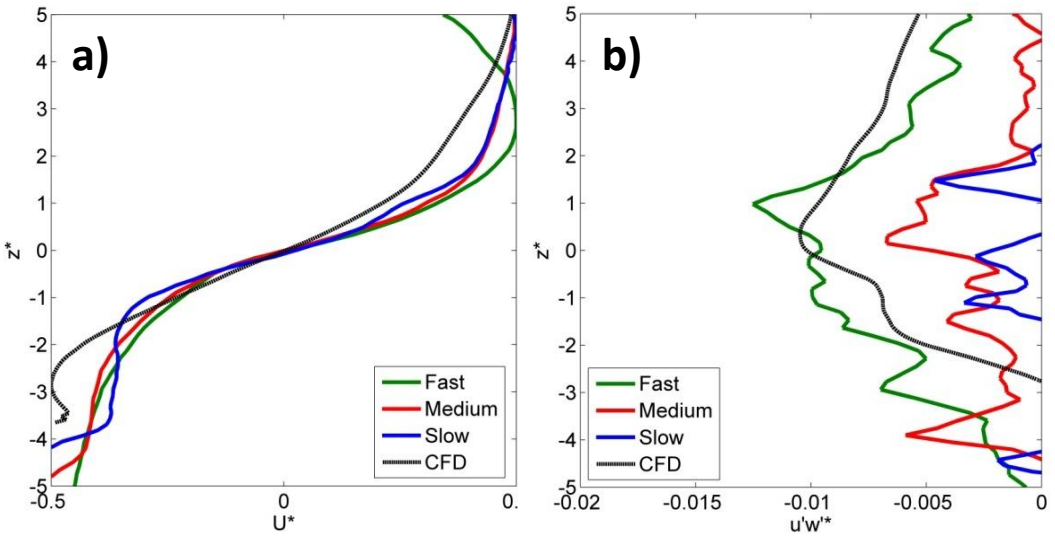

Figure 5.24: *(a) Shear layer velocity and (b) Reynolds stress profiles for the real vegetation experiments*

The Reynolds stress profiles show multiple peaks, with all profiles exhibiting a peak in or around the canopy top. The N-pendula model profile corresponds particularly well in terms of geometry and magnitude with the fast flow profile, though within the canopy its magnitude lies between the medium and fast flow scenarios as expected from Table 5.6. It is particularly noticeable that all of the PIV flow profiles exhibit at least one secondary peak. In particular, the fast, medium and N-pendula profiles all exhibit a secondary peak at roughly the same normalised depth into the canopy, suggesting the presence of either a moving shear layer, or secondary processes operating besides the shear layer. This will be discussed further in Chapter 6.

Figure 5.25 shows the mean vorticity plots from the real vegetation experiments. In each case there is clear evidence of shear layer vortices occurring at the canopy top. As the flow speed increases, the angle of the shear layer appears to decrease too which is consistent with the plant reconfiguring more as the flow and consequent drag force increases. The N-pendula vorticity plot in Figure 5.26 shows similar

evidence of shear layer vortices at the canopy top. Here, the shear layer appears flat, similar to the fast flume case.

It is possible that the numerical shear layer is flatter than the real vegetation cases because of the shorter stem length preventing the stems from protruding too far into the flow. Nevertheless, the shear layer alignment lies within the range of the flume data.

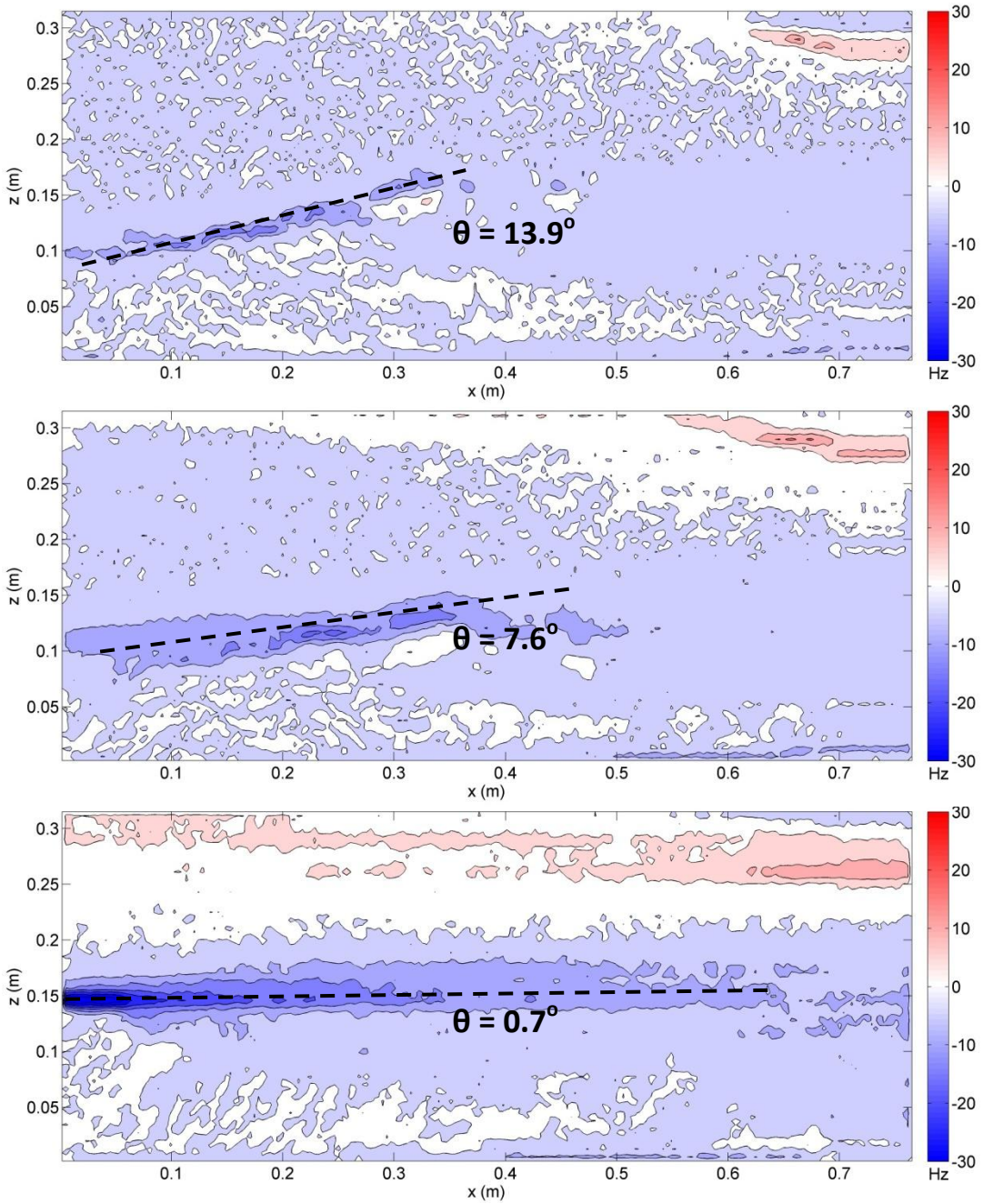

Figure 5.25: *Mean vorticity plots for the slow (top), medium (middle) and fast (bottom) 0.4m real canopies. The plot shows both clockwise (blue) and anticlockwise (red) vorticity. Dotted lines represent approximate shear layer angles.*

Overall, the results from the real vegetation experiments show good process agreement with the N-pendula model, both in terms of shear layer development and vortex regime. Whilst this validation is not as thorough as the beam model it is sufficient to be able to suggest that the N-pendula model may be useful in modelling simplified canopy dynamics in highly flexible canopies.

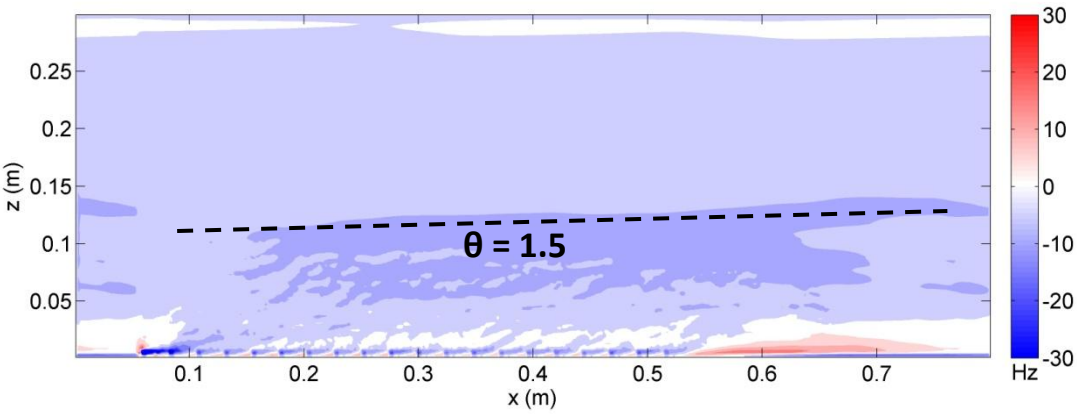

Figure 5.26: *Mean vorticity plot for N-pendula canopy model. The plot shows both clockwise (blue) and anticlockwise (red) vorticity.*

5.9 Wavelet Analysis

As discussed earlier in this chapter, it was not possible to compare the instantaneous turbulent signal from the model and flume results due to the lack of developed turbulence within the validation models and the error within the flume data. The errors in the flume data can be overcome by analysing the larger scale trends via wavelet analysis. Although the data is still noisy, larger scale trends are identifiable. The models used in the application in Chapter 6 use cyclic boundary conditions and therefore contain a more developed turbulent flow signal. Therefore, it is possible to qualitatively compare the wavelet signal from the flume, with those obtained from the numerical models in Chapter 6.

The models in Chapter 6 were not designed as exact analogues of the flume experiments and therefore quantitative analysis is not possible, however it is possible to compare general trends. Furthermore, some of the numerical experiments were conducted in similar canopy conditions. In particular, the rigid model (Section 6.2), the canopy beam model (Section 6.4) and the n-pendula

canopy (Section 6.6) closely resemble the flume experiments in vegetation configuration and flow conditions.

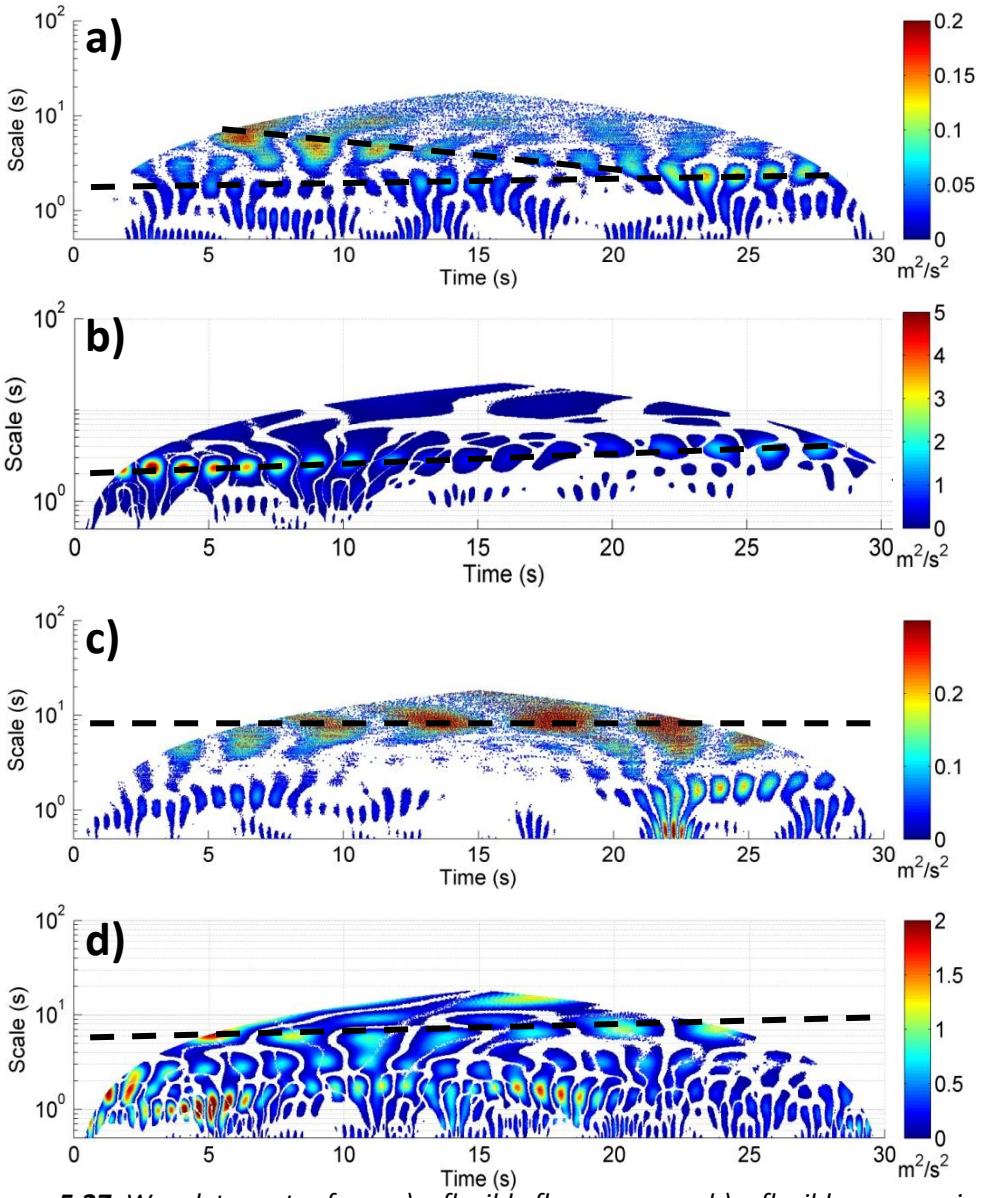

Figure 5.27: *Wavelet spectra from a) a flexible flume canopy, b) a flexible canopy simulation, c) a real flume canopy and d) a highly flexible canopy simulation. The black dotted lines highlight dominant turbulent scales.*

Figure 5.27 shows a series of wavelet spectra obtained from numerical (b and d) and flume experiments (a and c). The numerical spectra will be investigated in detail in Chapter 6, and therefore discussion here is limited to comparison between the spectra. The noise within the flume datasets is identifiable particularly at the higher time-scales, where there is a wide range in magnitude and fewer smooth patterns. For the flexible artificial canopy (a and b), there is evidence of turbulence

at a similar scale in both the flume and numerical data, suggesting that both are highlighting the same turbulent process, possibly related to the vegetated shear layer.

The flume data identifies a higher time-scale process too, which appears to merge with the lower time-scale signal. It is unclear what this signal relates to, but it is possible that it corresponds to flume-induced secondary circulation (Hardy *et al.*, 2009). Overall, the flume identifies turbulence at a wider range of scales than the numerical model and this is expected given that the model cannot fully represent all the turbulent processes operating.

For the highly flexible (or real vegetation) case, both the flume and numerical data identify two scales of turbulence, at different time-scales: one longer timescale, shown by the dotted black line, and one with much shorter timescale (approximately one second) which appears to oscillate through time. There is qualitatively good agreement between these two scales. Both spectra also pick up other turbulent scales, though in this case the numerical spectrum appears to identify a wider range of turbulent scales. This may be due to interference from the vegetation in the flume case, blocking flow through the interrogation region and dampening turbulence.

It is also noticeable that the magnitude of the peaks differs considerably between the flume and numerical data, with much larger magnitude peaks in the numerical data. This may be due to either the dampening of turbulence by interaction with a wider range of turbulence scales in the flume, or it may be due to the effect of the noise on the data.

Overall, the visual agreement between the wavelet spectra is encouraging. It appears that the numerical model does reproduce some of the key features observed in the flume spectra, though it must be noted that this does not represent a direct validation of the model.

5.10 Summary of validation

The validation of numerical models applied to natural systems is not straightforward and there are many nuances associated with the process. While the numerical data may appear at times to poorly represent the spot data obtained in the flume, there are complexities with the flume data that must be considered.

The flume data were collected using high resolution state of the art techniques, which allowed analysis of the holistic flow field. This offered mm/Hz scale measurement of the instantaneous two dimensional velocity field across the domain, over a given time period, and represents a much more accurate data source than single point measures such as acoustic Doppler velocimetry (ADV) or one dimensional methods such as Ultrasonic velocity profiling (UVP). Yet, even though the most appropriate methods were used there were still significant concerns about data quality

There were three significant sources of error within the flume data that have been identified and discussed in Section 5.6. First, the presence of the free surface in the images introduced error. This was not applicable for the deeper flow, but for the shallower flows, the presence of the free-surface within the images led to false 'particles' within the PIV image that were subsequently used to calculate the velocity field. This led to erroneous velocity vectors.

Second, the laser did not fully illuminate the whole domain, and there were regions of the domain where particles were not identified as a result. This lack of illumination led to lower velocities in regions where un-illuminated particles were not tracked.

Thirdly, the presence of the artificial vegetation canopy within the flow introduced error. Despite the artificial vegetation being transparent, there was evidence of reflection of light off the canopy, leading to erroneous velocity vectors. Furthermore, the canopy created regions of low light, where particles could not be identified, resulting in lower velocities. Finally, the visual effect of the perspective of the canopy meant that for much of the image, the stems occupied the entirety of

the canopy region, thereby acting as false, non-moving particles and creating false low velocity regions throughout the canopy region.

Steps were taken to minimise all three sources of error however it is not possible to eradicate them entirely as outlined above. Consequently, it may be considered that the flume data is at least equally as likely to contain error as the model itself (Lane, 1998).

The model uses a solution method and boundary condition technique (MFSA) which have been proven over a wide range of scales, from high resolution mm scale analyses (Lane *et al.*, 2002; Hardy *et al.*, 2007), to investigation over a geomorphological unit such as a meander (Ferguson *et al.*, 2003) or a confluence (Bradbrook *et al.*, 2000), through to investigation of flow in large rivers at the km scale (Sandbach *et al.*, 2012).

However, it is inevitable that the model fails to fully represent the entirety of canopy processes operating within the flume environment. This is another important consideration when validating numerical data against flume or field data. The experimental data contain the influences of processes which are intentionally not resolved by the model. The simplest example of this is upstream boundary conditions which affect background turbulence levels, which were not accounted for by the model inlet conditions. There are also other processes which are not fully modelled, such as those not captured due to the assumptions inherent within the turbulence model (Hardy *et al.*, 2003), as outlined in Chapter 3.

Resolution is another key aspect to consider. Differences in resolution and geolocation between the model and experimental data can introduce error. In this case the difference in resolution is relatively small (0.002m for the model and 0.0038m for the flume) but nevertheless it may introduce some error. Therefore, given these limitations in validation, it is important to evaluate model performance more broadly, for example using visualisation as a means of evaluating the model's ability to reproduce temporally evolving, spatially distributed processes (Lane *et al.*, 2005).

Notwithstanding the model's limitations, the flow structure within the numerical results agrees qualitatively with results obtained from previous studies, both experimental and numerical, into canopy flows (e.g. Ghisalberti and Nepf, 2006; Stoesser *et al.*, 2006; Stoesser *et al.*, 2010). Therefore it is reasonable to assume that a significant portion of the disparity between the numerical and flume data is a result of the experimental errors detailed above. Taking into consideration these issues, the validation experiments presented above have highlighted several key points with regard to the applicability of the numerical models to canopy flows.

1. There are some significant differences between the flume data and the numerical model. In particular, the model appears to under-predict vertical velocity fluctuations and consequently Reynolds stress magnitude.
2. However, it is clear that the rigid and beam models reproduce the key processes acting within canopy flows. Namely, it has been shown that wake-scale turbulence, canopy shear layer characteristics and shear layer vortex production are all captured by the numerical models and the results are in line with the experimental data and previous numerical work.
3. Furthermore, qualitative comparison between wavelet spectra obtained from flume and numerical data suggests that the numerical model represents the same turbulent processes as are seen in the flume data.
4. Flow speed and depth do lead to changes in the quality of model prediction, however this varied over the range of measures and no conditions led to a consistent decrease in prediction capabilities.
5. The N-pendula model shows good agreement with the real vegetation experiments, and whilst there was no direct analogy to compare the numerical data against, it has been shown that in terms of process representation, the N-pendula model is accurate.

Having assessed their accuracy, both models can now be applied to a range of different scenarios. Within this model application, the performance of the models can be assessed further by comparing the numerical results with previous work discussed in Chapter 2.

Chapter 6: Model application and analysis

6.1 Introduction

In Chapter 5, the two vegetation models introduced and developed in Chapter 3 were compared with flume data, to show the extent to which they can represent canopy flows. Both mean and turbulent flow quantities were shown to be reproduced well, over a range of different flow and vegetation conditions. Having validated the two biomechanical models, it is now possible to use the model predictions in more detail to explore the micro-scale processes, feedbacks and interactions operating within the canopy between the flow and vegetation in order to answer the research questions in Chapter 1. In this chapter, several scenarios are considered over a range of different canopy and flow conditions, as summarised in Table 6.1.

The aim of this chapter is not to provide analogy with the flume data, but to use the validated model to investigate the turbulent structure over the canopy top and to characterise the interaction between the turbulence and plant motion at higher spatial and temporal resolutions than possible in either the field or the flume. This will enable an improved insight into plant-flow interactions that to date has not been achieved.

Three key processes are investigated in this chapter: vortex generation and evolution, plant-flow interactions, and drag production. As discussed in Chapter 2, it has been hypothesised that drag production is one of the key linking processes which drives the interaction between flow and vegetation and therefore it is important to study the role of drag and in particular, the influence of drag calculation method on the numerical results.

These three processes are investigated over a range of vegetation types. First, vortex mechanics are considered over a rigid canopy. Second, the vortex mechanics

Simulation	Biomechanical model	Section	$\bar{U}$(m/s)	*Re**	*Fr*	Purpose/Real world analogy
Rigid canopy	n/a	6.2	0.3	25,600	0.19	Benchmark for comparison with previous experimental studies
Semi-rigid patch	Euler-Bernoulli beam	6.3	0.7	22,600	0.28	High velocity peak flows over isolated reed patches within a river.
Semi-rigid canopy	Euler-Bernoulli beam	6.4	0.3	19,200	0.17	Medium velocity floodplain flows over crop fields
Highly flexible patch	N-pendula	6.5	0.5	21,400	0.29	Local high velocity region within base-flow conditions over isolated macrophytes within a small river such as the Browney (see Chapter 8)
Highly flexible canopy	N-pendula	6.6	0.3	12,000	0.29	Base-flow conditions over an extended macrophyte canopy within a small river such as the Browney (see Chapter 8)
Single semi-rigid stem	Euler-Bernoulli beam	6.7	0.7	22,600	0.28	Simple case for testing the dynamic drag treatment

Table 6.1: *Outline of all the numerical simulations presented in Chapter 6. *The Reynolds numbers are low due to the size restriction and shape of the numerical domain. In practice, the scenarios are analogous to higher Reynolds number natural flows.*

and plant-flow interactions of a flexible patch and canopy are considered, using the Euler-Bernoulli beam model. Next, a similar analysis is carried out for a highly flexible patch and canopy using the N-pendula model. Finally, an investigation of the drag-calculation method is performed on a single stem simulation to eliminate plant-plant interactions which may complicate the drag signal.

In order to prevent bias in interpreting the results, a systematic analysis approach is followed throughout, in line with the methodology set out in Chapter 4. A full description of all the methods employed as well as references to previous application of these methods is also given in Chapter 4.

6.2 Vortex mechanics over rigid vegetation

In order to determine the role of flexibility in driving vortex mechanics, initially analysis was conducted on a simulation with a rigid vegetation canopy. A similar setup formed the basis of much of the experimental work into aquatic canopies (e.g. Nepf, 1999; Liu *et al.*, 2008) and therefore this provides a benchmark solution against which to compare the results.

6.2.1 Experimental setup

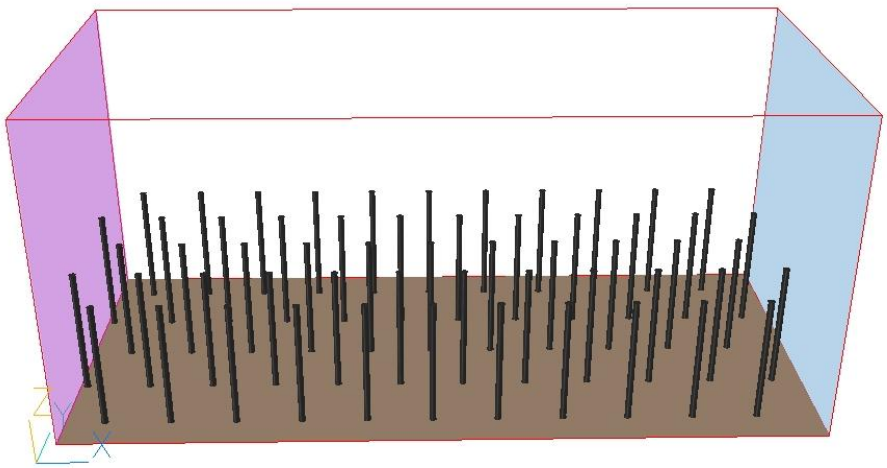

Figure 6.1: *Graphical view of the rigid vegetation domain. The pink region represents the inlet, and the blue region represents the outlet. Physical dimensions shown in Figure 6.2.*

For the rigid vegetation simulation the domain was set up as shown in Figures 6.1 and 6.2. The domain was 0.578m in length, including a recirculation region of 0.082m at the front of the domain. The width of the domain was 0.256m and the

wall conditions were set as smooth boundaries to prevent wall effects dominating the flow. The stalks were arranged in a staggered manner, with a cross-stream and downstream separation of 0.05m between adjacent (albeit staggered) stalks. The stalks were 0.1m high; approximately 0.4 of the overall flow depth which was 0.256m. Each stalk was represented by a cylinder of radius 0.005m with a no-slip boundary condition. The domain was 578 cells long, 256 cells wide and 256 cells high (nx=578, ny=256, nz=256) and therefore the resolution was set as 0.001m in each direction. This grid resolution was chosen, based on initial results in Chapter 3, to ensure grid independence and that the ratio of the stem diameter to grid resolution was such that key turbulent features at both stem and patch scale were resolved. The inlet flow velocity was set to 0.3m/s and consequently the Reynolds number was approximately 25,600. The Froude number was 0.19 and therefore the flow was subcritical.

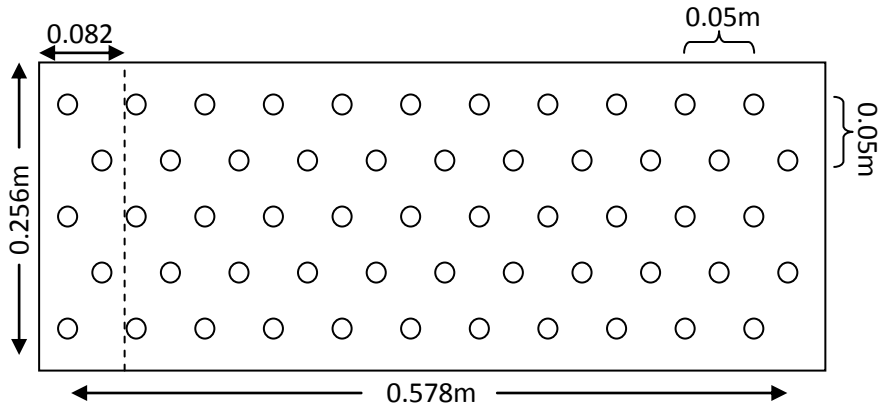

Figure 6.2: *Schematic of the rigid vegetation domain, not drawn to scale. The dotted line shows the boundary of the recirculation region.*

The simulation, which was run for 30 seconds at 50Hz temporal resolution, took 1,400hrs CPU time to complete on a high performance desktop PC. Unfortunately, during the simulation, a computational error within the code led to failure of the model to save the output data after the first 10 seconds of the simulation. Therefore the data collected are analysed here, but with the recognition that the time length is a significant limitation. All analysis was undertaken in the x-z plane at $y/w = 0.5$.

6.2.2 Mean flow profiles and turbulence characteristics

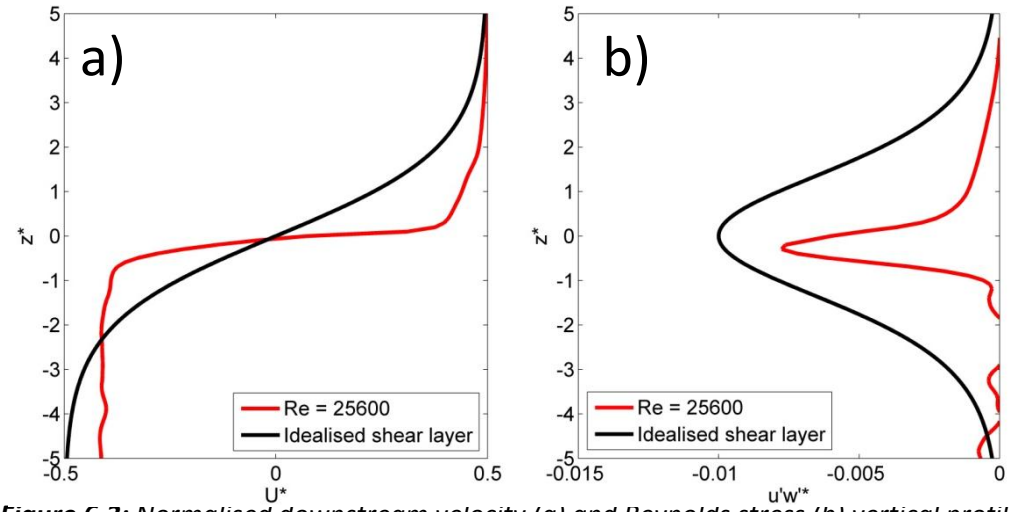

Figure 6.3: *Normalised downstream velocity (a) and Reynolds stress (b) vertical profiles for the rigid vegetation simulation. The black line represents the profile for an idealised shear mixing layer (Ghisalberti and Nepf, 2002).*

The mean vertical velocity and Reynolds stress profiles are shown in Figure 6.3. The signature shape of the mixing layer profile (Ghisalberti and Nepf, 2002) is present although the velocity profile exhibits a much sharper interface between the canopy zone and the flow above, compared to the typical mixing layer profiles discussed in Chapter 2. This suggests there is comparatively little mixing between the two flows. The average long-section of the downstream (u) velocity (Figure 6.4) confirms that there are two well-defined velocity regimes with little evidence of mixing. Due to the recirculating nature of the domain, there is no clear flow separation at the front of the canopy.

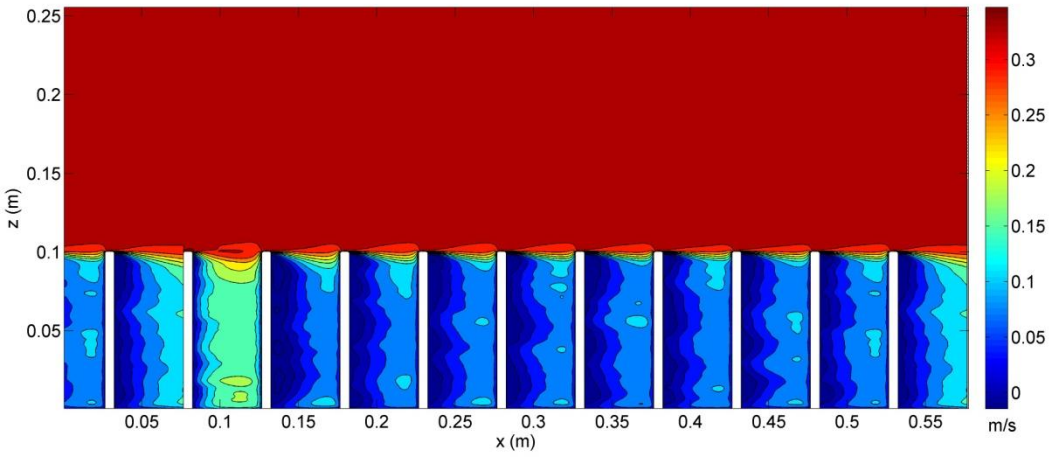

Figure 6.4: *Time-averaged long-section of downstream (u) velocity.*

The Reynolds stress profile (Figure 6.3b) also shows a sharp interface, illustrated by a sharper peak than the ideal mixing layer profile. This could be due to the vegetation spacing. The separation between stems in the downstream direction appears to be at a length scale similar to the wake length off the top of the stems. Therefore, it may be that skimming flow develops in the region just above the stems, thus, inhibiting penetration of faster flow into the canopy (Neumeier and Amos, 2006; Folkard, 2011).

The maximum Reynolds stress is also lower than expected for the peak of the shear layer, which may again relate to the correlation between vegetation spacing and wake length of the top of the stems. However, this could also be due to the relatively low vegetation density as it is well documented that density, via drag helps determine the velocity profile (see Section 2.3.2). Figure 6.5 shows regions of relatively high Reynolds stress, concentrated along the top of the canopy. These appear to correspond to individual stalks rather than a larger shear layer and therefore this is perhaps why the values are lower than expected with a sharper peak.

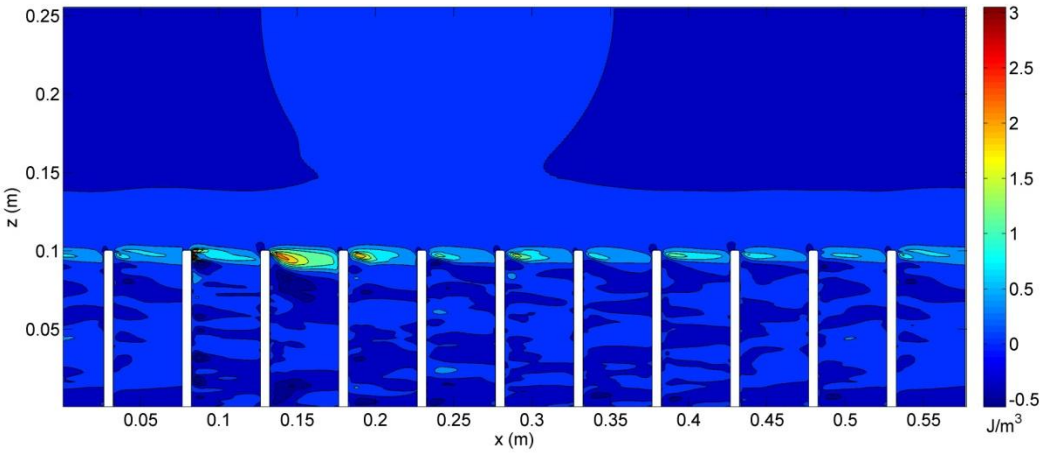

Figure 6.5: *Time-averaged long-section of Reynolds stress*

The distribution of turbulent kinetic energy in Figure 6.6 shows a similar pattern to the Reynolds stress, with energy concentrated at the canopy top and in the lee of individual stems. Similar to the Reynolds stress, there is little evidence of larger scale turbulent energy at the canopy top which might be associated with canopy scale turbulence. Both the TKE and Reynolds stress plots agree well with those of

Stoesser who used a similar numerical setup for modelling rigid vegetation canopies (Stoesser *et al.*, 2006; Stoesser *et al.*, 2009).

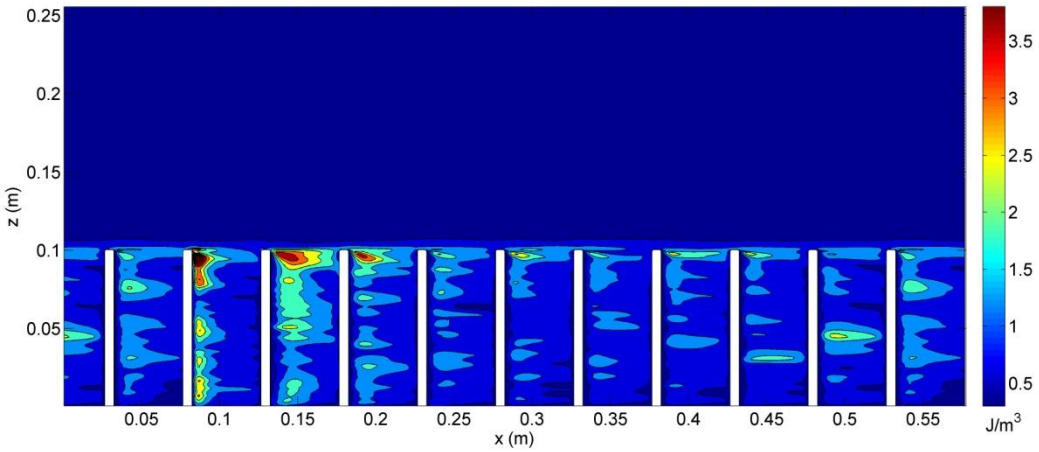

Figure 6.6: *Time-averaged long-section of turbulent kinetic energy*

The turbulence production plot in Figure 6.7 appears to be dominated by frequent, small in extent but large magnitude production regions. The graphs therefore fail to indicate spatial regions of significant turbulence of a more moderate magnitude. This was the same for a number of different analyses and therefore this measure is not used in any of the subsequent analyses.

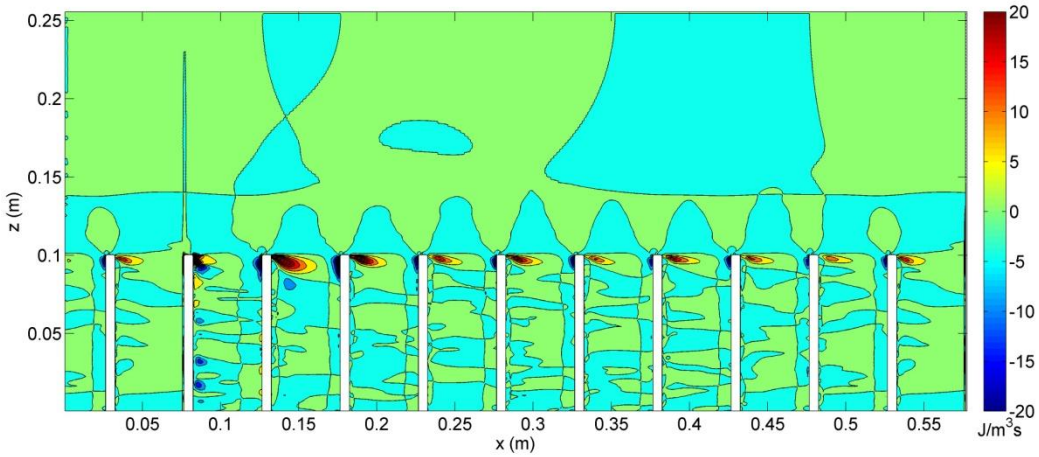

Figure 6.7: *Time-averaged long-section of turbulence production.*

Overall, the mean flow quantities suggest the presence of a weak canopy mixing layer, with a dominance of wake-scale turbulent events. However, in order to fully understand the turbulent dynamics, analysis of the fluctuating, time-dependent quantities is required.

6.2.3 Quadrant analysis

Figure 6.8a shows the vertical profile of the relative dominance of the different turbulent quadrant events over the length of the simulation, assuming a threshold of *H=0* (i.e. all flow events are considered). The profile has been taken at y/w=0.5 and averaged along the downstream direction as well as temporally. There is a clear dominance of both quadrant 2 and 4 events at the canopy top height (denoted by the dotted line). Here, sweeps (Q_4) dominate the flow, accounting for half of the flow events. The combined contribution of quadrant 1 and 3 events is less than 15%. Away from the canopy top, the distribution between the quadrants is more even. Quadrant 3 events are most prominent within the canopy, and there is an overall dominance of negative u' events (Q_2 & Q_3) within the canopy. Thus, the canopy exhibits a minority of stronger positive velocity pulses, amongst a majority of weaker negative events.

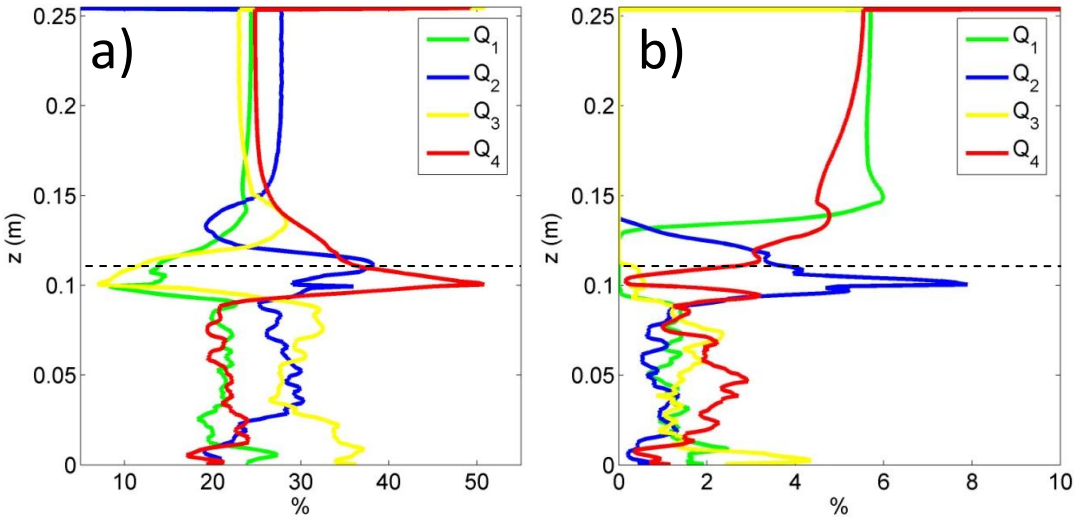

Figure 6.8: *Vertical profiles of quadrant occurrence as a percentage of the total time series, with a hole size of (a) H=0 and (b) H=2. The dotted line shows the canopy top.*

In order to extract the most energetic structures, the same analysis has been carried out using a hole size of *H=2*. The profile in Figure 6.8b shows the results from this analysis. These results show a similar dominance of Q_2 events at the canopy top as was demonstrated in Figure 6.8a. However, there are also far fewer Q_4 events. In fact, the percentage of time spent in sweep mode decreases to nearly zero at the canopy height. Instead, Q_4 events dominate a section just above the canopy top. Figure 6.9 shows the dominant quadrant regime throughout he

simulation for a long-section of the domain, using the *H=2* threshold. There are two clear layers in which Q_2 and Q_4 events dominate, at the canopy top. Into the canopy, there is little discernable pattern, with all quadrants present. Interestingly, above the canopy, there are also large sections where Q_1 events dominate.

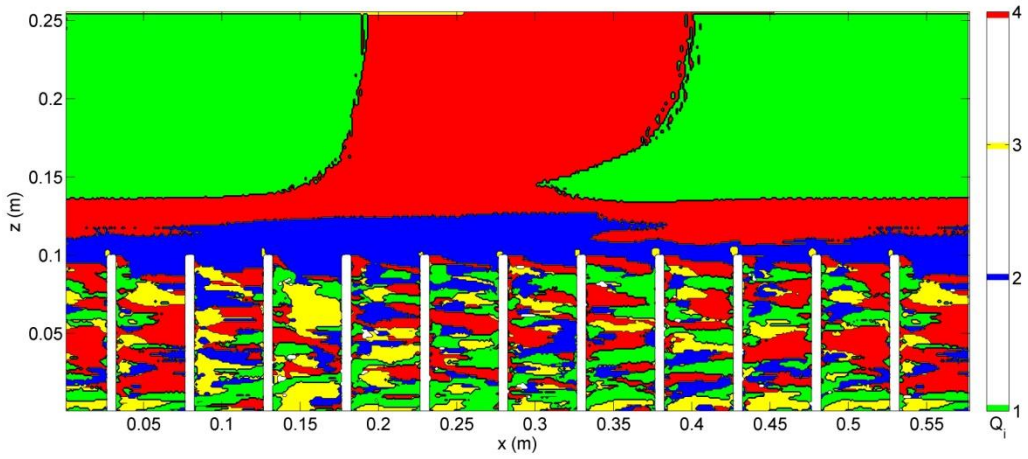

Figure 6.9: *Quadrant dominance across the domain using a hole size of H=2.*

Figure 6.10 highlights the clear spatial pattern of quadrant occurrence. In particular, it is evident that a large proportion of the quadrant 4 events relate to turbulent structures, formed in the lee of individual stems. In this region, Q_4 events account for up to 50% of the flow. These are generally small in magnitude and therefore, this explains why Q_4 occurrence drops significantly when the hole size increases. This stem-scale spatial structure is clearly visible in all four plots of Figure 6.10. However, it is also clear that there are larger scale forcings present. In particular, there is a clear layer at the top of the canopy where Q_2 dominates and this signal appears to be present in addition to the wake-induced structure. From Figure 6.9, the layering of the dominant quadrant regimes at the canopy top appears broadly similar throughout the long-section, suggesting that there may also be mixing layer turbulence present. This is investigated further in Sections 6.2.4 and 6.2.5.

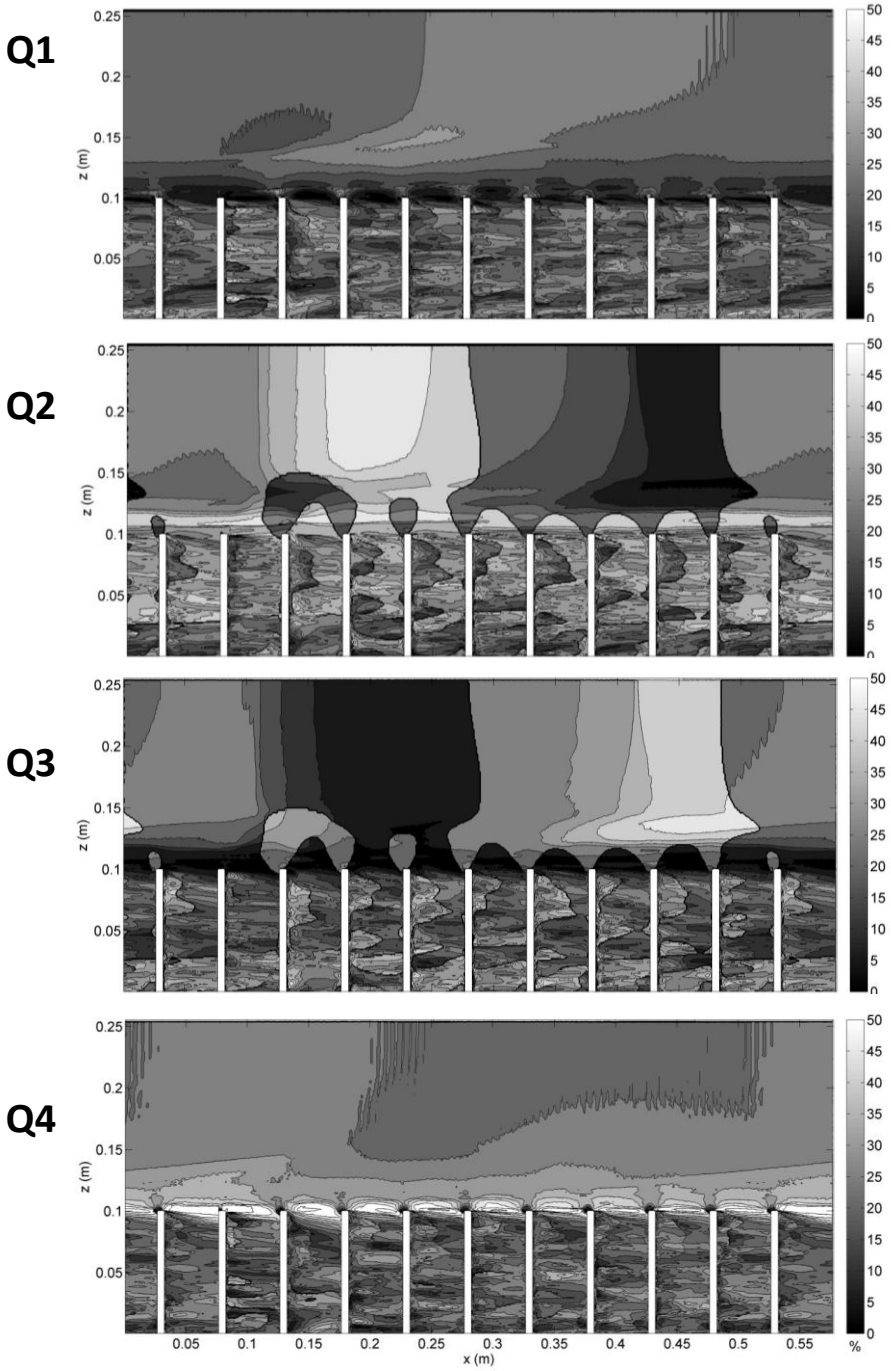

Figure 6.10: *Quadrant occurrence as a percentage of total time series, using hole size H=0.*

6.2.4 Vortex detection

Figure 6.11 shows the vorticity plot for the two dimensional long-section. A single time step snapshot has been selected, which it is suggested is representative of the dataset in terms of turbulence structure. There is a considerable amount of vorticity evident in the flow, particularly within the canopy. Here, clockwise (blue) and anti-

clockwise (red) stem-scale vortices are both prevalent within the canopy, which agrees well with the wide variety and pattern of quadrant events found to be present. In addition to the stem-generated vorticity, the oval in Figure 6.11 highlights a canopy-scale structure which moves along the canopy through time. There is very little evidence of vortices in the flow further above the canopy. This is probably due to the flow not being fully developed within the time-series.

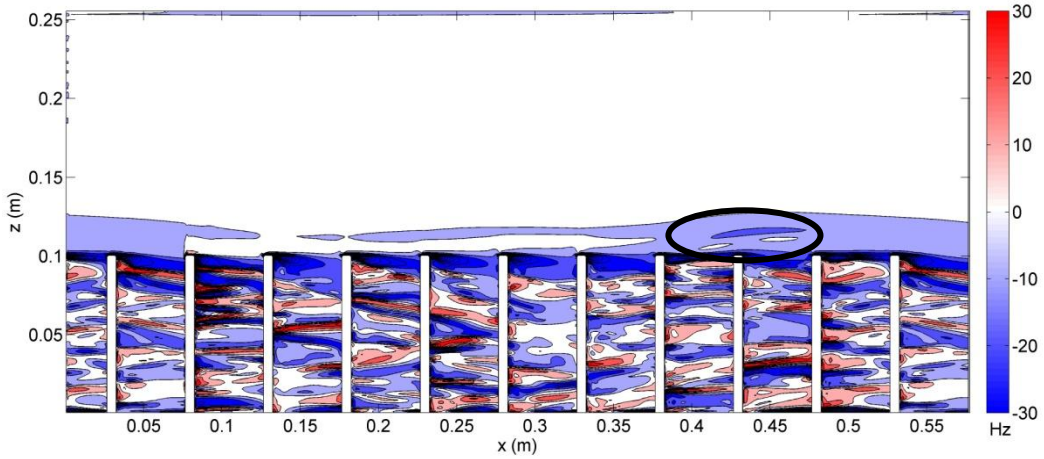

Figure 6.11: *Vorticity plot showing a downstream snapshot of clockwise (blue) and anticlockwise (red) spanwise vorticity. The oval highlights the shear-scale vortex.*

The three Eulerian vortex detection methods described in Chapter 4 are applied in Figure 6.12 and show a very similar pattern to the vorticity plot. There are minor differences between them, but overall they indicate a complex vortex structure within the canopy. The Q criterion is the only one to pick out strongly the canopy scale turbulence. For the Q and λ_2 criterion, the vortex threshold was taken as the standard value of 0. For the Δ criterion, a similar threshold resulted in the entire flow field being highlighted as a vortex. Thus, for the Δ criterion, a more restrictive positive threshold was chosen, such that the results show only the strongest vortices within the flow, without being too restrictive. The consequence of this alteration is that while the Δ criterion results are useful in their own right, they are not comparable to the other two Eulerian methods. Notably, the conditions highlighted in Figure 4.4 do not hold.

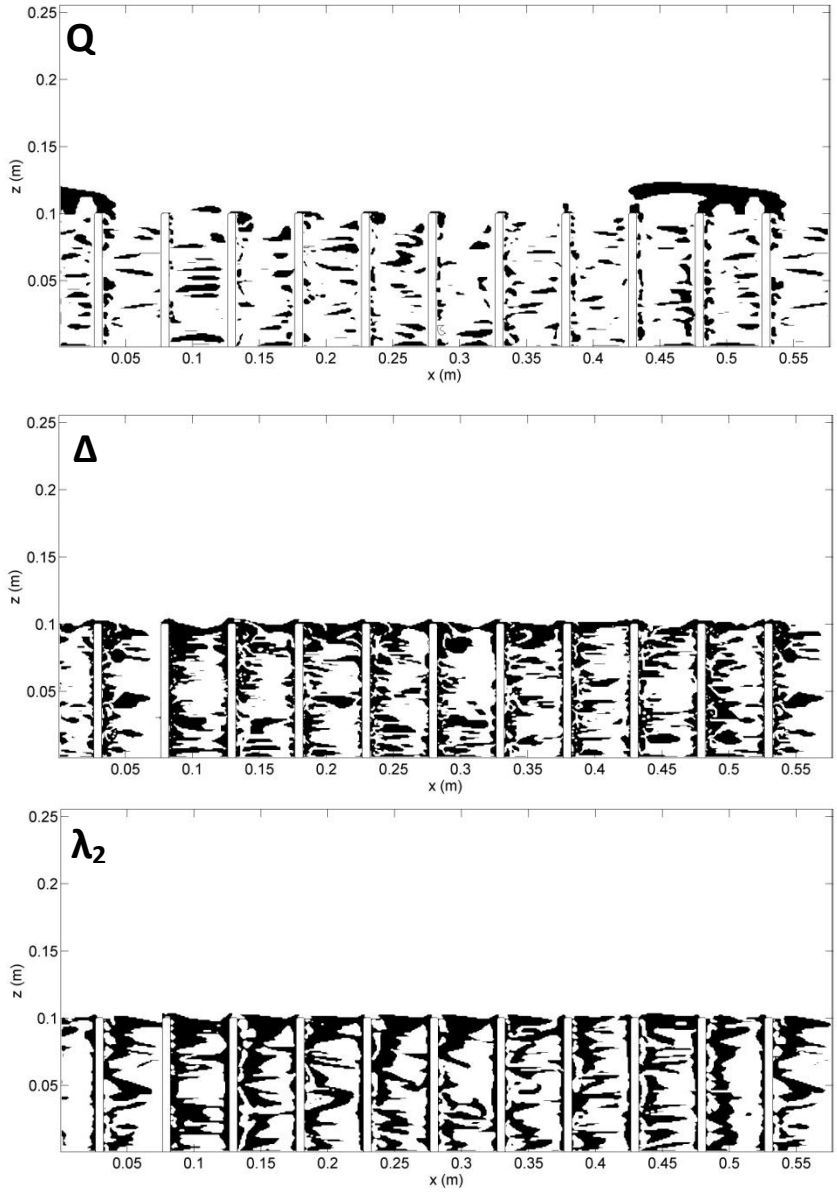

Figure 6.12: *Eulerian vortex methods, showing regions of vorticity in black.*

The FTLE plot in Figure 6.13 shows a similar pattern to all the other vortex detection methods, with evidence of vorticity behind the stems within the canopy as well as along the top of the canopy. Although the canopy top turbulence is picked up by the Q criterion as well as the vorticity plot and the FTLE, it is noticeable that the different methods appear to highlight different elements of the vortex. The vorticity picks up the core of the vortex, where vorticity is highest. The Q criterion highlights a section of the vortex which stretches further downstream and also appears connected to the stem tops. The FTLE ridges seem to highlight the edges of the vortex, particularly the back (upstream) end of the vortex.

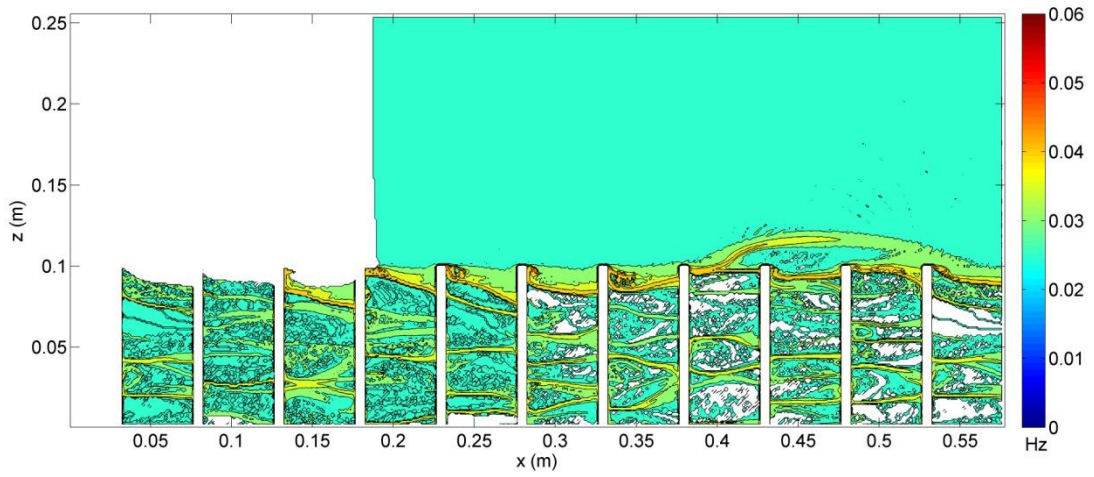

Figure 6.13: *FTLE plot showing areas of flow attraction. Areas in white represent regions where the trajectories could not be tracked sufficiently to give a reliable estimate.*

This pattern is similar to the expected results for the different methods outlined in Figure 4.10, though it is clear that the vortex, starting at approximately x=0.4, is not fully developed and most probably represents a roller vortex rather than a hairpin vortex. The vortex also appears to be significantly stretched in the downstream direction, potentially due to the sharp shear interface.

In order to attempt to investigate the evolution of the vortex through time, in Figure 6.14, the output of the ridge detection algorithm applied to the FLTE calculations, has been averaged over the vertical region of interest at the canopy top. Thus, the figure highlights the streamwise region of the domain length occupied by the canopy scale vortex, and how this changes through time. It shows that the vortex develops, or at least rises above the canopy, after roughly 4.6 seconds. The vortex is then advected downstream, and as it does so, the vortex size grows. Furthermore, this plot elucidates two vortex characteristics. First, it enables calculation of the propagation speed of the vortex. This can be calculated as approximately 0.26m/s. The inflection point velocity of the shear layer, calculated as the arithmetic mean between the canopy and free-stream velocity, is approximately 0.19m/s. Thus, as found by Nepf and Ghisalberti (2008), the vortex propagates downstream faster than the inflection point velocity. However, given the sharp velocity interface, this does not necessarily represent a significant upward shift of the vortex centre.

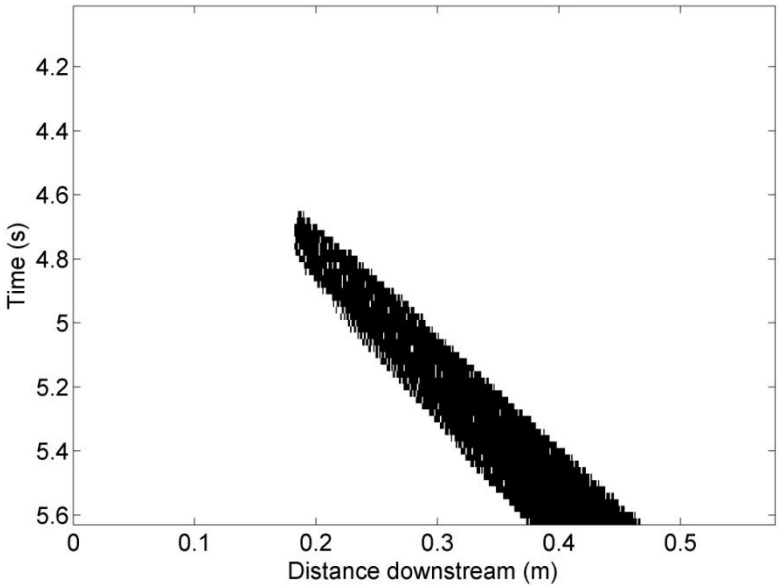

Figure 6.14: *Vortex evolution through time. The x-axis is the downstream coordinate and the y-axis is time. The black region represents the vortex, and the portion of the domain it covers at different time-steps.*

Second, it allows the growth rate of the vortex through time to be calculated. Figure 6.15 shows the vortex width plotted against distance downstream. It displays a distinctly non-linear growth rate. Here, vortex width is plotted against distance downstream rather than time, to permit comparison with the predicted growth rate ($d\delta/dx$) associated with a mixing layer, which is calculated as

$$\frac{d\delta}{dx} = \alpha . \frac{\Delta U}{\overline{U}} \tag{6.1}$$

Here, ΔU and $\overline{U}$ are the arithmetic mean and velocity difference of the mixing layer respectively, as discussed in Section 4.2. The term α is a constant, with values between 0.06-0.12 depending on initial conditions (Pope, 2000). The time variable was transformed into the distance downstream by multiplying through by the propagation speed of the vortex as calculated in this section. Both the horizontal (downstream) and vertical vortex widths have been plotted. If the vortex is symmetrical then these should be equal. However, as was shown by the earlier vortex detection methods, the vortex is significantly stretched in the downstream direction. This indicates that in this simulation, the canopy-top turbulence is anisotropic. Nevertheless, despite the difference in width, the growth rate seems to follow a similar pattern in both directions, suggesting that the shape is maintained.

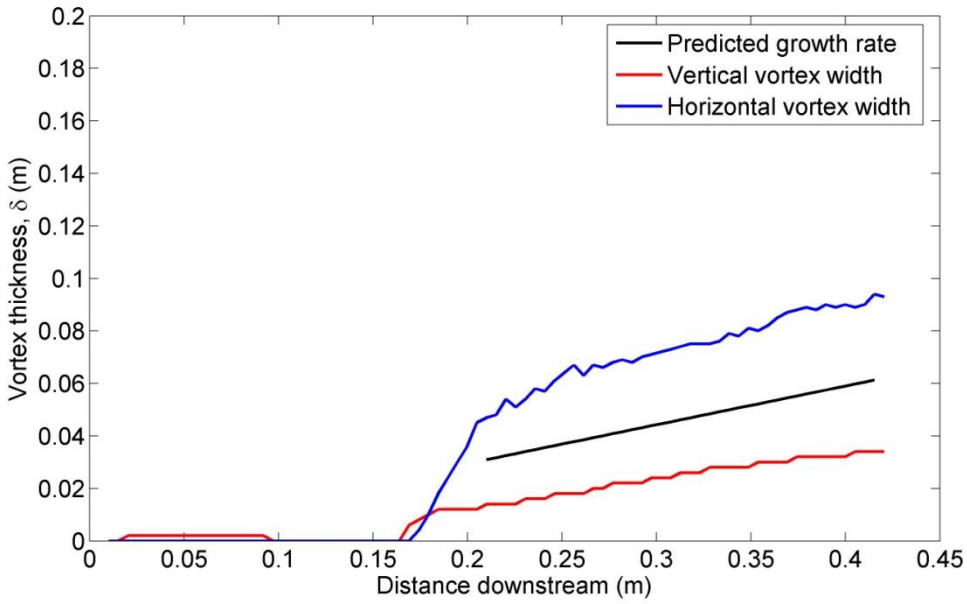

Figure 6.15: *Vortex growth through time, measured using vertical (red) and horizontal (blue) width. The black line shows the predicted vortex growth rate.*

Despite the overall non-linear appearance, after an initial rapid growth period, the rate of vortex growth does appear to follow an approximately linear trend in both the horizontal and vertical direction. The linear growth rate is similar to the predicted rate for the mixing layer, assuming $\alpha = 0.09$ (Sukhodolova and Sukhodolov, 2012).

This suggests that this vortex has been produced by the mixing layer, and furthermore, its growth is controlled by that mixing layer. Within the time-frame, there is no evidence of the depth-limitation of the flow having an effect on the vortex evolution, and this is expected as the vertical size of the vortex is already significantly limited. This severe vortex stretching may be due to the sharp velocity gradient across the canopy. Ikeda and Kanawanza (1996) found in their experiments over plant canopies that the vortices appeared elliptical in the downstream direction, though they also identified inclination of the vortices which is not evident here.

6.2.5 Velocity spectra

In order to determine the time-scales of the vortices a velocity time series was extracted from the data for analysis. Figure 6.16 shows a plot of the velocity spectra, taken from a location just above the canopy-top. It shows a clear spectral peak

between 1-2Hz (labelled A). In comparison, as seen in Table 6.2, the predicted Kelvin-Helmholtz vortex frequency for the mixing layer is 0.62Hz which corresponds to a very weak peak in the spectra (labelled B). However, the stem vortex shedding frequency is estimated as 1.43Hz, which corresponds well with the observed maximum peak in the velocity spectra. This confirms the idea that, as is suggested in the vorticity plots (Figures 6.11-13), the dominant scale of turbulence at this stage of the simulation is wake-scale, though there is some evidence of canopy-scale turbulence.

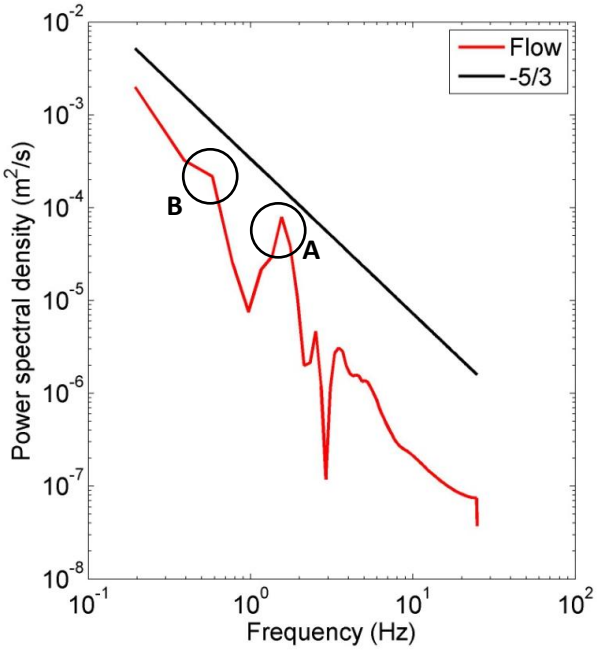

Figure 6.16: *Velocity power spectra from a single point above the canopy. The Kolmogorov decay rate is also shown in black for reference.*

Mechanism	Frequency
f_{KH}	0.62Hz
f_W	1.43Hz

Table 6.2: *Key frequencies active within the flow: f_W is the wake shedding frequency and f_{KH} is the Kelvin-Helmholtz vortex frequency as discussed in Chapter 4.*

The spectrum also exhibits a clear -5/3 slope, as is predicted for turbulence (Kolmogorov, 1941). Due to the computational error, the time-series is shorter than preferable, and this is clear from the smoothness of the profile. This also limits the scales of motion that can be identified and decreases the coherence of frequencies that are identified as the results are more sensitive to anomalies in the data.

The wavelet spectrum in Figure 6.17 shows the gradual development and strengthening of a periodicity at ≈1.5s timescale (as indicated by the dotted line). This agrees very well with the predicted K-H vortex frequency of 0.62Hz ($f = 1/scale$). This would suggest that the system is developing into a canopy-scale dominated turbulence regime, which is not fully developed within the time-frame. The stem-scale turbulence does not show up significantly within the wavelet spectrum and this suggests that when the canopy-scale turbulence had developed, it would dominate the turbulent energy spectrum.

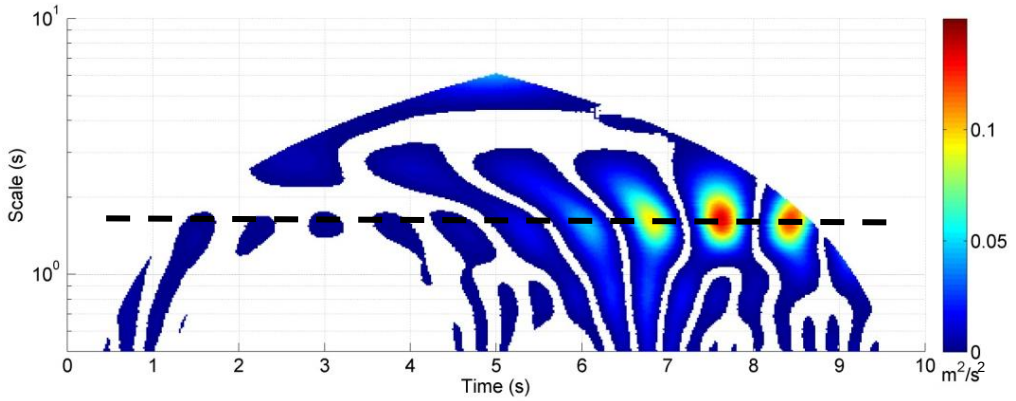

Figure 6.17: *Wavelet spectra of the same time series as the power spectra. Here the colour scale indicates magnitude (power). The dotted line indicates the shear layer scale.*

6.2.6 Summary

The results presented here from the simulation using rigid vegetation show evidence of all 3 of the criteria set out in Table 4.1. Namely, there is clear evidence of a developing canopy mixing layer, shown through the mean profiling and spectral analysis. Furthermore, the vortex growth rate has been shown to be linked directly to the mixing layer. In addition, there is a clear dominance of sweep and ejection events at the canopy top, linked to the passage of canopy-scale vortices, though there are also a number of quadrant events present that are linked to wake-scale processes. Similarly, the vortex methods highlight a large number of wake-scale vortices, but the FTLE and Q criterion also detect developing canopy-scale vortices.

Thus this simulation highlights the transition of a canopy system from the dominance of wake-scale eddies to a canopy-layer system, dominated by larger scale, higher energy roller vortices. Central to this transition is the extraction of

energy via canopy drag and wake scale turbulence which then creates and sustains the mixing layer.

6.3 Plant and flow dynamics above a small patch

This simulation was designed to allow investigation of both the flow and plant dynamics over a small patch (20 stems) of flexible grass or reed-like vegetation within a submergent environment. This case could, for example, represent flow over floodplain grasses/crops or bank-full flow over riparian reed patches (e.g. *Phragmites australis*). In this example, the Euler-Bernoulli beam model was applied.

6.3.1 Experimental setup

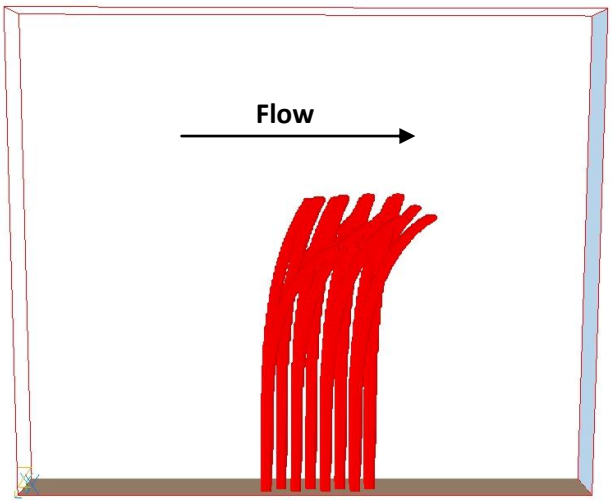

Figure 6.18: *Side view of the domain with the stalks in red, captured during the simulation. Flow is from left to right.*

For this case, the domain was 0.768m long, 0.068m wide and 0.64m high. The plant height was 0.4m, which is equivalent to 0.63 of the flow depth (h/z). The vegetation stalks had a radius of 0.005m, and were arranged in a dense staggered formation as shown in Figure 6.18 to ensure a sufficient drag discontinuity. The vegetation spacing was chosen such that the vegetation canopy frontal width was equal to the whole width of the patch, and therefore the flow could not simply streamline between vegetations stalks. The recirculation region occupied 0.128m at the front of the domain as shown in Figure 6.19. The domain was 384 cells long, 34 cells wide and 320 cells high (nx=384, ny=34, nz=320). The grid resolution was therefore 0.002m in each direction, which was determined as the coarsest resolution which

was still capable of reproducing the wake-scale turbulent characteristics. As this simulation was designed to reproduce high velocity flows, the inlet velocity was set at 0.7m/s, and consequently the Reynolds number of the flow was approximately 22,600. The Froude number was 0.28 and therefore the flow was subcritical. The flexural rigidity of the vegetation was 0.02Nm^2, as discussed in Section 5.2.2. The simulation was run for 30 seconds at a temporal resolution of 50Hz and took 400hrs CPU time to complete. All analysis was undertaken in the x-z plane at $y/w = 0.5$.

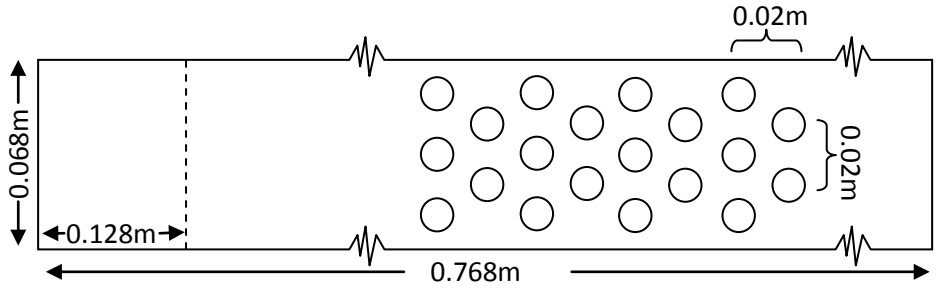

Figure 6.19: *Schematic of the numerical domain for the patch model. The dotted line indicated the recirculation region. This diagram is not to scale.*

6.3.2 Mean flow profiles and turbulence characteristics

Figure 6.20 shows the vertical profile for both the downstream velocity and Reynolds stress, calculated from the x-z long section and averaged both in time and in the downstream direction. The velocity profile, calculated as explained in Section 4.2 shows generally good agreement with the idealised shear layer, but similar to the rigid case above, the shear layer appears to be thinner and sharper. This is particularly noticeable in the bottom of the half of the profile, as the flow profile interacts with the canopy. Here it would appear that there is little penetration of the faster velocities into the canopy. However, the velocity does increase slightly in the canopy, suggesting the additional stem density at the top due to bending causes lower velocities than around the more rigid section of the stems.

There is also a peak in the velocity profile at the bed. This phenomenon was observed by Stoesser *et al.* (2006) and is thought to originate from the necklace/horseshoe vortex that forms around each stem, along the bed. It is clear that the entire velocity profile does not fit a shear layer profile. In fact it would be expected that the shear layer profile is limited to the region in which canopy shear

is dominant. However, the whole profile, selected as the region between which the flow obtains its minimum and maximum values, was used in the normalisation rather than individually selecting the profile, to prevent bias in choice of boundaries.

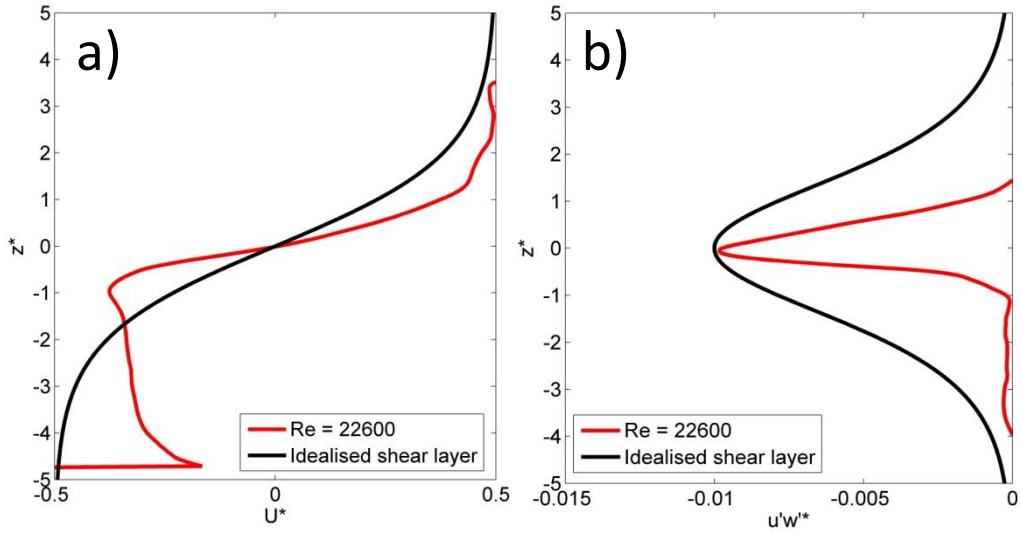

Figure 6.20: *Normalised vertical profiles of horizontally and temporally averaged downstream velocity(a) and Reynolds stress (b). The idealised shear layer profiles are shown in black.*

The Reynolds stress values at the canopy top match up well with the expected values, though the sharper interface is again reflected through a steep decline in Reynolds stress away from the canopy top. This implies a lower total stress than expected. This may be due to the relatively small size of the patch.

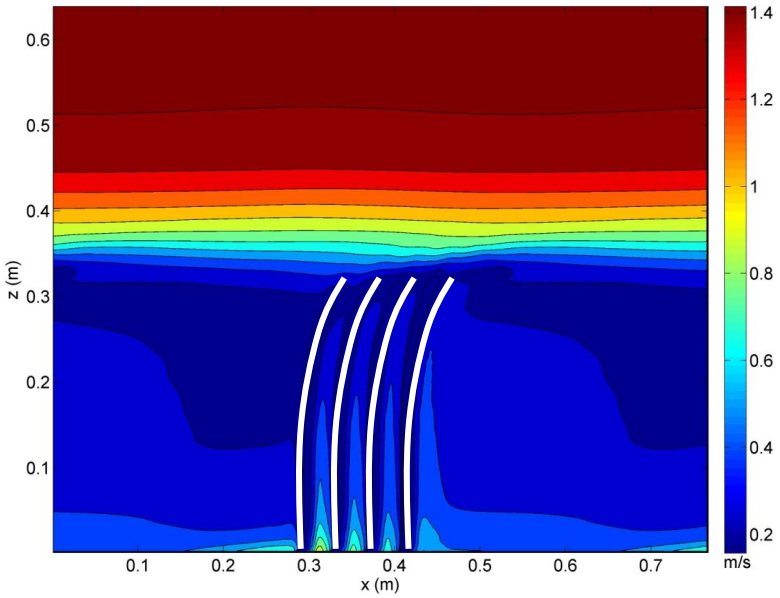

Figure 6.21: *Long-section of time-averaged downstream velocity. An approximate vegetation mask is included.*

The long-section time-averaged plot in Figure 6.21 shows little variation in mean flow structure downstream. Despite the small canopy size and the vegetation movement, there is still a very well defined separation into a slow canopy layer with faster flow above. The recirculation ensures that the wake effects behave as though the vegetation is in the middle of a patch, rather than at the front end.

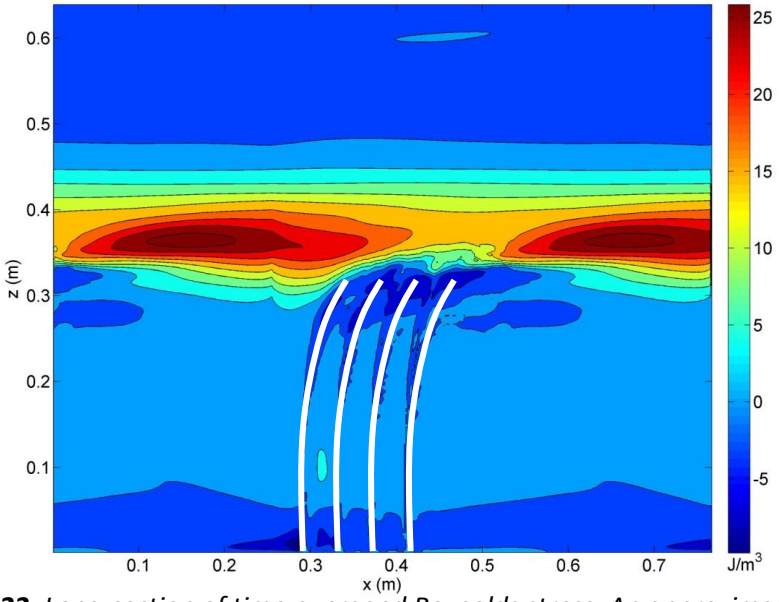

Figure 6.22: *Long-section of time-averaged Reynolds stress. An approximate vegetation mask is included.*

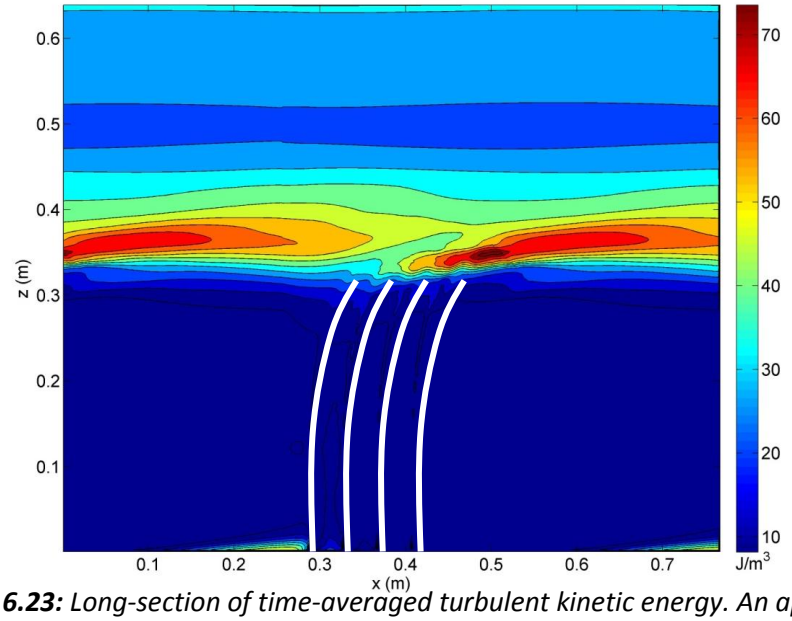

Figure 6.23: *Long-section of time-averaged turbulent kinetic energy. An approximate vegetation mask is included.*

Figures 6.22 and 6.23 show clear peaks in the Reynolds stress and turbulent kinetic energy at the top of the canopy, specifically just behind the main cluster of stems. There is some evidence of stem-scale turbulent energy and stress, however this is

clearly an order of magnitude smaller than the canopy top. It is noticeable that neither the stress nor the energy penetrate significantly into the canopy. This suggests that the bending of the stems limits transfer into the canopy

6.3.3 Quadrant analysis

The vertical profile of quadrant occurrence in Figure 6.24 shows a clear spatial pattern. As in the rigid case, Q_2 and Q_4 events (sweeps and ejections) dominate the region at the canopy top. With a hole size of *H=0*, ejections (Q_2) dominate, and the peak in their occurrence is just below the peak in sweeps (Q_4). When only the larger events are considered by applying a hole size of *H=2*, this pattern switches. Q_4 sweep events become most prevalent, and their peak occurs below the peak in Q_2 ejection events.

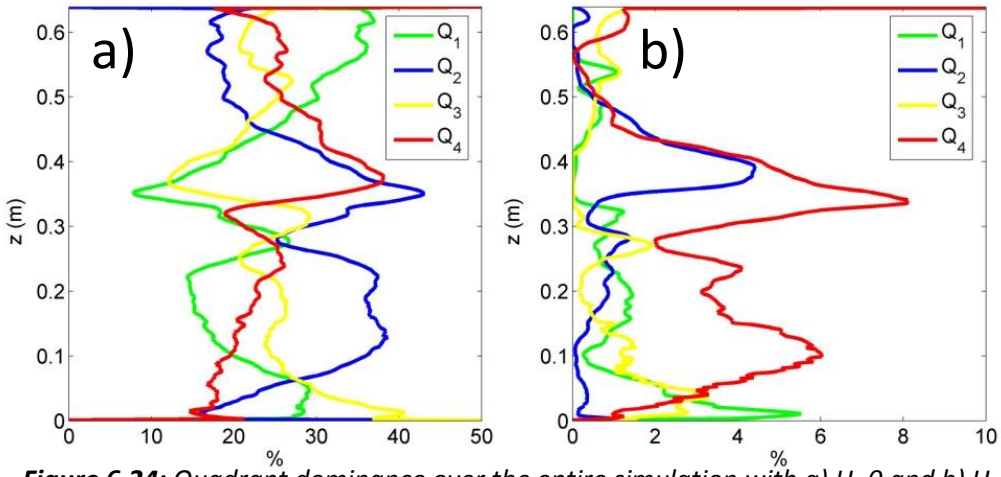

Figure 6.24: *Quadrant dominance over the entire simulation with a) H=0 and b) H=2.*

As discussed in the rigid case analysis, one potential explanation of this switch is the presence of two separate turbulent processes operating at different scales. The larger scale pattern revealed using the larger hole size is consistent with Finnigan *et al.'s* (2009) model for terrestrial canopies, whereby sweeps occur below ejections due to the position of the hairpin vortices. Ghisalberti and Nepf (2006) and Okamoto and Nezu (2009) also found the same pattern for vertical quadrant profiles over flexible vegetation canopies. It is also consistent with the findings of Nezu and Sanjou (2008), that sweeps dominate the mixing layer. The pattern of turbulent structure found using *H=0* could relate to smaller-scale wake-shedding turbulent processes off the top of the vegetation, though there is no direct evidence for this.

The other significant impact thresholding has is to diminish the relative contribution of quadrant 1 and 3 events. This suggests that they are not an integral part of the large-scale turbulent structure. The only region where there seem to be significant numbers of Quadrant 1 and 3 events is in the bed region.

Figure 6.25 shows the spatial pattern of quadrant dominance across the long-section of the domain for a hole size of *H=2*. This emphasises the dominance of Q_4 events, but also highlights the distinct spatial regions of quadrant dominance. The pattern is relatively homogenous along the domain, with the exception of two areas where quadrants 1 and 3 dominate, just behind the tops of the stems, which is caused by the presence of the stems.

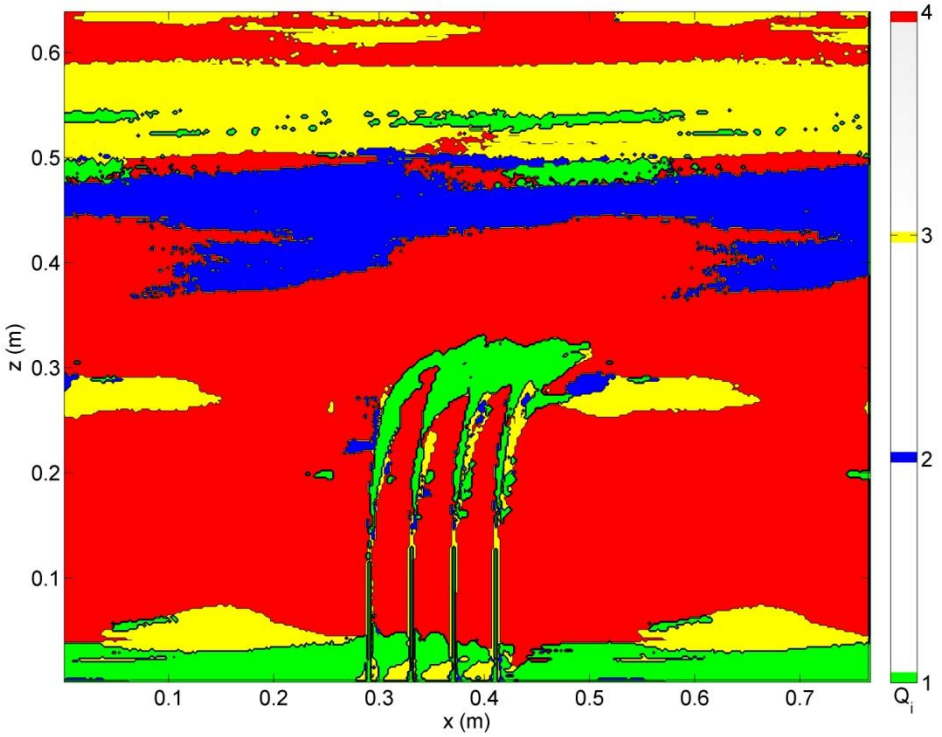

Figure 6.25: *Dominant quadrants across the domain using H=2.*

Figure 6.26 unpacks the spatial picture further by showing the individual occurrence across the long-section. This highlights the relative dominance of sweep events over any of the other three quadrants. Ejections also have a significant occurrence along the canopy top, but high-energy (*H=2*) sweeps alone account for up to 10% of the time series. The region of Q_1 and Q_3 events at the bed is still present. However, its significance is shown to be far less considerable than the canopy top turbulence.

Interestingly, there is a clear region of Q_4 dominance towards the bottom of the stalks which is unexplained.

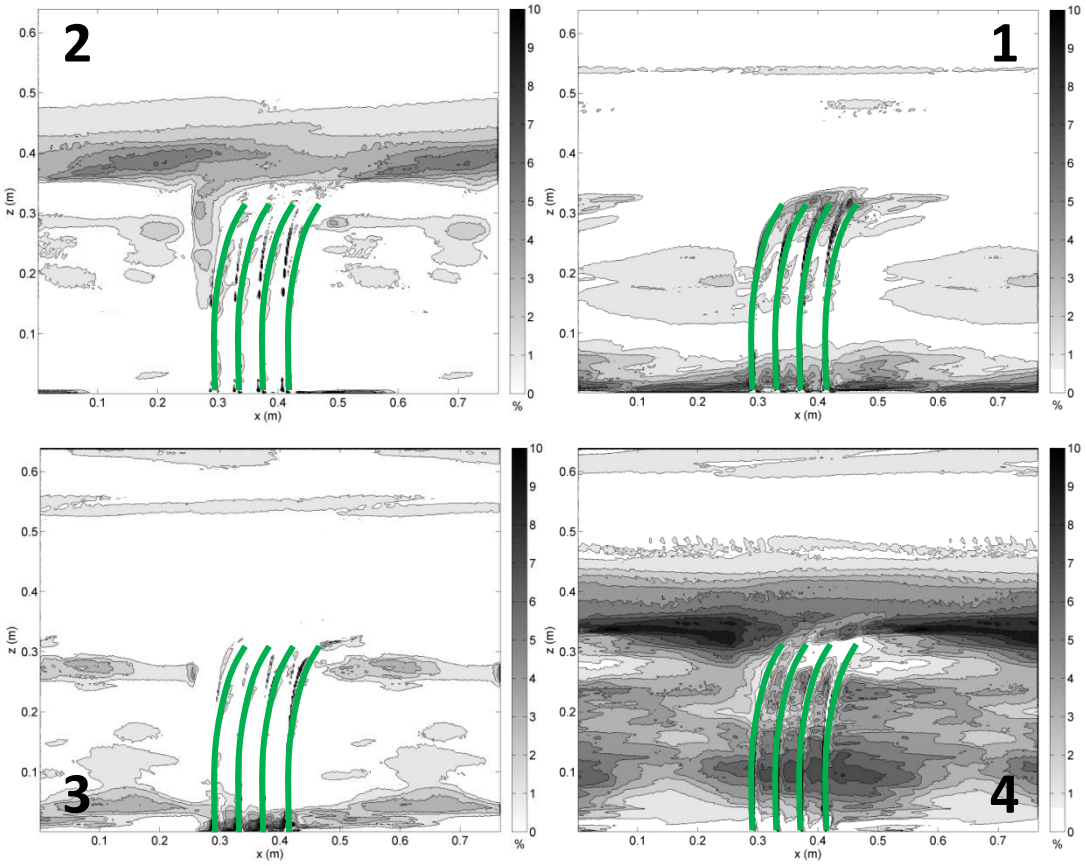

Figure 6.26: *Occurrence of different quadrant events as a percentage of the total simulation time, using a threshold hole size of H=2. Approximate canopy positions are shown in green.*

6.3.4 Vortex detection

The simulation was fully turbulent for the duration of the experiment and therefore there were a vast number of vortices which could have been analysed here. Some previous studies that have conducted similar vortex analysis over terrestrial canopies have used ensemble averaging to analyse the vortex characteristics over the entire simulation (e.g. Finnigan *et al.*, 2009). However, this was unfeasible due to computational power constraints. Instead, vortex detection and analysis was done based on an initial visual search for patterns within the FTLE and vorticity fields. From this, key examples of the vortex structure were drawn out for analysis.

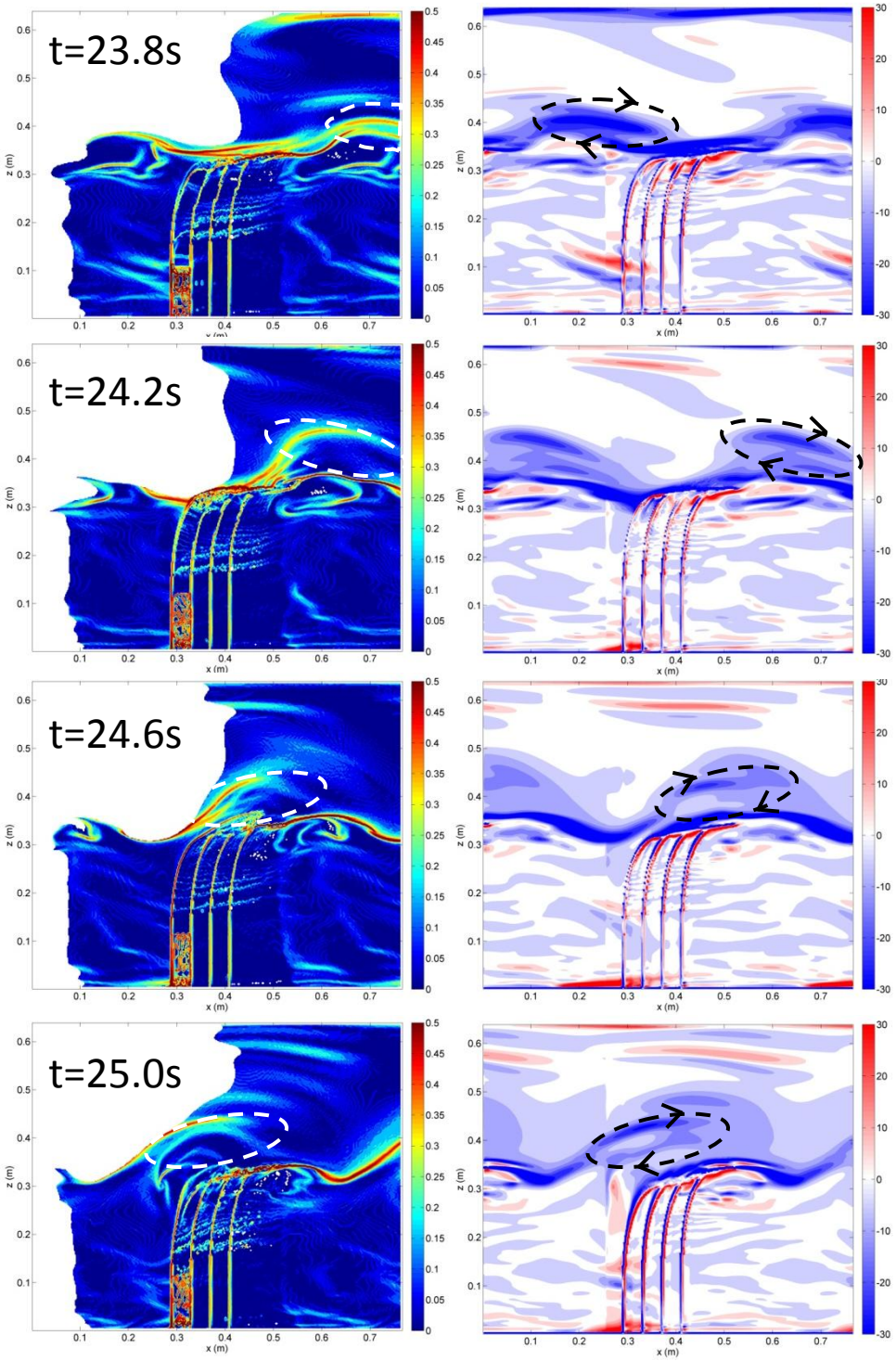

Figure 6.27: *FTLE (left) and vorticity (right) long-sections at a series of time-steps. The positions of identified vortices are shown using the dotted ovals. The white regions in the FTLE plot correspond to regions where the trajectories could not be fully tracked. In the vorticity plots, blue corresponds to clockwise vorticity and red to anti-clockwise vorticity.*

Figure 6.27 shows a series of FTLE snapshots which capture the motion of a turbulent eddy above the canopy as it propagates downstream. Here, the time

spacing has been chosen to highlight snapshots of vortex progression over the canopy. Each image shows the vortex as it passes through the domain once more. The vortex is visualised as an inclined FTLE ridge which curls over at the top. This is significantly different from the full hairpin signature shown in Figure 4.10. However, the presence of the strong FTLE ridge indicates the presence of a vortex, and in some of the snapshots, a potential lower limb of the vortex can be identified. Therefore further analysis was conducted on this vortex.

The shape of the vortex can be better seen in the vorticity plots also shown on the right in Figure 6.27. Here there are clearly identifiable regions of high clockwise vorticity present at the canopy top. Similar to the rigid case, the vortex appears to be significantly stretched in the downstream direction, implying anisotropy within the turbulence. Its inclination appears to alter significantly throughout the simulation. Within both the FTLE and vorticity plots there is evidence of smaller scale turbulence, generated by both the stems and bed, however this appears to occur at a much smaller magnitude. The vortex signal within both the FLTE and particularly the vorticity plot seems to weaken significantly through time, suggesting that the vortex does not persist or retain a well-defined form for long.

Figure 6.28 shows the results from the three Eulerian vortex detection methods (Q, λ_2 and Δ), for a series of snapshots from the flow, from 23.8 seconds through to 25.2 seconds into the simulation. As with the rigid case, a non-zero threshold was used for the Δ criterion and so these results are not strictly comparable with the other two, but provide additional stand-alone evidence of vortex passage. These images were extracted at double the temporal resolution of the FTLE and vorticity plots in order to aid vortex tracking. This time-period was ideal as it is towards the end of the simulation time (30s) and therefore the vortices are most likely to resemble those of a fully-developed canopy flow.

The three methods all detect a vortex, circled in Figure 6.28, at the canopy top which moves along the canopy, recirculating through the domain twice within the time period. The vortex is not very clearly defined and is irregular in shape in all three methods, most probably due to interference and potentially coalescence with

other turbulence when recirculating. Because the domain length is short, there is little time for the vortex to develop before it reaches the front of the canopy again, where it most likely is affected by the newly generated turbulence at the canopy front.

Nevertheless the vortex does persist and is still identifiable in the last snapshot, though here it begins to break down as it is split (Labelled A in Figure 6.28). This splitting appears to occur predominantly in the horizontal plane. Due to the irregular shape of the vortex it is difficult to analyse changes to size and position of the vortex relative to the canopy. However, it would appear that the size generally does increase and there may be a slight increase in vortex centre though this effect is minimal.

The positions of the vortex do broadly coincide with the areas enclosed by FTLE ridges as proposed in Figure 4.10. However, the FTLE appears to have a much weaker signal than the vorticity or Eulerian vortex methods. This may be due in part to the restriction on trajectory tracking imposed by the short domain in the FTLE method. There is also clear evidence for the existence of other vortices in the flow, shown by the multiple FTLE ridges and regions of high positive (and negative) vorticity. A number of these vortices appear to persist for a time but are broken up during recirculation.

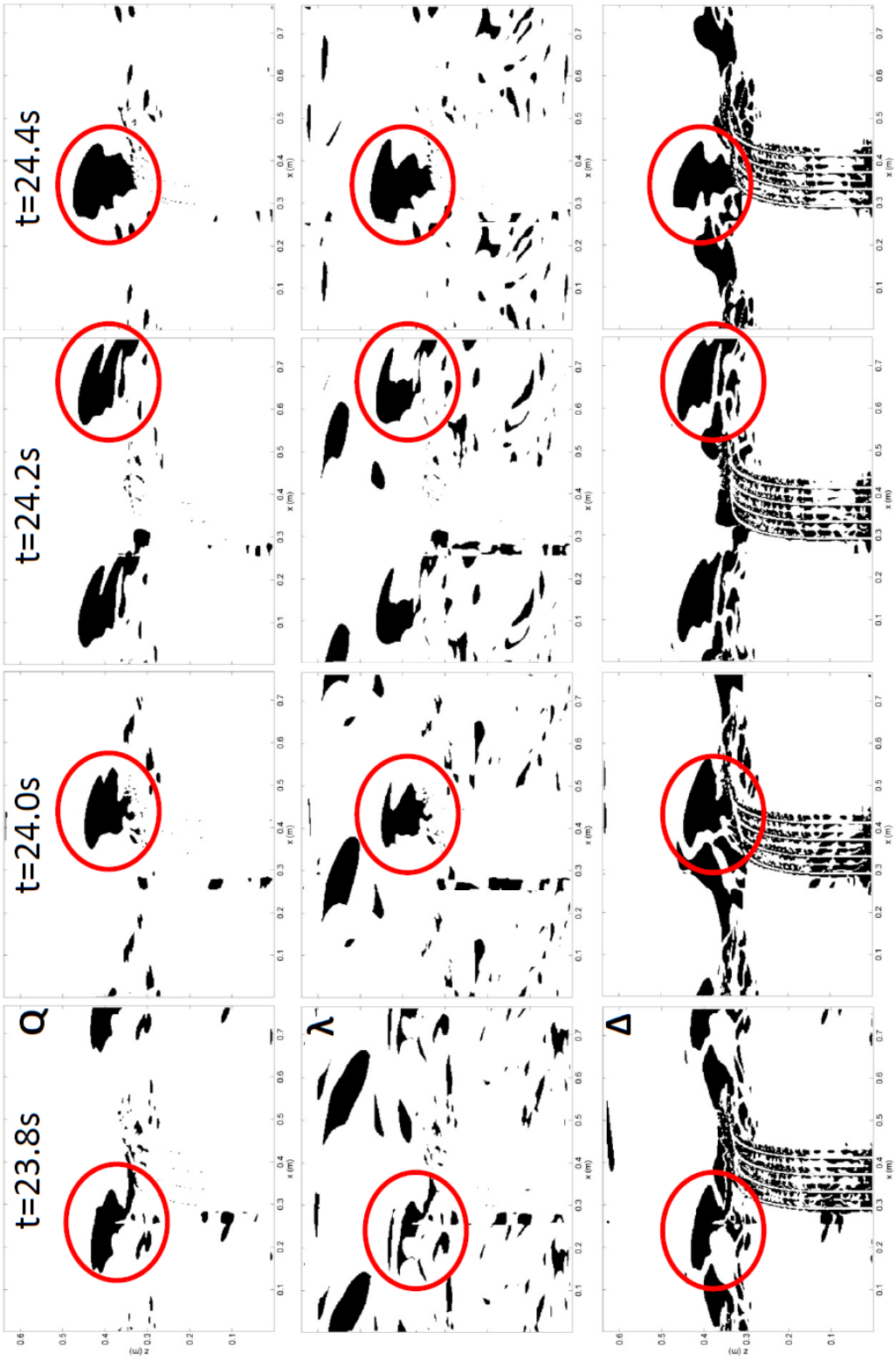

Figure 6.28: *Series of snapshots through time of vortex detection using the three Eulerian vortex methods (Q=top, λ=middle, Δ=bottom)*

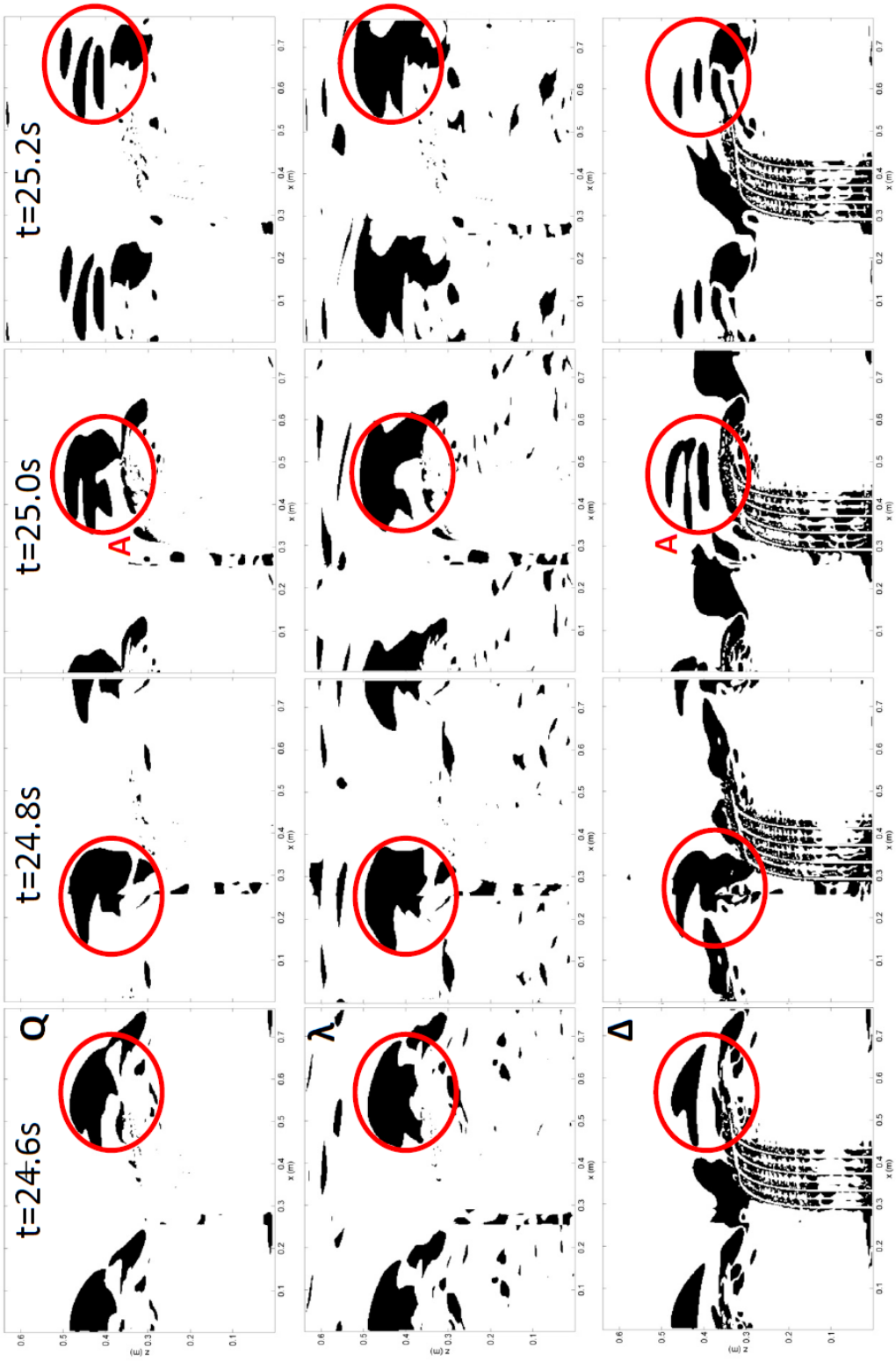

Figure 6.28 continued: *Series of snapshots through time of vortex detection using the three Eulerian vortex methods (Q=top, λ=middle, Δ=bottom)*

6.3.5 Velocity and plant spectra

The power spectra for the downstream velocity as well as the canopy height are shown in Figure 6.29. The plant spectrum was obtained by calculating the height of the canopy through time at a location in the middle of the canopy laterally and in the downstream direction. Therefore, this measure does not refer to the movement of an individual stem, but rather the canopy as a whole. The velocity spectrum was taken from the same downstream and lateral location, at a height just above the canopy.

The vegetation canopy height spectrum appears to decay linearly at a rate of -5/3, which is the rate predicted by Kolmogorov (1941) for turbulent decay. On top of this general trend there are two peaks in the spectrum. First, there is a slight peak at roughly 0.1-0.2Hz, labelled A. The second, more obvious peak appears like a wave-packet at roughly 2Hz, labelled B in Figure 6.29. A similar pattern is found in the flow velocity time series. Here, there is a large peak in the spectra at 2.05Hz, labelled C, and a smaller peak at roughly 0.1Hz, labelled D. There is also a third peak further up the spectrum at 4Hz.

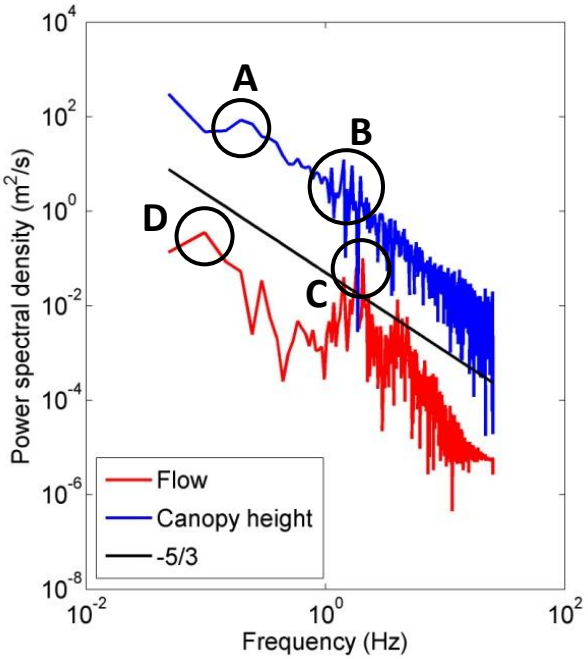

Figure 6.29: *Downstream velocity (red) and plant canopy height (blue) power spectra. The Kolmogorov -5/3 decay rate is also plotted in black for reference.*

Using Equation 4.10, the Kelvin-Helmholtz frequency can be calculated as 0.32Hz. This corresponds with the low frequency spectral peaks, though there is some discrepancy in values. This is most likely due to error in the predicted K-H frequency, caused by poor estimations of the shear layer properties. As mentioned in Section 6.3.2, these properties were calculated automatically using an approximation of the shear layer region, which in some cases was hard to define.

Mechanism	Frequency
f_{KH}	0.323Hz
f_N	2.12Hz
f_W	6Hz

Table 6.3: *Key frequencies active within the flow: f_W is the wake shedding frequency, f_N is the natural frequency of the vegetation and f_{KH} is the Kelvin-Helmholtz vortex frequency as discussed in Chapter 4.*

The higher frequency (≈2Hz) peak in the velocity spectra (B) appears to coincide with the natural frequency of the vegetation, which was calculated as 2.12Hz (see Table 6.3). This peak also appears in the canopy height spectra, reinforcing the idea that the peak is linked to plant characteristics. It is most likely that the third spectral peak in the velocity spectrum is also linked mechanistically to the natural frequency, occurring as it does at double the natural frequency. However, an explanation of that phenomenon is not given here and remains to be fully investigated. This peak does not appear in the canopy height spectra, and so would most likely be a response in the flow to the natural frequency, rather than a response of the canopy itself. The other possible frequency influence is the wake shedding frequency which was calculated as 6Hz. There is another small peak in the velocity spectrum around this frequency but it appears less significant than the others.

Thus, the spectral results highlight two key influences on plant-flow interactions: shear layer turbulence and subsequent decay and the natural frequency of the vegetation. The spectral results appear at first to have paradoxical implications. The canopy spectra seems to indicate that the plant has a largely passive role, moving in response to the turbulent flow and thus exhibiting the slope associated with turbulent flow, as well as a spectral peak corresponding to the canopy shear layer

vortex frequency. This suggests that following the formation of the shear layer, the vegetation is a largely passive reflection of the flow structure.

However, the flow velocity spectrum shows a clear forcing from the vegetation. Here, the spectral slope is significantly altered, and a significant peak appears in the spectrum, which related directly to the vegetation characteristics, through the natural frequency. Hence, the velocity spectrum indicates that the vegetation canopy is actively responding to the flow, modulating the velocity field through its vibrational response (Maitani, 1979; Ghisalberti and Nepf, 2006).

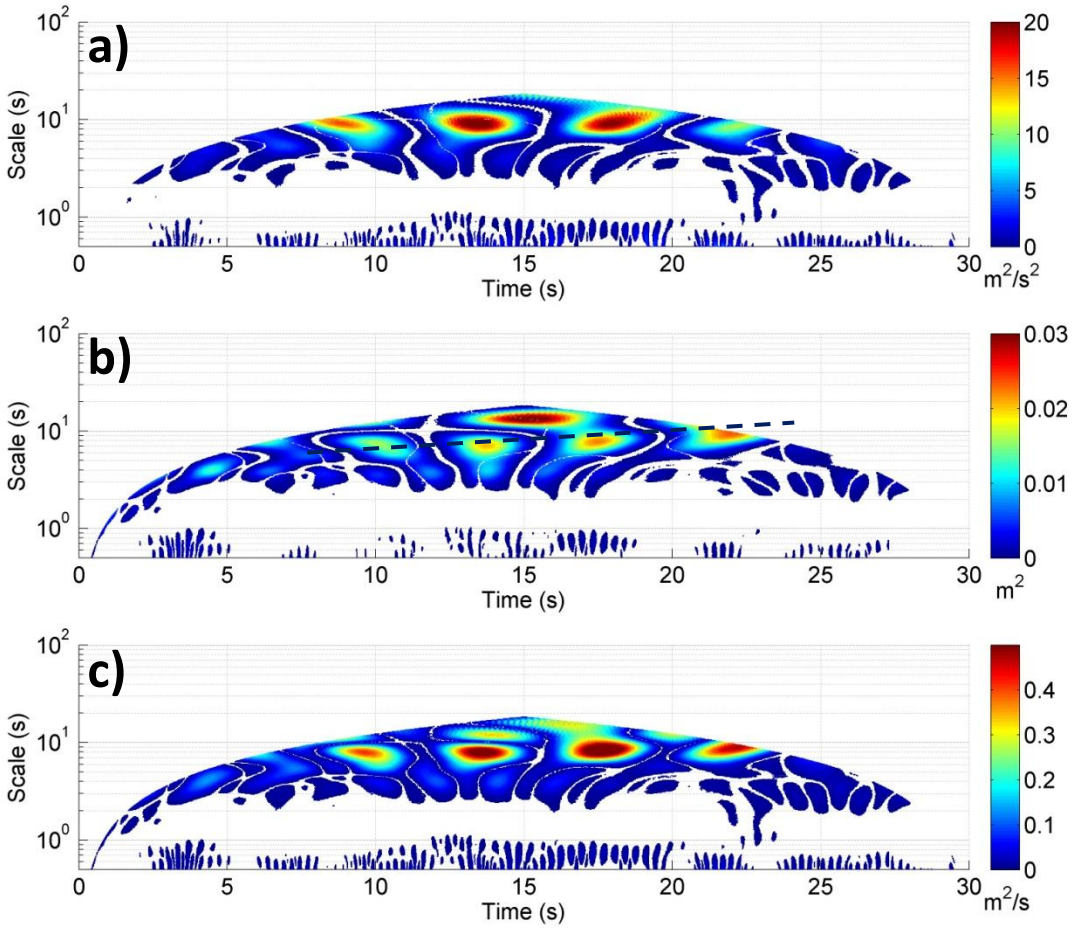

Figure 6.30: *Wavelet power spectra for the velocity (a) and canopy height (b) series and (c) cross spectra between the two time series.*

The wavelet analysis presented in Figure 6.30 shows a similar trend to the spectral analysis. Both the flow (a) and canopy height (b) wavelet spectra show the presence of a high frequency (low time scale) signal as well as a low frequency (high time scale) signal. The high frequency signal appears at a time scale of roughly 0.5-0.8s, whereas the low frequency signal appears at a time scale of roughly 5-10s. Both

these scales correspond well to the inverse frequencies shown in the power spectra (1-2Hz and 0.1-0.2Hz respectively).

However, in the canopy height spectra, the low frequency signal appears to occur at a lower frequency initially. The frequency then appears to change through time, increasing to something more similar to that in the velocity spectrum. This change is highlighted by the dotted line (Fig 6.30 b).

Thus it would appear that the oscillation of the canopy is being modulated by the velocity field, and in particular the canopy shear layer vortices, whilst there is also evidence of plant-generated turbulence linked to the natural frequency at much shorter timescales. The wavelet cross-spectrum (Fig 6.30 c) shows the high level of agreement between the low frequency peaks in the signals from the flow and canopy time series', and this signal too shows an increase in time-scale of the peaks through time. The cross-wavelet spectrum also confirms the coherence between the two signals in the high frequency low time scale region, where there appears to be a regular, periodic motion.

The absence of structure in the wavelet spectrum between 1-3 s implies that the two scales of turbulence, canopy shear layer and plant-generated, do not seem to interact or coalesce, but rather mutually coexist. This can also be seen in the time series' of the velocity and canopy height data shown in Figure 6.31 where there is clear superposition of the high frequency signal onto the lower frequency signal.

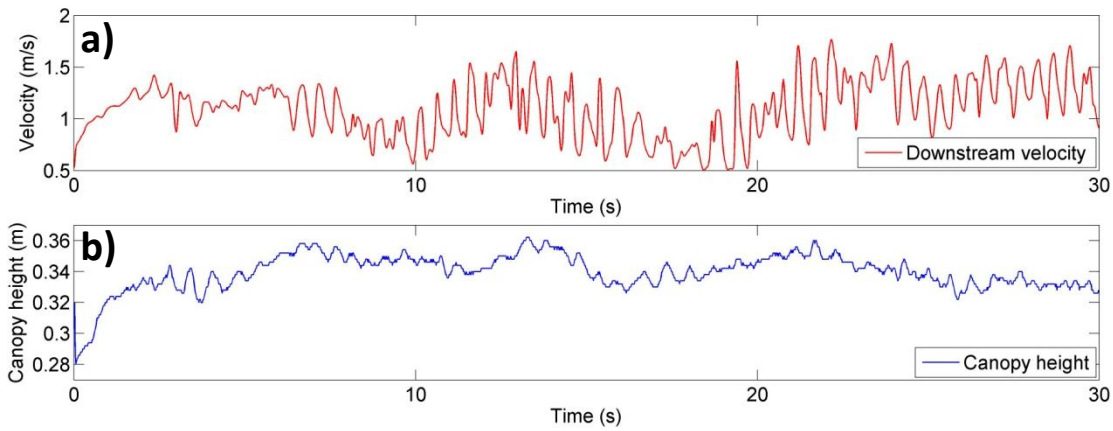

Figure 6.31: *Plot of the (a) velocity and (b) canopy height time series used in the spectral analysis.*

Therefore, in this particular simulation, neither the flow nor the vegetation characteristics act dominantly as a control on the system, due to the large difference in frequency.

6.3.6 Summary

This small-patch semi-rigid case shows the development of a canopy shear layer and the associated generation of roller vortices at the canopy top. Both the velocity and Reynolds stress profiles provide evidence of the formation of the inflected velocity profile, while the various vortex methods all identify canopy-scale vortices. This is supported by the distribution of sweep and ejection events at the canopy top. The spectral analysis reveals the dominance of particular frequencies within the flow that can be linked to the development of the canopy shear layer and the vibrational response of the vegetation.

The issue of frequency 'lock-in' between the vegetation and flow has received a considerable amount of attention in the terrestrial literature in recent years (Py *et al.*, 2006; Dupont *et al.*, 2010; Finnigan, 2010) and has been discussed in Chapter 2. Within the aquatic literature, there has been less investigation of the issue. To the author's knowledge, these results represent the first comprehensive numerical study into the dynamic interaction between flow and vegetation in aquatic flows.

In the case studied, it is clear that the lack of interaction and lock-in between the plant motion and canopy layer turbulence is due to the difference in frequency between the two. The canopy does move in response to the flow, and its initial bending response is modulated by the shear length scale however this is not affected by the natural frequency response of the vegetation. Further study, in conditions whereby the natural frequency of the vegetation matches the K-H vortex frequency more closely, is required to determine the interaction between the two mechanisms.

6.4 Plant and flow dynamics above a canopy

In this simulation, an entire vegetation canopy of 300 stems was used to investigate the processes explained above, over a larger spatial domain. Every stem was independently driven by the Euler-Bernoulli beam equation, designed to replicate semi-rigid vegetation. The larger canopy and domain reduces the effect of recirculation and should therefore provide better insight into vortex structure in particular over an extended canopy.

6.4.1 Experimental setup

The 300 stem patch model was also set up to be more analogous to the flume experiments. Here the domain had a length of 1m, a width of 0.16m and was 0.32m high as shown in Figure 6.32. While it would have been ideal to set the flow depth to 0.4m in line with the flume experiments, this was not possible due to computational memory limitations. The domain was 500 cells long, 80 cells wide and 160 cells high (nx=500, ny=80, nz=160) and therefore the spatial resolution was 0.002m. Each stem had a radius of 0.005m, and was 0.15m tall, 0.47 of the flow depth. The inlet flow velocity was set at 0.3m/s, representing a slightly faster flow than the flume experiments and consequently the Reynolds number of the flow was 19200. The Froude number of the flow was 0.17 and therefore the flow was subcritical. The flexural rigidity of the vegetation was set at 0.0003Nm^2 as explained in Section 5.2.2. The simulation was run for 30 seconds, at a temporal resolution of 50Hz and took 790hrs CPU. All analysis was undertaken in the x-z plane at $y/w = 0.5$.

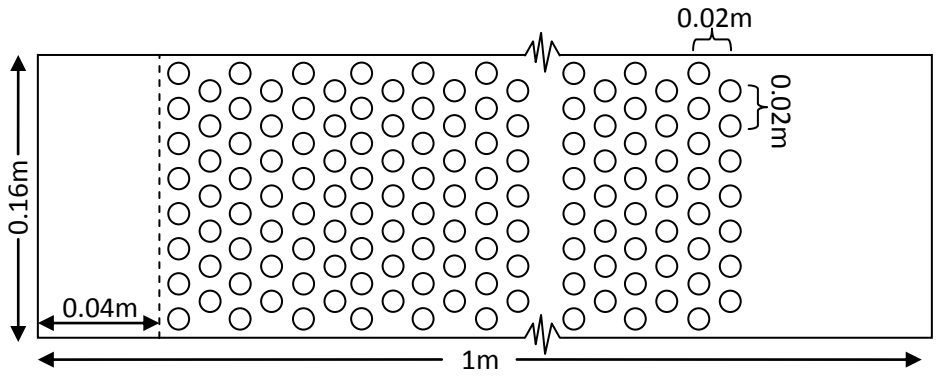

Figure 6.32: *Schematic of the numerical domain for the canopy simulation. The dotted line indicated the extent of the recirculation region. This diagram is not to scale.*

6.4.2 Mean flow profiles and turbulence characteristics

The vertical profile of the downstream velocity and Reynolds stress are shown in Figure 6.33. The modelled velocity profile closely resembles that expected of a free shear layer, although the interface at the canopy top appears to be sharper than expected. This suggests, as was the case in the previous simulations, that the development of the shear layer into the canopy is inhibited. However, above the canopy, the slope of the velocity profile is much closer to that of the classical mixing layer.

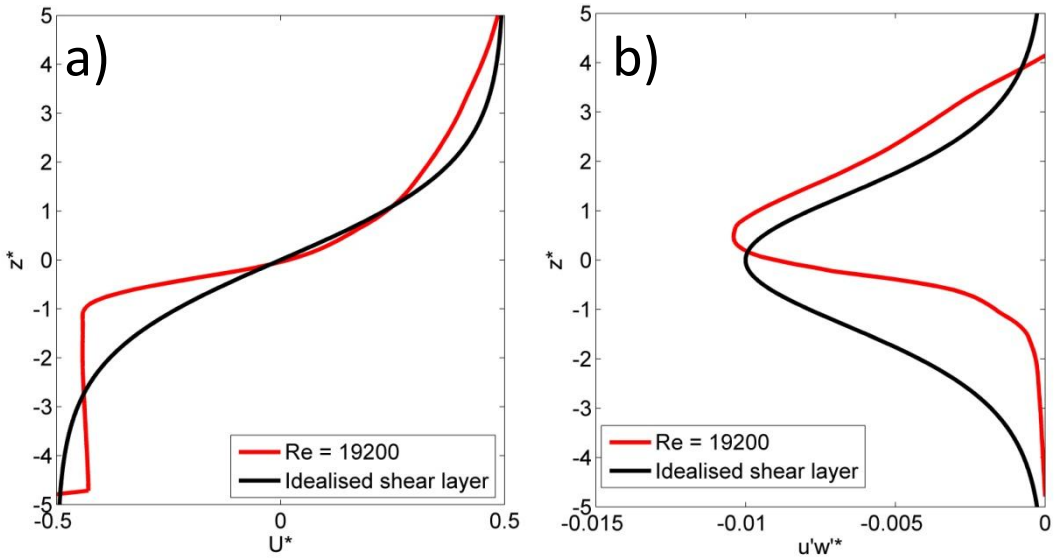

Figure 6.33: *Normalised vertical profiles of the horizontally and temporally averaged downstream velocity (a) and Reynolds stress (b). The idealised shear layer profiles are shown in black for comparison.*

This sharp interface at the canopy top is evident in the Reynolds stress profile too, which appears asymmetrical, with a much steeper curve into the canopy. In contrast to the small canopy run and the rigid experiment, the shear layer in the canopy experiment is much closer to the thickness in a free shear layer. This highlights the role of canopy density and length in forming the shear layer. As well as the steepened slope, the Reynolds stress peak is also shifted above the centre of the shear layer, as defined using the velocity profile. This suggests that the shear layer is actually pushed above the canopy layer. This finding is in contrast with Ghisalberti and Nepf (2006) who found that the peak actually moved down into the canopy. However, this may be due to differences in canopy density.

Figure 6.34 shows the mean velocity long-section which demonstrates the regularity of the velocity profile downstream through the canopy as well as the asymmetrical velocity gradient about the inflection point which causes the asymmetry in the Reynolds stress profile

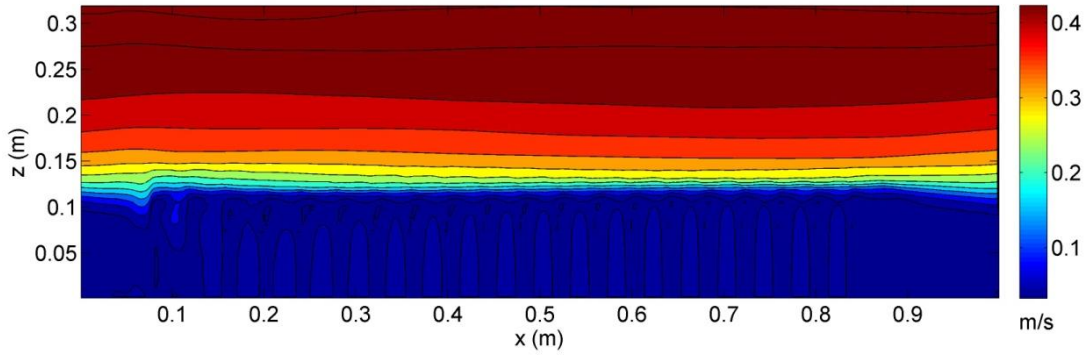

Figure 6.34: *Long-section of the time-averaged downstream (u) velocity. Due to the dynamic nature of the vegetation, it has not been blocked out.*

Figure 6.35 shows the time-averaged Reynolds stress. There is a clear peak along the top of the canopy as expected, though there also appears to be a peak at the top of the domain. This may be due to the rigid-lid approximation used for the top boundary condition. Despite the length of the canopy, there is still variation along the canopy, particularly at the front and back. This means the canopy cannot be analysed as one continuous canopy when recirculating the flow as the flow will still respond slightly differently at the ends of the domain. The overall pattern however, is far more homogeneous along the long-section than for the small patch, where the Reynolds stress corresponded to particular stalks instead of a continuous canopy. Therefore, these results are more useful in analysing longer time evolution of vortices in the flow.

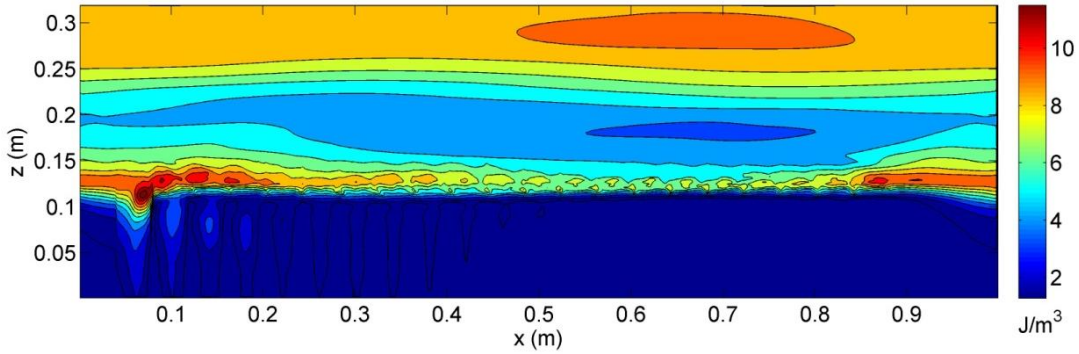

Figure 6.35: *Long-section of the time-averaged Reynolds stress.*

The turbulent kinetic energy plot in Figure 6.36 shows that this signal still shows specific peaks at the front and back ends of the canopy, though similar to the Reynolds stress, there is a small peak at the canopy top that extends along the entire canopy, suggesting canopy conditions have been obtained.

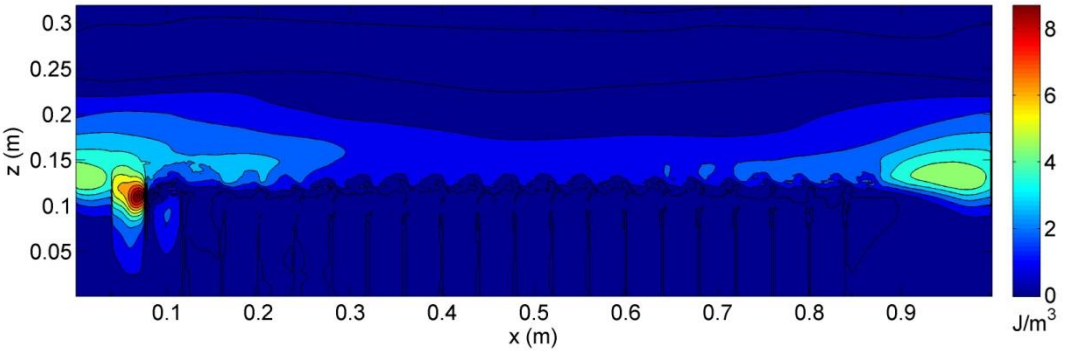

Figure 6.36: *Long-section of the time-averaged turbulent kinetic energy.*

6.4.3 Quadrant analysis

The vertical profiles of quadrant occurrence in Figure 6.37a show a similar pattern to the previous simulations, with Q_2 and Q_4, ejections and sweeps, dominating the flow at the canopy top. With an *H*=0 threshold, the distribution of sweeps and ejections is very similar throughout the bottom two thirds of the domain. As the threshold size increases to *H=2*, ejections dominate at the canopy top, with sweeps dominating in the region above. This contrasts with the previous case in Section 6.3 as well as previous published work (e.g. Okamoto and Nezu, 2009), where the pattern is reversed. One possible explanation is that, similar to the rigid case in Section 6.2, a different process is dominating the large-scale turbulent structure however this seems unlikely. This will be discussed further in Section 6.4.5.

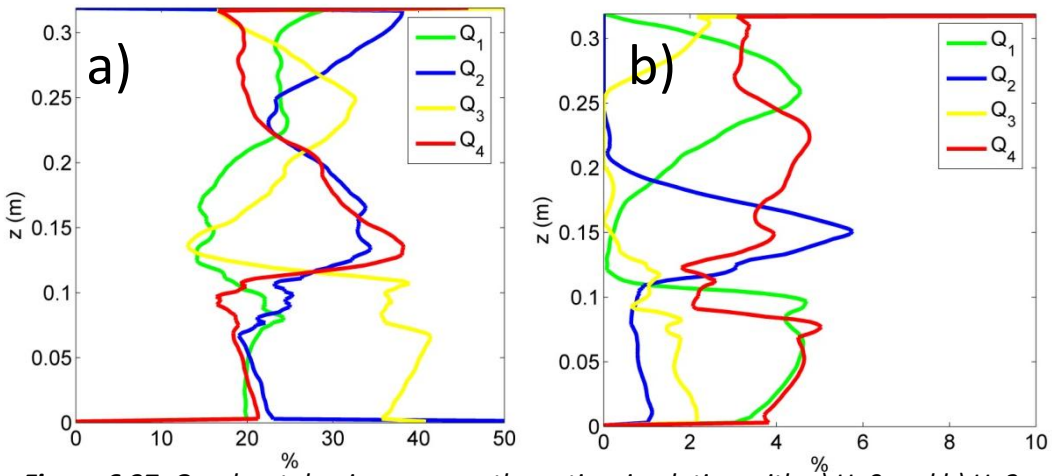

Figure 6.37: *Quadrant dominance over the entire simulation with a) H=0 and b) H=2.*

The long-section in Figure 6.38 shows the spatial pattern of quadrant dominance. This highlights the distinct layering of the flow, and the homogeneity along the canopy. The canopy is clearly divided into sections and there is little evidence of flow penetration into the canopy. This is clearly seen as Q_1 events dominate the canopy. This separation and lack of mixing might explain why Q_2 events dominate at the top of the canopy. If there is little penetration, the flow may resemble a stable boundary layer in which case ejections would be expected to dominate (Maitani, 1977). The vertical velocity profile in Figure 6.33 suggests that while there is evidently some mixing, this may be the case, as the profile above the canopy does resemble a logarithmic profile, with a much-reduced mixing layer.

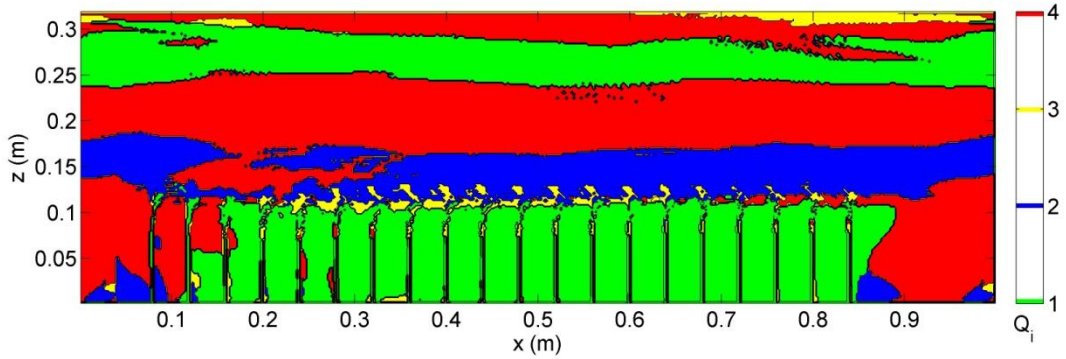

Figure 6.38: *Quadrant dominance using a threshold hole size of H=2.*

The individual quadrant plots in Figure 6.39 highlight the lack of penetration of any large scale sweeps or ejections. Sweep occurrence drops off sharply at the front of the canopy, with no sweeps penetrating more than half way into the canopy. Along the top of the canopy there is even less penetration, with a clear divide between the canopy zone and the flow above. The only significant quadrant events within the canopy are Q_1 outward interactions. Finnigan (1979b) also found a high occurrence of Q_1 events within the canopy, alongside Q_4 events.

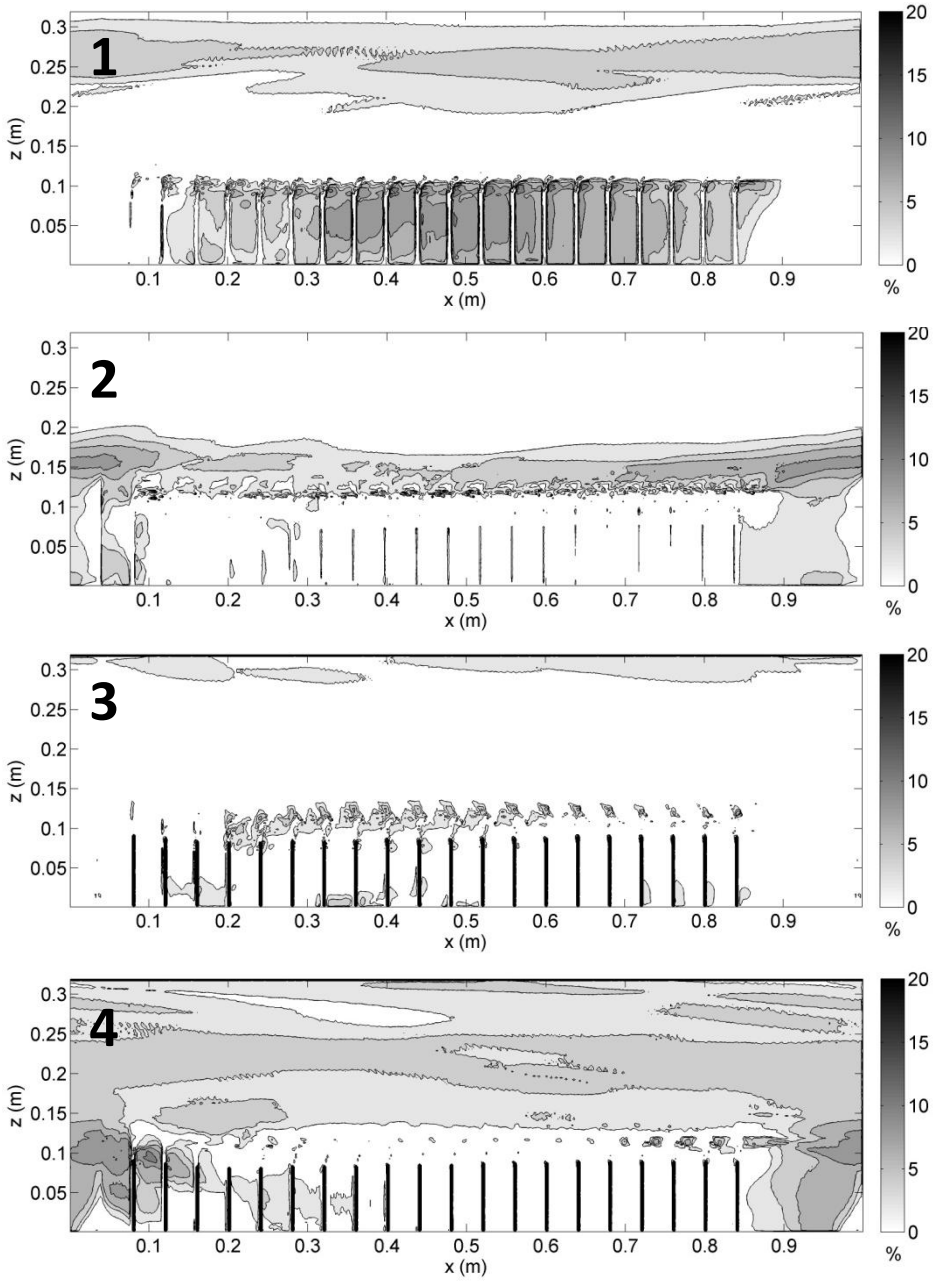

Figure 6.39: *Quadrant occurrence expressed as a percentage using a hole size H=2.*

6.4.4 Vortex detection

Similarly to the small patch simulation, the entire simulation was fully turbulent and therefore there were a large number of vortices which could have been analysed. Instead, examples are drawn from the simulation via visual analysis of the FTLE fields. Figures 6.40-43 show the progression over time of a vortex over the canopy, captured by each vortex detection method. The time-step in the figures has been chosen to highlight the progression of a single vortex.

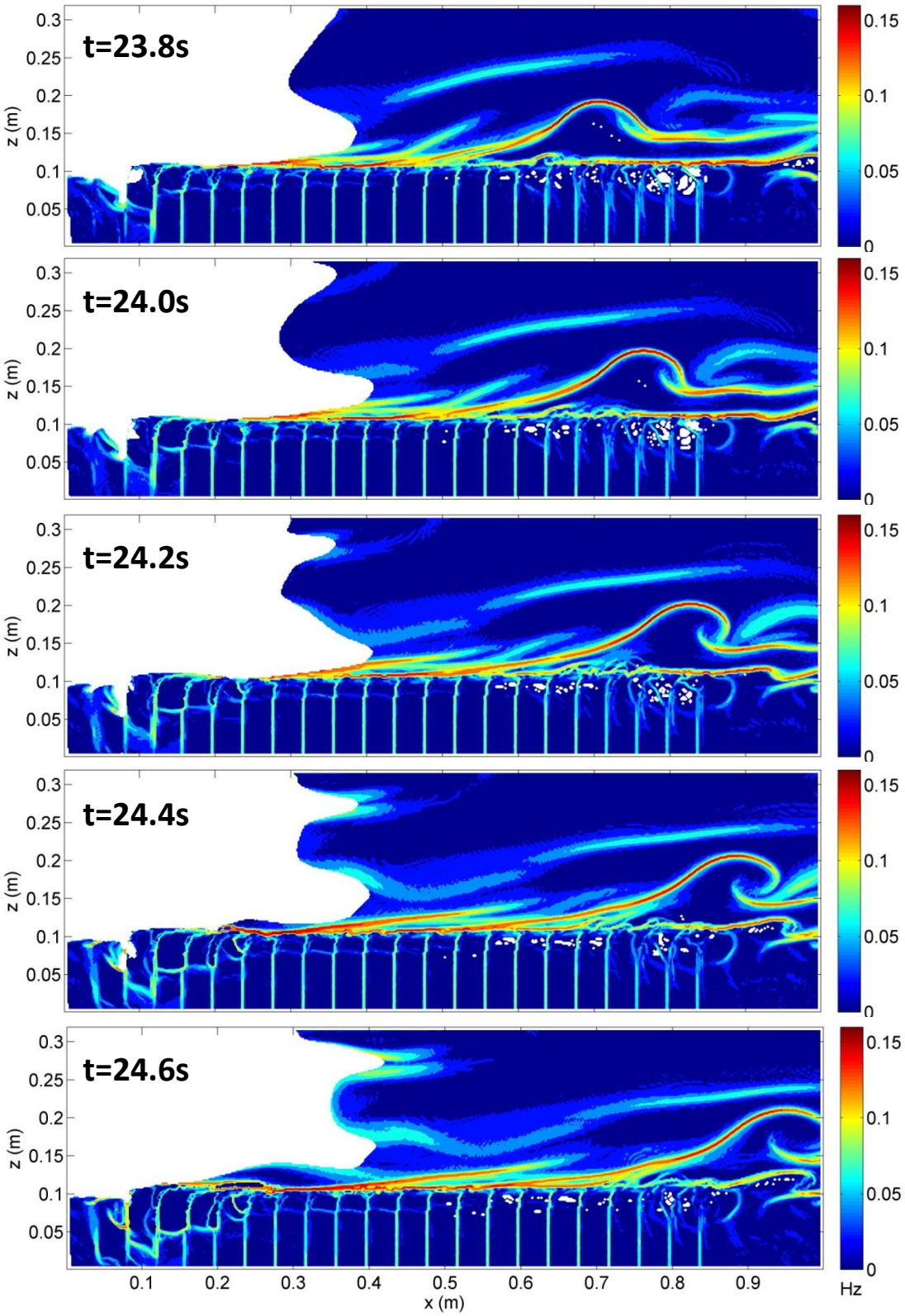

Figure 6.40: *FTLE vortex tracking. Areas in white represent regions where the trajectories could not be tracked sufficiently to give a reliable estimate. Ridges represent areas of greatest flow attraction.*

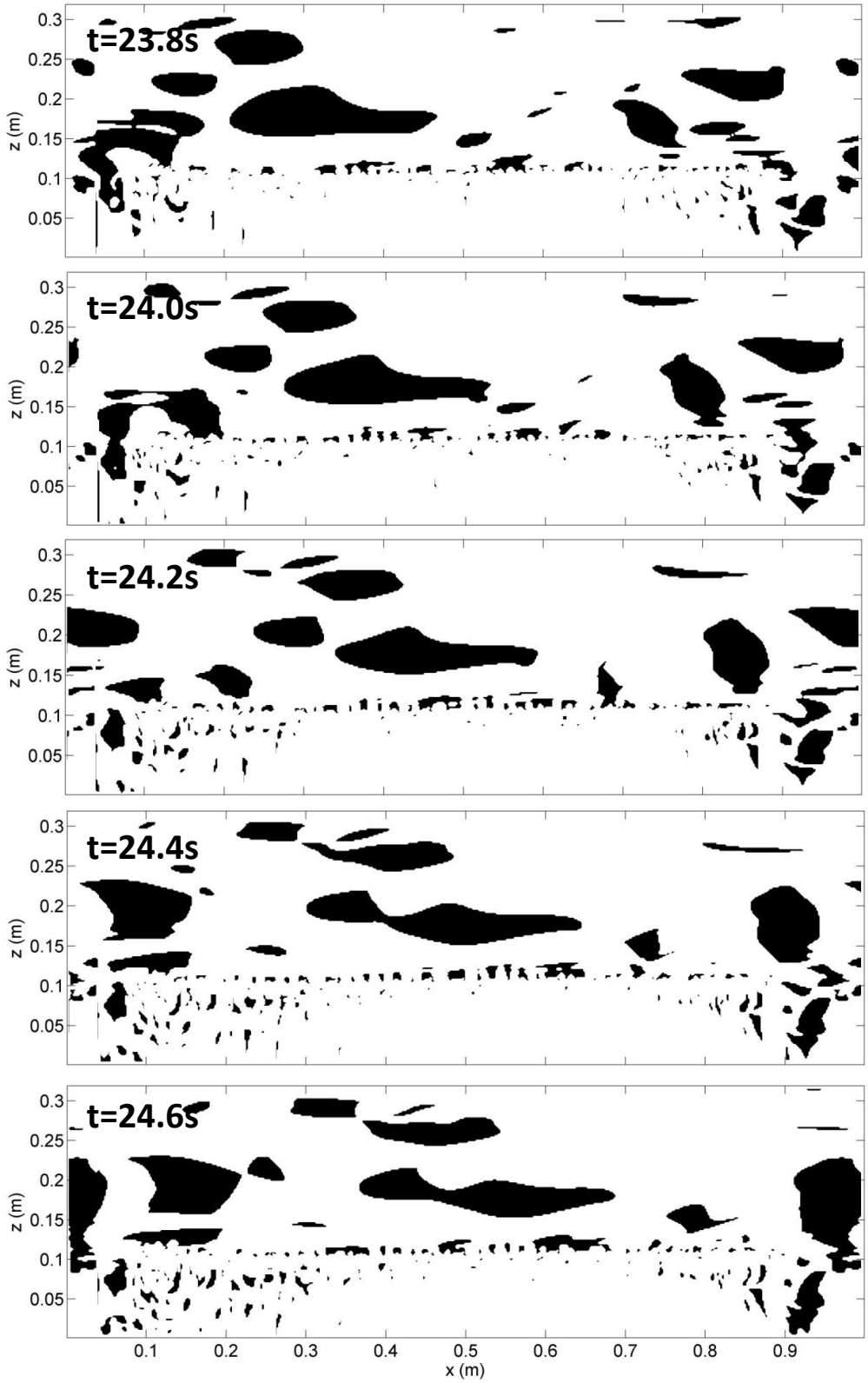

Figure 6.41: *Q criterion vortex detection results through time. Black areas represent vortices*

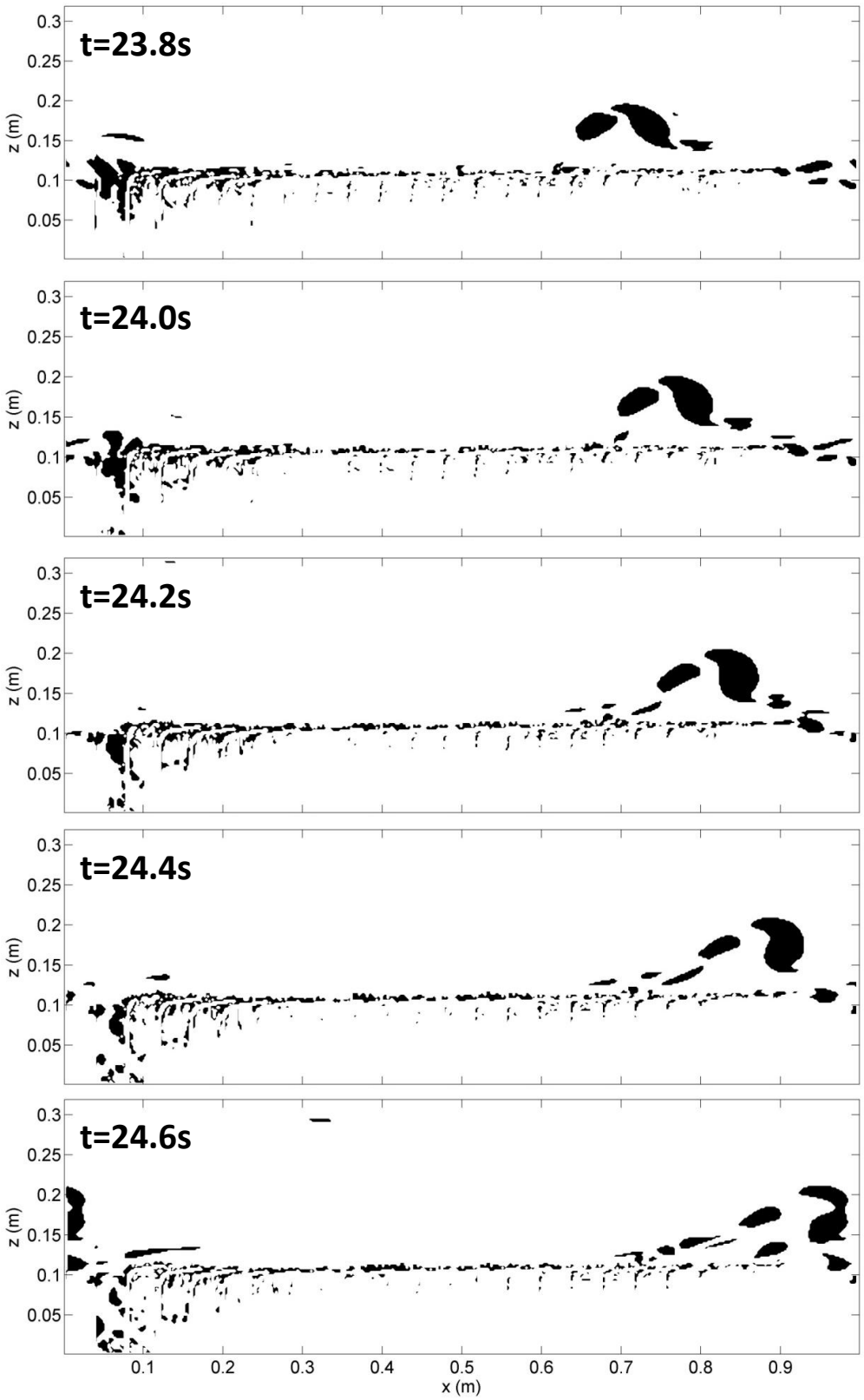

Figure 6.42: *Δ criterion vortex detection results. Black areas represent vortices*

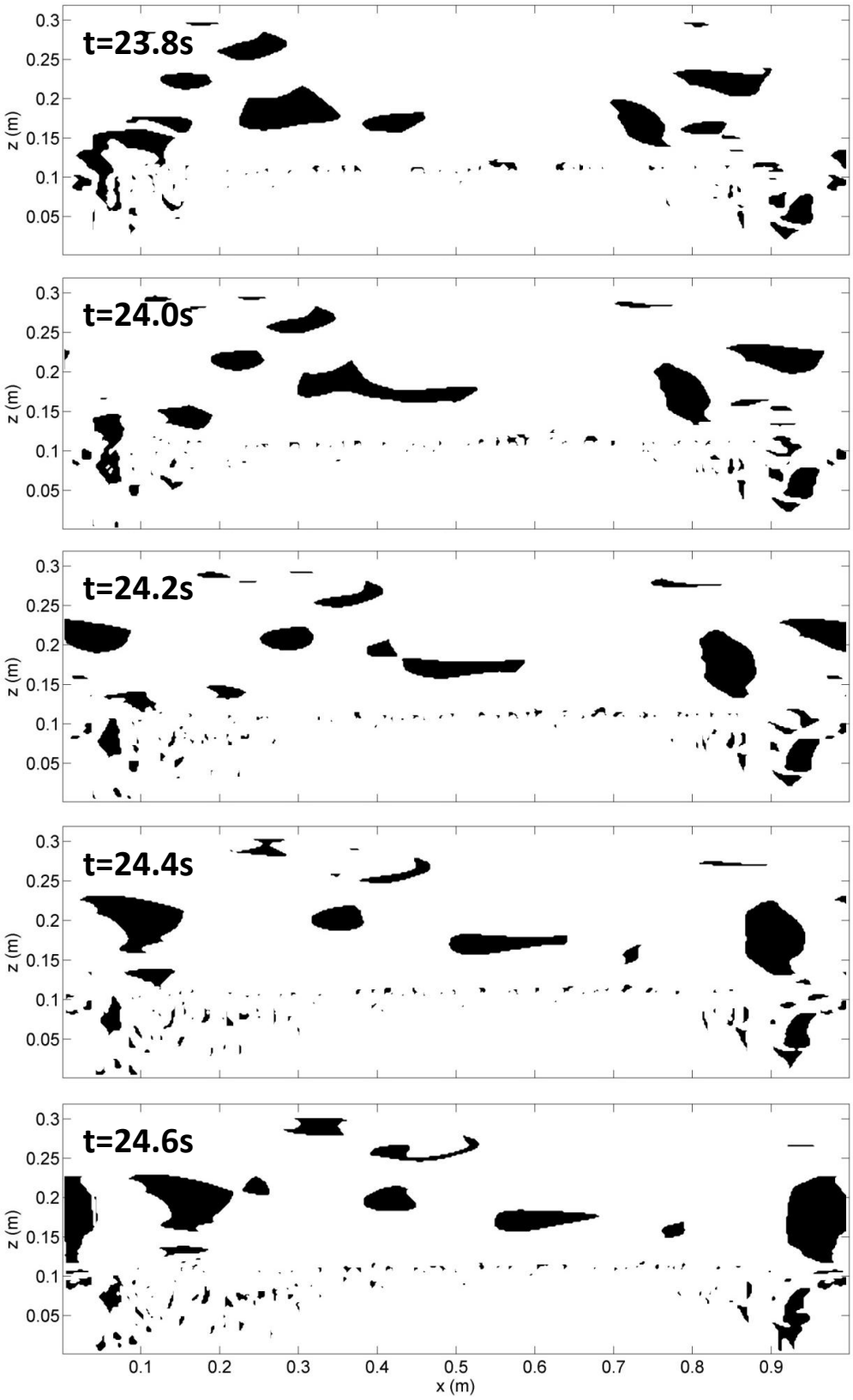

Figure 6.43: *λ_2 criterion vortex detection results. Black areas represent vortices*

The clearest one is arguably the FTLE plot, where the characteristic signature of a roller vortex (Figure 4.10), and perhaps a hairpin vortex, is clearly visible. This develops as the vortex progresses downstream.

The three Eulerian methods each pick up the vortex, and the Q and Δ criterion in particular highlight the growth and distortion of the vortex through time. The λ_2 criterion appears to pick up more of the structure besides the head of the roller vortex, whereas the other two approaches do not detect those structures. Similarly, the vorticity plot in Figure 6.44, only taken for one instant, also picks up the head of the vortex as well as a strong vorticity signal in the trailing part of the vortex.

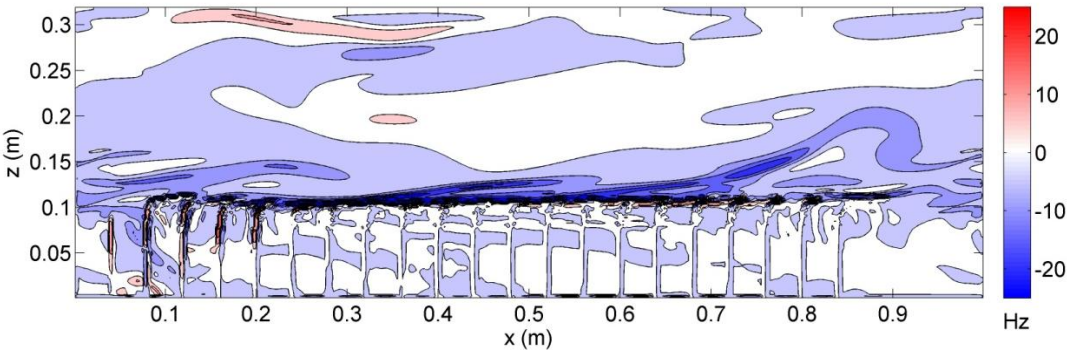

Figure 6.44: *Vorticity snapshot taken at t=24.4s, showing clockwise (blue) and anti-clockwise (red) vorticity.*

Figure 6.45 maps the results of the different vortex methods, FTLE and Eulerian, onto one another. There is clear agreement between them, and together they pick up the different components of the vortex well. It is also clear from this Figure that the λ_2 criterion is in this case a subset of the Q criterion. This would not necessarily be the case if these vortex quantities were calculated in three dimensions.

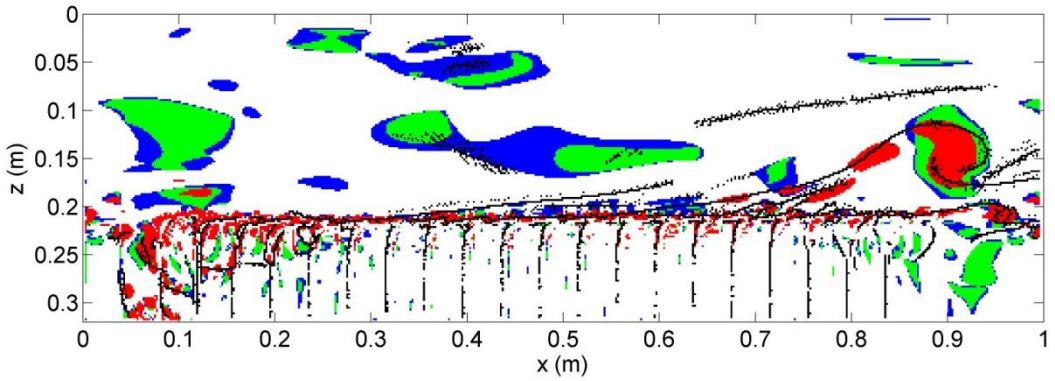

Figure 6.45: *Comparison between different vortex methods for t=24.4s. Q criterion vortices are shown in blue, λ_2 criterion vortices in green, Δ criterion vortices in red and FTLE ridges in black.*

As with the rigid case, the vortex detection results allow analysis of vortex evolution downstream. In contrast to the rigid case, rather than using the FTLE results to calculate the vortex size, the Eulerian methods were used. There are a number of reasons for this alteration to the method. Firstly, there is a much stronger background signal in the FTLE in this dataset, making it harder to identify and single out individual vortices. Secondly, the Eulerian methods produce much better results for this data than for the rigid simulation and therefore provide a more accurate method.

The radius of the vortex was calculated by first calculating the area of the vortex. To do this, a rectangular section of the domain was selected manually, such that it included the entire vortex of interest, and as few other vortices as possible. The area (A) of the vortex was then calculated by summing the areas of the binary maps shown in Figures 6.41-43. The radius was then calculated as

$$r_V = \sqrt{A_V/\pi} \tag{6.2}$$

This assumes inherently that the vortex is circular, which is a reasonable first order approximation given the results above. However, this assumption of isotropy would not have held in the previous cases. This procedure was carried out for each time-step and then the results were converted into downstream distance, using the convective velocity of the vortex which was calculated from the data to be 0.282m/s.

Figure 6.46 shows the changes in vortex thickness as the vortex travels downstream. It is clear that the results from the Δ criterion are unreliable. This is expected given the problems described with this method in Section 6.2.4. As with the rigid case, the assumption is that vortex growth should scale with mixing layer growth. Therefore, the results have been compared to the predicted mixing layer growth rate using Equation 6.1. There is good agreement between the predicted and modelled rates, suggesting that this simulation does represent a canopy mixing layer flow.

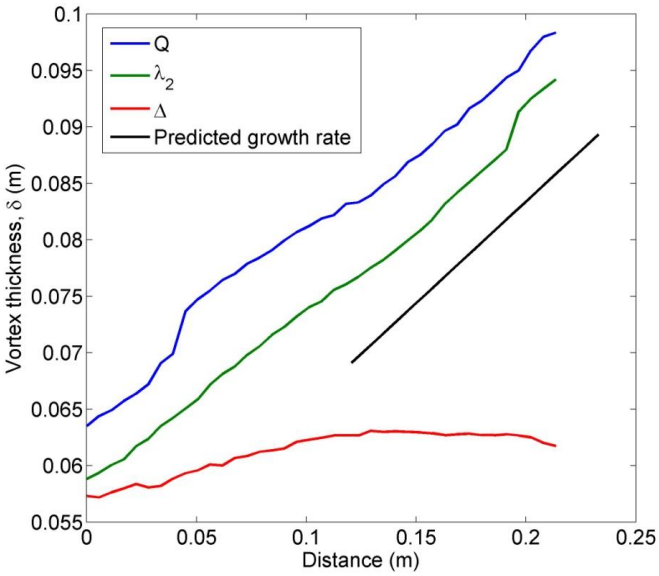

Figure 6.46: *Change in vortex thickness through time, using the Q (blue), λ_2 (green) and Δ (red) vortex criteria. The predicted growth rate is shown in black*

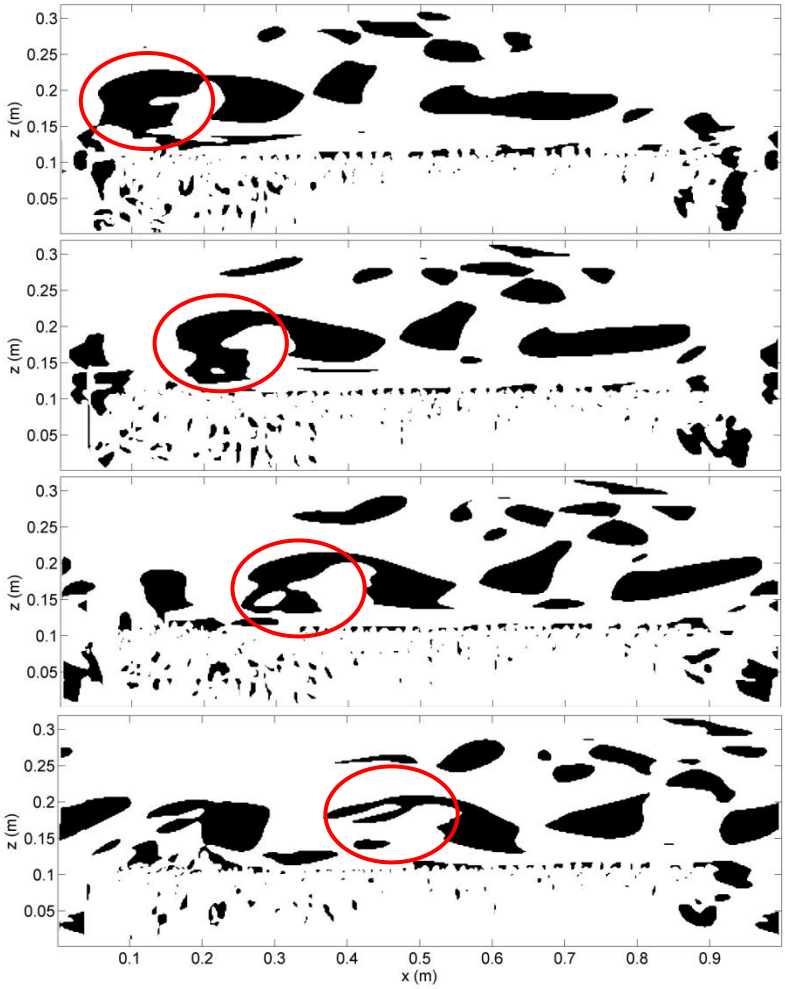

Figure 6.47: *Evolution and breakup of the vortex as detected by the Q criterion. The frames are taken at 0.2s intervals, between 24.8s (top) and 25.4s (bottom).*

Within the time period shown, the vortex does not reach a size great enough to be constrained by the flow depth. It is not possible to track the vortex further as it recirculates, making the calculations inaccurate. However, visual inspection in Figure 6.47 shows the vortex coalescing with another vortex and undergoing significant distortion within the next second. Therefore it is unlikely that even without the calculation problems associated with recirculation, the results may not be reliable.

In order to study the three dimensional structure of this vortex further, 3D-FTLE analysis was applied at the time-step where the vortex appears most well-defined (t=24.4s). Figure 6.48 shows the results from applying a ridge detection algorithm to these results. The structure of the roller vortex is clear, and exists consistently across the width of the domain. Both the upper and lower limb of the vortex are well defined. There are two structures upstream of the roller vortex which could potentially be the detached legs of a previous hairpin vortex (see annotation) however there is little further evidence to support this. The roller vortex appears to be smallest in the centre, with a widening of the vortex visible at either end.

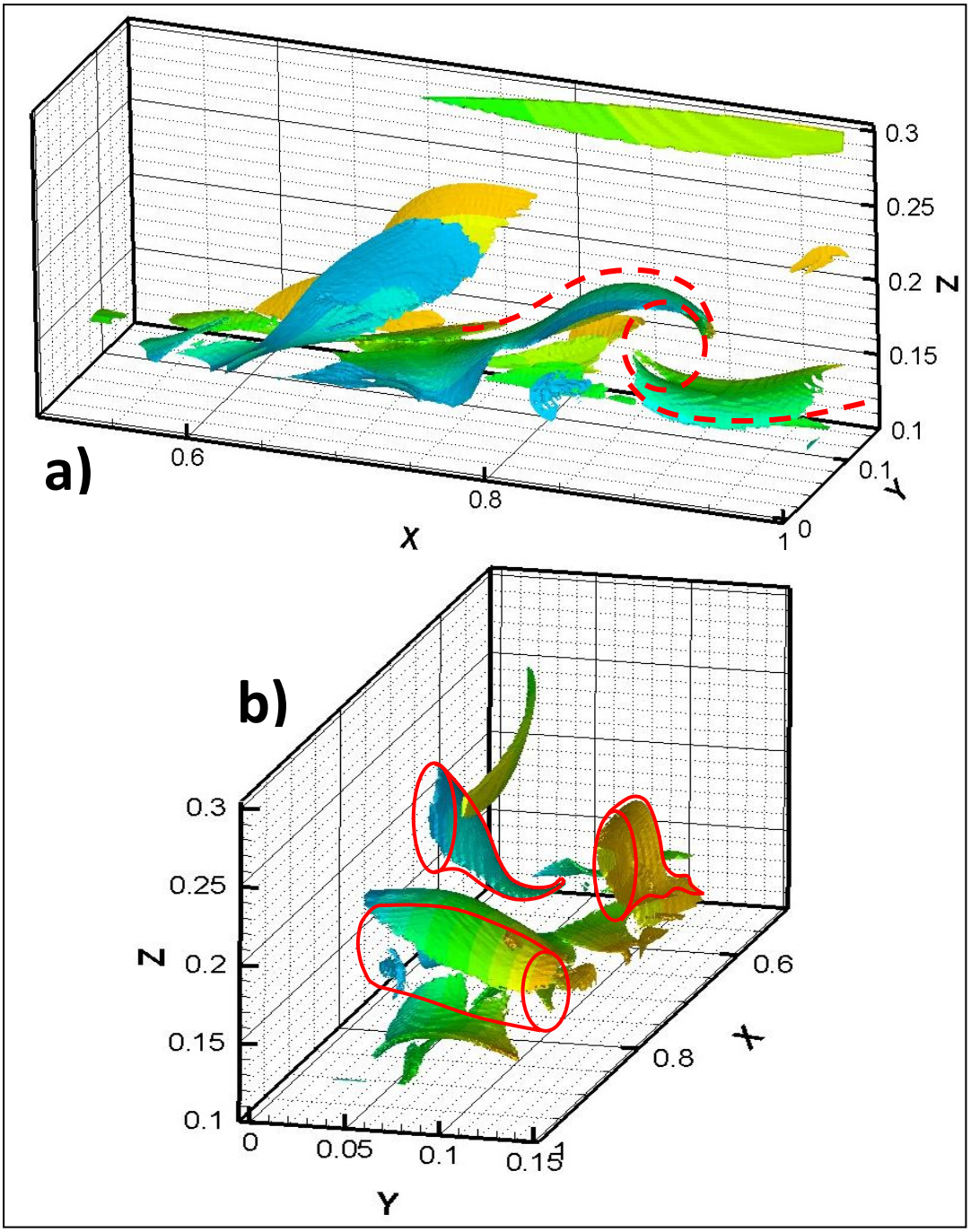

Figure 6.48: *Images of the 3D FTLE ridges viewed from (a) side-on to the domain with flow from left to right and (b) from the outlet, looking upstream. The surfaces are coloured according to their y-coordinate for visualisation purposes. The annotations in red highlight potential vortex structure.*

6.4.5 Velocity and plant spectra

Figure 6.49 shows the velocity and canopy height spectra taken at the same plan-view location. There is a high level of similarity between the plant and flow spectra. Both exhibit a dip at first, then a clear peak at approximately 0.5Hz (shown by the dotted line in Figure 6.49), followed by steady decay. The plant spectrum appears to follow the Kolmogorov spectrum well whereas, similar to the other LES simulations, the flow spectrum experiences a sharper drop-off possibly due to choice of SGS model, as discussed in Section 3.2.2.

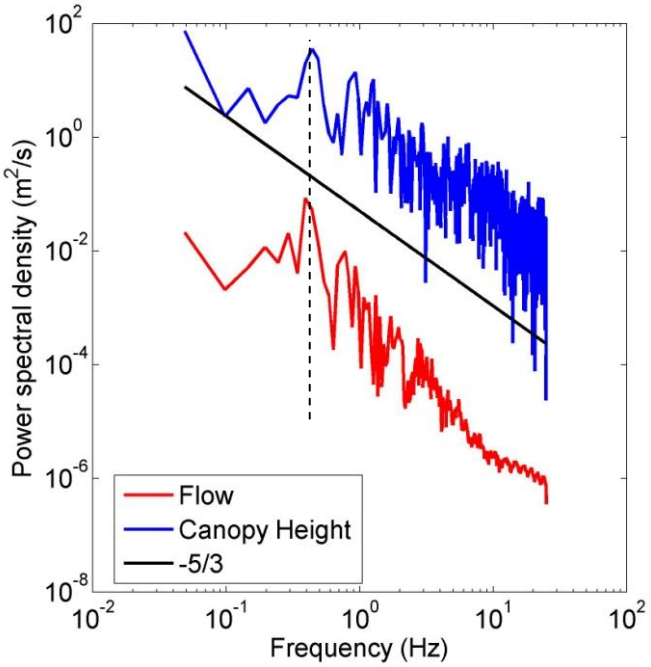

Figure 6.49: *Velocity (red) and canopy height (blue) spectra. The black line shows the Kolmogorov rate of decay. The dotted line is located at 0.5Hz.*

Mechanism	Frequency
f_{KH}	0.28Hz
f_N	5.81Hz
f_W	6.3Hz

Table 6.4: *Key frequencies active within the flow: f_W is the wake shedding frequency, f_N is the natural frequency of the vegetation and f_{KH} is the Kelvin-Helmholtz vortex frequency as discussed in Chapter 4.*

The low frequency peak in the spectra does not seem to match up very well with the predicted mixing layer K-H vortex frequency (Table 6.4). This may be due to inaccuracy in calculating the mixing layer properties, or it may be because the flow

does not represent a mixing layer. There is not any evidence of other powerful frequencies within the velocity spectrum. The plant spectrum potentially shows a peak at the natural frequency though this is not as clear as for the small patch.

However, the wavelet analysis, for both the flow and canopy, shown in Figure 6.50, does pick up two distinct periodicities. Firstly there is a low frequency signal at a time-scale of approximately 2s, which increases through time (as shown by the dotted line in Figure 6.50), to between 3 and 4s time scale. This correlates with the scale of the mixing layer instability. Secondly there is a much higher frequency, short time-scale signal which appears as a wave-packet at approximately 1s time-scale, though this frequency also appears to alter through time at approximately the same rate as the other signal.

These signals are much clearer in the velocity spectrum, and indeed almost die out completely in the canopy spectrum halfway into the simulation. The larger scale motions die out even earlier, at roughly 10 seconds into the simulation. This matches well with the visual evidence that canopy motion dies out fairly early on in the simulation as the canopy reaches an equilibrium position.

The cross-wavelet spectrum (Fig 6.50 c) indicates good agreement between the flow and vegetation signals. Furthermore, the magnitude of the peaks indicates that the motion is most similar between 5 and 10 seconds into the simulation. It is clear from the flow spectrum (Fig 6.50 a) that the largest magnitude peak occurs at the beginning of the simulation, after which the signal dies away. In contrast, the vegetation signal increases in magnitude after 5 seconds, potentially indicating a lag in response of the vegetation to the flow. The cross-spectrum highlights this region between 5-10 seconds when the periodicities coincide, either side of which, the magnitude dies away considerably. There is some agreement at the lower frequencies throughout the simulation; however in general, following the initial stages of the simulation, the canopy and flow do not seem to be linked. This may be in part due to a general decrease in canopy motion after the initial stages.

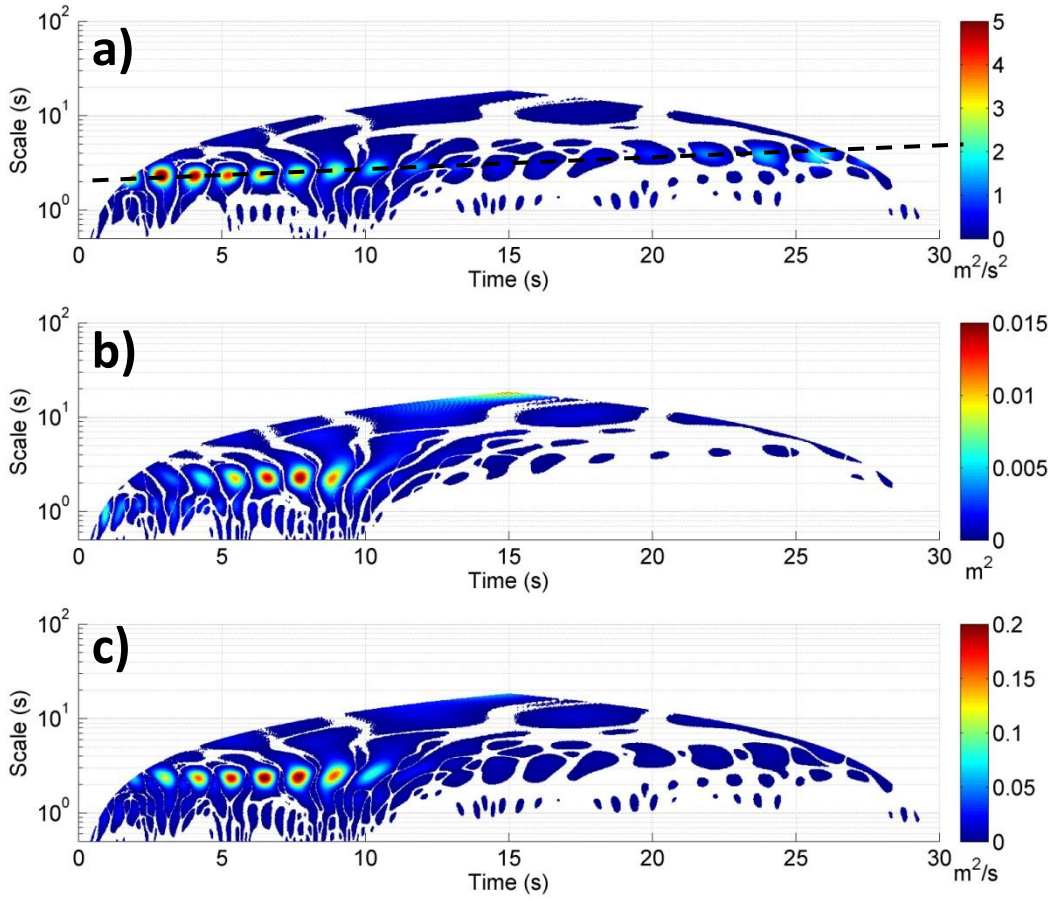

Figure 6.50: *Wavelet spectra for a) the velocity and b) the canopy height and c) cross-spectra between the two time-series. The dotted line highlights the observed increase in scale through time.*

There is obviously a linkage between the spectra, and based on the frequency, this is most likely through the mixing layer instability. However, there is no evidence of the plant actively responding to, or forcing the flow.

6.4.6 Summary

The results from the full canopy simulation show clear evidence of canopy flow regimes, with a region of slower flow throughout the canopy. However, in contrast to the small patch simulation, there is less evidence of a mixing layer between the two flows. The velocity profiles, and turbulent quadrant profiles hint at flow resembling more of a boundary layer above the canopy. It is suggested that this may be due to the density of the stems and the blocking effect they have between the flow above and within the canopy.

The vortex detection methods highlight vortices that are characteristic of the mixing layer, however it is possible these may be relics of hairpin vortices, which can also be produced in stable boundary layers (e.g. Adrian *et al.*, 2000). Therefore, it is possible that due to the high vegetation density at the canopy top, the momentum blockage is such that the flow above resembles a boundary layer. This would explain the dominance of ejection events over sweeps. However, the growth rate of the vortex does match well with the rate predicted for the mixing layer.

The spectral and wavelet analysis shows that in contrast to the small patch simulation, there is no long-lasting coupling between the flow and vegetation. Instead, the vegetation appears to reach a stable equilibrium condition whereby the flow conditions prevent the vegetation from moving. This may partly be due to the representation of drag within the model, whereby the drag does not re-adjust according to the plant position. This limitation is discussed, and a solution proposed in Section 6.7.

6.5 Flow and plant dynamics around a small highly flexible vegetation patch

Having investigated flow over semi-rigid canopies using the Euler-Bernoulli beam model, the next two sections use the N-pendula model to investigate how flow structure and plant-flow interactions differ in highly flexible vegetation canopies. These simulations are designed to represent submerged macrophytes such as *Callitriche platycarpa* and *Ranunculus penicillatus*, which was the vegetation used in the flume work in Chapter 5. These plants are highly flexible and generally assume a much more horizontal configuration within the flow. Similar to the beam model, two main investigations were carried out with this model, beginning with a simple, small patch of four stems. This configuration therefore represents either four single stemmed plants, or perhaps more likely, a single multiple-stemmed plant.

6.5.1 Experimental setup

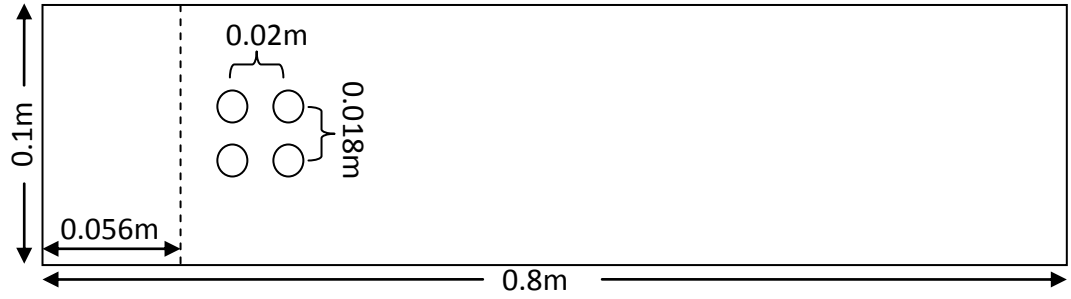

Figure 6.51: *Schematic of the numerical domain used for the small patch. The dotted line indicates the recirculation region.*

For this simulation, four individual stems were used within a cuboid domain of length 0.8m, width 0.1m and height 0.3m, as shown in Figure 6.51. The domain was 400 cells long, 50 cells wide and 150 cells high (nx=400, ny=50, nz=150) and therefore the spatial resolution was 0.002m. The stems were placed in a simple square alignment, 0.02m apart in the downstream direction, with a lateral separation of 0.018m. The stems were each 0.3m long with a radius of 0.003m. As this simulation was designed to represent highly flexible vegetation, the flexural rigidity of the stems was set at $0.001 Nm^2$ as discussed in Section 5.2.2. The inlet velocity was set to 0.5m/s, representing a Reynolds number of 21,400. The Froude number was 0.29 and therefore the flow was subcritical. In order to model fully-developed flow, a recirculation region of 0.056m was applied to the front of the domain. The simulation was run for 30 seconds, at a temporal resolution of 50Hz and took 552hrs CPU time. All analysis was undertaken in the x-z plane at $y/w = 0.5$.

6.5.2 Mean flow profiles and turbulence characteristics

The vertical velocity and Reynolds stress profiles in Figure 6.52 immediately indicate that this setup does not resemble a mixing layer. The velocity profile shows very poor agreement with the classical pattern observed for canopy flows. This is to be expected given the low density and high flexibility of the stems. The Reynolds stress profile shows some agreement, with a double peak at the canopy top, however it then drops away much faster than expected, above and beneath the canopy top.

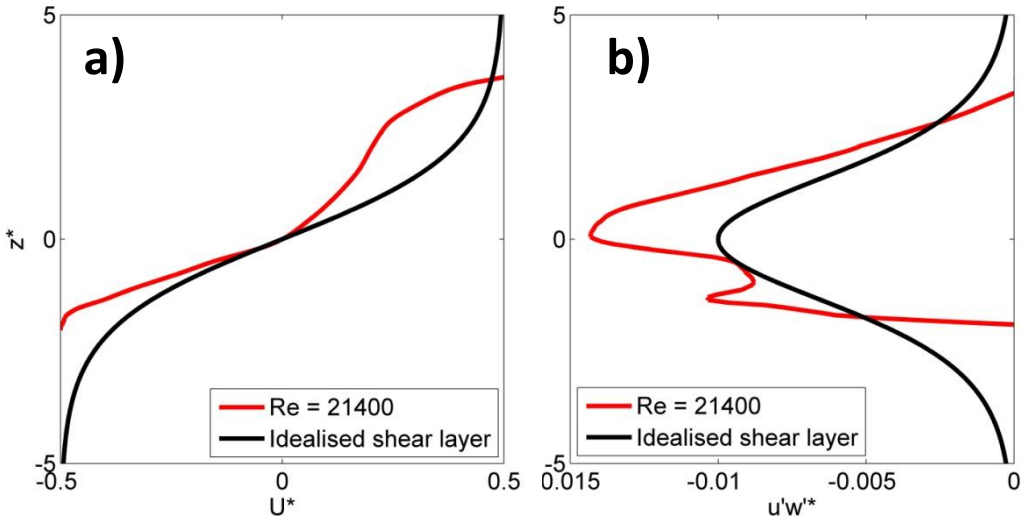

Figure 6.52: *Vertical profiles of a) downstream velocity and b) Reynolds stress.*

The mean downstream velocity profile in Figure 6.53 clearly shows the region of influence of the stems. Due to both the low stem density and stem configuration, there is no evidence of the formation of a canopy layer. Instead the vegetation has a large wake-region, where the flow is considerably below the average. Interestingly, this wake is not attached to the bed, but is confined mostly to the top half of the plant.

The fact that this case does not resemble a mixing layer has obvious implications for the analytical approach which was setup specifically to identify canopy mixing layer processes. Nevertheless, the same procedure is still applied here, in order to try and explain the general flow dynamics.

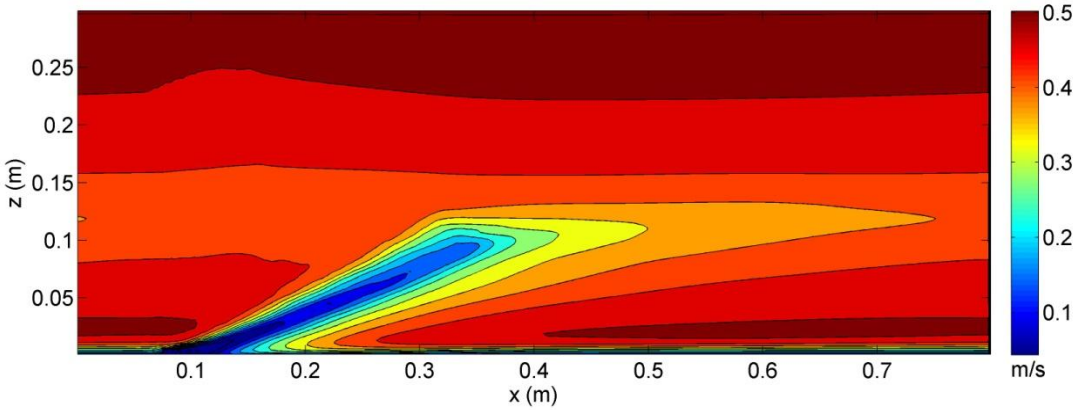

Figure 6.53: *Time-averaged long-section of the mean downstream (u) velocity field. Vegetation cannot be masked as it is dynamic.*

Both the Reynolds stress and TKE profiles (Figures 6.54 and 6.55) show a surprisingly local distribution of energy and stress, limited to the region immediately surrounding the stalk. This is far more local than the reach of the wake region in Figure 6.53. Some of these values may be skewed by the presence of the vegetation in the data, potentially creating an excessive peak near to the plant. The values of T.K.E. are significantly larger than those obtained for the rigid and Euler-Bernoulli beam simulations, but even when compared on similar scales there is very little evidence of high T.K.E. values beyond the immediate stalk area. Figures 6.54 and 6.55 both indicate a predominantly local distribution of energy and stress.

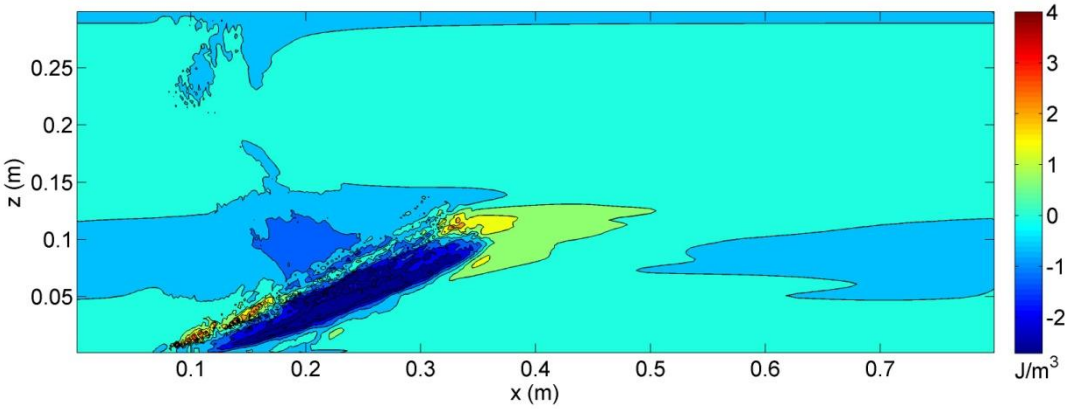

Figure 6.54: *Long-section of time-averaged Reynolds stress.*

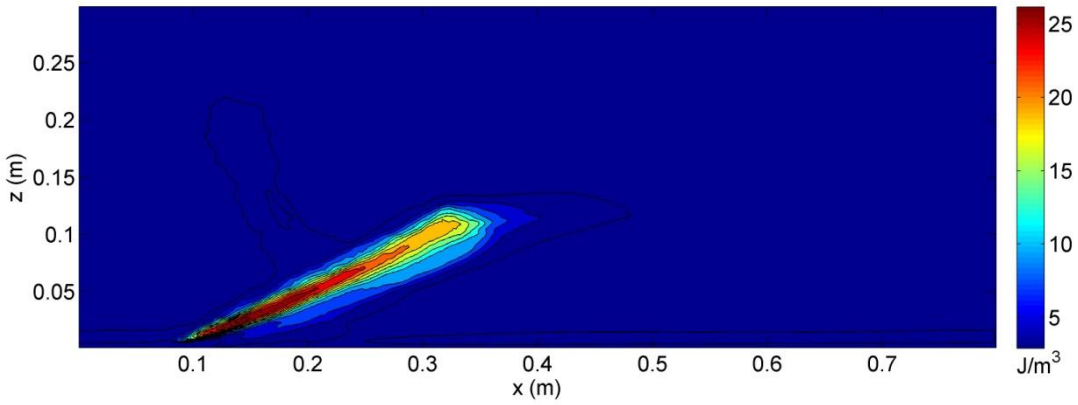

Figure 6.55: *Long-section of time-averaged TKE.*

6.5.3 Quadrant analysis

The vertical profiles of quadrant occurrence in Figure 6.56 show that sweeps (Q_4) and ejections (Q_2) dominate the flow both below and above the vegetation. Contrastingly, Q_1 and Q_3 events dominate in the height at which the wake is greatest. Applying a stricter threshold significantly diminishes the influence of Q_4

sweep events. Instead, ejections dominate the flow by far, except again for the wake region. As this isn't a canopy layer, it is more likely to resemble a classical boundary layer and therefore it is unsurprising that ejections dominate.

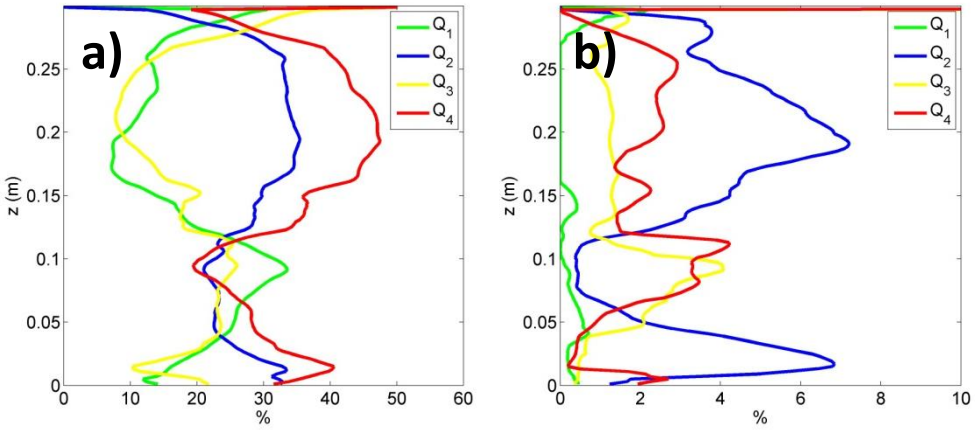

Figure 6.56: *Vertical profiles of quadrant occurrence using a) H=0 and b) H=2 threshold.*

The dominance of ejection events throughout the domain is highlighted in Figure 6.57. It is very clear that the driving factor in the additional quadrant distribution is the plant morphology. There are clear wake and stalk controlled regions as well as a region of Q_3 events up the front of the canopy. This morphology-driven structure is clearly shown in the individual quadrant plots in Figure 6.58.

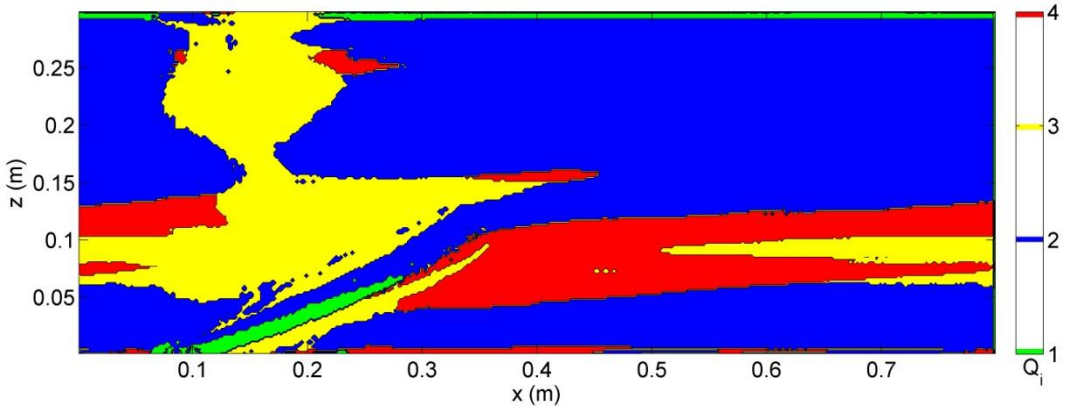

Figure 6.57: *Quadrant dominance using a threshold hole size of H=2.*

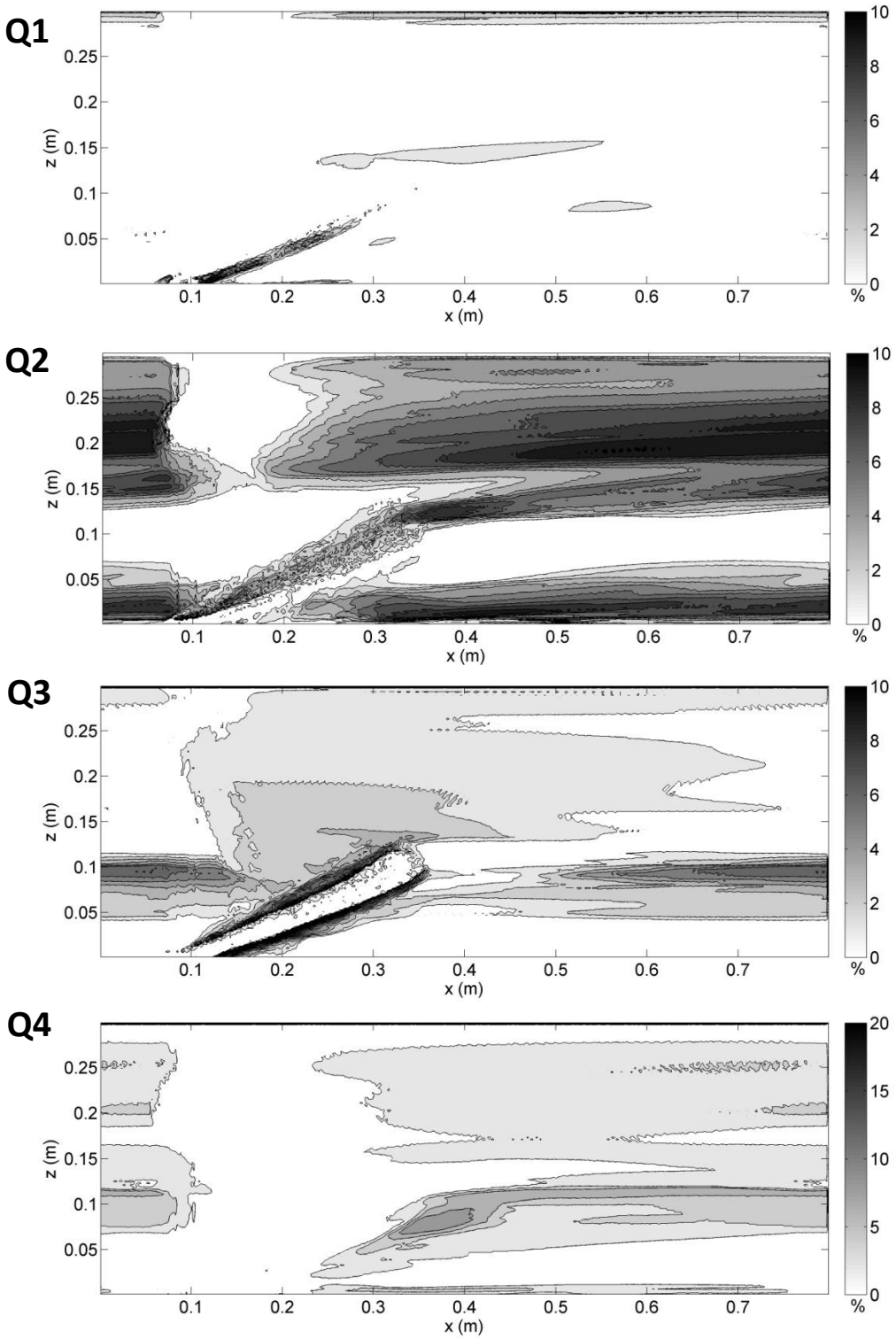

Figure 6.58: *Quadrant occurrence across the long-section as a percentage with H=2*

6.5.4 Vortex detection

Figure 6.59 shows an instantaneous vorticity plot taken from the simulation. There is clear evidence of small-scale vorticity at the top of the stalks. Here, vortices of both clockwise (blue) and anticlockwise (red) appear in a manner more akin to a flapping flag (Farnell *et al.*, 2004) than a canopy shear layer. There is some indication that this wake-flapping may develop into something larger as it detaches from the shear layer, however the other vortex methods fail to identify this within the flow.

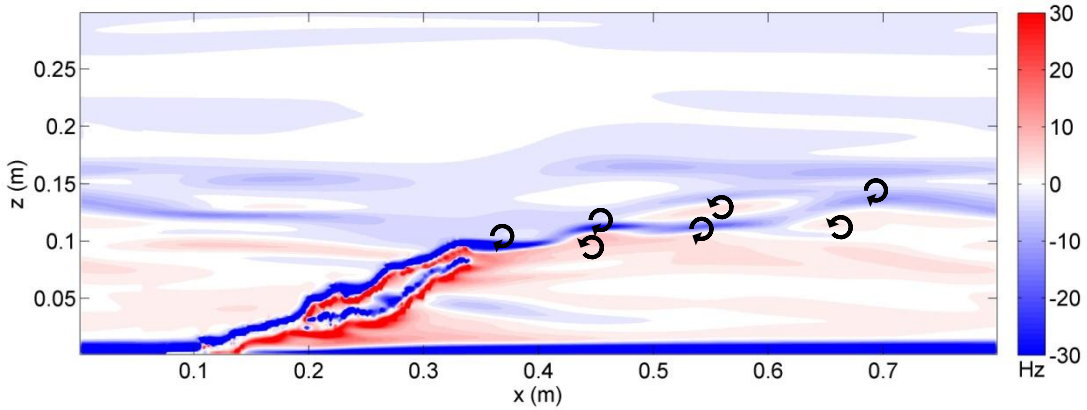

Figure 6.59: *Vorticity snapshot showing clockwise vorticity (blue) and anti-clockwise vorticity (red).*

The Q and Δ criterion (Figure 6.60) pick up clearly the stem-induced vorticity as well as the meandering flapping wake, however there is very little sign of larger-scale vortices above the canopy. The Q criterion appears to identify some larger scale vortices up the front of the vegetation. However most of these vortices have been recirculated and are not generated along the stem. At certain time-steps there is some evidence of vortices being advected along the stems; however, these tend to be much smaller in scale. The overall vortex regime is not sufficiently coherent to be able to analyse the evolution of individual vortices through time in the same manner as the previous cases.

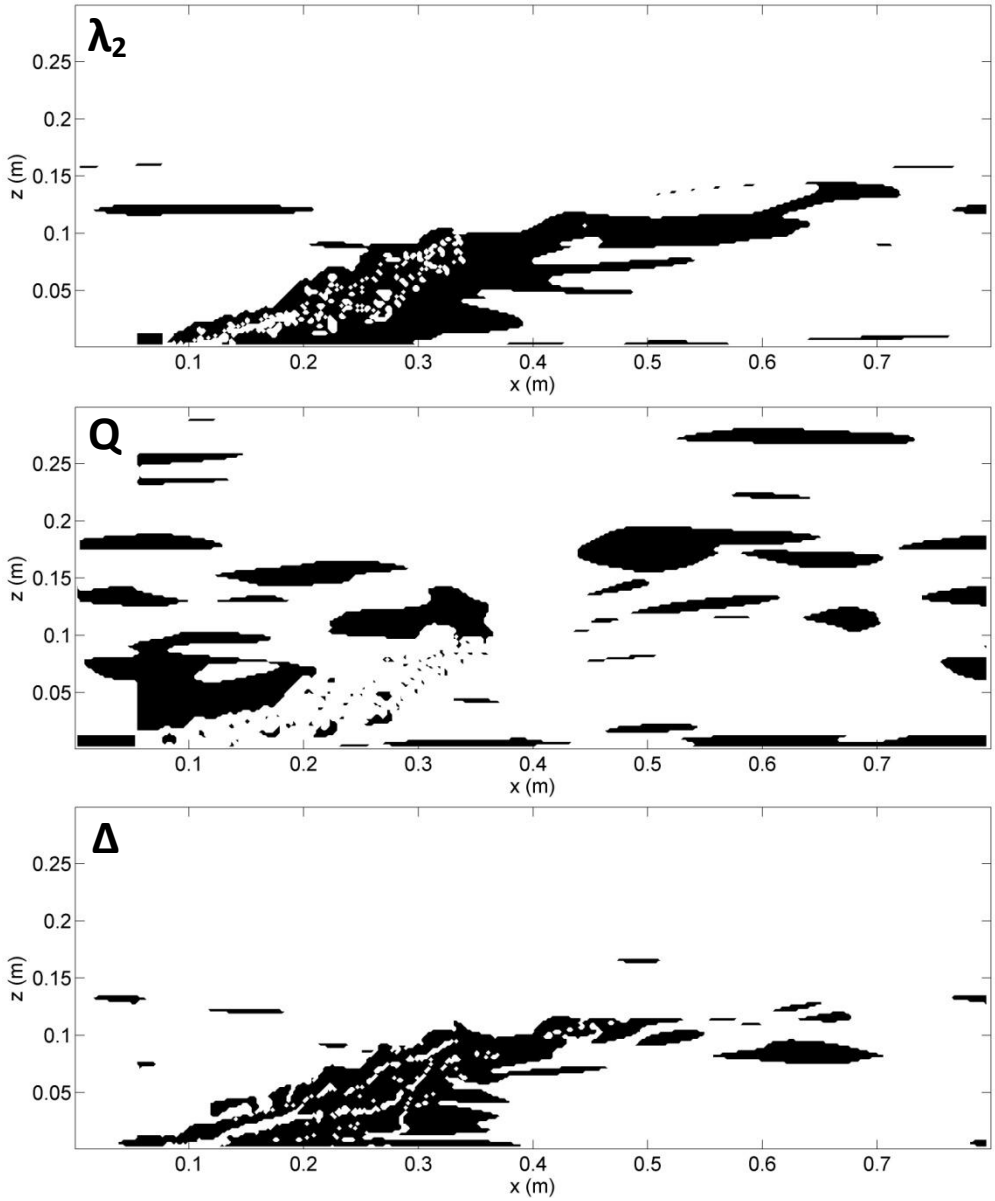

Figure 6.60: *Eulerian vortex detection results. Areas of black represent vortices.*

The FTLE plot in Figure 6.61 shows a convergent region of flow at the canopy top. As mentioned in Section 4.8, the FTLE highlights convergence of flow and therefore is not a direct proxy for vorticity. The ridges in the FTLE field agree well with the vorticity map suggesting that they may well correspond to vortices. However, it is also likely that the ridges are highlighting a region of strong shear in the flow.

Therefore, the different vortex methods hint at some larger scale structure in addition to the vortex shedding off the stems, however there is no conclusive evidence.

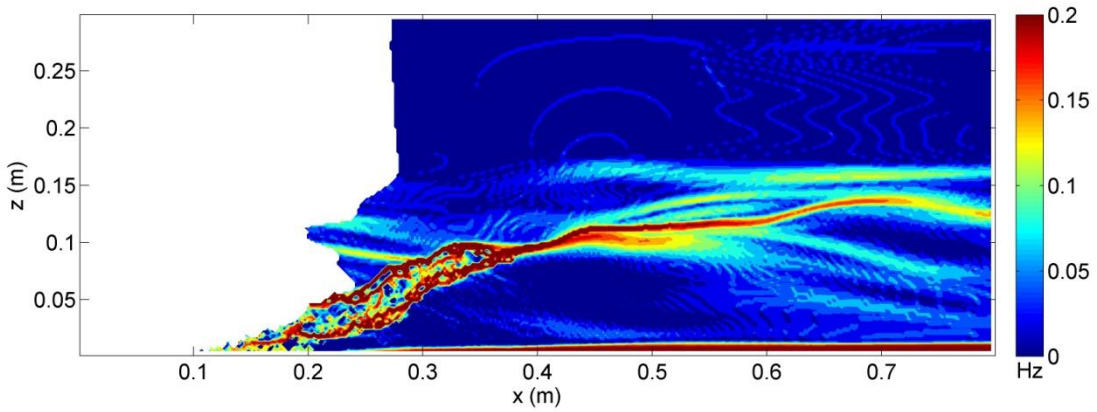

Figure 6.61: *FTLE vortex tracking. Areas in white represent regions where the trajectories could not be tracked sufficiently to give a reliable estimate. Ridges represent areas of greatest flow attraction.*

6.5.5 Velocity and plant spectra

Figure 6.62 shows the velocity and plant height spectra for this simulation. In contrast to the previous simulations, the velocity time series was not collected vertically above the vegetation, but instead was taken from downstream of the vegetation in order to avoid plant interference at a height just above the plant due to the large amount of plant movement. The canopy spectrum very closely follows the -5/3 Kolmogorov decay rate with little significant deviation from that trend at any frequency. This suggests that it is largely passive in response to the flow. This is to be expected given the low rigidity of the stems. The velocity spectrum exhibits a definite peak at roughly 0.7Hz as well as another potential lower frequency peak at roughly 0.1Hz. As has been discussed above, it is not appropriate to fit canopy shear layer vortex models to these results. Instead, the frequency should be compared to that associated with wake flapping.

However, this is not straightforward wake flapping behind a flagpole for instance; as the vegetation is attached to the bed and therefore the standard Strouhal number relationships do not apply. The wavelet analysis in Figure 6.63 again shows the dominance of a vortex of scale within the 1-2s band. This pattern is mirrored in the latter part of the plant height wavelet spectrum. This suggests that this vorticity is the result of a feedback between the flow and vegetation. The flow seems to be the driver of the motion, though this is most likely caused by the vegetation

configuration. The vegetation response to the flow is slow in initiating and appears to be a weaker signal.

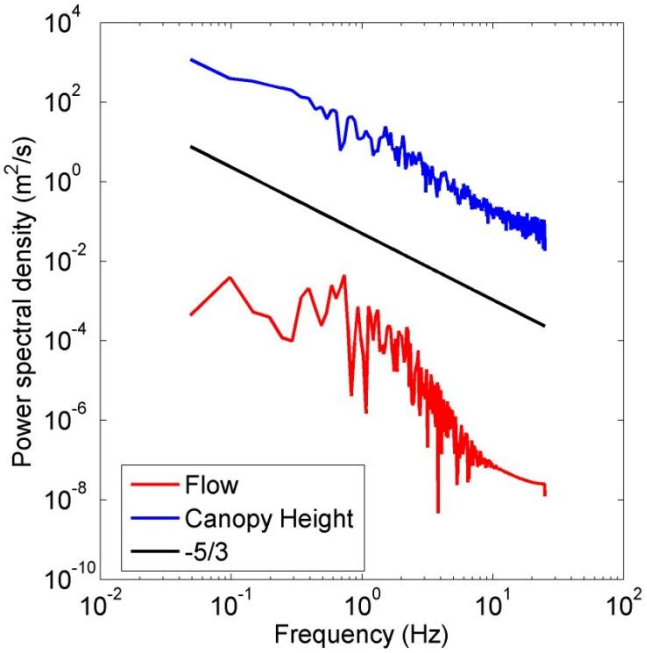

Figure 6.62: *Velocity (red) and canopy height (blue) spectra. The black line shows the Kolmogorov decay rate.*

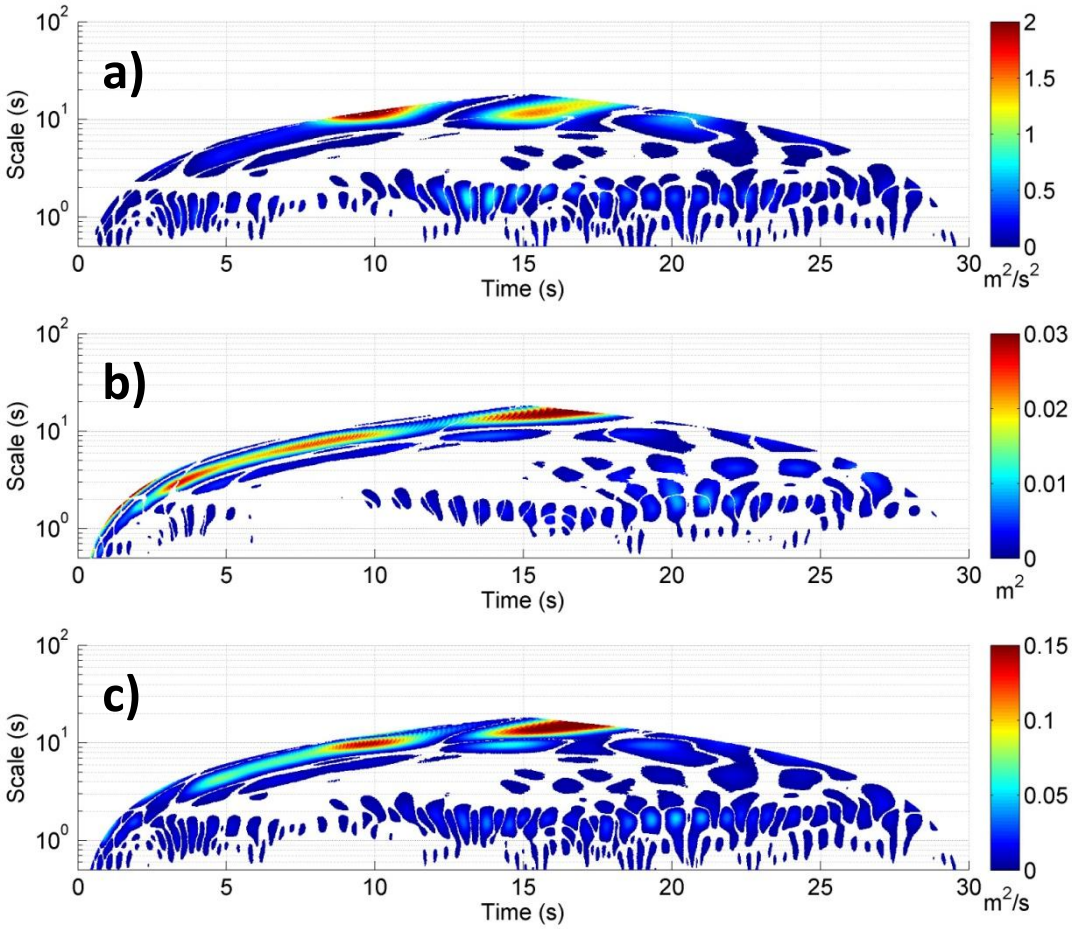

Figure 6.63: *Wavelet spectra for a) the velocity and b) canopy height time series and (c) cross spectra between the two time series.*

There is also some evidence of larger scale coherence in the both the flow and vegetation wavelet spectra, however as the majority of this occurs in the first half of the time series it is suggested that signal may correspond to initial reconfiguration of the plants. The cross-spectra in Figure 6.63 (c) highlights the association between the flow and vegetation signals for the high frequency 1-2s periodicity. Again, a large low frequency peak is detected, but it is suggested that this purely corresponds to the initial reconfiguration of the canopy.

6.5.6 Summary

In contrast to the simulations with the Euler-Bernoulli beam model, the results from this simulation with the N-pendula model cannot be characterised as a mixing layer profile. Instead, the individual stem position and morphology controls the local turbulence structure and vortex generation. The vortex detection methods and the spectral analysis both identify vortices within the flow, generated by the flapping stems and there are some hints that a larger scale feedback may exist between the flow and vegetation, however there is not enough evidence to fully explain this scenario.

In natural rivers, these plants are usually found in extended clumps or canopies, and therefore, to fully understand how they interact with the flow structure in natural rivers, a larger patch-size must be investigated.

6.6 Flow and plant dynamics over a large highly flexible canopy

In order to fully investigate the relevance of the canopy shear layer analogy over highly flexible vegetation, an entire canopy simulation is tested. In these circumstances one would expect the drag of the canopy to form a significant enough canopy zone to generate canopy layer vortices.

6.6.1 Experimental setup

For this simulation, a canopy of 300 stems was used within the same domain as the previous section (nx=400, ny=50, nz=150). The stems were placed in a staggered

arrangement, with a lateral and downstream separation of 0.012m. All other flow conditions were set as described in Section 6.5. The extra stems in the canopy led to a decrease in recirculated mean velocity, to approximately 0.3m/s and a Reynolds number of 12000. The simulation was run for 30 seconds, at a temporal resolution of 50Hz and took 936hrs CPU time. All analysis was undertaken in the x-z plane at $y/w = 0.5$.

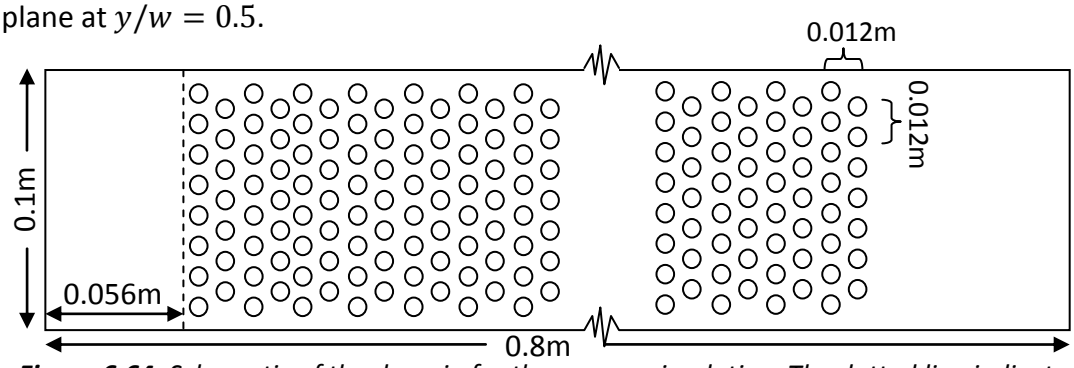

Figure 6.64: *Schematic of the domain for the canopy simulation. The dotted line indicates the extent of the recirculation region. This diagram is not to scale.*

6.6.2 Mean flow profiles and turbulence characteristics

In contrast to the small patch in the previous section, the larger canopy does appear to develop into a canopy shear layer, as shown by the profiles in Figure 6.65. There is very good agreement with the ideal velocity profile, and also significant similarities within the Reynolds stress profile. The differences within the Reynolds stress profiles suggests that although there is a canopy shear layer, there are other processes too which are contributing to the Reynolds stress.

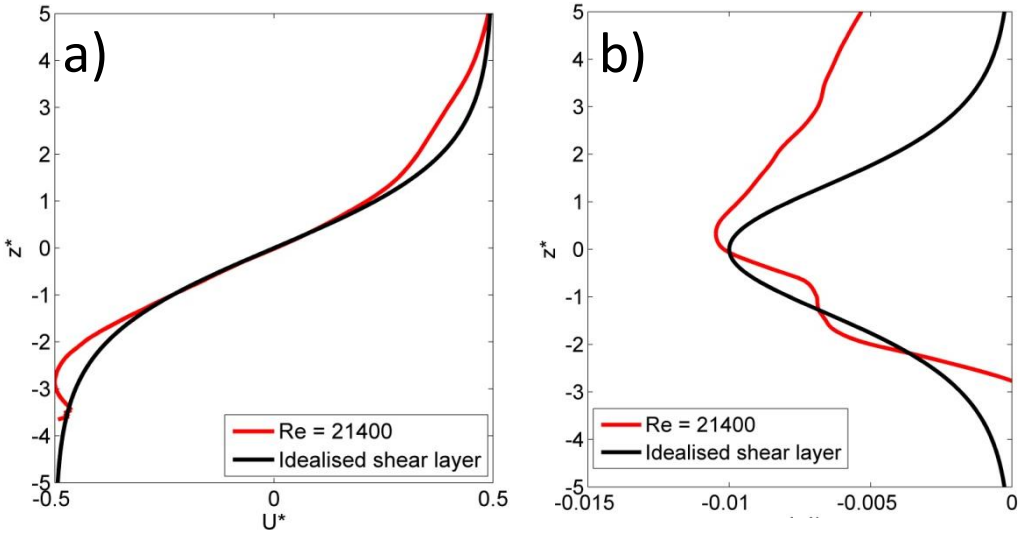

Figure 6.65: *Normalised vertical velocity profiles of the horizontally and temporally averaged (a) downstream velocity and (b) Reynolds stress. The idealised shear layer profiles are shown in back for comparison*

The time-averaged velocity map (Figure 6.66) indicates that the canopy shear layer extends along the whole domain, with little change due to plant morphology. This suggests that the canopy density is great enough that the dominant flow structure relates to the canopy shear layer, as in Section 6.4.

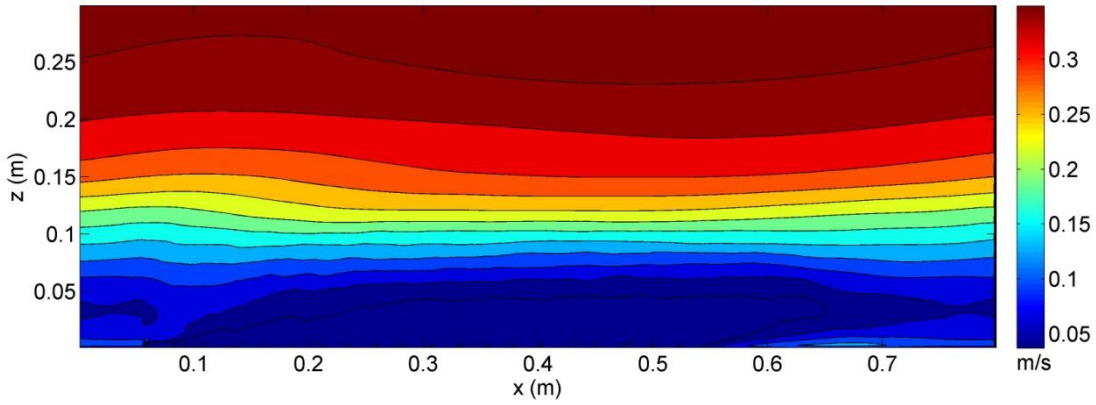

Figure 6.66: *Long-section of the time-averaged downstream (u) velocity.*

Despite the appearance of a consistent canopy shear layer profile throughout the domain, the time-averaged turbulent quantities identify regions of heterogeneity within the flow. Within the Reynolds stress signal there is a clear dominance at the front and back end of the canopy, presumably relating to wake and flow separation effects. It is in fact possible that the peak at the front canopy is caused merely by the recirculated wake effects rather than due to flow separation.

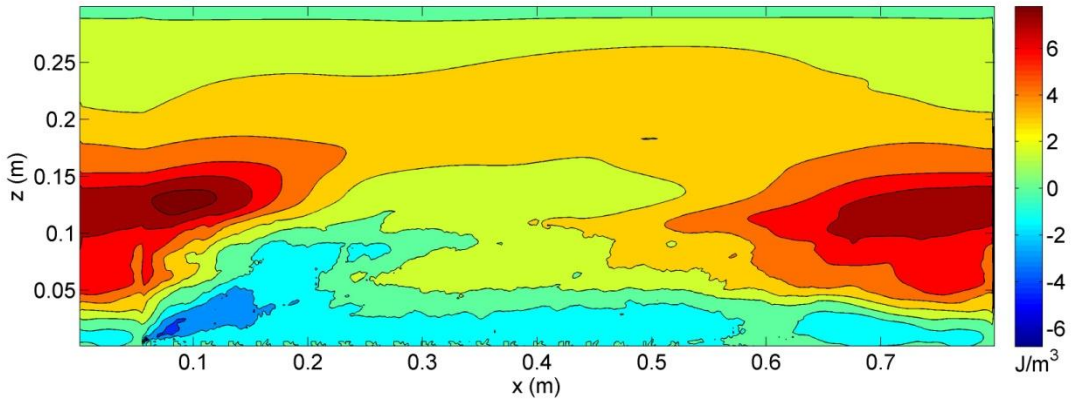

Figure 6.67: *Long section of the time-averaged Reynolds stress.*

The turbulent kinetic energy shows a more homogeneous pattern with high values of TKE along the entirety of the canopy top, though there are still obvious peaks at the front and back of the canopy. The TKE plot suggests that there is very little

penetration of turbulence into the canopy itself, with very low values in the mean canopy region

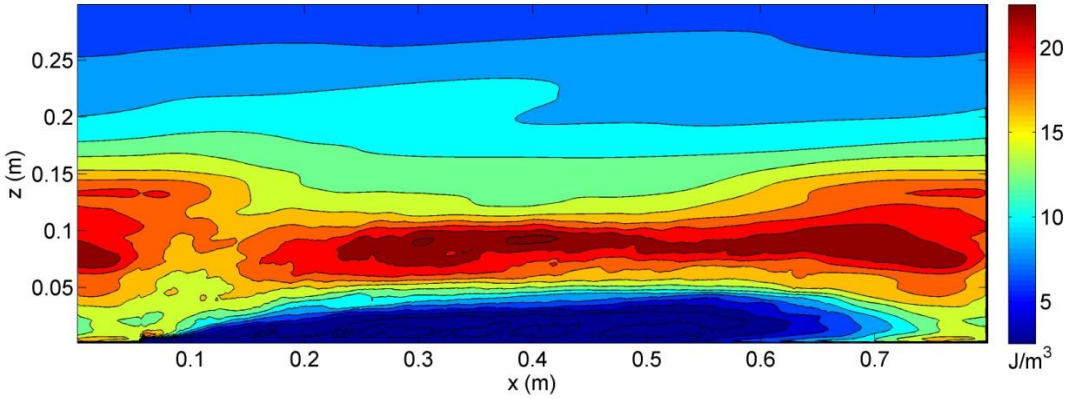

Figure 6.68: *Long-section of the time-averaged turbulent kinetic energy.*

6.6.3 Quadrant analysis

The vertical quadrant plots in Figure 6.69 show that when considering all turbulent events, there is a dominance of quadrant 4 sweep events at the canopy top and in the shear layer. Within the canopy, Q_3 events dominate, which is consistent with the findings in Section 6.4.3. Quadrant 2 ejection events are also present and appear to peak just above the canopy top suggesting that shear layer processes may be operating in that region.

When a hole size of H=2 is applied, the contribution of Q_2 and Q_3 events diminishes dramatically and only Q_1 and Q_4 events appear to contribute significantly. There is a clear peak in Q_4 sweep events at the canopy top, with Q_1 events dominating in the canopy. It is not clear why there is such a dominance of Q_2 and Q_4 events over Q_1 and Q_3 events.

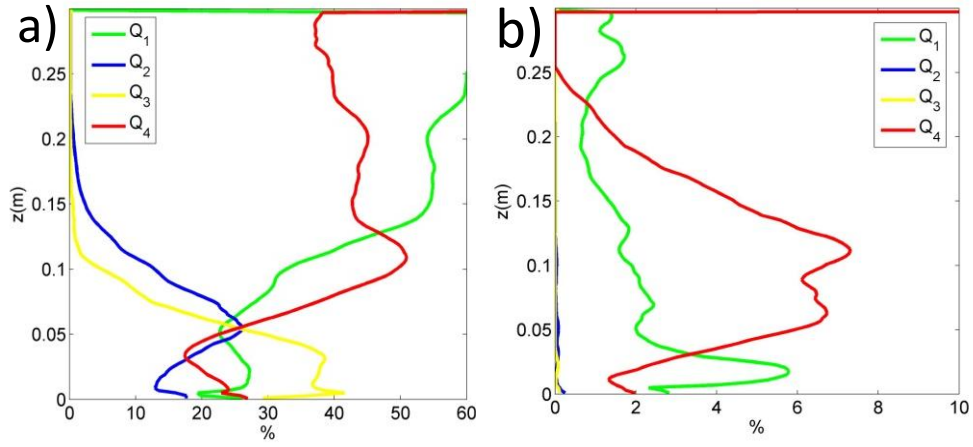

Figure 6.69: *Quadrant dominance over the entire simulation with a) H=0 and b) H=2*

Figure 6.70 highlights the spatial dominance of Q_4 events within the region of interest, except towards the front of the domain, where Q_1 events seem to dominate, potentially related to flow separation off the front of the canopy

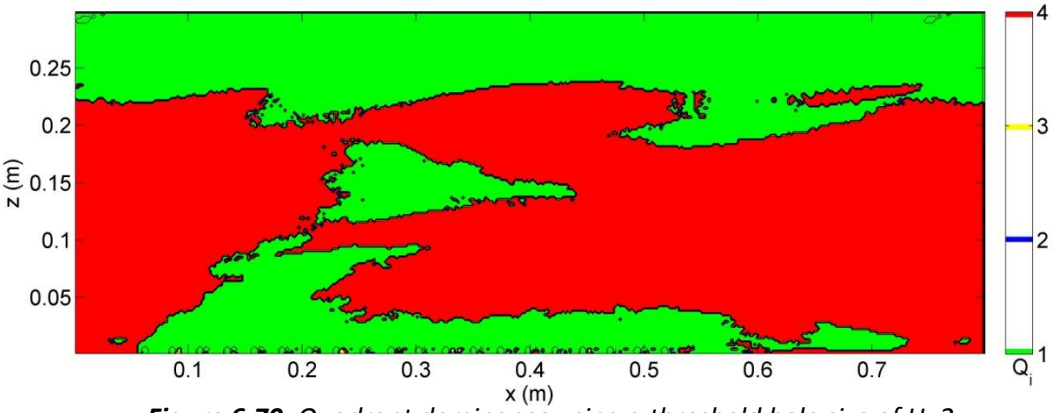

Figure 6.70: *Quadrant dominance using a threshold hole size of H=2.*

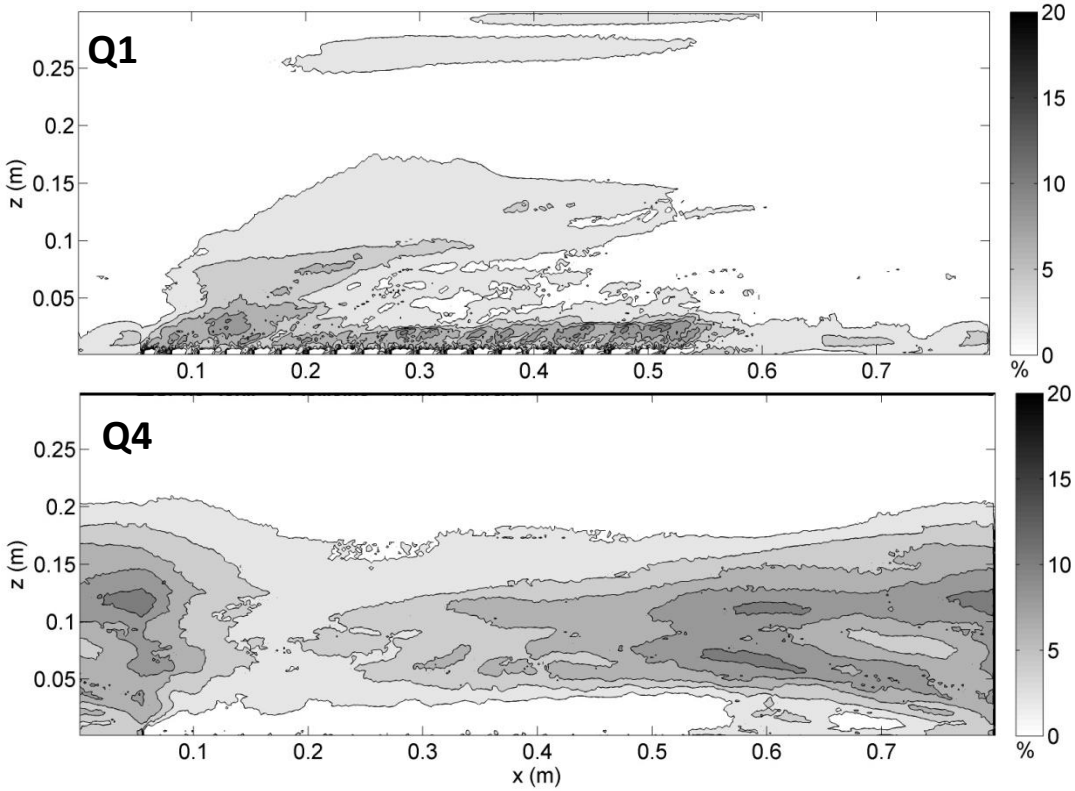

Figure 6.71: *Quadrant occurrence across the long-section as a percentage with H=2. The figures for Q2 and Q3 contained no signal and therefore have not been included.*

This is confirmed in Figure 6.71 that shows that with the exception of the canopy front, the distribution of Q_4 sweep events is reasonably uniform. This figure also shows that in some areas of the domain, high magnitude Q_4 events account for up to 15% of the flow which demonstrates a huge dominance of energy within sweep motions.

6.6.4 Vortex detection

A visual analysis of the FTLE fields and the different vortex methods reveals a highly complex pattern of vorticity across the domain. There is evidence of the existence of large-scale coherent structures as shown for a number of different instances in the FTLE snapshots in Figure 6.72. The predominant vortex generation mechanism appears to be K-H induced roller vortices, and there is generally good agreement with the schematic in Figure 4.10. However, the behaviour of some of these roller-type vortices is not as expected for a shear layer, with much higher angles in the flow and less obvious correspondence with the canopy shear layer (Figure 6.72c). Initially, this pattern looks similar to the FLTE trace caused by the wake flapping vortices in the small patch case. However, the corresponding vorticity plot (Figure 6.73c) shows that clockwise vorticity is very dominant in this region, suggesting that it more likely relates to a K-H instability.

There are also clear examples of K-H instabilities in the wake of the vegetation patch (Fig 6.72 b&d), which similarly do not follow the shear layer prediction of vortex evolution, occurring purely because of the recirculation region at the back of the canopy. Figure 6.72e shows the formation of a large wake vortex, caused by the sinking of a vortex created at the back end of the canopy and enhanced by the recirculation region. Figure 6.72a appears to show canopy shear layer generated vortices, though even here, the vortices appear to be displaced further above the canopy, perhaps due to the influence of the flow separation at the canopy front.

These results suggest that there are a number of active vortex generating mechanisms within the flow. It is difficult to classify exactly which have been generated by the canopy-shear layer mechanism as they have all been produced by similar K-H regimes. The first case however none of these are sufficiently well-defined within the flow to allow tracking of individual vortices.

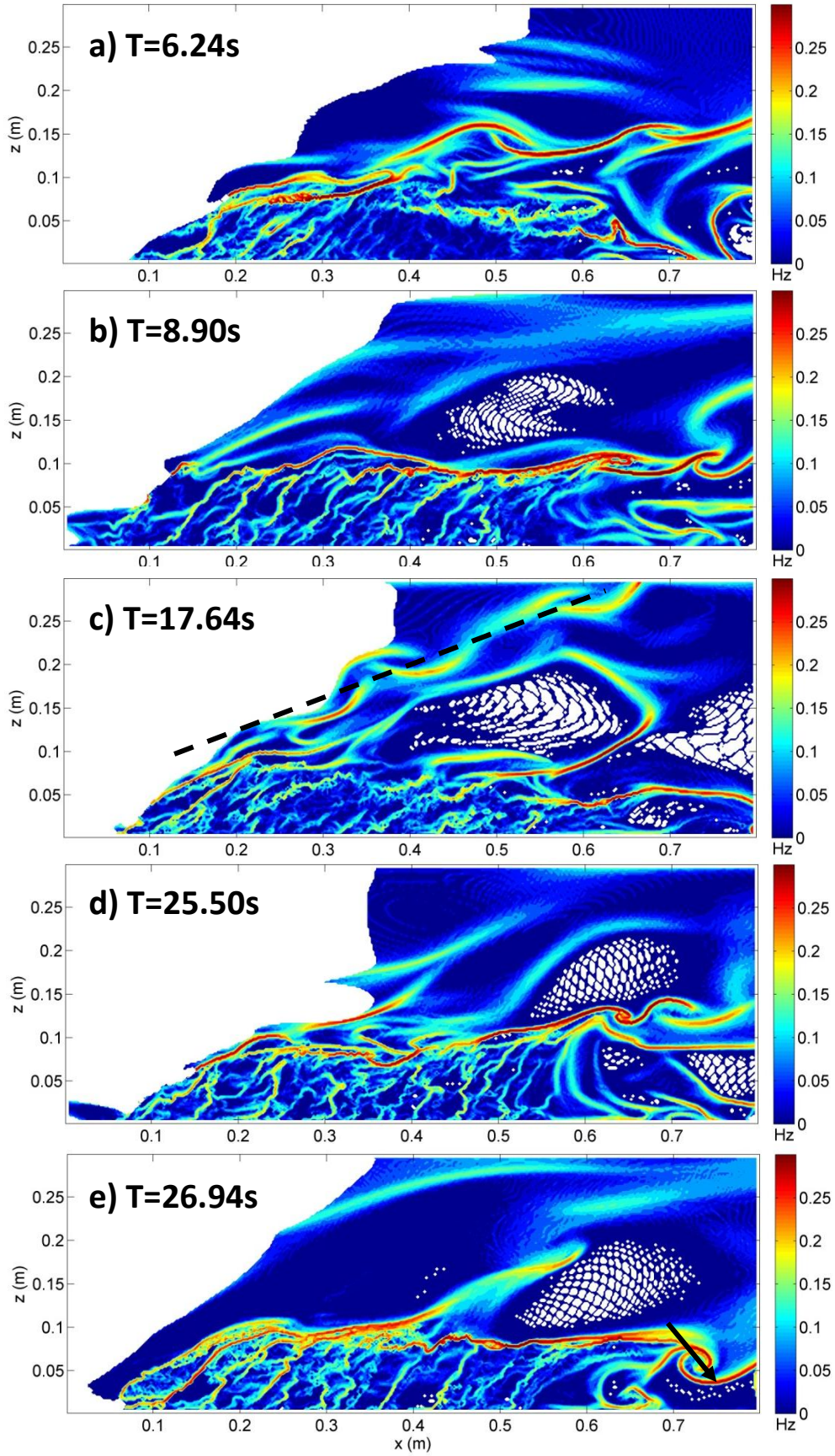

Figure 6.72: *Snapshots from the FTLE field at particular time-steps showing different vortex generating mechanisms.*

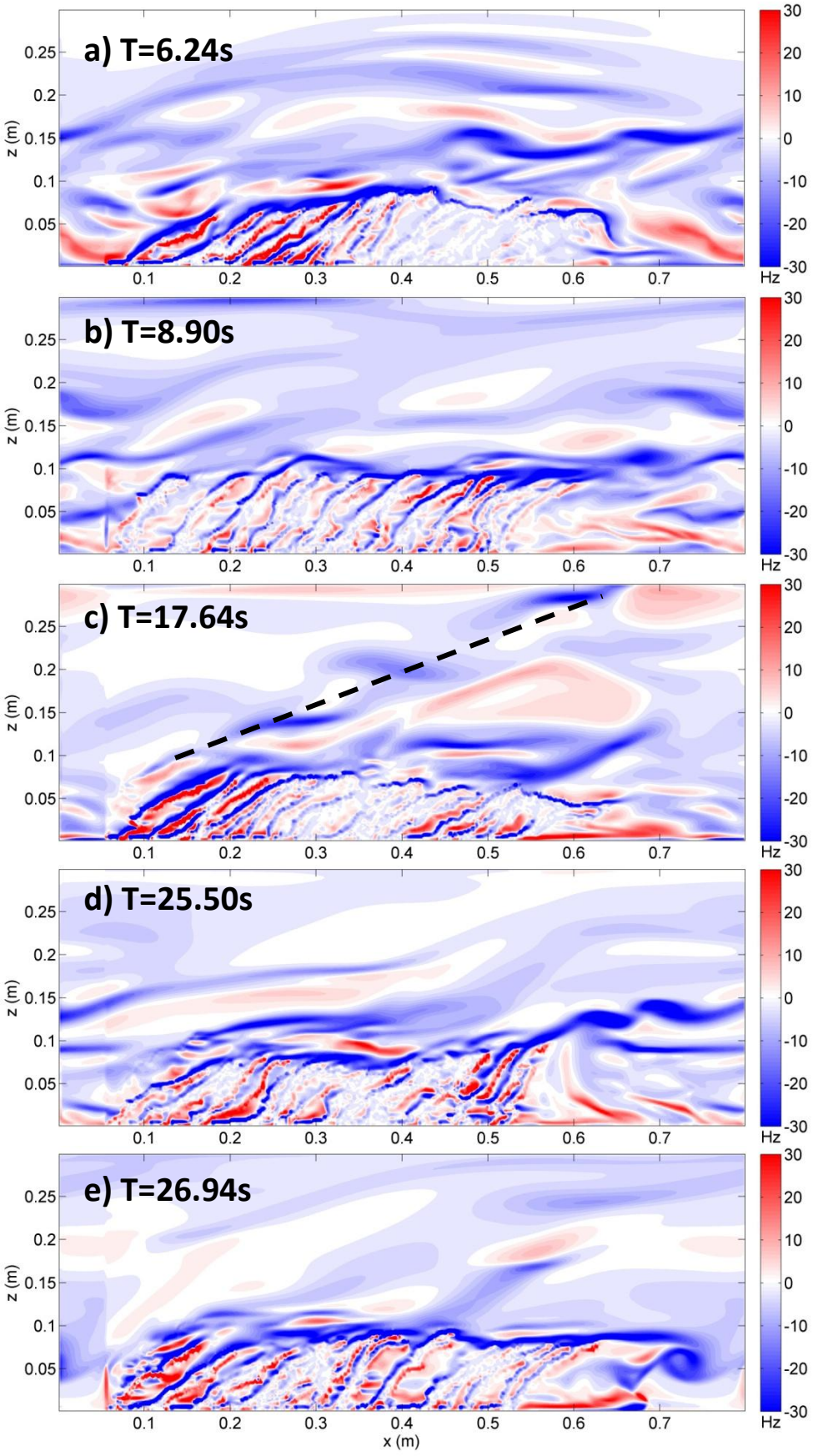

Figure 6.73: *Snapshots from the vorticity field at particular time-steps showing clockwise (blue) and anticlockwise (red) vorticity.*

The corresponding vorticity plots (Figure 6.73) for the FTLE snapshots in Figure 6.72 show good agreement with the expected vortex locations. Compared to the Euler-Bernoulli beam model patch and canopy cases, there is more anti-clockwise vorticity present, suggesting the presence of a wake-flapping mechanism. However, the clockwise vorticity generally has a larger magnitude above the canopy, implying that shear-generated K-H instabilities dominate over individual wake flapping.

The Eulerian vortex method results are not included here as the turbulence signal was too noisy to allow extraction of information regarding the evolution of individual vortices. The results do support the FTLE results (Figure 6.72), with corresponding regions of vorticity identified in each case, but do not add anything to the analysis in this case.

6.6.5 Velocity and plant spectra

The velocity spectrum taken for a point just above the canopy (Figure 6.74) shows a wide peak with a maximum at approximately 0.6-0.7Hz followed by a steep decay. In contrast, the plant spectra follows a slope of -5/3 until approximately 5Hz at which point the spectrum flattens considerably.

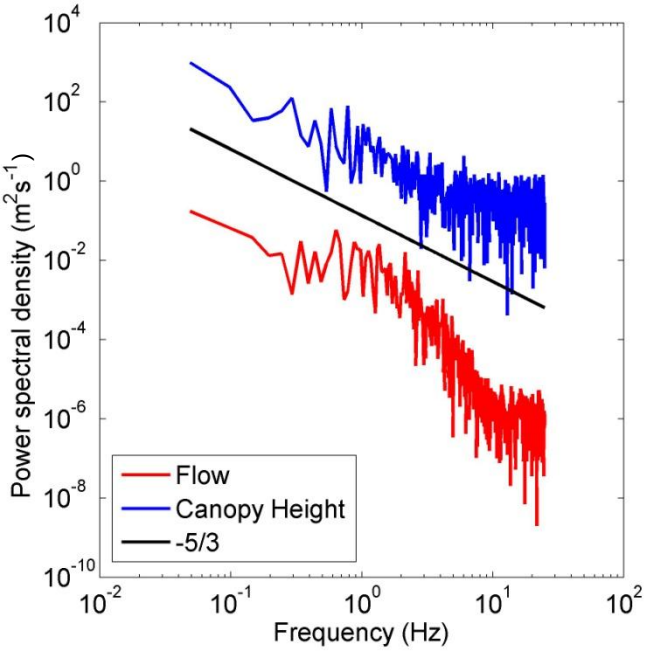

Figure 6.74: *Velocity (red) and canopy height (blue) spectra. The black line shows the Kolmogorov rate of decay*

This figure is substantially different to the predicted shear layer frequency (Table 6.5) thus confirming that a high proportion of the turbulence does not directly relate to canopy shear scale turbulence. The peak between 0.6 and 0.7Hz does agree well with the frequency found in Section 6.5 with the small patch, suggesting that both have a common turbulent production mechanism. This would seem to most likely relate to the plant flapping motion, though there is not a clear indication of this scale of motion within the plant canopy spectrum.

Mechanism	Frequency
f_{KH}	0.44Hz

Table 6.5: *Key frequencies active within the flow. f_{KH} is the Kelvin-Helmholtz frequency. Wake-scale turbulence is not included her as the inclination of the stems means that the effective radius is substantially different.*

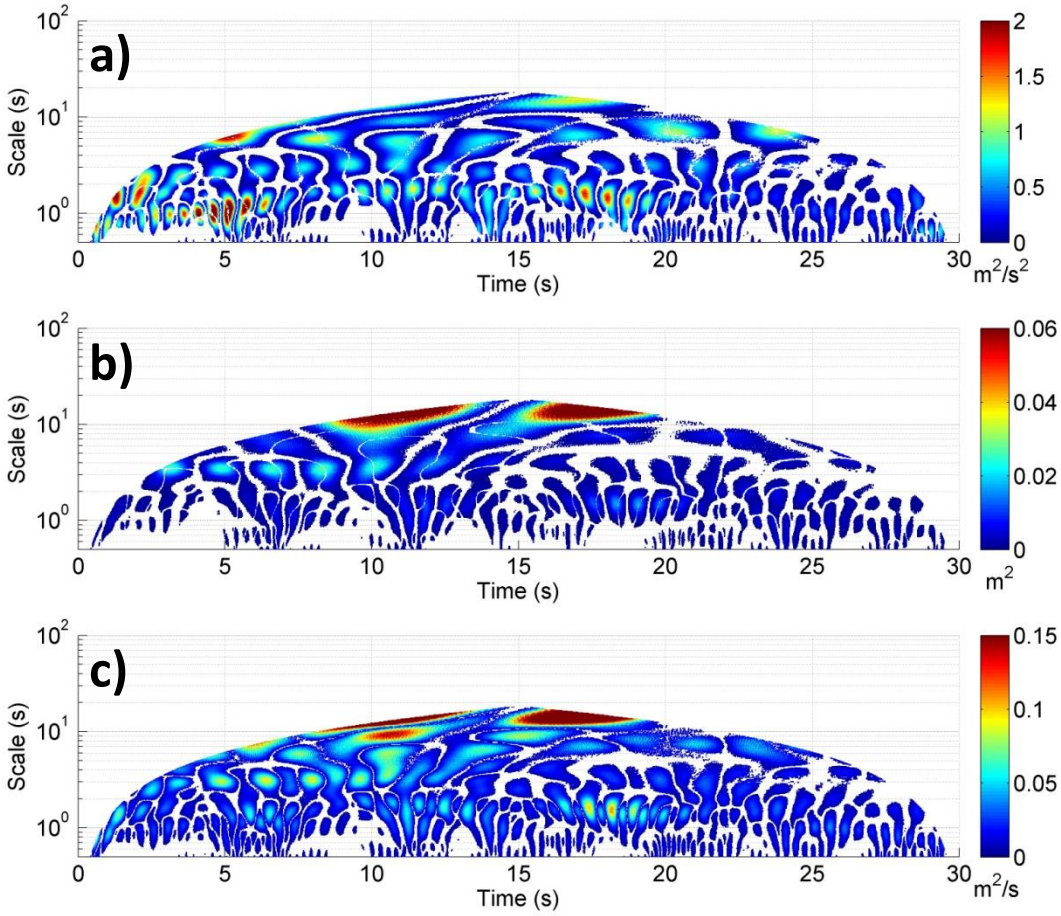

Figure 6.75: *Wavelet spectra for a) the velocity and b) canopy height time series and (c) cross-spectra between the two time series.*

The wavelet spectra confirm the presence of a dominant frequency between 1-2s (0.5-1Hz), which similarly to the small patch case seems to oscillate between different scales through time. There is also evidence of a lower frequency signal, particularly at the beginning of the simulation, which may be related to the recirculation of turbulence caused by the initial canopy reconfiguration. The complexity of the turbulence in comparison to the other cases is demonstrated by the wide range of scales of turbulence within the flow as well as the connections between the scales, which contrasts with the beam model cases which displayed distinct scales with limited interaction.

6.6.6 Summary

Implementing the N-pendula model for an entire patch it has been shown that within highly flexible canopies an inflected velocity profile develops, similar to that found in semi-rigid canopies, as shown through vertical flow profiling.

However, the turbulent signal is far more complex than that found over semi-rigid canopies. There appears to be a weaker canopy shear scale turbulence signal, and interaction between a number of different vortex generation mechanisms, including individual plant motion. The dominant frequency within the flow does not appear to correspond to the canopy shear scale, but instead is similar to the peak found in the small patch case (Section 6.5) and therefore it is hypothesised that this relates to plant flapping, though this is inconclusive from the canopy spectra.

This case has demonstrated the complexity of highly flexible canopies and the difference in processes compared to those operating in semi-rigid vegetation. It is clear therefore that the treatment of highly flexible canopies should therefore be distinct from generic canopy layer theory, as developed for semi-rigid terrestrial canopies.

6.7 Drag as a driver of stem motion

As previously discussed in Chapters 2 and 3, drag is a key force which drives the dynamic interaction between flow and vegetation. The assumption often used in models of vegetation is that the drag coefficient, used to calculate the drag force, is

constant and is equal to 1 (e.g. Fischer-Antze *et al.*, 2001). In order to investigate the validity of that assumption, two test model runs were conducted, each with a single vegetation stem, modelled using the Euler-Bernoulli beam equation.

One model was driven using the assumption of a constant drag coefficient equal to 1, whilst the other was driven by an in-built drag calculation procedure as outlined in Chapter 3. This in-built drag procedure calculates the drag from the pressure distribution around the stem.

6.7.1 Experimental setup

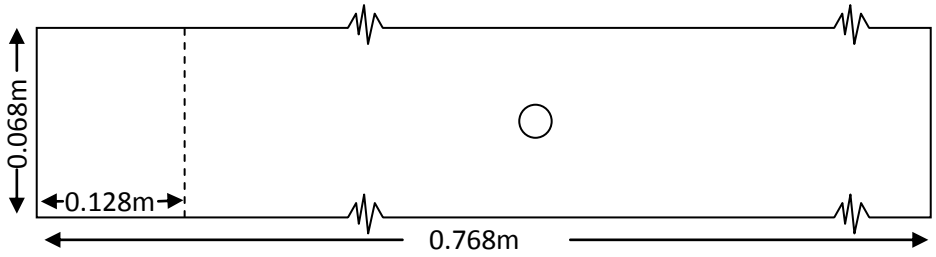

Figure 6.76: *Schematic of the numerical domain for the single stem simulation.*

For this simulation the domain was setup identically to the small patch case in Section 6.3 except that only a single stalk was used (Figure 6.76). This stalk was placed in the centre of the domain. The simulation was run for 30 seconds at a temporal resolution of 50Hz and took 400hrs CPU time to complete. In order to identify the effect variable drag has on plant position, motion and consequently on flow, time series from the flow and vegetation will be analysed visually and using wavelets.

6.7.2 Comparison of flow and vegetation data

The plant height time series for the constant and variable drag simulations are shown in Figure 6.77. Two differences are immediately apparent. First, the stem with the constant drag coefficient maintains a lower position in the flow throughout the simulation. Second, there is much greater variation in canopy height in the directly calculated drag model. The first observation can be explained by the fact that plant reconfiguration is a drag reduction mechanism of vegetation (Sand-Jensen, 2003). Therefore, as the plant reconfigures, drag will naturally reduce, however this reduction is not accounted for by the constant drag coefficient.

Therefore, the drag remains high and the plant is subject to further reconfiguration, thus occupying a lower position in the flow.

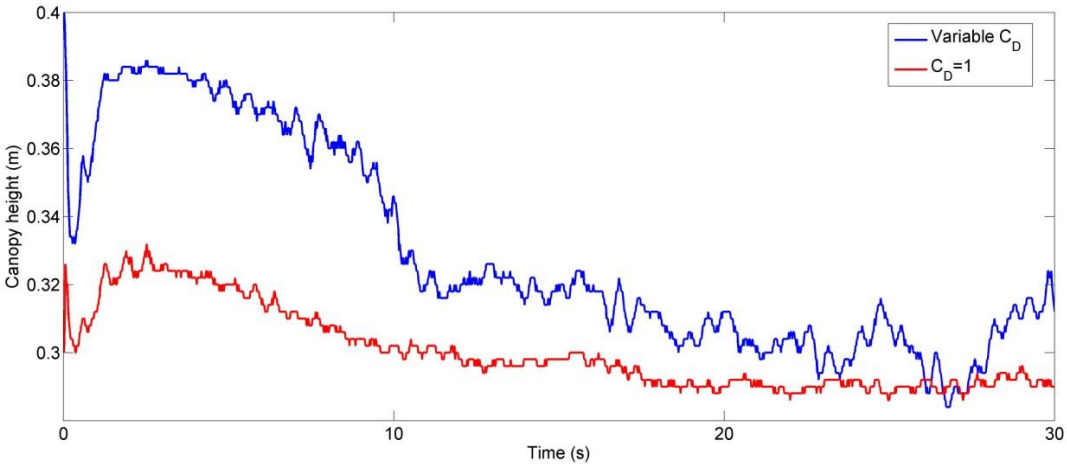

Figure 6.77: *Canopy height time series from the constant (red) and variable (blue) drag coefficient simulations.*

The second observation is a consequence of the model reaching a stable equilibrium for the constant drag coefficient. This does not mean that there is no plant movement, as shown in Section 6.3 where there was clear plant response to the flow. However it does mean that drag acts as a constant dampening effect on the flow, effectively reducing the variability in the drag, which is one of the key forces driving the flow. The drag is still dependent on local velocity, but every other term is constant. These results confirm the idea that constant drag coefficients are inaccurate and inappropriate for modelling flexible vegetation, as they lead to both a false average canopy height and variation in canopy height.

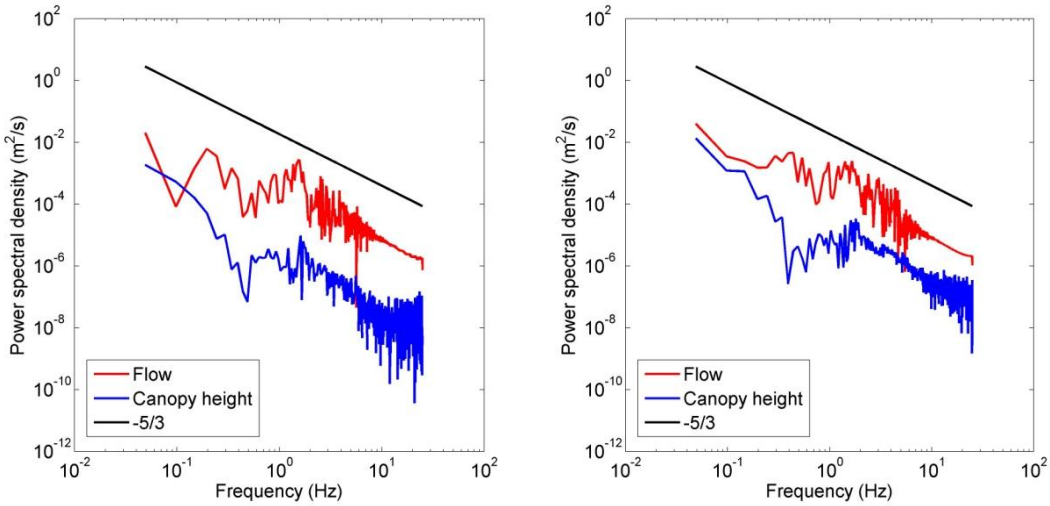

Figure 6.78: *Flow and canopy height spectra from the constant (left) and variable (right) drag coefficient simulations*

Figure 6.78 shows the velocity and plant spectra from the two different model runs. Both graphs have the same overall shape, though there is a definite upward translational shift of the plant spectrum in the drag-calculation case, suggesting that there is more energy and therefore more oscillation. There is a sharper peak at the natural frequency (≈2Hz) in the constant drag coefficient case. This is expected as the vegetation motion is less directly coupled to flow conditions and therefore there is less feedback and interference with the signal from the vegetation. However, there is no clear evidence of an increased coupling between the vegetation and the flow vortex frequency in the variable drag simulation.

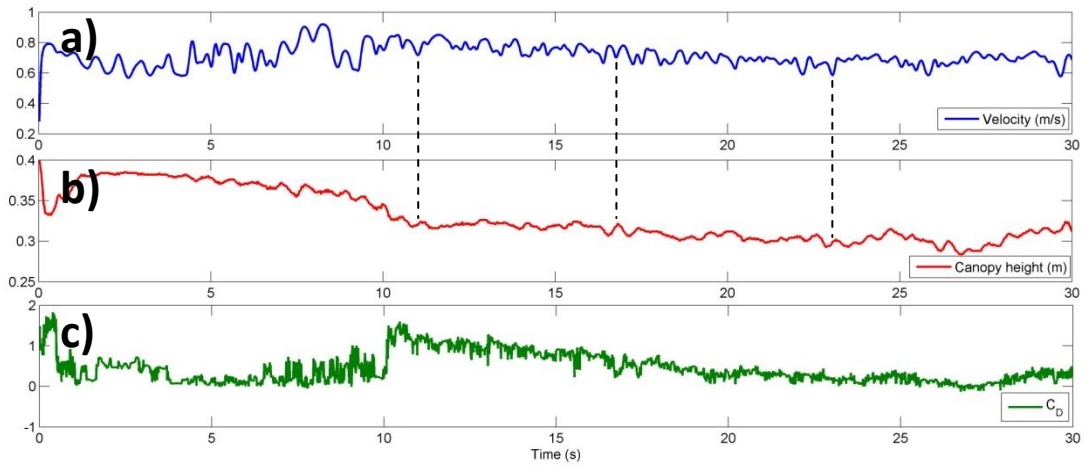

Figure 6.79: *Time series for the (a) flow, (b) canopy height and (c) drag coefficient for the variable drag simulation.*

Figure 6.79 shows that again, there is little visual evidence of direct coupling between flow structures and canopy height. There a few incidences where lower canopy height clearly corresponds to higher velocities, as shown by the dotted lines. In these cases there is a very slight lag, with the vegetation reconfiguring after the velocity spike. There is also a clear connection between drag coefficient and canopy height, with drag decreasing as canopy height decreases and the plant reconfigures.

The drag profile up the entire stem through time is shown in Figure 6.80. There is a clear spatial pattern, with much lower values for the drag coefficient at the top of the stem, where reconfiguration is greatest. It is notable that there is an order of magnitude difference between the drag coefficient values at the top and bottom of the stem. Furthermore, Figure 6.80 highlights the temporal variation in drag. Even

in the stable, rigid region of the stem near the bed, there is significant variation in drag through time. This variation appears oscillatory in nature.

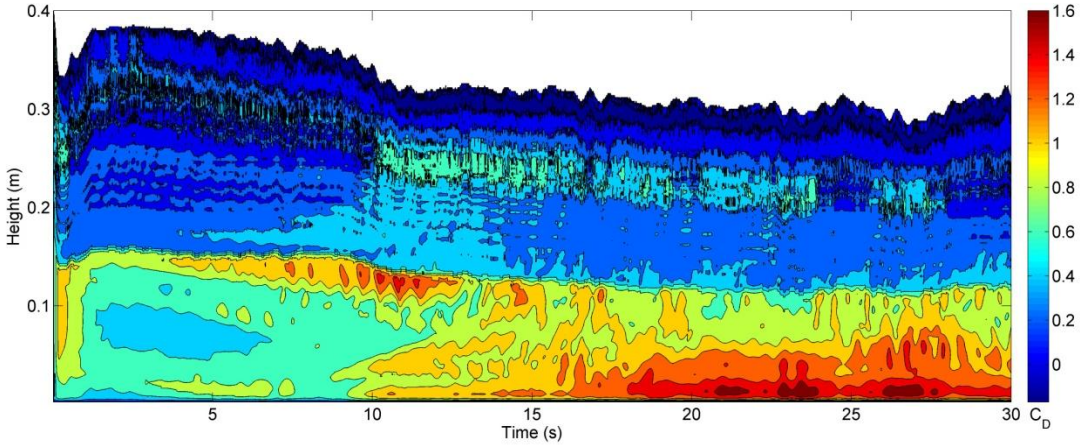

Figure 6.80: *Drag coefficient profile along the stalk and through time.*

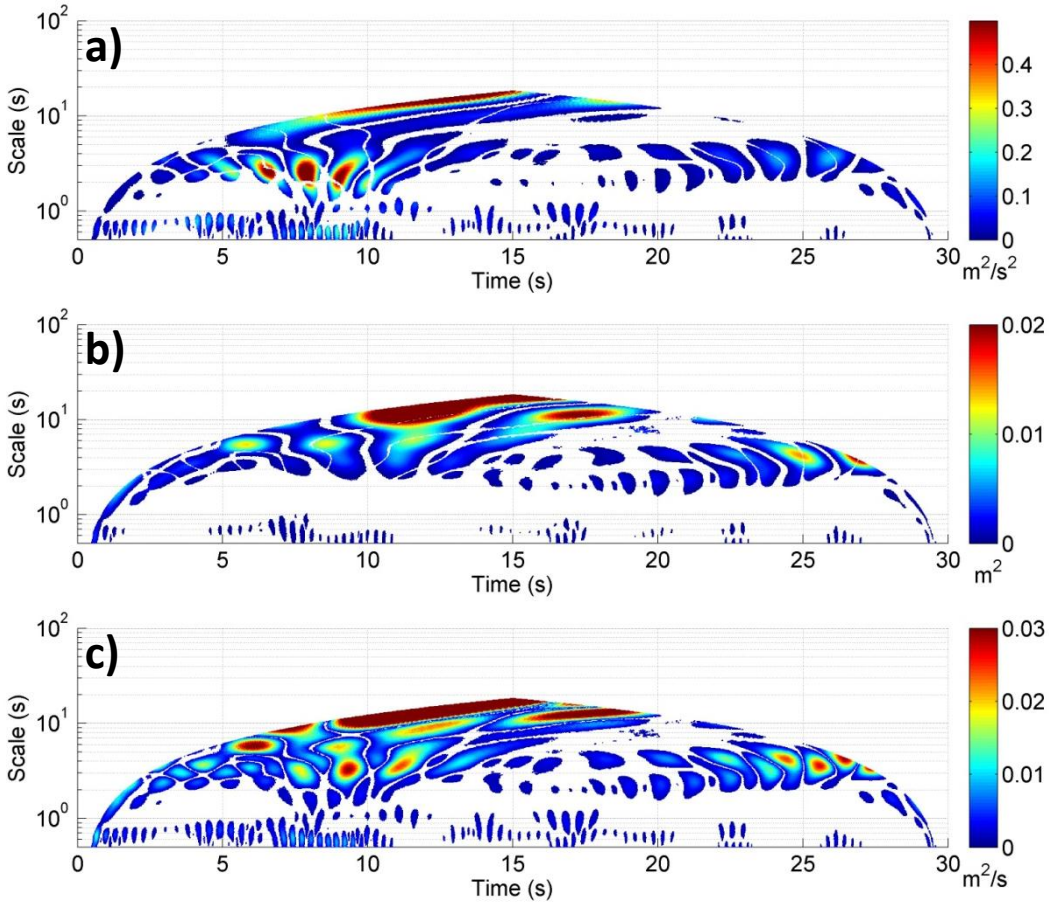

Figure 6.81: *Wavelet spectra for the variable drag simulation. The three graphs correspond to the (a) flow, (b) canopy height and (c) cross wavelet spectra.*

In places, the values of the drag coefficient appear higher than expected. There are a number of potential reasons for this. The vegetation is represented in the domain using a porosity approach. Therefore, although the blockage represents a cylinder,

it is represented within a hexahedral grid and this may represent a slightly rougher boundary, causing higher drag values

Figure 6.81 and Figure 6.82 shows the wavelet spectra from both the variable and constant drag simulations. The spectra are broadly similar, with evidence of both small scale and large scale turbulence visible. There is a noticeable difference in magnitude between the canopy spectra, with the variable drag simulation showing peaks over twice the magnitude.

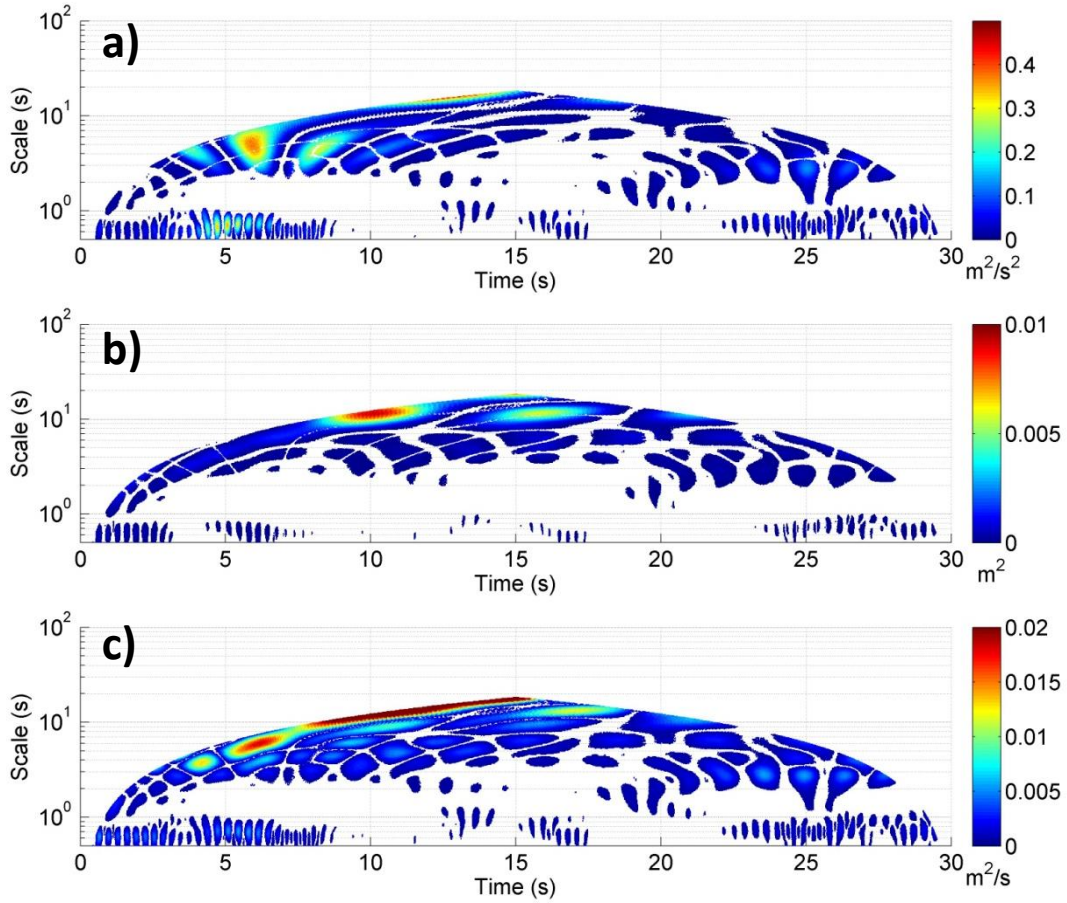

Figure 6.82: *Wavelet spectra for the constant drag coefficient simulations. The three graphs show the (a) flow, (b) plant and (c) cross wavelet spectra.*

Furthermore, the cross-spectra (Figure 6.82-3, c) show the emergence of regions of association between the flow and canopy in the variable drag simulation. These do exist within the constant drag simulation but are an order of magnitude smaller.

6.7.3 Summary

The introduction of a variable drag coefficient into the beam model significantly alters the predicted vegetation movement. In particular, the vegetation assumes a

higher position in the flow due to the reduction in drag achieved by reconfiguration and the plant is also subject to greater movement throughout the simulation due to the explicit dynamic linkage of the drag force to the flow field.

This variability in drag force is shown to be both temporal and spatial in nature, and this impacts upon the plant motion and consequently turbulence structure as evidenced in the spectral and wavelet plots. Thus, although no direct evidence has been found of a distinct change in the flow-plant interaction for the variable drag case, it is hypothesised that over a larger canopy simulation, this difference would become apparent.

These results highlight the ineffectiveness of constant drag coefficients in flexible vegetation models, and introduce a new methodology for high resolution drag modelling. Furthermore the results also highlight the natural spatial and temporal variability of drag along the stem, questioning the applicability of a constant drag value of 1 to even rigid stem models.

Further work is required to implement this approach within a canopy environment and to refine the drag calculation mechanism. In addition, work is required to apply the implications of these results within lower resolution models.

6.8 Conclusion

This chapter has investigated the flow and plant dynamics in a range of different types of canopy flows. Both of the models developed in Chapter 3 are shown to be useful as research tools for investigating the turbulent flow dynamics around vegetation, and the interaction between vegetation and the flow in canopy flows.

The Euler-Bernoulli beam model has been used to investigate canopy dynamics and the evolution of vortices over large and small canopies and the nature of the feedbacks and interactions between flow and vegetation in mixing layer environments with semi-rigid vegetation. The results have been shown to agree well with existing literature as well as giving insight into processes, such as the coupling of plant motion and velocity signals, not previously studied.

The N-pendula model has been used to investigate the dynamics of highly flexible vegetation canopies and single plants. Using this model it was shown that within smaller canopies, the turbulence appears to be dominated by vortices shed due to the flapping of the stem, rather than any wake-shedding or shear layer vortices. With a larger canopy of stems, there is more evidence of the development of a canopy shear layer, though the vortex signal is far noisier and still shows a clear influence from the plant flapping vortex mechanism. This model therefore provides an alternative method for modelling highly flexible vegetation, where the driving processes are distinctly different.

Finally, it has been demonstrated that there is a need for a new, dynamic treatment of drag within high resolution vegetation models. A new methodology has been proposed and tested for a simple case. The results indicate that this is a promising alternative to the constant drag approach, which offers a better process-representation of the dynamic interactions between plants and the flow. However there was little evidence that across the board, these conditions led to a significant canopy layer development.

The results of this chapter support existing theories regarding canopy layer theory as well as providing additional insight in certain topics. Therefore it is important to incorporate these findings within our current understanding of canopy layers. To that end, the results of this chapter are synthesised and discussed, within the context of current canopy layer theory in Chapter 7.

Chapter 7: Discussion of micro-scale processes in vegetated channels

7.1 Introduction

The aim of this chapter is to set the findings of Chapters 5 and 6 within the context of our current understanding of aquatic flow-vegetation interaction as presented in Chapter 2. Specifically, this chapter focuses on comparing the results with the most recent state-of-the-art reviews of vegetated channel hydrodynamics of Nikora (2010) and Nepf (2012a; 2012b).

One of the most significant contributions of these reviews has been the distinction between different types of vegetation, each driven by different force balances. This classification framework is revisited in Section 7.2. Having established this, the results from Chapters 5 and 6 are synthesised within this framework. Finally, the implications of these results for future vegetation modelling are discussed.

7.2 Classification by force balance

Chapter 2 discussed in detail the current theories relating to terrestrial and open-channel vegetated flows. Until recently, little effort had been made to categorise these vegetation types by biomechanical characteristics and, as a result, generalised canopy layer theory was developed without allowance for different vegetation types. Given that the origins of canopy layer theory lie in terrestrial canopies, much of this theory has been developed under the assumption of rigid or semi-rigid vegetation, such as reeds, crops and grasses. Therefore, this generalised theory is not necessarily transferable to other, less idealised canopies.

Generalised canopy layer theory is typically applied to aquatic vegetation, with most experiments (Luhar and Nepf, 2013) and numerical models (e.g. Kutija and Hong, 1996; Ikeda *et al.*, 2001; Kim and Stoesser, 2011) assuming a similar rigid or

semi-rigid vegetation structure. However, a small number of flume and field experiments (e.g. O'Hare *et al.*, 2007; Siniscalchi and Nikora, 2012) with real vegetation have been conducted. Furthermore, recent numerical model developments within the fields of coastal and estuarine flow (e.g. Abdelrhman, 2007; Backhaus and Verduin, 2008; Dijkstra and Uittenbogaard, 2010) have also sought to deal with the case of more flexible vegetation. These studies have involved both aquatic macrophytes and marine seagrasses. Thus our current understanding has begun to recognise and distinguish between vegetation of significantly different biomechanical characteristics and the corresponding, variations in canopy processes.

As discussed in Section 2.3.4, this distinction was initially made by Nikora (2010) who used the terms 'tensile' and 'bending' plants to refer to those plants experiencing different physical controls on plant motion. This classification is made by analysing the ratios between internal and external forces acting on the vegetation. The three most significant forces acting on the vegetation are the drag force (F_D), the buoyancy force (F_B) and the rigidity or bending force (F_R) (Ghisalberti and Nepf, 2002). Nepf (2012b) identifies two parameters which define these force balances: i) the Cauchy number (*Ca*) which is the ratio of the drag force and the rigidity force and; ii) the Buoyancy number (*B*) which is the ratio of the buoyancy and rigidity forces.

$$B = F_B/F_R \tag{7.1}$$

$$Ca = F_D/F_R \tag{7.2}$$

Nikora (2010) distinguishes between different plant morphologies (tensile and bending) based only upon the Cauchy number. A high value of the Cauchy number implies a 'tensile' plant, whereas a low value indicates a 'bending' plant. The Cauchy number, described as the elastohydrodynamical number (Schouveiler and Boudaoud, 2006), has been used in various studies to try to parameterise drag and the reconfiguration of flexible bodies in fluid flows according to plant morphology (e.g. Gosselin *et al.*, 2010; Gosselin and de Langre, 2011).

Luhar and Nepf (2011) extended this approach by characterising the vegetation behaviour using both the Cauchy and the Buoyancy number. They used these two parameters and their ratio ($B^{-1}Ca$), which between them represent the three different force balances, to predict plant reconfiguration. Thus, this categorisation approach has been shown to be a useful framework within which to characterise and study the interactions between plants and flow. Therefore, the findings of Chapters 5 and 6 will be summarised within this framework.

For terrestrial canopies, due to the low density of the fluid (approximately 1.7kgm^{-3}), no vegetation is positively buoyant and therefore it is a reasonable assumption that the vast majority of plants are 'bending' plants. For aquatic vegetation, given the relatively high density of the fluid (approximately 998.1kgm^{-3}) and the fact that many plants contain gas filled lacunae or cavities (Penhale and Wetzel, 1983), it is possible for aquatic plants to be positively buoyant (Luhar and Nepf, 2011). Therefore, aquatic plants might be classified as either 'bending' or 'tensile'.

For the purpose of this thesis, only two categories (bending and tensile) have been considered. It is important to note that plants may not fall into either category but may be transitional, being equally subjected to both tensile and bending forces. Similarly, the Cauchy and Buoyancy numbers represent a spectrum of different force balances rather than two simple categories. Nevertheless, this categorisation provides a useful initial framework and therefore the results of this thesis are classified within this framework, defined in terms of both the Cauchy and Buoyancy numbers.

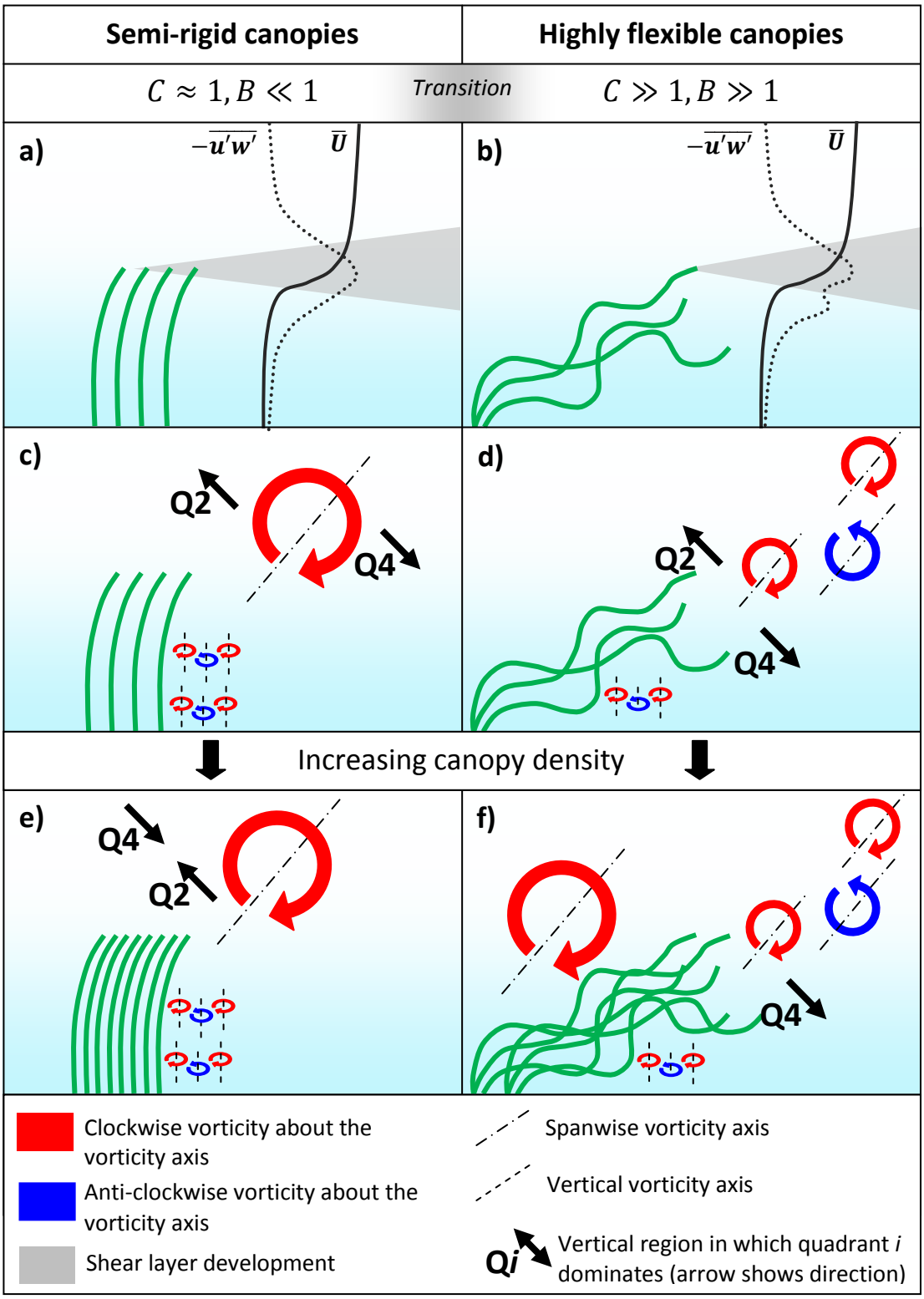

Figure 7.1: *Schematic diagram showing the canopy layer velocity and shear profiles (a & b), and turbulent processes within sparse (c & d) and dense (e & f) canopies. The canopies are split by Nikora's (2010) classification into semi-rigid (bending) plants and highly flexible (tensile) plants.*

7.3 Processes in semi-rigid, bending canopies

The results in Chapter 6 showed that for semi-rigid, bending canopies (e.g. grasses, *Phragmites australis*) the canopy shear layer velocity profile (Figure 7.1a) agrees well with that found in previous studies (e.g. Ikeda and Kanazawa, 1996; Ghisalberti and Nepf, 2002). Similarly the Reynolds stress profiles showed good agreement with previous work (Rogers and Moser, 1994; Ghisalberti and Nepf, 2006), while the actual magnitude and thickness of the Reynolds stress peak exhibited a dependence on stem density. The predicted canopy shear layer was shown to develop in a linear fashion similar to that predicted for an analogous free shear layer (Sukhodolova and Sukhodolov, 2012).

As discussed in Chapter 6, simulations were run for a few stems (small patch) and then 300 stems (large patch). Assuming the entire lower portion of the domain is considered as the canopy region, these two conditions can be generalised as low density, heterogeneous canopies and higher density more homogeneous canopies respectively. This is reflected in the results in Chapter 6, where the increased number of stems caused a more homogeneous and stronger canopy shear layer, consistent with a higher stem density (Nepf and Ghisalberti, 2008). Therefore, this generalisation of high and low density canopies is used in analysing the results.

For the more heterogeneous system, with a lower canopy density (Figure 7.1c), the canopy shear layer led to the generation of spanwise roller vortices (Finnigan, 2000). Analysing the high magnitude turbulent events revealed a dominance of quadrant 4 (sweep) events at the canopy top with a dominance of quadrant 2 (ejection) events just above, as previously observed by Okamoto and Nezu (2009). This is in agreement with the model of Finnigan *et al.* (2009), previously developed for terrestrial canopy flows, which linked the occurrence of sweep and ejection events to the passage of hairpin vortex pairs (Figure 7.2).

As the stem density was increased to form a more homogeneous and higher stem density canopy (Figure 7.1e), the effects of canopy blockage and subsequent limit of transfer between the canopy and the flow above led to a change in distribution

of turbulent quadrant events. The canopy-scale roller vortices were still present, however the distribution of quadrant events resembled more closely the model of Adrian *et al.* (2000) for terrestrial boundary layers (Figure 7.3). Thus, it is hypothesised that for particularly high canopy densities, the momentum blockage at the canopy top increases such that the flow above the canopy behaves like a boundary layer.

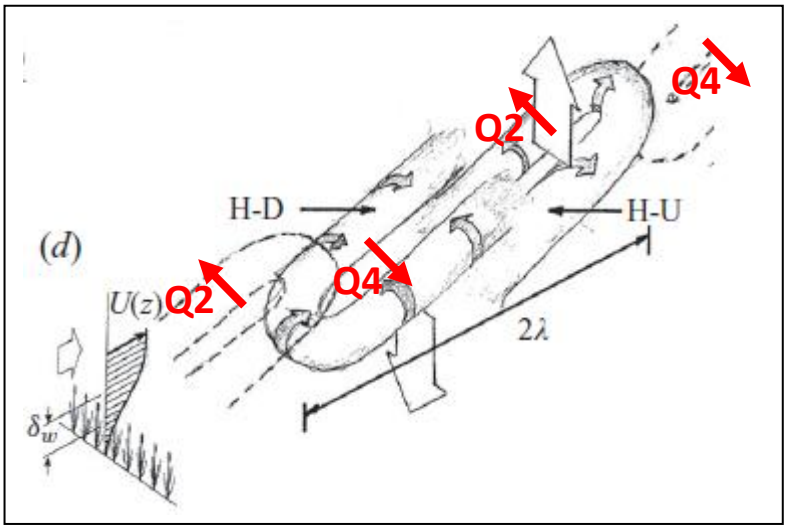

Figure 7.2: *Model for canopy turbulence structure from Finnigan et al., (2009).*

.

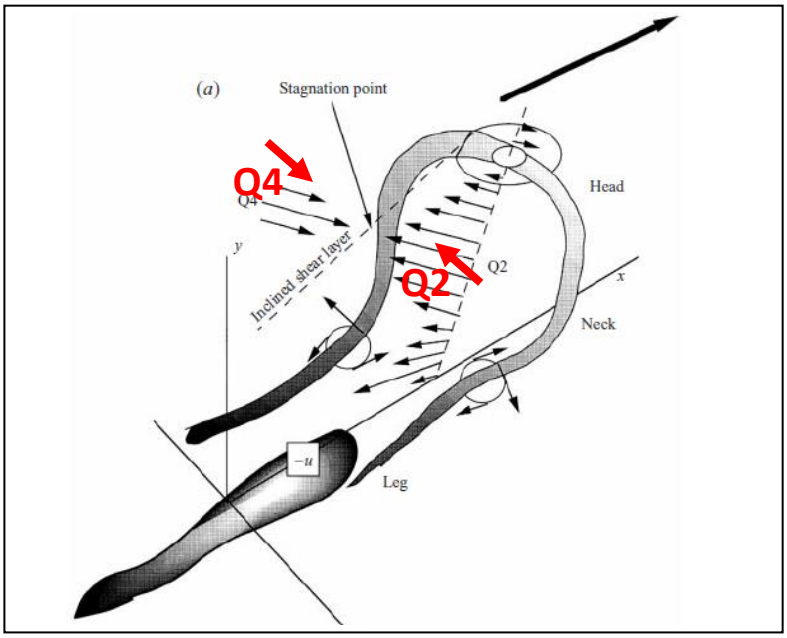

Figure 7.3: *Model for boundary layer turbulence structure from Adrian et al., (2000)*

Finally, the results from the biomechanical model identified an active interaction between the flow and vegetation. It was demonstrated that the plant motion and the fluid turbulence regime both contain signals associated with the fluid (shear

layer) turbulence as well as the vegetation (rigidity) characteristics, via the natural frequency of the vegetation

The main driver of this flow-vegetation interaction is the effect of drag on the vegetation and consequently the flow. Section 6.7 highlighted that this is a highly variable interaction and therefore simulations which used a constant drag coefficient may have dampened this interaction.

7.4 Processes in highly flexible, tensile canopies

The numerical experiments with highly flexible canopies, which representing tensile canopies (e.g. *Ranunculus penicillatus, Callitriche platycarpa*), reveal that for both small and large vegetation patches the mean velocity profile (Figure 7.1b) still resembles a canopy shear layer profile in line with previous studies (e.g. Abdelrhman, 2007; Dijkstra and Uittenbogaard, 2010). The Reynolds stress profile is similar to the semi-rigid vegetation, but contains an additional secondary peak below the main shear-layer peak (Figure 7.1b). This peak occurs for low and high density patches, and possibly relates to the additional complex plant flapping processes which cause velocity fluctuations further within the canopy. This second peak was also identified within some of the flume experiments with real vegetation in Chapter 5 (Figure 5.24). To the author's knowledge, no previous studies have detected this phenomenon and therefore there is a need to investigate this phenomenon further.

For the low density patch (Figure 7.1d), the flow profile is dominated by vortices shedding off the flapping vegetation, via a mechanism which appears qualitatively similar to that observed behind flapping flags (e.g. Zhang *et al.*, 2000). However, in the case of a flag the vortices are shed from a leading edge which is situated midstream, whereas with aquatic vegetation the leading edge is attached to the bed (Figure 7.1b). Therefore these structures cannot be characterised using the wake vortex shedding frequency given in Equation 4.24. This means it is difficult to identify theoretical, dominant frequencies against which to compare the observations. In the low density simulation, quadrant 4 sweep events dominate

directly behind the canopy, with a region of quadrant 2 ejection events directly above. This could correspond to the canopy shear layer model (Finnigan *et al.*, 2009) as described for the semi-rigid case, however there was no evidence of canopy-scale vortices over the small canopy.

When a canopy with greater overall vegetation density is introduced (Figure 7.1f), shear layer vortices are identified along the canopy top as previously suggested (although not directly observed) for highly flexible aquatic canopies (Ackerman and Okubo, 1993; Grizzle *et al.*, 1996). These exist in conjunction with the smaller flapping-induced vortices shed from the vegetation, and consequently there is interaction and coalescence which creates a highly complex velocity and vorticity field. In this simulation, when considering the largest (*H=2*) turbulent events, quadrant 4 (sweep) events appear to dominate across a much larger portion of the domain, with no equivalent region of quadrant 2 (ejection) dominance.

7.5 Comparison between vegetation types

The preceding sections have drawn out a number of key features relating to flow structure in both bending and tensile canopies. There are several key similarities and differences between the two cases. In both cases, the velocity profile resembles that of a shear layer which, given a high enough stem density, leads to the development of shear-scale vortices. The vegetation also impacts the flow in both cases, though the mechanisms differ. In the semi-rigid canopies, plant motion is controlled by the flexural rigidity whereas in the highly flexible canopies it is controlled by a flapping mechanism that is likely to be indirectly related to the plant biomechanical properties.

These plant-flapping-scale vortices are one of the key differences between the two cases. These contribute significantly to the total kinetic energy and also interact with the larger vortices, creating a more complex vorticity pattern than in the semi-rigid case.

By combining this process understanding, a new conceptual model of flow through aquatic vegetation is proposed from Figure 7.1. This is structured on Nikora's (2010)

classification of bending and tensile plants, but also scaled upon stem density. It suggests that for semi-rigid ($C \approx 1, B \ll 1$) aquatic canopies, roller vortices dominate the flow profile in line with the model of Finnigan *et al.* (2009) up until a certain stem density, above which the system transitions into the boundary layer model of Adrian *et al.* (2000). However, when the plant rigidity decreases ($C \gg 1, B \gg 1$) an additional vortex generation mechanism emerges. This plant flapping mechanism occurs in addition to the background shear layer turbulence signal, and therefore arguably roller vortices no longer dominate the flow profile.

7.6 Implications for modelling vegetation

It is suggested that these findings have a significant impact on how aquatic vegetation is modelled. Firstly, it is important to recognise that, at the individual stem-scale, the behaviour of vegetation is strongly dependent on the force balance. Therefore, the model conceptualisation must be informed by the force balance. In theory a single universal model, incorporating both morphologies discussed, should be possible. However, there are complexities, particularly surrounding the different distances over which processes such as plant bending occur (Luhar and Nepf, 2011). Therefore, it would be difficult to include both within a single all-encompassing vegetation model.

Secondly, it has been demonstrated in Chapter 6 that a constant drag coefficient is not suitable for modelling vegetation. Therefore, within stem-scale models a dynamic drag treatment, which calculates the changes in drag force through time, is required in order to fully represent the vegetation-flow interactions.

These findings also have implications for how vegetation should be represented in reach-scale models. Firstly, when modelling highly flexible (tensile) vegetation it is necessary to consider the effects of vortex shedding induced by plant flapping, in addition to the shear layer vortices typically represented in analytical models (e.g. Huthoff *et al.*, 2007; Konings *et al.*, 2012). Secondly, within semi-rigid canopies, 'bending' plants cause a significant feedback on the flow due to their rigidity.

Therefore it is essential that models used to represent semi-rigid vegetated flows account for the forcing from the vegetation motion.

7.7 Chapter Summary

This chapter has reviewed the findings of the numerical models applied in Chapters 5 and 6, setting them within the context of the current literature. The key results are shown in Figure 7.1 and represent schematically the flow structure and turbulent processes identified by the different models. In general, these results show good agreement with previous findings, though there are aspects which are novel and require further investigation; particularly relating to flow structure over highly flexible canopies. The results have several implications for vegetation modelling across a range of scales, particularly relating to the representation of the effects of dynamic drag and vegetation interaction with flow-vegetation models. Therefore, in the next chapter, these findings are scaled up and applied to the reach-scale.

Chapter 8: Applying process knowledge to the reach scale

8.1 Introduction

Currently, as was discussed in Chapter 2, there is a lack of process representation of the effects of vegetation in industry standard models which are used for river management. Most one- and two-dimensional models use a reach-averaged roughness term (typically Manning's n) to account for the additional flow resistance (e.g. ISIS, HEC-RAS, LISFLOOD). However, this has been shown to be inappropriate due to the effect of vegetation on flow structure (Naden *et al.*, 2006), as demonstrated throughout this thesis. Previously, some lower resolution research-focused models have been developed which treat vegetation using a drag term (e.g. Fischer-Antze *et al.*, 2001), as explained in Section 2.6.1. This is a more physically realistic approach but depends on either *a priori* knowledge or basic approximations of the drag coefficient. As previously discussed, this is based upon the assumption of cylindrical stalks in steady flow and has been shown to be a limitation in Section 6.7, as this approach does not account for vegetation movement, where drag can vary dynamically.

In this chapter, a new model is proposed and developed that begins to account for the effects of vegetation on the flow, described in this thesis, within a lower resolution model. The aim is to demonstrate the potential of using the findings at the micro-scale, summarised in Chapter 7, to inform the representation of vegetation at the reach-length scale in order to improve predictive ability and management. It is intended to illustrate the applicability of the high resolution process understanding to lower-resolution reach-scale models. This chapter is not intended as a comprehensive study of reach-scale vegetated channels. Instead, it provides a particular case-study which highlights the possible direction of further research in this field.

In order to assess the new model, it is compared against an existing model which has been previously used in canopy flows (Fischer-Antze *et al.*, 2001; Lopez and Garcia, 2001). This model uses a bulk drag term to represent the vegetation and is referred to as the static drag model in this chapter. This model was chosen as a benchmark as it has been widely applied to both terrestrial and aquatic canopy flows (e.g. Shaw and Schumann, 1992; Fischer-Antze *et al.*, 2001) and has been shown to reproduce vertical velocity profiles and patch scale flow structure well in compound channels.

The static drag model, described in Section 8.4.2, uses a constant drag term to represent areas of vegetation within either a RANS or LES modelling framework. In contrast, the proposed new model uses a dynamic drag term, driven by a plant motion equation developed herein. This equation is based upon the key vortex frequencies as identified in Chapter 7 and is used to predict the spatial movement of the drag region through time. This model is, by definition, unsteady and therefore low spatial (0.05-0.2m) and temporal (10Hz) resolution LES is used. The performance of the two models over a range of grid resolutions (0.05-0.2m) is assessed with comparison to a field dataset collected over a small reach of the River Browney in Durham, UK.

It is not suggested that these models are directly analogous to those currently used by river managers as they still use a level of complexity in computation (RANS and LES) that is not currently applied at the management scale. However, the purpose of the new model is to attempt to bridge the gap between high-resolution research models and low resolution industry models. With the predicted increases in computational power and capability, it is also possible that models like these may be more feasibly applied to entire rivers and subsequently used by river managers in the near future.

This chapter begins with a description of the field site and methods, followed by the numerical methodology and specifically the details regarding the new vegetation models developed in this chapter. Following this, results from the model application are discussed and compared, in order to assess their relative performance.

8.2 River Browney Fieldwork

The fieldwork was carried out on a section of the River Browney in County Durham. The selected reach (Figure 8.1) lies to the West of Durham city, just outside the village of Bearpark, a few kilometres upstream of the confluence with the River Wear. The reach was chosen due to its straight channel shape (Figure 8.2), simple channel form, well defined banks, abundance of suitable vegetation and ease of access. The river reach flows through agricultural land, with significant riparian vegetation along both banks (Figure 8.3) and has a low stream gradient (0.007). The vegetation was mainly *Ranunculus penicillatus* (Figure 8.4) with a few reed patches.

Figure 8.1: *The field site location shown in OS 1:25 000. The river reach is shown in the red oval and the coordinates are given with respect to the British National Grid.*

Figure 8.2: *Aerial photo of the field site, with the reach indicated by the red line. The river flows from North to South.*

Figure 8.3: *Photo of the field site, taken in September, looking downstream. Field assistant shown for scale.*

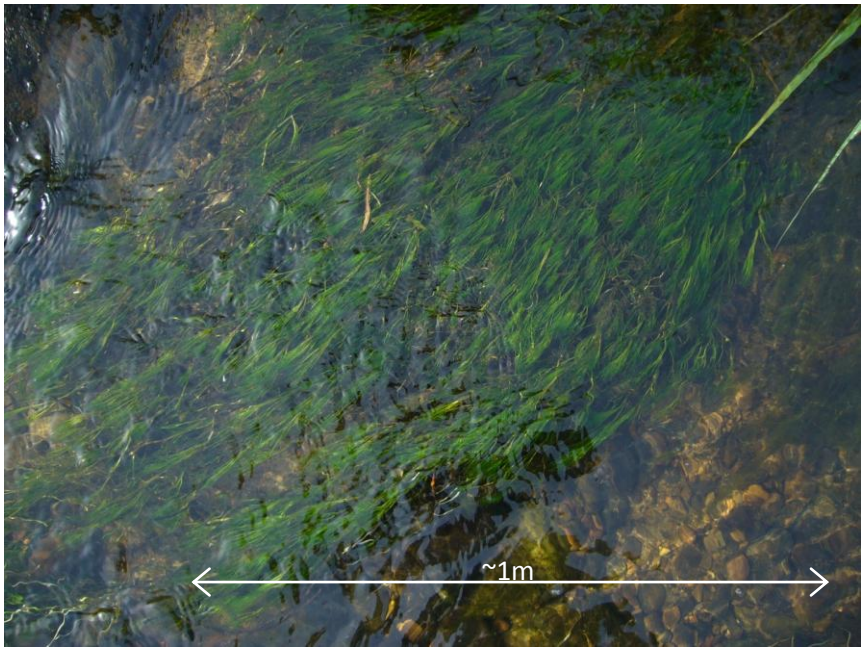

Figure 8.4: *Patch of Ranunculus penicillatus within the river reach. The water depth was approximately 0.2m.*

8.3 Field methodology

In order to produce a digital elevation model (DEM) for the numerical modelling, topographic data were collected using a Total Station electronic distance meter (EDM). Measurements were taken at a series of cross-sections, approximately 0.2m apart in the downstream direction, with a similar separation between points in the

lateral direction. The resulting DEM had a point density of over 20 points per square metre (Figure 8.5a) for the majority of the domain. Based upon previous work, this has been shown to obtain a good representation of gravel bed rivers with less than 15% loss of information (Lane *et al.*, 1994). However, it is worth noting that both the 0.1m and 0.05m simulations had a greater spatial resolution than the DEM. This is not necessarily an issue as the primary purpose of the increase in model resolution was better representation of the vegetation rather than the bed. The DEM (Figure 8.5b) shows a relatively even surface with a slight pool at the end of the domain. There are also a few micro-topographic features which might affect the flow significantly.

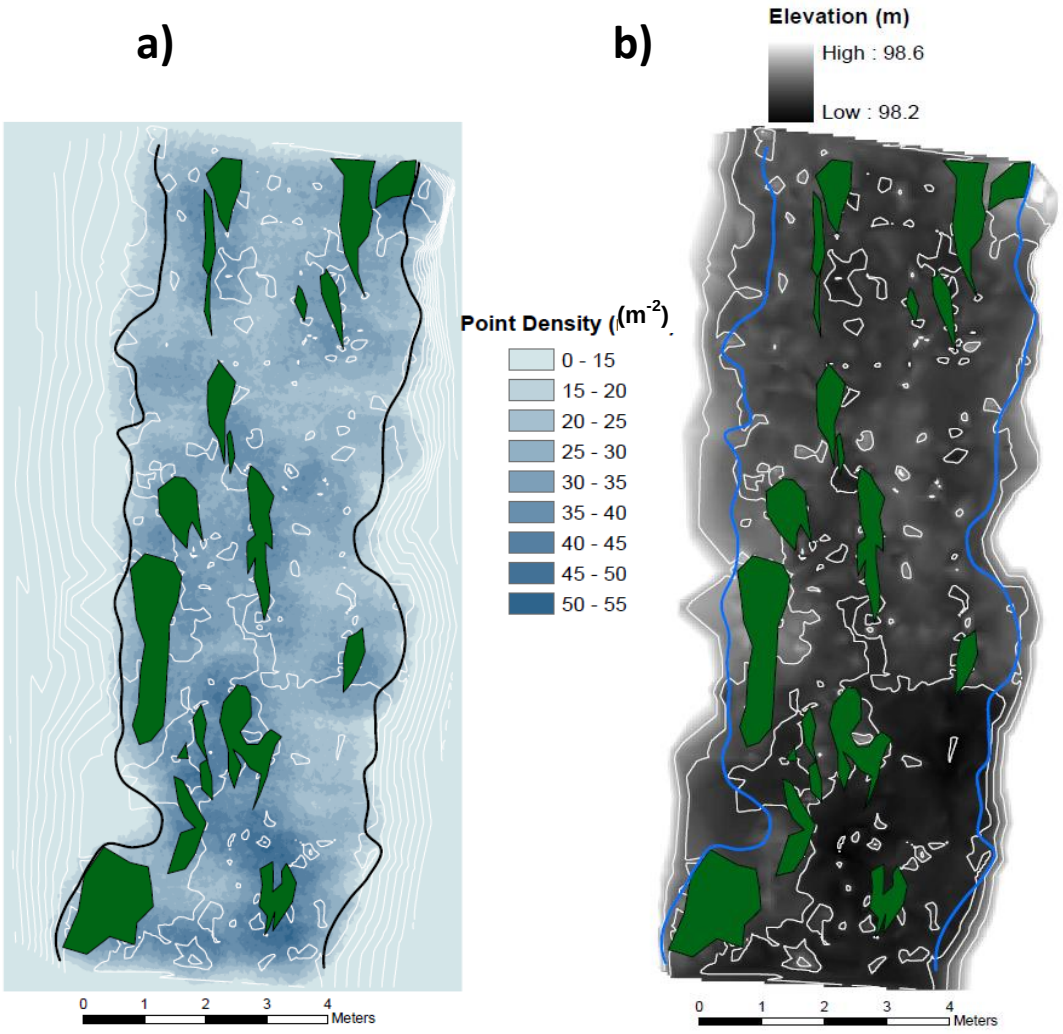

Figure 8.5: *Map of the (a) DEM point densities across the numerical domain and (b) topography across the domain. The white contours mark every 0.1m change in topography. Green areas show vegetation patches. The water surface edge is shown by the black/blue line with different colours used for clarity.*

Vegetation positions were geo-located by mapping the shape of each patch using the Total Station EDM. These outlines were converted into polygon vegetation maps for the numerical model. In addition, key characteristics of each patch were measured; namely submergence depth and mean stem length within the patch. These were intended to be semi-qualitative measurements, as both these quantities are spatially and temporally variable.

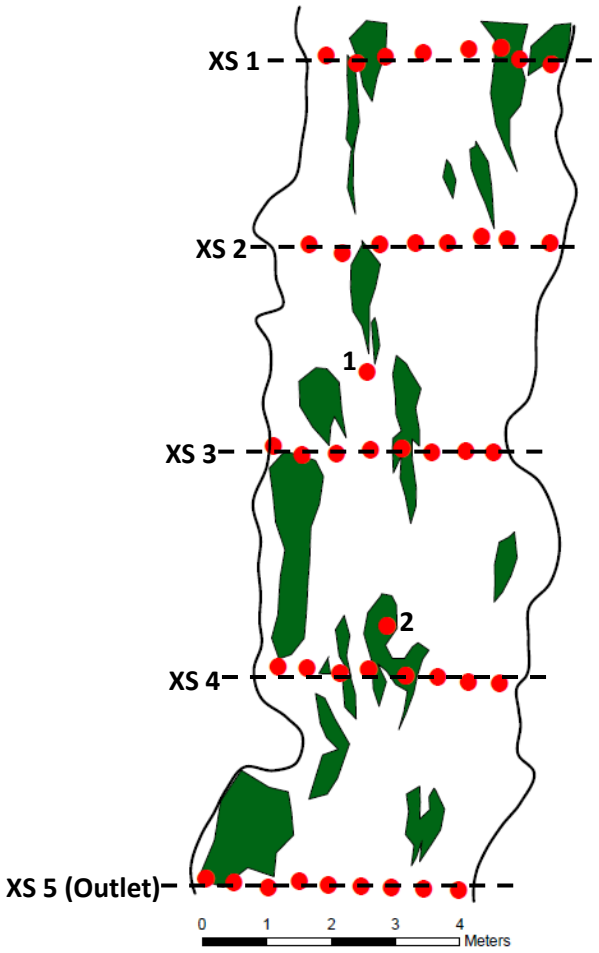

Figure 8.6: *Location of the ADV measurement points (red dots) and associated cross-sections. The cross-sections are referred to by these numbers throughout.*

Flow measurements were taken using a Sontek Acoustic Doppler Velocimeter (ADV) at five cross-sections including the inlet and outlet of the domain to provide both boundary conditions and validation data (Figure 8.6). Each time series was collected for 1 minute, at 10Hz resolution, to provide a stationary time series (Buffin-Bélanger and Roy, 2005). Velocity measurements were taken at 0.4 of the depth, in order to obtain a depth-averaged velocity estimate at each location. Two additional measurements were made at points of particular interest in relation to vegetation

configuration. The first of these (labelled 1 in Figure 8.6) was taken directly downstream of a large vegetation patch and the second (labelled 2) was taken in the canopy shear layer flow just above a vegetation patch. These two time series were collected for longer (3-7 minutes), to allow more in-depth analysis of the turbulent signal.

8.4 Numerical methodology

Previous work in reach-scale vegetation modelling has been reviewed in Section 2.6.1. The methodology developed and applied in this section builds upon those approaches. Here, two different models were developed, a static vegetation density model and a dynamic vegetation density model. These two models were applied in order to evaluate the benefit of increased process representation in reach-scale models. The static vegetation model was run as a test case, comparable with other previous work (e.g. Fischer-Antze *et al.*, 2001). The dynamic vegetation model is a novel approach based upon the results of Chapter 7. Each of the models is explained in detail following a description of the general domain setup.

8.4.1 Numerical model

For each simulation, a regular Cartesian grid was used, and the topography was represented using the mass flux scaling algorithm as described in Chapter 3 (Lane *et al.*, 2002; 2004; Hardy *et al.*, 2005). The domain was 13m long, 7m wide and 0.4m high. In order to evaluate the effect of discretisation on the performance of both models, each model was applied within 3 different spatial resolutions: 0.05m (nx=260, ny=130, nz=8); 0.1m (nx=130, ny=70, nz=4) and; 0.2m (nx=65, ny=35, nz=2). This enabled investigation of both the process representation and resolution requirements for accurate modelling of the reach. For the remainder of the chapter, the 0.05m, 0.1m and 0.2m discretisations are referred to as high, medium and low resolution, respectively. For each different resolution, the DEM and vegetation information was discretised into a raster array which was then used as an input for the model. The free surface was represented using a rigid-lid approximation. Within this scale model, it is the simplest to implement, and should not introduce

significant error over shallow water slopes in a straight channel. Therefore an average water surface was taken, which may cause minor changes to the water surface edge in the model but should not have a significant impact due to the morphology of the river reach.

The inlet data was interpolated from the time-averaged ADV readings, and all three time-averaged velocity components as well as the kinetic energy were applied at the inlet. An average velocity and kinetic energy was used throughout the domain to initialise the model and aid convergence. The static model was run with a standard RNG $k-\epsilon$ turbulence closure model (Yakhot and Orszag, 1986), whereas the dynamic model was run using Large Eddy Simulation with a Smagorinsky (1963) sub-grid model, hot-started from a converged RNG $k-\epsilon$ solution. Some previous studies have sought to model the additional sub-grid turbulent kinetic energy production due to vegetation (e.g. Lopez and Garcia, 2001). However, within this application, the stem diameter was sufficiently small that the majority of steam-generated turbulence will dissipate into heat and therefore this term was not included in the turbulence closure equations.

8.4.2 Static vegetation density model

In the simplest method developed, the vegetation was represented using a drag term that was implemented as a momentum source term in the Navier-Stokes equations (e.g. Wilson and Shaw, 1977; Fischer-Antze *et al.*, 2001; Lopez and Garcia, 2001) . The drag term was calculated using Equation 8.1, which gives the total drag loss per unit mass (Nepf, 1999).

$$F_D = 0.5 C_D M 2 r_p u^2 \tag{8.1}$$

Here, C_D is the drag coefficient, M is the stem density (per square metre of the bed), r_p is the stem radius (m) and u is the local velocity (m/s). The drag coefficient was taken as 1, in line with previous studies (Kim and Stoesser, 2011). There are limitations with the assumption of $C_D = 1$ as previously discussed in Chapters 3 and 6, and a more effective drag estimation is potentially one key way of improving reach-scale model accuracy (Kim and Stoesser, 2011). However, the philosophy

applied in the development of this model means that a high-resolution, computationally expensive drag treatment is neither appropriate and nor was sufficient field data collected to be able to accurately calculate a more appropriate value.

The stem density was estimated as 10,000 stems/m^2 based on field observations and similarly the stem diameter was estimated as 0.003m. Figure 8.7 shows the difficulty associated with assigning a single value for stem density and stem diameter due to the significant variation between different parts of the plant. Given such variation in stem diameter and density within a single plant and between plants, it was necessary to estimate a mean value for both quantities and this was performed using image analysis from the laboratory and field.

Figure 8.7: *Vegetation sample collected from the field.*

Vegetation locations were geo-located within the domain using the field data collected with the EDM, as well as data collected in the field regarding submergence depths of the various patches. It was assumed that each patch of vegetation filled the height of the domain up to its measured canopy top height. This is another simplification as there is likely to be a region of low vegetation density beneath each buoyant patch. The cells above the canopy top were then treated as free from vegetation. In the top vegetated cell, where the vegetation did not occupy the entire cell, the drag force was then scaled linearly accordingly to the percentage of cell that was considered vegetated, similar to the MFSA approach described in Chapter 3 (Lane *et al.*, 2004) .

8.4.3 Dynamic vegetation density model

The novel, dynamic model developed herein, is more sophisticated in its treatment of turbulence as it aims to resolve the turbulence rather than use a simple statistical approximation. It is based upon the previous model and uses a similar computational technique to the dynamic mass flux scaling algorithm (Section 3.2.3), whereby a spatial drag map is created and moves dynamically within the domain (Figure 8.8). Thus, there are drag fluctuations which enable variation in mean and turbulent flow quantities. In order to consider the unsteady, dynamic nature of the flow-vegetation interactions, an LES model was used, which enables representation of the larger (shear and flapping) canopy turbulent scales.

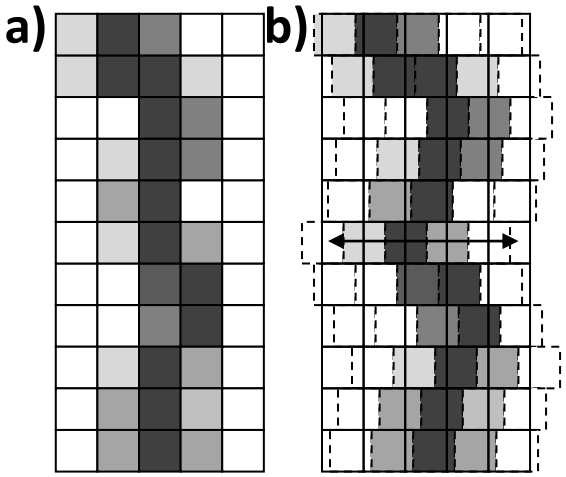

Figure 8.8: *Schematic showing the lateral motion of the drag mask. The solid grid represents the domain grid whereas the dotted grid represents the plant grid. Darker values correspond to higher drag values. The original plant position (a) is altered as each section shifts laterally (b) according to the wave equation (Equation 8.2).*

The final implementation of the drag term within the momentum equations is performed in a similar manner to the static model, though in this case the values of drag at each location in the domain vary dynamically through time and therefore must be remapped at each time step. This encourages the development of dynamic canopy-scale turbulence which may not otherwise be resolved by the steady model. The approach could also be viewed as a temporally variable drag coefficient.

The motion of the dynamic drag patch is driven by a representative canopy model. This model was designed to be simple, and therefore was approximated as a wave

equation, such that the lateral displacement, y, of the canopy from its mean lateral position at a x distance downstream of the plant front at a time t is given by;

$$y(x,t) = \delta(x)\sin\left(\frac{2\pi f_{KH}x}{v} - 2\pi f_{KH}t\right) + A_f \sin(2\pi f_V x/v - 2\pi f_V t) \quad (8.2)$$

Here, f_{KH} and f_V are the vortex frequencies associated with the shear-scale Kelvin Helmholtz instability and vegetation flapping respectively (calculated as described below), v is the propagation speed of the vortex, $\delta(x)$ is a vortex size function and A_f is a constant which defines the wave amplitude. In this initial application, this model only deals with lateral motion of the plant. This is in contrast to the previous chapters that focussed on the shear layer at the top of the vegetation. However, White and Nepf (2007) showed lateral shear layers to be similar to canopy top shear layers in terms of process and observed flow structure. Furthermore, in this particular case study, given the low submergence depth across the reach, lateral shear layers are more likely to affect the reach-scale spatial flow structure. The model could be extended to include a vertical fluctuation at the canopy top via a similar mechanism.

As discussed in Chapter 2, one of the key criteria used in the development of this type of predictive model is that they should only depend on terms which do not require *a priori* knowledge of the flow. Therefore, all the terms in Equation 8.2 need to be known or solvable at the time of calculation.

The shear layer term has previously received considerable attention (e.g. Ghisalberti and Nepf, 2006; Ghisalberti, 2009) and therefore, is simplest to parameterise. As discussed in Chapter 4, the vortex shedding frequency can be estimated using Equation 8.3 (Ghisalberti and Nepf, 2002);

$$f_{KH} = 0.032\frac{\overline{\overline{U}}}{\theta_M} \quad (8.3)$$

where, the terms $\overline{U}$ and θ (as defined in Section 4.2) depend purely on the flow characteristics of the shear layer and so can be approximated from the mean flow conditions.

The vortex size function can similarly be estimated (Equation 8.4) using the theoretical vortex growth rate, $\partial\delta(x)/\partial x$ (see Section 6.2.4), which relies upon shear layer variables $\overline{U}$ and ΔU as defined in Section 4.2. For simplicity, in this work, the initial vortex size, $\delta_0(x)$, was taken as 0, effectively assuming that shear layer vortices are shed from the front of the canopy.

$$\delta(x) = \frac{1}{2}\left(\delta_0(x) + 0.09\frac{\Delta U}{\overline{U}}x\right) \tag{8.4}$$

The propagation speed of the vortices (v) is assumed to be equal to the mean velocity at the canopy edge ($\overline{U}$). This does not account for the observed displacement of the vortices from the canopy edge (Nepf, 2012a). However, given the spatial resolution of the model it is not possible to accurately calculate this shift directly, and the difference is likely to be sub-grid anyway.

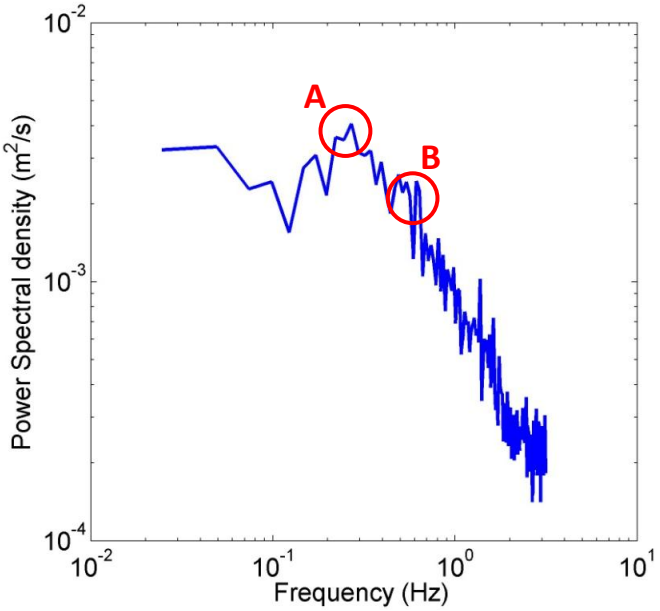

Figure 8.9: *Lateral velocity power spectra for the time series taken behind the vegetation patch. The red circles highlight two key frequencies, which it is suggested correspond to the (a) shear and (b) flapping scale.*

In summary, Equation 8.2 depends only upon the parameters ΔU, $\overline{U}$, θ_M , A_f and f_V. The first three terms require an approximation of the shear layer within the flow, whereas the latter 2 require some knowledge of the flapping mechanism. For these experiments, the shear layer was parameterised using the RNG $\kappa - \epsilon$ model results from the previous model described in Section 8.4.2 ($\Delta U = 0.2, \overline{U} = 0.15, \theta_M = 0.02$). This provided a constant shear layer approximation throughout the

simulation, which is beneficial for model convergence, and requires less computational run-time than calculating the values at each time-step.

The flapping frequency and amplitude parameters were calculated using the velocity power spectrum of the time series taken in the field in the wake of a vegetation patch (Figure 8.9). The spectrum of lateral velocity shows a peak at approximately 0.27Hz (A) which agrees well with the predicted K-H scale, (0.24Hz) and a secondary peak at approximately 0.6Hz (B) which it is suggested corresponds to the plant flapping scale. Therefore this value (0.6) was used for f_V and consequently, the amplitude was worked out as 0.06m ($A_f = \overline{U}/4f_V$).

8.5 Results

The results from the static and dynamic model are presented together, to allow comparison between the predictive capabilities of both models and are grouped by grid resolution which is the other key variable for assessing predictive capability. In order to compare the field and model datasets effectively, both datasets have been time and depth averaged. The LES data were tested for stationarity to ensure the validity of time-averaging.

As outlined in the methodology set out above, the static and dynamic models use different turbulence closure schemes. It is therefore, important to identify any differences in flow structure caused simply by the turbulence closure model rather than the dynamic aspect of the model. Therefore, the static model was also implemented within an LES framework. The downstream ($\bar{u}$) and lateral ($\bar{v}$) velocity results from the two static models and the dynamic model are shown in Figures 8.10 and 8.11.

Visual comparison in Figure 8.10 shows that there is some difference in prediction of downstream velocity between the static RANS (8.10a) and LES (8.10b) models. For instance, behind some patches there is a difference in wake shape (dashed circles in Figure 8.10b). However, there is also significant difference between the static (8.10b) and dynamic (8.10c) LES models. This is particularly evident in changes

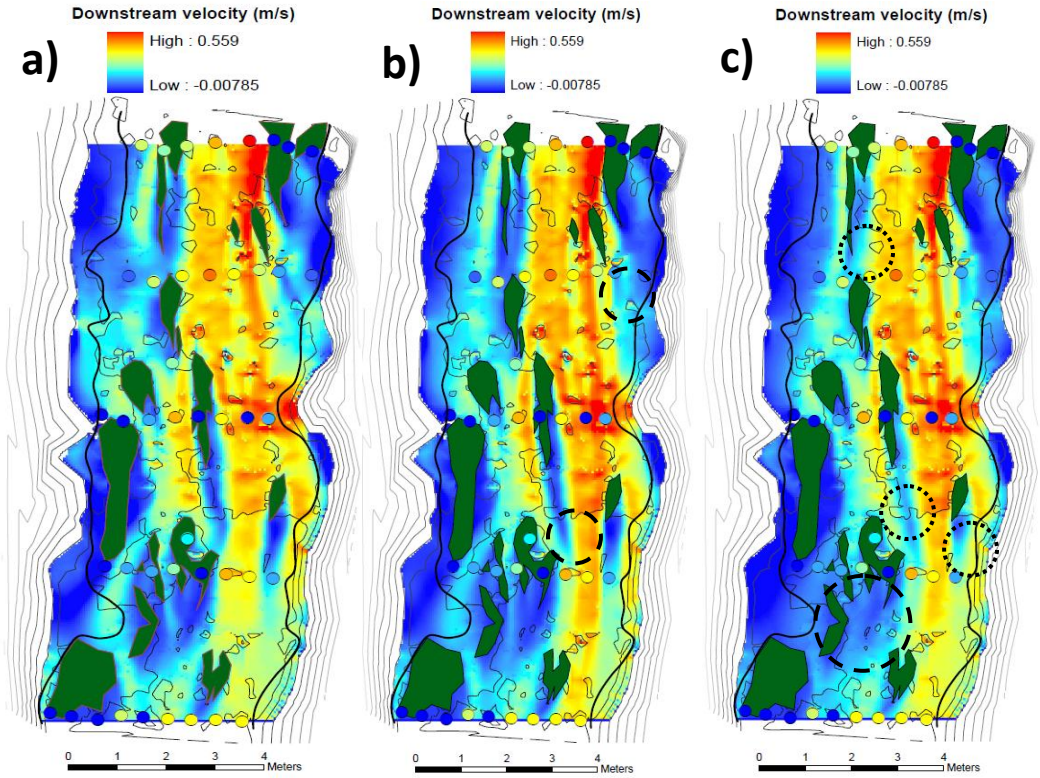

Figure 8.10: *Comparison between downstream velocities from the a) RNG k-e, b) LES and c) dynamic LES models. The dots show the corresponding field-measured values. The thick black lines show the measured water surface edge. The dashed circles highlight changes in wake shape and the dotted circles highlight changes in wake velocity magnitude.*

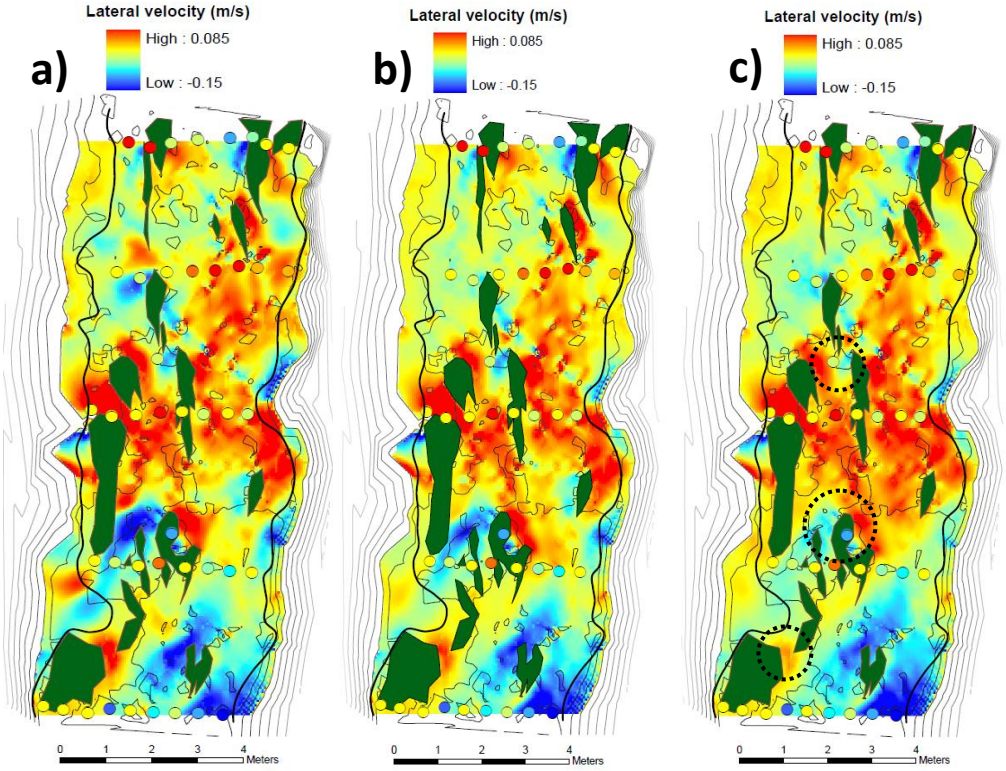

Figure 8.11: *Comparison between lateral velocities from the a) RNG k-e, b) LES and c) dynamic LES models. The dots show the corresponding field-measured values. The thick black lines show the measured water surface edge. The dotted circles highlight changes in wake velocity magnitude.*

in velocity magnitude in the wake regions (dotted circles in Figure 8.10c). There is less of an identifiable change in wake shape, though the reduction in wake velocity magnitude does cause the wakes to become wider and more diffuse with much less clear wake boundaries (dashed circle in Figure 8.10c).

Considering the lateral velocities, Figure 8.11 shows that there is some difference between the static RANS (Figure 8.11a) and LES (Figure 8.11b) cases, with generally lower magnitude velocity peaks in the LES case (see dotted circles in Figure 8.11b). The dynamic model increases this effect further, with significantly lower velocity peaks associated with regions of flow separation and reattachment (see dotted circles in Figure 8.11c). This would be expected as the introduction of turbulent eddies and plant motion increases the movement of the wake and therefore there is a less well defined wake area which alters through time and therefore average velocities in the wake regions are not as low as the static, RANS case.

Based on these results, it is reasonable to attribute changes in flow structure in the dynamic model at least in part to the plant motion and not purely the turbulence closure. Therefore, for the remainder of the discussion, only the RANS static model and dynamic LES will be compared, with the acknowledgement that some of the differences attributed to the dynamic model may in fact be due to the turbulence closure model.

8.5.1 High resolution results

The key differences in prediction between the high resolution RANS and LES models have already been discussed in the preceding section. Therefore, the focus in this section is on the agreement between the models and field data. The downstream velocity maps for the high resolution models (shown again in Figure 8.12) both show relatively good qualitative agreement with the field data particularly across cross-sections 2, 4 and 5. In cross-section 4 for example, both models predict the position of the vegetation wake (labelled w in Figure 8.12) well. In this case, the RANS model (a) appears to perform better, with the LES producing a slightly shorter wake. Cross-section 3 shows greater error in both models, particularly at the true left of the channel (circled in Figure 8.12) where both models predict high velocities.

This suggests that this error may be due to the discretisation of the problem rather than the particular vegetation modelling approach as it appears in both models.

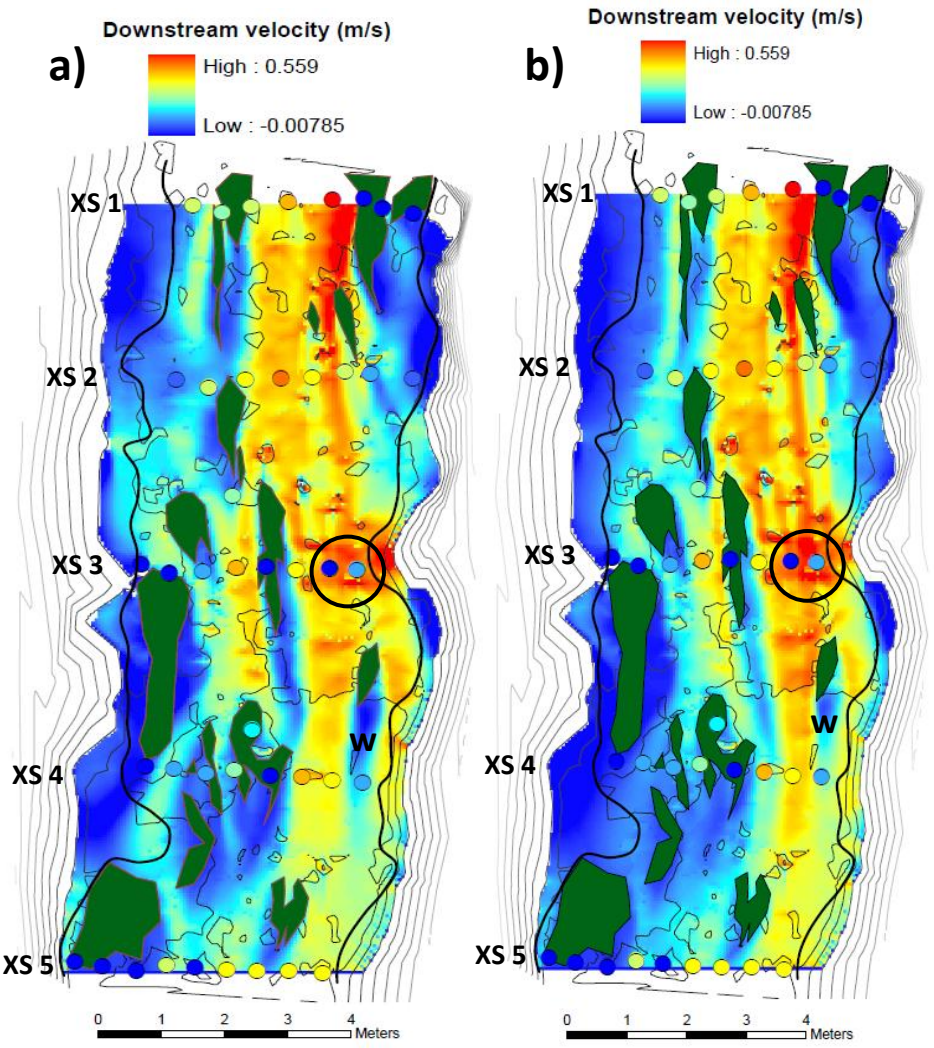

Figure 8.12: *Downstream velocity maps for the (a) static and (b) dynamic high resolution models. The circles show values measured in the field.*

The lateral velocity plots (Figure 8.13) show a similar trend. As with the downstream velocity, cross-section 3 shows particularly poor agreement with the field data. Both models predict substantially higher cross-stream velocities in most locations than measured in the field. Elsewhere, at the other cross-sections, the overall velocity trends are similar but there is still significant error. In particular, the models both predict flow towards the true right in two locations in cross-sections 2 and 4 (circled in Figure 8.13) which appears logical given the location of nearby vegetation but is not seen in the field data. The outlet (cross-section 5) appears to

show best agreement with regions of positive and negative cross-stream velocity both identified correctly.

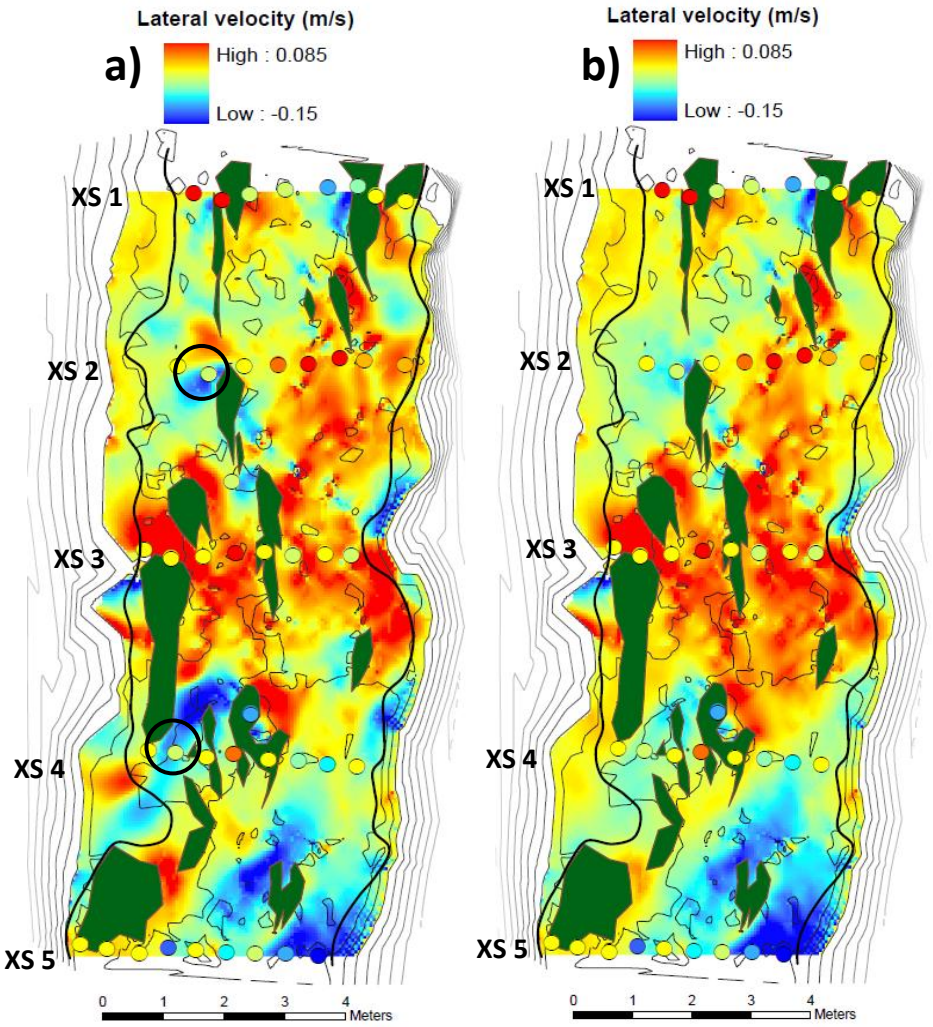

Figure 8.13: *Lateral velocity maps for the (a) static and (b) dynamic high resolution models. Flow from true right to true left is considered positive. The circles show values measured in the field.*

Though the effect of the dynamic model on wake structure is clear, it is difficult to assess visually whether or not it leads to an improved prediction of velocity or not. In order to quantify the performance of the model predictions, ordinary least squares linear regression was performed on the field data and corresponding model values. The plot of measured against modelled velocities (Figure 8.14) shows that there is significant discrepancy within the values for both the downstream and lateral velocities. Both graphs show close pairing between static and dynamic model predictions. This suggests that the overall discrepancy between the model and field data is as a result of the general model discretisation rather than the

behaviour of the vegetation models. There is no clear, consistent pattern across the dataset as to which model reduces the error most.

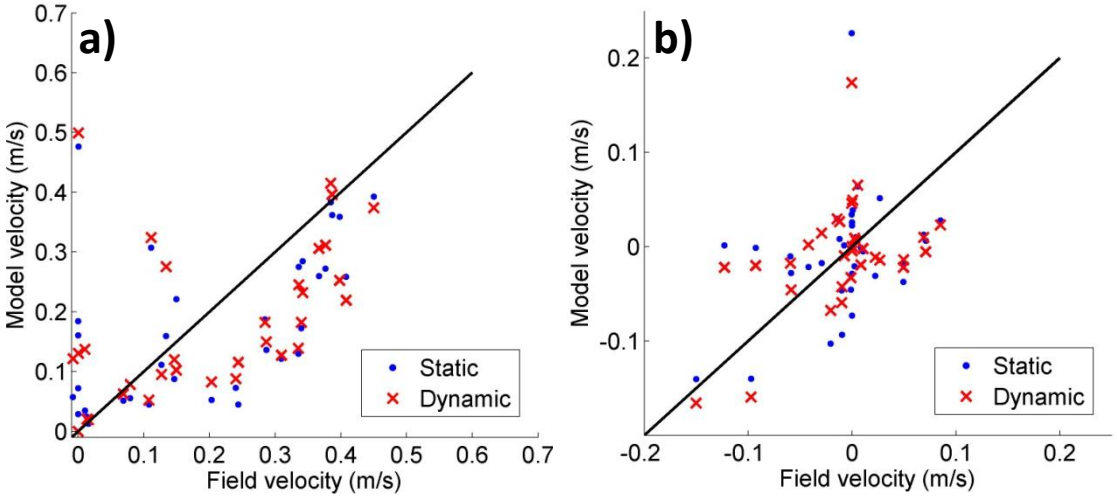

Figure 8.14: *Scatter plots showing agreement between measured and modelled (a) downstream and (b) lateral velocities. The black line represents a perfect fit.*

Run		±U (m/s)	±V (m/s)
0.05m	Static	**0.130**	**0.062**
	Dynamic	**0.136**	**0.053**
0.1m	Static	**0.159**	**0.060**
	Dynamic	**0.170**	**0.061**
0.2m	Static	**0.180**	**0.069**
	Dynamic	**0.179**	**0.051**

Table 8.1: *RMSE values for the different model simulations*

U	Static model			Dynamic model		
Resolution	Intercept	Gradient	R^2	Intercept	Gradient	R^2
High	0.058	0.535	0.382	0.077	0.47	0.321
Medium	0.104	0.556	0.266	0.107	0.538	0.226
Low	0.112	0.380	0.128	0.150	0.262	0.079

Table 8.2: *Regression coefficients and R^2 values for downstream velocity*

V	Static model			Dynamic model		
Resolution	Intercept	Gradient	R^2	Intercept	Gradient	R^2
High	-0.004	0.468	0.147	-0.003	0.546	0.240
Medium	-0.001	0.425	0.141	-0.001	0.471	0.156
Low	-0.001	0.198	0.030	-0.009	0.360	0.172

Table 8.3: *Regression coefficients and R^2 values for lateral velocity*

The RMSE values (Table 8.1) show that the dynamic model marginally improves the lateral velocity accuracy, but marginally worsens the downstream velocity accuracy. Overall though, the RMSE is relatively large with ±0.13m/s error in the downstream

velocity and no model substantially improves prediction over the other. This error is evident from the low R^2 values obtained from the regression analysis. As well as differing significantly from the expected values (intercept=0, gradient=1), the regression (Table 8.2 & 8.3) shows a wide spread of data with poor goodness of fit (R^2=~0.3-0.4). This poor correlation across both models suggests that the general model contains a significant level of error encountered during the conceptualisation and discretisation of the model.

For example, it is noticeable in all the velocity maps that the modelled water surface edge is significantly different from the measured water surface edge along much of the domain, but particularly on the true right bank. It is suggested that this is due to uncertainty in defining the water surface edge in the field. There is a clear topographic limit to the water surface edge as the banks rise steeply, but close to the water's edge there is some ambiguity as the edges of the channel are lined with dense vegetation.

As discussed in Section 8.4.1, the model water surface edge is based upon the DEM and a prescribed water level and therefore assumes flow right up to the bottom of the bank. In the field, this region was very densely vegetated and there was no flow evident in this region. On the true right bank, the velocities are generally very low and so although the spatial region of error is larger, this may not provide as significant a source of continuity error as the true-left bank, where there are higher velocities near the bank. Furthermore, the change in water surface consequently causes a change in channel shape which may influence the mean velocities, particularly for the lateral velocity component. This error in the water surface edge is found in all of the results across the three different resolutions.

Another potential source of error is the choice of model parameters. It is not known whether these represent an optimal parameter combination. All the parameters were chosen based upon physical characteristics calculated from the flow measurements which may contain error. Some parameters (such as $\overline{U}$ and ΔU) were also reach-averaged which may introduce local error.

Overall, the effect of the dynamic vegetation model can clearly be seen from the velocity maps. In particular, there is a noticeable difference between the wake-structure and velocity magnitude alongside and behind the vegetation patches, which suggests that at this high resolution, the dynamic model is successfully representing processes which the static model fails to. However, this improvement does not lead to an increase in accuracy when compared to the field data, where the agreement is still poor and in some cases, worse.

8.5.2 Medium resolution results

With the decrease in resolution from the previous case, the models still both clearly resolve and identify wake regions behind the vegetation patches (Figure 8.15). The effect of the dynamic model appears to be similar to the high-resolution case, in making the wakes more diffuse (circled in Figure 8.15), however, this effect is much reduced. As well as being more diffuse, the vegetation wakes are marginally wider in the dynamic model, and this causes a noticeable increase in peak velocity towards the end of the domain, where flow is more streamlined (shown by dashed line in Figure 8.15b). As with the high resolution case, the model qualitatively appears to predict the downstream velocity well through cross-sections 2, 4 and to a lesser extent 5, with poorer performance along cross-section 3.

The lateral velocity results (Figure 8.16) again show a very similar pattern between the two models, with only very minor differences to the high resolution case. The decrease in resolution appears to improve the prediction at cross-section 2, but there is still significant error in cross-section 3, where the models over-predict the lateral velocity considerably.

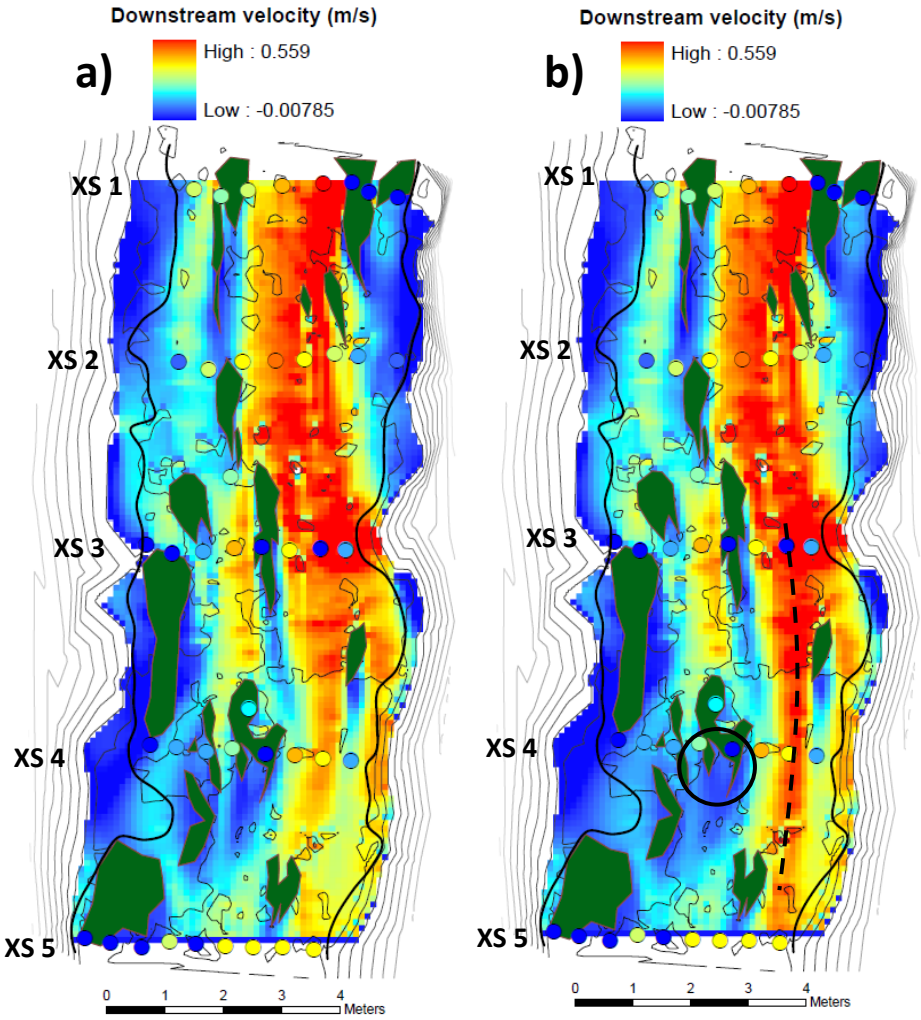

Figure 8.15: *Downstream velocity maps for the (a) static and (b) dynamic medium resolution models. The dots show values measured in the field. The dotted line indicates the region of faster streamlined flow and the circle represents a region of diffuse wakes.*

The comparison between modelled and measured values (Figure 8.17) shows slightly worse agreement with the field data than the high resolution model, particularly relating to errors at cross-section 3 which are identifiable within both graphs (circled in Figure 8.17). Figure 8.17(a) shows a slight tendency for the dynamic model to over-predict in the higher velocity regions and under-predict in the low velocity regions, compared to both the static model and field observations however this is not the case universally across the domain.

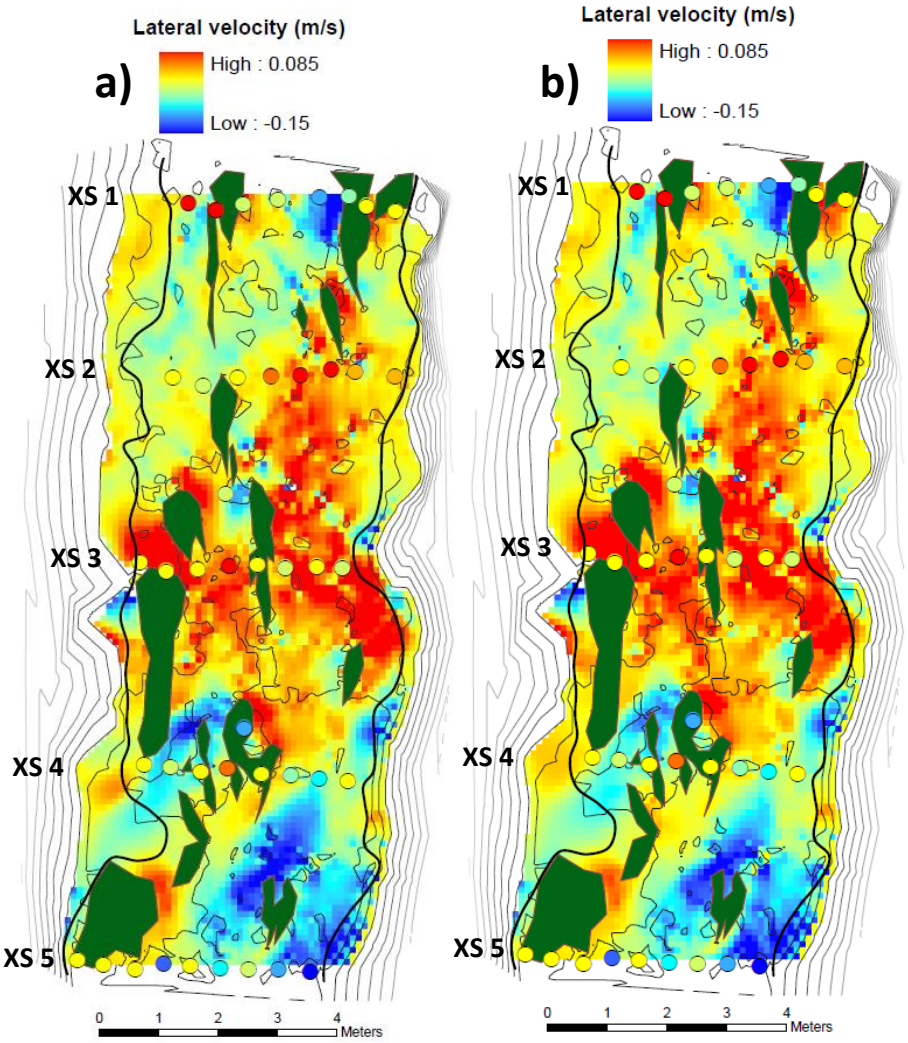

Figure 8.16: *Lateral velocity maps for the (a) static and (b) dynamic medium resolution models. Flow from true right to true left is considered positive. The circles show values measured in the field.*

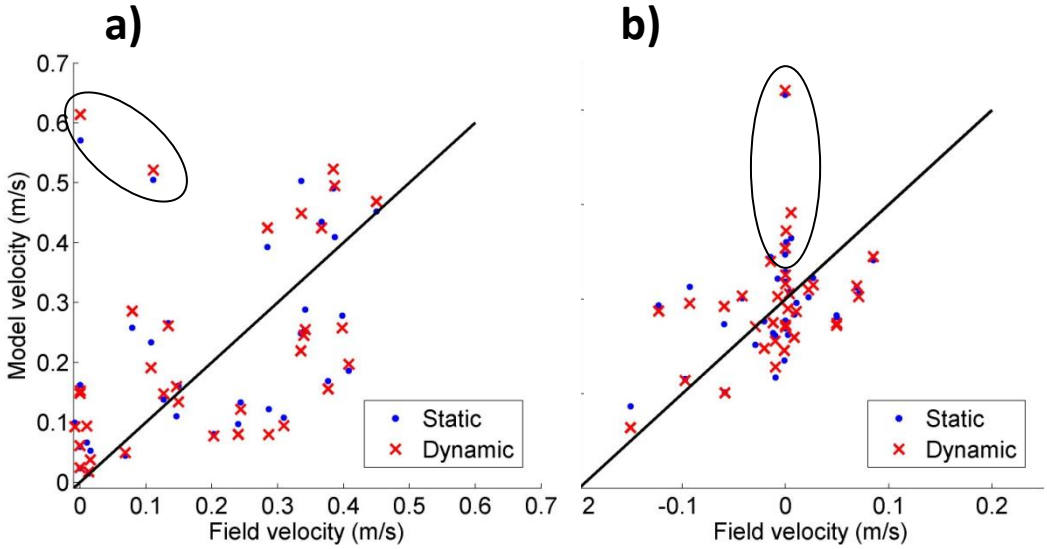

Figure 8.17: *Scatter plots showing agreement between measured and modelled (a) downstream and (b) lateral velocities. The black line represents a perfect fit. The ovals highlight regions of poor fit associated with cross-section 3.*

Table 8.1 shows that the performance of the two models is very similar, but that as with the high resolution case, the static model actually outperforms the dynamic model for both velocity components. However, as previously stated, it is difficult to comment on the relative performance of the vegetation models given the large underlying error between the field and numerical data. The regression for both the downstream and vertical velocities (Tables 8.2 & 8.3) again show significantly different gradients from the expected 1:1 fit. Furthermore, the downstream velocity also shows a significantly non-zero intercept (~0.1) suggesting an offset in the model data.

Overall, the medium resolution provides an increase in similarity between the two models and a slight decrease in predictive capability for both models from the high resolution models. Thus the merits of the dynamic model are reduced compared to the high resolution model, though the simulations are less computationally intensive.

8.5.3 Low resolution results

Reducing the resolution further, the resulting downstream velocity maps (Figure 8.18) show a broadly similar spatial velocity pattern between the two models. Both models pick out the wake structure behind most of the patches well, though in the static model, the wakes are stronger (i.e. larger negative velocities). Consequently, the flow in-between the vegetation patches is significantly faster in the static model, particularly in the first half of the domain (shown by the dotted line in Figure 8.18). Here, the dynamic model velocities appear to agree better with the field results.

For cross-section 2, both models reproduce the measured velocities well, with the dynamic model performing marginally better due to the reduction in peak flow velocity. Similarly both models perform well at cross-section 4, where the two models predict very similar flow velocities. However, the model performs less well at cross-section 3, as with the other cases, where there is a significant over-prediction of the velocity in the region of faster flow.

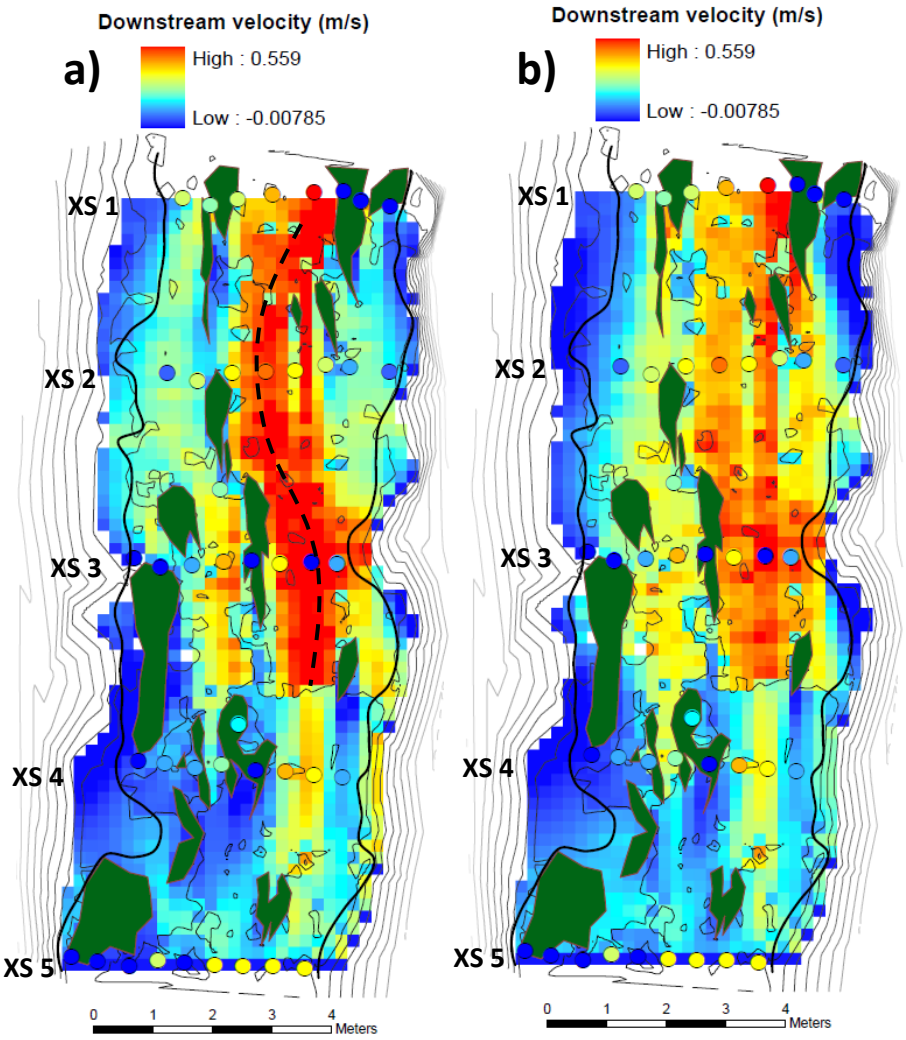

Figure 8.18: *Downstream velocity maps for the (a) static and (b) dynamic low resolution models. The dots show values measured in the field. The dashed line highlights the region of fast flow.*

The lateral velocity plots (Figure 8.19) again show good qualitative agreement between the two models. Compared to the field data, both models appear to significantly over-predict the lateral velocities particularly in the middle region of the domain, around cross-section 3 as seen with the other cases. As with the higher resolution cases, the dynamic model predicts lower peak velocities in several flow separation regions (dashed circle in Figure 8.19b). There is one exception to this (dotted circle in Figure 8.19b) whereby the dynamic model predicts a significantly higher velocity. It is not possible to assess which is the more accurate as there are no nearby field measurements.

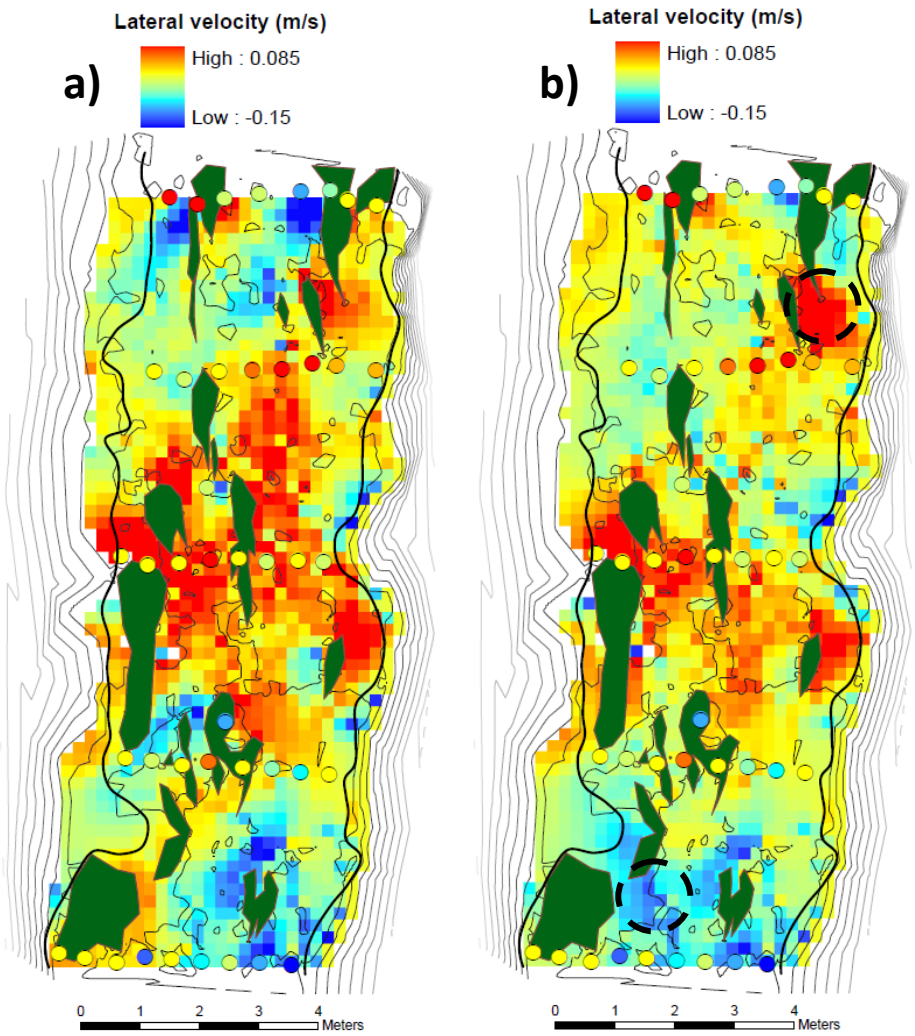

Figure 8.19: *Lateral velocity maps for the (a) static and (b) dynamic low resolution models. Flow from true right to true left is considered positive. The dots show values measured in the field.*

The comparison between measured and modelled values (Figure 8.20), again shows a wide spread of values for the downstream velocities. Within the lateral velocity plot (Figure 8.20b) there is a high level of error particularly relating to cross section 3. However, there is reasonable visual correlation for some of the lateral velocities, though there appears to be an offset in the data (dotted line in Figure 8.20). Similar to the downstream velocities, there is little evidence of an improvement in predictive capability of the dynamic model. Table 8.1 confirms that in terms of RMSE, the dynamic model does outperform the static model for both the downstream and lateral velocities, though only slightly.

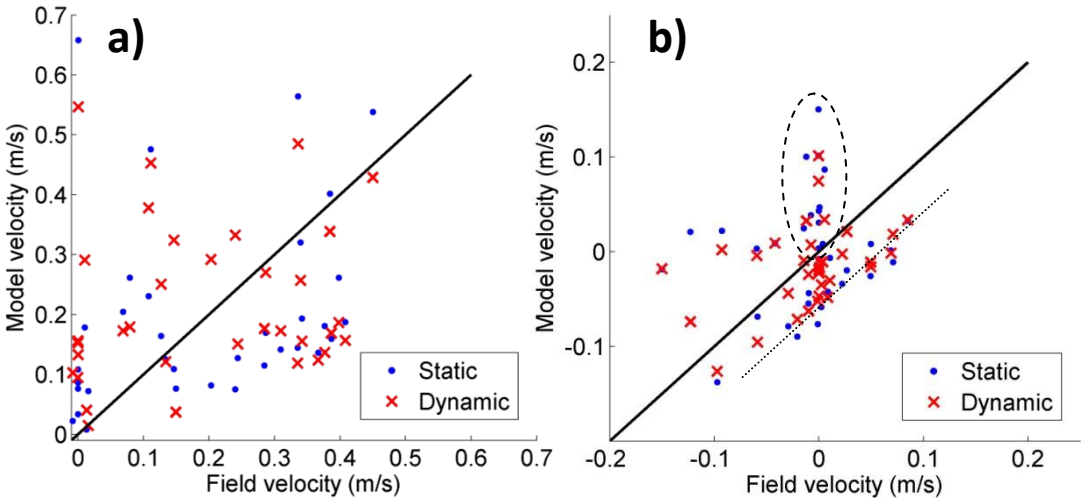

Figure 8.20: *Scatter plots showing agreement between measured and modelled (a) downstream and (b) lateral velocities. The dotted circle highlights poor data relating to cross-section 3. The black line represents a perfect fit. The dotted line shows the offset,*

The R^2 values for the downstream velocities (Table 8.2) show a significantly worse fit in the low resolution model. This trend is present but less clear in the lateral velocities. Overall, the performance of the low resolution models is worse than the higher resolution models for the downstream velocities (Table 8.1). However, the dynamic low resolution model shows the greatest level of agreement with lateral velocities collected in the field, though the improvement is small (~0.01m/s). At the lowest resolution, the dynamic model does outperform the static model slightly for both velocities.

8.6 Impact of resolution within the dynamic model

The influence of resolution on model velocity prediction has been discussed throughout the preceding sections, however, for ease of comparison, the results from the three dynamic models are compared briefly here. The results (Figure 8.21) show that for the dynamic model, resolution has little effect on the spatial pattern of flow, with wake regions and high velocity regions agreeing well across all three. The resolution does appear to have an effect on velocity magnitude however, with the results showing a particularly marked difference in the 0.1m model, with significantly higher velocity peaks. In terms of predictive capability, though there is

little visually distinguishable difference in performance, Table 8.1 does indicate that an increase in resolution does lead to a modest increase in performance.

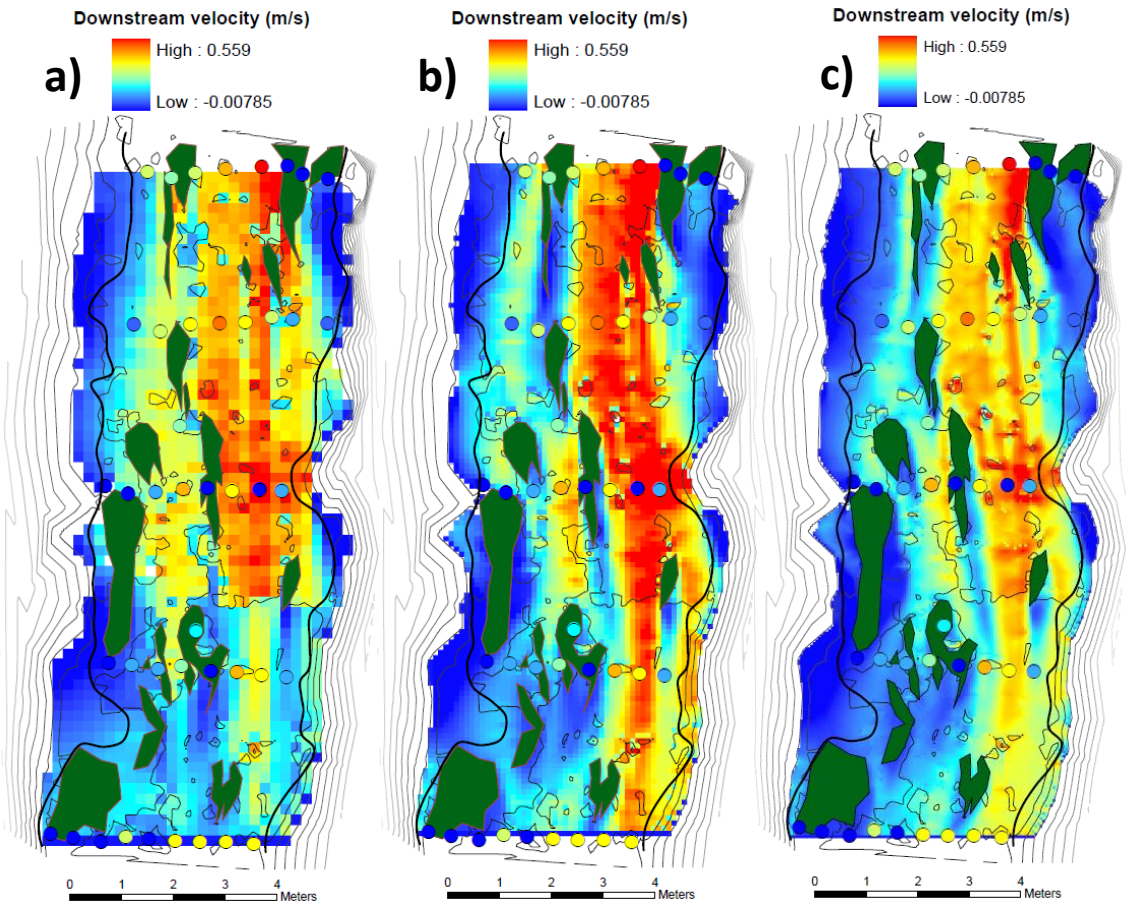

Figure 8.21: *Downstream velocity as predicted by the dynamic model for (a) low, (b) medium and (c) high resolution grids. The thick black lines show the measured water surface edge. The dots represent the field-measured velocities.*

Similarly, with the lateral velocities (Figure 8.22) there are only minor differences in the spatial flow pattern between the different resolutions. The largest difference is in one particular upstream location (circled), as discussed in Section 8.5.3. This location aside, the increase in resolution seems to add detail and alter velocity magnitude slightly, but the effect is small. This is illustrated by Tables 8.1-8.3 which show no significant improvement in either correlation or error with increasing resolution.

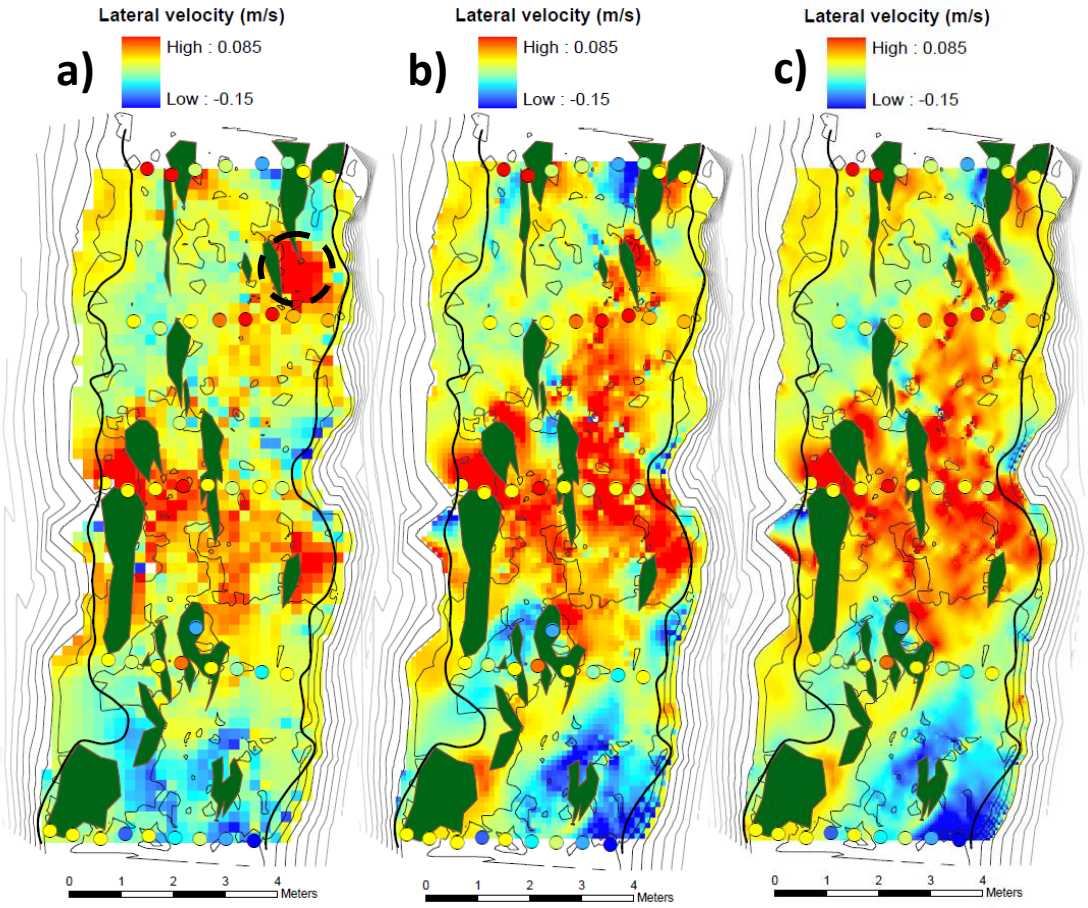

Figure 8.22: *Lateral velocity as predicted by the dynamic model for (a) low, (b) medium and (c) high resolution grids. The thick black lines show the measured water surface edge. The dots represent the field-measured velocities*

Figure 8.23 shows how the difference in prediction between the static and dynamic models, at the ADV measurement locations, changes with resolution. There is little evidence of bias within the model results in either the downstream or lateral velocities. Particularly at the high and medium grid resolutions, the models perform very similarly. At the low resolution, there is some evidence that the dynamic model predicts higher minimum velocities and lower maximum velocities, which is in agreement with the visual observations that velocity magnitudes seem to be smaller in the dynamic case.

However, the ADV measurement locations do not necessarily accurately represent the entire domain. Therefore, a similar analysis has been carried out for the velocities at each point within the domain (Figure 8.24). For the downstream velocity, at the low resolution there is a clear trend of the dynamic model over-predicting the velocity relative to the static model. This trend weakens as the

resolution increases and the graph becomes more symmetrical. It is noticeable that the best agreement between models occurs at the medium resolution with a qualitatively much better fit than the other two cases.

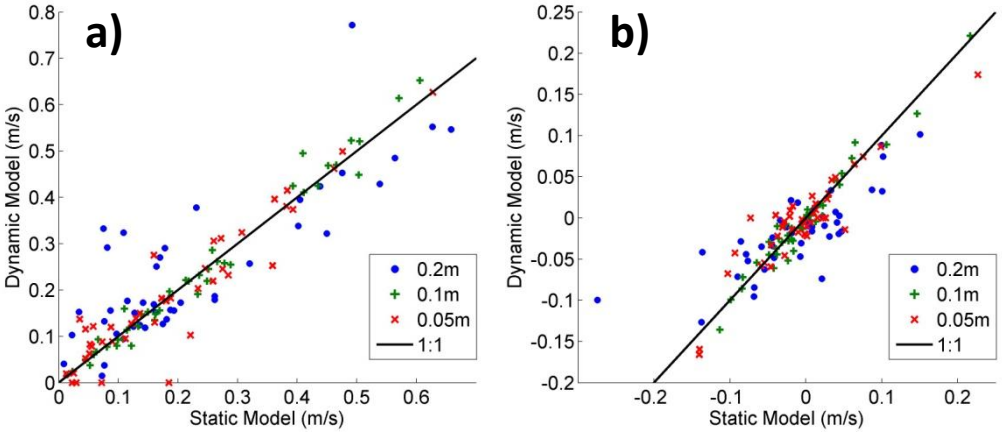

Figure 8.23: *Dynamic model velocity plotted against static model velocity for (a) downstream and (b) lateral velocities at each of the ADV measurement locations. Each graph shows the low (green), medium (green) and high (red) resolution results.*

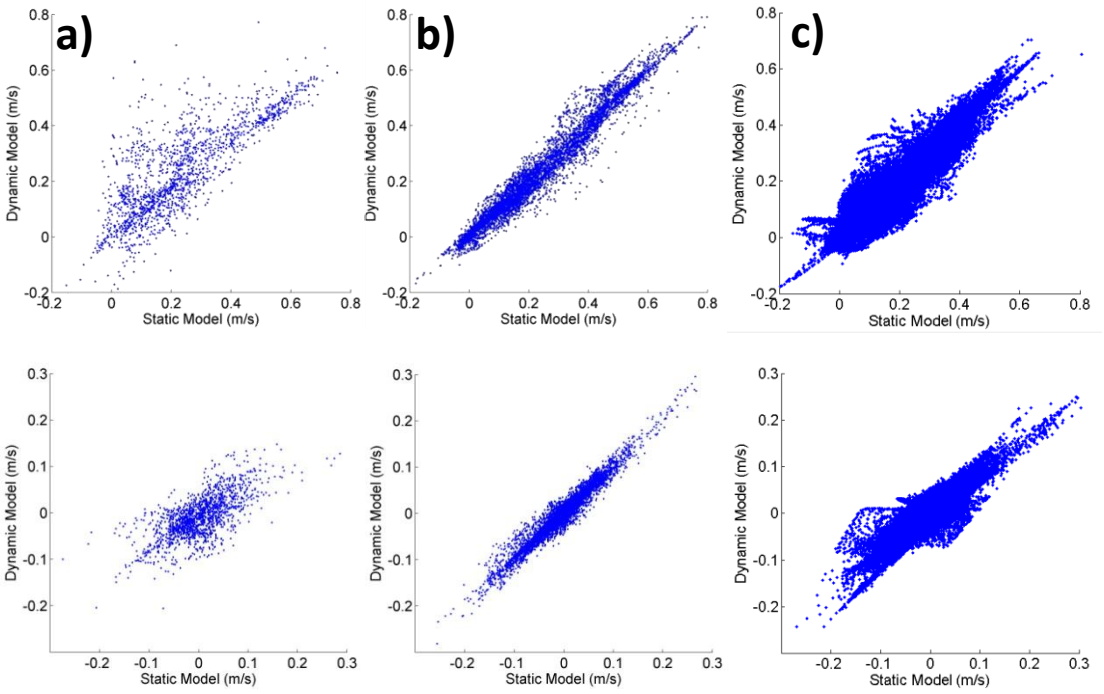

Figure 8.24: *Dynamic model downstream (top) and lateral (bottom) velocity plotted against static model velocity for the whole domain with grid resolutions (a) 0.2m, (b) 0.1m and (c) 0.05m.*

The patterns are very similar for the lateral velocities, however there appears to be greater difference between the velocities in the high resolution case. Here there

appears to be a portion of the domain in which the static model predicts values with a range of approximately 0.3m/s whereas the dynamic model only has a range of 0.1m/s. This region is visualised as parallelogram within Figure 8.24c (bottom). It is unclear whether this corresponds to a particular spatial area of the domain, or to a particular flow condition, experienced at several locations across the domain. One possibility is that it relates to wakes behind vegetation patches, where separation and therefore lateral velocity is intensified within the static model compared to the dynamic model.

In summary, resolution has a clear impact upon the performance of the two models, and the extent to which the models agree. Both models show an increase in performance with increased grid resolution and this is to be expected. It is interesting to note that the two models are most similar at the medium resolution, as shown in Figure 8.24 and also from the regression in Table 8.2. This suggests that for this particular reach, the dynamic model has least effect at this resolution. In contrast, Figure 8.23 and 8.24 suggest that the difference between the models is greatest at the lowest resolution.

8.7 Comparison with previous work

Most of the studies which have applied similar drag methodologies within RANS frameworks (e.g. Fischer-Antze *et al.*, 2001; Lopez and Garcia, 2001) have focussed on the vertical velocity profiles rather than looking at the spatial distribution of depth-averaged velocities. Fischer-Antze *et al.* (2001) did look at the spatial flow patterns though not round complex patch structures. To the author's knowledge there have been no studies conducted that investigate the effect of vegetation on flow structure in a similar manner to that presented here. It can be viewed as an extension of the work regarding blockage factors in channels (e.g.Green, 2005a; Nepf, 2012b), except that in those studies, blockage values are collapsed down to a single roughness value.

This study thus represents a step change in the calculation of depth-averaged flow in vegetated channels at a reach-scale. Until recently, such improvements have not

been possible due to computational and field data collection limitations. However, with improved computational capability and the ability to collect high resolution, high precision reach-scale data (Lane, 2005), this type of modelling may soon become feasible at the reach-scale for management purposes.

8.8 Chapter summary

The aim of this chapter was to demonstrate how information from high resolution numerical simulations might be used to improve the representation of vegetation within reach-scale models. To this end, a novel dynamic vegetative drag model was developed and its performance was compared to that of a static vegetative drag model over a range of grid resolutions. The accuracy of the simulations, when compared to the field data collected in this study is shown in Table 8.1 by the root mean square (RMS) error for each of the runs and the regression analysis (Tables 8.2 & 8.3).

These figures do not necessarily represent the accuracy of the models over the whole domain, but rather at the locations at which ADV data were collected. Therefore it is necessary to judge the models visually in addition to their performance at the validation points, as measurement error in the field may skew these results. Nevertheless, the RMS error values provide a quantitative overview of the performance of the models over the range of variables.

Table 8.1 suggests that for the downstream velocity, resolution has a significant impact on model accuracy. This effect is less consistent for the lateral velocity values. The difference between the two model performances also varies. The simpler static model actually outperforms the dynamic model for both the medium and high resolution cases. This is reversed in the low resolution case where the dynamic model outperforms the static model slightly.

The dynamic model took approximately 24 times the computational time required for the static run. Similarly, for each doubling in resolution, the computational time increased by a factor of eight. The consequence of this is that the dynamic, 0.05m resolution simulation took approximately 1500 times the simulation time required

for the static 0.2m model. This dramatic increase in computational time only resulted in a modest decrease in RMS error of approximately 0.04m/s for the downstream velocity, and 0.007m/s for the lateral velocity.

This is a surprising result, and despite the fact that it is clear that increasing both the resolution and modelling complexity does increase process representation, from a management perspective it is obvious that in this case the additional complexity is not cost-effective. The inaccuracy of the results across a range of resolutions calls into question the accuracy of both the discretisation of the channel and the field velocity measurements. The field data is an obvious source of error, and as discussed in Chapter 5, model data can often be more accurate than the field or flume data. In particular there is likely to be some orientation error within the ADV measurements.

However, the model setup may also contain significant error. The similarity in values between the two different vegetation models suggests there may be some inherent error within the numerical setup. There are a number of different sources of error within the simulations, which may have caused differences in the results.

1) Free surface boundary conditions

This source of error includes both the assumption of a rigid-lid as well as the subsequent assumption of a constant water surface. Both the numerical treatment and the parameterisation of the water surface introduce potential error into the simulation. The parameterisation of the water surface created a wider river than measured in the field, potentially affecting velocity values throughout the domain. Together with the rigid lid assumption, this also had an effect in those shallower regions of the flow, such as the middle section of the domain, where free-surface effects of the flow are not negligible and have an impact on velocities and turbulence. This may be the reason for the increased velocities within the centre of the domain.

2) Topographic boundary conditions

As discussed earlier, the resolution of the DEM used within the models may be a limitation on accuracy. It is likely that the river featured significant topographic variation at a scale smaller than 0.2m which was therefore a sub-grid element of the topography. It is possible that this topography may have had a profound effect on the local velocity measurements at some of the ADV locations.

3) Model parameters

The two main parameterisations within the model were the drag value for the canopies and the plant motion variables. Given the overall similarity between the two model results, it is unlikely that the model plant motion variables were responsible for widespread error across the domain, however they may have under-represented the effects of plant motion. The drag parameterisation has a key effect on flow structure and velocity magnitudes across the domain and therefore it is possible that inaccurate estimation of the drag value skewed the results. This illustrates the problem explained in Chapter 7 and demonstrates the need for more accurate methods of drag modelling at a range of scales.

4) Grid resolution and convergence

Although the models were tested at a range of resolutions, it is still possible that the finest resolution was below the resolution required in order to effectively model the processes operating in the channel. For example, in chapter 3 it was discussed that to begin to resolve wake-scale effects behind a vegetation element, a width of at least 4 grid cells was optimal, whereas for many of the patches, even in the 0.05m simulations, the patches were only 2 or 3 cells wide. Verification analysis with the models could help determine the potential error within the different resolution models.

Finally, there may be errors in geo-location between the field and model data. The numerical values represent cell averages over volumes of 125-8000cm^3 whereas the ADV data represent data collected over a much smaller sampling volume (0.25cm^3). This is particularly a case for the low resolution model, however even at the highest

resolution, there is still an order of magnitude difference in averaging volume which may introduce errors.

Nevertheless, considering the various sources of error, these results have demonstrated a new methodology for including the effects of vegetation within reach-scale models. Though the agreement is quantitatively poor, the visual results show that the model is reproducing the general flow structure observed in vegetated channels. It is worth noting that even the simple static drag model represents a step change in modelling methodology, from the current reach-averaged vegetation roughness terms.

This chapter has begun to investigate how the results from high-resolution vegetation modelling might begin to inform reach-scale modelling of vegetation. For the preliminary study shown here, the inclusion of a dynamic vegetation model did improve the process representation within the model, for example altering the wake structures and turbulence production rates within the flow. However this increase in process representation did not lead to a significant increase in predictive capability, as judged by comparison with field data.

Further work is required to identify at which resolutions increases in model complexity are cost-effective, and to establish the applicability of low resolution CFD to reach-scale modelling. Nevertheless, this chapter has begun to explore ways in which high resolution modelling can be used to inform lower-complexity models.

Chapter 9: Conclusions

9.1 Introduction

In this chapter, the overall aims of the thesis and research questions that were initially developed in Chapter 1 are revisited. The aim of the thesis (Section 1.2) was divided into a methodological (*A1*) and a research aim (*A2*). These were:

A1. To develop a model capable of simulating the interaction between flow and vegetation from the individual plant scale through to the canopy scale,

and

A2. To investigate the controls on the turbulent processes exhibited in canopy flows.

In order to fulfil these aims, a series of research questions were devised. Each of these questions is now addressed in turn. Having considered each of the research questions, suggestions are presented regarding potential directions of future research to further develop this field as well as possible applications of the research.

9.2 Research Questions

The research questions, initially developed in Section 1.3, are considered below.

Q1. What turbulent processes are present within canopy flows?

As a benchmark, the conceptual model of Nikora (2010) was applied to analyse the results. In Nikora's model, six different scales of turbulence were identified (see Figure 9.1). The flume and numerical data in Chapters 5 and 6 confirmed the existence of turbulent processes operating at several different scales. Of the six scales Nikora included, three scales were clearly identified within these results. These include: i) canopy shear (process 2 in Figure 9.1), ii) stem-wakes (process 5 in Figure 9.1) and; iii) a plant flapping related scale which it is suggested here is a combination of processes 4 and 6 (Figure 9.1). Evidence for shear and wake scale turbulence was found both in the vortex detection (e.g. Figures 6.11, 6.28 & 6.40) and spectral analysis results (e.g. Figures 6.17 & 6.29). The evidence for the plant-

flapping-scale is less well defined but was identified through wavelet analysis (e.g. Figures 6.63 & 6.75).

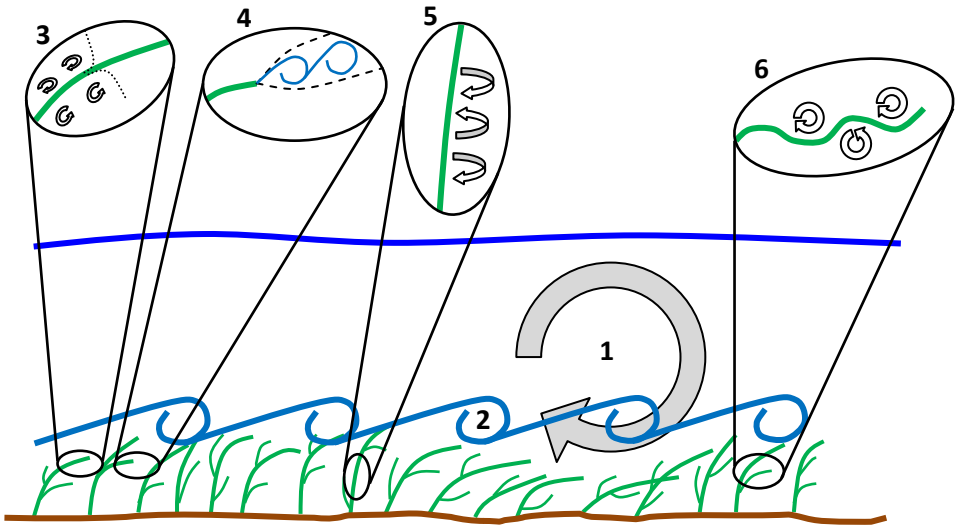

Figure 9.1: *The six scales of turbulence within vegetated channels as proposed by Nikora (2010). The six scales are; 1) boundary layer; 2) canopy shear layer; 3) leaf boundary layer; 4) leaf mixing layer; 5) stem wake and; 6) plant flapping scale.*

This leaves two scales (channel and leaf boundary layer) which were not identified in this thesis. It is suggested that the spatial resolution was not fine enough in either the numerical simulations (the grid discretisation) or flume measurements (PIV interrogation window) to be able to detect evidence of plant boundary layer turbulence (process 3 in Figure 9.1). Furthermore, both the numerical simulations and flume experiments considered depth-limited aquatic flows and therefore it was not possible to identify channel boundary layer turbulence (Figure 9.1 process 1). This has implications for research question 2.

In summary, the results presented in this thesis support the general conceptual model of Nikora (2010). However, it was not possible to distinguish between the leaf mixing layer (4) and plant flapping (6) scales. As such, it is suggested that this conceptual model could be modified as these two scales appear to interact to form a single plant morphology-governed scale.

Q2. How do aquatic canopy flows differ from terrestrial canopy flows?

As noted above, the first key difference between aquatic and terrestrial canopies is that aquatic flows, in a fluvial context, are typically depth-limited. This tends to inhibit the development of a boundary layer above the canopy layer. The second important difference, as discussed in Chapter 7, is the weighting in the force balance. Aquatic plants are surrounded by a higher-density fluid. This has two implications: i) they experience much greater drag than terrestrial canopies (Denny and Gaylord, 2002) and; ii) it implies that it is possible for aquatic plants to be positively buoyant (Luhar and Nepf, 2011).

This different weighting in the force balance leads to a change in plant form, whereby aquatic plants must find a balance between drag reduction and photosynthetic capacity (Bal *et al.*, 2011). Therefore, many aquatic plants (e.g. *Ranunculus penicillatus, Callitriche platycarpa*) exhibit very low stem rigidities to allow reconfiguration and minimisation of drag (Sand-Jensen, 2003). This represents a significantly different form of vegetation to the rigidity-driven grass or reed stems often used in terrestrial studies. Therefore, vegetation can be classified as either tensile or bending (as per Nikora (2010)) based on the force balance (see Section 7.2).

This classification does not strictly distinguish between terrestrial and aquatic canopies, although all previous terrestrial work has focussed on bending plants. Furthermore, while some aquatic work has assumed a bending plant form (e.g. Ikeda *et al.*, 2001), the majority of aquatic macrophytes can be classed as tensile plants (Siniscalchi and Nikora, 2012).

It has been shown that these two vegetation types require very different model frameworks to represent the different ways, and scales over which, the internal and external forces interact. Accordingly, two vegetation models were developed in Chapter 3: the Euler-Bernoulli beam model (Figure 9.2a) to represent bending vegetation and the N-pendula (Figure 9.2b) model to represent tensile vegetation. The application of these different models (Figure 9.2) revealed that they generate

different flow characteristics, mainly through vortex production, due to the difference in interaction between flow and vegetation (Figure 9.2c & d).

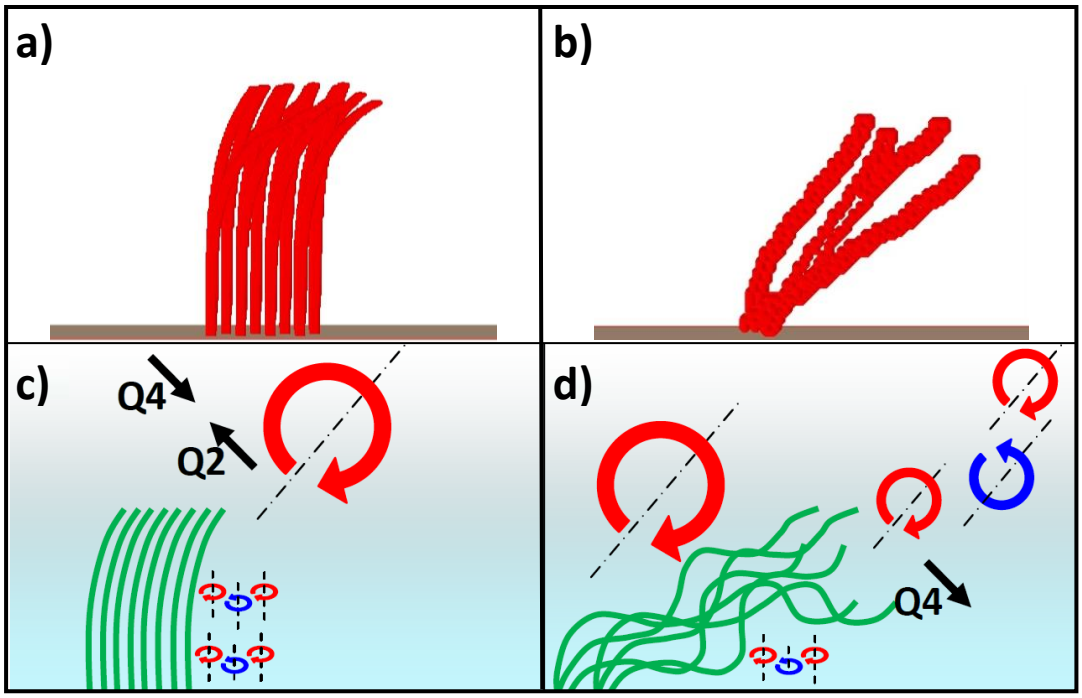

Figure 9.2: *Schematics of the (a) Euler-Bernoullli beam and (b) N-pendula models above an excerpt of Figure 7.1 showing the differences in vortex generation between the two vegetation types.*

This thesis has clearly shown that while there may be similar characteristics between aquatic and terrestrial canopy flows, aquatic canopies exhibit far more complex behaviour in response to their different force balance. In particular, this thesis has identified a strong, flapping-controlled vortex generation mechanism.

Q3. How do structural and biomechanical properties of river plants determine turbulence dynamics within plant canopies?

It has been shown that the vortex dynamics within the canopy depend on the nature of the vegetation and resultant force balance as shown in Figure 9.2. Thus, key biomechanical and structural features such as flexural rigidity, stem diameter, stem length and plant density, which determine the plant resistive and buoyancy forces, are fundamental in controlling the turbulence structure generated. In the simplest case of rigid vegetation, stem diameter and patch-scale properties such as stem density and arrangement characterise the drag discontinuity (Nepf *et al.*, 2007)

which in turn determine the inflected velocity profile that generates the shear scale turbulence.

Furthermore, in the case of flexible vegetation, the results in Chapters 6 and 7 show that flexural rigidity and buoyancy interact with the flow forces in a complex manner, which controls the plant reconfiguration. The results in this thesis demonstrate that this temporally dynamic plant reconfiguration drives turbulence production at the flapping scale (Figure 9.1, process 6). Thus, it is suggested here that the biomechanical properties are crucial in defining turbulence dynamics in canopy flows.

Q4. What feedback mechanisms are present between the flow and vegetation characteristics?

Chapter 6 highlighted a key feedback mechanism between the flow and vegetation movement whereby the vegetation motion both responds to and actively affects the turbulent spectrum of the flow itself. More specifically, the low frequency vegetation oscillation appears to be modulated by the canopy shear scale vortices while the turbulent flow spectrum shows a clear peak at the natural frequency of the vegetation (Figure 9.3c).

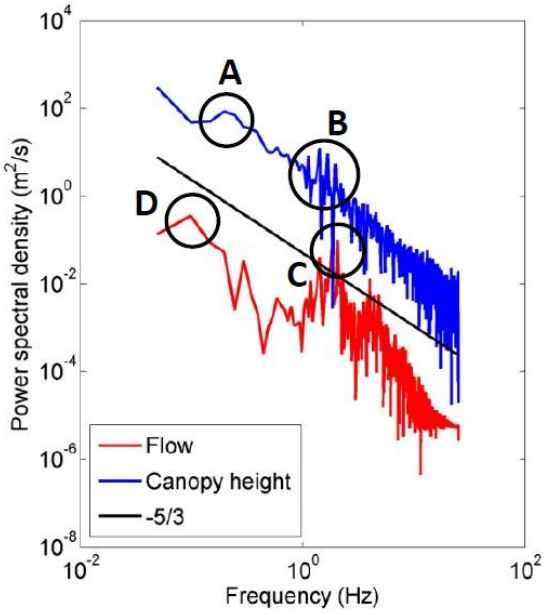

Figure 9.3: *Downstream velocity and canopy height spectra showing interaction and feedback between the two as shown in Figure 6.29. The circles highlight the potential shear layer signals (A and D) and the natural frequency signals (B and C).*

In the case shown in Section 6.3.5, the frequencies were sufficiently different that both scales existed independently within the plant and flow data. The interplay between these two processes in cases where the natural and shear layer frequencies are similar requires further investigation in order to determine whether the plant or flow controls the turbulence in such circumstances. This has implications for the representation of vegetation within numerical models as it dictates whether the flow or vegetation frequency dominates the vortex regime.

Q5. What key processes need to be represented within high-resolution vegetation models?

It has been shown that the most dominant turbulent process in canopy flows is the formation of the canopy shear layer and associated vortex generation. These vortices are responsible for the majority of mass and momentum transport (Ghisalberti and Nepf, 2009) and therefore have implications for the movement of sediment and nutrients within the flow (Okamoto and Nezu, 2009). Thus, an appropriate representation of the shear layer processes is vital in models designed to further our understanding of the hydraulic, geomorphic and ecological aspects of canopy flows.

It has been shown throughout this thesis that one of the fundamental processes which causes the development of the shear layer is the turbulence generated at the stem-scale. Moreover, this removal of energy from the mean flow within the canopy controls the inflection in the velocity profile. Therefore, in order to accurately model the shear-scale processes it is crucial that stem-scale processes are sufficiently represented. This involves using spatial grid resolutions that ensure that wake processes can be adequately resolved.

The most significant process which drives this extraction of mean energy from the flow at the wake-scale is drag (Raupach and Thom, 1981). If the wake-scale processes are fully captured, then the effect of drag on the flow is accounted for directly. However, this drag is also one of the main forces driving plant motion. Therefore, it is essential that the process of energy extraction via drag is included, in order to drive the plant motion which will in turn affect the large-scale vortex

generation processes. As shown in Chapter 6, this requires a dynamic drag treatment, whereby the force induced by the drag is back-calculated directly from the flow field (Figure 9.4). The inclusion of a drag-calculation method is a novel approach which, it is suggested, is a significant development in flow-vegetation modelling.

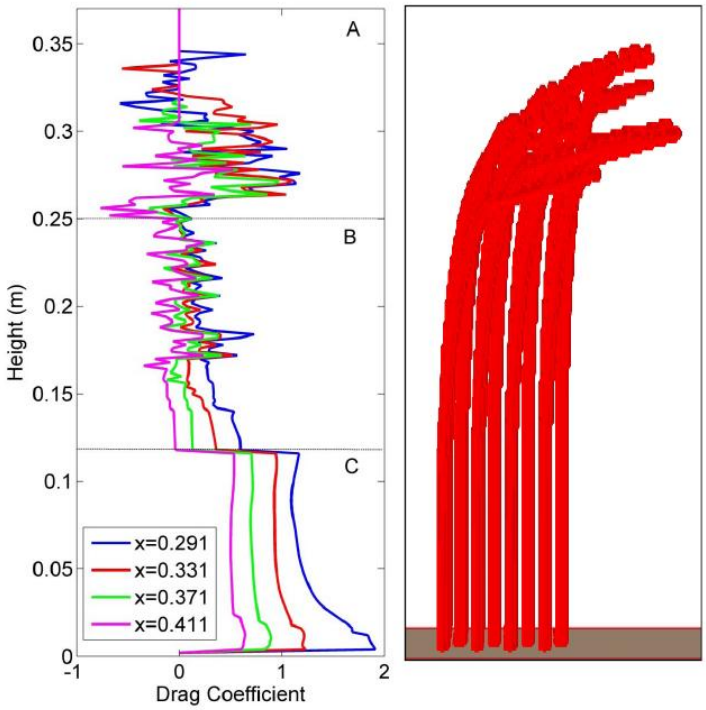

Figure 9.4: *Vertical drag coefficient profile taken from the Euler beam model at different points downstream through the canopy as shown in Figure 3.20*

Q6. Is it possible to improve the representation of vegetation in management-scale models, by applying a more process-based approach?

The response to question 5 highlighted two key processes which could be better represented within reach-scale models: drag and large-scale turbulent structure. Vegetation motion is a third process which is intrinsically linked to both these processes. In Chapter 8, a reach-scale model was developed which included a physically-based drag term, and a vegetation motion model based upon the key vortex characteristics discussed in Chapter 7. Thus, this model represented all three key processes, and avoided the use of empirical roughness terms. The results showed that the dynamic model resulted in different flow patterns. However, it was

difficult to assess any possible improvement in representation due to disparity between the field and model data across all of the models.

Though this was purely an example case study, some conclusions may be drawn from these results. Firstly, the simple static drag model demonstrated the potential for the application of a drag-based treatment at the reach-scale, given the availability of good quality vegetation data. Secondly, the dynamic model demonstrated a method for simulating reach-scale canopy dynamics with relatively low computational cost, which is dependent on only a few physically-based parameters. Though both of these models use a CFD framework, which represents an increase in computational time compared to current methods, it is suggested that given the increasing availability of low-cost, high performance computing such methods may be appropriate in the near future.

9.3 Further research

The major methodological aim of this thesis was the development of a high resolution numerical model capable of simulating flow-vegetation interactions. While this was achieved, there are a number of aspects of the two models which could be extended further. Firstly, the present models do not currently deal with plant collisions, which in terrestrial canopies have been shown to have a significant effect on canopy behaviour (Doare *et al.*, 2004). This process may act to dampen the vegetation response to the flow and therefore should be considered. Secondly, the current models are single stemmed with no mechanism for including foliage. Foliage can inhibit momentum transfer into the canopy (Wilson *et al.*, 2003) and so is an important vegetation characteristic. Finally, all the models within this thesis assumed a constant flexural rigidity along the stems. This was due to a lack of information regarding variation in flexural rigidity along the vegetation. Such information could easily be incorporated within the existing models to investigate the role of factors such as vegetation age and spatial variability in rigidity in determining flow-vegetation interactions.

Though these developments were beyond the scope of this thesis, the model framework allows these features to be included later. The extension of the models to include these three aspects will further increase the model accuracy and applicability to a range of natural vegetation types.

Furthermore, a new approach for the calculation of drag within vegetation models was developed in Section 3.7. The importance of including a dynamic drag calculation was demonstrated in a single-stalk simulation in Section 6.7. It was shown that a constant drag coefficient both underestimated plant motion and resulted in a false canopy height. Therefore, a necessary further development of the model will be to implement the dynamic drag treatment within the full canopy simulations.

As well as further model developments, there were a number of scenarios which were not able to be fully investigated due to time constraints. Most notably, Section 6.3 drew attention to the case of flow-vegetation feedbacks where the natural frequency of the plants and the shear-layer frequencies are similar. As discussed in Section 9.2, under research question 4, investigation of this scenario would allow the dominant control within canopy flows to be determined.

A common theme between Chapters 5 and 8 was the need for high quality flume and field data to validate the vegetation models. It has been demonstrated in this thesis that field and flume data measurement techniques still appear to lag behind those required for model boundary conditions and for full assessment of the processes and the model. Therefore, there is a need to develop methods which improve our ability to measure both vegetation and flow in the field at a greater spatial and temporal resolution. In particular, there is a need to identify methods for collecting flow and vegetation data simultaneously to allow validation of numerical vegetation motion and flow data accurately.

Finally, Chapter 8 showed an example of how high resolution results might be used to inform lower resolution reach-scale models. In order to improve the predictive capability of flood models applied to vegetated channels and floodplains, it is

necessary to develop a novel treatment of vegetative roughness that is more physically based than the standard empirical methods.

9.4 Potential applications

The results of this thesis, and in particular the two high-resolution biomechanical models, provide a tool for river management. As discussed in Chapter 1, understanding the interaction between flow and vegetation is key to effective river management. Therefore these models should be used to further investigate the role of vegetation across a range of scenarios and to inform management decisions.

With the current balance within river management between EU legislation such as the Water Framework Directive (2000/60/EC) and the Biodiversity Framework (2011/2307(INI)), and the flood management needs of local communities, these models could prove vital in quantifying the effects of vegetation at a local scale. Furthermore, these results could be developed as discussed in the previous section, to improve prediction of flow and sediment dynamics at the reach and catchment scale.

Finally, the models developed within this thesis, using the dynamic mass flux scaling algorithm, are generic fluid-structure interaction models. They could therefore be adapted for use in a wide range of generic dynamic flows in different environmental, biological and engineering contexts.

9.5 Concluding remarks

This thesis has developed a new approach for the modelling of aquatic vegetation. It has demonstrated the effect that vegetation has on drag and consequently turbulence within river channels. The new model approach enables an examination of flow-vegetation interaction in a manner hitherto not possible, which has significant potential for river management.

References

Abdelrhman, M. A. (2007). "Modeling coupling between eelgrass Zostera marina and water flow." Marine Ecology Progress Series **338**: 81-96.

Ackerman, J. D. and A. Okubo (1993). "Reduced Mixing in a Marine Macrophyte Canopy." Functional Ecology **7**(3): 305-309.

Adrian, R. J., C. D. Meinhart and C. D. Tomkins (2000). "Vortex organization in the outer region of the turbulent boundary layer." Journal of Fluid Mechanics **422**: 1-54.

Albayrak, I., V. Nikora, O. Miler and M. O'Hare (2011). "Flow-plant interactions at a leaf scale: effects of leaf shape, serration, roughness and flexural rigidity." Aquatic Sciences - Research Across Boundaries: 1-20.

Alben, S. and M. J. Shelley (2008). "Flapping states of a flag in an inviscid fluid: Bistability and the transition to chaos." Physical Review Letters **100**(7): 4.

Anderson, J. D. (1984). Fundamentals of Aerodynamics. New York, McGraw-Hill.

ASME (1993). "Statement upon the Control of Numerical Accuracy." American Society of Mechanical Engineers, Journal of Fluids Engineering.

Aurell, E., G. Boffetta, A. Crisanti, G. Paladin and A. Vulpiani (1997). "Predictability in the large: An extension of the concept of Lyapunov exponent." Journal of Physics a-Mathematical and General **30**(1): 1-26.

Backhaus, J. O. and J. J. Verduin (2008). "Simulating the interaction of seagrasses with their ambient flow." Estuarine, Coastal and Shelf Science **80**(4): 563-572.

Baker, J. W. (2007). "Quantitative Classification of Near-Fault Ground Motions Using Wavelet Analysis." Bulletin of the Seismological Society of America **97**(5): 1486-1501.

Bal, K. D., T. J. Bouma, K. Buis, E. Struyf, S. Jonas, H. Backx and P. Meire (2011). "Trade-off between drag reduction and light interception of macrophytes: comparing five aquatic plants with contrasting morphology." Functional Ecology **25**(6): 1197-1205.

Bartlett, M. S. (1948). "Smoothing Periodograms from Time-Series with Continuous Spectra." Nature **161**(4096): 686-687.

Bates, P. D., M. S. Horritt and T. J. Fewtrell (2010). "A simple inertial formulation of the shallow water equations for efficient two-dimensional flood inundation modelling." Journal of Hydrology **387**(1–2): 33-45.

Bennett, S. J. and J. L. Best (1995). "Mean flow and turbulence structure over fixed, two-dimensional dunes: implications for sediment transport and bedform stability." Sedimentology **42**(3): 491-513.

Bergström, H. and U. Högström (1989). "Turbulent exchange above a pine forest II. Organized structures." Boundary-Layer Meteorology **49**(3): 231-263.

Booker, D. J., D. A. Sear and A. J. Payne (2001). "Modelling three-dimensional flow structures and patterns of boundary shear stress in a natural pool-riffle sequence." Earth Surface Processes and Landforms **26**(5): 553-576.

Boussinesq, J. (1877). Essai sur la théorie des eaux courantes. Mémoires présentes pars divers savants à l'Académie des Sciences. Paris.

Bradbrook, K. F., P. M. Biron, S. N. Lane, K. S. Richards and A. G. Roy (1998). "Investigation of controls on secondary circulation in a simple confluence geometry using a three-dimensional numerical model." Hydrological Processes **12**(8): 1371-1396.

Bradbrook, K. F., S. N. Lane and K. S. Richards (2000). "Numerical simulation of three-dimensional, time-averaged flow structure at river channel confluences." Water Resources Research **36**(9): 2731-2746.

Bradbrook, K. F., S. N. Lane, K. S. Richards, P. M. Biron and A. G. Roy (2000). "Large Eddy Simulation of periodic flow characteristics at river channel confluences." Journal of Hydraulic Research **38**(3): 207-215.

Buffin-Bélanger, T. and A. G. Roy (2005). "1 min in the life of a river: selecting the optimal record length for the measurement of turbulence in fluvial boundary layers." Geomorphology **68**(1–2): 77-94.

Buffin-Bélanger, T., A. G. Roy and A. D. Kirkbride (2000). "On large-scale flow structures in a gravel-bed river." Geomorphology **32**(3–4): 417-435.

Chakraborty, P., S. Balachandar and R. J. Adrian (2005). "On the relationships between local vortex identification schemes." Journal of Fluid Mechanics **535**: 189-214.

CHAM. (2005). "CHAM Technical Report: TR 001, PHOENICS Overview." 2012, from http://www.cham.co.uk/phoenics/d_polis/d_docs/tr001/tr001.htm.

CHAM. (2005). "Numerical Convection Schemes in PHOENICS." from http://www.cham.co.uk/phoenics/d_polis/d_lecs/numerics/scheme.htm#3.3%20Hybrid-Differencing%20Scheme.

CHAM. (2007). "PHOENICS Encyclopaedia." from http://www.cham.co.uk/phoenics/d_polis/d_enc/encindex.htm.

CHAM. (2008). "Solution Techniques." from http://www.cham.co.uk/phoenics/d_polis/d_lecs/numerics/solution.htm#sst.

Chong, M. S., A. E. Perry and B. J. Cantwell (1990). "A general classification of three-dimensional flow fields." Physics of Fluids A: Fluid Dynamics **2**(5): 765-777.

Chow, V.-T. (1959). Open Channel Hydraulics. New York, McGraw-Hill College.

Clarke, S. J. (2002). "Vegetation growth in rivers: influences upon sediment and nutrient dynamics." Progress in Physical Geography **26**(2): 159-172.

Connell, B. S. H. and D. K. P. Yue (2007). "Flapping dynamics of a flag in a uniform stream." Journal of Fluid Mechanics **581**: 33-68.

Constantinescu, G., S. Miyawaki, B. Rhoads, A. Sukhodolov and G. Kirkil (2011). "Structure of turbulent flow at a river confluence with momentum and velocity ratios close to 1: Insight provided by an eddy-resolving numerical simulation." Water Resources Research **47**(5): W05507.

Cowan, W. L. (1956). "Estimating hydraulic roughness coefficients." Agricultural Engineering **37**(7): 473-475.

Cucitore, R., M. Quadrio and A. Baron (1999). "On the effectiveness and limitations of local criteria for the identification of a vortex." European Journal of Mechanics - B/Fluids **18**(2): 261-282.

Daubechies, I. (1990). "The wavelet transform time-frequency localization and signal analysis." IEEE Trans. inform. Theory **36**: 961-1004.

Davidson, P. A. (2004). Turbulence: An Introduction for Scientists and Engineers. Oxford, Oxford University Press.

De Doncker, L., P. Troch, R. Verhoeven, K. Bal, N. Desmet and P. Meire (2009). "Relation between resistance characteristics due to aquatic weed growth and the hydraulic capacity of the river Aa." River Research and Applications **25**(10): 1287-1303.

Deardorff, J. W. (1970). "A numerical study of three-dimensional turbulent channel flow at large Reynolds numbers." Journal of Fluid Mechanics **41**(02): 453-480.

Deck, S., P. Duveau, P. d'Espiney and P. Guillen (2002). "Development and application of Spalart–Allmaras one equation turbulence model to three-dimensional supersonic complex configurations." Aerospace Science and Technology **6**(3): 171-183.

Defina, A. and A. C. Bixio (2005). "Mean flow and turbulence in vegetated open channel flow." Water Resources Research **41**(7): 12.

Denny, M. and B. Gaylord (2002). "The mechanics of wave-swept algae." Journal of Experimental Biology **205**(10): 1355-1362.

Devaney, R. (2003). An Introduction to Chaotic Dynamical Systems, 2nd Edition, {Westview Pr (Short Disc)}.

Dijkstra, J. T. and R. E. Uittenbogaard (2010). "Modeling the interaction between flow and highly flexible aquatic vegetation." Water Resour. Res. **46**(12): W12547.

Doare, O., B. Moulia and E. d. Langre (2004). "Effect of Plant Interaction on Wind-Induced Crop Motion." Journal of Biomechanical Engineering **126**(2): 146-151.

Dunn, C., F. Lopez and M. H. Garcia (1996). "Mean flow and turbulence in a laboratory channel with simulated vegetation." UIUL-ENG-96-2009, University of Illinois, Urbana.

Dupont, S. and Y. Brunet (2008a). "Edge Flow and Canopy Structure: A Large-Eddy Simulation Study." Boundary-Layer Meteorology **126**(1): 51-71.

Dupont, S. and Y. Brunet (2008b). "Influence of foliar density profile on canopy flow: A large-eddy simulation study." Agricultural and Forest Meteorology **148**(6–7): 976-990.

Dupont, S., Y. Brunet and J. J. Finnigan (2008). "Large-eddy simulation of turbulent flow over a forested hill: Validation and coherent structure identification." Quarterly Journal of the Royal Meteorological Society **134**(636): 1911-1929.

Dupont, S., F. Gosselin, C. Py, E. De Langre, P. Hemon and Y. Brunet (2010). "Modelling waving crops using large-eddy simulation: comparison with experiments and a linear stability analysis." Journal of Fluid Mechanics **652**: 5-44.

Dwyer, M. J., E. G. Patton and R. H. Shaw (1997). "Turbulent kinetic energy budgets from a large-eddy simulation of airflow above and within a forest canopy." Boundary-Layer Meteorology **84**(1): 23-43.

E.A. (2004). "Reducing uncertainty in River Conveyance." W5A-057/PR/1.

Erduran, K. S. and V. Kutija (2003). "Quasi-three-dimensional numerical model for flow through flexible, rigid, submerged and non-submerged vegetation." Journal of Hydroinformatics **5**(3): 189-202.

ETC/BD (2008). "Article 17 Technical Report (2001-2006)." available at http://forum.eionet.europa.eu/x_habitat-art17report/library/datasheets/habitats/freshwater_habitats/freshwater_habitats/3260-water_ranunculionpd/download/1/3260-Water%20courses%20of%20plain%20to%20montane%20level%20%28Ranunculion..%29.pdf.

Evans, E. P., J. Simm, C. Thorne, N. W. Arnell, R. Ashley, T. Hess, S. Lane, J. Morris, R. J. Nicholls, E. Penning-Rowsell, N. Reynard, A. Saul, S. Tapsell, A. Watkinson and H. Wheater (2009). An update of the Foresight Future Flooding 2004 qualitative risk analysis.

Farge, M. (1992). "Wavelet Transforms and their Applications to Turbulence." Annual Review of Fluid Mechanics **24**(1): 395-458.

Farnell, D. J. J., T. David and D. C. Barton (2004). "Numerical simulations of a filament in a flowing soap film." International Journal for Numerical Methods in Fluids **44**(3): 313-330.

Felippa, C. A., K. C. Park and C. Farhat (2001). "Partitioned analysis of coupled mechanical systems." Computer Methods in Applied Mechanics and Engineering **190**(24-25): 3247-3270.

Ferguson, R. (2010). "Time to abandon the Manning equation?" Earth Surface Processes and Landforms **35**(15): 1873-1876.

Ferguson, R. I., D. R. Parsons, S. N. Lane and R. J. Hardy (2003). "Flow in meander bends with recirculation at the inner bank." Water Resour. Res. **39**(11): 1322.

Ferguson, R. I., D. R. Parsons, S. N. Lane and R. J. Hardy (2003). "Flow in meander bends with recirculation at the inner bank." Water Resources Research **39**(11): 1322.

Finnigan, J. (1979a). "Turbulence in waving wheat I. Mean statistics ans Honami." Boundary-Layer Meteorology **16**(2): 181-211.

Finnigan, J. (1979b). "Turbulence in waving wheat II. Structure of Momentum Transfer." Boundary-Layer Meteorology **16**(2): 213-236.

Finnigan, J. (2000). "Turbulence in Plant Canopies." Annual Review of Fluid Mechanics **32**(1): 519-571.

Finnigan, J. J. (2010). "Waving plants and turbulent eddies." Journal of Fluid Mechanics **652**: 1-4.

Finnigan, J. J. and P. J. Mulhearn (1978). "Modelling waving crops in a wind tunnel." Boundary-Layer Meteorology **14**(2): 253-277.

Finnigan, J. J., R. H. Shaw and E. G. Patton (2009). "Turbulence structure above a vegetation canopy." Journal of Fluid Mechanics **637**: 387-424.

Fischer-Antze, T., T. Stoesser, P. Bates and N. R. B. Olsen (2001). "3D numerical modelling of open-channel flow with submerged vegetation." Journal of Hydraulic Research **39**(3): 303-310.

Fisher, K. (1992). "The Hydraulic Roughness of Vegetated Channels." Hydraulics Research Ltd: Wallingford.

Flesch, T. K. and R. H. Grant (1991). "The translation of turbulent wind energy to individual corn plant motion during senescense." Boundary-Layer Meteorology **55**(1): 161-176.

Flynn, M. R. and A. D. Eisner (2004). "Verification and validation studies of the time-averaged velocity field in the very near-wake of a finite elliptical cylinder." Fluid Dynamics Research **34**(4): 273-288.

Folkard, A. (2011). "Flow regimes in gaps within stands of flexible vegetation: laboratory flume simulations." Environmental Fluid Mechanics **11**(3): 289-306.

Fourier, J. B. J. (1878). The Analytical Theory of Heat. Harvard university, The University Press. Translated by A. Freeman

Franklin, P., M. Dunbar and P. Whitehead (2008). "Flow controls on lowland river macrophytes: A review." Science of The Total Environment **400**(1–3): 369-378.

Gao, W., R. H. Shaw and K. T. Paw U (1989). "Observation of organized structure in turbulent flow within and above a forest canopy." Boundary-Layer Meteorology **47**(1): 349-377.

García Díaz, R. (2005). "Analysis of Manning coefficient for small-depth flows on vegetated beds." Hydrological Processes **19**(16): 3221-3233.

George, W. K., P. D. Beuther and R. E. A. Arndt (1984). "Pressure spectra in turbulent free shear flows." Journal of Fluid Mechanics **148**: 155-191.

Germano, M., U. Piomelli, P. Moin and W. H. Cabot (1991). "A dynamic subgrid-scale eddy viscosity model." Physics of Fluids A: Fluid Dynamics **3**(7): 1760-1765.

Ghisalberti, M. (2009). "Obstructed shear flows: similarities across systems and scales." Journal of Fluid Mechanics **641**: 51-61.

Ghisalberti, M. and H. Nepf (2006). "The Structure of the Shear Layer in Flows over Rigid and Flexible Canopies." Environmental Fluid Mechanics **6**(3): 277-301.

Ghisalberti, M. and H. Nepf (2009). "Shallow Flows Over a Permeable Medium: The Hydrodynamics of Submerged Aquatic Canopies." Transport in Porous Media **78**(3): 385-402.

Ghisalberti, M. and H. M. Nepf (2002). "Mixing layers and coherent structures in vegetated aquatic flows." Journal of Geophysical Research-Oceans **107**(C2): 11.

Ghisalberti, M. and H. M. Nepf (2004). "The limited growth of vegetated shear layers." Water Resour. Res. **40**(7): W07502.

Gosselin, F. and E. de Langre (2009). "Destabilising effects of plant flexibility in air and aquatic vegetation canopy flows." European Journal of Mechanics - B/Fluids **28**(2): 271-282.

Gosselin, F., E. de Langre and B. A. Machado-Almeida (2010). "Drag reduction of flexible plates by reconfiguration." Journal of Fluid Mechanics **650**: 319-341.

Gosselin, F. P. and E. de Langre (2011). "Drag reduction by reconfiguration of a poroelastic system." Journal of Fluids and Structures **27**(7): 1111-1123.

Graf, W. H. (1998). Fluvial Hydraulics: Flow and transport processes in channels of simple geometry. Chichester, John Wiley and Sons.

Green, J. C. (2005a). "Comparison of blockage factors in modelling the resistance of channels containing submerged macrophytes." River Research and Applications **21**(6): 671-686.

Green, J. C. (2005b). "Modelling flow resistance in vegetated streams: review and development of new theory." Hydrological Processes **19**(6): 1245-1259.

Green, J. C. (2006). "Effect of macrophyte spatial variability on channel resistance." Advances in Water Resources **29**(3): 426-438.

Green, M. A., C. W. Rowley and G. Haller (2007). "Detection of Lagrangian coherent structures in three-dimensional turbulence." Journal of Fluid Mechanics **572**: 111-120.

Grizzle, R. E., F. T. Short, C. R. Newell, H. Hoven and L. Kindblom (1996). "Hydrodynamically induced synchronous waving of seagrasses: 'monami' and its possible effects on larval mussel settlement." Journal of Experimental Marine Biology and Ecology **206**(1–2): 165-177.

Gurnell, A. (2013). "Plants as river system engineers." Earth Surface Processes and Landforms: n/a-n/a.

Haller, G. (2000). "Finding finite-time invariant manifolds in two-dimensional velocity fields." Chaos: An Interdisciplinary Journal of Nonlinear Science **10**(1): 99-108.

Haller, G. (2005). "An objective definition of a vortex." Journal of Fluid Mechanics **525**: 1-26.

Haller, G. and G. Yuan (2000). "Lagrangian coherent structures and mixing in two-dimensional turbulence." Physica D: Nonlinear Phenomena **147**(3–4): 352-370.

Hanjalic, K. and B. E. Launder (1972). "A Reynolds stress model of turbulence and its application to thin shear flows." Journal of Fluid Mechanics **52**(04): 609-638.

Hardy, R. J., J. L. Best, S. N. Lane and P. E. Carbonneau (2009). "Coherent flow structures in a depth-limited flow over a gravel surface: The role of near-bed turbulence and influence of Reynolds number." Journal of Geophysical Research-Earth Surface **114**: 18.

Hardy, R. J., S. N. Lane, R. I. Ferguson and D. R. Parsons (2003). "Assessing the credibility of a series of computational fluid dynamic simulations of open channel flow." Hydrological Processes **17**(8): 1539-1560.

Hardy, R. J., S. N. Lane, R. I. Ferguson and D. R. Parsons (2007). "Emergence of coherent flow structures over a gravel surface: A numerical experiment." Water Resources Research **43**(3): 14.

Hardy, R. J., S. N. Lane, M. R. Lawless, J. L. Best, L. Elliott and D. B. Ingham (2005). "Development and testing of a numerical code for treatment of complex river channel topography in three-dimensional CFD models with structured grids." Journal of hydraulic research. **43**(5): 468-480.

Hardy, R. J., S. N. Lane and D. Yu (2011). "Flow structures at an idealized bifurcation: a numerical experiment." Earth Surface Processes and Landforms **36**(15): 2083-2096.

Haslam, S., C. Sinker and P. Wolseley (1975). "British Water Plants." Field Studies **4**: 243-351.

Hinze, J. O. (1975). Turbulence. New York, McGraw-Hill.

Ho, C. M. and P. Huerre (1984). "Perturbed Free Shear Layers." Annual Review of Fluid Mechanics **16**: 365-424.

Hodskinson, A. and R. I. Ferguson (1998). "Numerical modelling of separated flow in river bends: model testing and experimental investigation of geometric controls on the extent of flow separation at the concave bank." Hydrological Processes **12**(8): 1323-1338.

Hoffmann, M. R. (2004). "Application of a simple space-time averaged porous media model to flow in densely vegetated channels." Journal of Porous Media **7**(3): 183-191.

Huang, H., D. Dabiri and M. Gharib (1997). "On errors of digital particle image velocimetry." Measurement Science and Technology **8**(12): 1427.

Hunt, J. C. R., A. A. Wray and P. Moin (1988). "Eddies, stream and convergence zones in turbulent flows."

Huthoff, F., D. C. M. Augustijn and S. Hulscher (2007). "Analytical solution of the depth-averaged flow velocity in case of submerged rigid cylindrical vegetation." Water Resources Research **43**(6): 10.

Ikeda, S. and M. Kanazawa (1996). "Three-dimensional organized vortices above flexible water plants." Journal of Hydraulic Engineering-Asce **122**(11): 634-640.

Ikeda, S., M. Kanazawa and K. Ohta (1995). "Flow over flexible vegetation and 3-D structure of organized vortex associated with honami." Journal of Hydraulic, Coastal and Environmental Enginerring, **515**: 33-43.

Ikeda, S., T. Yamada and Y. Toda (2001). "Numerical study on turbulent flow and honami in and above flexible plant canopy." International Journal of Heat and Fluid Flow **22**(3): 252-258.

Ingham, D. B. and L. Ma (2005). Fundamental equations for CFD in river flow simulations. Computational Fluid Dynamics:Applications in Environmental Hydraulics. P. Bates, S. N. Lane and R. I. Ferguson, Wiley.

Inoue, E. (1955a). "Studies of the phenomenon of waving plants ("Honami") caused by wind. I. Mechanism of waving and characteristics of waving plants phenomena." Journal of Agricultural Meteorology (Tokyo) **11**: 18-22.

Inoue, E. (1955b). "Studies of the phenomenon of waving plants ("Honami") caused by wind. II Spectra of waving plants and plants vibration." Journal of Agricultural Meteorology (Tokyo) **11**: 87-90.

Inoue, E. (1963). "On the Turbulent Structure of Airflow within Crop Canopies." Journal of the Meteorological Society of Japan. Ser II **41**(6): 317-326.

James, C. S., A. L. Birkhead, A. A. Jordanova and J. J. O'Sullivan (2004). "Flow resistance of emergent vegetation." Journal of Hydraulic Research **42**(4): 390-398.

Jarvela, J. (2002). "Flow resistance of flexible and stiff vegetation: a flume study with natural plants." Journal of Hydrology **269**(1-2): 44-54.

Jeong, J. and F. Hussain (1995). "On the identification of a vortex." Journal of Fluid Mechanics **285**: 69-94.

Jirka, G. H. and W. S. J. Uijttewaal (2004). Shallow Flows. London, Taylor & Francis.

Kadlec, R. H. and R. L. Knight (1996). Treatment Wetlands. Boca Raton, FL, Lewis Publishers.

Kaiser, G. (1994). A Friendly Guide to Wavelets, Birkhäuser.

Kanda, M. and M. Hino (1994). "Organized structures in developing turbulent flow within and above a plant canopy, using a Large Eddy Simulation." Boundary-Layer Meteorology **68**(3): 237-257.

Kemp, J. L., D. M. Harper and G. A. Crosa (2000). "The habitat-scale ecohydraulics of rivers." Ecological Engineering **16**(1): 17-29.

Keylock, C. J., R. J. Hardy, D. R. Parsons, R. I. Ferguson, S. N. Lane and K. S. Richards (2005). "The theoretical foundations and potential for large-eddy simulation (LES) in fluvial geomorphic and sedimentological research." Earth-Science Reviews **71**(3-4): 271-304.

Kim, J., P. Moin and R. Moser (1987). "Turbulence statistics in fully developed channel flow at low Reynolds number." Journal of Fluid Mechanics **177**: 133-166.

Kim, S. J. and T. Stoesser (2011). "Closure modeling and direct simulation of vegetation drag in flow through emergent vegetation." Water Resources Research **47**(10): W10511.

Kolmogorov, A. N. (1941). "On degeneration of isotropic turbulence in an incompressible viscous fluid." Comptes Rendus (Doklady) de l'Academie des Sciences de l'U.R.S.S., **31**: 538-540.

Konings, A. G., G. G. Katul and S. E. Thompson (2012). "A phenomenological model for the flow resistance over submerged vegetation." Water Resour. Res. **48**(2): W02522.

Kouwen, N. (1980). "Biomechanics of vegetated channel linings." Journal of the Hydraulics Division-Asce **106**: 1085-1203.

Kouwen, N., R. M. Li and D. B. Simons (1981). "Flow Resistance in Vegetated Waterways." Transactions of the Asae **24**(3): 684-&.

Kouwen, N. and T. E. Unny (1973). "Flexible roughness in open channels." Journal of the Hydraulics Division-Asce **101**(NHY1): 194-196.

Kouwen, N., T. E. Unny and H. M. Hill (1969). "Flow retardance in vegetated channels." Journal of the Irrigation and Drainage Division **95**(2): 329-342.

Kutija, V. and H. T. M. Hong (1996). "A numerical model for assessing the additional resistance to flow introduced by flexible vegetation." Journal of Hydraulic Research **34**(1): 99-114.

Lane, S. N. (1998). "Hydraulic modelling in hydrology and geomorphology: a review of high resolution approaches." Hydrological Processes **12**(8): 1131-1150.

Lane, S. N. (2005). "Roughness - time for a re-evaluation?" Earth Surface Processes and Landforms **30**(2): 251-253.

Lane, S. N., K. F. Bradbrook, K. S. Richards, P. A. Biron and A. G. Roy (1999). "The application of computational fluid dynamics to natural river channels: three-dimensional versus two-dimensional approaches." Geomorphology **29**(1–2): 1-20.

Lane, S. N. and R. J. Hardy (2002). Porous rivers: A new way of conceptualizing and modelling river and floodplain flows. Transport Phenomena in Porous Media. D. B. Ingham and I. Pop. **2**.

Lane, S. N., R. J. Hardy, L. Elliott and D. B. Ingham (2002). "High-resolution numerical modelling of three-dimensional flows over complex river bed topography." Hydrological Processes **16**(11): 2261-2272.

Lane, S. N., R. J. Hardy, L. Elliott and D. B. Ingham (2004). "Numerical modeling of flow processes over gravelly surfaces using structured grids and a numerical porosity treatment." Water Resources Research **40**(1): 18.

Lane, S. N., R. J. Hardy, R. I. Ferguson and D. R. Parsons (2005). A framework for model verification and validation of CFD schemes in natural open channel flows. Computational Fluid Dynamics:Applications in Environmental Hydraulics. P. Bates, S. N. Lane and R. I. Ferguson. Chichester, Wiley.

Lane, S. N., K. S. Richards and J. H. Chandler (1994). "Developments in monitoring and modelling small-scale river bed topography." Earth Surface Processes and Landforms **19**(4): 349-368.

Launder, B. E., G. J. Reece and W. Rodi (1975). "Progress in the development of a Reynolds-stress turbulence closure." Journal of Fluid Mechanics **68**(03): 537-566.

Le, H., P. Moin and J. Kim (1997). "Direct numerical simulation of turbulent flow over a backward-facing step." Journal of Fluid Mechanics **330**: 349-374.

Lesieur, M. (2008). Turbulence in Fluids. New York, Springer-Verlag.

Li, C. W. and J. F. Xie (2011). "Numerical modeling of free surface flow over submerged and highly flexible vegetation." Advances in Water Resources **34**(4): 468-477.

Lien, F. S. and M. A. Leschziner (1994). "Assessment of turbulence-transport models including non-linear rng eddy-viscosity formulation and second-moment closure for flow over a backward-facing step." Computers & Fluids **23**(8): 983-1004.

Lipinski, D. and K. Mohseni (2010). "A ridge tracking algorithm and error estimate for efficient computation of Lagrangian coherent structures." Chaos: An Interdisciplinary Journal of Nonlinear Science **20**(1): 017504-017509.

Liu, C. and Y.-m. Shen (2008). "Flow structure and sediment transport with impacts of aquatic vegetation." Journal of Hydrodynamics, Ser. B **20**(4): 461-468.

Liu, D., P. Diplas, J. D. Fairbanks and C. C. Hodges (2008). "An experimental study of flow through rigid vegetation." J. Geophys. Res. **113**.

López, F. and M. García (1998). "open-channel flow through simulated vegetation: Suspended sediment transport modeling." Water Resources Research **34**(9): 2341-2352.

Lopez, F. and M. H. Garcia (2001). "Mean flow and turbulence structure of open-channel flow through non-emergent vegetation." Journal of Hydraulic Engineering-Asce **127**(5): 392-402.

Lu, S. S. and W. W. Willmart (1973). "Measurements of the structure of the Reynolds stress in a turbulent boundary layer." Journal of Fluid Mechanics **60**(SEP18): 481-511.

Luettich, R. A. and J. W. Westerlink (1994). Continental Shelf Scale Convergence Studies with a Baratropic Tidal Model. Quantitative Skill Assessment of Coastal Ocean Models. L. D.R. and D. A.M., AGU Press.

Luhar, M., S. Coutu, E. Infantes, S. Fox and H. Nepf (2010). "Wave-induced velocities inside a model seagrass bed." Journal of Geophysical Research: Oceans **115**(C12): n/a-n/a.

Luhar, M. and H. M. Nepf (2011). "Flow-induced reconfiguration of buoyant and flexible aquatic vegetation." Limnology and Oceanography **56**(6): 2003-2017.

Luhar, M. and H. M. Nepf (2013). "From the blade scale to the reach scale: A characterization of aquatic vegetative drag." Advances in Water Resources **51**(0): 305-316.

Luhar, M., J. Rominger and H. Nepf (2008). "Interaction between flow, transport and vegetation spatial structure." Environmental Fluid Mechanics **8**(5-6): 423-439.

Maitani, T. (1977). "Vertical transport of turbulent kinetic energy in the surface layer over a paddy field." Boundary-Layer Meteorology **12**(4): 405-423.

Maitani, T. (1978). "On the downward transport of turbulent kinetic energy in the surface layer over plant canopies." Boundary-Layer Meteorology **14**(4): 571-584.

Maitani, T. (1979). "An observational study of wind-induced waving of plants." Boundary-Layer Meteorology **16**(3): 49-65.

Maltese, A., E. Cox, A. M. Folkard, G. Ciraolo, G. La Loggia and G. Lombardo (2007). "Laboratory Measurements of Flow and Turbulence in Discontinuous Distributions of Ligulate Seagrass." Journal of Hydraulic Engineering **133**(7): 750-760.

Marquis, G. A. and A. G. Roy (2011). "Bridging the gap between turbulence and larger scales of flow motions in rivers." Earth Surface Processes and Landforms **36**(4): 563-568.

Michelin, S., S. G. L. Smith and B. J. Glover (2008). "Vortex shedding model of a flapping flag." Journal of Fluid Mechanics **617**: 1-10.

Miler, O., I. Albayrak, V. Nikora and M. O'Hare (2012). "Biomechanical properties of aquatic plants and their effects on plant-flow interactions in streams and rivers." Aquatic Sciences **74**(1): 31-44.

Moin, P. and K. Mahesh (1998). "Direct Numerical Simulation: A Tool in Turbulence Research." Annual Review of Fluid Mechanics **30**(1): 539-578.

Na, Y. and P. Moin (1998). "Direct numerical simulation of a separated turbulent boundary layer." Journal of Fluid Mechanics **374**: 379-405.

Naden, P., P. Rameshwaran, O. Mountford and C. Robertson (2006). "The influence of macrophyte growth, typical of eutrophic conditions, on river flow velocities and turbulence production." Hydrological Processes **20**(18): 3915-3938.

Nepf, H. and M. Ghisalberti (2008). "Flow and transport in channels with submerged vegetation." Acta Geophysica **56**(3): 753-777.

Nepf, H. and M. Ghisalberti (2008). Flow and transport in channels with submerged vegetation. 5th Workshop on Double-Averaging Methodology, Lisbon, PORTUGAL, Versita.

Nepf, H., M. Ghisalberti, B. White and E. Murphy (2007). "Retention time and dispersion associated with submerged aquatic canopies." Water Resources Research **43**(4): 10.

Nepf, H., J. Rominger and L. Zong (in press). Coherent Flow Structures in Vegetated Channels. Coherent Structures at the Earth's Surface. J. G. Venditti, M. Church, J. L. Best and R. J. Hardy, John Wiley and Sons.

Nepf, H. M. (1999). "Drag, turbulence, and diffusion in flow through emergent vegetation." Water Resources Research **35**(2): 479-489.

Nepf, H. M. (2012a). "Flow and Transport in Regions with Aquatic Vegetation." Annual Review of Fluid Mechanics **44**(1): 123-142.

Nepf, H. M. (2012b). "Hydrodynamics of vegetated channels." Journal of Hydraulic Research **50**(3): 262-279.

Nepf, H. M. and E. W. Koch (1999). "Vertical secondary flows in submersed plant-like arrays." Limnology and Oceanography **44**(4): 1072-1080.

Nepf, H. M. and E. R. Vivoni (2000). "Flow structure in depth-limited, vegetated flow." Journal of Geophysical Research-Oceans **105**(C12): 28547-28557.

Neumeier, U. R. S. and C. L. Amos (2006). "The influence of vegetation on turbulence and flow velocities in European salt-marshes." Sedimentology **53**(2): 259-277.

Nezu, I. and K. Onitsuka (2001). "Turbulent structures in partly vegetated open-channel flows with LDA and PIV measurements." Journal of Hydraulic Research **39**(6): 629-642.

Nezu, I. and M. Sanjou (2008). "Turburence structure and coherent motion in vegetated canopy open-channel flows." Journal of Hydro-environment Research **2**(2): 62-90.

Nicholas, A. P. (2001). "Computational fluid dynamics modelling of boundary roughness in gravel-bed rivers: an investigation of the effects of random variability in bed elevation." Earth Surface Processes and Landforms **26**(4): 345-362.

Niklas, K. J. (1992). Plant Biomechanics: An engineering Approach to Plant Form and Function, University of Chicago Press.

Nikora, V. (2010). "Hydrodynamics of aquatic ecosystems: An interface between ecology, biomechanics and environmental fluid mechanics." River Research and Applications **26**(4): 367-384.

O'Hare, M. T., K. A. Hutchinson and R. T. Clarke (2007). "The drag and reconfiguration experienced by five macrophytes from a lowland river." Aquatic Botany **86**(3): 253-259.

O'Hare, M. T., C. McGahey, N. Bissett, C. Cailes, P. Henville and P. Scarlett (2010). "Variability in roughness measurements for vegetated rivers near base flow, in England and Scotland." Journal of Hydrology **385**(1–4): 361-370.

Okamoto, T.-A. and I. Nezu (2009). "Turbulence structure and "Monami" phenomena in flexible vegetated open-channel flows." Journal of Hydraulic Research **47**: 13.

Olsen, N. R. B. and S. Stokseth (1995). " 3-dimensional numerical modelling of water-flow in a river with large bed roughness." Journal of Hydraulic Research **33**(4): 571-581.

Oreskes, N., K. Shraderfrechette and K. Belitz (1994). "Verification, validation, and confirmation of numerical-models in the earth sciences." Science **263**(5147): 641-646.

Pantakar, S. V. (1980). Numerical Heat Transfer and Fluid Flow. New York, Hemisphere.

Panton, R. L. (1984). Incompressible Flow. New York, Wiley-Interscience.

Parseval, M. A. (1799). Mémoire sur les séries et sur l'intégration complète d'une équation aux différences partielles linéaires du second ordre, à coefficents constants.

Patankar, S. V. and D. B. Spalding (1972). "A calculation procedure for heat, mass and momentum transfer in three-dimensional parabolic flows." International Journal of Heat and Mass Transfer **15**(10): 1787-1806.

Penhale, P. A. and R. G. Wetzel (1983). "Structural and functional adaptations of eelgrass (Zostera marina L.) to the anaerobic sediment environment." Canadian Journal of Botany **61**(5): 1421-1428.

Percival, D. B. and A. T. Walden (2000). Wavelet methods for Time Series Analysis. Cambridge, Cambridge University Press.

Petryk, S. and G. Bosmajian (1975). "Analysis of flow through vegetation." Journal of the Hydraulics Division-Asce **101**(7): 871-884.

Pierrehumbert, R. T. and H. Yang (1993). "Global Chaotic Mixing on Isentropic Surfaces." Journal of the Atmospheric Sciences **50**(15): 2462-2480.

Pitt, M. (2008). "Learning lessons from the 2007 floods." DEFRA.

Pope, S. B. (2000). Turbulent Flows. Cambridge, Cambridge University Press.

Prandtl, L. (1925). "Liber die ausgebildete turbulenz." Z. Angew. Math. Mech. **5**(136-139).

Py, C., E. de Langre and B. Moulia (2004). "The mixing layer instability of wind over a flexible crop canopy." Comptes Rendus Mécanique **332**(8): 613-618.

Py, C., E. de Langre and B. Moulia (2006). "A frequency lock-in mechanism in the interaction between wind and crop canopies." Journal of Fluid Mechanics **568**: 425-449.

Raupach, M. R. (1989). "A practical Lagrangian method for relating scalar concentrations to source distributions in vegetation canopies." Quarterly Journal of the Royal Meteorological Society **115**(487): 609-632.

Raupach, M. R., J. J. Finnigan and Y. Brunet (1996). "Coherent eddies and turbulence in vegetation canopies: The mixing-layer analogy." Boundary-Layer Meteorology **78**(3-4): 351-382.

Raupach, M. R. and R. H. Shaw (1982). "Averaging procedures for flow within vegetation canopies." Boundary-Layer Meteorology **22**(1): 79-90.

Raupach, M. R. and A. S. Thom (1981). "Turbulence in and above plant canopies." Annual Review of Fluid Mechanics **13**: 97-129.

Ree, W. O. (1958). "Retardation coefficients for row crops in division terraces." Transactions of ASAE **1**(1): 78-80.

Reynolds, O. (1895). "On the dynamical theory of incompressible viscous fluids and the determination of the criterion." Phil. Trans. R. Soc. **186A**: 123-164.

Rhee, D. S., H. Woo, B. A. Kwon and H. K. Ahn (2008). "Hydraulic resistance of some selected vegetation in open channel flows." River Research and Applications **24**(5): 673-687.

Roache, P. J. (1993). A method for uniform reporting of grid refinement studies. Proceedings of the 11th AIAA Computational Fluid Dynamics Conference, Orlando, FL.

Roache, P. J. (1994). "Perspective - A method for uniform reporting of grid refinement studies." Journal of Fluids Engineering-Transactions of the Asme **116**(3): 405-413.

Roache, P. J. (1997). "Quantification of uncertainty in computational fluid dynamics." Annual Review of Fluid Mechanics **29**: 123-160.

Roache, P. J. (1998). Verification and validation in computational science and engineering. Albuquerque, Hermosa.

Rodi, W. (1997). "Comparison of LES and RANS calculations of the flow around bluff bodies." Journal of Wind Engineering and Industrial Aerodynamics **69–71**(0): 55-75.

Rogallo, R. S. and P. Moin (1984). "Numerical Simulation of Turbulent Flows." Annual Review of Fluid Mechanics **16**(1): 99-137.

Rogers, M. M. and R. D. Moser (1992). "The three-dimensional evolution of a plane mixing layer: the Kelvin–Helmholtz rollup." Journal of Fluid Mechanics **243**: 183-226.

Rogers, M. M. and R. D. Moser (1994). "Direct simulation of a self-similar turbulent mixing layer." Physics of Fluids **6**(2): 903-923.

Rotta, J. (1951). "Statistische Theorie nichthomogener Turbulenz." Zeitschrift für Physik A Hadrons and Nuclei **129**(6): 547-572.

Sand-Jensen, K. (2003). "Drag and reconfiguration of freshwater macrophytes." Freshwater Biology **48**(2): 271-283.

Sand-Jensen, K. A. J., E. Jeppesen, K. Nielsen, L. Van Der Bijl, L. Hjermind, L. W. Nielsen and T. M. Ivlrsln (1989). "Growth of macrophytes and ecosystem consequences in a lowland Danish stream." Freshwater Biology **22**(1): 15-32.

Sandbach, S. D., S. N. Lane, R. J. Hardy, M. L. Amsler, P. J. Ashworth, J. L. Best, A. P. Nicholas, O. Orfeo, D. R. Parsons, A. J. H. Reesink and R. N. Szupiany (2012). "Application of a roughness-length representation to parameterize energy loss in 3-D numerical simulations of large rivers." Water Resources Research **48**(12): W12501.

Schouveiler, L. and A. Boudaoud (2006). "The rolling up of sheets in a steady flow." Journal of Fluid Mechanics **563**: 71-80.

Schuster, A. (1898). "On the investigation of hidden periodicities with application to a supposed 26 day period of meteorological phenomena." Terrestrial Magnetism and Atmospheric Electricity **3**: 13-41.

Seginer, I., P. J. Mulhearn, E. F. Bradley and J. J. Finnigan (1976). "Turbulent flow in a model plant canopy." Boundary-Layer Meteorology **10**(4): 423-453.

Shadden, S. C., F. Lekien and J. E. Marsden (2005). "Definition and properties of Lagrangian coherent structures from finite-time Lyapunov exponents in two-dimensional aperiodic flows." Physica D-Nonlinear Phenomena **212**(3-4): 271-304.

Shaw, R. H. and U. Schumann (1992). "Large-eddy simulation of turbulent flow above and within a forest." Boundary-Layer Meteorology **61**(1): 47-64.

Shimizu, Y., M. W. Schmeeckle and J. M. Nelson (2001). "Direct Numerical Simulation of Turbulence Over Two-Dimensional Dunes Using CIP Method." Journal of Hydroscience and Hydraulic Engineering **19**(2): 85-92.

Shucksmith, J. D., J. B. Boxall and I. Guymer (2011). "Bulk Flow Resistance in Vegetated Channels: Analysis of Momentum Balance Approaches Based on Data Obtained in Aging Live Vegetation." Journal of Hydraulic Engineering **137**(12): 1624-1635.

Siniscalchi, F. and V. I. Nikora (2012). "Flow-plant interactions in open-channel flows: A comparative analysis of five freshwater plant species." Water Resources Research **48**(5): W05503.

Smagorinsky, J. (1963). "GENERAL CIRCULATION EXPERIMENTS WITH THE PRIMITIVE EQUATIONS." Monthly Weather Review **91**(3): 99-164.

Sotiropoulos, F. (2005). Introduction to statistical turbulence modelling for hydraulic engineering flows. Computational Fluid Dynamics:Applications in Environmental Hydraulics. P. Bates, S. N. Lane and R. I. Ferguson. Chichester, Wiley.

Spalart, P. R. (1988). "Direct simulation of a turbulent boundary layer up to Rθ = 1410." Journal of Fluid Mechanics **187**: 61-98.

Spalart, P. R. (2008). "Detached-Eddy Simulation." Annual Review of Fluid Mechanics **41**(1): 181-202.

Spalart, P. R. and S. R. Allmaras (1994). "A One-Equation Turbulence Model for Aerodynamic Flows." La Rech. Aérospatiale **1**: 5-21.

Spalding, D. B. (1980). "Mathematical Modelling of Fluid Mechanics, Heat Transfer and Mass Transfer Processes." HTS-8-1, Mech. Eng. Dept., Imperial College of Science, Technology and Medicine, London.

Spalding, D. B. (1985). The computation of flow around ships with allowance for free-surface and density-gradient effects. Proceedings of the First Intercontinental Symposium on Maritime Simulation.

Speziale, C. G. (1991). "Analytical Methods for the Development of Reynolds-Stress closures in Turbulence." Annual Review of Fluid Mechanics **23**: 107-157.

Sprott, J. C. (2003). Chaos and Time Series Analysis. Oxford, Oxford University Press.

Stephan, U. and D. Gutknecht (2002). "Hydraulic resistance of submerged flexible vegetation." Journal of Hydrology **269**(1–2): 27-43.

Stoesser, T., S. Kara, B. MacVicar and J. L. Best (2010). Turbulent Flow over a mildly sloped pool-riffle sequence. Proceedings of the IAHR River Flow 2010 Conference, Bundesanstalt fuer Wasserbau**:** 409-417.

Stoesser, T., S. J. Kim and P. Diplas (2010). "Turbulent Flow through Idealized Emergent Vegetation." Journal of Hydraulic Engineering-Asce **136**(12): 1003-1017.

Stoesser, T., C. Liang, W. Rodi and G. Jirka (2006). Large eddy simulation of fully-developed turbulent flow through submerged vegetation. River Flow 2006, Two Volume Set, Taylor & Francis.

Stoesser, T., G. P. Salvador, W. Rodi and P. Diplas (2009). "Large Eddy Simulation of Turbulent Flow Through Submerged Vegetation." Transport in Porous Media **78**(3): 347-365.

Stoica, P. and R. Moses (1997). Introduction to Spectral Analysis. Upper Saddle River, Prentice-Hall.

Stone, B. M. and H. T. Shen (2002). "Hydraulic Resistance of Flow in Channels with Cylindrical Roughness." Journal of Hydraulic Engineering-Asce **128**(5): 500-506.

Sukhodolov, A. N. and T. A. Sukhodolova (2010). "Case Study: Effect of Submerged Aquatic Plants on Turbulence Structure in a Lowland River." Journal of Hydraulic Engineering **136**(7): 434-446.

Sukhodolova, T. A. and A. N. Sukhodolov (2012). "Vegetated mixing layer around a finite-size patch of submerged plants: 1. Theory and field experiments." Water Resources Research **48**(10): n/a-n/a.

Tanino, Y. and H. Nepf (2008). "Laboratory Investigation of Mean Drag in a Random Array of Rigid, Emergent Cylinders." Journal of Hydraulic Engineering **134**(1): 34-41.

Tennekes, H. and J. L. Lumley (1972). A First Course in Turbulence, MIT Press.

Torrence, C. and G. P. Compo (1998). "A Practical Guide to Wavelet Analysis." Bulletin of the American Meteorological Society **79**(1): 61-78.

Tritton, D. J. (1988). Physical Fluid Dynamics. Oxford, Oxford University Press.

Velasco, D., A. Bateman, J. M. Redondo and V. Demedina (2003). "An open channel flow experimental and theoretical study of resistance and turbulent characterization over flexible vegetated linings." Flow Turbulence and Combustion **70**(1-4): 69-88.

Watanabe, T. (2004). "Large-Eddy Simulation of Coherent Turbulence Structures Associated with Scalar Ramps Over Plant Canopies." Boundary-Layer Meteorology **112**(2): 307-341.

Weerakoon, S. B. and N. Tamai (1989). "Three-dimensional calculation of flow in river confluences using boundary fitted coordinates-." J. Hydrosci. Hydraul. Engng **7**(51-62).

Welch, P. (1967). "The use of fast Fourier transform for the estimation of power spectra: A method based on time averaging over short, modified periodograms." Audio and Electroacoustics, IEEE Transactions on **15**(2): 70-73.

Westerlink, J. W. and P. J. Roache (1997). Issues in Convergence in Geophysical Flow Computations. Next Generation Environmental Models and Computational Methods. G. Delic and M. F. Wheeler. Bay City, SIAM.

Westerweel, J. (1997). "Fundamentals of digital particle image velocimetry." Measurement Science & Technology **8**(12): 1379-1392.

White, B. L. and H. M. Nepf (2007). "Shear instability and coherent structures in shallow flow adjacent to a porous layer." Journal of Fluid Mechanics **593**: 1-32.

Wilmott, P. (1995). The Mathematics of Financial Derivatives: A Student Introduction. Cambridge, Cambridge University Press.

Wilson, C., T. Stoesser, P. D. Bates and A. B. Pinzen (2003). "Open channel flow through different forms of submerged flexible vegetation." Journal of Hydraulic Engineering-Asce **129**(11): 847-853.

Wilson, C. A. M. E., T. Stoesser and P. Bates (2005). Modelling of open channel flow through vegetation. Computational Fluid Dynamics: Applications in Environmental Hydraulics. P. Bates, S. N. Lane and R. I. Ferguson, Wiley.

Wilson, J. D., D. P. Ward, G. W. Thurtell and G. E. Kidd (1982). "Statistics of atmospheric turbulence within and above a corn canopy." Boundary-Layer Meteorology **24**(4): 495-519.

Wilson, N. R. and R. H. Shaw (1977). "A Higher Order Closure Model for Canopy Flow." Journal of Applied Meteorology **16**(11): 1197-1205.

Wright, N. G. (2005). Introduction to numerical methods for fluid flow. Computational Fluid Dynamics: Applications in Environmental Hydraulics. P. Bates, S. N. Lane and R. I. Ferguson. Chichester, Wiley.

Yagci, O. and M. S. Kabdasli (2008). "The impact of single natural vegetation elements on flow characteristics." Hydrological Processes **22**(21): 4310-4321.

Yakhot, V. and S. A. Orszag (1986). "Renormalization group analysis of turbulence. I. Basic theory." Journal of Scientific Computing **1**(1): 3-51.

Yue, W. S., C. Meneveau, M. B. Parlange, W. H. Zhu, R. van Hout and J. Katz (2007). "A comparative quadrant analysis of turbulence in a plant canopy." Water Resources Research **43**(5): 14.

Yue, W. S., M. B. Parlange, C. Meneveau, W. H. Zhu, R. van Hout and J. Katz (2007). "Large-eddy simulation of plant canopy flows using plant-scale representation." Boundary-Layer Meteorology **124**(2): 183-203.

Zhang, J., S. Childress, A. Libchaber and M. Shelley (2000). "Flexible filaments in a flowing soap film as a model for one-dimensional flags in a two-dimensional wind." Nature **408**(6814): 835-839.

Zhou, J., R. J. Adrian, S. Balachandar and T. M. Kendall (1999). "Mechanisms for generating coherent packets of hairpin vortices in channel flow." Journal of Fluid Mechanics **387**: 353-396.

Zong, L. and H. Nepf (2010). "Flow and deposition in and around a finite patch of vegetation." Geomorphology **116**(3–4): 363-372.